Late Permian and Basal Triassic Paleoenvironments and Stable Isotope Geochemistry in the Nanpanjiang Basin (South China)

Dissertation

zur

Erlangung der naturwissenschaftlichen Doktorwürde
(Dr. sc. nat.)

vorgelegt der

Mathematisch-naturwissenschaftlichen Fakultät

der

Universität Zürich

von

Borhan Bagherpour

Aus dem

Iran

Promotionskommission

Prof. Dr. Hugo Bucher (Vorsitz und Leiter der Dissertation , Universität Zürich)
Prof. Dr. Torsten Vennemann (Université de Lausanne)
Prof. Dr. Christoph Zollikofer (Universität Zürich)
Prof. Dr. Hans Peter Linder (Universität Zürich)

Zürich, 2018

Dedicated to the memory of my father, Gholamali Bagherpour.

Abstract 2

Zusammenfassung 4

Introduction...9

Chapter I Early Wuchiapingian (Lopingian, Late Permian) drowning event in the South China Block related to a late eruptive phase of Emeishan Large Igneous Province?.19

Chapter II Coupled carbon and strontium isotope chemostratigraphy from early Late Permian: influence of prolonged Emeishan volcanism? 45

Chapter III Are Late Permian carbon isotope excursions of local or of global significance?.......95

Chapter IV Onset, development, and cessation of basal Early Triassic microbialites (BETM) in the Nanpanjiang pull-apart Basin, South China Block............................161

Appendix

Appendix A Conodonts from the Early Triassic microbialite of Guangxi (South China): implications for the definition of the base of the Triassic System..193

Appendix B Competition in slow motion: the unusual case of benthic marine communities in the wake of the end-Permian mass extinction..217

Appendix C Timing of global regression and microbial bloom linked with the Permian-Triassic boundary mass extinction: implications for driving mechanisms 251

Acknowledgements...259

Curriculum Vitae 260

Abstract:

The largest mass extinction of the Phanerozoic coincided with the Permian-Triassic Boundary (PTB), which was associated with profound paleoenvironmental changes, such as a pronounced perturbation in the global carbon cycle, in climate and in sedimentary regime. In comparison to the PTB and its aftermath, the preceding paleoenvironmental changes and carbon cycle dynamics during the Lopingian (Late Permian) were hitherto poorly understood. The present dissertation utilizes a multi-disciplinary approach for studying the paleoenvironmental changes and chemostratigraphic time series from the Late Permian to basal Triassic interval in different marine sedimentary settings.

In a first step, the detailed biostratigraphic dating of Emeishan Large Igneous Province (ELIP) eruptive pulses and associated paleoenvironmental effects are discussed. The key area for studying ELIP volcanic activity is South China. Applying sedimentary facies analyses and high-resolution conodont biostratigraphy to several south Chinese successions, a substantial drowning event (named Mapojiao event) during early Late Permian times is documented for the first time. It ends with volcanogenic turbidites, suggesting a relation with volcanism. The compilation of new, comprehensive sedimentological and field data with published sedimentary records across the G-L interval reveals the repetition of similar drowning events with comparable facies architecture during three time intervals in south China; 1: middle Capitanian, 2: latest Capitanian, and 3: early Wuchiapingian (Mapojiao event). The first drowning event is attributed to a rapid subsidence associated with the (ELIP) volcanism. The striking similarity of all three drowning events suggests a similar driving mechanism in all cases.

In a second step, perturbations in carbon and strontium isotope records of the Mapojiao Event are addressed in detail. Carbonate carbon isotope ($\delta^{13}C_{carb}$) and strontium isotope ($^{87}Sr/^{86}Sr$) data both document a substantial excursion toward lower values concomitant with this event, whereas organic carbon isotope data ($\delta^{13}C_{org}$) display a concurrent shift toward higher values. The short-lived excursion in $^{87}Sr/^{86}Sr$, superimposed on the global trend toward higher values, is best interpreted as an enhanced hydrothermal flux limited to a short pulse of ELIP-related volcanism. This supports that Mapojiao Event represents the youngest known episode of ELIP activity. The excursion toward lower values in $\delta^{13}C_{carb}$ is not laterally reproducible and is only present when associated with a drowning event (the Mapojiao Event). This implies that the Carbon Isotope Excursion (CIE) due to changes in bathymetry and increased burial of terrestrial organic matter was local, rather than a global perturbation of the carbon cycle. Rock-Eval and palynofacies analyses reveal that the decoupling between $\delta^{13}C_{carb}$ and $\delta^{13}C_{org}$ is best explained by mixing of different organic carbon pools that contributed jointly to the $\delta^{13}C_{org}$ curve.

The third goal of the thesis is to assess the global *vs.* local significance of changes in carbon cycling during the Late Permian. After removing diagenetic overprints, C isotope record from the basal Wuchiapingian to the basal Triassic reveals three remarkable negative CIEs in southern Guizhou (south China); 1: A short-lived CIE during the early Wuchiapingian (Mapojiao Event), 2: a protracted CIE ending shortly after the Wuchiapingian-Changhsingian Boundary (WCB), and 3: a CIE straddling the PTB. Comparison of our new $\delta^{13}C_{carb}$ and $\delta^{13}C_{org}$ data with available C isotope data from contemporaneous sections reveals that only the CIE at the PTB represents a global signal. Thus, the mechanisms involved into the carbon budget of the Late Permian must be different from those spanning the PTB and the Early Triassic, during which C isotope data represent global synchronous variations. Despite extension of ELIP volcanism into the Late Permian, fundamental differences with Siberian Traps (as the source of PTB and Early Triassic CIEs) can explain the inconsistencies of CIEs during the Late Permian. Differences between the two large igneous provinces include the respective volume of erupted lava (ca. ten-fold smaller ELIP), paleolatitude, and submarine *vs.* subaerial emplacement. Therefore, utilizing the C isotope records as a correlation tool during the Late Permian is called into question. Moreover, Late Permian CIEs are not associated with any known change in biodiversity and/or ecology.

In the last part of the thesis, the biotic and abiotic consequences of the PTB in different sedimentary settings are investigated. The earliest Triassic horst and graben paleotopography of the Nanpanjiang Basin was inherited from the Late Permian pull-apart basin with deposition of shallow-marine microbialites (Luolou Fm.) on the uplifted blocks and black-shales (Daye/Ziyun Formations) in the troughs. Sedimentary facies and C isotope analyses across the PTB indicate continuous sedimentation in the grabens and a substantial stratigraphic gap on the uplifted blocks (at the base of microbialite) due to a global regression. Microfacies analyses of this erosional surface indicate both chemical dissolution and mechanical erosion, although evidence of subaerial exposures (e.g. karstification) was not found. The upward changes from tabular to domical microbialite build-ups indicate a gentle sea-level rise during the earliest Triassic. Finally, a regional rapid tectonic drowning accompanied by volcanoclastic led to the cessation of the microbialites, independent from changes in the water chemistry. This reconstruction highlights the role of regional tectonic in the spatial distribution of anoxic black-shale and well-oxygenated microbialites and undermines the existence of alleged global anoxia in the immediate aftermath of the PTB crisis.

Zusammenfassung:

Das grösste Massenaussterben des Phanerozoikums ereignete sich an der Perm-Trias Grenze (PTG). Dieses war verbunden mit tiefgreifenden ökologischen Veränderungen, sowie Änderungen des globalen Kohlenstoffkreislaufes und der vorherrschenden sedimentären Prozesse. Die Ereignisse während und direkt nach der PTG sind verhältnismässig gut bekannt. Im Vergleich dazu sind jedoch die vorangegangenen Spätpermischen Änderungen der Umweltbedingungen und des Kohlenstoffkreislaufes kaum bekannt. Um die Veränderungen der Paläoumwelt und des Kohlenstoffkreislaufs zu untersuchen, wurden Abfolgen unterschiedlicher sedimentärer Ablagerungsräume im Zeitabschnitt vom Späten Perm bis zur basalen Trias mit unterschiedlichen Methoden untersucht.

Zunächst wurden die eruptiven Phasen der Emeishan Large Igneous Province (ELIP) biostratigraphisch genau datiert und ihre Auswirkungen auf die Paläoumwelt diskutiert. Ein Referenzgebiet für die Untersuchung der ELIP-Aktivität ist Südchina. Mit Methoden der Sedimentologie und hochauflösender Conodonten Biostratigraphie konnte für mehrere sedimentäre Abfolgen in Südchina eine signifikante Subsidenz des Beckens während des frühen Spätperms (Wuchiapingium) zum ersten Mal nachgewiesen werden. Die als Mapojiao Ereignis bezeichnete Sedimentabfolge dieser Subsidenz endet mit der Ablagerung von Turbiditen. Eine umfängliche Kompilation von neuen und publizierten sedimentologischen Daten, die den Zeitabschnitt vom Guadalupium bis zum Lopingium einschliessen, zeigt, dass ähnliche Subsidenzereignisse mit wiederkehrender Sedimentarchitektur insgesamt drei Mal dokumentiert werden können: Das erste im mittleren Capitanium, das zweite im spätesten Capitanium, und das dritte im frühen Wuchiapingium, welches dem bereits erwähnten Mapojiao Ereignis entspricht. Das erste Subsidenzereignis konnte auf die Aktivität des ELIP Vulkanismus zurückgeführt werden. Die auffällige Ähnlichkeit der drei Ereignisse legt nahe, dass die Ursachen in allen drei Fällen sehr ähnlich waren.

Des Weiteren wurden Veränderungen in der Kohlenstoffisotopen- und Strontiumisotopen-Geochemie während des Mapojiao Ereignisses genauer untersucht. Während des frühen Wuchiapingiums dokumentieren Kohlenstoffisotopendaten von Karbonaten ($\delta^{13}C_{carb}$) und Strontiumisotopendaten ($^{87}Sr/^{86}Sr$) signifikante negative Anomalien. Wohingegen die organischen Kohlenstoffisotopendaten ($\delta^{13}C_{org}$) zur gleichen Zeit einen positiven Trend aufzeigen. Die kurzzeitige negative $^{87}Sr/^{86}Sr$ Anomalie, die den globalen positiven Trend kurzzeitig unterbricht, kann mit erhöhtem hydrothermalen Einfluss einer späten Phase des ELIP Vulkanismus erklärt werden. Somit dokumentiert das Mapojiao Ereignis die jüngste bekannte Episode der ELIP Aktivität. Die negative $\delta^{13}C_{carb}$ Anomalie ist lateral nicht kontinuierlich vorhanden. Sie ist nur dort dokumentiert, wo das Mapojiao Ereignis in der sedimentologischen Abfolge vorhanden ist. Dies impliziert, dass die Kohlenstoffanomalie auf lokale bathymetrische Änderungen und damit verbundenem erhöhten Eintrag von terrestrischen organischem Material zurückzuführen ist und daher nicht mit Änderungen des globalen Kohlenstoffkreislaufes zusammenhängt. Rock Eval Daten und Palynofaziesanalysen beweisen, dass die unterschiedlichen Verläufe in den $\delta^{13}C_{org}$ und $\delta^{13}C_{carb}$ Kurven am besten mit Veränderungen der Zusammensetzung des organischen Materials erklärt werden, die sich in den $\delta^{13}C_{org}$ niederschlagen.

In einem weiteren Schritt wurden die Signifikanz der Änderungen in der Kohlenstoffisotopen-Geochemie bezüglich ihrer globale beziehungsweise lokale Relevanz im Späten Perm untersucht. Nach Abzug von diagenetischen Veränderungen, zeigen die Kohlenstoffisotopendaten vom basalen Wuchiapingium bis hin zur basalen Trias drei markante negative Anomalien in Süd Guizhou (Südchina). Eine kurzzeitig negative Anomalie während des frühen Wuchiapingiums (Mapojiao Ereignis), eine zweite

zeitlich ausgedehnte negative Anomalie, die kurz nach der Wuchiapingium-Changhsingium Grenze endet und eine dritte negative Anomalie an der PTG. Ein Vergleich der neuen $\delta^{13}C_{org}$ und $\delta^{13}C_{carb}$ Datensätze mit publizierten Kohlenstoffisotopendaten aus gleich alten Profilen zeigt, dass nur die negative Anomalie an der PTG ein globales Signal repräsentiert. Daher müssen andere Mechanismen für die spätpermischen lokalen Anomalien verantwortlich sein im Vergleich zu jenen, die die globalen Veränderungen im Kohlenstoffkreislauf während des PTG und der Frühen Trias verursacht haben. Ein fundamentaler Unterschied besteht zwischen den beiden magmatischen Grossprovinzen, die für die Änderungen in der Kohlenstoffisotopen Geochemie zur Erklärungen herangezogen werden können, die Siberische Trapp Provinz im Falle der PTG und Frühen Trias beziehungsweise die ELIP für die Spätpermischen Anomalien. Unterschiede zwischen beiden bestehen bezüglich der Paläobreite der Eruptionszentren als auch des Magmavolumens, zudem eruptierte erstere an der Erdoberfläche wohingegen die ELIP submarine auftrat. Daher ist die Anwendung spätpermischer Kohlenstoffisotopendaten zur Korrelationen sedimentärer Abfolgen fraglich. Zudem sind die spätpermischen Kohlenstoffisotopen-Anomalien nicht mit bekannten Änderungen in der Biodiversität oder ökologischen Änderungen verbunden.

Zuletzt wurden die biotischen und abiotischen Konsequenzen der Ereignisse um die PTG in verschiedenen sedimentären Milieus untersucht. Die Horst und Graben Paläotopographie des Nanpanjiang Beckens in der frühesten Trias rührte von einem Spätpermischen Pull-Apart Becken her. Auf flachmarinen Horsten lagerten sich mikrobielle Kalke (Luoluo Fm.) und in den Gräben Schwarzschiefer (Daye/Ziyun Formationen) ab. Sowohl die Sedimentfazies- als auch die Kohlenstoffisotopenanalyse deuten auf eine kontinuierliche Sedimentation in den Gräben und auf einen signifikanten Sedimentationsunterbruch auf den Horsten hin. Mikrofaziesanalysen dieser letztgenannten Erosionsoberflächen zeigen, dass sowohl chemische Lösungsvorgänge als auch mechanische Erosionprozesse aktiv waren. Einen Beiweis für subaerische Exposition konnte jedoch nicht gefunden werden. Die Änderungen von flächigen zu knollig abgelagerten mikrobiellen Kalken deuten auf einen langsamen Meeresspiegelanstieg während der frühesten Trias hin. Das Ende er Ablagerung der mikrobiellen Kalke erfolgte aufgrund eines markantes Subsidenzereignisses und war nicht durch Änderungen in der Meerwasserchemie verursacht. Dies unterstreicht den starken Einfluss der lokalen Tektonik auf die Ablagerungbedingungen. So konnten Schwarzschiefer unter anoxischen Bedingungen und mikrobielle Kalke unter oxyischen Bedingungen auf geographisch kleinem Raum zeitgleich abgelagert werden. Eine global existierende Anoxia unmittelbar nach der PTG ist daher fraglich.

Introduction

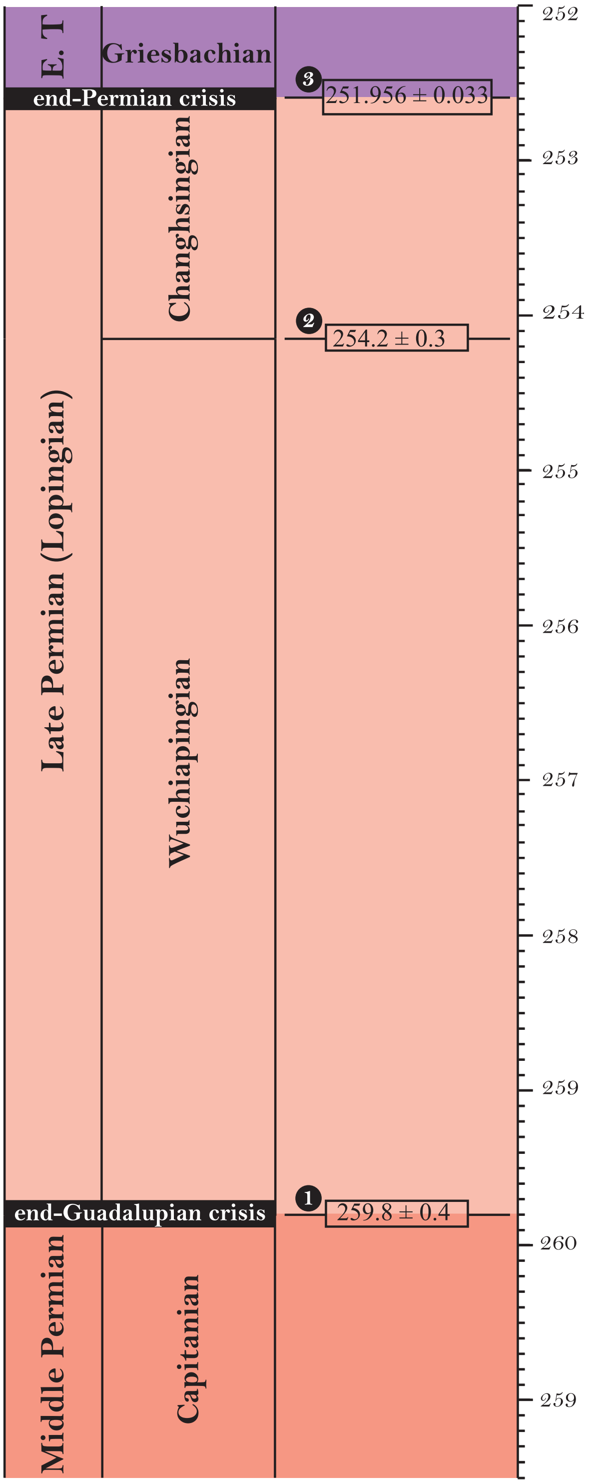

1- Geological background

a. Chronological setting

The Permian system is divided into three series: Cisuralian, Guadalupian, and Lopingian (in ascending order). The Lopingian (Late Permian) is further subdivided into two the Wuchiapingian and Changhsingian stages (Henderson et al., 2012) (Fig. 1). The absolute age of the Guadalupian-Lopingian Boundary (GLB) has yet to be constrained and only the interpolated 259.8±0.4 Ma is given for this stage boundary (Henderson et al., 2012). On the other hand, the end of the Lopingian (Permian-Triassic Boundary: PTB) is well dated at 251.956±0.035 Ma by means of radiometric ages (Baresel et al., 2017a). The lower and upper boundaries of the Lopingian respectively coincide with the GLB and PTB mass extinctions (e.g. Sepkoski, 1984; Stanley and Yang, 1994).

b. GLB and PTB mass extinctions

The GLB extinction was first identified by Jin et al. (1994) and Stanley and Yang (1994), but its detailed timing is still under debate. This extinction mostly impacted fusulinacean foraminifers and calcareous algae. Corals, bryozoans, brachiopods, bivalves, and ammonoids suffered to a lesser degree (Bond et al., 2010). According to these authors, this extinction abruptly occurred during the middle Capitanian and is correlated with the onset of volcanism of the Emeishan Large Igneous Province (ELIP). However, Clapham et al. (2009) showed that the extinction was characterized by a gradual decline of diversity from the Wordian to the end of Permian.

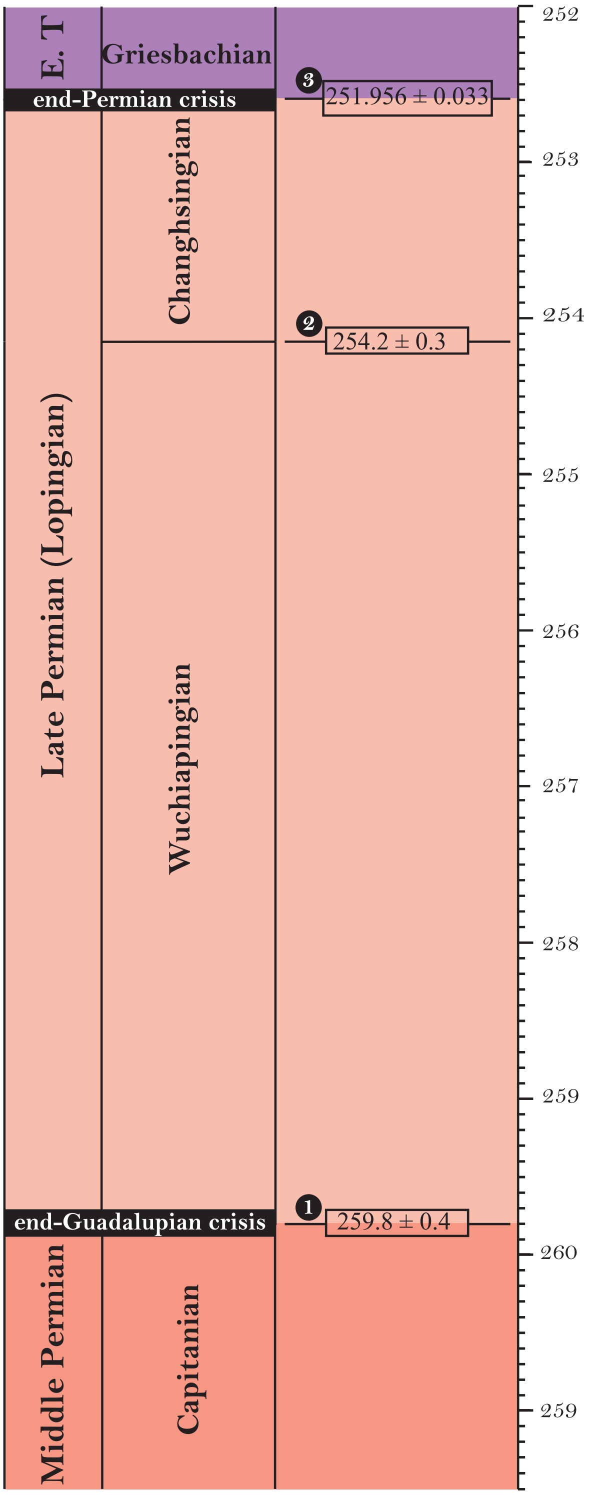

Fig. 1 Late Permian subdivisions. (1 and 2) Henderson et al. (2012); (3) Baresel et al. (2016).

The PTB coincides with the largest mass extinction of the Phanerozoic (Fig. 2), which occurred in a short interval between 251.941±0.037 and 251.880±0.031 Ma (Burgess et al., 2016). About 90% of marine species went extinct (e.g. Raup, 1979; Sepkoski, 1984) and terrestrial plant communities underwent a short-term but profound ecological deterioration without

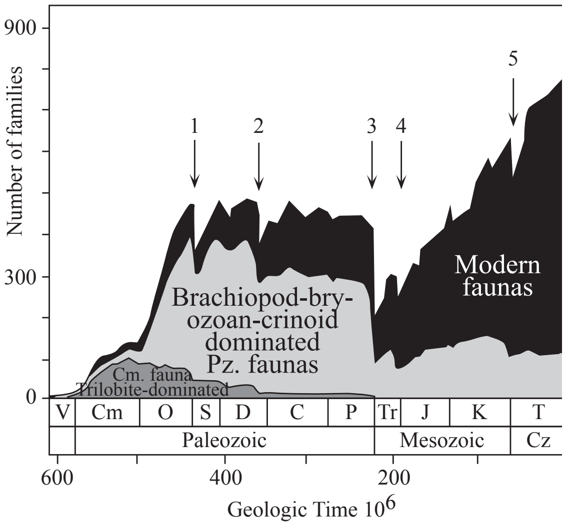

Fig. 2 Diversity of marine animal families through the Phanerozoic. The arrows represent the mass-extinctions, (1) End-Ordovician, (2) Late Devonian, (3) End-Permian, (4) End-Triassic and (5) End-Cretaceous. Modified from Sepkoski (1984).

a significant extinction peak (e.g. Hochuli et al., 2010). The PTB mass extinction is synchronous with the onset of the Siberian Traps volcanism (Burgess and Bowring, 2015). Several causal mechanisms have been proposed as trigger for the mass extinction, such as oceanic anoxia (e.g. Wignall and Twitchett, 1996), global regression (e.g. Yin et al., 2014), global sea-level rise (Hallam and Wignall, 1999), ocean acidification (e.g. Payne et al., 2010), global warming (e.g. Joachimski et al., 2012), global cooling (Baresel et al., 2017b) and increased sedimentation rates (Algeo and Twitchett, 2010).

2- Questions and objectives

Extensive amounts of data show that the PTB and Early Triassic times were characterized by a substantial perturbation in the global carbon cycle, closely correlated with the episodic activity of the Siberian Traps volcanism (e.g. Galfetti et al., 2007; Horacek et al., 2009; Hermann et al., 2010; Korte and Kozur, 2010 Meyer et al., 2013; Grasby et al., 2013; Sanson-Barrera et al., 2015). However, the C-isotope record of the Lopingian, prior to the onset of the Siberian Traps, is hitherto not well constrained in time. Hence, this is an open question whether the Carbon Isotope Excursions (CIEs) during the PTB and the Early Triassic are extraordinary instabilities after an interval of stable C isotope values during the Late Permian, or if the global CIEs already started in the Late Permian. The accurate answer to this question has crucial implications for the evaluation of carbon isotope time series as a chemostratigraphic tool.

The influence of ELIP volcanism on Lopingian paleoenvironments is also a matter of debate. Conodont age constraints indicate a middle Capitanian age for the onset of ELIP volcanism (Sun et al., 2010). However, the timing of later phases of the ELIP and associated paleoenvironmental effects, despite its profound impact on environmental deteriorations and possibly extinction patterns, is still poorly known. The influence of ELIP volcanic activity on Lopingian paleoenvironments is addressed in the **First and Second chapters**, and the complete carbon isotope record of the Lopingian (from the Pingtang syncline; Fig. 3) is provided and further discussed in the **Third chapter** (Fig. 4).

In spite of the well-known timing, extinction pattern, C isotope record, and sedimentology of the PTB, the consequences of PTB in different sedimentary settings have been largely overlooked. Oblique convergence between the Indochina and South China blocks during the Late Permian resulted in the development of Nanpanjiang Basin as a pull-apart basin in a back arc context in the eastern Tethys. Associated block faulting initiated a system of horsts and grabens around the Wuchiapingian-Changhsingian boundary (WCB) (Bagherpour et al., 2017, Chapter 4). In the down-thrown blocks (e.g. Pingtang syncline; Fig. 3), the WCB coincides with a rapid deepening event form shallow-marine limestone of the Wuchiaping Fm.

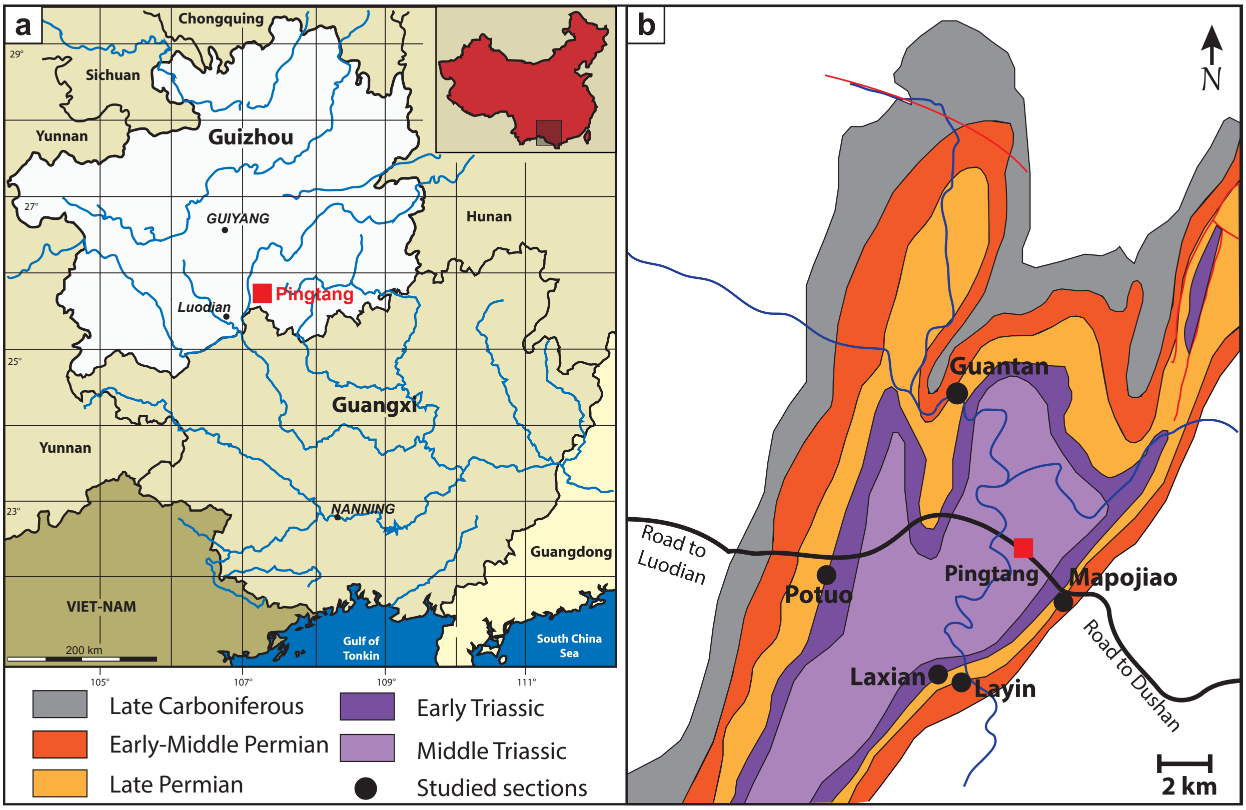

Fig. 3 Location of the Pingtang syncline. **a**, Present day geographic position of the Pingtang syncline. **b**, Geologic map of the Pingtang Syncline in S. Guizhou Province (modified from Guizhou Bureau, 1987).

to organic matter (OM)-rich, radiolarian bearing, siliceous mudstone of the Talung Fm. The OM-rich, O_2-depleted, deep-marine condition persisted into the basal Early Triassic black shales of the Ziyun Fm.

On the up-thrown blocks (e.g. Great Bank of Guizhou, Lehrmann et al., 1998; Luolou Platform, Bagherpour et al., 2017), shallow-marine limestone in well oxygenated waters (Heshan Fm.) were deposited until the PTB and were subsequently replaced by microbial limestone during the basal Early Triassic (Luolou Fm.) (Fig. 5). The sedimentology and carbon isotope record of the PTB transition in a deep marine setting is discussed in the **Third chapter**, while the **Forth Chapter** focuses on the PTB and basal Early Triassic microbialites that formed under shallow marine conditions (Fig. 4).

3- Thesis outline

The **First chapter** documents a substantial drowning event during the early Wuchiapingian in the Pingtang syncline (southern Guizhou) (Fig. 3). This drowning event (named here the Mapojiao Event) resulted in a drastic facies change from shallow-marine bioclastic limestone to deep-marine limestone with abundant radiolarian and sponge spicules, followed by volcanogenic distal turbidites. Compilation of the sedimentary record around the GLB in south China reveals that such drowning events occur in three time intervals; early to middle Capitanian, latest Capitanian, and early Wuchiapingian. The first cluster of drowning events is overlain by ELIP volcanic rocks or ELIP-driven volcaniclastic deposits and has been related to a subsidence event accompanied by the onset of ELIP activity (e.g. Sun et al., 2010). The striking similarities of the Mapojiao Event with Capitanian events suggest a common driving mechanism for these three phases of drowning/ eruptive events. These

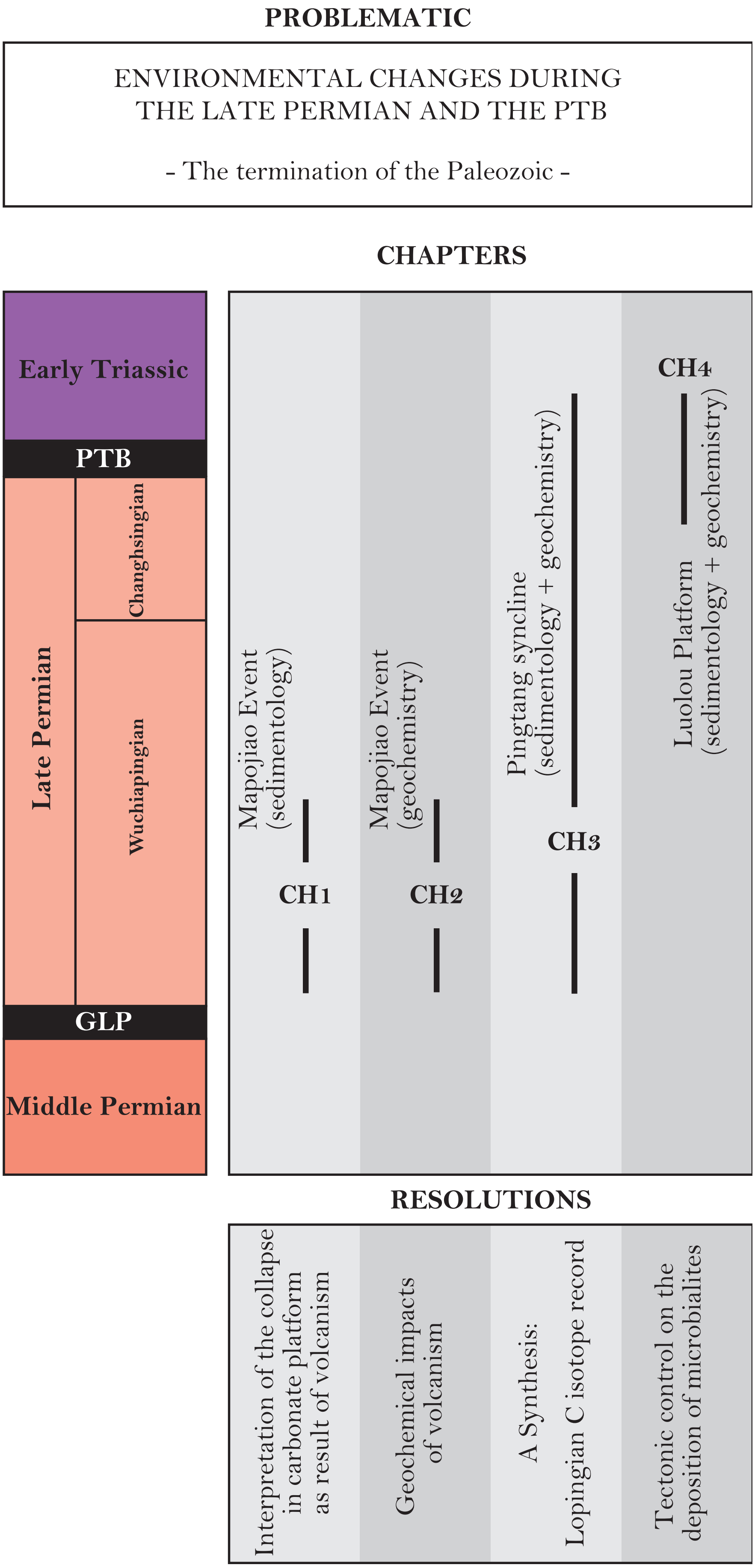

Fig. 4 Outline of the thesis with problematic and resolutions of each chapter against time scale.

results suggest that the episodic ELIP volcanism extended into early Late Permian times.

The **Second chapter** addresses geochemical proxies such as carbonate carbon and oxygen isotopes ($\delta^{13}C_{carb}$, $\delta^{18}O_{carb}$), organic carbon isotope ($\delta^{13}C_{org}$), strontium isotope ($^{87}Sr/^{86}Sr$), Rock-Eval and palynofacies analyses associated with the Mapojiao Event. This study documents a remarkable shift toward lower values in $\delta^{13}C_{carb}$ concomitant with the Mapojiao Event. This interval is characterized by a minor shift toward higher values in $\delta^{13}C_{org}$ as a result of substantial input of terrestrial OM during the drowning event. Furthermore, the $^{87}Sr/^{86}Sr$ data also display a shift toward lower values, which indicates an enhanced hydrothermal flux from mafic sources such as a large igneous province. Comparison of the CIE in $\delta^{13}C_{carb}$ with other sections reveals that this CIE solely occurs when associated to a drowning event (the Mapojiao Event). The same type of CIEs associated with ELIP-related drowning events is also known from some other sections (Xiong Jia Chang and Chaotian) prior to the GLB in south China. Hence, this indicates strong control of local environmental factors such as bathymetry and accumulation of terrestrial OM on the carbon budget.

The **Third chapter** provides a complete carbon isotope ($\delta^{13}C_{carb}$ and $\delta^{13}C_{org}$) record from early Lopingian to basal Griesbachian in the Pingtang syncline. This study also includes facies analysis, Rock-Eval data and palynofacies. Our new data indicates remarkable shifts toward lighter carbon isotope values in three time intervals, including a short-lived CIE during the early Wuchiapingian, a protracted CIE ending shortly after the Wuchiapingian-Changhsingian Boundary (WCB), and a third CIE straddling the PTB. Then, comparison of the Late Permian carbon isotope time series from south China with those from the western parts of the Tethys revealed inconsistencies in trends and magnitudes of the early Wuchiapingian and WCB CIEs. These discrepancies are in sharp contrast with the synchronous global signals during the PTB and the Early Triassic. In this chapter, we argue that the regional carbon isotope signals during the Late Permian versus global signals at PTB and during Early Triassic reflect the global dispersion of volatiles from the Siberian Traps as opposed to poor dispersion of ELIP-derived volatiles. The much larger amount of volcanic gasses, high-latitude position, and aerial eruption of the Siberian Traps (contrary to small size, equatorial position and submarine eruption of the Emeishan LIP) likely facilitated the global dispersal of volcanic gases from the Siberian Traps. This study indicates fundamental limitations of utilizing the carbon isotope record as a correlation tool for the Late Permian and highlights the importance of stablishing the nature of the OM that can be remineralized. In addition, comparisons of CIEs and biodiversity changes during the Late Permian undermine any systematic relation between perturbations in the carbon isotope and extinction events.

The **Fourth chapter** highlights the impact of regional paleotopography of the Nanpanjiang Basin on spatial distribution of the O_2-depleted black shales in troughs and well-oxygenated microbialites on the up-lifted blocks during the griesbachian. C-isotope data from up-lifted blocks display an abrupt CIE toward lower values at the PTB indicating a stratigraphical gap. Detailed facies analyses revealed that both chemical dissolution and physical erosion may have been at play. This study suggests that the vertical change in the growth of microbialites (domical *vs.* tabular buildups) is a response to the Early Triassic sea-level rise. Finally, I present evidences for an abrupt cessation of microbialite formation due to the tectonic drowning of the platform. This new finding emphasizes the role of regional tectonics rather than changes in water chemistry on the cessation of the earliest Triassic microbialites.

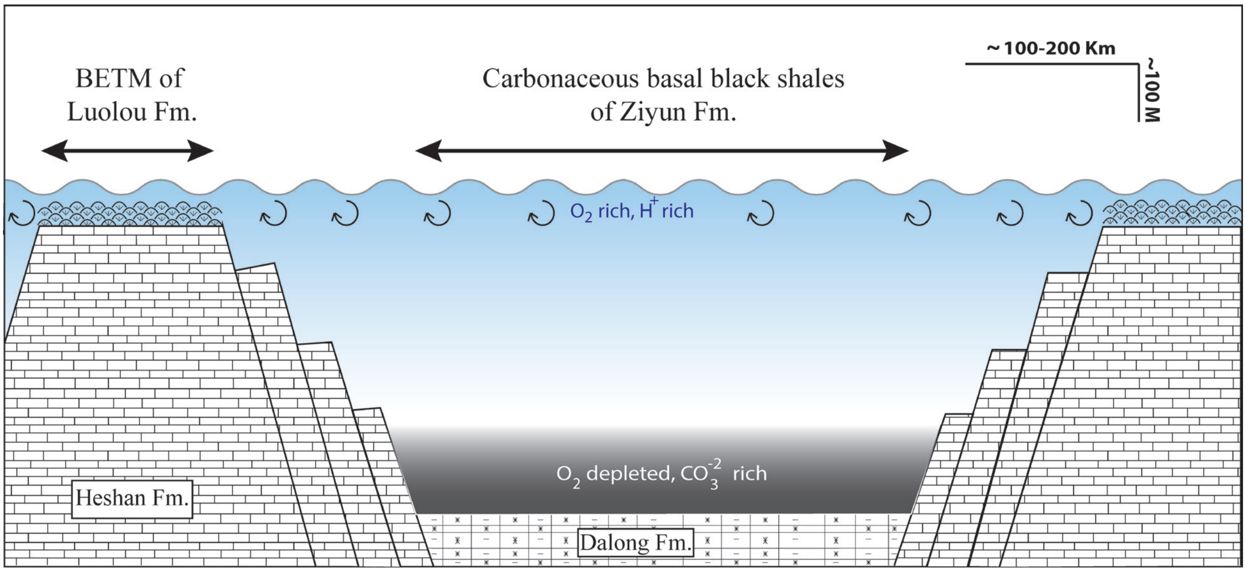

Fig. 5 Spatial relations between Late Permian to earliest Triassic depositional environments in the Nanpanjiang Basin.

References:

Algeo, T.J., Twitchett, R.J., 2010. Anomalous Early Triassic sediment fluxes due to elevated weathering rates and their biological consequences. Geology 38, 1023–1026.

Baresel, B., Bucher, H., Brosse, M., Cordey, F., Guodun, K., Schaltegger, U., 2017a. Precise age for the Permian–Triassic boundary in South China from high-precision U-Pb geochronology and Bayesian age–depth modelling. Solid Earth 8, 361–378.

Baresel, B., Bucher, H., Bagherpour, B., Brosse, M., Guodun. K., Schaltegger, U., 2017b. Timing of global regression and microbial bloom linked with the Permian-Triassic boundary mass extinction: implications for driving mechanisms. Scientific Reports 7, 43630.

Bond, D.P.G., Hilton, J., Wignall, P.B., Ali, J.R., Stevens, L.G., Sun, Y.D., Lai, X.L., 2010. The Middle Permian (Capitanian) mass extinction on land and in the oceans. Earth-Science Reviews 102, 100–116.

Burgess, S.D., Bowring, S., Shen, S.Z., 2014. High-precision timeline for Earth's most severe extinction. Proceedings of the National Academy of Sciences 111, 3316–3321.

Burgess, S.D., Bowring, S.A., 2015. High-precision geochronology confirms voluminous magmatism before, during, and after Earth's most severe extinction. Science Advances 1(7), 1-14.

Clapham, M.E., Shen, S., Bottjer, D.J., 2009. The double mass extinction revisited: reassessing the severity, selectivity, and causes of the end-Guadalupian biotic crisis (Late Permian). Paleobiology 35, 32–50.

Galfetti, T., Bucher, H., Brayard, A., Hochuli, P.A., Weissert, H., Kuang, G., Atudorei, V., Guex, J., 2007. Late Early Triassic climate change: insights from carbonate carbon isotopes, sedimentary evolution and ammonoid paleobiogeography. Palaeogeography, Palaeoclimatology, Palaeoecology 243, 394–411.

Grasby, S.E., Beauchamp, B., Embry, A., Sanei, H., 2013. Recurrent Early Triassic anoxia. Geology 41, 175–178.

Guizhou Bureau of Geology and Mineral Resources., 1987. Regional Geology of Guizhou Province: Geological Memoires, Ser. 1, no. 6, [in Chinese, English summary; Geologic map 1:500,000].

Hallam, A., Wignall, P.B., 1999. Mass extinctions and sea level changes: Earth-Science Reviews 48, 217–250.

Henderson, C.M., Davydov, D.I., Wardlaw, B.R., 2012. The Permian Period. *In*: Gradstein, F.M., Ogg, J.G., Schmitz, M.D., Ogg, G.M. (Eds.), The Geologic Time Scale 2012. Elsevier, pp. 653-679.

Hermann, E., Hochuli, P.A., Bucher, H., Vigran, J.O., Weissert, H., Bernasconi, S.M., 2010. Close-up view on the Permian–Triassic boundary based on extended organic carbon isotope records from Norway (Trøndelag and Finnmark Platform). Global and Planetary Change 74, 156-167.

Hochuli, P.A., Hermann, E., Vigran, J.S., Bucher, H., Weissert, H., 2010. Rapid demise and recovery of plant ecosystems across the end-Permian extinction event. Global and Planetary Change 74, 144–155.

Horacek, M., Koike, T., Richoz, S., 2009. Lower Triassic d13C isotope curve from shallow-marine carbonates in Japan, Panthalassa realm: confirmation of the Tethys d13C curve. Journal of Asian Earth Sciences 36, 481–490.

Jin, Y.G., Zhang, J., Shang, Q.H., 1994. Two phases of the end-Permian mass extinction. Canadian Society of Petroleum Geologists Memoir 17, 813–822.

Joachimski, M.M., Lai, X., Shen, SZ., Jiang, H., Luo, G., Chen, B., Chen, J., Sun, Y., 2012. Climate warming in the latest Permian and the Permian–Triassic mass extinction. Geology 40(3), 195-198.

Korte, C., Kozur, H.W., 2010. Carbon-isotope stratigraphy across the Permian–Triassic boundary: A review. Journal of Asian Earth Sciences 39, 215–235.

Meyer, K.M., Yu, M., Lehrmann, D., van de Schootbrugge, B., Payne, J.L., 2013. Constraints on Early Triassic carbon cycle dynamics from paired organic and inorganic carbon isotope records. Earth and Planetary Science Letters 361, 429–435.

Payne, J.L., Turchyn, A.V., Paytan, A., DePaolo, D.J., Lehrmann, D.J., Yu, M., Wei, J., 2010. Calcium isotope constraints on the end-Permian mass extinction. Proceedings of the National Academy of Sciences 107, 8543–8548.

Raup, D.M., 1979. Size of the Permo-Triassic bottleneck and its evolutionary implications. Science 206, 217–218.

Sanson-Barrera, A., Hochuli, P.A., Bucher, H., Schneebeli-Hermann, E., Meier, M., Weissert, H., Bernasconi, S., 2015. Late Permian-earliest Triassic high resolution organic carbon isotope and palynofacies records from Kap Stosch (northeast Greenland). Global and Planetary Change 133, 149–166.

Sepkoski Jr., J.J., 1984. A kinetic-model of Phanerozoic taxonomic diversity 3. Post-Paleozoic families and mass extinctions. Paleobiology 10, 246–267.

Stanley, S.M., Yang, X., 1994. A double mass extinction at the end of the Paleozoic era. Science 266, 1340–1344.

Sun, Y., Lai, X., Wignall, P.B., Widdowson, M., Ali, J.R., Jiang, H., Wang, W., Yan, C., Bond, D.P.G., Vedrine, S., 2010. Dating the onset and nature of the Middle Permian Emeishan large igneous province eruptions in SW China using conodont biostratigraphy and its bearing on mantle plume uplift models. Lithos 119, 20–33.

Wignall, P.B., Twitchett, R.J., 1996. Oceanic anoxia and the End Permian mass extinction. Science 272, 1155–1158.

Yin, H.F., Jiang, H.S., Xia, W.C., Feng, Q.L., Zhang, N., Shen, J., 2014. The end-Permian regression in South China and its implication on mass extinction. Earth-Science Reviews 173, 19–33.

Chapter I

EARLY WUCHIAPINGIAN (LOPINGIAN, LATE PERMIAN) DROWNING EVENT IN THE SOUTH CHINA BLOCK RELATED TO A LATE ERUPTIVE PHASE OF EMEISHAN LARGE IGNEOUS PROVINCE?

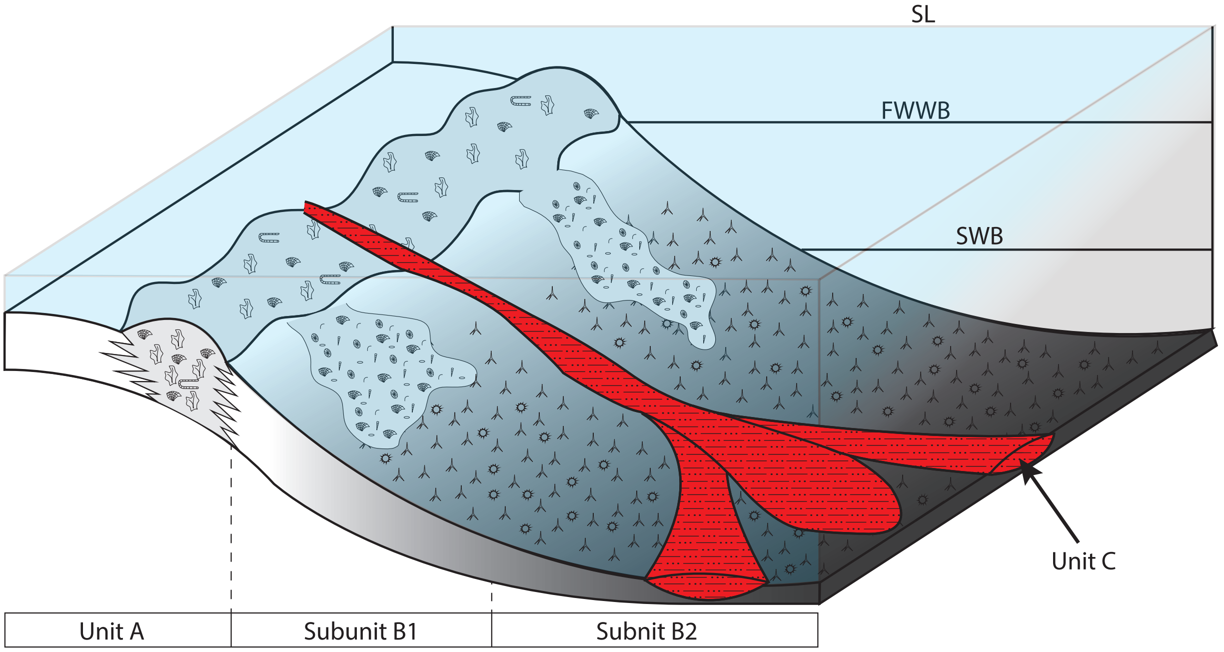

Global and Planetary Change (in review)

Early Wuchiapingian (Lopingian, Late Permian) drowning event in the South China Block related to a late eruptive phase of Emeishan Large Igneous Province?

Borhan Bagherpour[1*], Hugo Bucher[1], Dong-xun Yuan[2], Marc Leu[1], Chao Zhang[2], Shu-zhong Shen[2]

1- Paleontological institute, University of Zurich, Karl Schmid-Strasse 4, 8006 Zürich, Switzerland.

2- State Key Laboratory of Palaeobiology and Stratigraphy, Nanjing Institute of Geology and Palaeontology, Chinese Academy of Sciences, Nanjing 210008, China.

Abstract

Although the precise age and magnitude of the end-Guadalupian biodiversity crisis is still debated, this “mass” extinction has been customarily linked with the onset of massive volcanism in the Emeishan Large Igneous Province (ELIP) in South China. The onset of ELIP eruptive activity at least partly coincides in time with episodes of regional subsidence interrupting the predominant regime of carbonate platforms during Capitanian times.

Here, we present a strikingly similar but younger (early Wuchiapingian) subsidence episode from the Pingtang syncline in southern Guizhou, here named as the Mapojiao Event. Shallow-marine, light-grey, massive bioclastic limestone of the Wuchiaping Fm. (Unit A) are overlain by deep-marine radiolarian-sponge spicule, thin-bedded black limestone (Unit B). The latter is followed by volcanogenic distal turbidites (Unit C). The base of the next overlying unit consists of cherty, nodular limestone (Unit D) rich in radiolarians and sponge spicules, whose respective abundances decline up-ward within a few meters. Concomitant replacement by a shallow marine benthic fauna documents the uplift that terminates the event. A total of five index species of *Clarkina* conodonts indicating an early Wuchiapingian age were obtained from Units A and B. Brachiopods of Wuchiapingian age were also documented in units A, B and D.

Compilation of drowning events in the Guadalupian-Lopingian (G-L) interval suggests that comparable events tend to cluster in three age groups; 1: middle Capitanian, 2: latest Capitanian, 3: early Wuchiapingian. The first drowning event is overlain by ELIP volcanics in sections near the center of the volcanic province. In peripheral areas, this first drowning is intercalated within carbonate platforms (e.g. Maoershan), where not obscured by the unconformity associated with the eustatic regression around the G-L boundary. Overlying this unconformity, the Wangpo Shale, which contains ELIP-derived volcanic materials, rests either on the first (e.g. Chaotian) or on the second drowning event (e.g. Dukou, Maoershan). The striking similarities of the facies architecture shared by all these drowning events suggest a similar driving mechanism. Hence, we propose that the Mapojiao Event represents the youngest burst of ELIP eruptive activity during early Wuchiapingian. Comparative timing of the three episodes of ELIP-related tecto-volcanism with changes in diversity of marine clades remains unclear. The extinction has been correlated either with the 1st or with the 2nd episode, while the new 3rd episode occurred within a diversification phase.

Keywords:

Emeishan Large Igneous Province; South China; conodonts; facies analysis; drowning event

1. Introduction

The end-Guadalupian extinction was first recognized by Jin (1993) and discussed by Jin et al. (1994) and Stanley and Yang (1994). It was then perceived as the first phase of the end-Permian mass extinction. This extinction has been reported to occur in both marine and terrestrial realms (Bond et al., 2010a; Lucas 2017). Among the main affected marine clades are fusulinacean foraminifers and calcareous algae. Corals, bryozoans, brachiopods, bivalves, and ammonoids also suffered, but to a lesser degree (Bond et al., 2010a). Two different timing and patterns of extinction have been proposed: (i) an abrupt extinction in the mid-Capitanian (Bond et al., 2010a; 2010b) or (ii) a gradual decrease in diversity from the Wordian to the end of Permian (Clapham et al., 2009; Groves and Wang, 2013). Several causal mechanisms have been suggested for this extinction. Although the ultimate cause is still under debate, the synchronicity of the eruptive phase of the Emeishan Large Igneous Province (ELIP) with the end-Guadalupian extinction in South China led several authors to propose volcanism as causal mechanism (e.g. Wang and Sugiyama, 2000; Zhou et al., 2002; He et al., 2007; Wignall et al., 2009a; Bond et al., 2010a; Xu et al., 2010; Shellnutt et al., 2012). The mostly submarine ELIP volcanism (Ukstins Peate and Bryan, 2008) is known to be concomitant with several paleoenvironmental changes in South China (e.g. collapse in carbonate platforms, perturbation of the carbon cycle, and increase of sea surface temperature) during the Guadalupian-Lopingian (G-L) interval (e.g. Wignall et al., 2009a; Sun et al., 2010; Bond et al., 2010a; 2010b; Chen et al., 2011; 2013). In Sichuan, Yunnan and Guizhou provinces the carbonate platform of the Guadalupian Maokou Fm. ends with an abrupt drowning. Bioclastic limestone of the Maokou Fm. is succeeded by deep water radiolarian-spiculitic facies, which is in turn followed by Emeishan volcanics or derived clastic rocks (Lai et al., 2008; Wignall et al., 2009a; Sun et al., 2010). This drowning indicates rapid subsidence related to ELIP activity during middle Capitanian time (*Jinogondolella altudaensis* Interval Zone (IZ), which is generally considered as the onset of the ELIP volcanism (Sun et al., 2010).

Several studies documented a mid-Capitanian age for the main phase of ELIP activity. However, the detailed timing of ELIP eruptions and associated paleoenvironmental effects are still unresolved. Whereas eruptive activity was either episodic or protracted remains one of the main open questions, whose answer has potential implications for causal links with patterns of extinction.

Here, we provide new evidence from the Pingtang Syncline (S. Guizhou) (Fig. 1a) that the same type of collapse in carbonate platform occurred again during the early Wuchiapingian, thus suggesting a late episode of ELIP activity during post-Capitanian times. Rapid drowning and associated volcanism was documented in a consistent stratigraphic position in three sections (Mapojiao, Layin, Guantan) distributed in both limbs of the Pingtang Syncline (Fig. 1b). Exceptional exposures are found along the Mapojiao section (Fig. 2a, b; 25°49′21.8″N; 107°21′16.3″E). The two other sections are located in deep canyons cutting across thick successions of Permian limestone (Fig. 3a, b). For the sake of simplicity, this drowning and associated volcanogenic clastics are here referred to as the “Mapojiao Event”. We provide a high resolution conodont biostratigraphic control establishing the early Wuchiapingian age of the Mapojiao Event. Changes in depositional environments defining this event are compared to those of other known ELIP-related drownings throughout South China. The timing of these ELIP-related drowning events is then compiled in order to discuss putative links with the end-Guadalupian extinction.

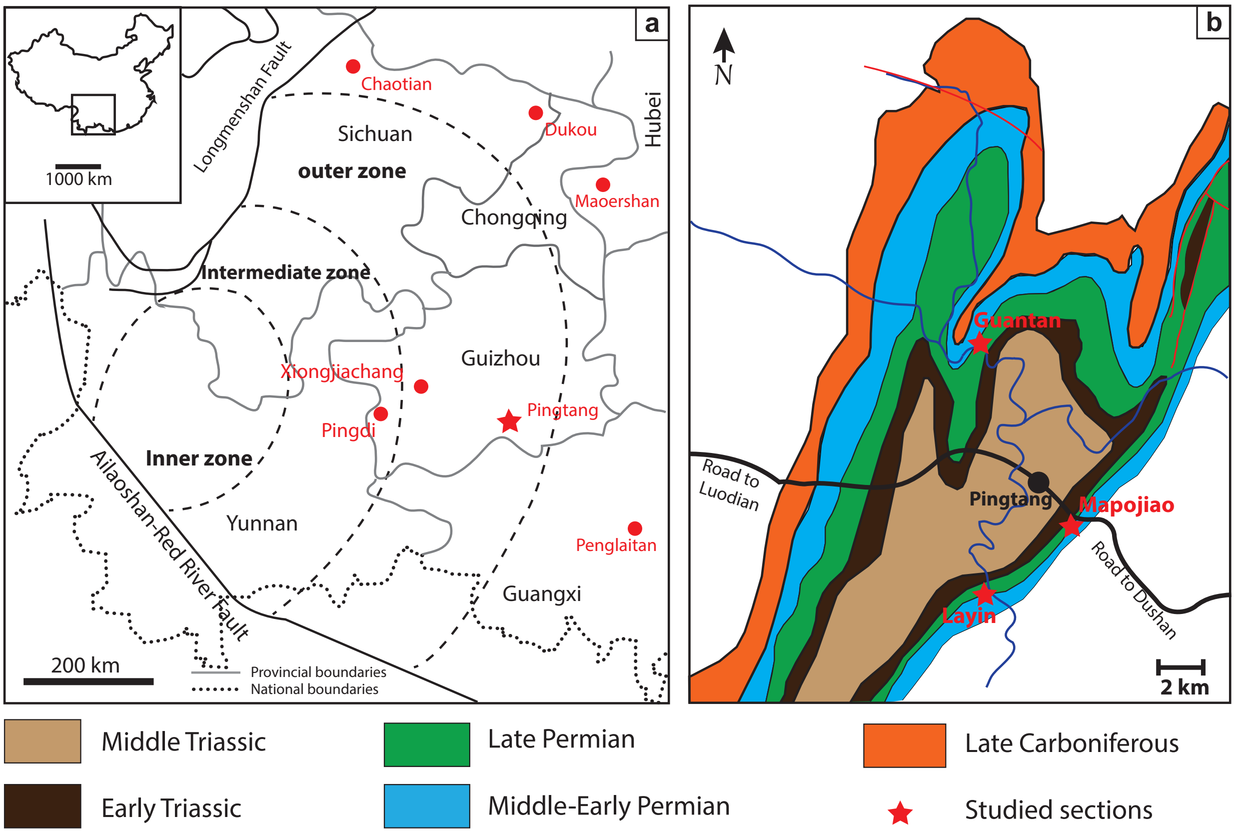

Fig. 1 Location of studied sections**.** **a**, Distribution of the G-L interval sections in concentric inner, intermediate and outer zones around the hypothetical core of the surficial uplift (modified from He et al., 2003; Zhao et al., 2016). Red circles: relevant sections taken from the literature and discussed in the paper. Red star: Pingtang Syncline with new sections. **b**, Geologic map of the Pingtang Syncline in S. Guizhou Province (modified from Guizhou Bureau, 1987).

2. Geological setting and studied sections

The Nanpanjiang Basin belongs to the South China Block, which occupied an equatorial position during the Permian (Boucot et al., 2013). This basin, whose age ranges from the Late Proterozoic to Late Triassic (Enos, 1995), extends over present-day Guangxi, eastern Yunnan, and Guizhou provinces. The Middle-Late Permian transition in the Nanpanjiang Basin is associated with ELIP volcanism (Zhou et al., 2002; He et al., 2007). Exposures of Emeishan basalts cover at least 0.3×10^6 km^2 of SW China and northern Vietnam (Shellnutt, 2014). ELIP eruptive rocks were deposited in the westernmost part of the Nanpanjiang Basin and are reported to thin eastward into western Guizhou (Lehrmann et al., 2005). In central and eastern Guizhou, the Guadalupian Maokou Fm. is unconformably overlain by the Wangpo Shale, which contains volcaniclastic material derived from ELIP (e.g. He et al., 2007). The Wangpo Shale is overlain by the Wuchiaping Fm. In Yunnan and western Guizhou, the Maokou Fm. is overlain by ELIP volcanic rocks (Bond et al., 2010b; Wignall et al., 2009a). Based on the amount of erosion that affected the Maokou Fm., He et al. (2003) outlined three semi-concentric zones around the Emeishan LIP (Fig. 1a). In the "inner zone" (W. Yunnan and S. Sichuan), the Maokou Fm. is strongly eroded with an estimated >1km uplift prior to the eruption. The thickness of Maokou Fm. increases in the "intermediate zone" (E. Yunnan and N. Sichuan), suggesting

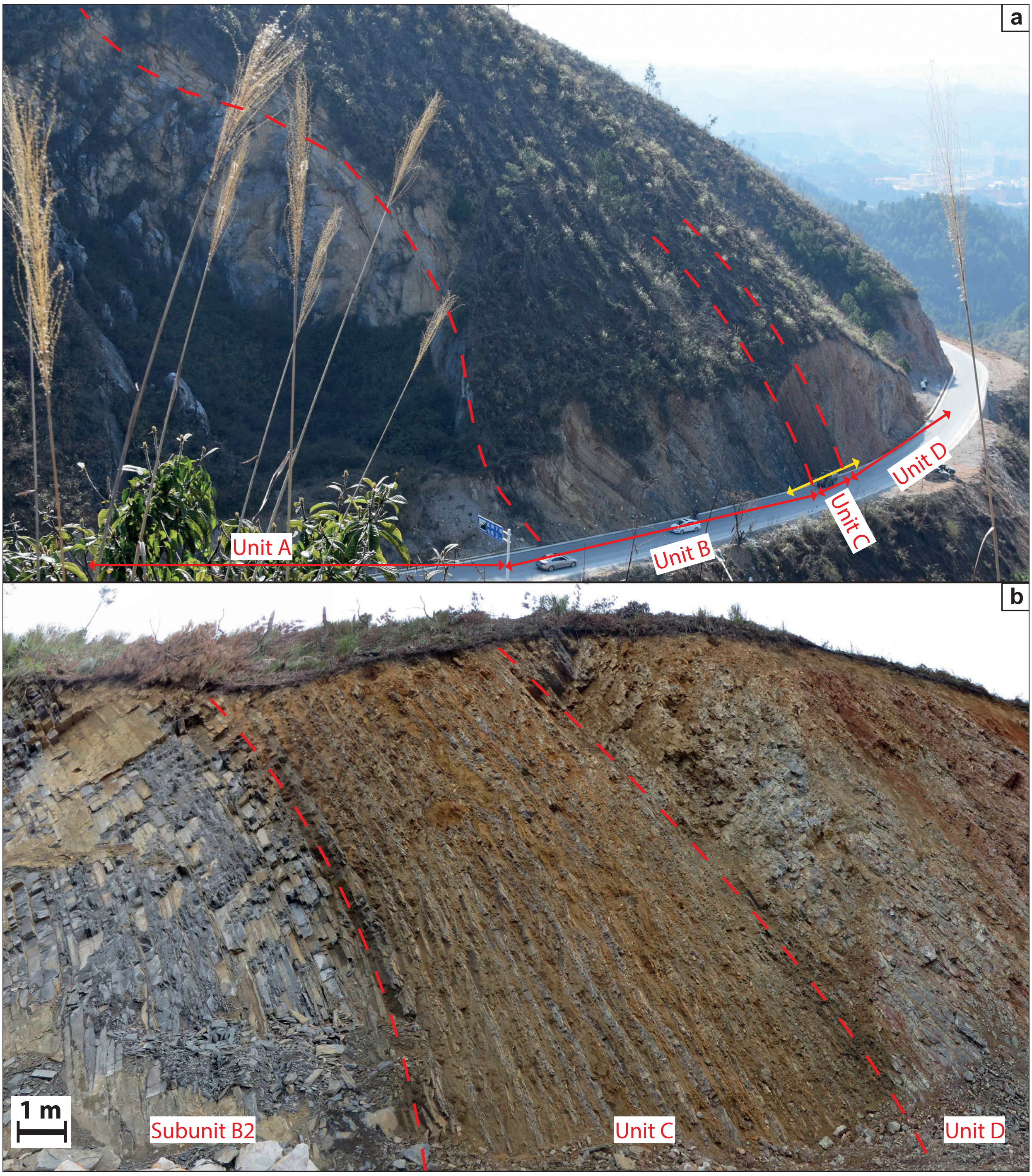

Fig. 2 Field photographs of the studied Mapojiao section. **a,** Landscape view of the freshly exposed road-cut. Dashed lines mark the boundary between the units. **b**, Enlargement of the interval marked by the yellow arrows in Fig 2a. Close-up view of the upper part of thin-bedded black limestone (Subunit B2), alternating fine-volcanogenic sand and siltstone (Unit C), and cherty nodular limestone (Unit D). Note the sharp and conformable contacts between all units.

less uplift. Finally, the Maokou Fm. reaches its maximum thickness in the "outer zone", where the amount of erosion was comparatively small. According to He et al. (2003), the fusulinid-based age of the erosional upper boundary of the Maokou Fm. displays a younging trend combined with decreasing erosion away from the inner zone, thus suggesting pre-eruption uplift. However, the initial phase of the Emeishan volcanism is represented by hydromagmatic deposits and submarine

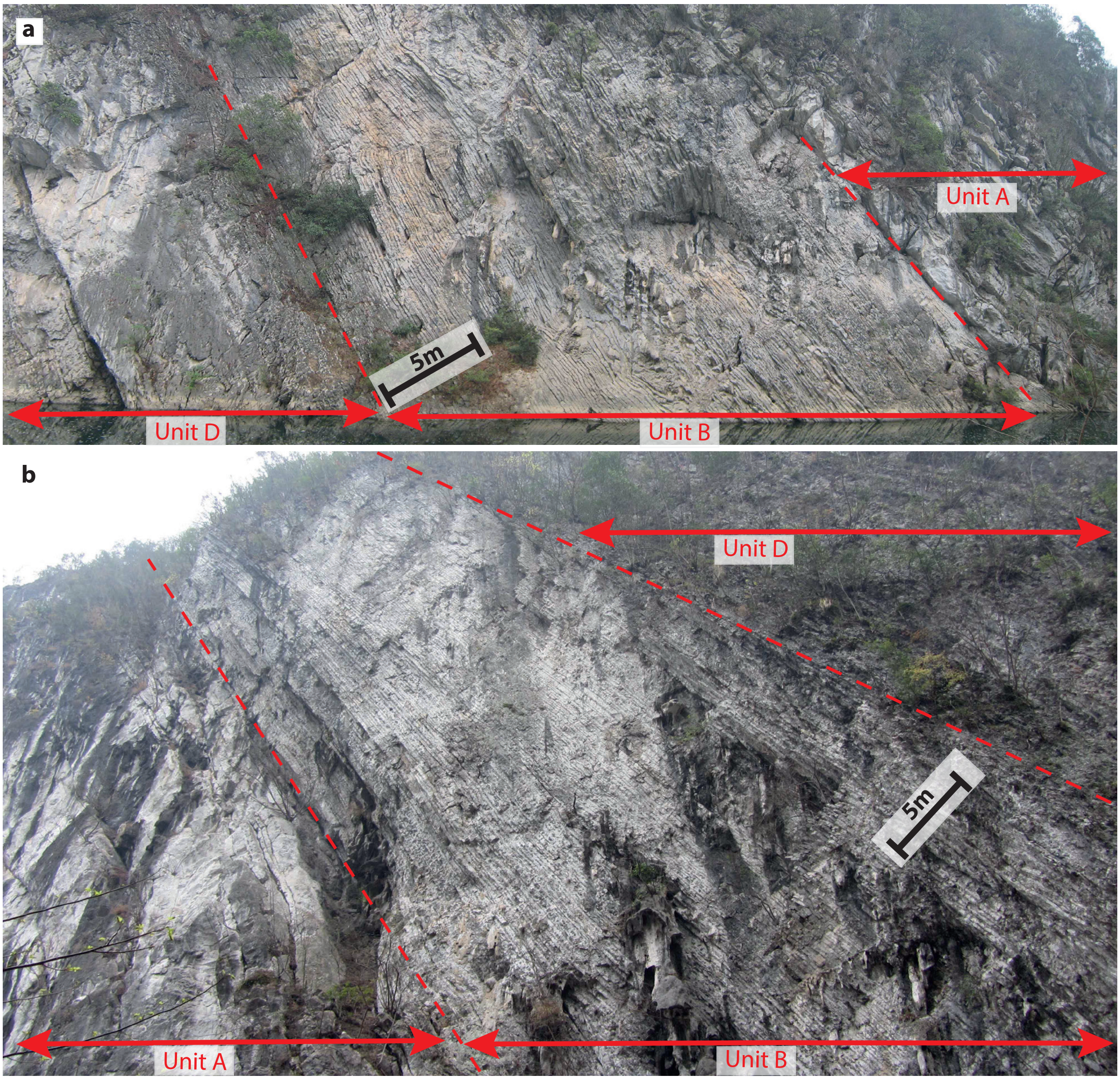

Fig. 3 Field photographs of the Layin and Guantan sections. **a,** Landscape view of the overturned Layin section. Dashed lines mark the boundary between the units. Note the absence of Unit C. **b,** Landscape view of the Guantan section. Dashed lines mark the boundary between the units. Note the absence of Unit C.

extrusions suggesting emplacement at or below sea-level (Ukstins Peate and Bryan, 2008), which stands in striking contrast with the pre-eruption uplift model. Biostratigraphic evidence supporting this uplift is based on fusulinids that do not provide a high-resolution time framework and which is largely facies-controlled. Neither did a conodont-based biostratigraphy (Sun et al., 2010) confirm any substantial diachronism at the top of Maokou Fm. Previous studies documented the occurrence of ELIP volcanics mainly in the "inner" and "intermediate" zones, but recent discoveries of ELIP-related basalts in western Guangxi (Fan et al., 2008) and eastern Sichuan (Li et al., 2016) indicate that ELIP basalts did reach the "outer zone". The studied Pingtang Syncline is located within this "outer zone" in the northern part of the Nanpanjiang Basin (Fig. 1a).

In the studied area, Middle to Late Permian strata are assigned to the Maokou and Wuchiaping formations (Guizhou Bureau, 1987). The two formations are extensively exposed in both limbs of the 50 km long, NE-SW Pingtang Syncline

(Fig. 1b). The lower part of the Wuchiaping Fm. represents a remarkable and substantial facies change from thick-bedded bioclastic to thin-bedded black limestone in Mapojiao (Fig. 1b: 2a, b), Layin (Fig. 1b; 3a) and Guantan (Fig. 1b; 3b). Paleontological data from an auxiliary section (Mapojiao B) expands the base of Mapojiao main section. Mapojiao B is located on strike on the same structural ridge, ca 800m SW of the main section.

3. Material and methods

The stratigraphic section was logged bed by bed and analyzed in detail in the field. Rock samples for thin sections, polished slabs, and extraction of conodont elements were collected from the main Mapojiao section.

A total of 8 from Mapojiao B and 36 samples from Mapojiao main section, 5 kg each, were collected for conodont extraction. Conodont samples were dissolved and concentrated following the procedure of Jeppsson et al. (1999) and Jeppsson and Anehus (1999). Concentrated residues were sieved with a 0.075-mm mesh, and handpicked using Stemi508 ZEISS binoculars. The conodont elements were coated with platinum, and then photographed using a LEO 1530 VP SEM. The conodont collection is curated in Nanjing Institute of Geology and Palaeontology (NIGP).

Fifty samples were selected for the preparation of thin sections. Petrographic description of carbonate rocks follows the classification of Dunham (1962). Thin sections were stained with Alizarin red S in order to reveal the presence of dolomite. Occurrence and relative abundance of each fossil group were plotted against the lithological profile.

4. Lithological subdivisions and age control

The Mapojiao section is subdivided into four units (Units A-D; Fig. 2a, b; 4). Unit A is composed of massive, light-grey bioclastic limestone with sparse diagenetic siliceous concretions. Unit A did not yield fusulinids and calcareous algae, which are typically abundant in the underlying Guadalupian Maokou Fm. The overlying Unit B begins with dark-grey, medium-bedded limestone containing few chert concretions at its base (Subunit B1). Unit B quickly grades into thin-bedded, cherty black limestones (Subunit B2). Unit B is conformably overlain by an 8 m-thick succession comprising ca. 20 volcanogenic turbidites (Unit C). Above C, Unit D consists of grey, medium-bedded, nodular limestones with wavy bedding planes and diagenetic chert concretions (Fig. 2b). Layin and Guantan sections display a similar lithological succession, except that the volcanogenic Unit C is missing and Unit D conformably overlies thin-bedded black limestones of Unit B (Fig. 3a, b).

High biostratigraphic resolution age control is based on conodonts for the G-L interval. A total of five conodont index species of Wuchiapingian age, all assigned to the genus *Clarkina*, were recovered from Unit A and B (Figs. 5, 6). No conodonts were recovered from the uppermost ten meters of Subunit B2, from Unit C, nor from Unit D (Fig. 2, 4).

Clarkina ?dukouensis occurs at the base of the section. However, scarcity of specimens combined to the fact that juveniles and small specimens of *Clarkina asymmetrica* and *C. dukouensis* can hardly be distinguished makes this identification likely but not certain. Following an 18 meters thick barren interval, *C. asymmetrica*, *Clarkina leveni*, *Clarkina guangyuanensis*, and *Clarkina transcaucasica* (or transitional forms between *C. guangyuanensis* and *C. transcaucasica*) sequentially appear through Units A and B (Fig. 4). However, typical *C. asymmetrica*, *C. leveni*

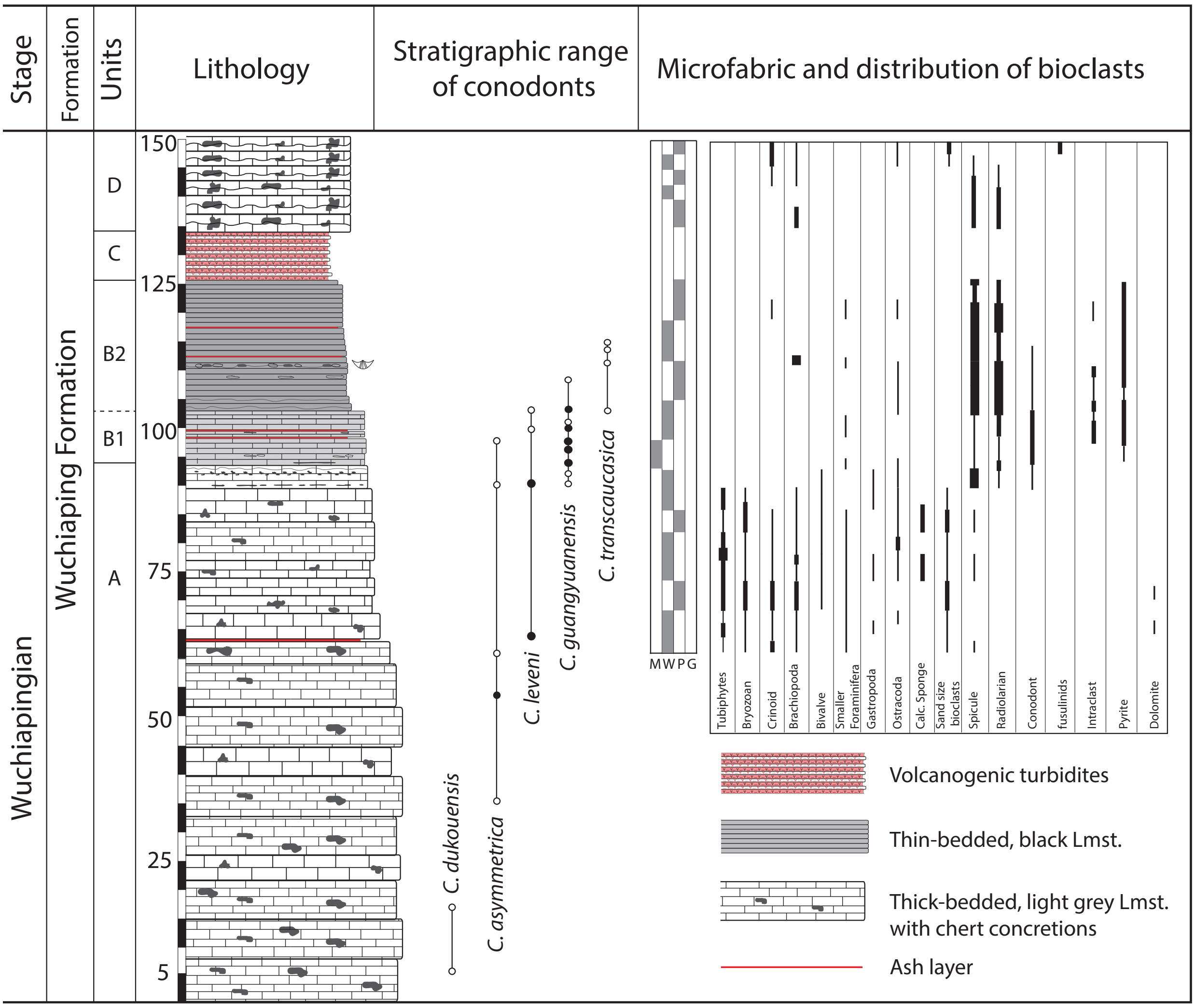

Fig. 4 Mapojiao section with stratigraphic range of conodont taxa (open circles indicate identifications without certainty), microfabric and distribution of bioclasts. M: Mudstone, W: Wackestone, P: Packstone, G: Grainstone

and *C. guangyuanensis* (Figs. 4, 5, 6) indicate that these strata belong to the early Wuchiapingian. Thus, Unit A and Subunit B1 are assigned to the upper *C. asymmetrica* IZ, *C. leveni* IZ and *C. guangyuanensis* IZ. Subunit B2 is assigned to the upper *C. guangyuanensis* IZ and/or to the lower part of *C. transcaucasica* IZ. The continuous range of *C. guangyuanensis* across the boundary between Units A and B suggests a conformable boundary between these two units.

The G-L boundary is defined by the First Appearance Datum (FAD) of *Clarkina postbitteri postbitteri* (Jin et al., 2006), which was not retrieved from the sampled interval. All younger conodonts recognized here are index species widely used to construct the Wuchiapingian second to sixth IZs (e.g. Mei et al., 1994a; Mei et al., 1998; Shen and Mei, 2010; Shen et al., 2010; Yuan et al., 2017). Because the youngest *Clarkina orientalis* IZ represents about two thirds of the Wuchiapingian in most South Chinese sections (based on high-precision CA-ID-TIMS dates at Shangsi, see Shen et al., 2010), the conodonts identified here univocally indicate an early Wuchiapingian age for the Mapojiao section. In the Pingtang Syncline, Unit D is ca. 300 meters thick, the Wuchiapingian-Changhsingian boundary coinciding with the sharp transition to the Talung Fm.

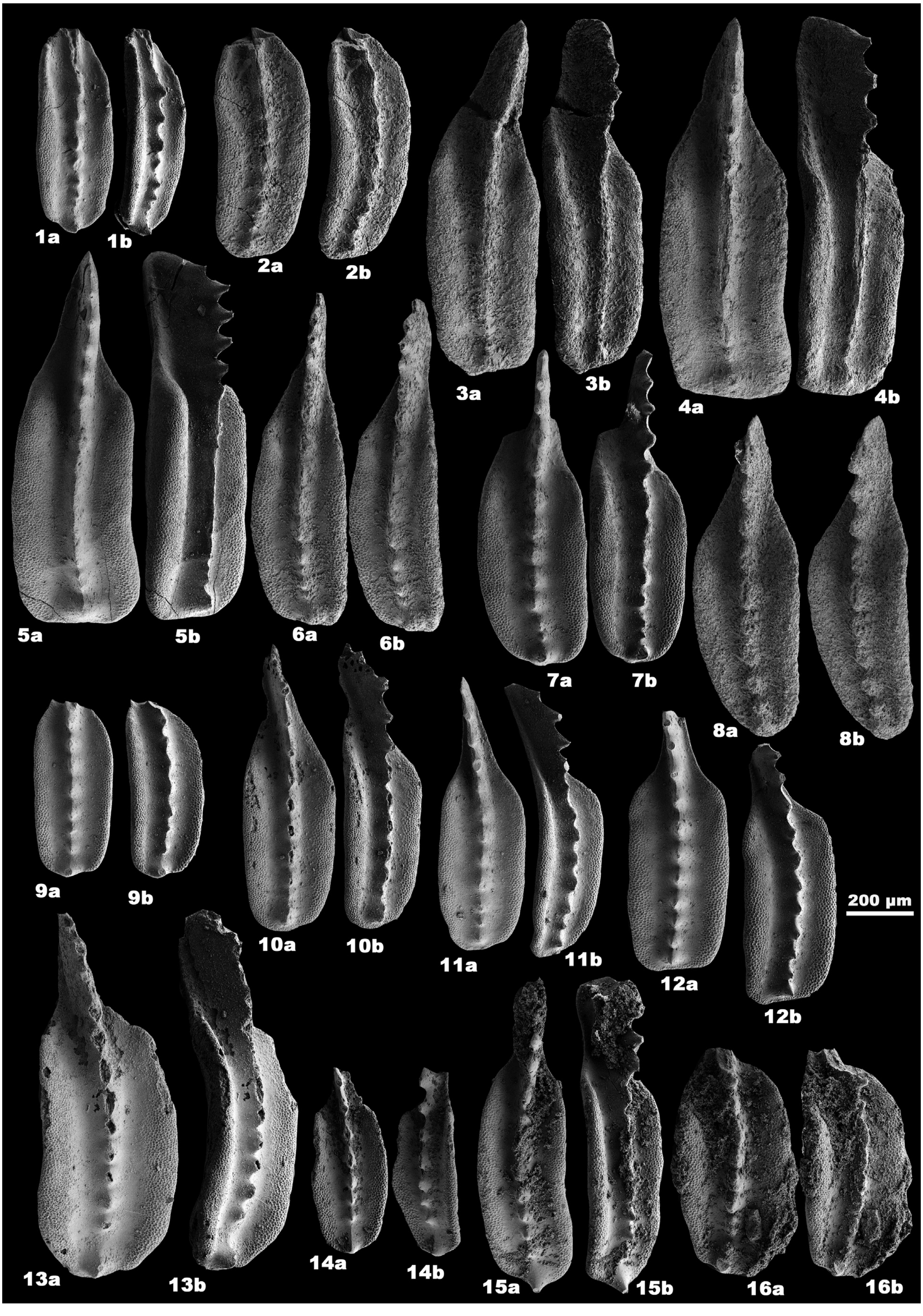

Fig. 5 Conodont P_1 elements from the main Mapojiao section. 1-2, *Clarkina ?dukouensis* (NIGP166280-NIGP166281). 3-7, *Clarkina asymmetrica* (NIGP166282-NIGP166286). 8-12, *Clarkina leveni* (NIGP166287-NIGP166291). 13-16, *Clarkina guangyuanensis* (NIGP166292-NIGP166295).

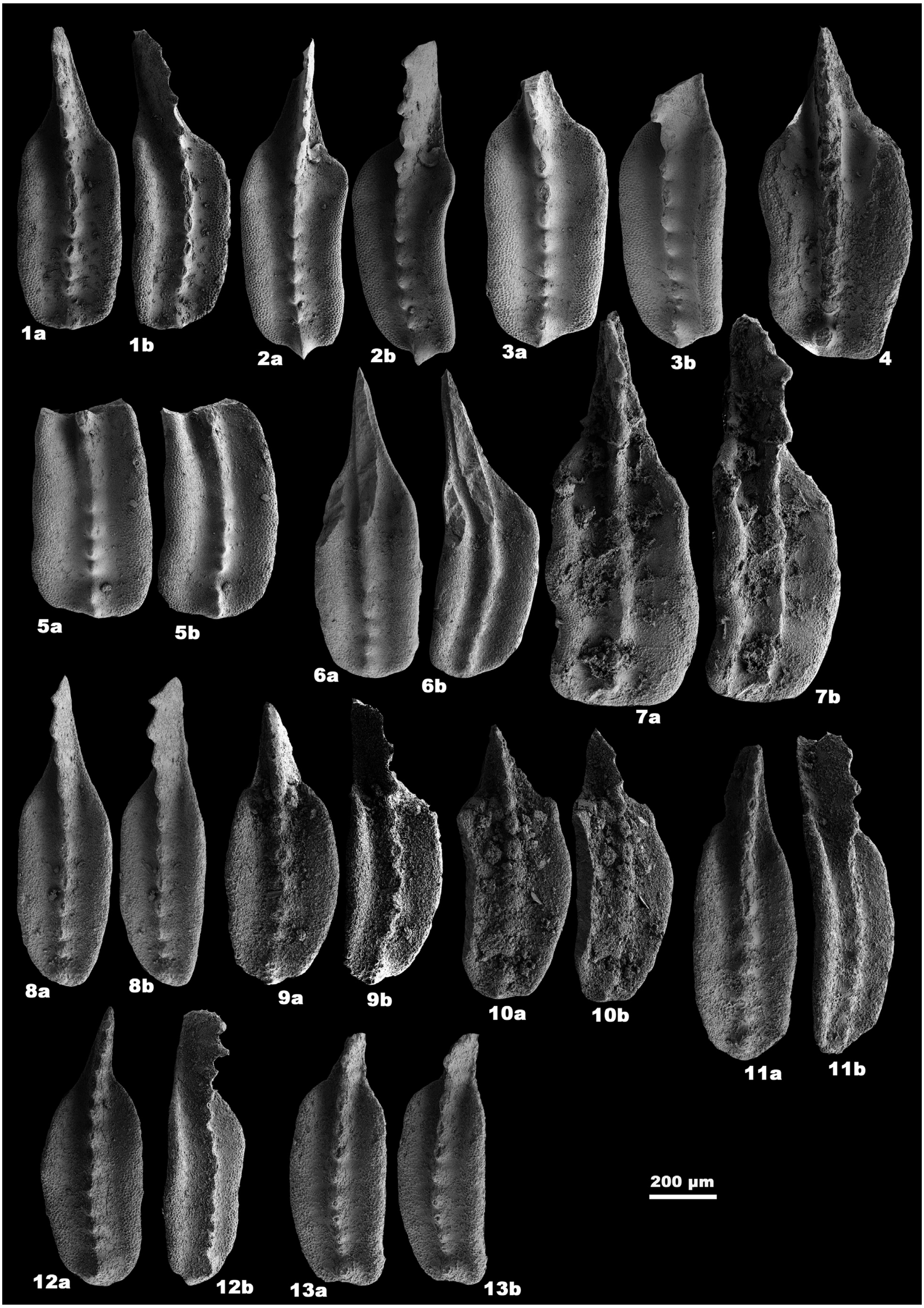

Fig. 6 Conodont P_1 elements from the main Mapojiao section and nearby ancillary Mapojiao B section. 1-4, 8-13, *Clarkina guangyuanensis* (1-4, NIGP166296-NIGP166299; 8-13, NIGP166300-NIGP166305). 5-7, *Clarkina* ?*transcaucasica* (NIGP166306-NIGP166308).

5. Results

5.1. Facies analysis

The shallow marine fauna of Unit A is well diversified. In order of decreasing relative abundance, it includes brachiopods, *Tubiphytes*, bryozoans, calcareous sponges, crinoids, and ostracods, smaller foraminifera, rugose corals and bivalves in packstone-wackestone dominated textures (Fig. 7a). Calcareous sponges and bryozoans are occasionally encrusted with *Archaeolithoporella* and *Tubiphytes* (Fig. 7b). Undifferentiated sand-sized bioclasts are particularly abundant in packstone-dominated horizons. No evidence of mechanical sorting was observed and burrows are rarely seen. The microfacies is more or less homogeneous and constant throughout this unit. Minor secondary dolomitization is detected only at the base of the unit.

The transitional Subunit B1 contains abundant disseminated pyrite crystals, monaxon and siliceous spicules of hexactinellid sponges, conodonts, subordinate radiolarians, and rare smaller foraminifera and ostracods (Fig. 7c). Burrows occasionally occur in this subunit. A few centimetric tempestites are also noticed in Subunit B1. These thin tempestites (~2 cm) are characterized by a sharp erosional base and a distinctive graded bedding (Fig. 7d). The lower part of these layers displays a grainstone-packstone texture and bioclasts similar to the shallow water fauna of Unit A (Fig. 7e). The finer upper part shows wackestone texture with sponge spicules.

Thin-bedded, black, cherty limestones of Subunit B2 (Fig. 2b) are made of abundant radiolarians and hexactinellids sponge spicules, rare small foraminifera, ostracods and fragmented shells within a packstone-wackestone texture (Fig. 8a). Fragmented brachiopods shells that have been transported are restricted to a single layer in the lower part of this unit (see Fig. 4).

Unit C is composed of ca. 20 graded cycles of volcaniclsatics, each cycle being on average ca. 40 cm thick (Fig. 2b). Thin sections from this carbonate-free unit show fine detrital volcanic crystals in a siliceous groundmass (Fig. 8b). The finest hemipelagic fraction of the cycles displays thin lenticular, organic-rich clay (Fig. 8c).

Limestones at the base of Unit D contain radiolarians and sponge spicules (Fig. 8d, e), whose abundance gradually declines upward. The lowermost ~5m of Unit D also exhibit extensive diagenetic silicification (Fig. 8e). Silicification decreases up-section and brachiopods, crinoids, ostracods, smaller foraminifera and small fusulinids occur again in the upper most part of Unit D (Fig. 8f).

5.2. Brachiopods

Unit A yielded an abundant typical Wuchiapingian brachiopod fauna with a total of 17 species belonging to 15 genera. These include: *Permophricodothyris elegantula*; *P. squamularioides*; *Transennatia gratiosa*; *Alphaneospirifer anshunensis*; *Enteletes kayseri*; *Leptodus nobilis*; *Qinglongia zhongyingensis*; *Spinomarginifera lopingensis*; *Juxathryis zhijinensis*; *Paraspiriferina multiplicata*; *P. kwangtungensis*?; *Haydenoides orientalis*?; *Martinia abrupta*; *M. triquetra*; *Notothyris crassa*?; *Paramarginifera kwangtungensis*; *Haydenella* sp.

Abundance of brachiopods drastically decreases above Unit A and only three species (*Spinomarginifera lopingensis*; *Transennatia gratiosa*; *Haydenella kiangsiensis*), which are among the most common species in the Wuchiapingian in South China, were identified from the brachiopod horizon in Subunit B2. A few

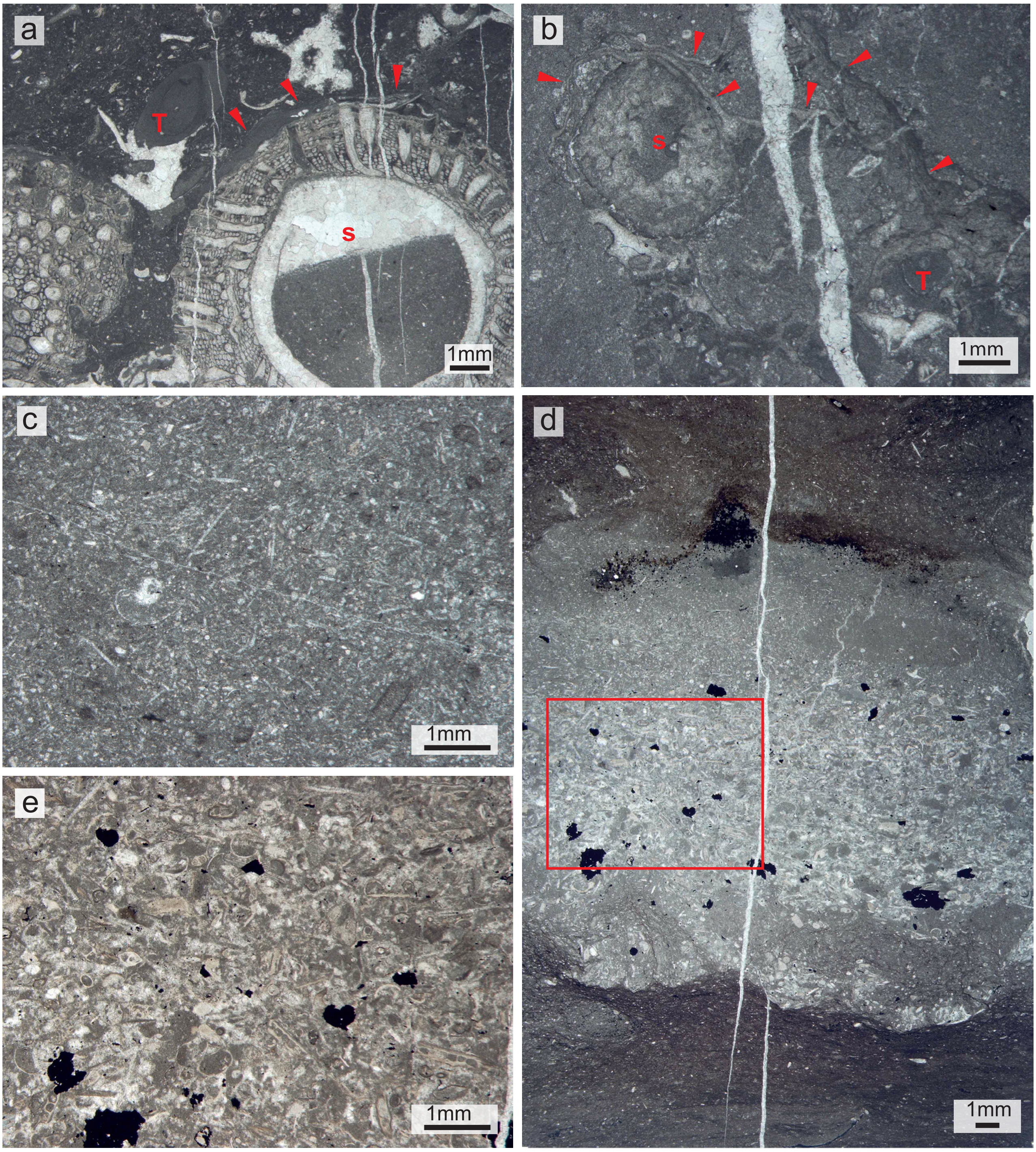

Fig. 7 Photomicrographs of microfacies of Unit A and Subunit B1. **a**, Bioclast packstone of Unit A. Bioclasts are sponge (S) and *Tubiphytes* (T). Red arrows are indicating encrusting *Tubiphytes*. **b**, Bioclast packstone of Unit A. Red arrows indicates encrusting *Archaeolithoporella*. **c**, Spiculite packstone-wackestone of Subunit B1. **d**, Storm deposits intercalated within the dark grey spiculitic limestone of Subunit B1. Note the sharp and erosional lower contact. **e**, Enlargement of the red rectangle in Fig. 7d showing shallow marine bioclastic packstone fabric.

specimens of *Haydenella kiangsiensis* also occur in the lower part of Unit D.

6. Discussion

6.1. Reconstruction of depositional settings

Facies analyses reveal drastic environmental changes across Units A-D. Abundant and diverse benthic bioclasts of Unit A indicate a shallow marine setting. Abundant reef builder and encrusting organisms such as *Tubiphytes*, *Archaeolithoporella*, calcareous sponges, and bryozoans in the thick-bedded Unit A are interpreted as peri-reefal, subtidal settings within the euphotic zone. In addition, sand size bioclasts in packstone texture indicates occasional wave agitation and deposition of this unit above fair weather wave base (Fig. 9).

The drastic decrease of benthic bioclasts at the boundary with the following Subunit B1 on one hand and increase in monaxon and hexactinellid sponge spicules, radiolarian, gondolellid conodonts on the other hand indicate a deeper depositional setting for Subunit B1. Presence of thin tempestites made of shallow marine benthic bioclasts intercalated with deeper water wackestone of Subunit B1 also suggests that Subunit B1 was deposited on a slope, above the storm wave base (Fig. 9). The change from medium-bedded, grey limestone of Subunit B1 to thin-bedded, black siliceous limestone of Subunit B2, with abundant radiolarians and absence of benthic organisms indicates an even deeper depositional setting for Subunit B2. The absence of storm deposits in this unit also suggests deposition in a basinal setting, below storm wave base. Strongly reduced burrowing in this unit indicates a poorly oxygenated sediment-water interface (Fig. 9).

Intercalation of a series of ca. 20 volcaniclastic turbidites marks the culmination of the stepwise drowning event. The 40 cm average thicknesses of these turbidites, the absence of scouring, of channeling and of large sized-clasts suggest a relatively distal submarine lobe. The absence of such turbidites between units B and D in Layin and Guantan supports the presence of feeding canyons for those areally-restricted turbidite lobes.

The dominance of radiolarians and sponge spicules in the packstone-wackestone texture of the base of Unit D indicates persistent deep marine conditions, but without any sign of oxygen depletion. The upward gradual change to packstone texture made of shallow marine bioclasts in Unit D indicates a shallowing trend until depositional settings similar to those of Unit A prevailed again throughout most of the Wuchiaping Fm. The observed silicification in the base of Unit D is likely related to the diagenetic contamination from the silica-rich Unit C.

To summarize, the Mapojiao Event represents a significant drowning event of at least several hundred meters depth within time interval lasting approximatively three conodont IZs (*C. leveni, C. guangyuanensis* and *C. transcaucasica*). Shen et al. (2010) provide an order of magnitude of ~0.5 Myr for the duration of these three IZs, but additional radio-isotopic age calibrations and interpolations are still needed. The deepest deposits typically display an oxygen poor water-sediment interface that may result either from tectonically silled water masses or from high fluxes of organic matter, or a combination of both. The abrupt deposition of volcanogenic clastics of unknown radio-isotopic age suggests either reworking of older volcanic material through vertical tectonic movements in neighboring areas and/or a coeval burst of eruptive activity.

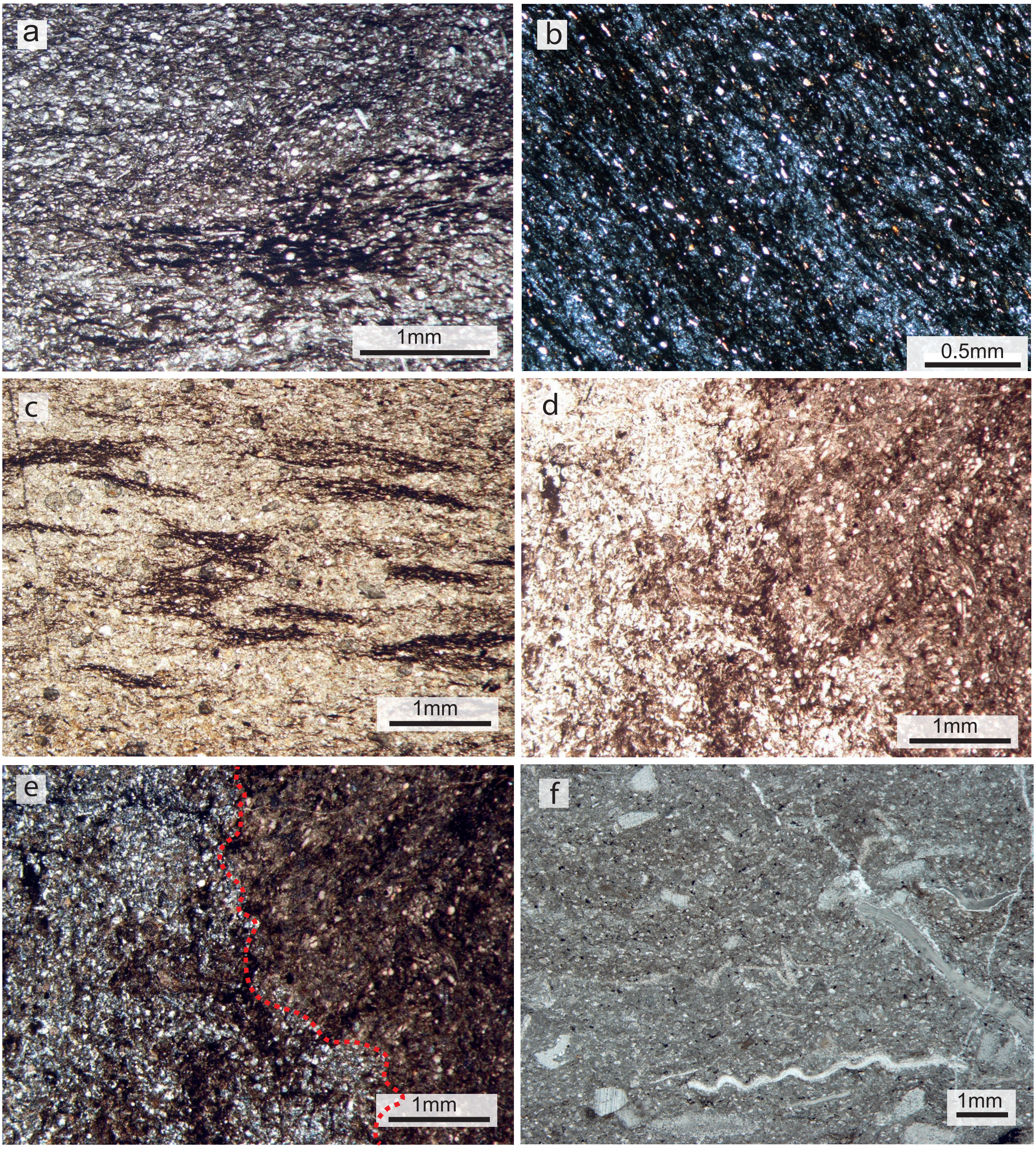

Fig. 8 Photomicrographs of microfacies of Subunit B2, Unit C and Unit D. **a**, Radiolarian- spiculitic packstone of Subunit B2. **b**, Volcanogenic facies of Unit C (polarized light). **c**, volcanogenic facies of Unit C. Note the thin lenticular clay laminae. **d**, Radiolarian- spiculitic wackestone from the lower part of Unit D. **e**, Radiolarian- spiculitic wackestone of Unit D, polarized light (same thin section as shown in 8d). Note the silicification in the left side of the dashed red line. **f**, bioclastic (crinoid-brachiopod) wackestone in the upper part of Unit D.

6.2. Correlation with other sections in South China

Compilation of the published sedimentary records spanning G-L interval indicates that drowning events similar to the Mapojiao Event tend to cluster around three discrete time intervals.

6.2.1. First cluster of drowning events

The oldest cluster (drowning episode 1, Fig. 10) represents drowning events of early to middle Capitanian age. The drowning event at Pingdi (intermediate zone, western Guangxi) and Xiongjiachang (outer zone, western Guangxi) occurred during the *J. altudaensis* IZ. The deep marine radiolarian-spiculitic chert deposited at the top of Maokou Fm. is overlain by the ELIP volcanic rocks in these two sections (Sun et al., 2010; Wignall et al., 2009a). A slightly older (*Jinogondolella postserrata*- *Jinogondolella shannoni* IZs) drowning event belonging to this cluster is documented in Chaotian (northeastern Sichuan) by Saitoh et al. (2013). In Chaotian, the "volcanics" succeeding the radiolarian-spiculitic chert are known as the Wangpo Shale and are also generally agreed to be of ELIP origin (e.g. Huang et al., 2016). There, the Maokou Fm. of Capitanian age is composed of shallow-marine bioclastic limestone and referred to as "The Limestone Unit" by Saitoh et al. (2013). This large fusulinids-bearing unit represents a sedimentary environment similar to Unit A of Mapojiao. It is overlain by a 12 m thick interval of thin-bedded, black siliceous mudstone referred to as "The Mudstone Unit" by Saitoh et al. (2013). Detailed facies analyses indicate a close resemblance in depositional environment for Unit B of Mapojiao and for "The Mudstone Unit" of Chaotian. The only difference between these two sections is the presence of ammonoids and the absence of sponge spicules in "The Mudstone Unit", whereas sponge spicules are abundant and ammonoids are absent in Unit B of Mapojiao. The next unconformably overlying unit in Chaotian is the 2 m thick Wangpo Shale, which yielded a SHIRIMP U-Pb age of 260±4 Ma (He et al., 2007). How much time is included in this unconformity is not precisely known, but the next available age control point below the unconformity is within the *J. shannoni* IZ. Three different interpretations have been proposed for the genesis of the Wangpo Shale. Isozaki et al. (2004) and Lai et al. (2008) interpreted this unit as an ash layer, but He et al. (2007, 2010) and Huang et al. (2016) proposed that it consist of erosional products of ELIP volcanics. Finally, Deconinck et al. (2014) and Zhao et al. (2016) brought new arguments showing that the Wangpo Shale is in fact a mixture of ELIP derived clastics with volcanic tuffs. Lai et al. (2008) noticed substantial quick lateral variation in the thickness of the Wangpo Shale between Shangsi and Chaotian, which would be somehow unusual if it was a true ash layer deposited in a deep water setting. In the Chaotian section, a 1 m-thick black mudstone bed with intercalated coal seams follows the Wangpo Shale. This black mudstone was termed "Heshan beds" and assigned to the base of the Wuchiaping Fm. by Lai et al. (2008), a denomination followed by Saitoh et al. (2013). It is in turn overlain by typical shallow marine bioloclastic limestone of the Wuchiaping Fm. Although robust age control is lacking, the G-L boundary has been tentatively placed at the base of the Wuchiaping Fm. in Chaotian (Isozaki et al., 2008; Saitoh et al., 2013). There are no strata equivalent to these so-called "Heshan beds" associated with the Mapojiao event. Chemical characterization of the Mapojiao volcaniclastic turbidites is still needed to secure any genetic link with ELIP, as is also the case for the older Wangpo Shale.

In Maoershan, the interruption of the Maokou Fm. carbonate deposition by a short episode of sponge spiculite chert was assigned to the *J.*

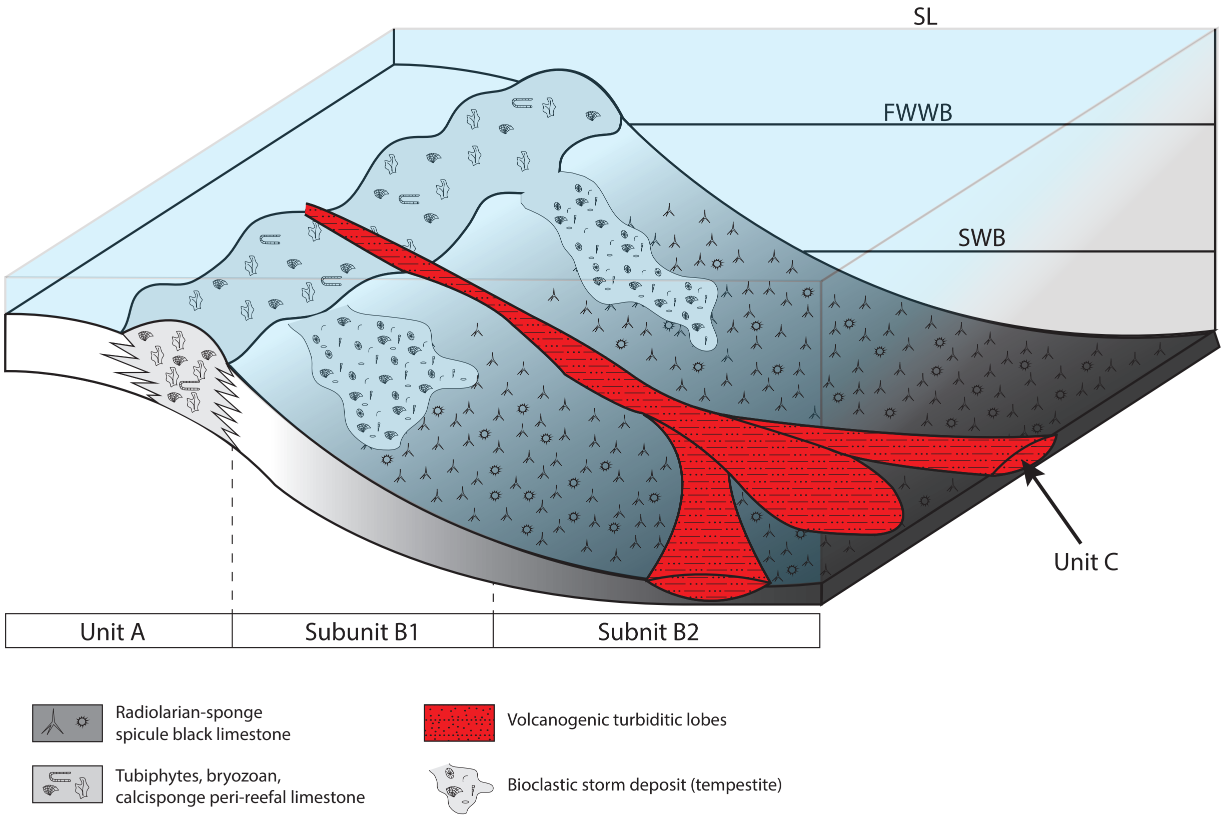

Fig. 9 Depositional model for the early Wuchiapingian carbonate platform of the Wuchiaping Fm. in the Pingtang Syncline. (SL: Sea-level, FWWB: Fair weather wave base, SWB: Storm wave base).

altudaensis IZ by Zhang et al. (2008). This age was subsequently utilized by Sun et al. (2010) to relate this drowning event to the onset of ELIP volcanic activity. However, poor preservation and rough illustrations of these conondonts by Zhang et al. (2008) make this age uncertain. Regardless of the precise age of the drowning in Maoershan, this event starts within the *J. shannoni* IZ in Chaotian (Lai et al., 2008) and, provided that FOs of index species are diachronous (e.g. Brosse et al., 2016), within the next younger *J. altudaensis* IZ in Pingdi (Sun et al., 2010) and in Xiongjiachang (Wignall et al., 2009a; Sun et al., 2010).

Most of the G-L interval in the Penglaitan section is composed of deep-water chert alternating with packages of limestone, the youngest and shallowest of all being referred to as the Laibin Limestone (Jin et al., 2006; Shen et al., 2007). The Laibin limestone documents a rapid regression at top of the Maokou Fm., which overlaps in time with the end-Capitanian eustatic regression (He et al., 2005). Recognition of the first drowning event in Penglaitan is nevertheless obscured by discrepancies in the lithological succession (i.e. number of drowning events, stratigraphic thickness) and by differences in conodont IZs between Shen et al. (2007) and Sun et al. (2010). Only one deepening event prior to the Laibin limestone is arbitrarily shown in our compilation (Fig. 10). It is assigned to the basal *J. altudaensis* IZ by Shen et al. (2007) and Sun et al. (2010), an age which is in agreement with the onset of volcanism in the center of the province.

6.2.2. Second cluster of drowning events

The second cluster of drowning episodes is of latest Capitanian age (Fig. 10). This second event is documented in Maoershan and Dukou (Fig.

1a) by a change from shallow-water limestone of the Maokou Fm. to black, argillaceous cherts of the Kuhfeng Fm. The latter resembles Unit B in Mapojiao.

In Maoershan and Dukou, the Wangpo Shale unconformably follows the radiolarian-spiculitic chert assigned to the Kuhfeng Fm. (Mei et al., 1994a; Zhang et al., 2008). In Maoershan, the onset of this deepening event at is at the base of the *Clarkina postbitteri hongshuiensis* IZ (latest Capitanian). Here again, conodont identifications by Zhang et al. (2008) are uncertain. For instance, *C. postbitteri hongshuiensis* of Zhang et al. (2008) has characteristic serrations found in *Jinogondolella* species. The Kuhfeng chert at Dukou did not yield any conodonts. However, the Kuhfeng chert and Wangpo Shale are bracketed by the *Jinogondolella xuanhanensis* IZ and the *C. dukouensis* IZ in Dukou. Absence of three conodont IZs opens the possibility for a hiatus associated with this drowning event in Dukou. In Penglaitan, a slightly younger deep-water chert unit assigned to the *C. postbitteri postbitteri* IZ rests on the top of the Laibin Limestone and potentially belongs to the second cluster.

6.2.3. Third cluster of drowning events

The youngest drowning event of early Wuchiapingian age is here newly recognized and is well exemplified by the Mapojiao section (Fig. 10). The onset of the Mapojiao Event coincides with the base of the *C. guangyuanensis* IZ. The duration of the radiolarian-spiculitic facies also includes the next younger *C. transcaucasica* IZ. Although Unit C and Unit D did not yield any conodonts, other sections in the Pingtang syncline yielded *C. ?transcaucasica* and *C. orientalis* near the top of the *ca*. 300 m thick Unit D, a few meters below the sharp transition with the Talung Fm. This age constraint suggests a *C. transcaucasica* or a *C. orientalis* IZ age for the base of Unit D in Mapojiao without further precision.

In Dukou, Mei et al. (1994b) report a ca. 20 m thick unit of thin-bedded cherts intercalated within shallow water limestone. These authors indicated an age at the base of the *C. orientalis* IZ for this drowning event. Even in the apparent absence of volcaniclastics in Dukou, this drowning is a likely correlative of the Mapojiao event.

6.3. Episodic drowning events and ELIP volcanism

According to Sun et al. (2010), Emeishan volcanism started in the *J. altudaensis* IZ and intensified during the *J. xuanhanensis* IZ. The first cluster of drowning events overlaps in time (*J. shannoni* to *J. altudaensis* IZs) with a base level fall in the periphery of ELIP (Sun et al., 2010). Our compilation (Fig. 10) across the G-L interval reveals the repetition of the same type of drowning episodes which postdate the first volcanic phase of ELIP. The recognition of two younger subsidence episodes opens up the possibility of a causal relationship with additional pulses of ELIP activity. No obvious spatial trend emerges from the geographical distribution of these drowning events but it cannot be excluded that any such trend could be largely obscured by the random position of a few sections only.

Lithospheric flexuration closely preceding LIPs volcanism is frequently related to mantle plumes (Saunders et al., 2007; Leng and Zhong et al., 2010; Shellnutt, 2014), as well as to smaller sized intrusive bodies (Delaney and McTigue, 1994). However, uplift or doming related to LIPs can be lacking (Burov and Guillou-Frottier, 2005; Elkins-Tanton, 2007; Sheth, 2007; Ukstins Peate and Bryan, 2008).

Similarly, several recent studies argued against the surficial uplift model prior to the ELIP eruption (Ukstins Peate and Bryan, 2008, 2009; Sun et al.,

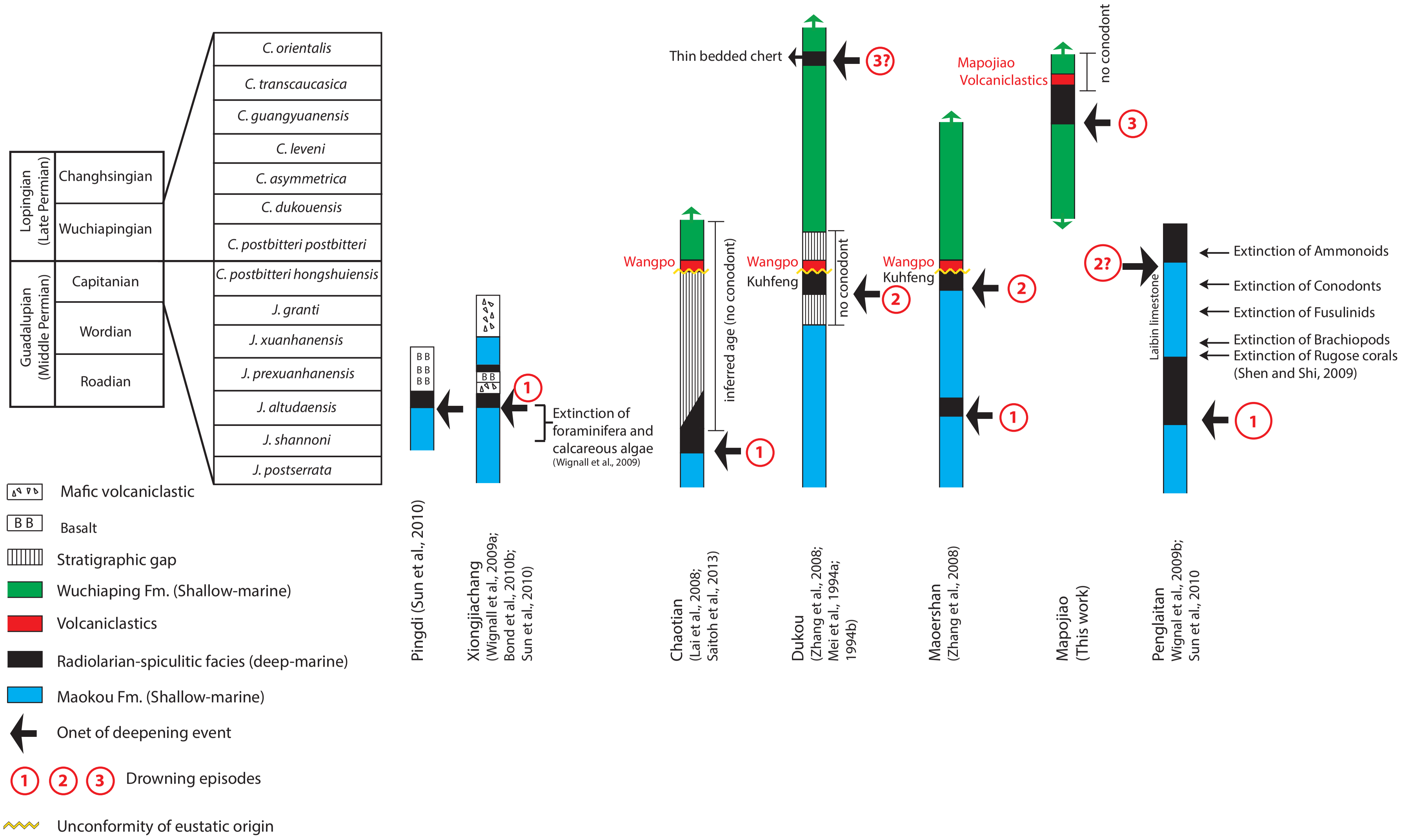

Fig. 10 Comparison of the sedimentary record across G-L interval in the ELIP center and periphery (modified from Sun et al., 2010).

2010; Ukstins Peate et al., 2011; Shellnutt et al., 2014; Jerran et al., 2016). In contrast to the ~500 m uplift proposed by He et al. (2010), several sections near the hypothetical core of the alleged surficial uplift indicate that the earliest eruption of ELIP was at or below sea-level (Ukstins Peate and Bryan, 2008; Ukstins Peate et al., 2011; Jerram et al., 2016). Biostratigraphic and sedimentological constraints also suggest a widespread and rapid subsidence prior to the main eruptive phase and absence of significant erosion at the top of the Maokou Fm. (Ukstins Peate and Bryan, 2008, 2009; Wignall et al., 2009a; Sun et al., 2010; Ukstins Peate et al., 2011; Jerram et al., 2016).

According to Leng and Zhong (2010), surficial uplifts related to LIPs are explained by the plume model as advocated by many authors (e.g. Richards et al., 1991; Griffiths and Campbell, 1991; Farnetani and Richards, 1994; He et al., 2003; Saunders et al., 2007; Campbell, 2007). However, mechanistic models linking surficial subsidence to the extrusion of flood basalts are still debated (Richards et al., 1991; Czamanske et al., 1998; Hales et al., 2005; Ukstins Peate and Bryan, 2008). Leng and Zhong (2010) proposed two models explaining the relationship between plume models and observed subsidence events related to LIPs. The first model involves precocious (tens of Myrs) surficial subsidence resulting from the high temperature of the plume head reaching the 660-km deep phase change. The second model calls upon the peripheral propagation of subsidence around the center of a LIP due to surficial volcanic loading. This second model is in a better agreement with our time/space compilation but cannot be formally tested because of the insufficient number of validation points in space. Another common attribute of all three subsidence events is the absence of breccia related to synsedimentary block faulting. Higher up in the Permian stratigraphic succession of the Nanpanjiang Basin, kilometric wedges of breccia are associated with the pull-apart structuration of the basin around the Wuchiapingian-Changhsingian boundary (Bagherpour et al. 2017). Therefore, the remarkable absence of fault breccia in relation with the three subsidence clusters suggests a flexural rather than a block faulting regime as commonly found in extensional or trans-tensional basins. If the correlation between flexuration/drowning events and ELIP eruptive pulses holds true, then peaks of volcanic loading can be seen as a potential triggers for the flexuration/drowning episodes, in agreement with the second model of Leng and Zhong (2010).

Another model calling upon rapid subsidence - such as the three clusters recognized here - refers to the tensional instability generated by the flattening of the plume head (Burov et al., 2007). This model produces extensional basins separated by highs with a wavelength of 300 to 500 km, but it lacks the time dimension for a meaningful comparison with our time/space distribution of the drowning events. Moreover, absence of fault breccia is hardly reconcilable with an extensional regime.

According to Bryan and Ernst (2008), recognition of the initial phase of LIPs magmatism is more straightforward than identifying the terminal phase of it. This applies to ELIP, whose onset is well constrained but whose cessation is still unclear. Moreover, it is still unknown if the ELIP volcanism represents a single phase as opposed to multiple phases of volcanism (Zhong et al., 2014). According to Shellnutt, (2014), the ELIP eruption lasted over a period of ≤ 2 Ma and more recently, Huang et al. (2016) decreased the inferred duration of the main basaltic eruptive phase to >1 Ma. However, this short duration of the ELIP does not imply an abrupt cessation of plutonic magmatism (Shellnutt, 2014). Shellnutt (2014) listed ELIP radio-isotopic ages ranging from ~266 to ~236 Ma, with several post-260 Ma (G-L boundary) ages. However, such wide range in age may also partly originate from utilization of different radio-isotopic methods. The moderate to low precision of these ages does not allow recognizing different phases of ELIP activity, as suggested by our three clusters of drowning events. However, several post-Capitanian ages indicate additional and younger ELIP magmatism that overlap in time with the Mapojiao Event.

Higher resolution and accuracy radio-isotopic ages as well as geochemical evidence supporting an ELIP-related source of the ash layers and volcanogenic sediments of Unit C at Mapojiao are still needed (Ovtcharova et al. ongoing work). The strikingly similar pattern of facies succession between the younger Mapojiao Event and previous Capitanian examples (e.g. Chaotian) suggests a common underlying mechanism (culmination of eruptive phases) for all three clusters of subsidence events. One must conclude that the tecto-sedimentary records of G-L carbonate platforms in South China represent a more complex history than that of a single uplift or subsidence event related to ELIP.

6.4. Is there any relationship between drowning events and the end-Guadalupian extinction?

In order to evaluate the relationship between the extinction and the determined pulses of ELIP activity here, timing of both phenomena is crucial. Bond et al. (2010a; b) proposed that the end-Guadalupian "mass" extinction abruptly occurred during mid-Capitanian time (*J. altudaensis* IZ) and that it coincided with the onset of ELIP magmatism (i.e. the first cluster of drowning events). These authors suggested that ELIP flood basalt triggered the extinction. They also documented an associated negative shift of the carbon isotope record in a few South Chinese sections. However, negative excursions of the G-L carbon isotope record lack lateral reproducibility in time and may be influenced by local diagenetic controls as convincingly concluded by Jost et al. (2014). Absence of a coeval and paleogeographically widespread negative excursion in C-isotope record undermines the causal relation between the onset of ELIP volcanism and any alleged "mass" extinction. In Penglaitan, Shen and Shi (2009) also documented that the timing of extinction of many marine clades is not synchronous and that it occurred in late- not mid-Capitanian time (Fig. 10).

Finally, Clapham et al. (2009) documented that the end-Guadalupian extinction represents a prolonged and gradual extinction from the Wordian to the end of the Permian, without any peak in extinction rates (see also Groves and Wang, 2013). These authors also concluded that a gradual decline in diversity had already started before ELIP volcanism, thus questioning the existence of any mid or late Capitanian "mass" extinction.

Regardless of the reliability of any mid- or late Capitanian "mass" extinction, only the first drowning event coincides with the proposed mid Capitanian "mass" extinction of Bond et al. (2010a). The early Wuchiapingian Mapojiao Event does not correlate with any known extinction peak but is within a time interval that witnessed a marine recovery and radiation (Villier and Korn, 2004; Chen et al., 2005; Shen and Shi 2009; Brayard et al., 2009; Shen et al., 2011). Additionally, the brachiopod fauna of Unit A at Mapojiao is nearly identical to that of younger Wuchiapingian faunas. This brachiopod assemblage from Unit A also reveals some affinities with latest Capitanian faunas and indicates that brachiopod recovery and radiation had already started prior to the G-L boundary, which coincides with the second cluster of drowning event (Shen and Zhang, 2008; Shen and Shi, 2009).

7. Conclusion

1- In the Pingtang syncline (South Guizhou), deposition of shallow marine limestone of the Wuchiapingian Fm. was interrupted by a radiolarian-spiculitic deep water limestone documenting a drowning event. This deep water episode is immediately followed by deposition of volcanogenic turbidites.

2- Five index species of *Clarkina* from the shallow marine limestone (Unit A) and lower part of the radiolarian-spiculitic facies (Unit B) have been identified.

3- *C. dukouensis*, *C. asymmetrica*, *C. leveni*, *C. guangyuanensis*, and *C. transcaucasica* (or *C. guangyuanensis* transitional to *C. transcaucasica*) are identified in stratigraphically ascending order. The conodont assemblage indicates an early Wuchiapingian age.

4- Compilation of the published South Chinese sedimentary records across G-L interval reveals that such drowning events cluster around three discrete time intervals.

5- The similar facies evolution of the Capitanian ELIP-related Chaotian drowning event, of the latest Capitanian Dukou/Maoershan drowning event and of the early Wuchiapingian Mapojiao Event suggest that peaks of ELIP eruptive activity are associated with regional drowning episodes temporarily interrupting the preponderant deposition of shallow water carbonate.

6- It remains to be established if the ash layers and volcanogenic turbidites associated with the Mapojiao Event are genetically related to ELIP.

7- Any causal relation between episodic ELIP tecto-volcanic activity and peaks of extinction among marine clades remains obscure. Only the mid-Capitanian “mass” extinction of Bond et al. (2010) seems to correlate with the first cluster of drowning events, but the robustness of this “mass” extinction is still elusive.

Acknowledgments: Constructive reviews by XXX, XXX, XXX, and editor XXX are deeply acknowledged. This research is supported by the Swiss NSF projects 135446 and 160055 (to H.B.) and by the National Natural Science Foundation of China 41420104003 and 41702007 (to DXY and SZS). Insightful discussions during this work with Jean-Pierre Burg, Michael

Hautmann and Morgane Brosse are deeply acknowledged.

References:

Bagherpour, B., Bucher, H., Baud, A., Brosse, M., Vennemann, T., Martini, R., Goudun, K., 2017. Onset, development, and cessation of basal Early Triassic microbialites (BETM) in the Nanpanjiang pull-apart Basin, South China Block. Gondwana Research 44, 178–204.

Bond, D.P.G., Hilton, J., Wignall, P.B., Ali, J.R., Stevens, L.G., Sun, Y.D., Lai, X.L., 2010a. The Middle Permian (Capitanian) mass extinction on land and in the oceans. Earth-Science Reviews 102, 100–116.

Bond, D.P.G., Wignall, P.B., Wang, W., Izon, G., Jiang, H.S., Lai, X.L., Sun, Y.D., Newton, R.J., Shao, L.Y., Védrine, S., Cope, H., 2010b. The mid-Capitanian (Middle Permian) mass extinction and carbon isotope record of South China. Palaeogeography, Palaeoclimatology, Palaeoecology 292, 282–294.

Boucot, A.J., Xu, C., Scotese, C.R. and Morley, R.J., 2013. Phanerozoic paleoclimate: an atlas of lithologic indicators of climate. Society of Economic Paleontologists and Mineralogists.

Brayard, A., Escarguel, G., Bucher, H., Monnet, C., Brühwiler, T., Goudemand, N., Galfetti, T., Guex, J., 2009. Good Genes and Good Luck: Ammonoid Diversity and the End-Permian Mass Extinction. Science 325(5944), 1118-1121.

Brosse, M., Bucher, H., Goudemand, N., 2016a. Quantitative biochronology of the Permian–Triassic boundary in South China based on conodont unitary associations. Earth-Science Reviews 155, 153–171.

Bryan, S.E., Ernst, R.E., 2008. Revised definition of large igneous provinces (LIPs). Earth-Science Reviews 86, 175-202.

Burov, E., Guillou-Frottier, L., 2005. The plume head–continental lithosphere interaction using a tectonically realistic formulation for the lithosphere. Geophysical Journal International 161, 469–490.

Burov, E., Guillou-Frottier, L., d'Acremont, E., Le Pourhiet, L., Cloetingh, S., 2007. Plume head–lithosphere interactions near intra-continental plate boundaries. Tectonophysics 434, 15–38.

Campbell, I.H., 2007. Testing the plume theory. Chemical Geology 241, 153–176.

Chen, Z.Q., Campi, M.J., Shi, G.R., Kaiho, K., 2005. Post‒extinction brachiopod faunas from the Late Permian Wuchiapingian coal series of South China. Acta Palaeontologica Polonica 50(2), 343-363.

Chen, B., Joachimski, M.M., Sun, Y.D., Shen, S.Z., Lai, X.L., 2011. Carbon and conodont apatite oxygen isotope records of Guadalupian–Lopingian boundary sections: climatic or sea-level signal? Palaeogeography, Palaeoclimatology, Palaeoecology 311, 145–153.

Chen, B., Joachimski, M.M., Shen, S.Z., Lambert, L.L., Lai, X.L., Wang, X.D., Chen, J.,

Yuan, D.X., 2013. Permian ice volume and palaeoclimate history: Oxygen isotope proxies revisited. Gondwana Research 24, 77-89.

Clapham, M.E., Shen, S., Bottjer, D.J., 2009. The double mass extinction revisited: reassessing the severity, selectivity, and causes of the end-Guadalupian biotic crisis (LatePermian). Paleobiology 35, 32–50.

Czamanske, G.K., Gurevitch, A.B., Fedorenko, V., Simonov, O., 1998. Demise of the Siberian plume: paleogeographic and paleotectonic reconstruction from the prevolcanic and volcanic record, north-central Siberia. International Geology Review 40, 95–115.

Deconinck, J.F., Crasquin, S., Bruneau, L., Pellenard, P., Baudin, F., Feng, Q., 2014. Diagenesis of clay minerals and K-bentonites in Late Permian/Early Triassic sediments of the Sichuan Basin (Chaotian section, Central China). Journal of Asian Earth Sciences 81, 28–37.

Delaney, P.T., McTigue, D.F., 1994. Volume of magma accumulation or withdrawal estimated from surface uplift or subsidence, with application to the 1960 collapse of Kilauea Volcano. Bulletin of Volcanology 56, 417–424.

Dunham, R.J., 1962. Classification of carbonate rocks according to depositional texture. *American Association* of Petroleum Geologists memoir 1,108–121.

Elkins-Tanton, L.T., 2007. Continental magmatism volatile recycling, and a heterogeneous mantle caused by lithospheric gravitational instabilities. Journal of Geophysical Research 112 (B03405), 1-13. doi:10.1029/2005JB004072

Enos, P., 1995, Permian of China, in P. A. Scholle, T. M. Peryt, D. S. Ulmer-Scholle, eds., The Permian of northern Pangea: Berlin, Springer-Verlag 2, 225–256.

Fan, W., Zhang, C., Wang, Y., Guo, F., Peng, T., 2008. Geochronology and geochemistry of Permian basalts in western Guangxi Province, southwest China: evidence for plume-lithosphere interaction. Lithos 102, 218-236.

Farnetani, C.G., Richards, M.A., 1994. Numerical investigations of the mantle plume initiation model for flood basalt events. Journal of Geophysical Research 99, 13813–13833.

Griffiths, R.W., Campbell, I.H., 1991. Interaction of mantle plume heads with the Earth's surface and onset small-scale convection. Journal of Geophysical Research 96, 18,275–18,310.

Groves, J. R., Wang, Y., 2013. Timing and size selectivity of the Guadalupian (Middle Permian) fusulinoidean extinction. Journal of Paleontology 87(2), 183-196.

Guizhou Bureau of Geology and Mineral Resources., 1987. Regional Geology of Guizhou Province: Geological Memoires, Ser. 1, no. 6, [in Chinese, English summary; Geologic map 1:500,000].

Hales, T.C., Abt, D.L., Humphreys, E.D., Roering, J.J., 2005. A lithospheric instability origin for Columbia River flood basalts and Wallowa Mountains uplift in northeast Oregon. Nature 438, 842–845.

He, B., Xu, Y., Chung, Sun-Lin, Xiao, L., Wang, Y., 2003. Sedimentary evidence for a rapid, kilometer-scale crustal doming prior to the eruption of the

Emeishan flood basalts. Earth and Planetary Science Letters 213, 391–405.

He, B., Xu, Y. G., Wang, Y. M., and Xiao, L., 2005, Nature of the Dongwu Movement and its temporal and spatial evolution. Earth Science-Journal of China University of Geosciences, 30(1), 89-96.

He, B., Xu, Y., Huang, X., Luo, Z., Shi, Y., Yang, Q., Yu, S., 2007. Age and duration of the Emeishan flood volcanism, SW China: geochemistry and SHRIMP zircon U–Pb dating of silicic ignimbrites, post-volcanic Xuanwei Formation and clay tuff at the Chaotian section. Earth and Planetary Science Letters 255, 306–323.

He, B., Xu, Y.G., Zhong, Y.T., Guan, J.P., 2010. The Guadalupian–Lopingian boundary mudstones at Chaotian (SW China) are clastic rocks rather than acidic tuffs: implication for a temporal coincidence between the end-Guadalupian mass extinction and the Emeishan volcanism. Lithos 119, 10–19.

Huang, H., Cawood, P.A., Hou, M.C., Yang, J.H., Ni, S.J., Du, Y.S., Yan, Z.K., Wang, J., 2016. Silicic ash beds bracket Emeishan Large Igneous province to b1 m.y. at ~260 Ma. Lithos 264, 17-27.

Isozaki, Y., Yao, J.X., Matsuda, T., Sakai, H., Ji, Z.S., Shimizu, N., Kobayashi, N., Kawahata, H., Nishi, H., Takano, M., Kubo, T., 2004. Stratigraphy of the Middle–Upper Permian and Lowermost Triassic at Chaotian, Sichuan, China — record of Late Permian double mass extinction event. Proceedings of Japan Academy, Series B 80, 10–16.

Isozaki, Y., Yao, J.X., Ji, Z.S., Saitoh, M., Kobayashi, N., Sakai, H., 2008. Rapid sea-level change in the Late Guadalupian (Permian) on the Tethyan side of South China: litho- and biostratigraphy of the Chaotian section in Sichuan. Proceedings of Japan Academy, Series B 80, 344–353.

Jeppsson, L., Anehus, R., 1999. A new technique to separate conodont elements from heavier minerals. Alcheringa 23 (1), 57–62.

Jeppsson, L., Anehus, R., Fredholm, D., 1999. The optimal acetate buffered acetic acid technique for extracting phosphatic fossils. Journal of Paleontology 73 (5), 964–972.

Jerram, D.A., Widdowson, M., Wignall, P.B., Sun, Y., Lai, X., Bond, D.P.G., Torsvik, T.H., 2016. Submarine palaeoenvironments during Emeishan flood basalt volcanism, SW China: Implications for plume–lithosphere interaction during the Capitanian, Middle Permian (‘end Guadalupian’) extinction event. Palaeogeography, Palaeoclimatology, Palaeoecology 441, 65–73.

Jin, Y. G., 1993. Pre-Lopingian benthos crisis, Comptes Rendus XII ICC-P, Volume 2: Buenos Aires, 269-278.

Jin, Y.-G., Zhang, J., Shang, Q.-H., 1994. Two phases of the end-Permian mass extinction.

Canadian Society of Petroleum Geologists Memoir 17, 813–822.

Jin, Y., Shen, S., Henderson, C.M., Wang, X., Wang, W., Wang, Y., Cao, C., Shang, Q., 2006. The Global Stratotype Sectionand Point (GSSP) for the boundary between the Capitanian and Wuchiapingian Stage (Permian). Episodes 29, 253–262.

Jost, B. A., Mundil, R., He, B., Brown, T. S., Altiner, D., Sun, Y., DePaolo, D. J., Payne L. L., 2014. Constraining the cause of the end-Guadalupian extinction with coupled records carbon and calcium isotopes. Earth and Planetary Science Letters. 396, 201-212.

Lai, X., Wei, Wang, Wignall, P.B., Bond, D.P.G., Jiang, H., Ali, J.R., John, E.H., Sun, Y., 2008. Palaeoenvironmental change during the end-Guadalupian (Permian) mass extinction in Sichuan, China. Palaeogeography, Palaeoclimatology, Palaeoecology 269, 78–93.

Lehrmann, D.J., Enos, P., Payne, J.L., Montgomery, P., Wei, J., Yu, Y., Xiao, J., Orchard, M.J., 2005. Permian and Triassic depositional history of the Yangtze platform and Great Bank of Guizhou in the Nanpanjiang basin of Guizhou and Guangxi, south China. Albertiana 33, 147–166.

Leng, W., Zhong, S., 2010. Surface subsidence caused by mantle plumes and volcanic loading in large igneous provinces. Earth and Planetary Science Letters 291, 207–214.

Li, H., Zhang, Z., Santosh, M., Lü, L., Han, L., Liu, W., 2016. Late Permian basalts in the Yanghe area, eastern Sichuan Province, SW China: Implications for the geodynamics of the Emeishan Large Igneous Province and Permian global mass extinction. Journal of Asian

Earth Sciences 134, 293-308.

Lucas, S., 2017. Permian tetrapod extinction events. Earth-Science Reviews 170, 31–60.

Mei, S.L., Jin, Y.G., Wardlaw, B.R., 1994a. Zonation of conodonts from the Maokouan-Wuchiapingian boundary strata, South China. In: Permian Stratigraphy, Environments and Resources, Jin, Y.G., Utting, J.,Wardlaw, B.R. (eds). Palaeoworld 4, 225–233.

Mei, S.L., Jin, Y.G., Wardlaw, B.R., 1994b. Succession of Wuchiapingian conodonts from northeastern sichuan and its worldwide correlation. Acta Micropalaeontologica Sinica 11, 121–139. (in Chinese with English abstract).

Mei, S.L., Jin, Y.G., Wardlaw, B.R., 1998. Conodont succession of the Guadalupian-Lopingian boundary strata in Laibin of Guangxi, China and West Texas, USA. In: Permian Stratigraphy, Environments and Resources, Jin, Y.G., Wardlaw, B.R., Wang, Y. (eds). China University of Science and Technology Press, Hefei, Palaeoworld 9, 53–76.

Richards, M.A., Jones, D.L., Duncan, R.A., Depaolo, D.J., 1991.A mantle plume initiation model for the Wrangellia flood basalt and other oceanic plateaus. Science 254, 263–267.

Saitoh, M., Isozaki, Y., Yao, J., Ji, Z., Ueno, Y., Yoshida, N., 2013. The appearance of an oxygen-depleted condition on the Capitanian disphotic slope/basin in South China: Middle–Upper Permian stratigraphy at Chaotian in northern Sichuan. Global and Planetary Change 105, 180–192.

Saunders, A.D., Jones, S.M., Morgan, L.A., Pierce, K.L., Widdowson, M., Xu, Y.-G., 2007. Regional uplift associated with continental large igneous provinces: the roles of mantle plumes and the lithosphere. Chemical Geology 241, 282–318.

Shellnutt, J.G., Denyszyn, S., Mundil, R., 2012. Precise age determination of mafic and felsic intrusive rocks from the Permian Emeishan large igneous province (SW China). Gondwana Research 22, 118-126.

Shellnutt, J.G., 2014. The Emeishan large igneous province: A synthesis. Geoscience Frontiers 5, 369-394.

Shen, S.Z., Wang, Y., Henderson, C.M., Cao, C.Q., Wang, W., 2007. Biostratigraphy and lithofacies of the Permian System in the Laibin–Heshan area of Guangxi, South China. Palaeoworld16, 120–139.

Shen, S.Z., Zhang, Y.C., 2008. Earliest Wuchiapingian (Lopingian, late Permian) brachiopods in southern Hunan, South China: implications for the pre-Lopingian crisis and onset of Lopingian recovery/radiation. Journal of Paleontology 82(5), 924-937.

Shen, S.Z., Shi, G.R., 2009. Latest Guadalupian brachiopods from the Guadalupian/Lopingian boundary GSSP section at Penglaitan in Laibin, Guangxi, South China and implications for the timing of the pre-Lopingian crisis. Palaeoworld 18, 152-161.

Shen, S.Z., Mei, S.L., 2010. Lopingian (Late Permian) high-resolution conodont biostratigraphy in Iran with comparison to South China zonation. Geological Journal 45, 135–161.

Shen, S.Z., Henderson, C.M., Bowring, S.A., Cao, C.Q., Wang, Y., Wang, W., Zhang, H., Zhang, Y.C., Mu, L., 2010. High-resolution Lopingian (LatePermian) timescale of South China. Geological Journal 45, 122–134.

Shen, S.Z., Crowley, J.L., Wang, Y., Bowring, S.A., Erwin, D.H., Sadler, P.M., Cao, C.Q., Rothman, D.H., Henderson, C.M., Ramezani, J., Zhang, H., Shen, Y., Wang, X.D., Wang, W., Mu, L., Li, W.Z., Tang, Y.G., Liu, X.L., Liu, L.J., Zeng, Y., Jiang, Y.F., Jin,Y.G., 2011. Calibrating the end-Permian mass extinction. Science 334, 1367–1372.

Sheth, H.C., 2007. Plume related regional pre-volcanic uplift in the Deccan traps: absence of evidence, evidence of absence. In: Foulger, G.R., Jurdy, D.M. (Eds.), Plates, Plumes and Planetary Processes. Geological Society of America, 785-813. Special Paper 430.

Stanley, S.M., Yang, X., 1994. A double mass extinction at the end of the Paleozoic era.

Science 266, 1340–1344.

Sun, Y., Lai, X., Wignall, P.B., Widdowson, M., Ali, J.R., Jiang, H., Wang, W., Yan, C., Bond, D.P.G., Vedrine, S., 2010. Dating the onset and nature of the Middle Permian Emeishan large igneous province eruptions in SW China using conodont biostratigraphy and its bearing on mantle plume uplift models. Lithos 119, 20–33.

Ukstins Peate, I., Bryan, S.E., 2008. Re-evaluating plume-induced uplift in the Emeishan large igneous province. Nature Geoscience 1, 625–629.

Ukstins Peate, I., Bryan, S.E., 2009. Pre-eruptive uplift in the Emeishan? Nature Geoscience 2, 531–532.

Ukstins Peate, I., Bryan, S.E., Wignall, P.B., Jerram, D.A., Ali, J.R., 2011. Comment on 'Paleokarst on the top of the Maokou Formation: further evidence for domal crustal uplift prior to the Emeishan flood volcanism'. Lithos 125, 1006-1008.

Villier, L., Korn, D., 2004. Morphological Disparity of Ammonoids and the Mark of Permian Mass Extinctions. Science 306(5694), 264-6.

Wang, X.D., Sugiyama, T., 2000. Diversity and extinction patterns of Permian coral faunas of China. Lethaia 33, 285–294.

Wignall, P.B., Sun, Y., Bond, D.P.G., Izon, G., Newton, R.J., Védrine, S., Widdowson, M., Ali, J.R., Lai, X., Jiang, H., Cope, H., Bottrell, S.H., 2009a. Volcanism, mass extinction, and carbon isotope fluctuations in the Middle Permian of China. Science 324, 1179–1182.

Wignall, P.B., Védrine, S., Bond, D.P.G., Wang, W., Lai, X., Ali, J.R., Jiang, H., 2009b. Facies analysis and sea-level change at the Guadalupian–Lopingian Global Stratotype (Laibin, South China), and its bearing on the end-Guadalupian mass extinction. Journal of the Geological Society London 166, 655–666.

Yuan, D. X., Shen, S. Z., Henderson, C. M., 2017. Revised Wuchiapingian conodont taxonomy and succession of South China. Journal of Paleontology 00(0), 1–21. doi: 10.1017/jpa.2017.71

Xu, Y.G., Chung, S.L., Shao, H., He, B., 2010. Silicic magmas from the Emeishan large igneous province, Southwest China: petrogenesis and their link with the end-Guadalupian biological crisis. Lithos 119, 47–60.

Zhang, L.L., Zhang, N., Xia, W.C., 2008. Conodont succession in the Guadalupian Lopingian boundary interval (upper Permian) of the Maoershan section, Hubei Province, China. Micropaleontology 53, 433–446.

Zhao, L., Dai, S., Graham, I.T., Li, X., Zhang, B., 2016. New insights into the lowest Xuanwei Formation in eastern Yunnan Province, SW China: Implications for Emeishan large igneous province felsic tuff deposition and the cause of the end-Guadalupian mass extinction. Lithos 264, 375–391.

Zhong, Y.T., He, B., Mundil, R., Xu, Y.G., 2014. CA-TIMS zircon U–Pb dating of felsic ignimbritefrom the Binchuan section: implications for the termination age of Emeishan large igneous province. Lithos 204, 14–19.

Zhou, M. F., Malpas, J., Song, X. Y., Robinson, P. T., Sun, M., Kennedy, A. K., Lesher, C. M., Keays, R. R., 2002. A temporal link between the Emeishan large igneous province (SW China) and the end-Guadalupian mass extinction. Earth and Planetary Science Letters 196 (3-4), 113-122.

CHAPTER II

COUPLED CARBON AND STRONTIUM ISOTOPE CHEMOSTRATIGRAPHY FROM EARLY LATE PERMIAN: INFLUENCE OF PROLONGED EMEISHAN VOLCANISM?

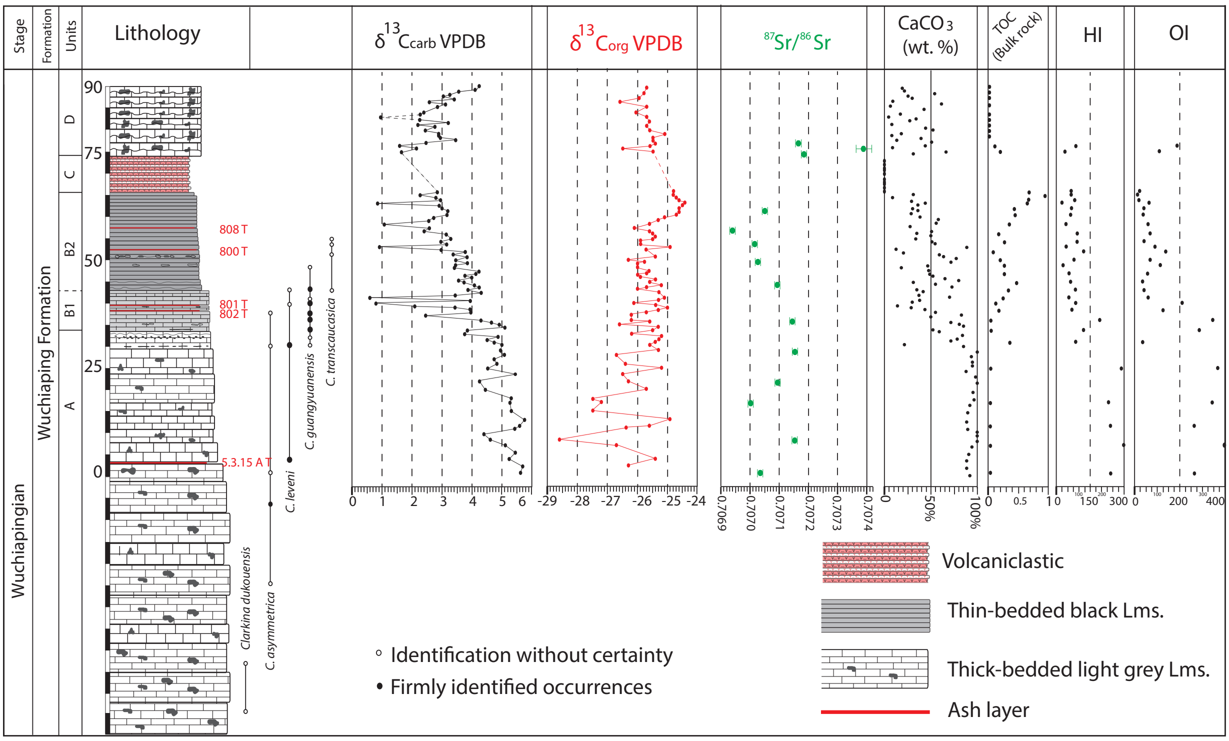

Gondwana Research (in review)

Coupled carbon and strontium isotope chemostratigraphy from early Late Permian: influence of prolonged Emeishan volcanism?

Borhan Bagherpour[1*], Hugo Bucher[1], Elke Schneebeli-Hermann[1], Torsten Vennemann[2], Massimo Chiaradia[3], Shu-zhong Shen[4]

1- Paleontological institute, University of Zürich, Karl Schmid-Strasse 4, 8006 Zürich, Switzerland.

2- Institute of Earth Surface Dynamics, University of Lausanne, Géopolis, 1015 Lausanne, Switzerland.

3- Department of Earth Sciences, University of Geneva, Geneva, 1205, Switzerland.

4- Nanjing Institute of Geology and Palaeontology, Chinese Academy of Sciences, Nanjing 210008, China.

Abstract

Carbonate carbon isotope compositions ($\delta^{13}C_{carb}$) document a new 3.5 ‰ CIE toward lower values concomitant with an ELIP-related drowning event (Mapojiao Event, southern Guizhou) during the early Wuchiapingian. Organic carbon isotope data ($\delta^{13}C_{org}$) have a 2 ‰ shift toward higher values across the drowning event, showing decoupling with the $\delta^{13}C_{carb}$ evolution. Rock-Eval and palynofacies analyses suggest an elevated flux of terrestrial OM during the temporary drowning episode. Therefore, the decoupling between $\delta^{13}C_{carb}$ and $\delta^{13}C_{org}$ is best explained by the mixing of different organic carbon pools in the $\delta^{13}C_{org}$ curve. Strontium isotope data ($^{87}Sr/^{86}Sr$) also show a transient shift from 0.70715 to 0.70694 associated with this early Wuchiapingian CIE, which is superimposed on the late Permian prolonged global rising trend. This short-lived $^{87}Sr/^{86}Sr$ excursion is best interpreted as an enhanced hydrothermal flux related to a short pulse of ELIP-related volcanism.

Comparison of the Mapojiao Event with other C isotope records from South China and other parts of Tethys reveals substantial discrepancies. Moreover, older Capitanian CIEs concomitant with ELIP-related drownings are also not laterally reproducible in time. The local distribution of CIEs across G-L interval indicates the influence of local factors such as bathymetry and accumulation of terrestrial OM, rather than perturbations in the global carbon cycle to due volcanism. This prevents the C isotope record to be used as a global correlation tool during Capitanian and Wuchiapingian times. Comparison of palaeobiodiversity changes with perturbations in C isotope compositions across the G-L interval shows that only the oldest CIE was associated with a modest extinction event as documented in South China. Hence, this study undermines any systematic coupling between extinctions and iterative perturbations of the C isotope record during the G-L interval.

Keywords

South China; Wuchiapingian; Carbon isotope; Strontium isotope; Emeishan Large Igneous Province

1. Introduction

The end-Guadalupian crisis represents a distinct extinction event preceding Permian-Triassic mass extinction (Stanley and Yang, 1994; Jin et al., 1994). The end-Guadalupian extinction is recorded in both marine and terrestrial realms, and had a profound effect on fusulinids and calcareous algae, but also affected corals, bryozoans, brachiopods, bivalves, ammonoids, and ostracods (Bond et al., 2010a and references therein; Zazzali et al., 2015). However, a more recent study revealed that there was no associated terrestrial extinction (Rubidge et al., 2013). According to Bond et al. (2010a; 2010b), this “mass” extinction occurred in a short time interval during the mid-Capitanian and coincided with the onset of the Emeishan Large Igneous Province (ELIP). This is in marked contrast with Clapham et al. (2009), who argued that this extinction represents a prolonged and gradual decline of diversity from the Wordian to the end of the Permian without any extinction peak. Although the ultimate trigger for the end-Guadalupian extinction is still unclear, its close temporal association with the ELIP volcanism led several authors to suggest a cause-effect relationship between these two phenomena (e.g., Wang and Sugiyama, 2000; Ali et al., 2002; Zhou et al., 2002; Lai et al., 2008; Wignall et al., 2009; Li et al., 2016). However, the Wordian to end-Permian gradual decline of diversity “precludes the need to invoke drastic extinction mechanisms” (Clapham et al., 2009).

The Guadalupian-Lopingian (G-L) boundary in South China coincides with formational boundary between the Maokou and Wuchiaping formations. It is associated with several environmental changes such as sedimentary facies change (e.g., Sun et al., 2010; Saitoh et al., 2013a), carbon cycle perturbations (e.g. Bond et al., 2010b; Yan et al., 2013), and a temperature rise (Chen et al., 2011).

The top of Maokou Fm. is marked by remarkable drowning events associated with ELIP volcanism (drowning events 1 and 2 in Fig. 1) due to pre-eruption subsidence (Ukstins-Peate and Bryan, 2008; Sun et al., 2010; Jerram et al., 2016). Recently, Bagherpour et al. (in review) showed that the same type of drowning in association with volcanic activity occurred again during the early Wuchiapingian time (Mapojiao Event, drowning events 3 in Fig. 1) in the Pingtang syncline in Southern Guizhou Province (Fig. 2). Similar sedimentary architecture of Capitanian drowning events (drowning events 1 and 2 in Fig. 1) and of the Mapojiao Event strongly suggests a common underlying driving mechanism related to episodic pulses of the ELIP activity (Fig. 1). In addition to bathymetric change, several studies also recognized pronounced Carbon Isotope Excursions (CIEs) in the South China records during the Capitanian or at the G-L boundary. ELIP volcanism has been often designated as the most plausible cause for these CIEs toward lower values (Wignall et al., 2009; Bond et al., 2009b; Chen

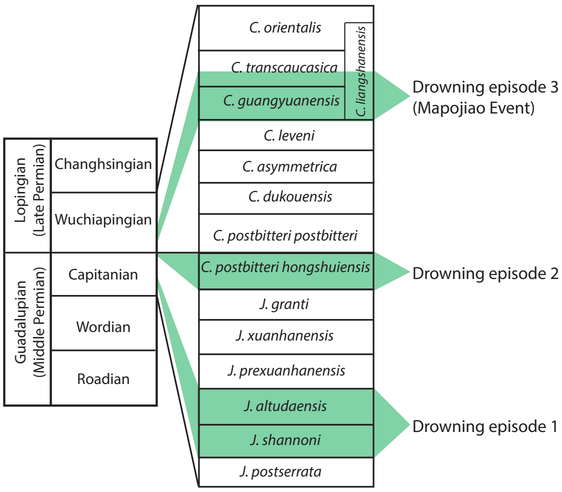

Fig. 1 Conodont zonation of the Capitanian and Wuchiapingian (Mei et al., 1998; Shen et al., 2010), as well as biostratigraphic position of the drowning and volcanic events (Bagherpour et al., in review).

et al., 2011; Wei et al., 2012). However, alternative mechanisms such as upwelling of oxygen depleted waters (Saitoh et al., 2013b) and diagenetic alteration (Jost et al., 2014) have also been considered. Unlike the end-Permian mass extinction, which is accompanied by a synchronous and worldwide CIE toward lower values (e.g. Korte and Kozur, 2010), C isotope excursions spanning G-L interval occurred at different times as indicated by biostratigraphic age controls (Saitoh et al., 2013b; Jost et al., 2014; Shen et al., 2013). Moreover, these CIEs are only present when associated with drowning events. This strongly calls into question the significance of released light C from Emeishan volcanism as the main driver of CIEs during the G-L interval.

Most studies focused on the Capitanian and only limited data were available for the Wuchiapingian. In order to assess any extension of ELIP volcanism in time and related paleoenvironmental consequences in post-Capitanian times, this study includes new data from high-resolution coupled carbon (carbonate and organic) and strontium isotope records of the Mapojiao Event (Bagherpour et al., in review) (Mapojiao section, Fig. 2, 3). Rock-Eval and palynofacies analyses are used to establish the relative proportions of terrestrial and marine organic matter and contribute to a sound interpretation of the C isotope record.

2. Geological setting and studied sections

2.1. Overview

During the Late Permian, the South China Block was located near the equator in the eastern margin of the Paleotethys (Fig. 2a) (Enkin et al., 1992). The Middle to Late Permian transition in South China is associated with the emplacement of ELIP, which covers an area of at least 0.3×10^6 km^2 distributed across South China (Guizhou, Yunnan, and Sichuan provinces) and northern Vietnam (Songpan-Ganzi terrane) (Ali et al., 2002; Shellnutt, 2014). With estimated volumes ranging from ~0.3×10^6 km^3 to ~0.6×10^6 km^3, the ELIP represents a modest-sized LIP with respect to others, such as Siberian Traps (Shellnutt et al., 2014). Shortly before ELIP eruption, SW China was partially covered with epeiric seas (Jerram et al., 2016). In Yunnan and western Guizhou, the Guadalupian shallow-marine limestone Maokou Fm. ended with the deposition of ELIP volcanic

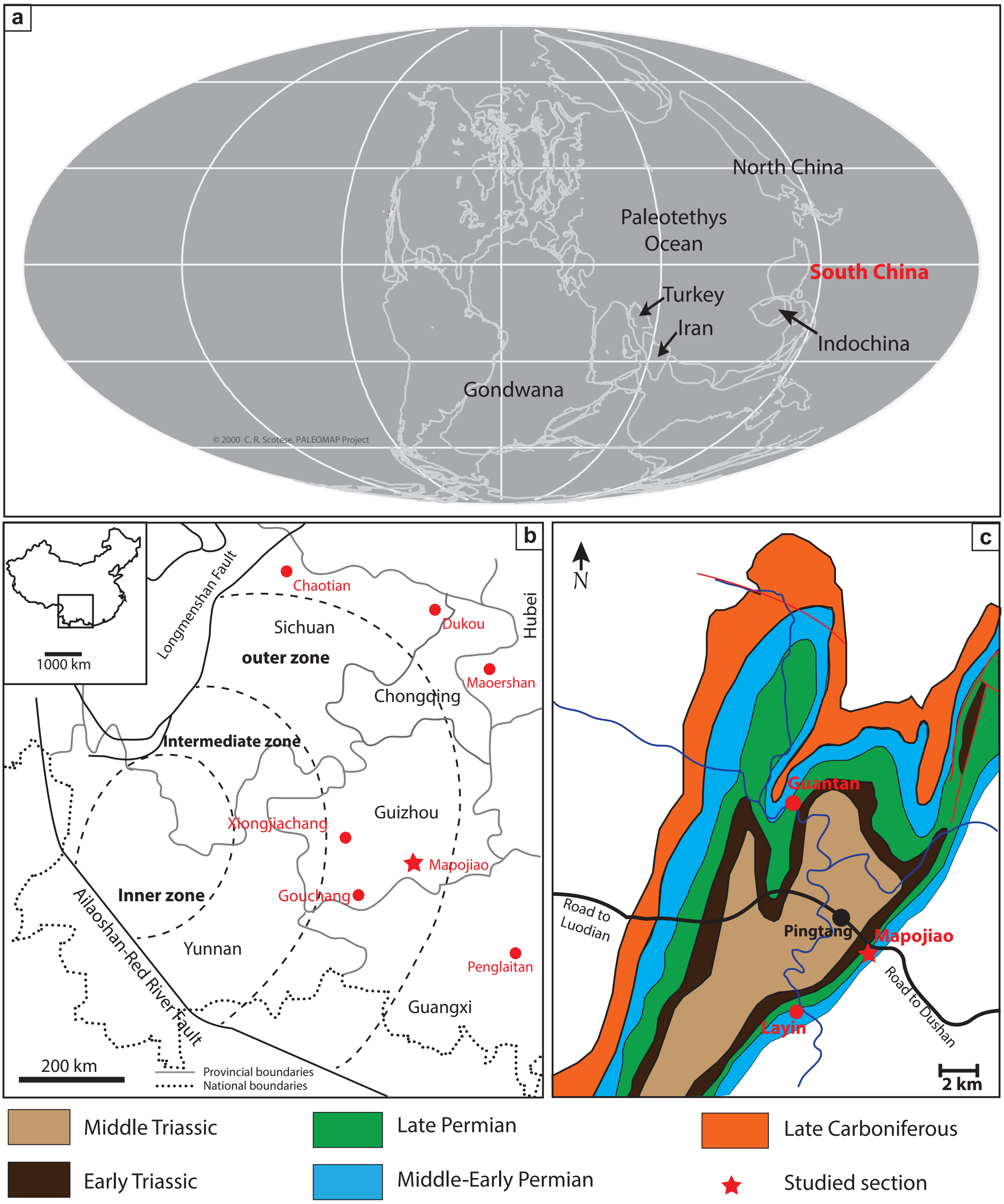

Fig. 2 Location of the study site**. a,** Paleogeographic map of the late Permian (modified from PALEOMAP Project; www.scotese.com) **b**, Distribution of the G-L interval sections with carbon isotope records in concentric inner, intermediate and outer zones around the hypothetical core of the surficial uplift (modified from He et al., 2003; Zhao et al., 2016). **c**, Geologic map of the Pingtang syncline and location of the studied sections in S. Guizhou (modified from Guizhou Bureau, 1987).

rocks, which are thinning eastward. In eastern Guizhou, the volcanic flows of ELIP are absent but their erosional products (e.g., Wangpo Shale) are intercalated between the Maokou and Wuchiaping formations. Based on differential pre-volcanism erosion, He et al. (2003) recognized three concentric zones around the ELIP (Fig. 2b). In the “inner zone” (W. Yunnan and S. Sichuan), the top of Maokou Fm. is strongly eroded due to a pre-eruption uplift. The thickness of Maokou Fm. progressively increases in the surrounding “intermediate zone” (E. Yunnan and N. Sichuan), where lesser amount of uplift and erosion occurred. Beyond this intermediate zone is the “outer zone”, which is characterized by even less erosion as suggested by the maximal thickness Maokou Fm. According to He et al. (2003), fusulinids-based biostratigraphic ages at the top of the Maokou Fm. also show a younging trend toward the “outer zone”, thus supporting the uplift model. However, hydromagmatic deposits of the initial phase of ELIP indicate submarine volcanism, which apparently contradicts the pre-eruption uplift model (Ukstins Peate and Bryan, 2008). Moreover, conodont biostratigraphy does not confirm any younging trend of the upper boundary of the Maokou Fm. and the previous diachronous ages have been argued to result from a low resolution of fusulinid biostratigraphy and/or a strong influence of facies control (Sun et al., 2010).

The studied area is located in Pingtang County (S. Guizhou) in the outer zone of the ELIP. A Carboniferous to Middle Triassic succession is exposed in both limbs of the 50 km long NE-SW Pingtang syncline (Fig. 2b, c). The Middle and Late Permian succession in the Pingtang syncline includes the Guadalupian Maokou Fm. and the Lopingian, Wuchiaping and Talung formations. The Mapojiao Event consistently occurs in the lower part of the Wuchiaping Fm. as documented at the Mapojiao, Layin and Guantan sections. The Mapojiao section (25°49′21.8″N; 107°21′16.3″E) is well exposed along a fresh road-cut in the eastern limb of the Pingtang syncline (Figs. 2c, 3) and is used here as a reference section. In order to obtain additional geochemical data from the lowermost part of the section, an additional section named Mapojiao B was also investigated. It is located 800 m SW of the main section in an intermittently exploited quarry.

2.2. Lithological subdivision, facies, and depositional setting

The studied interval at Mapojiao is subdivided into four lithostratigraphic units (Units A-D) (Fig. 3a, b, 4). The lower 35 m of the section (Unit A) is composed of light-grey massive limestone (Fig. 3a) yielding an abundant and diversified shallow-marine benthic fauna including calcareous sponges, bryozoans, *Tubiphytes*, brachiopods and crinoids. One ash layer is intercalated in the basal part of this unit. Additionally,

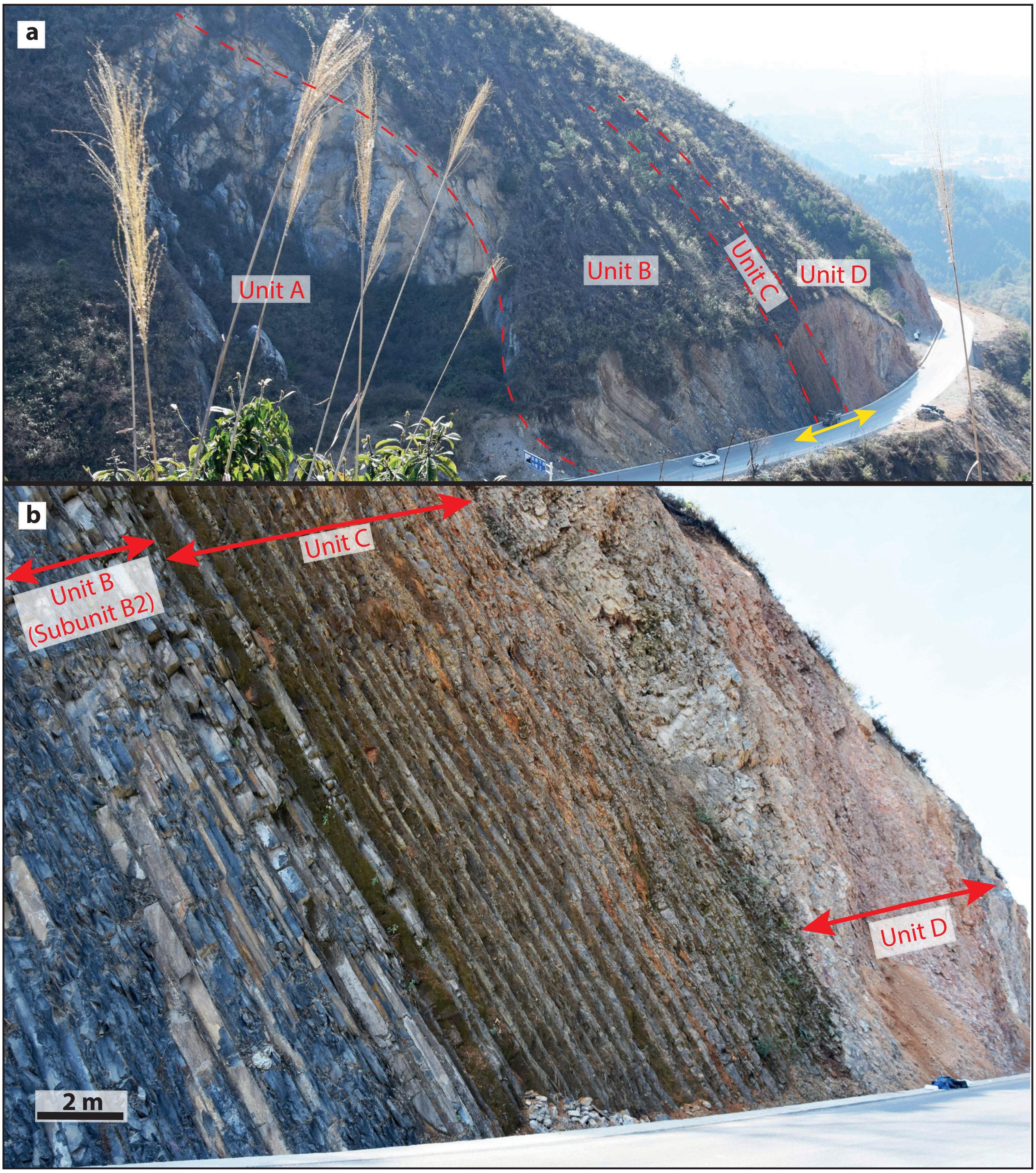

Fig. 3 Outcrop photographs of the Mapojiao section. **a,** Panoramic view of the road-cut Mapojiao main section. Dashed lines mark the boundaries between the units. **b**, Close-up photograph of the interval marked by the yellow arrows in Fig. 3a showing the uppermost part of thin-bedded black limestone of Unit B, alternating volcanogenic silt and sandstone of Unit C, and lower part of limestone of Unit D. Note the sharp and conformable contacts between the units.

two ash layers were also found from the lateral equivalent of Unit A at Mapojiao B. The carbonate content in Unit A is very high (>88 %) and remains stable throughout the unit (Fig. 4). The overlying 31 m-thick Unit B is further subdivided into two subunits (B1 and B2). Subunit B1 is characterized by medium-bedded, dark-grey limestone containing abundant disseminated pyrite, siliceous sponge spicules, conodonts, some radiolarians, and rare smaller foraminifera and ostracods. Two volcanic ash layers are intercalated within Subunit B1. The following Subunit B2 consists of organic-rich, thin-bedded black limestone (Fig. 3b), with abundant disseminated pyrite crystals, radiolarian, hexactinellids sponge spicules, and rare smaller foraminifera and ostracods. Two ash layers are also present in the middle part of Subunit B2. Carbonate content progressively declines from the base of Subunit B1 and reaches a minimum of ~30 % at the top of Subunit B2 (Fig. 4). The overlying (8 m-thick) Unit C consists of about 20 carbonate-free, graded volcanogenic sandstone and silt cycles (averaging 40 cm in thickness) interpreted as distal turbidites. The section ends with medium-bedded, cherty, nodular limestone of Unit D (Fig. 3b, 4). The lower half of Unit D consists of silicified limestone yielding radiolarian and sponge spicules, whose abundance progressively decrease in the upper half of the unit where they are replaced by benthic faunas. Carbonate content remains low in the lower part of the unit but increases up section. Reconstruction of sedimentary environments indicates a remarkable drowning event here termed Mapojiao Event with deposition of Unit A in a shallow subtidal setting, followed by slope to basinal facies of Subunit B1 and Subunit B2. Deposition of Unit B was interrupted by the intercalation of volcanogenic turbidites of Unit C, and ended with Unit D that records a shallowing upward trend from basinal to subtidal settings (Bagherpour et al., in review).

2.3. Age control

A high resolution biostratigraphic data from the recent study of the conodont fauna from the Mapojiao section by Bagherpour et al. (in review) is used. Five index species in Units A and B were recognized and all were assigned to *Clarkina*. No conodonts were retrieved from the uppermost part of Subunit B2 and higher units. *Clarkina ?dukouensis* is the stratigraphically oldest conodont recovered from the Mapojiao section. After a 20 m barren interval, *Clarkina asymmetrica*, *Clarkina leveni*, *Clarkina guangyuanensis*, and *Clarkina ?transcaucasica* (or *Clarkina guangyuanensis* transitional to *Clarkina transcaucasica*) successively appear in ascending order and range through Unit A and Unit B (Fig. 4). The upper two thirds of the Wuchiaping Fm. are commonly assigned to the *Clarkina orientalis* Interval Zone (IZ) in South China (Shen et al., 2010), which is consistent with the entire development of the

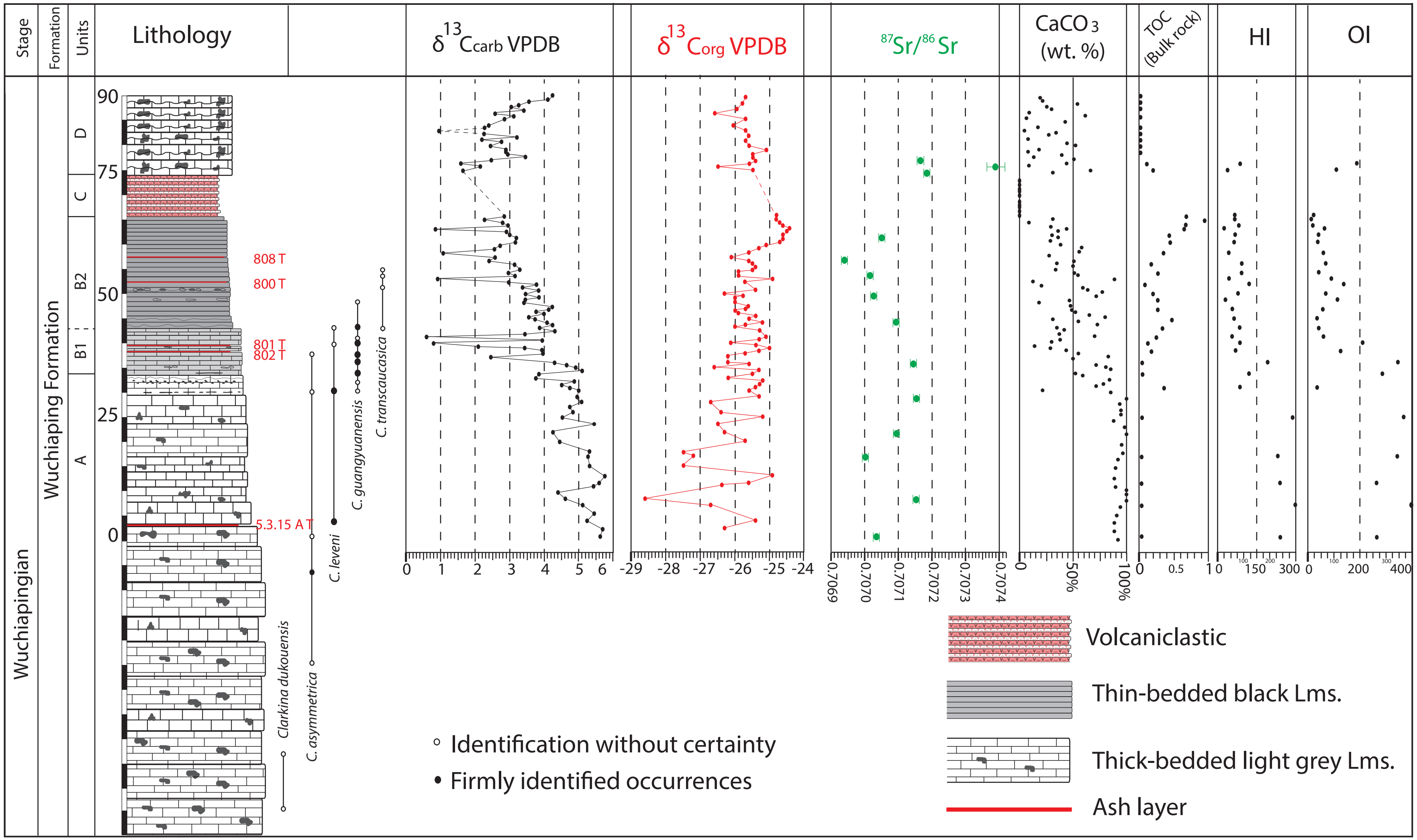

Fig. 4 δ $^{13}C_{carb}$, δ $^{13}C_{org}$, $^{87}Sr/^{86}Sr$, carbonate content, TOC, hydrogen index (HI), and oxygen index (OI) data of the Mapojiao section. Stratigraphic range of conodont taxa are from Bagherpour et al. (in review).

formation in Pingtang syncline and the age constraints obtained for its lower part.

3. Material and methods

The Mapojiao section was logged bed by bed and rock samples for carbon, oxygen and strontium isotope compositions ($\delta^{13}C_{carb}$, $\delta^{18}O_{carb}$, $^{87}Sr/^{86}Sr$) of bulk micrite, bulk organic carbon isotope ($\delta^{13}C_{org}$) and composition of organic matter (Rock-Eval and palynofacies) were collected.

3.1. Carbonate carbon and oxygen stable isotope analyses

A total of 116 unweathered rock samples (21 from Unit A, 58 from Unit B, 11 from Unit C, and 26 from Unit D) (Supplementary material S1) for $\delta^{13}C_{carb}$ and $\delta^{18}O_{carb}$ measurements of bulk micrite were collected. Samples were carefully cleaned, cut, and drilled to produce a fine powder. Diagenetic calcite veins, cracks, stylolites, and large skeletal particles were excluded.

Additionally, a total of 126 ultrahigh-resolution samples (Supplementary material S2) were also collected from OM-poor, shallow-marine limestone beds bracketing ash layers of Unit A in Mapojiao B section (Supplementary material S3, S4), and from OM-rich, deep-marine limestone beds adjacent to the ash layers of Unit B in Mapojiao main section, (Supplementary material S5, S6, S7).

The C- and O- isotope composition of the carbonates were measured with a GasBench II linked to a DeltaPlus XL mass spectrometer (Thermo-Fisher Scientific) according to a method adapted after Spötl and Vennemann (2003). Carbonates were reacted at 70 ºC with 100 % orthophosphoric acid and the extracted CO_2 calibrated against a number of in-house Carrara Marble (CM) replicates for acid fractionation and normalization of the $d^{13}C$ and $d^{18}O$ values expressed at the permil scale. The CM standard was, in turn, calibrated against $\delta^{13}C$ and $\delta^{18}O$ values of NBS-19 (+1.95 and –2.20 ‰, relative to VPDB). Average reproducibility of about 8 CM's analysed in each run of 40 samples is better than 0.06 ‰ for $d^{13}C$ and 0.08 ‰ for $d^{18}O$ values.

3.2. Organic carbon stable isotope analyses

In order to measure the bulk organic carbon isotope composition ($\delta^{13}C_{org}$), 88 samples (17 Unit A, 54 Unit B, 0 Unit C, and 17 Unit D) (Supplementary material S1) were pulverized to <100 µm using a puck mill. About 5 g of powdered samples were dissolved in 6 M hydrochloric acid to remove all carbonates. After centrifuging, residues were rinsed with deionized water and centrifuged until neutrality was reached. The residues were dried over night at 45 ˚C and $\delta^{13}C_{org}$ values of the

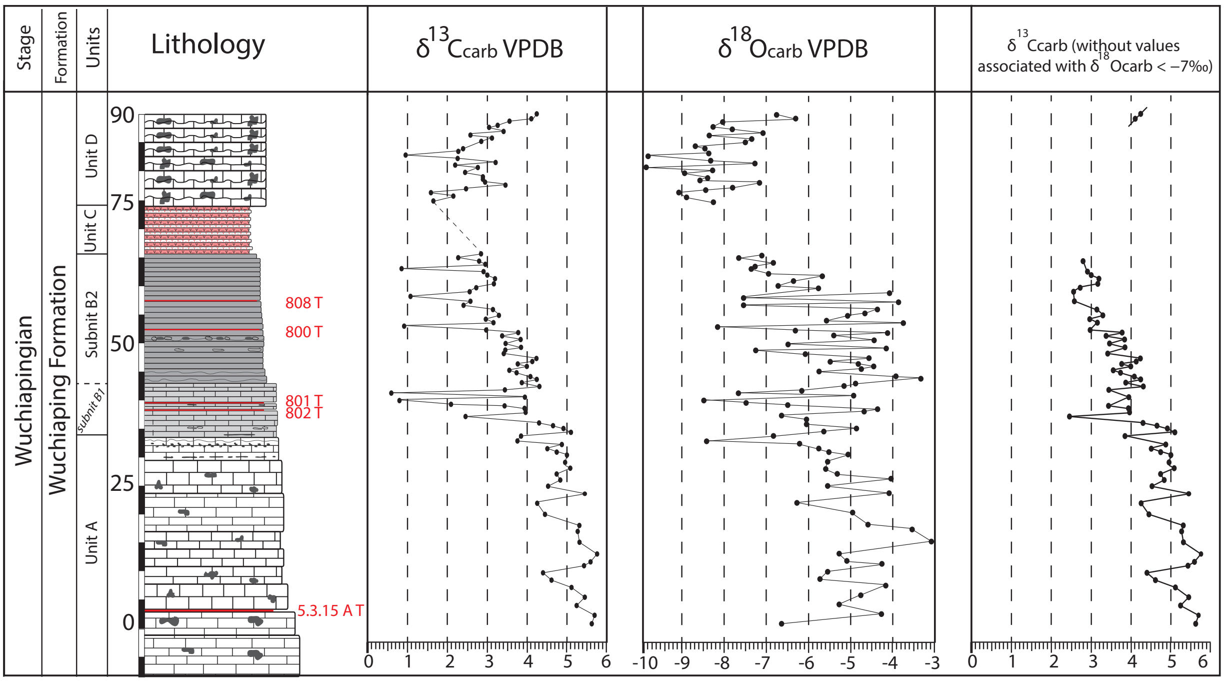

Fig. 5 Comparing $\delta^{13}C_{carb}$ and $\delta^{18}O_{carb}$ and $\delta^{13}C_{carb}$ profile after removing samples with $\delta^{18}O_{carb}$ values < −7 ‰.

homogenized residues were measured using a Carlo Erba 1500 elemental analyser connected to a ThermoFisher Delta V Plus mass spectrometer. The samples were individually wrapped in tin foil cups and sequentially allowed to react with an injected quantity of oxygen while continuously flushed with He carrier gas. The sample was oxidized in the reactor at about 1050ºC using cobalt(II) oxide as the catalyst. Excess oxygen in the He-stream was adsorbed in a reactor column filled with metallic Cu held at 500 ºC. The CO_2 produced was passed over a magnesium perchlorate (Mg[ClO4]2) trap to remove H_2O and a gas chromatograph to separate the N_2 from the CO_2, before the CO_2 is carried by the He-stream into the mass spectrometer for isotopic analysis. The reproducibility of several in-house standards used is better than 0.1 ‰ and calibrated against USGS-24 graphite (–16.0 ‰ VPDB) and NBS-22 oil (–29.6 ‰ VPDB).

3.3. Rock-Eval analyses and palynofacies

The quantification and characterization of the organic matter of 39 samples (5 from Unit, 22 from Unit B, 0 from Unit C, and 12 from Unit D) (Supplementary material S1) were performed on powdered whole rock using a Rock-Eval 6 following the method described by Espitalié et al. (1985, 1986) and Behar et al. (2011). The IFP 160000 standard was used to calibrate the measurements. The measured values include total organic carbon (TOC), the Hydrogen Index (HI as mg HC/g TOC), and the Oxygen Index (OI as mg CO2/g TOC), which permit an overall characterization of the sedimentary organic matter (OM). The HI and OI indices are proportional to the H/C and O/C ratios of the organic matter, respectively, and can be used for OM classification in Van-Krevelen-type diagrams (Espitalié et al. 1985, 1986).

In order to gain a better understanding of the terrestrial and marine fraction of OM in each unit, 8 samples were selected and treated with hydrochloric and hydrofluoric acid following the standard techniques of Traverse (2007). The residues were sieved with a 15 µm mesh screen and mounted on slides for analysis of the particulate organic matter (POM or kerogen). The POM has been divided into terrestrial and marine OM fractions. The terrestrial POM includes mainly translucent and opaque woody particles and rare spores and pollen. The marine POM includes a main fraction of amorphous organic matter (AOM) and a smaller fraction of acritarchs and foraminiferal test linings.

3.4. Strontium isotope compositions ($^{87}Sr/^{86}Sr$)

A total of 14 bulk rock samples (5 from Unit A, 6 from Unit B, 0 from Unit C, and 3 from Unit D) (Supplementary material S1) were carefully cleaned, cut, and drilled to produce a fine powder. Diagenetic calcite veins, cracks, stylolites, and large skeletal particles were excluded.

A few mg of the powdered carbonate material were dissolved in 2.2 M high purity acetic acid during 1 to 2 hours at room temperature in conical shaped 2 ml vials. The solutions were centrifuged and the supernatant was recovered and transferred to Teflon vials, where it was dried down on a hot plate. The residue was redissolved in a few drops of 14 M HNO3 and dried down again, before Sr separation from the matrix using a Sr-Spec resin. The Sr separate was redissolved in 5 ml of ~2% HNO3 solutions and ratios were measured using a Thermo Neptune PLUS Multi-Collector ICP-MS in static mode. The 88Sr/86Sr (8.375209) ratio was used to monitor internal fractionation during the run. Interferences at masses 84 (84Kr), 86 (86Kr) and 87 (87Rb) were also corrected in-run by monitoring 83Kr and 85Rb. The SRM987 standard was used to check external reproducibility, which on the long-term (more than 100 measurements during one year) was 10 ppm (1σ). The internally corrected 87Sr/86Sr values were further corrected for external fractionation (due to a systematic difference between measured and a nominal standard ratio of the SRM987 of 87Sr/86Sr = 0.710248: McArthur et al., 2001) by a value of -0.039‰ per amu. The 2-sigma analytical uncertainties of Sr isotope measurements are ranging between 0.000006 and 0.000028.

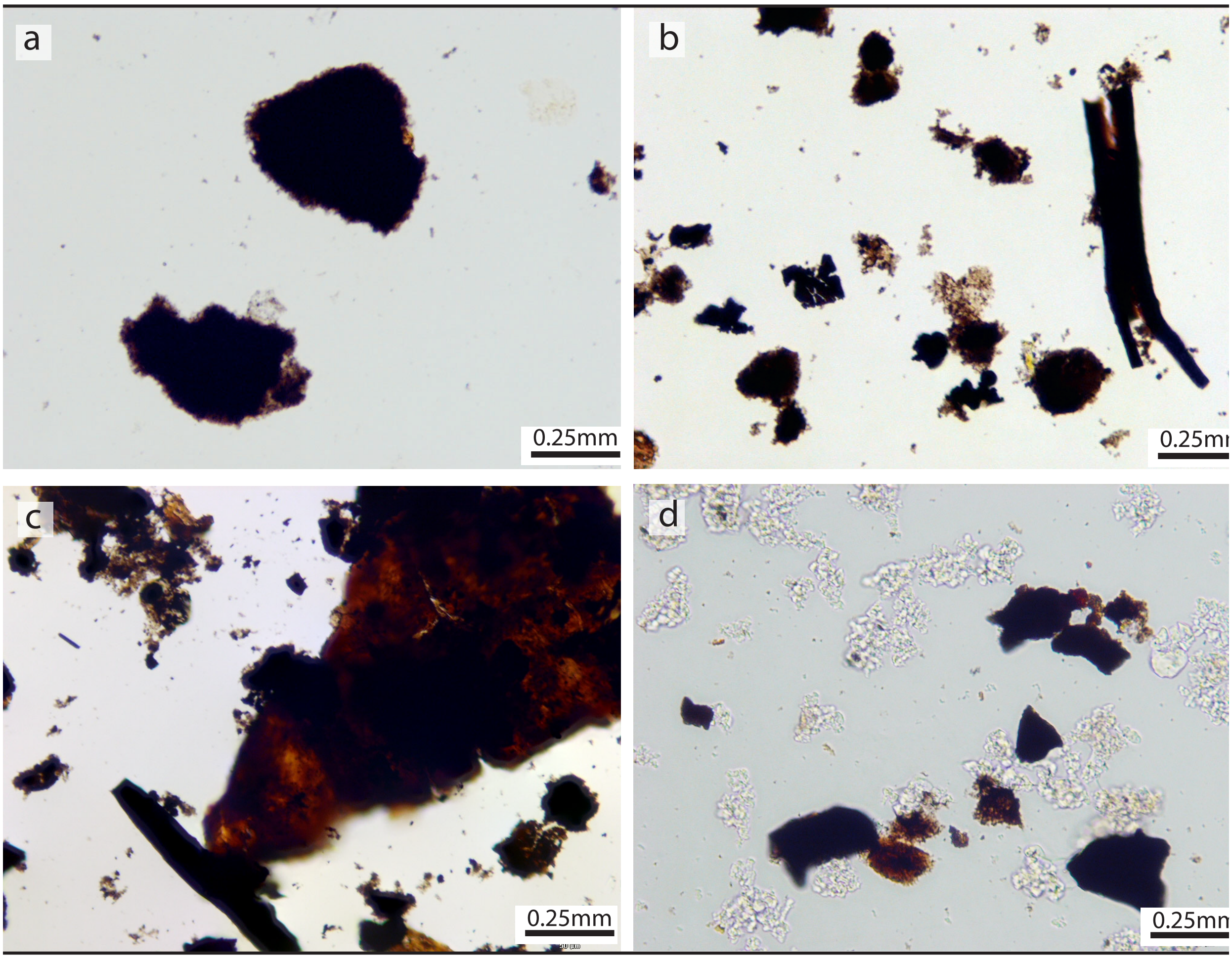

Fig. 6 Photomicrographs of sieved palynofacies slides from the Mapojiao section. **a,** AOM dominated palynofacies from Unit A. **b**, Palynofacies with equal amount of terrestrial and marine POM from Subunit B1. **c,** Terrestrial POM dominated palynofacies from Subunit B2. **d,** AOM dominated palynofacies from Unit D.

4. Results

4.1. Carbon and oxygen isotope composition of Carbonates

The $\delta^{13}C_{carb}$ profile shows a plateau of high values at around 5 ‰ (ranging 4.5 to 5.5 ‰) for the shallow-marine bioclastic limestone of Unit A (Fig. 4). The stability of the C isotope profile in this unit is confirmed by the ultrahigh-resolution record around the ash layers found in the auxiliary section Mapojiao B (Supplementary material S3, S4).

The $\delta^{18}O_{carb}$ values in Unit A have a range between -3 and -7 ‰ and tend to covary with $\delta^{13}C_{carb}$ (Fig. 5).

Above this interval, $\delta^{13}C_{carb}$ values are lower by 1–1.5 ‰ from 5 ‰ to 3.5–4 ‰ in the dark-grey limestone of Subunit B1 (Fig. 4). The upper part of this excursion toward lower values is marked by two low-$d^{13}C_{carb}$ peaks down to 0.8 ‰ and 0.6 ‰ just above two ash layers (801T and 802T). The ultrahigh-resolution carbon isotope records around these ash layers are given in Supplementary material S5. They show 2 ‰ and

1 ‰ CIEs towards lower values below and above the upper ash layer (801T), respectively.

The $\delta^{18}O_{carb}$ values of Subunit B1 have a range between -4 and -8 ‰ and do not show any covariation with $\delta^{13}C_{carb}$ (Fig. 5). However, a correlation between $\delta^{18}O_{carb}$ and $\delta^{13}C_{carb}$ values around the upper ash layer (801T) in this subunit is noted (Supplementary material S5).

In the basal 7 m of Subunit B2, $\delta^{13}C_{carb}$ values are homogeneous around 4 ‰ and gradually decrease to values between 2.5 and 3 ‰ in the upper part of this subunit. Within the upper part, fluctuations are of higher amplitude than in the lower part of Subunit B2. Three horizons with values as low as 1 ‰ are measured in Subunit B2. Two of these three peaks are in beds immediately overlying ash layers (800T and 808T) (Fig. 4). The ultrahigh-resolution $\delta^{13}C_{carb}$ data around the lower ash layer (800T, Supplementary material S6) have a 2.5 ‰ CIE towards lower values immediately below the ash layer 800T and a shift towards higher values just above it. The $\delta^{13}C_{carb}$ record around the upper ash layer (808T, Supplementary material S7) shows a decrease in $\delta^{13}C_{carb}$ of 1 ‰ below and of 2.5 ‰ above the ash layer.

The $\delta^{18}O_{carb}$ values of Subunit B2 vary between -3 and -8 ‰ and do not show any covariation with $\delta^{13}C_{carb}$ (Fig. 5). Here again, a correlation between $\delta^{18}O_{carb}$ and $\delta^{13}C_{carb}$ is observed around the ash layers in this subunit (Supplementary material S6, S7).

The absence of carbonate rocks in Unit C generates the gap in the $\delta^{13}C_{carb}$ record.

At the base of Unit D, $\delta^{13}C_{carb}$ values have a minimum value of 2 ‰ that returns to values of 4 ‰ in the next overlying layers. Within Unit D, one bed with a sharp decrease of 1 ‰ is recorded in Unit D, but no preserved ash layer could be observed near this peak.

The $\delta^{18}O_{carb}$ values in this unit have a range between -6 and -10 ‰ and show a covariation with $\delta^{13}C_{carb}$ (Fig. 5).

The overall changes of $\delta^{13}C_{carb}$ values document a plateau of high values (ca. 5 ‰) in Unit A followed by a 3.5-4 ‰ decrease starting at the base of Unit B and a 2 ‰ increase again in Unit D. This general trend is interrupted by outliers towards lower values reaching ca. 1 ‰. Most of these are associated with ash layers intercalated within OM-rich limestone. These outliers may result from the diagenetic alteration of $\delta^{13}C_{carb}$ values (remineralization of OM) in higher TOC limestone adjacent to volcanic ashes. The $\delta^{18}O_{carb}$ values have a range between -3 and -10 ‰ and do not show covariation with the $\delta^{13}C_{carb}$ in Units A and B, although a covariation is detected in Unit D.

4.2. Carbon isotope compositions of organic matter

Unit A is characterized by $\delta^{13}C_{org}$ values ranging from -25 to -28.5 ‰ with a median value

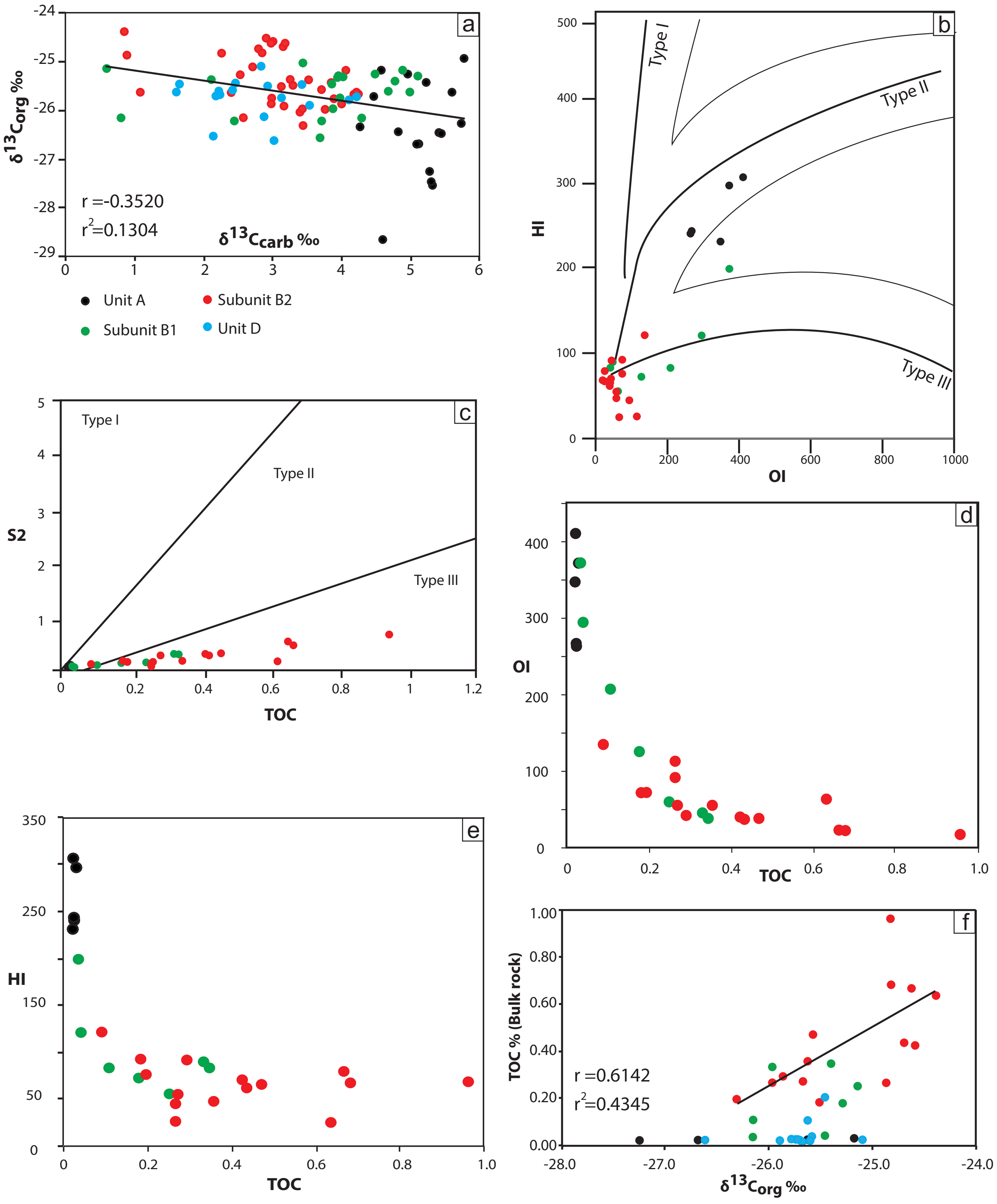

Fig. 7. a, $\delta^{13}C_{carb}$ and $\delta^{13}C_{org}$ cross-plot. **b,** Oxygen index (OI) and hydrogen index (HI) cross-plot, and the kerogen types fields as defined in Tyson (1995). **c**, S2 and TOC cross-plot (Langford & Blanc-Valleron, 1990). **d**, OI and TOC cross-plot. **e,** HI and TOC cross-plot.

of -26.4 ‰ and major fluctuations of up to 3.5 ‰ (Fig. 4).

In Subunit B1, the amplitude of the fluctuations decreases and the values have a range between -25 and -26 ‰, with a median value of -25.4 ‰. These stable values extend to the lower 15 m of Subunit B2, with a median value of 25.6 ‰. Subsequently, the upper part of Subunit B2 is marked by a rapid 1 ‰ change towards higher $\delta^{13}C_{org}$ values with a maximum of -24.5 ‰ (median: -24.7 ‰).

In Unit D, above the volcanogenic silt and sandstones of Unit C, the $\delta^{13}C_{org}$ profile displays a 1 ‰ decrease and again the values have a range between -25 and -26 ‰ (median value: -25.7‰).

The overall change in the $\delta^{13}C_{org}$ profile has a 2 ‰ increase in $d^{13}C_{org}$ shift in Units A and B, followed by a 1 ‰ shift to lower values again in Unit D. Moreover the variation in the range of the values decreases from shallow-marine, light-grey limestones of Unit A to basinal and organic-rich limestones of Unit B (Fig. 4).

4.3. Rock-Eval pyrolysis and palynofacies

In Unit A, TOC values of bulk rock samples are low. At the base of Subunit B1 they start increasing and reach a maximum of 1 % at the top of Subunit B2, although a decrease back to 0.3 % is recorded in the lower part of Subunit B2. The base of Unit D is characterized by a return to low TOC values (Fig. 4).

In Unit A, HI values range from 230 to 305 mg HC/g TOC and decrease in Unit B where the values are ranging from 25 to 198 mg HC/g TOC. Subunits B1 and B2 show a minor decreasing trend. HI values remain low (varying from 39 to 84 mg HC/g TOC) in the basal part of Unit D. In the upper part of Unit D, the low TOC content did not allow to measure the HI index values.

OI values in Unit A have a range from 410 to 263 mg HC/g TOC and decrease throughout Unit B, where they range from 16 to 372 mg HC/g TOC. At the base of Unit D, OI values increase but very low TOC does not allow the measurement of the OI values in the upper part of this unit.

Based on palynofacies observations, Unit A is dominated by marine POM (Fig. 6a). In Unit B, marine POM decreases and terrestrial POM increases progressively. In Subunit B1, each fraction constitutes about half of the POM (Fig. 6b) and subsequently, terrestrial POM reaches a maximum of 80 % and marine POM a decrease to 20 % in Subunit B2 (Fig. 6c). Marine POM again becomes dominant in low TOC limestones of Unit D (Fig. 6d). The boundary between Unit A and B is characterized by a significant input of terrestrial POM, whose dominance progressively increases up-section, until the end of unit B.

In general, the change in $\delta^{13}C_{org}$ towards higher values is associated with an input of terrestrial POM, increasing TOC values, and decreasing HI and OI values.

4.4. Strontium isotope ($^{87}Sr/^{86}Sr$)

$^{87}Sr/^{86}Sr$ values have a range from 0.70738 to 0.70694 throughout the Mapojiao section. Unit A is characterized by fluctuation in $^{87}Sr/^{86}Sr$ around 0.7071 and a minor positive excursion (from 0.70700 to 0.70715) in the upper half of this unit (Fig. 4). The overlying Unit B (Subunits B1 and lower half of Subunit B2) have much lower values, from 0.70714 to the minimum of 0.70694 in the middle of Subunit B2. Subsequently, this change is followed by ratios that reach a maximum of 0.70738 in Unit D. The overall changes in $^{87}Sr/^{86}Sr$ indicate a change to low ratios in Unit B, which is followed by an excursion in the upper part of Subunit B2 and Unit D towards higher ratios.

5. Discussion

5.1. Comparison of $\delta^{13}C_{carb}$ records across G-L interval

Comparison of C isotope records across G-L interval indicates that the magnitude and biostratigraphic age of the supposed global CIE toward lower values at the G-L boundary is highly variable between different sections in South China and elsewhere, as already stressed by Jost et al. (2014). In the Chaotian section, the oldest CIE toward lower values has a magnitude of 7 ‰ in $d^{13}C_{carb}$, started in the *Jinogondolella postserrata* – *Jinogondolella shannoni* IZ (early Capitanian) and ended at the inferred G-L boundary (Saitoh et al., 2013b). The Xiongjiachang section documents a younger CIE with a magnitude of 7 ‰ from the *Jinogondolella altudaensis* IZ (mid-Capitanian) up to the *Jinogondolella xuanhanensis* IZ (Bond et al., 2010b; Wignall et al., 2009). Intriguingly, the entire Capitanian stage represents a plateau of heavy values (around 4 ‰) at the Penglaitan section, and only a minor excursion toward lower values (ca. 1 ‰) is recorded in earliest Wuchiapingian (Jost et al., 2014). At the nearby Tieqiao section, however, a CIE toward lower values with a magnitude of 6.5 ‰ in the earliest Wuchiapingian has been documented (Yan et al., 2013). Finally, the Mapojiao section represents a distinct, stratigraphically younger excursion with a magnitude of 3.5 to 4 ‰ towards lower values. It starts in the *Clarkina guangyuanensis* IZ and ends in the *Clarkina transcaucasica* IZ. Unpredictably, contemporaneous intervals in Shangsi and Dukou sections are characterized by homogeneous high values (Shen et al., 2013). The temporal and geographic distribution of C isotope excursions during G-L interval indicates different processes compared to the end-Permian, where a significant and synchronous global excursion toward lower values is recorded in numerous sections (e.g. Korte and Kozur, 2010).

The sedimentology indicates that the Capitanian (Chaotian and Xiongjiachang sections) and early Wuchiapingian (Tieqiao and Mapojiao sections) CIEs toward lower values were all recorded in deep-marine, organic-rich radiolarian-spiculitic rocks. However, in the Gouchang section (W. Guizhou), a significant (7 ‰) CIE toward lower values within shallow-water carbonates bracketed between basaltic flows has been argued to be associated with the mid-Capitanian "mass" extinction. This CIE has been correlated, without independent paleontological age control, with CIEs toward lower values documented in Chaotian and Xiongjiachang with the assumption that it represents a global signal across different types of depositional environments (Wignall et al., 2009). The disparity of CIEs in time and space makes $\delta^{13}C$ curves a misleading tool for correlations in the Capitanian-Wuchiapingian time interval. The local association of CIEs toward lower values with distinctive drowning episodes (clusters 1 to 3 of Bagherpour et al. in review) during this interval suggests the influence of local factors, rather than global changes in the carbon cycle.

5.2. Mechanisms for the excursions towards lower $\delta^{13}C_{carb}$ values

ELIP volcanic activities have been the most commonly invoked causal mechanism among different hypotheses for C isotope excursions in the G-L interval (e.g. Ganino and Arndt, 2009; Wignall et al., 2009; Bond et al., 2010b; Chen et al., 2011). According to Wignall et al. (2009) and Ganino and Arndt (2009), the amplitude of the Capitanian excursion towards lower values is too large to be solely attributed to volcanic CO_2, and release of thermogenic C from contact metamorphism has been called upon. These authors suggested that carbon release from heating of dolomite ($\delta^{13}C$ = 0 ‰) and metamorphic release of CO_2 from organic carbon ($\delta^{13}C$ = -22 ‰) due to the emplacement of the ELIP resulted in the large change in $d^{13}C_{carb}$ during the end-Guadalupian. Retallack and Jahren (2008) proposed that a voluminous release of isotopically light methane from the contact metamorphism of the ELIP resulted in an excursion toward lower values at the base of Wuchiapingian. However, Saitoh et al. (2013) argued that the early Capitanian change toward lower values at the Chaotian started two conodont zones earlier than the onset of the ELIP (during the *Jinogondolella altudaensis* IZ), which excludes the input of associated volcanic CO_2 gas. These authors rather suggested that "the input of inorganic carbon of low $\delta^{13}C$ values by upwelling of the oxygen-depleted waters" caused this shift toward lower values. Alternatively, the lack of any covariation between $\delta^{13}C$ and $\delta^{44/40}Ca$ records from Chaotian and Penglaitan, as would be expected in case of massive volcanic CO_2 or methane clathrate destabilization, led Jost et al. (2014) to relate the perturbation in C isotope across the G-L interval to "local burial conditions or diagenetic effects", with which our interpretation is compatible.

Comparison of the excursions in C-isotope compositions towards lower values with concomitant facies changes may contribute to distinguish the plausible driving mechanism for C isotope perturbations during this interval. According to Sun et al. (2010), the middle Capitanian facies change (e.g., at Chaotian and Xiongjiachang) from shallow-marine limestone of the Maokou Fm. to radiolarian-spiculitic facies represents an ELIP-related drowning and volcanic event. Later occurrences of the same type of events again at the G-L boundary (Maoershan and Dukou) and early Wuchiapingian (Mapojiao) support a repetition of the same sedimentary processes associated with similar changes in isotopic composition. Despite the lack of high-resolution C-isotope data from Maoershan and Dukou, coincidence of excursions toward lower values and ELIP-related drowning events is well exemplified from Chaotian (Saitoh et al., 2013b) and Xingjiachang (Wignall et al., 2009) (first cluster of drowning events) and Mapojiao (third and youngest cluster of drowning events). The lack of lateral reproducibility of theses CIEs in South China and elsewhere undermines any global perturbation in the global carbon cycle. Hence, the association of CIEs and ELIP-related drowning events indicates the influence of local conditions such as bathymetry and increased burial of terrestrial organic matter on C-isotope record.

5.3. Diagenetic alteration of $\delta^{13}C_{carb}$

Lowering of the $\delta^{13}C_{carb}$ values can result from global changes in the carbon cycle, regional isotopic variation of seawater, or from diagenetic alteration. In comparison to $\delta^{13}C_{carb}$, $\delta^{18}O_{carb}$ values are more prone to diagenetic alternation (e.g. Given and Lohmann, 1985; Weissert et al., 2008) and covariation of $\delta^{13}C_{carb}$ and $\delta^{18}O_{carb}$ may indicate a diagenetic alteration of $\delta^{13}C_{carb}$ (e.g. Brand and Veizer, 1981). However, correlation between $\delta^{13}C_{carb}$ and $\delta^{18}O_{carb}$ does not systematically imply diagenetic alteration (Marshall, 1992; Ullmann and Korte, 2015; Schobben et al., 2016). Moreover, based on the fact that limestone with $\delta^{18}O_{carb}$ values lower than -7 ‰ imply precipitation at > 45 °C for 0 ‰ seawater (Hays and Grossman, 1991), Jost et al. (2014) convincingly argued that samples with $\delta^{18}O_{carb}$ lower than -7 ‰ also indicate diagenetic alteration.

Comparison of $\delta^{13}C_{carb}$ and $\delta^{18}O_{carb}$ records from the Mapojiao main section (Fig. 5) only shows a covariation in Unit D. Moreover, after removing samples whose $\delta^{18}O_{carb}$ values < -7 ‰, the first order trend of $\delta^{13}C_{carb}$ recorded in Unit A and Unit B does not change but the positive shift and most of the samples of Unit D disappeared (Fig. 5). Two points in the upper most part of Unit D with relatively high $\delta^{13}C_{carb}$ values (4 ‰) remain after this filtering and support that these shifts towards high values can be interpreted as primary. Petrographic analysis (at the thin section scale) of samples from the Mapojiao section did not show any diagenetic microfacies (e.g., dolomitization) accompanying the change towards lower values in Unit B. However, silicification in the lower part of Unit D is reported by Bagherpour et al. (under review), which may have been accompanied by diagenetic alteration of $\delta^{13}C_{carb}$ values in this interval.

Following the same approach for assessing diagenetic alteration, the change towards lower values in Tieqiao disappears, but that of Chaotian do subsist (Jost et al., 2014). Unfortunately, $\delta^{18}O_{carb}$ data from Xiongjiachang are not available for assessing diagenetic alteration.

The ultrahigh-resolution $\delta^{13}C_{carb}$ records from limestone beds bracketing the ash layers show substantial excursions toward lower values in the organic-rich limestone of Unit B, whereas limestone beds adjacent to ash layers in the organic-poor limestone of Unit A (from Mapojiao B) do not display any change toward lower values. The excursions towards lower values around the ash layers are characterized by $\delta^{18}O_{carb}$ values < -7 ‰, thus indicating the influence of diagenetic alteration apparently fostered by the presence of high TOC values (Supplementary material S5, S6, S7). Moreover, the strong positive correlation between $\delta^{18}O_{carb}$ and $\delta^{13}C_{carb}$ around the ash layers also supports remineralization of OM for these negative outliers. However, detailed diagenetic processes that led to the alteration of the $\delta^{13}C_{carb}$ signal of OM-rich limestone adjacent to ash layers are unknown.

5.4. Organic geochemistry and palynofacies

Paired organic and inorganic C isotope records provide a potential tool to assess the variation in Dissolved Inorganic Carbon (DIC) pool. Covariation between $\delta^{13}C_{org}$ and $\delta^{13}C_{carb}$ is expected when the changes in $\delta^{13}C_{carb}$ indicate variation in the past DIC (Oehlert and Swart, 2014 and references therein). Therefore, comparing both C isotopes from the same section is of special interest for discriminating primary changes in sea water DIC from a possible diagenetic overprint. However, special care should be taken for the interpretation of excursions in $\delta^{13}C_{org}$, because these values are highly dependent on the composition of organic matter and environmental condition during plant growth (Jahren et al., 2008). For instance, during the late Permian the isotopic composition of terrestrial OM was significantly heavier (^{13}C enriched) in comparison with marine OM, a reverse situation in comparison to modern OM (Arthur et al., 1985).

Paired $\delta^{13}C_{org}$ and $\delta^{13}C_{carb}$ analysis at Mapojiao reveals an opposite trend throughout the section (Fig. 4). Cross-plot of $\delta^{13}C_{org}$ versus $\delta^{13}C_{carb}$ also shows a negative correlation (r = -0.3520 and $r^2 = 0.1304$) for Units A-D at Mapojiao (Fig. 7a). This negative correlation might indicate a diagenetic alteration and/or changes in the respective contribution of the terrestrial and marine pools of organic carbon. Hence, before utilizing the $\delta^{13}C_{org}$ as a correlation tool or before assuming variations in DIC, the composition of OM must be first determined.

The HI/OI cross-plot shows that samples from limestones of Unit A fall into the type-II kerogen field (Fig. 7b), which indicates (relatively hydrogen-rich) autochthonous marine origin of OM. Samples from Subunits B1 and B2 are characterized by lower HI and OI values and correspond to type-III kerogen (Fig. 7b), indicating that the OM is essentially derived from terrestrial plants (Tissot and Welte, 1984). The S2/TOC cross-plot shows a linear relationship between the two factors and also indicates type II and type III kerogen for samples from Unit A and Unit B, respectively (Fig. 7c). Moreover, both diagrams show that the dominance of kerogen type III progressively increase from Subunit B1 to Subunit B2. In addition, the OI/TOC and HI/TOC cross-plots (Fig. 7d, e) show a negative logarithmic relation; the higher TOC values being associated with lower OI and HI (terrestrial origin) values and vice versa. The most $\delta^{13}C_{org}$ positive values are also associated with the highest TOC values (Fig 7.f) and therefore, with the presence of type III kerogen of terrestrial origin. Hence, Rock-Eval parameters indicate a substantial input of terrestrial OM concomitant with lithological change from shallow-marine limestone to deep marine and organic-rich limestone, thus explaining the positive trend of the $\delta^{13}C_{org}$ curve.

Palynofacies analyses also confirm the substantial change from marine dominated OM of Unit A (Fig. 6a) to terrestrial dominated OM in Unit B, where the TOC and contribution of terrestrial OM progressively increase upward in this unit (Fig. 6b, c). In Unit D, marine OM dominates POM assemblages again (Fig. 6d).

Studies of the Permian-Triassic interval from Norway and Australia indicate that the primary isotopic value of terrestrial OM varies around −22‰ to −23‰ and marine OM around−31‰ to −32‰ (Thomas et al., 2004; Hermann et al., 2010). Therefore, according to significant differences in the isotopic composition of marine and terrestrial end-members, one of the most important factors which can bias the $\delta^{13}C_{org}$ is the mixing of two different pools of organic carbon (Herrmann et al., 2011). Moreover, several studies show that diagenesis has a minor (~1‰) effect on the variation of the $\delta^{13}C_{org}$ (e.g., Freudenthal et al., 2001, Meyers et al., 1995). Thermal maturity of organic matter is also considered to shift the $\delta^{13}C_{org}$ record toward heavier values (Hayes et al., 1999), but this process would not alter the overall trend of the isotopic record (Des Marais et al., 1992). Hence, we conclude that the decoupling of $\delta^{13}C_{org}$ and $\delta^{13}C_{carb}$ is in better agreement with the mixing of different pools of organic carbon than with the influence of diagenetic alteration.

Comparison of the $\delta^{13}C_{org}$ record of the Chaotian section (Saitoh et al., 2014) with Mapojiao indicates that the similarity between these two events of different age even extends to the $\delta^{13}C_{org}$ record. Chaotian shows a positive shift in $\delta^{13}C_{org}$ in the OM-rich, radiolarian-spiculitic facies associated with a shift toward lower values in $\delta^{13}C_{carb}$. Unfortunately, composition of the bulk OM from Chaotian is not available for further comparison. Nevertheless, the $\delta^{13}C_{org}$ record indicates another similarity between the episodic drowning events that occurred during the G-L interval.

5.5. Strontium and carbonate carbon isotopic records

The strontium isotopic composition ($^{87}Sr/^{86}Sr$) of marine carbonates provides valuable information about sources from which the $^{87}Sr/^{86}Sr$ profile is modified. Sea water $^{87}Sr/^{86}Sr$ is determined by the relative influence of radiogenic Sr from the continental crust (riverine flux) and less radiogenic Sr from the Earth's mantle (hydrothermal or other mafic igneous sources of the oceanic crust) (Palmer and Edmond 1989; Taylor and Lasaga 1999). Hence, changes in the $^{87}Sr/^{86}Sr$ record indicate relative variation in the riverine and hydrothermal oceanic crustal sources of strontium (Veizer and Compston, 1974; Palmer and Edmonds, 1989, Veizer, 1989; Martin and Macdougall, 1995; Veizer et al., 1999). In general, an increasing $^{87}Sr/^{86}Sr$ indicates relative increase of continental weathering, and a decreasing trend indicates higher contribution of volcanogenic, ocean-crust derived Sr (Bralower et al., 1997).

The lowest $^{87}Sr/^{86}Sr$ value (ca. 0.7068) in the Phanerozoic is recorded during the Capitanian stage (Veizer et al., 1999; McArthur and Howarth, 2004; Kani et al., 2013). Subsequently, a rapid $^{87}Sr/^{86}Sr$ rise started immediately after the Capitanian minimum near the G-L boundary and continued throughout the late Permian, reaching a value of 0.7082 at the end of the Early Triassic (Korte et al., 2003; Kani et al., 2013). This protracted increase in $^{87}Sr/^{86}Sr$ indicates input of a large amount of terrigenous clastic material enriched in radiogenic Sr from Pangea into Panthalassa (Kani et al., 2008), and/or cessation of widespread basaltic activity in the entire Paleotethys (Korte et al., 2006). However, other causal links such as changes in "global tectonic, sea-level, climate, weathering rate, and diagenetic processes" for the late Permian $^{87}Sr/^{86}Sr$ rise have also been proposed (Kani et al., 2013 and references therein).

The Sr-isotope profile from the Mapojiao section provides a useful tool to assess the enhanced hydrothermal flux of volcanic origin concomitant with the Mapojiao Event. High resolution $^{87}Sr/^{86}Sr$ record at Mapojiao represents an interval of a decrease in $^{87}Sr/^{86}Sr$ from 0.70715 to 0.70694 corresponding to organic-rich, thin-bedded limestone of Unit B. This transient decreasing trend intercalated within a longer increasing trend is compatible with a short pulse of ELIP-related volcanic activity. In addition to enhanced hydrothermal flux, riverine input from weathered less-radiogenic basalts from the ELIP may also contribute to decrease of $^{87}Sr/^{86}Sr$. According to Jones and Jenkyns (2001), the most likely mechanism to lower the average of riverine $^{87}Sr/^{86}Sr$ is to expose low $^{87}Sr/^{86}Sr$ volcanic rocks such as continental flood basalts or formation of new volcanic arcs. Basalts are of particular importance in this case, because they are easily weathered compared to more siliceous rocks and, hence, they are more likely to release Sr (Bluth and Kump, 1994; Taylor and Lasaga, 1999). Therefore, both mechanisms, inputs of less radiogenic Sr from volcanism and lowering the average of $^{87}Sr/^{86}Sr$ riverine (erosion of ELIP), may have contributed to lowering the Sr-isotope ratio at Mapojiao. Whether this decrease of $^{87}Sr/^{86}Sr$ at Mapojiao is triggered by increased hydrothermal flux from the oceanic ridges or by other sources such as ELIP cannot be assessed directly. However, differences in order of magnitude between the duration of tectonic processes and volcanic activities suggests that such a relatively short-term excursion in the $^{87}Sr/^{86}Sr$ ratio supports Emeishan volcanism as a cause rather than an increased flux from the mid-oceanic ridges. Moreover, explaining the excursion toward lower values in $^{87}Sr/^{86}Sr$ record at Mapojiao with ELIP activity can be supported by other indications of volcanism, such as a climate warming during this time (Chen et al., 2011). In addition to the composition of conodont assemblages that indicates a warming trend during the Wuchiapingian (Mei et al., 2002), the conodont apatite $\delta^{18}O$ record from the Tieqiao section provides a potential temperature proxy. The Tieqiao section represents two warming episodes during the G-L transition. The first episode occurred in the Capitanian (*Jinogondolella xuanhanensis* IZ to *Jinogondolella granti* IZ) and has been related to the widespread eruption of the ELIP. The second warming episode occurred in the *Clarkina leveni* to *Clarkina liangshanensis* IZs in the base of the Heshan Fm. (lateral equivalent of Wuchiaping Fm.) (Chen et al., 2011). The commonly used *Clarkina liangshanensis* IZ (Wang and Wang, 1981) in South China partly overlaps with *Clarkina guangyuanensis*, *Clarkina transcaucasica,* and lower part of the *Clarkina orientalis* IZs (Fig. 1) (Shen et al., 2010). Hence, the biostratigraphic position of the second warming episode at Tieqiao perfectly overlaps in time with the interval of the excursion toward lower $^{87}Sr/^{86}Sr$ values at Mapojiao and their coexistence support a concomitant ELIP-related volcanic activity.

The termination age of Emeishan flood basalts is known from Binchuan section (Yunnan Province, inner zone) at 259.1±0.5 Ma (Shellnutt et al., 2012; Zhong et al., 2014). Pending high-precision radiometric dating of the Mapojiao Event (Ovtcharova et al., in prep), biostratigraphic data here indicates extension of ELIP volcanism into the Wuchiapingian. The Wuchiapingian age (257.6±0.5 Ma) of ELIP plutonism and dyking is also known from Panxi region (Sichuan Province, inner zone) (Shellnutt et al., 2012). However, any further explicit correlation between Mapojiao

Event and known Wuchiapingian ELIP activity cannot be performed here.

5.6. Remarks on the $\delta^{18}O_{phosphate}$ record from South China

In South China, the $\delta^{18}O_{phosphate}$ composite record measured from conodonts documents a period of low, homogeneous values during the end-Capitanian to Wuchiapingian time interval, with two superimposed short excursions towards even lower values of late Capitanian and early Wuchiapingian ages, respectively (Chen et al., 2013). How robust these two short term excursions are remains to be established by documenting them from single sections with appropriate paleontological age control. The composite section with substantial gaps in their $\delta^{18}O_{phosphate}$ records combined with the application of a running mean may result in unreliable peaks. The late Capitanian excursion has nevertheless been assigned to ELIP volcanic activity, while the origin of the second excursion has not been addressed (Chen et al., 2013). It is worth noting here that this second short excursion overlaps in age with the Mapojiao Event, but any direct or indirect linkage with the $\delta^{18}O_{phosphate}$ record would first require a better resolved time series, as stressed above. Chen et al. (2013) could not discriminate between a temperature change, sea-level changes and conodont habitats to explain these changes in $\delta^{18}O_{phosphate}$. In addition, local pH changes related to ELIP eruptions may also have contributed to fluctuations and noise in the $\delta^{18}O_{phosphate}$ time series.

6. Conclusions

The Mapojiao Event is a newly recognized drowning and volcanic event during the early Wuchiapingian in S. Guizhou (Pingtang Syncline). This event resulted in regional progressive drowning of the carbonate platforms and deposition of organic-rich, radiolarian-spiculitic facies ending with the intercalation of volcanogenic turbidites. The remarkable absence of synsedimentary breccias indirectly argue in favor of flexuration rather than block faulting for this accelerated regional subsidence phase. During this event, $\delta^{13}C_{carb}$ data show a 3.5–4 ‰ excursion towards lower values, but the $\delta^{13}C_{org}$ record does not show any covariation. Rock-Eval and palynofacies analyses support increased inputs of terrestrial OM as the cause for increased burial of OM that shifts the primary (marine OM dominated) $\delta^{13}C_{org}$ signal toward heavier values. The terrestrial origin of the OM buried during the Mapojiao Event excludes the presence of upwelling as a driver for increased marine bioproductivity. Strontium isotope compositions indicate an excursion to lower ratios, concomitant with the shift in the $\delta^{13}C_{carb}$ record, which suggests an enhanced hydrothermal flux from mafic sources such as ELIP. Weathering of basalts from ELIP may have also contributed to lower the $^{87}Sr/^{86}Sr$ ratios. Comparison of the C isotope record of the Mapojiao Event to other contemporaneous records from South China and Iran indicates that this excursion represents only a regional perturbation and not a global phenomenon. Comparing the Mapojiao Event with the Capitanian CIEs toward lower values (at Chaotian and Xiongjiachang) reveals the iteration of the same CIE associated with ELIP-related drownings. As a consequence, it is proposed that these CIEs are resulted from local environmental factors such as bathymetry and increased burial rate of organic matter. . Unlike the Capitanian, which is characterized by either gradual or abrupt decreasing marine diversity, the Wuchiapingian stage represents an interval of recovery and radiation (Chen et al., 2005; Shen and Shi 2009; Brayard et al., 2009; Villier and Korn, 2004) and the Mapojiao Event does not coincide in time with any noticeable extinction. In a broader perspective, the extended duration of ELIP volcanic pulses may better compare with that of other LIPs (Wei et al., 2014; Percival et al., 2017). But the mainly submarine volcanic eruptions and the comparatively smaller size of the equatorial ELIP are in agreement with the moderate impact it had in terms of environmental perturbations and extinctions, both during the initial eruptive phase and during subsequent pulses.

***Acknowledgments**:* This work is supported by the Swiss NSF projects 135446 and 160055 (to H.B.). SSZ's work is supported by NSFC project 41420104003. Constructive reviews by Gregory Shellnutt, an anonymous reviewer, and editor Shoujie Liu are deeply appreciated. Jean-Pierre Burg is thanked for stimulating discussions on the tectonic interpretations of the sedimentary signal. The assistance of Chao Zhang and Marc Leu in the field is deeply appreciated.

References

Ali, J.R., Thompson, G.M., Song, X.Y., Wang, Y.L., 2002. Emeishan Basalts (SW China) and the 'end-Guadalupian' crisis: magnetobiostratigraphic constraints. Journal of the Geological Society London 159, 21–29.

Ali, J.R., Thompson, G.M., Zhou, M.F., Song, X.Y., 2005. Emeishan large igneous province, SW China. Lithos 79, 475-489.

Arthur, M.A., Dean, W.E., Claypool, G.E., 1985. Anomalous 13C enrichment in modern marine organic carbon. Nature 315, 216–218.

Bagherpour, B., Bucher, H., Yuan, DX., Leu, M., C, Zhang., Shen, SZ., in review. Early Wuchiapingian (Lopingian, Late Permian) drowning event in the South China Block related to a late eruptive phase of Emeishan Large Igneous Province? Global and planetary change XXX, XXX-XXX.

Behar, F., Beaumont, V., Penteado, H.L.D., 2001. Rock-Eval 6 technology: performances and developments. Oil & Gas Science and Technology 56, 111-134.

Bluth, G.J.S., Kump, L.R., 1994. Lithologic and climatologic controls of river chemistry. Geochimica et Cosmochimica Acta 58, 2341–2359.

Bond, D.P.G., Hilton, J., Wignall, P.B., Ali, J.R., Stevens, L.G., Sun, Y.D., Lai, X.L., 2010a. The Middle Permian (Capitanian) mass extinction on land and in the oceans. Earth-Science Reviews 102, 100–116.

Bond, D.P.G., Wignall, P.B., Wang, W., Izon, G., Jiang, H.S., Lai, X.L., Sun, Y.D., Newton, R.J., Shao, L.Y., Védrine, S., Cope, H., 2010b. The mid-Capitanian (Middle Permian) mass extinction and carbon isotope record of South China. Palaeogeography, Palaeoclimatology, Palaeoecology 292, 282–294.

Bralower, T.J., Fullagar, P.D., Paull, C.K., Dwyer, G.S., Leckie, R.M., 1997. Mid-Cretaceous strontium-isotope stratigraphy of deep-sea sections. Geological Society of America Bulletin 109, 1421–1442.

Brayard, A., Escarguel, G., Bucher, H., Monnet, C., Brühwiler, T., Goudemand, N., Galfetti, T., Guex, J., 2009. Good Genes and Good Luck: Ammonoid Diversity and the End-Permian Mass Extinction. Science 325(5944), 1118-1121.

Brand, U., Veizer, J., 1981. Chemical diagenesis of a multicomponent carbonate system — 2: stable isotopes. Journal of Sedimentary Petrology 51, 987–997.

Chen, Z.Q., Campi, M.J., Shi, G.R., Kaiho, K., 2005. Post−extinction brachiopod faunas from the Late Permian Wuchiapingian coal series of South China. Acta Palaeontologica Polonica 50(2), 343-363.

Chen, B., Joachimski, M.M., Sun, Y.D., Shen, S.Z., Lai, X.L., 2011. Carbon and conodont apatite oxygen isotope records of Guadalupian–Lopingian boundary sections: climatic or sea-level signal? Palaeogeography, Palaeoclimatology, Palaeoecology 311, 145–153.

Chen, B., Joachimski, M.M., Shen, S.Z., Lambert, L.L., Lai, X.L.,Wang, X.D., Chen, J., Yuan, D.X., 2013. Permian ice volume and palaeoclimate history: oxygen isotope proxies revisited. Gondwana Research 24, 77–89.

Clapham, M.E., Shen, S., Bottjer, D.J., 2009. The double mass extinction revisited: reassessing the severity, selectivity, and causes of the end-Guadalupian biotic crisis (LatePermian). Paleobiology 35, 32–50.

Des Marais, D.J., Strauss, H., Summons, R.E., Hayes, J.M., 1992. Carbon isotope evidence for the stepwise oxidation of the Proterozoic environment. Nature 359, 605–609.

Enkin, R.J., Zhenyu, Yang, Yan, Chen, Courtillot, V., 1992. Paleomagnetic constraints on the geodynamic history of the major blocks of China from the Permian to the present. Journal of Geophysical Research 97 (B10), 13953–13989.

Espitalié, J., Deroo, G., Marquis, F., 1985. La pyrolyse Rock-Eval et ses applications: Première partie. Rev. Inst. Fr. Pétr., 40, 563–579.

Espitalié, J., Deroo, G., Marquis, F., 1986. La pyrolyse Rock-Eval et ses applications: Troisième partie. Rev. Inst. Fr. Pétr., 41, 73–89.

Freudenthal, T., Wagner, T., Wenzhöfer, F., Zabel, M., Wefer, G., 2001. Early diagenesis of organic matter from sediments of the eastern subtropical Atlantic: evidence from stable nitrogen and carbon isotopes. Geochimica et Cosmochinica Acta 65, 1795–1808.

Ganino, C., Arndt, N.T., 2009. Climate changes caused by degassing of sediments during the emplacement of large igneous provinces. Geology 37, 323–326.

Given, R.K., Lohmann, K.C., 1985. Derivation of the original isotopic composition of Permian marine cements. Journal of Sedimentary Petrology 55(3), 430-439.

Guizhou Bureau of Geology and Mineral Resources., 1987. Regional Geology of Guizhou Province: Geological Memoires, Ser. 1, no. 6, [in Chinese, English summary; Geologic map 1:500,000].

Hays, P.D., Grossman, E.L., 1991. Oxygen isotopes in meteoric calcite cements as indicators of continental paleoclimate. Geology19(5), 441.

Hayes, J.M., Strauss,H., Kaufman,A.J., 1999. The abundance of ^{13}C in marine organic matter and isotopic fractionation in the global biogoechemical cycle of carbon during the past 800 Ma. Chemical Geology 161,103–125.

He, B., Xu, Y.-G., Chung, S.-L., Xiao, L., Wang, Y., 2003. Sedimentary evidence for a rapid, kilometer-scale crustal doming prior to the eruption of the Emeishan flood basalts. Earth and Planetary Science Letters 213, 391-405.

Hermann, E., Hochuli, P.A., Bucher, H., Vigran, J.O., Weissert, H., Bernasconi, S.M., 2010. Close-up view on the Permian–Triassic boundary based on extended organic carbon isotope records from Norway (Trøndelag and Finnmark Platform). Global and Planetary Change 74, 156-167.

Hermann, E., Hochuli, P.A., Méhay, S., Bucher, H., Brühwiler, T., Ware, D., Hautmann, M., Roohi, G., Ur-Rehman, K., Yaseen, A., 2011. Organic matter and palaeoenvironmenta signals during the Early Triassic biotic recovery: the Salt Range and Surghar Range records. Sedimentary Geology 234, 19–41.

Jahren, A.H., Arens, N.C., Harbeson, S.A., 2008. Prediction of atmospheric δ13CO2 using fossil plant tissues. Review of Geophysics 46, RG I002. doi:10.1029/2006RG000219.

Jerram, D.A., Widdowson, M., Wignall, P.B., Sun, Y., Lai, X., Bond, D.P.G., Torsvik, T.H., 2016. Submarine palaeoenvironments during Emeishan flood basalt volcanism, SW China: Implications for plume–lithosphere interaction during the Capitanian, Middle Permian (‘end Guadalupian’) extinction event. Palaeogeography, Palaeoclimatology, Palaeoecology 441, 65–73.

Jin, Y.G., Zhang, J., Shang, Q.-H., 1994. Two phases of the end-Permian mass extinction.

Canadian Society of Petroleum Geologists Memoir 17, 813–822.

Jones, C.E., Jenkyns, H.C., 2001. Seawater strontium isotopes, Oceanic Anoxic Events, and seafloor hydrothermal activity in the Jurassic and Cretaceous. American Journal of Science 301, 112–149.

Jost, B. A., Mundil, R., He, B., Brown, T. S., Altiner, D., Sun, Y., DePaolo, D. J., Payne L. L., 2014. Constraining the cause of the end-Guadalupian extinction with coupled records carbon and calcium isotopes. Earth and Planetary Science Letters. 396, 201-212.

Kani, T., Fukui, M., Isozaki, Y., Nohda, S., 2008. The Paleozoic minimum of 87Sr/86Sr initial ratio in the upper Guadalupian (Permian) mid-oceanic carbonates: a critical turning point in the Late Paleozoic. Journal of Asian Earth Sciences 32, 22–33.

Kani, T., Hisanabe, C., Isozaki, Y., 2013. The Capitanian (Permian) minimum of 87Sr/86Sr ratio in the mid-Panthalassan paleo-atoll carbonates and its demise by the deglaciation and continental doming. Gondwana research 24, 212-221.

Korte, C., Kozur, H.W., Bruckschen P., and Veizer, J., 2003. Strontium isotope evolution of Late Permian and Triassic seawater: Geochimica et Cosmochimica Acta 67, 47-62.

Korte, C., Jasper, T., Kozur, H.W., Veizer, J., 2006. 87Sr /86Sr record of Permian seawater. Palaeogeography, Palaeoclimatology, Palaeoecology 240, 89–107.

Korte, C., Kozur, H.W., 2010. Carbon-isotope stratigraphy across the Permian–Triassic boundary: A review. Journal of Asian Earth Sciences 39, 215–235.

Lai, X., Wei, Wang, Wignall, P.B., Bond, D.P.G., Jiang, H., Ali, J.R., John, E.H., Sun, Y., 2008. Palaeoenvironmental change during the end-Guadalupian (Permian) mass extinction in Sichuan, China. Palaeogeography, Palaeoclimatology, Palaeoecology 269, 78–93.

Langford, F.F., Blanc-Valleron, M.M., 1990. Interpreting Rock-Eval Pyrolysis data using graphs of pyrolizable hydrocarbons versus total organic carbon, American Association of Petroleum Geologists 74(6), 799–804.

Li, H., Zhang, Z., Santosh, M., Lü, L., Han, L., Liu, W., 2016. Late Permian basalts in the Yanghe area, eastern Sichuan Province, SW China: Implications for the geodynamics of the Emeishan Large Igneous Province and Permian global mass extinction. Journal of Asian Earth Sciences doi: http://dx.doi.org/10.1016/j.jseaes.2016.11.029

Marshall, J.D., 1992. Climatic and oceanographic isotopic signals from the carbonate rock record and their preservation. Geological Magazine 129, 143–160.

Martin, E.E., Macdougall, J.D., 1995. Sr and Nd isotopes at the Permian/Triassic boundary: a record of climate change. Chemical Geology 125, 73–99.

McArthur, J.M., Howarth, R.J., Bailey, T.R., 2001. Strontium Isotope Stratigraphy: LOWESS Version 3: Best Fit to the Marine Sr□Isotope Curve for 0–509 Ma and Accompanying Look□up Table for Deriving Numerical Age. The Journal of Geology 109 (2), 155-170.

McArthur, J.M., Howarth, R.J., 2004. Strontium Isotope Stratigraphy. In: Gradstein, F.M., Ogg, J.M., Smith, A.G. (Eds.), A geologic time scale 2004. Cambridge University Press, Cambridge, p. 96.

Mei, S.L., Jin, Y.G., Wardlaw, B.R., 1998. Conodont succession of the Guadalupian-Lopingian boundary strata in Laibin of Guangxi, China and West Texas, USA. Palaeoworld 9, 53-76.

Mei, S., Henderson, C.M., Wardlaw, B.R., 2002. Evolution and distribution of the conodonts *Sweetognathus* and *Iranognathus* and related genera during the Permian, and their implications for climate change. Palaeogeography, Palaeoclimatology, Palaeoecology 180, 57-91.

Meyers, P.A., Leenheer, M.J., Bourbonniere, R.A., 1995. Diagenesis of vascular plant organic matter components during burial in lake sediments. Aquatic Geochemistry 1, 35–52.

Oehlert, A.M., Swart, P.K., 2014. Interpreting carbonate and organic carbon isotope covariance in the sedimentary record. Nature Communications 5, 4672.

Palmer, M.R., Edmond, J.M., 1989. The strontium isotope budget of the modern ocean. Earth and Planetary Science Letters 92, 11–26.

Percival, L.M.E., Ruhl, M., Hesselbo, S.P., Jenkyns, H.C., Mather, T.A., Whiteside, J.H., Mercury evidence for pulsed volcanism during the end-Triassic mass extinction. Proceedings of the National Academy of Sciences 114(30), 7929–7934.

Retallack, G.J., Jahren, A.H., 2008. Methane release from igneous intrusion of coal during Late Permian extinction events. The Journal of Geology 116, 1–20.

Rubidge, B.S., Erwin, D.H., Ramezani, J., Bowring, S.A., de Klerk, W.J., 2013. High-precision temporal calibration of Late Permian vertebrate biostratigraphy: U-Pb zircon constraints from the Karoo Supergroup, South Africa. Geology 41, 363–366.

Saitoh, M., Isozaki, Y., Yao, J., Ji, Z., Ueno, Y., Yoshida, N., 2013a. The appearance of an oxygen-depleted condition on the Capitanian disphotic slope/basin in South China: Middle–Upper Permian stratigraphy at Chaotian in northern Sichuan. Global and Planetary Change 105, 180–192.

Saitoh, M., Isozaki, Y., Ueno, Y., Yoshida, N., Yao, J., Ji, Z., 2013b. Middle–Upper Permian carbon isotope stratigraphy at Chaotian, South China: pre-extinction multiple upwelling of oxygen-depleted water onto continental shelf. Journal of Asian Earth Sciences 67–68, 51–62.

Saitoh, M., Ueno, Y., Isozaki, Y., Nishizawa, M., Shozugawa, K., Kawamura, T., Yao, J., Ji, Z., Takai, K., Yoshida, N. and Matsuo, M., 2014. Isotopic evidence for water-column denitrification and sulfate reduction at the end-Guadalupian

(Middle Permian). Global and Planetary Change123, 110-120.

Schobben, M., Ullman, C.V., Leda, L., Korn, D., Struck, U., Reimold, W.U., Ghaderi, A., Algeo, T., Korte, C., 2016. Discerning primary versus diagenetic signals in carbonate carbon and oxygen isotope records: An example from the Permian–Triassic boundary of Iran. Chemical Geology 422, 94-107.

Shellnutt, J.G., Denyszyn, S., Mundil, R., 2012. Precise age determination of mafic and felsic intrusive rocks from the Permian Emeishan large igneous province (SW China). Gondwana Research 22, 118-126.

Shellnutt, J.G., 2014. The Emeishan large igneous province: A synthesis. Geoscience Frontiers 5, 369-394.Shen, S.Z., Shi, G.R., 2009. Latest Guadalupian brachiopods from the Guadalupian/Lopingian boundary GSSP section at Penglaitan in Laibin, Guangxi, South China and implications for the timing of the pre-Lopingian crisis. Palaeoworld 18, 152-161.

Shen, S.Z., Mei, S.L., 2010. Lopingian (Late Permian) high-resolution conodont biostratigraphy in Iran with comparison to South China zonation. Geological Journal 45, 135–161.

Shen, S.Z., Cao, C.Q., Zhang, H., Bowring, S.A., Henderson, C.M., Payne, J.L., Davydov, V.I., Chen, B., Yuan, D.X., Zhang, Y.C., Wang, W., Zheng, Q.C., 2013. High-resolution δ13Ccarb chemostratigraphy from latest Guadalupian through earliest Triassic in South China and Iran. Earth and Planetary Science Letters 375, 156–165.

Spötl C., and Vennemann T.W., 2003. Continuous-flow IRMS analysis of carbonate minerals. Rapid Communications in Mass Spectrometry, V. 17, p. 1004-1006.

Stanley, S.M., Yang, X., 1994. A double mass extinction at the end of the Paleozoic era.

Science 266, 1340–1344.

Sun, Y., Lai, X., Wignall, P.B., Widdowson, M., Ali, J.R., Jiang, H., Wang, W., Yan, C., Bond, D.P.G., Vedrine, S., 2010. Dating the onset and nature of the Middle Permian Emeishan large igneous province eruptions in SW China using conodont biostratigraphy and its bearing on mantle plume uplift models. Lithos 119, 20–33.

Taylor, A.S., Lasaga, A.C., 1999. The role of basalt weathering in the Sr isotope budget of the oceans. Chemical Geology 161, 199–214.

Thomas, B.M., Willink, R.J., Grice, K., Twitchett, R.J., Purcell, R.R., Archbold, N.W., George, A.D., Tye, S., Alexander, R., Foster, C.B., Barber, C.J., 2004. Unique marine Permian-Triassic boundary section from Western Australia. Australian Journal of Earth Sciences 51, 423–430.

Tissot, B.P., Welte, D.H., 1984. Petroleum Formation and Occurrence, 2nd edition, Springer-Verlag, Berlin. 699 pp.

Traverse, A., 2007. Paleopalynology. Topics in Geobiology 28. Springer.

Ukstins Peate, I., Bryan, S.E., 2008. Re-evaluating plume-induced uplift in the Emeishan large igneous province. Nature Geoscience 1, 625–629.

Ullmann, C.V., Korte, C., 2015. Diagenetic alteration in low-Mg calcite frommacrofossils: A review. Geological Quarterly 59, 3–20.

Veizer, J., Compston,W., 1974. 87Sr/86Sr composition of seawater during the Phanerozoic. Geochimica et Cosmochimica Acta 38, 1461–1484.

Veizer, J., 1989. Strontium isotopes in seawater through time. Annual Review of Earth and Planetary Sciences 17, 141–167.

Veizer, J., Ala, D., Azmy, K., Bruckschen, P., Buhl, D., Bruhn, F., Carden, G.A.F., Diener, A., Ebneth, S., Goddéris, Y., Jasper, T., Korte, C., Pawellek, F., Podlaha, O.G., Strauss, H., 1999. 87Sr/86Sr, δ13C and δ18O evolution of Phanerozoic seawater. Chemical Geology 161, 59–88.

Villier, L., Korn, D., 2004. Morphological Disparity of Ammonoids and the Mark of Permian Mass Extinctions. Science 306(5694), 264-6.

Wang, C.Y.,Wang, Z.H. 1981. Permian conodont biostratigraphy of China. Geological Society of America Special Paper 187, 227–236.

Wang, X.D., Sugiyama, T., 2000. Diversity and extinction patterns of Permian coral faunas of China. Lethaia 33, 285–294.

Wignall, P.B., Sun, Y., Bond, D.P.G., Izon, G., Newton, R.J., Védrine, S., Widdowson, M., Ali, J.R., Lai, X., Jiang, H., Cope, H., Bottrell, S.H., 2009. Volcanism, mass extinction, and carbon isotope fluctuations in the Middle Permian of China. Science 324, 1179–1182.

Wei, H., Chen, D., Yu, H., Wang, J., 2012. End-Guadalupian massextinction and negative carbon isotope excursion at Xiaojiaba, Guangyuan, Sichuan. Science China Earth Sciences 55(9),1480–1488.

Wei, H., Shen, J., Schoepfer, S.D., Krystyn, L., Richoz, S., Algeo, T., 2014. Environmental controls on marine ecosystem recovery following mass extinctions, with an example from the Early Triassic. Earth-Science Reviews 149, 108–135.

Weissert, H., Joachimski, M.M., Sarnthein, M., 2008. Chemostratigraphy. Newsletters on Stratigraphy 42, 145–179.

www.scotese.com

Yan, D., Zhang, L., Qiu, Z., 2013. Carbon and sulfur isotopic fluctuations associated with the end-Guadalupian mass extinction in South China. 24, 1276–1282.

Zazzali, S., Crasquin, S., Deconinck, J.S., Feng, Q., 2015. Biodiversity across the Guadalupian-Lopingian Boundary: first results on the ostracod (Crustacea) fauna, Chaotian section (Sichuan Province, South China). Geodiversitas 37(3), 283-313.

Zhao, L., Dai, S., Graham, I.T., Li, X., Zhang, B., 2016. New insights into the lowest Xuanwei Formation in eastern Yunnan Province, SW China: Implications for Emeishan large igneous province felsic tuff deposition and the cause of the end-Guadalupian mass extinction. Lithos 264, 375–391.

Zhong, Y.T., He, B., Mundil, R., Xu, Y.G., 2014. Ca-TIMS zircon U-Pb dating of felsic ignimbrite from the Binchuan section: implications for the termination age of Emeishan large igneous province. Lithos 204, 14-19.

Zhou, M.F., Malpas, J., Song, X.Y., Robinson, P.T., Sun, M., Kennedy, A.K., Lesher,

C.M., Keays, R.R., 2002. A temporal link between the Emeishan large igneous

province (SW China) and the end-Guadalupian mass extinction. Earth and Planetary Science Letters 196, 113–122.

Supplementary material S1 d^{13}C$_{carb}$, d^{18}O$_{carb}$, d^{13}C$_{org}$, ^{87}Sr/^{86}Sr, carbonate content, and Rock-Eval data measured from the Wuchiapingian Fm. at Mapojiao main section.

	Sample No.	Section	Formation	Position (m	Lithology	Ccarb	Ocarb
Unit A	MAP 537	Mapojiao	Wuchiaping	0.1	Light color Bioclastic lime	5.66	-6.66
Unit A	MAP 536	Mapojiao	Wuchiaping	2	Light color Bioclastic lime	5.74	-5.13
Unit A	MAP 530	Mapojiao	Wuchiaping	4	Light color Bioclastic lime	5.24	-5.02
Unit A	MAP 531	Mapojiao	Wuchiaping	5.1	Light color Bioclastic lime	5.44	-4.76
Unit A	MAP 532	Mapojiao	Wuchiaping	7	Light color Bioclastic lime	5.13	-4.16
Unit A	MAP 533	Mapojiao	Wuchiaping	8	Light color Bioclastic lime	4.60	-5.75
Unit A	MAP 534	Mapojiao	Wuchiaping	9.5	Light color Bioclastic lime	4.40	-5.95
Unit A	MAP 535	Mapojiao	Wuchiaping	11	Light color Bioclastic lime	5.42	-4.26
Unit A	MAP 505	Mapojiao	Wuchiaping	11.5	Light color Bioclastic lime	5.61	-5.10
Unit A	MAP 504	Mapojiao	Wuchiaping	13	Light color Bioclastic lime	5.78	-5.30
Unit A	MAP 503	Mapojiao	Wuchiaping	15	Light color Bioclastic lime	5.33	-3.08
Unit A	MAP 502	Mapojiao	Wuchiaping	17	Light color Bioclastic lime	5.28	-3.53
Unit A	MAP 501	Mapojiao	Wuchiaping	18	Light color Bioclastic lime	5.31	-4.59
Unit A	MAP 500	Mapojiao	Wuchiaping	20	Light color Bioclastic lime	4.47	-4.96
Unit A	MAP 499	Mapojiao	Wuchiaping	22	Light color Bioclastic lime	4.27	-6.29
Unit A	MAP 498	Mapojiao	Wuchiaping	24	Light color Bioclastic lime	5.45	-4.06
Unit A	MAP 497	Mapojiao	Wuchiaping	25	Light color Bioclastic lime	4.58	-5.59
Unit A	MAP 496	Mapojiao	Wuchiaping	26.5	Light color Bioclastic lime	4.83	-4.01
Unit A	MAP 495	Mapojiao	Wuchiaping	27.7	Light color Bioclastic lime	4.73	-5.31
Unit A	MAP 494	Mapojiao	Wuchiaping	28.7	Light color Bioclastic lime	5.10	-5.56
Unit A	MAP 493	Mapojiao	Wuchiaping	29.5	Light color Bioclastic lime	4.96	-5.55
Unit B1	MAP 600	Mapojiao	Wuchiaping	30	Dark organic rich limesto	5.00	-5.16
Unit B1	MAP 601	Mapojiao	Wuchiaping	30.6	Dark organic rich limesto	4.78	-5.52
Unit B1	MAP 602	Mapojiao	Wuchiaping	31.1	Dark organic rich limesto	4.49	-5.75
Unit B1	MAP 603	Mapojiao	Wuchiaping	31.8	Dark organic rich limesto	4.89	-6.20
Unit B1	MAP 604	Mapojiao	Wuchiaping	32.6	Dark organic rich limesto	3.72	-8.41
Unit B1	MAP 605	Mapojiao	Wuchiaping	33.6	Dark organic rich limesto	3.86	-6.82
Unit B1	MAP 606	Mapojiao	Wuchiaping	34.4	Dark organic rich limesto	5.11	-5.62
Unit B1	MAP 607	Mapojiao	Wuchiaping	34.8	Dark organic rich limesto	4.92	-4.83
Unit B1	MAP 608	Mapojiao	Wuchiaping	35.3	Dark organic rich limesto	4.68	-6.05
Unit B1	MAP 609	Mapojiao	Wuchiaping	35.7	Dark organic rich limesto	4.30	-6.07
Unit B1	MAP 610	Mapojiao	Wuchiaping	36.8	Dark organic rich limesto	2.45	-6.66
Unit B1	MAP 611	Mapojiao	Wuchiaping	37.3	Dark organic rich limesto	3.98	-4.63
Unit B1	MAP 612	Mapojiao	Wuchiaping	38	Dark organic rich limesto	3.96	-4.37
Unit B1	MAP 613	Mapojiao	Wuchiaping	38.7	Dark organic rich limesto	3.44	-6.50
Unit B1	MAP 614	Mapojiao	Wuchiaping	39	Dark organic rich limesto	2.11	-7.50
Unit B1	MAP 615	Mapojiao	Wuchiaping	39.7	Dark organic rich limesto	0.80	-8.56
Unit B1	MAP 616	Mapojiao	Wuchiaping	40.4	Dark organic rich limesto	3.95	-4.96
Unit B1	MAP 617	Mapojiao	Wuchiaping	40.9	Dark organic rich limesto	0.59	-7.65
Unit B1	MAP 618	Mapojiao	Wuchiaping	41.5	Dark organic rich limesto	3.47	-6.15
Unit B1	MAP 619	Mapojiao	Wuchiaping	42.2	Dark organic rich limesto	4.03	-5.18
Unit B1	MAP 620	Mapojiao	Wuchiaping	42.9	Dark organic rich limesto	3.88	-4.88
Unit B2	MAP 621	Mapojiao	Wuchiaping	43.6	Dark organic rich limesto	4.25	-3.33
Unit B2	MAP 622	Mapojiao	Wuchiaping	44.1	Dark organic rich limesto	4.07	-3.94
Unit B2	MAP 623	Mapojiao	Wuchiaping	44.7	Dark organic rich limesto	3.71	-5.77
Unit B2	MAP 624	Mapojiao	Wuchiaping	45.3	Dark organic rich limesto	3.53	-4.75

	Sample No.	Section	Formation	Position (m	Lithology	Ccarb	Ocarb
Unit B2	MAP 625	Mapojiao	Wuchiaping	45.9	Dark organic rich limesto	4.00	-4.48
Unit B2	MAP 626	Mapojiao	Wuchiaping	46.1	Dark organic rich limesto	3.77	-4.80
Unit B2	MAP 627	Mapojiao	Wuchiaping	46.5	Dark organic rich limesto	4.18	-5.50
Unit B2	MAP 628	Mapojiao	Wuchiaping	47.2	Dark organic rich limesto	4.22	-4.54
Unit B2	MAP 629	Mapojiao	Wuchiaping	47.9	Dark organic rich limesto	3.40	-6.09
Unit B2	MAP 630	Mapojiao	Wuchiaping	48.5	Dark organic rich limesto	3.44	-7.23
Unit B2	MAP 631	Mapojiao	Wuchiaping	49.2	Dark organic rich limesto	3.89	-4.16
Unit B2	MAP 632	Mapojiao	Wuchiaping	49.8	Dark organic rich limesto	3.44	-6.50
Unit B2	MAP 633	Mapojiao	Wuchiaping	50.5	Dark organic rich limesto	3.85	-4.43
Unit B2	MAP 634	Mapojiao	Wuchiaping	51.1	Dark organic rich limesto	3.38	-5.40
Unit B2	MAP 635	Mapojiao	Wuchiaping	51.8	Dark organic rich limesto	3.79	-4.11
Unit B2	MAP 636	Mapojiao	Wuchiaping	52.4	Dark organic rich limesto	2.99	-6.30
Unit B2	MAP 637	Mapojiao	Wuchiaping	53.1	Dark organic rich limesto	0.89	-7.18
Unit B2	MAP 638	Mapojiao	Wuchiaping	53.7	Dark organic rich limesto	3.17	-3.77
Unit B2	MAP 639	Mapojiao	Wuchiaping	54.3	Dark organic rich limesto	2.98	-5.59
Unit B2	MAP 640	Mapojiao	Wuchiaping	54.9	Dark organic rich limesto	3.30	-5.06
Unit B2	MAP 641	Mapojiao	Wuchiaping	55.5	Dark organic rich limesto	3.26	-4.68
Unit B2	MAP 642	Mapojiao	Wuchiaping	56	Dark organic rich limesto	3.13	-4.33
Unit B2	MAP 643	Mapojiao	Wuchiaping	56.6	Dark organic rich limesto	2.40	-7.55
Unit B2	MAP 644	Mapojiao	Wuchiaping	57.1	Dark organic rich limesto	2.58	-3.86
Unit B2	MAP 645	Mapojiao	Wuchiaping	58.2	Dark organic rich limesto	1.08	-7.10
Unit B2	MAP 646	Mapojiao	Wuchiaping	59.1	Dark organic rich limesto	2.53	-4.09
Unit B2	MAP 647	Mapojiao	Wuchiaping	59.7	Dark organic rich limesto	2.71	-5.72
Unit B2	MAP 648	Mapojiao	Wuchiaping	60.3	Dark organic rich limesto	3.16	-6.71
Unit B2	MAP 649	Mapojiao	Wuchiaping	60.9	Dark organic rich limesto	3.18	-6.37
Unit B2	MAP 650	Mapojiao	Wuchiaping	61.6	Dark organic rich limesto	3.01	-5.64
Unit B2	MAP 651	Mapojiao	Wuchiaping	62.4	Dark organic rich limesto	2.91	-6.98
Unit B2	MAP 652	Mapojiao	Wuchiaping	63	Dark organic rich limesto	0.85	-7.38
Unit B2	MAP 653	Mapojiao	Wuchiaping	63.6	Dark organic rich limesto	2.98	-7.23
Unit B2	MAP 654	Mapojiao	Wuchiaping	64.1	Dark organic rich limesto	2.80	-6.86
Unit B2	MAP 655	Mapojiao	Wuchiaping	64.7	Dark organic rich limesto	2.26	-7.69
Unit B2	MAP 656	Mapojiao	Wuchiaping	65.3	Dark organic rich limesto	2.85	-7.11
Unit C	MAP 657	Mapojiao	Wuchiaping	66	fine sandstone and siltsto	N/A	N/A
Unit C	MAP 658	Mapojiao	Wuchiaping	66.8	fine sandstone and siltsto	N/A	N/A
Unit C	MAP 659	Mapojiao	Wuchiaping	67.6	fine sandstone and siltsto	N/A	N/A
Unit C	MAP 660	Mapojiao	Wuchiaping	68.4	fine sandstone and siltsto	N/A	N/A
Unit C	MAP 661	Mapojiao	Wuchiaping	69.2	fine sandstone and siltsto	N/A	N/A
Unit C	MAP 662	Mapojiao	Wuchiaping	70	fine sandstone and siltsto	N/A	N/A
Unit C	MAP 663	Mapojiao	Wuchiaping	70.9	fine sandstone and siltsto	N/A	N/A
Unit C	MAP 664	Mapojiao	Wuchiaping	71.8	fine sandstone and siltsto	N/A	N/A
Unit C	MAP 665	Mapojiao	Wuchiaping	72.7	fine sandstone and siltsto	N/A	N/A
Unit C	MAP 666	Mapojiao	Wuchiaping	73.6	fine sandstone and siltsto	N/A	N/A
Unit C	MAP 667	Mapojiao	Wuchiaping	74.5	fine sandstone and siltsto	N/A	N/A
Unit D	MAP 668	Mapojiao	Wuchiaping	75	Cherty Limestone	1.65	-8.28
Unit D	MAP 669	Mapojiao	Wuchiaping	75.5	Cherty Limestone	2.14	-8.96
Unit D	MAP 670	Mapojiao	Wuchiaping	76	Cherty Limestone	1.60	-9.07
Unit D	MAP 671	Mapojiao	Wuchiaping	76.5	Cherty Limestone	2.46	-8.46

	Sample No.	Section	Formation	Position (m	Lithology	Ccarb	Ocarb
Unit D	MAP 672	Mapojiao	Wuchiaping	77	Cherty Limestone	3.43	-7.80
Unit D	MAP 673	Mapojiao	Wuchiaping	77.5	Cherty Limestone	2.93	-7.18
Unit D	MAP 907	Mapojiao	Wuchiaping	78	Cherty Limestone	2.84	-8.56
Unit D	MAP 908	Mapojiao	Wuchiaping	78.5	Cherty Limestone	2.84	-8.39
Unit D	MAP 909	Mapojiao	Wuchiaping	80	Cherty Limestone	2.42	-8.95
Unit D	MAP 910	Mapojiao	Wuchiaping	80.5	Cherty Limestone	2.76	-8.27
Unit D	MAP 911	Mapojiao	Wuchiaping	81	Cherty Limestone	2.18	-9.95
Unit D	MAP 912	Mapojiao	Wuchiaping	81.5	Cherty Limestone	3.20	-7.22
Unit D	MAP 913	Mapojiao	Wuchiaping	82	Cherty Limestone	2.22	-8.30
Unit D	MAP 914	Mapojiao	Wuchiaping	82.5	Cherty Limestone	0.95	-9.90
Unit D	MAP 915	Mapojiao	Wuchiaping	83	Cherty Limestone	2.24	-8.37
Unit D	MAP 916	Mapojiao	Wuchiaping	83.5	Cherty Limestone	2.39	-8.43
Unit D	MAP 917	Mapojiao	Wuchiaping	84	Cherty Limestone	0.69	-8.69
Unit D	MAP 918	Mapojiao	Wuchiaping	84.5	Cherty Limestone	2.88	-7.54
Unit D	MAP 919	Mapojiao	Wuchiaping	85	Cherty Limestone	3.13	-7.32
Unit D	MAP 920	Mapojiao	Wuchiaping	85.5	Cherty Limestone	2.58	-8.34
Unit D	MAP 921	Mapojiao	Wuchiaping	86	Cherty Limestone	3.41	-7.05
Unit D	MAP 922	Mapojiao	Wuchiaping	86.5	Cherty Limestone	3.02	-7.80
Unit D	MAP 923	Mapojiao	Wuchiaping	87	Cherty Limestone	3.28	-8.24
Unit D	MAP 924	Mapojiao	Wuchiaping	87.5	Cherty Limestone	3.54	-8.02
Unit D	MAP 925	Mapojiao	Wuchiaping	88	Cherty Limestone	4.11	-6.39
Unit D	MAP 926	Mapojiao	Wuchiaping	88.5	Cherty Limestone	4.22	-6.77

Sample No.	CaCo3%	TOC(carbon	Corg	PC	RC	TOC	MINC
MAP 537	93			0.01	0.02	0.02	9.46
MAP 536	88	0.5	-26.3				
MAP 530	88	1.9	-25.4				
MAP 531	91						
MAP 532	94	0.3	-26.7	0.01	0.01	0.02	8.65
MAP 533	105	0.2	-28.6				
MAP 534	102						
MAP 535	104	0.4	-26.4				
MAP 505	90	1.7	-25.6	0.01	0.02	0.02	8.68
MAP 504	88	1.6	-24.9				
MAP 503	89	0.9	-27.5				
MAP 502	93	0.9	-27.2	0.01	0.02	0.02	9.90
MAP 501	96	0.5	-27.5				
MAP 500	94	0.4	-25.7				
MAP 499	107	0.3	-26.3				
MAP 498	97	1.4	-26.5				
MAP 497	87	0.8	-25.2	0.01	0.02	0.03	8.87
MAP 496	95	1.2	-26.4				
MAP 495	95						
MAP 494	94	4.4	-26.7				
MAP 493	110	0.2	-25.3				
MAP 600	85	0.2	-25.6				
MAP 601	21	1.5	-25.4	0.03	0.32	0.35	10.04
MAP 602	71	1.7	-25.3				
MAP 603	78	1.5	-25.2				
MAP 604	84	0.9	-26.2				
MAP 605	59	1.0	-25.5	0.01	0.03	0.04	9.86
MAP 606	52	0.5	-25.3				
MAP 607	85	0.1	-26.6				
MAP 608	81	0.1	-25.6				
MAP 609	71	0.1	-26.2	0.01	0.03	0.03	9.16
MAP 610	50	0.2	-26.2				
MAP 611	83	1.0	-25.7				
MAP 612	55	0.3	-25.3	0.02	0.16	0.18	5.05
MAP 613	43	0.5	-25.0				
MAP 614	28	0.2	-25.4				
MAP 615	14	0.6	-26.1	0.01	0.09	0.11	6.03
MAP 616	30	0.6	-25.3				
MAP 617	39	0.5	-25.1	0.02	0.23	0.25	6.54
MAP 618	70						
MAP 619	37	0.5	-25.3				
MAP 620	41	0.6	-26.0	0.03	0.30	0.33	6.35
MAP 621	35	0.3	-25.7				
MAP 622	73	1.3	-25.2				
MAP 623	55	0.7	-25.6	0.03	0.44	0.47	5.51
MAP 624	31	0.6	-25.4				

Sample No.	CaCo3%	TOC(carbon	Corg	PC	RC	TOC	MINC
MAP 625	80	0.5	-25.9				
MAP 626	65	0.3	-26.0				
MAP 627	51	0.6	-25.7	0.02	0.25	0.27	7.06
MAP 628	49	0.8	-25.6				
MAP 629	48	0.9	-26.0				
MAP 630	17	0.5	-26.0	0.01	0.25	0.27	6.56
MAP 631	47	0.4	-25.8				
MAP 632	71	0.5	-26.3	0.02	0.18	0.20	7.48
MAP 633	76	0.6	-25.4				
MAP 634	64						
MAP 635	69			0.01	0.08	0.09	9.76
MAP 636	20	0.5	-25.7				
MAP 637	12	0.4	-24.9	0.02	0.25	0.27	4.11
MAP 638	88	0.7	-25.9				
MAP 639	55	0.4	-25.9	0.03	0.27	0.29	4.46
MAP 640	51	0.6	-25.5				
MAP 641	33	0.8	-25.4				
MAP 642	50	0.6	-25.5	0.02	0.16	0.18	9.11
MAP 643	30	0.8	-25.6				
MAP 644	51	0.6	-26.1				
MAP 645	22	0.6	-25.6	0.02	0.34	0.36	5.32
MAP 646	56	0.5	-25.3				
MAP 647	53	0.6	-25.1				
MAP 648	37	1.1	-24.7	0.03	0.41	0.44	6.07
MAP 649	28	0.9	-24.6				
MAP 650	36	1.1	-24.6	0.03	0.39	0.42	7.44
MAP 651	30	1.3	-24.5				
MAP 652	36	1.0	-24.4	0.02	0.61	0.64	5.72
MAP 653	43	1.5	-24.6	0.05	0.62	0.67	5.53
MAP 654	29	1.4	-24.7				
MAP 655	9	1.4	-24.8	0.06	0.90	0.96	1.72
MAP 656	31	1.2	-24.8	0.04	0.64	0.68	4.00
MAP 657	0	N/A	N/A	N/A	N/A	N/A	N/A
MAP 658	0	N/A	N/A	N/A	N/A	N/A	N/A
MAP 659	0	N/A	N/A	N/A	N/A	N/A	N/A
MAP 660	0	N/A	N/A	N/A	N/A	N/A	N/A
MAP 661	0	N/A	N/A	N/A	N/A	N/A	N/A
MAP 662	0	N/A	N/A	N/A	N/A	N/A	N/A
MAP 663	0	N/A	N/A	N/A	N/A	N/A	N/A
MAP 664	0	N/A	N/A	N/A	N/A	N/A	N/A
MAP 665	0	N/A	N/A	N/A	N/A	N/A	N/A
MAP 666	0	N/A	N/A	N/A	N/A	N/A	N/A
MAP 667	0	N/A	N/A	N/A	N/A	N/A	N/A
MAP 668	31	0.2	-25.5	0.01	0.19	0.20	1.84
MAP 669	66	0.1	-26.5				
MAP 670	9	0.1	-25.6	0.01	0.09	0.11	1.91
MAP 671	44	0.5	-25.4				

Sample No.	CaCo3%	TOC(carbon	Corg	PC	RC	TOC	MINC
MAP 672	51	0.1	-25.5				
MAP 673	13	0.1	-25.5				
MAP 907	40	0.09	-25.09	0.01	0.02	0.02	7.69
MAP 908	7						
MAP 909	18	0.06	-25.58	0.01	0.03	0.04	3.21
MAP 910	52						
MAP 911	44	0.05	-25.70	0.00	0.02	0.02	8.48
MAP 912	9						
MAP 913	28	0.06	-25.60	0.02	0.03	0.02	7.26
MAP 914	34						
MAP 915	4	0.04	-25.67	0.00	0.01	0.01	1.78
MAP 916	16						
MAP 917	1						
MAP 918	43	0.05	-26.13				
MAP 919	6	0.03	-25.74	0.01	0.02	0.02	4.22
MAP 920	61						
MAP 921	9						
MAP 922	30	0.13	-26.61	0.00	0.02	0.02	10.09
MAP 923	25						
MAP 924	54	0.06	-25.89	0.00	0.02	0.02	6.75
MAP 925	21	0.04	-25.78	0.01	0.02	0.03	4.06
MAP 926	19	0.04	-25.72	0.01	0.02	0.03	3.37

Sample No.	HI	OI	Tmax	S1	S2a	S2b	S3	87Sr/86Sr
MAP 537	240	263	452	0.00	0.06	0.00	0.07	0.70703443
MAP 536								
MAP 530								
MAP 531								
MAP 532	305	410	447	0.01	0.07	0.00	0.09	
MAP 533								0.70715363
MAP 534								
MAP 535								
MAP 505	242	266	453	0.00	0.06	0.00	0.07	
MAP 504								
MAP 503								
MAP 502	230	347	447	0.00	0.05	0.00	0.07	0.71
MAP 501								
MAP 500								
MAP 499								0.70709527
MAP 498								
MAP 497	296	371	448	0.01	0.09	0.00	0.11	
MAP 496								
MAP 495								
MAP 494								
MAP 493								0.70715211
MAP 600								
MAP 601	83	38	443	0.02	0.29	0.00	0.13	
MAP 602								
MAP 603								
MAP 604								
MAP 605	121	294	455	0.00	0.05	0.00	0.12	
MAP 606								
MAP 607								
MAP 608								
MAP 609	198	372	452	0.00	0.07	0.00	0.13	0.70714505
MAP 610								
MAP 611								
MAP 612	72	125	449	0.01	0.13	0.00	0.22	
MAP 613								
MAP 614								
MAP 615	83	207	458	0.01	0.09	0.00	0.22	
MAP 616								
MAP 617	55	59	446	0.01	0.14	0.00	0.15	
MAP 618								
MAP 619								
MAP 620	89	45	446	0.02	0.30	0.00	0.15	
MAP 621								
MAP 622								
MAP 623	65	37	451	0.02	0.31	0.00	0.18	0.70709456
MAP 624								

Sample No.	HI	OI	Tmax	S1	S2a	S2b	S3	87Sr/86Sr
MAP 625								
MAP 626								
MAP 627	55	55	452	0.01	0.15	0.00	0.15	
MAP 628								
MAP 629								
MAP 630	26	112	486	0.00	0.07	0.00	0.30	
MAP 631								
MAP 632	76	71	440	0.01	0.15	0.00	0.14	0.70702766
MAP 633								
MAP 634								
MAP 635	121	134	453	0.01	0.11	0.00	0.12	
MAP 636								
MAP 637	45	91	464	0.01	0.12	0.00	0.24	
MAP 638								
MAP 639	91	41	456	0.02	0.27	0.00	0.12	0.70701909
MAP 640								
MAP 641								
MAP 642	92	71	454	0.01	0.17	0.00	0.13	
MAP 643								
MAP 644								0.70694019
MAP 645	47	55	457	0.01	0.17	0.00	0.19	
MAP 646								
MAP 647								
MAP 648	62	36	455	0.02	0.27	0.00	0.16	
MAP 649								
MAP 650	70	39	453	0.02	0.30	0.00	0.17	0.70705233
MAP 651								
MAP 652	25	63	469	0.01	0.16	0.00	0.40	
MAP 653	79	22	458	0.03	0.53	0.00	0.15	
MAP 654								
MAP 655	68	16	462	0.05	0.66	0.00	0.16	
MAP 656	67	22	463	0.03	0.46	0.00	0.15	
MAP 657	N/A	N/A	N/A	N/A	N/A	N/A	N/A	
MAP 658	N/A	N/A	N/A	N/A	N/A	N/A	N/A	
MAP 659	N/A	N/A	N/A	N/A	N/A	N/A	N/A	
MAP 660	N/A	N/A	N/A	N/A	N/A	N/A	N/A	
MAP 661	N/A	N/A	N/A	N/A	N/A	N/A	N/A	
MAP 662	N/A	N/A	N/A	N/A	N/A	N/A	N/A	
MAP 663	N/A	N/A	N/A	N/A	N/A	N/A	N/A	
MAP 664	N/A	N/A	N/A	N/A	N/A	N/A	N/A	
MAP 665	N/A	N/A	N/A	N/A	N/A	N/A	N/A	
MAP 666	N/A	N/A	N/A	N/A	N/A	N/A	N/A	
MAP 667	N/A	N/A	N/A	N/A	N/A	N/A	N/A	
MAP 668	39	108	466	0.01	0.08	0.00	0.22	0.70718555
MAP 669								
MAP 670	84	191	445	0.01	0.09	0.00	0.20	0.70738852
MAP 671								

Sample No.	HI	OI	Tmax	S1	S2a	S2b	S3	87Sr/86Sr
MAP 672								0.70716681
MAP 673								
MAP 907	0	897	481	0.01	0.00	0.00	0.21	
MAP 908								
MAP 909	29	297	482	0.02	0.01	0.00	0.11	
MAP 910								
MAP 911	0	488	481	0.00	0.00	0.00	0.11	
MAP 912								
MAP 913	0	4299	483	0.01	0.00	0.00	0.19	
MAP 914								
MAP 915	0	367	483	0.02	0.00	0.00	0.05	
MAP 916								
MAP 917								
MAP 918								
MAP 919	0	491	303	0.02	0.00	0.00	0.12	
MAP 920								
MAP 921								
MAP 922	0	476	482	0.01	0.00	0.00	0.11	
MAP 923								
MAP 924	0	330	480	0.02	0.00	0.00	0.07	
MAP 925	0	507	483	0.02	0.00	0.00	0.13	
MAP 926	44	317	291	0.03	0.01	0.00	0.08	

Supplementary material S2 Ultrahigh-resolution $d^{13}C_{carb}$, $d^{18}O_{carb}$, and carbonate content data measured from limestone beds bracketing ash layers in Mapojiao main section and Mapojiao B section.

Sample No.	Position (cm)	$d^{13}C$ VPDB	$d^{18}O$ VPDB Calcite	$d^{18}O$ VSMOW Calcite	Yield % (as CaCO3)
MAP C3	29	4.19	-6.37	24.35	93
MAP C2	27	4.56	-5.74	24.99	102
MAP C1	25	4.92	-6.07	24.65	100
MAP B4	23	4.60	-5.69	25.04	110
MAP B3	20	4.85	-5.60	25.14	82
MAP B2	15	4.80	-5.27	25.48	115
MAP B1	12	4.86	-5.17	25.58	94
MAP A5	10	4.57	-4.64	26.12	110
MAP A4	8	4.98	-4.48	26.30	101
MAP A3	5	4.86	-4.75	26.01	87
MAP A2	2	4.76	-5.20	25.55	104
MAP A1	0.05	4.61	-4.97	25.78	107
MAP (B) 955	0	Ash Layer			
MAP D2	-1	5.33	-5.80	24.93	59.7
MAP D1	-6	5.23	-5.80	24.93	66.3
MAP E	-10	5.37	-3.64	27.16	112
MAp F	-16	5.01	-3.94	26.85	94

Sample No.	Position (cm)	$d^{13}C$ VPDB	$d^{18}O$ VPDB Calcite	$d^{18}O$ VSMOW Calcite	Yield % (as CaCO3)
I	78	6.01	-5.37	25.38	96
H	52	5.98	-4.51	26.26	110
G	38	4.61	-5.66	25.08	82
F	20.00	4.99	-4.72	26.05	87
E	5.00	4.92	-4.01	26.78	71
MAP B 954	0	Ash Layer			
A	-5	5.18	-4.42	26.35	58
B	-20	4.98	-4.30	26.48	76
C	-30	3.29	-4.64	26.13	80
D	-45	1.37	-6.83	23.86	106

Sample No.	Psition (cm)	$\delta^{13}C$ VPDB	$\delta^{18}O$ VPDB Calcite	$\delta^{18}O$ VSMOW Calcite	Yield % (as CaCO3)
MAP 637 A4	40	2.89	-6.00	24.73	30.41
MAP 637 A3	37	2.74	-5.93	24.80	59.87
MAP 637 A2	33	3.01	-3.99	26.80	83.79
MAP 637 A1	30	0.76	-2.69	28.14	44.93
MAP 637 B2	26	3.52	-3.61	27.18	75.78
MAP 637 B1	23	3.41	-3.64	27.16	64.28
MAP 637 C2	18	3.39	-4.50	26.27	72.17
MAP 637 C1	16	3.47	-3.95	26.84	69.48
MAP 637 D2	11	3.40	-4.47	26.30	70.71
MAP 637 D1	7	3.35	-4.68	26.09	73.47
MAP 637 E4	6	3.49	-4.55	26.22	55.79
MAP 637 E3	4	3.38	-4.87	25.89	42.81
MAP 637 E2	2	2.98	-5.40	25.34	68.33
MAP 637 E1	1	2.17	-6.45	24.26	23.17
MAP 800 T	0	Ash Layer			
MAP 636 A4	-0.50	1.20	-6.71	24.00	51.89
MAP 636 A3	-1.00	2.53	-6.74	23.96	40.30
MAP 636 A2	-3.00	2.27	-7.35	23.34	37.67
MAP 636 A1	-5.00	1.97	-7.51	23.17	36.61
MAP 636 B4	-8.00	2.27	-7.42	23.26	25.82
MAP 636 B3	-10.00	3.25	-5.72	25.02	52.53
MAP 636 B2	-12.00	3.56	-5.00	25.75	56.88
MAP 636 B1	-16.00	3.58	-4.35	26.42	80.16
MAP 636 C4	-19.00	3.01	-6.67	24.03	54.55
MAP 636 C3	-22.00	2.69	-7.28	23.41	60.79
MAP 636 C2	-26.00	2.99	-6.53	24.17	41.06
MAP 636 C1	-29.00	2.20	-7.22	23.47	13.95

Sample No.	Position (cm)	$d^{13}C$ VPDB	$d^{18}O$ VPDB Calcite	$d^{18}O$ VSMOW Calcite	Yield % (as CaCO3)
MAP 645 A5	37	1.90	-5.16	25.59	26
MAP 645 A4	33	2.52	-3.66	27.13	68
MAP 645 A3	30	2.66	-3.13	27.68	58
MAP 645 A2	28	2.59	-3.29	27.52	88
MAP 645 A1	26	2.02	-5.83	24.90	25
MAP 645 B2	23	1.73	-4.77	25.99	19
MAP 645 B1	21	1.25	-7.44	23.24	15
MAP 645 C6	18	2.05	-6.22	24.50	28
MAP 645 C5	17	2.38	-6.55	24.16	26
MAP 645 C4	15	2.17	-6.32	24.40	39
MAP 645 C3	13	1.85	-6.22	24.50	23
MAP 645 C2	11	0.69	-7.34	23.34	16
MAP 645 C1	9	0.69	-7.70	22.97	11
MAP 645 D5	8	1.13	-7.21	23.48	20
MAP 645 D4	6	2.03	-6.73	23.98	30
MAP 645 D3	5	2.83	-4.39	26.38	70
MAP 645 D2	2.5	2.99	-4.27	26.51	67
MAP 645 D1	1	2.63	-5.03	25.72	51
MAP 808 T	0	Ash Layer			
MAP 644 A4		NA	NA	NA	0
MAP 644 A3		NA	NA	NA	0
MAP 644 A2		NA	NA	NA	0
MAP 644 A1		NA	NA	NA	0
MAP 644 B3		NA	NA	NA	0
MAP 644 B2		NA	NA	NA	0
MAP 644 B1		NA	NA	NA	0
MAP 644 C3	-10	1.82	-7.34	23.35	20
MAP 644 C2	-14	2.36	-7.35	23.33	25
MAP 644 C1	-17	2.32	-7.44	23.24	28
MAP 644 D3	-20	2.62	-4.23	26.55	74
MAP 644 D2	-22	2.73	-3.56	27.24	72
MAP 644 D1	-24	1.96	-5.06	25.69	65

Sample No.	Position (cm)	d^{13}C VPDB	d^{18}O VPDB Calcite	d^{18}O VSMOW Calcite	Yield % (as CaCO3)
MAP 615 A5	176	3.79	-5.58	25.16	63
MAP 615 A4	173	3.65	-6.26	24.46	16
MAP 615 A3	170	3.60	-6.34	24.37	58
MAP 615 A2	167	3.38	-6.75	23.95	30
MAP 615 A1	164	3.17	-7.03	23.66	49
MAP 615 B3	161	3.18	-5.14	25.61	95
MAP 615 B2	158	2.75	-5.61	25.13	72
MAP 615 B1	154	3.30	-7.06	23.63	40
MAP 615 C5	151	3.01	-7.88	22.79	19
MAP 615 C4	149	3.34	-6.56	24.15	8
MAP 615 C3	147	3.77	-5.21	25.54	3
MAP 615 C2	145	3.47	-6.48	24.23	13
MAP 615 C1	143	3.78	-6.37	24.34	38
MAP 801 T	Ash Layer				
MAP 614 A6	131	3.08	-6.76	23.94	46
MAP 614 A5	129	2.75	-7.79	22.88	32
MAP 614 A4	126	1.94	-7.28	23.41	33
MAP 614 A3	122	2.48	-7.17	23.52	56
MAP 614 A2	119	2.01	-7.51	23.17	19
MAP 614 A1	117	1.79	-7.56	23.12	29
MAP 614 B3	114	2.29	-7.70	22.97	34
MAP 614 B2	110	2.48	-5.79	24.95	22
MAP 614 B1	107	3.46	-4.61	26.16	32
MAP 614 C2	103	2.87	-7.56	23.12	33
MAP 614 C1	100	2.91	-7.50	23.18	22
MAP 613 A3	96	3.83	-5.76	24.97	56
MAP 613 A2	92	3.82	-5.19	25.56	62
MAP 613 A1	90	3.97	-5.41	25.34	49
MAP 613 B5	85	3.88	-5.08	25.67	69
MAP 613 B4	80	3.93	-5.60	25.14	31
MAP 613 B3	78	3.86	-5.25	25.49	68
MAP 613 B2	73	3.99	-5.45	25.29	55
MAP 613 B1	69	3.96	-5.71	25.02	35
MAP 613 C4	66	3.70	-6.62	24.09	27
MAP 613 C3	64	3.69	-6.63	24.07	48
MAP 613 C2	62	3.69	-6.53	24.18	29
MAP 613 C1	61	3.76	-6.34	24.38	52
MAP 613 D4	59	3.71	-6.54	24.17	61
MAP 613 D3	56	3.79	-6.47	24.24	52
MAP 613 D2	54	3.70	-6.33	24.38	61
MAP 613 D1	52	3.81	-6.51	24.20	44
MAP 802 T	Ash Layer				
MAP 612 A4	41	4.36	-4.54	26.23	83

Sample No.	Position (cm)	$d^{13}C$ VPDB	$d^{18}O$ VPDB Calcite	$d^{18}O$ VSMOW Calcite	Yield % (as CaCO3)
MAP 612 A2	37	4.39	-5.38	25.36	58
MAP 612 A1	33	4.48	-4.40	26.37	92
MAP 612 B5	29	3.85	-5.98	24.75	71
MAP 612 B4	25	3.92	-5.42	25.32	61
MAP 612 B3	21	4.17	-4.31	26.46	34
MAP 612 B2	17	4.19	-4.50	26.27	44
MAP 612 B1	13	4.14	-4.90	25.86	53
MAP 612 C3	11	4.03	-3.55	27.25	86
MAP 612 C2	8	4.02	-5.93	24.79	73
MAP 612 C1	2	3.98	-3.38	27.43	79

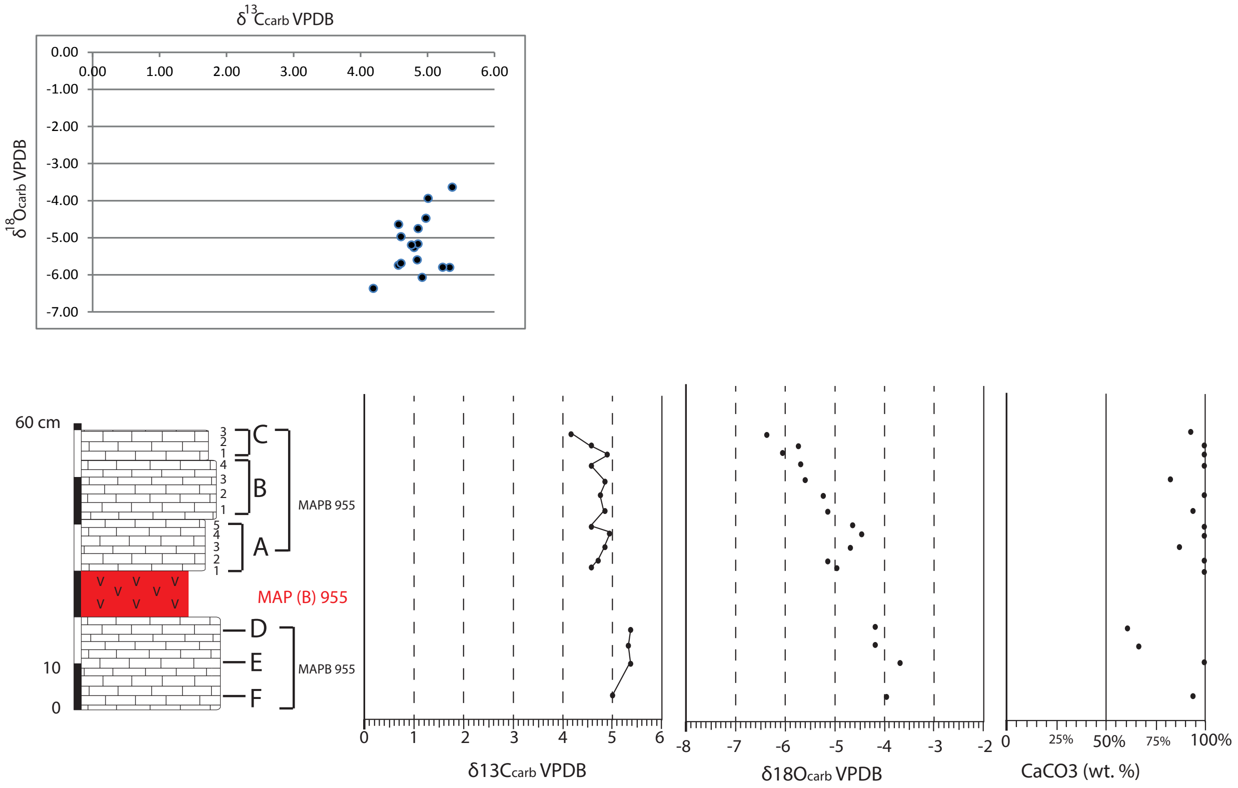

Supplementary material S3 δ $^{13}C_{carb}$, δ $^{18}O_{carb}$, carbonate content, and δ $^{13}C_{carb}$ versus δ $^{18}O_{carb}$ cross-plot around an ash layer in the lateral equivalent of Unit A from the Mapojiao B quarry section.

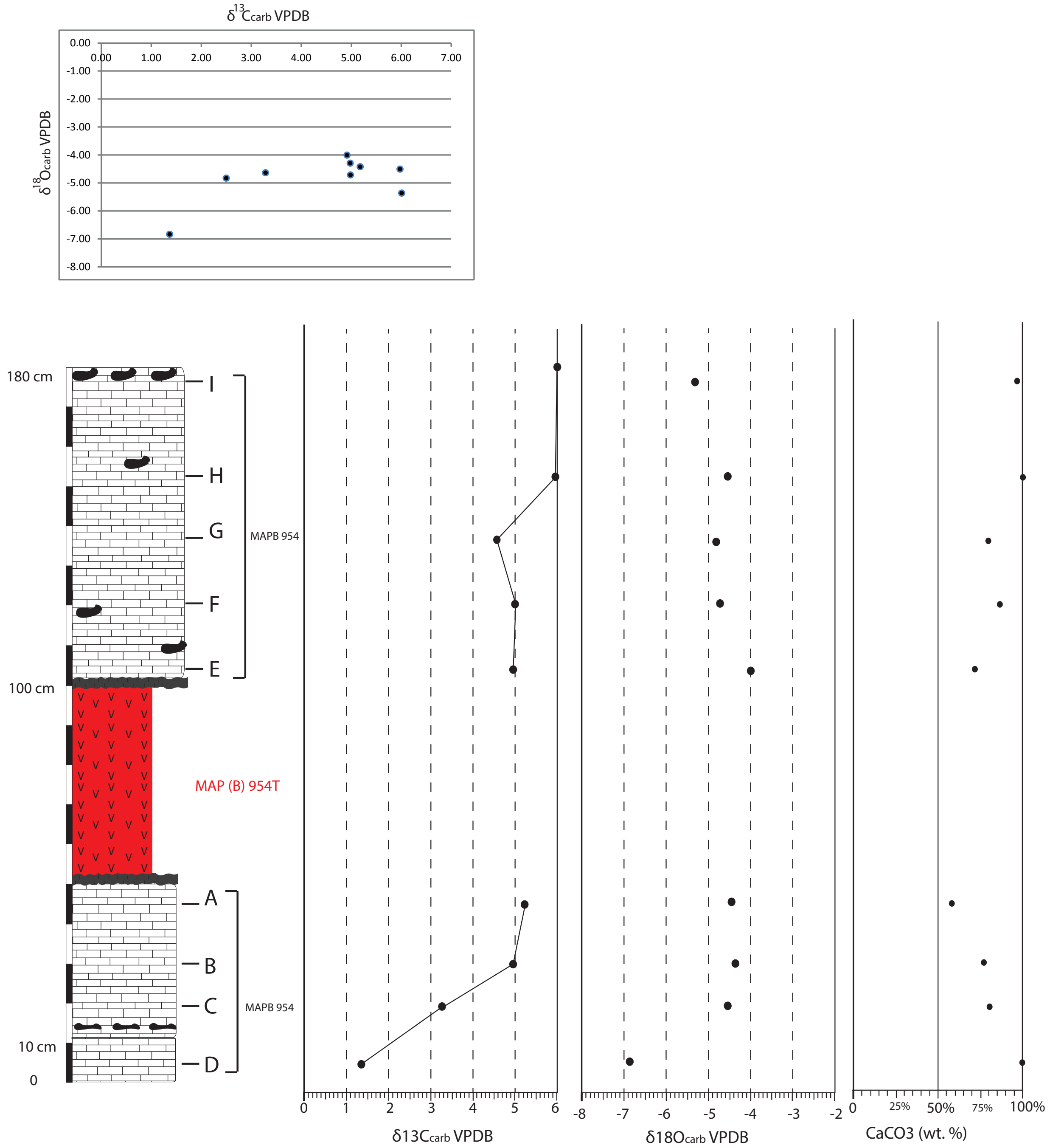

Supplementary material S4 δ ^{13}C$_{carb}$, δ ^{18}O$_{carb}$, carbonate content, and δ ^{13}C$_{carb}$ versus δ ^{18}O$_{carb}$ cross-plot around an ash layer in the lateral equivalent of Unit A from the Mapojiao B quarry section.

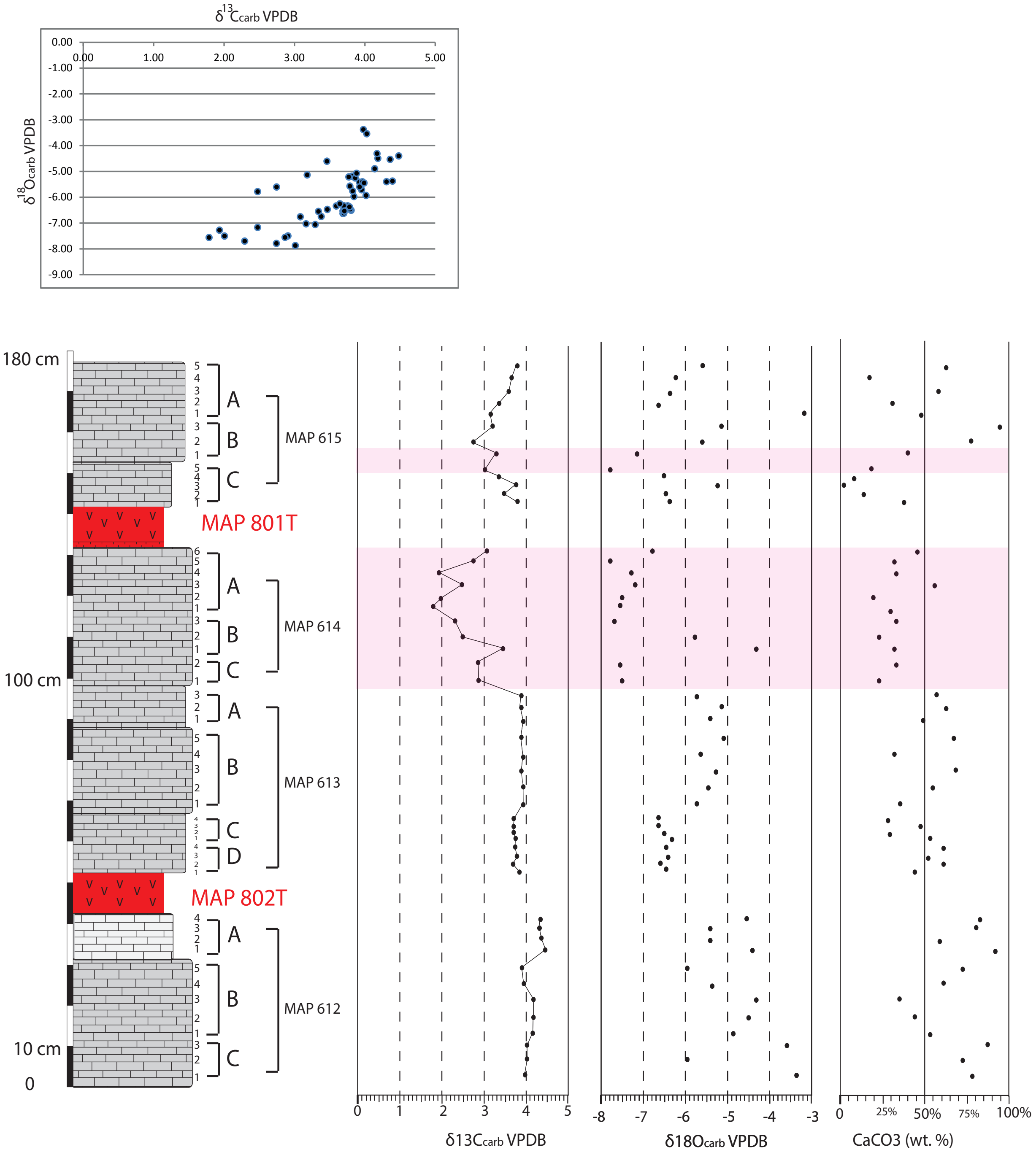

Supplementary material S5 $\delta^{13}C_{carb}$, $\delta^{18}O_{carb}$, carbonate content, and $\delta^{13}C_{carb}$ versus $\delta^{18}O_{carb}$ cross-plot around the ash layers (801 T-802 T) in Subunit B1 from the Mapojiao main section. Horizons with $\delta^{18}O_{carb}$ values < −7 ‰ are highlighted with pink intervals.

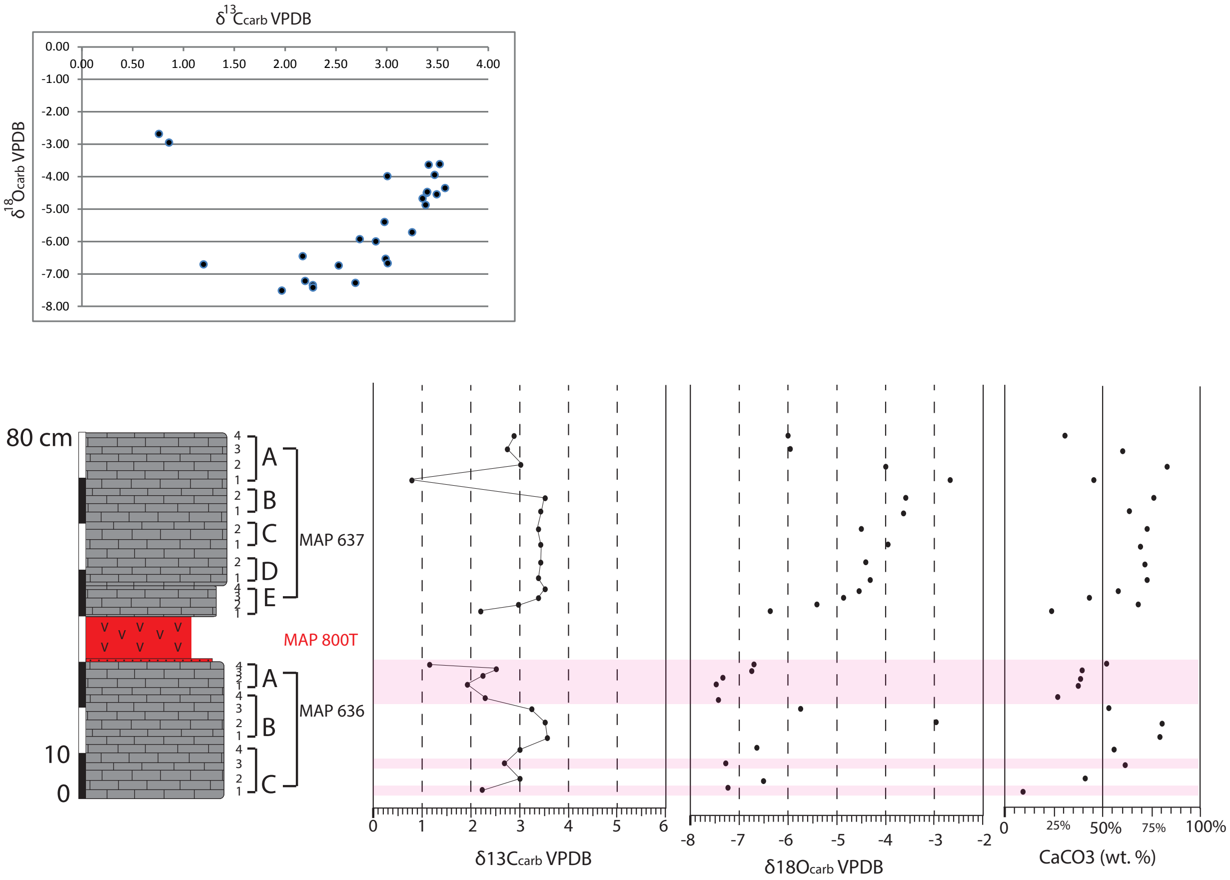

Supplementary material S6 δ $^{13}C_{carb}$, δ $^{18}O_{carb}$, carbonate content, and δ $^{13}C_{carb}$ versus δ $^{18}O_{carb}$ cross-plot around the lower ash layer (800 T) in Subunit B2 from the Mapojiao main section. Horizons with δ $^{18}O_{carb}$ values < −7 ‰ are highlighted with pink intervals.

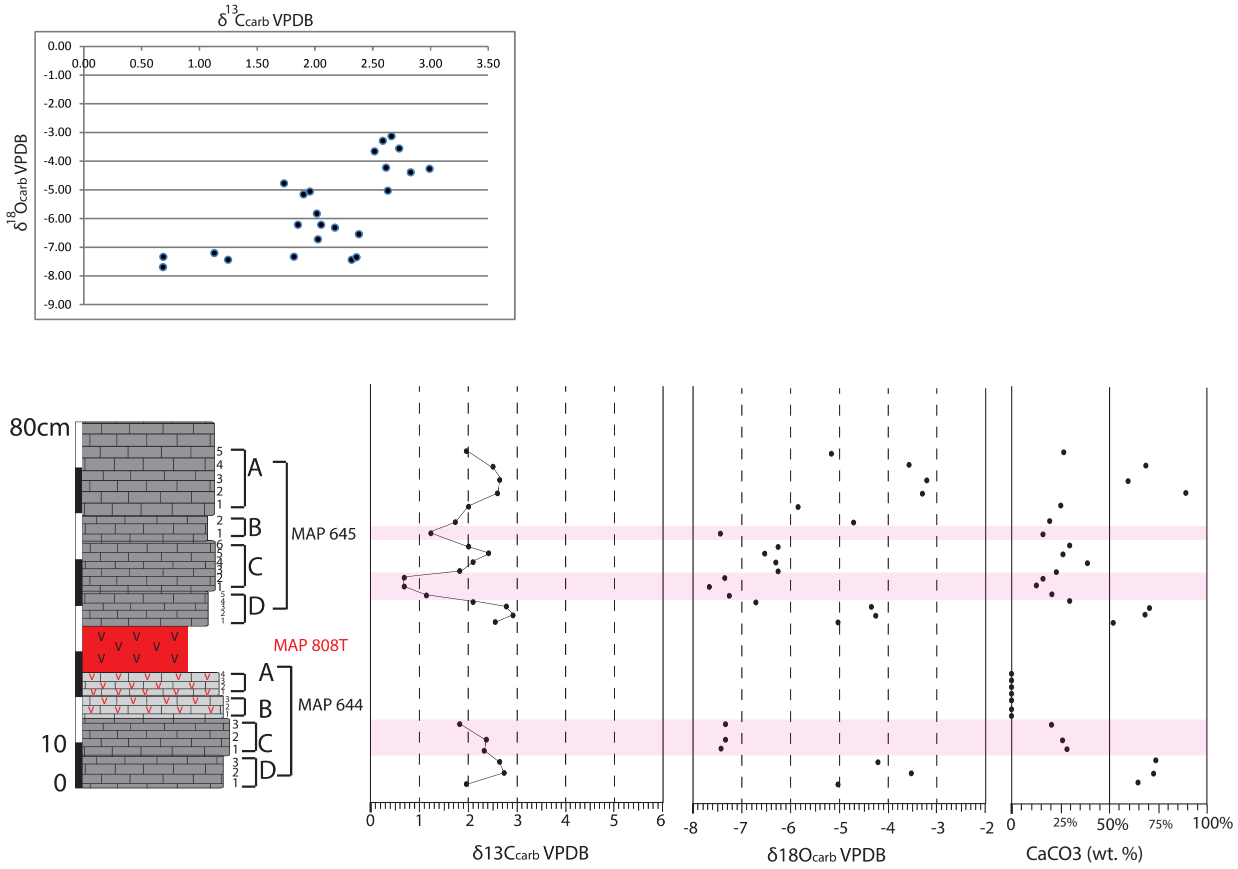

Supplementary material S7 δ ^{13}C$_{\text{carb}}$, δ ^{18}O$_{\text{carb}}$, carbonate content, and δ ^{13}C$_{\text{carb}}$ versus δ ^{18}O$_{\text{carb}}$ cross-plot around the upper ash layer (808 T) in Subunit B2 from the Mapojiao main section. Horizons with δ ^{18}O$_{\text{carb}}$ values < −7 ‰ are highlighted with pink intervals.

Chapter III

ARE LATE PERMIAN CARBON ISOTOPE EXCURSIONS OF LOCAL OR OF GLOBAL SIGNIFICANCE?

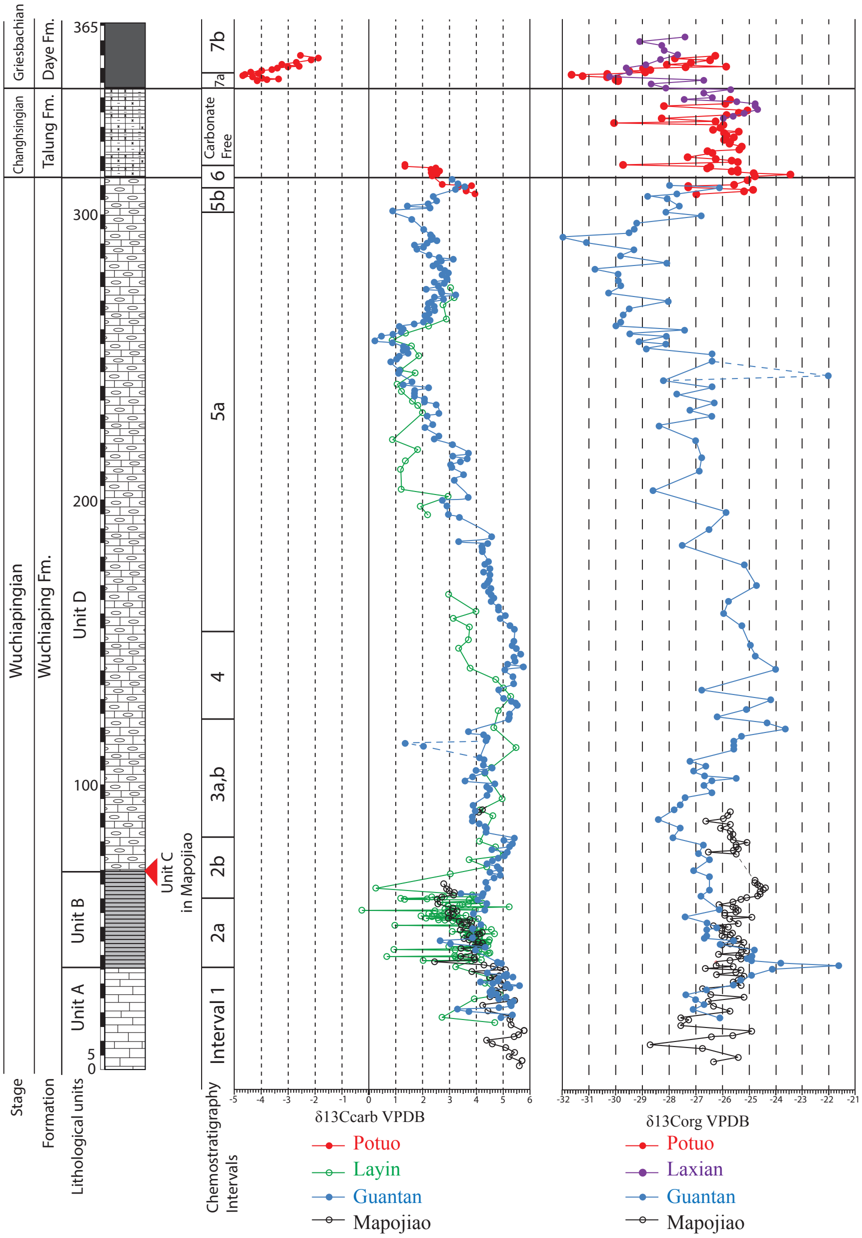

GSA Bulletin (in review)

Are Late Permian carbon isotope excursions of local or of global significance?

Borhan Bagherpour[1*], Hugo Bucher[1], Torsten Vennemann[2], Elke Schneebeli-Hermann[1], Dong-xun Yuan[3], Marc Leu[1] , Chao Zhang[3] & Shu-Zhong Shen[3]

1- Paleontological Institute, University of Zurich, Karl Schmid-Strasse 4, 8006 Zürich, Switzerland.

2- Institute of Earth Surface Dynamics, University of Lausanne, Géopolis, 1015 Lausanne, Switzerland.

3- Nanjing Institute of Geology and Palaeontology, Chinese Academy of Sciences, Nanjing 210008, China.

ABSTRACT

We present a new, biostratigraphically calibrated organic and inorganic C-isotope record spanning basal Wuchiapingian to basal Griesbachian (late Permian-earliest Triassic) time from southern Guizhou (South China). After fluctuations attributable to diagenetic overprint were removed, three negative Carbon Isotope Excursions (CIEs) persist. These include a short-lived CIE during the early Wuchiapingian, a protracted CIE ending shortly after the Wuchiapingian–Changhsingian Boundary (WCB), and a third CIE straddling the PTB. Comparison of our new C-isotope record with those from other south Chinese sections reveals the influence of local bathymetry and increased burial of terrestrial organic matter. Comparison with other time series outside South China also highlights that only the negative CIE at PTB is a global signal. This suggests fundamental differences in the carbon cycling between the late Permian on the one hand and the PTB and Early Triassic on the other. This divergence is explained by the different volumes of erupted basalts between the mid-Capitanian Emeishan and the late Permian-Triassic Siberian large igneous provinces and their distinct eruptive modalities. Emeishan volcanism was largely submarine, implying that sea water was an efficient buffer against atmospheric propagation of volatiles. The equatorial position of Emeishan was also an additional obstacle for volatiles to reach the stratosphere and benefit from an efficient global distribution. Consequently, the local significance of these CIEs calls into question correlations based on C-isotope chemostratigraphy during the late Permian. The timing of the late Permian Chinese CIEs is also not reflected in changes in species diversity or ecology, unlike the sudden and global PTB crisis and subsequent Early Triassic upheavals.

Keywords: Permian; Triassic; Carbon isotope; China; Emeishan Large Igneous Province; Siberian Traps.

1. INTRODUCTION

The largest mass extinction of the Phanerozoic occurred at the Permian-Triassic Boundary (PTB) between 251.941±0.037 and 251.880±0.031 Ma (Burgess et al., 2014), an age range recently supported by new stratigraphically closely spaced U-Pb dates (251.939±0.030 Ma in Dongpan, South China) from a deep water depositional environment with no stratigraphic gap at the PTB (Baresel et al., 2017a).

During the PTB about 80 to 90% of marine species went extinct (e.g. Raup, 1979; Sepkoski, 1989; Stanley, 2016). Terrestrial plant communities underwent a marked but short term ecological deterioration synchronous with the mass extinction in marine ecosystem (Zhang et al., 2016), although without a significant increase of extinction rate (Hochuli et al., 2010, 2016, 2017; Schneebeli-Hermann, 2015, 2017). The mass extinction was also accompanied by a global excursion toward lighter values (negative shift) in the carbon isotope record (e.g. Hermann et al., 2010; Korte and Kozur, 2010; Shen et al., 2013), as well as by drastic changes of the composition of sediments deposited on marine shelves (e.g. Kershaw et al., 2012; Bagherpour et al., 2017) and of sedimentation rates (Algeo and Twitchett, 2010; Baresel et al., 2017b). On the one hand, the sudden (Shen et al., 2011) PTB mass extinction has been perceived as the final peak of an extended ~8 Myr long time interval of decreasing biodiversity, starting around the Guadalupian-Lopingian boundary (GLB) extinction event (e.g. Bottjer et al., 2008; Clapham et al., 2009). Some authors (e.g. Isozaki et al., 2007; Bottjer et al., 2008) also suggested that the GLB represents the onset of a 20 Myr long time interval of unstable carbon cycling. Nevertheless, the GLB and PTB extinctions are generally considered to be two independent and unrelated phenomena (e.g. Shen and Shi, 1996, 2002; Wang and Sugiyama, 2000).

The PTB and Early Triassic CIEs represent some of the largest known Phanerozoic fluctuations in the C-isotope record, which have revealed robust and global isotopic changes of the dissolved inorganic carbon (DIC) reservoir of the world ocean (e.g. Payne et al., 2004; Galfetti et al., 2007a; Horacek et al., 2009; Meyer et al., 2013; Grasby et al., 2013; Sanson-Barrera et al., 2015). However, the lateral variability in the amplitude of these CIEs, as well as the offset of average absolute values along an onshore-offshore gradient, remains poorly documented. The synchronicity of these events is nevertheless very well documented by a wealth of analyses, thus establishing their global significance. In contrast, there is a comparatively limited amount of studies documenting the carbon isotope record of late Permian time. Here, available carbonate carbon isotopic records appear to be extremely variable in time and space, with little or no consistency that would compare with those around the PTB and during the Early Triassic. There are even fewer available data for the organic carbon isotope record, which is only sporadically known (e.g. Cao et al., 2009; Baud et al., 2012; Yan et al., 2013). Therefore, the amount of late Permian data is insufficient for assessing whether the PTB and Early Triassic CIEs are singular instabilities after a stable late Permian interval or, alternatively, if these CIEs are protracted perturbations of the carbon cycle from the late Permian into the Early Triassic. Moreover, validation of C-isotope chemostratigraphy in the Late Permian at the global scale - as utilized for the Early Triassic - directly hinges on the synchronicity and lateral reproducibility of these CIEs.

Further comparison of independently age-controlled late Permian C-isotope time series should help settle this open question. In this endeavor, we investigate a new Lopingian to basal Griesbachian, paleontologically age-controlled and expanded succession in the Pingtang syncline (southern Guizhou) of the Nanpanjiang Basin (South China). This new coupled carbonate and organic C-isotope time series is supplemented by Rock-Eval data and palynofacies analyses in order to evaluate the relative proportions of terrestrial *vs.* marine organic matter, a prerequisite for a sound interpretation of CIEs. Detailed facies analysis is also conducted for reconstructing depositional environments and for assessing the potential linkages between fluctuations of C-isotope values and facies change and/or diagenetic alteration (e.g. dolomitization).

Then, a comparison of the Lopingian and basal Early Triassic C-isotope time series within South China and with other Tethyan locales (e.g. Iran) is presented. This allows the disentangling of local *vs*. global C-isotope signals. Finally, we discuss potential driving mechanisms and processes that best account for the observed discrepancies in the lateral reproducibility of the signal between late Permian and Early Triassic CIEs.

The first and main phase of Emeishan volcanism is mid-Capitanian in age (Sun et al., 2010). However, extension of protracted and modest Emeishan volcanism into Wuchiapingian time is supported by facies analysis (Bagherpour et al., under revision a), strontium isotope (Bagherpour et al., under revision b), hafnium isotope (Ovtcharova et al., ongoing work), and radiometric ages (Shellnut, 2014; Ovtcharova et al., ongoing work). Hence, the respective impact of large igneous provinces such as the Permian Emeishan and the PTB-Early Triassic Siberia large igneous provinces are discussed in this perspective.

2. GEOLOGICAL CONTEXT AND STUDIED SECTIONS

2.1. Paleogeographical Context

Oblique convergence between the Indochina and South China blocks in the eastern equatorial Tethys resulted in the development of the Nanpanjiang pull-apart basin within a back arc context (Bagherpour et al., 2017). The main tectonic phase of the basin is manifested by local intercalations of wedges of breccia at the transition between the Wuchiaping Fm. and the Talung Fm., close to the Wuchiapingian-Changhsingian boundary (WCB). In some parts of the basin (e.g. northwestern Guangxi), these wedges reach several tens of meter in thickness and can be traced laterally over tens of kilometer. These breccias, as well as the persisting paleogeographic patterns in bathymetry inherited from the WCB into the Changhsingian and the Early Triassic, illustrate the primary control exerted by block faulting tectonics on the architecture of the basin. This tectonism initiated a horst and graben paleotopography during the Changhsingian, with deposition of shallow marine limestone (Heshan Fm.) on uplifted blocks and coeval deposition of deep-marine siliceous mudstone (Talung Fm.) on downthrown blocks. The earliest Triassic paleotopography was directly inherited from the latest Permian one, leading to the deposition of microbial limestone (basal Luolou Fm.) on highs (e.g. Great Bank of Guizhou, see Lehrmann et al. 1998; Luolou Platform, see Bagherpour et al. 2017) and contemporaneous deposition of black shales (basal Ziyun and Daye formations) in troughs and at the bottom of the slope. Depositional environments on highs were characterized by well oxygenated waters, whereas circulation was restricted in the troughs (Bagherpour et al., 2017; Baresel et al., 2017b).

The Pingtang syncline is located in the present-day northern part of the Nanpanjiang Basin (Fig. 1a). The late Permian to Early Triassic succession in the 50 km long, NE-SW trending Pingtang syncline (Fig. 1b) includes the Wuchiaping, Talung, and Daye formations, in ascending order (Fig. 1c). Transition from the Daye Fm. to the Luolou Fm. occurs at the middle-late Smithian boundary in this syncline (Leu et al., ongoing work). Deposition of the shallow marine Wuchiaping Fm. abruptly ended with a synsedimentary breccia and was succeeded by the deposition of deep water, organic matter-rich marine siliceous mudstones of the Talung Fm. Earliest Triassic black shale of the Daye Fm. conformably rests on top of the Talung Fm. These troughs document settings where poorly oxygenated, silled water mater masses persisted across the PTB, with continuous deposition (Bagherpour et al., 2017; Baresel et al., 2017a).

2.2. Lithological Subdivisions

Here, we present a 365 m-thick, early late Permian to earliest Triassic composite section combining five partial sections distributed within the Pingtang syncline; namely, the Mapojiao, Guantan, Layin, Potuo and Laxian sections (Fig. 1b, c). Lithological markers consistently found within the entire syncline have been used for constructing the composite section.

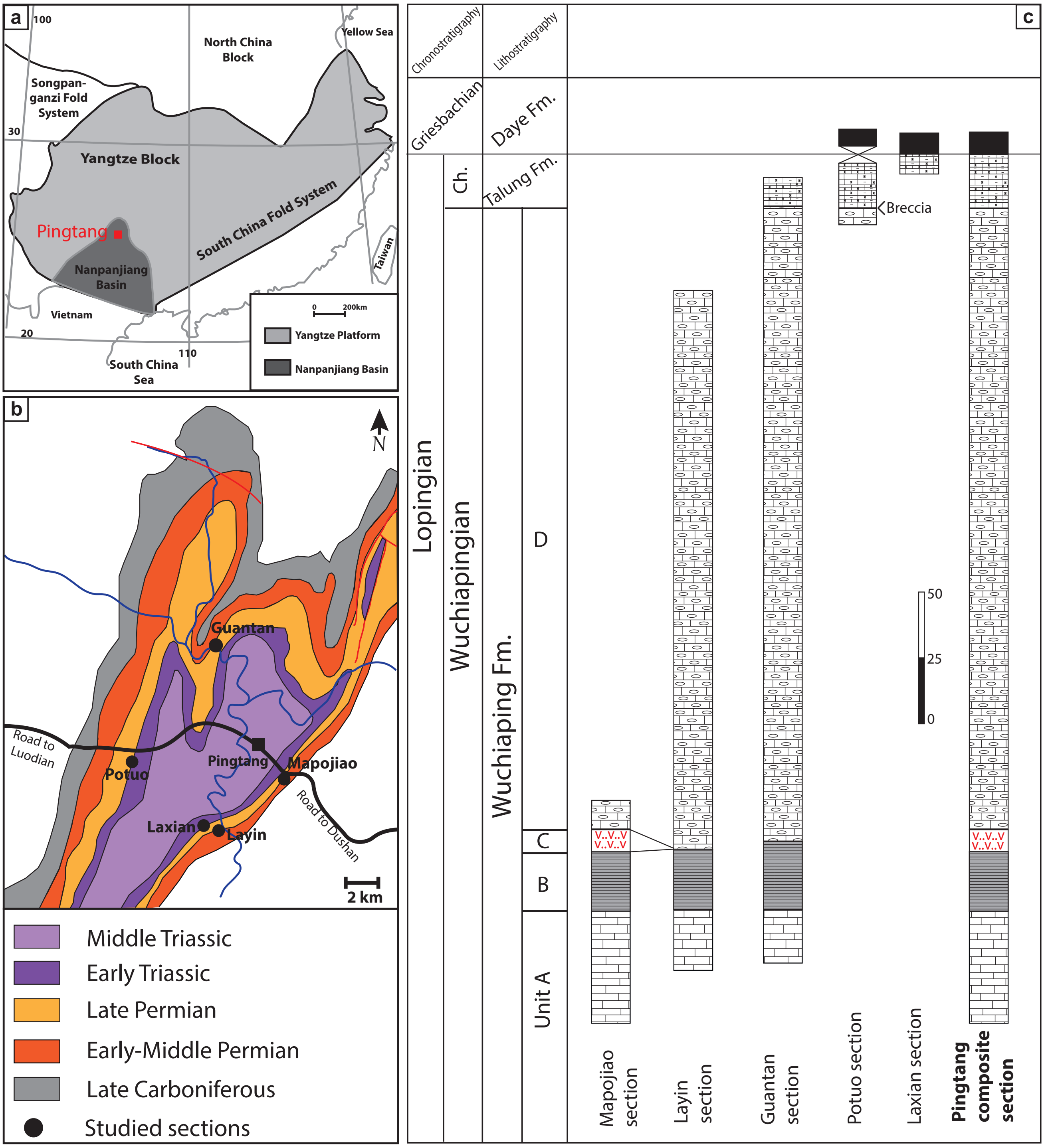

Fig. 1 Tectonic map, geologic map, and lithostratigraphy of the Late Permian-earliest Triassic of Pingtang syncline. **a**, Tectonic map of the South China Block including the Yangtze Craton, the South China fold system and the Nanpanjiang Basin (modified from Lehrmann et al., 1998). **b**, Geologic map of the Pingtang syncline and locations of the studied sections (modified from Bureau of Geology and mineral resources of Guizhou Province 1986). **c**, Studied sections (Mapojiao, Layin, Guantan, Potuo and Laxian) and their stratigraphic position in the Pingtang composite section. A-D refers to the lithostratigraphic units of Wuchiaping Fm.

In the Pingtang syncline, we subdivide the Wuchiaping Fm. into five lithostratigraphic units (Units A-E) (Table 1). Unit A is characterized by thick-bedded, light grey limestone rich in shallow-marine benthic organisms and with few chert concretions. The overlying Unit B is characterized by thin-bedded, black, siliceous limestone. The very distinctive facies and lateral continuity of this unit provide a useful lithological marker for correlation. Unit B is conformably overlain by Unit C, an 8 m-thick succession of 20-30 cm thick volcanogenic distal turbidites. The overlying Unit D consists of medium to thick-bedded, grey, bioclastic limestone containing abundant centimetric diagenetic concretions of dark chert and a few volcanic ashes. This unit represents the thickest part of the Wuchiaping Fm. A 0.8 m-thick breccia containing centimetric, angular chert and limestone clasts of Permian age ends the Wuchiaping Fm. It is followed by the Talung Fm., which predominantly consists of thin-bedded siliceous mudstone, frequent ash layers, and rare concretionary limestone beds near its base. The Talung Fm. is in turn conformably overlain by the Daye Fm., whose lower part typically consists of carbonaceous, finely laminated black shales, occasional ash layers and a few horizons of centimetric to decimetric carbonate concretions.

2.3. Studied Sections

2.3.1. *Mapojiao Section*

This 90 m-thick section is located along a fresh road-cut in the eastern limb of the Pingtang syncline (25˚49´21.8″N; 107˚21´16.3″E, Fig. 1b) and comprises units A, B, C, and the basal part of Unit D of the Wuchiaping Fm. (Fig. 1c, 2a). Analyses of depositional environments and conodont biostratigraphy of this section were documented by Bagherpour et al. (Bagherpour et al., under revision a), and carbon and strontium isotope records were presented by Bagherpour et al. (Bagherpour et al., under revision b) (Fig. 3). The lowermost 35 m of this section corresponds to thick-bedded and massive limestone of Unit A. The conformably overlying Unit B consists of 31 m of medium- to thin-bedded, siliceous limestone. The lower part (ca. 9 m) of this unit is characterized by medium-bedded, dark grey limestone (Subunit B1), which represents the transitional interval from Unit A to the thin-bedded, black, siliceous limestone of the upper part of Unit B (Subunit B2). Unit B is conformably overlain by an 8 m-thick interval of volcanogenic turbidites (Unit C), which is in turn followed by Unit D (15 m).

2.3.2. *Guantan And Layin Sections*

The Guantan section (25˚53´21.9″N; 107˚18´29.9″E) is located in the northern part of the Pingtang syncline (Fig. 1b) and exposes almost the entire Wuchiaping Fm. including units A, B, and D (Fig. 1c, 2b, 4). The upper 295 m of the formation were logged and sampled with

Age	Formation	Unit	Thickness	Lithology	Age diagnostic fossils	Description	Depositional environment
Griesbachian	Daye	Lower part	~15 m	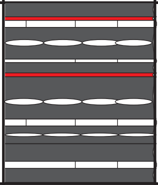	*Hindeodus parvus*	Laminated, OM-rich black shale. Interbedded with occasional ash layers and thin-bedded micritic limestone layers.	Basin
Changhsingian	Talung		30 m	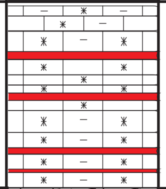	*Clarkina subcarinata*	Thin-bedded, OM rich, siliceous, mudstone rich in radiolarian. Interbedded with numerous ash layers.	Basin
Wuchiapingian	Wuchiaping	Unit D	0.8 m		—	Breccia containing centimetric/decimetric clasts of Wuchiaping Fm.	Synsedimentary tectonic breccia
			242 m	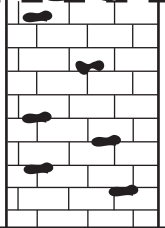	*Clarkina longicuspidata* *Clarkina orientalis* *Clarkina ?transcaucasica* *Clarkina liangshanensis* *Avushoceras* sp. *Prototoceras* sp.	Medium to thick-bedded, grey, limestone rich in shallow marine bioclasts and diagenetic chert nodules.	Shallow subtidal carbonate platform
		Unit C	8 m	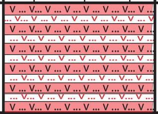	—	Upward thinning alteration of volcanogenic silt and sandstone (only in Mapojiao section).	Distal turbiditic fans
		Unit B	23-31 m	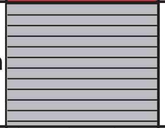	*Clarkina ?transcaucasica* *Clarkina guangyuanensis* *Clarkina leveni*	Thin-bedded, black, cherty, OM-rich limestone containing intraclasts and abundant radiolarian and sponge spicules.	Slope to basin
		Unit A	~35 m	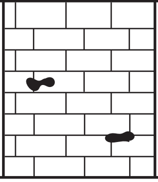	*Clarkina leveni* *Clarkina asymmetrica* *Clarkina ?dukouensis*	Massive light-grey bioclastic limestone with reefal community.	Shallow subtidal carbonate platform

Table 1 Age control, lithological subdivision, discerption and depositional environments from the Pingtang syncline.

high resolution. The basal 20 m of the logged part consist of thick-bedded and massive limestones belonging to Unit A. Unit B consists of 33 m of medium- to thin-bedded, dark grey to black limestone. The lower ~6 m of this unit (Subunit B1) are characterized by medium-bedded, dark grey limestone and represent a transitional facies between Unit A and Subunit B2, the latter being typified by thin-bedded, black, cherty limestone. The submarine lobe of volcanogenic turbidites of Unit C is locally missing in this section. Unit D conformably overlies Unit B, is 242 m thick, and represents most of the Wuchiaping Fm. Only the basal part of the Talung Fm. is visible.

The Layin section (25˚47′05.1″N; 107˚18′28.5″E) is located in the eastern limb of the Pingtang syncline (Fig. 1b). The lithological succession is overturned and consists of 260 m of Wuchiaping Fm. (Fig. 2c, 5). The Guantan and Layin sections share identical lithological successions. In Layin, a 20 m-thick interval in the middle of Unit D is obscured by a fault. However, the perfect exposure of a laterally equivalent interval at Guantan fills this gap.

2.3.3. *Potuo And Laxian Sections*

The Potuo section (25˚49′34.9″N; 107˚14′55.1″E) is located on the western limb of the Pingtang syncline (Fig. 1b) and comprises ~33 m of upper Permian to Lower Triassic sediments (Fig. 1c, 6). The basal 6 m of this section corresponds to the uppermost part of Unit D (Fig. 7a). A 0.8 m thick breccia is intercalated in the upper part of Unit D (Fig. 7b). Above the breccia, 2 m of medium- to thin-bedded limestone of the Wuchiaping Fm. and intercalated ash layers, are conformably overlain by 24 m of thin-bedded, siliceous, mudstone of the Talung Fm., which contains numerous ash layers. Above a ca. 3 m thick covered interval, 6 m of thin-bedded, carbonaceous, laminated, black-shale of the basal Daye Fm. (Fig. 7c) terminate the logged part of this section.

The formational boundary between the Talung and the Daye formations is well exposed at Laxian (25˚47′19.7″N; 107˚17′51.4″E) in the eastern limb of the Pingtang syncline (Fig. 1b). The base of the Laxian section comprises the uppermost 7 m of the Talung Fm., which is conformably overlain by a 15 m-thick interval of brown weathering black shales with frequent ash layers typical of the base of Daye Fm. (Fig. 7d, 8).

3. AGE CONTROL

Clarkina ?dukouensis is the stratigraphically oldest conodont that has been retrieved from the studied interval of Wuchiaping Fm. in the Pingtang syncline (50 m below the detailed studied interval at both Mapojiao and Guantan sections). Above an 18 m thick conodont

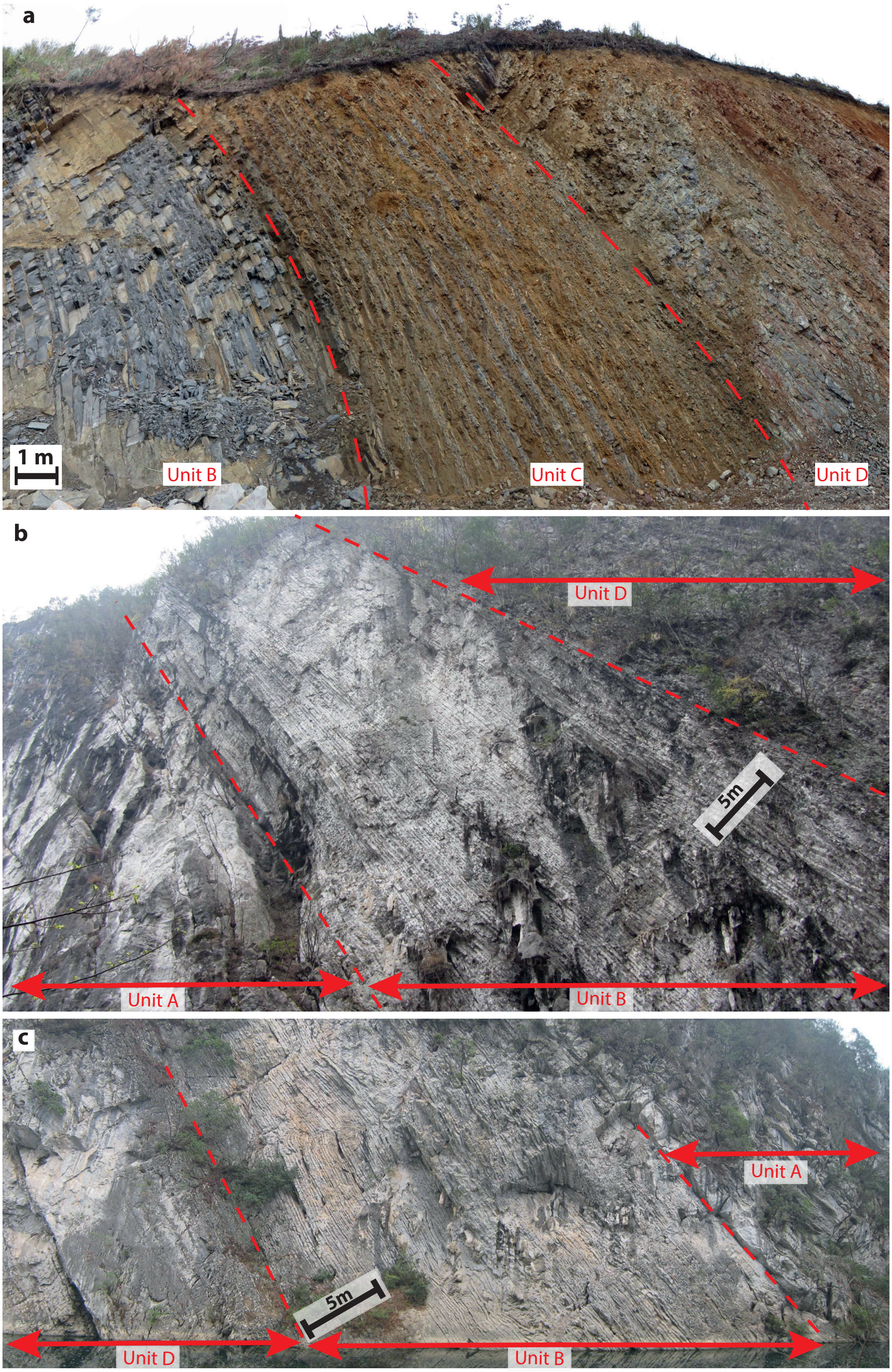

Fig. 2 Field photographs of exposures of Unit A, Unit B, Unit C and base of Unit D. **a**, Mapojiao section. **b**, Guantan section. **c**, Layin overturned section. Dashed lines separate the lithostratigraphic units. Note the absence of Unit C in Guantan and Layin sections.

barren interval, *C. asymmetrica*, *C. leveni*, *C. guangyuanensis*, and *C. ?transcaucasica* sequentially appear from Unit A to the middle of Unit B at Mapojiao (Fig. 3). Hence, Unit A and (lower part of) Unit B correspond to the *C. asymmetrica* Interval Zone (IZ), *C. leveni* IZ, *C. guangyuanensis* IZ and perhaps *C. transcaucasica* IZ in the early Wuchiapingian (Bagherpour et al., Under review a).

At Potuo the uppermost bed of the Wuchiaping Fm. is characterized by the presence of *Clarkina orientalis*, *C. longicuspidata*, and *C. longicuspidata* transitional to *C. wangi* (Fig. 9). Next, 1 m above the base of the Talung Fm. in Potuo, *C. subcarinata* is retrieved from two limestone beds intercalated with siliceous mudstone in the basal part of the Talung Fm. (Fig. 9). *Clarkina orientalis* IZ represents the youngest conodont zone of the Wuchiapingian stage, whose uppermost part is characterized by the overlapping *C. longicuspidata* (Shen and Mei 2010). The base of the Changhsingian has been defined by the First Appearance Datum (FAD) of *C. wangi* (Jin et al., 2006; Shen and Mei 2010), which has not been retrieved here. However, *C. subcarinata* represents the second conodont IZ of the Changhsingian Stage (Shen and Mei 2010), and therefore indicates that the Wuchiapingian-Changhsingian boundary (WCB) is within the basal 1 m of the Talung Fm. The ammonoids *Avushoceras* sp. and *Prototoceras* sp. (Fig. 10), indicating a Wuchiapingian age (Ehiro and Bando, 1985), were also retrieved from the uppermost bed of the Wuchiapingian Fm. at Potuo, which confirms that the top of the Wuchiaping Fm. is still within the Wuchiapingian Stage.

The PTB is biostratigraphically defined by the FAD of the conodont *Hindeodus parvus* (Yin et al., 2001), which is retrieved ca. 6 m above the formational boundary between the Talung and Daye formations at Potuo. However, the accuracy of this paleontological definition of the PTB is largely dependent on local ecological controls (facies) and on sampling effort. Recently, a comprehensive study proposed a reliable conodont zonation based on Unitary Association Zones (UAZs) instead of the traditional IZs and placed the PTB between UAZ2 and UAZ 3 (Brosse et al., 2016). Moreover, a recent study of the precise age of PTB in South China revealed that the Talung and Ziyun formational boundary in Dongpan and Penglaitan represents a synchronous time line bracketed by UAZ2 and UAZ3 in Meishan (Brosse et al., 2016; Baresel et al., 2017a). Hence, we place the PTB at the sharp and conformable formational boundary between late Permian Talung Fm. and the Early Triassic Ziyun/Daye formations.

4. MATERIAL AND METHODS

Sections were logged bed by bed and samples were collected for analyses of carbonate

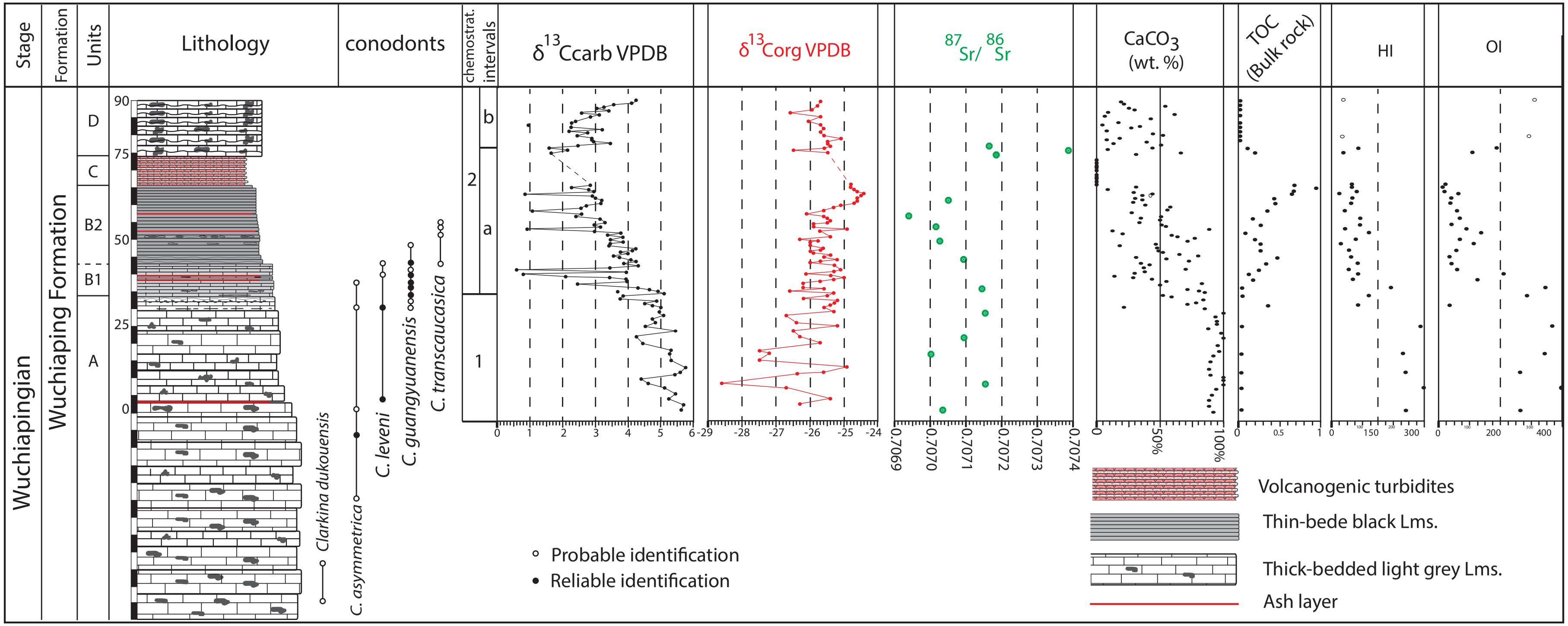

Fig. 3 Detailed stratigraphic log of the Mapojiao section with $\delta^{13}C_{carb}$, $\delta^{13}C_{org}$, $^{87}Sr/^{86}Sr$, carbonate content, TOC, hydrogen index (HI), and oxygen index (OI) data of the Mapojiao section (Bagherpour et al., under revision b). Stratigraphic range of conodont taxa are from Bagherpour et al. (under review a).

carbon and oxygen isotopes ($\delta^{13}C_{carb}$, $\delta^{18}O_{carb}$), bulk organic carbon isotope ($\delta^{13}C_{org}$), composition of organic matter (Rock-Eval and palynofacies), and preparation of thin sections.

A total of 510 hand samples (305 from Guantan, 143 from Layin, and 62 for Potuo) for $\delta^{13}C_{carb}$ and $\delta^{18}O_{carb}$ measurement of bulk micrite were collected. In order to avoid calcite veins, weathered parts, large bioclasts, cracks and stylolites, samples were carefully cleaned, cut and selectively drilled to produce a fine powder.

The C- and O- isotope composition of the carbonates were measured with a GasBench II linked to a DeltaPlus XL mass spectrometer (Thermo-Fisher Scientific) according to a method adapted after Spötl and Vennemann (2003). Carbonates were reacted at 70 ºC with 100 % orthophosphoric acid, and the extracted CO_2 calibrated against a number of in-house Carrara Marble (CM) replicates for acid fractionation and normalization of the $d^{13}C$ and $d^{18}O$ values expressed at the permil scale. The CM standard was, in turn, calibrated against $\delta^{13}C$ and $\delta^{18}O$ values of NBS-19 (+1.95 and –2.20 ‰, relative to VPDB). Average reproducibility of about 8 CM's analysed in each run of 40 samples is better than 0.06 ‰ for $d^{13}C$ and 0.08 ‰ for $d^{18}O$ values.

A total of 197 samples (111 Guantan, 62 Potuo and 24 Laxian) for $\delta^{13}C_{org}$ measurements of bulk organic matter (OM) were selected. Samples were cleaned and surfaces were trimmed off, then ground to <100 µm using a puck mill and treated with 6 M HCL for 24 hours. Residues were repeatedly rinsed with deionized water and centrifuged till neutrality was reached. The residues were dried over night at 45 ˚C and $\delta^{13}C_{org}$ values of the homogenized residues were measured using a Carlo Erba 1500 elemental analyser connected to a ThermoFisher Delta V Plus mass spectrometer. The samples were individually wrapped in tin foil cups and sequentially allowed to react with an injected quantity of oxygen while continuously flushed with He carrier gas. The sample was oxidized in the reactor at about 1050ºC using cobalt(II) oxide as the catalyst. Excess oxygen in the He-stream was adsorbed in a reactor column filled with metallic Cu held at 500 ºC. The CO_2 produced was passed over a magnesium perchlorate (Mg[ClO4]2) trap to remove H_2O and a gas chromatograph to separate the N_2 from the CO_2, before the CO_2 is carried by the He-stream into the mass spectrometer for isotopic analysis. The reproducibility of several in-house standards used is better than 0.1 ‰ and calibrated against USGS-24 graphite (–16.0 ‰ VPDB) and NBS-22 oil (–29.6 ‰ VPDB).

A total of 128 samples (111 Guantan and 17 Potuo) were selected for the quantification and characterization of the OM using a Rock-Eval 6 device following the method described by Espitalié et al. (1985, 1986) and Behar et al. (2001). The IFP 160000 standard was used to calibrate the measurements. The determined parameters such as the total organic carbon (TOC) content,

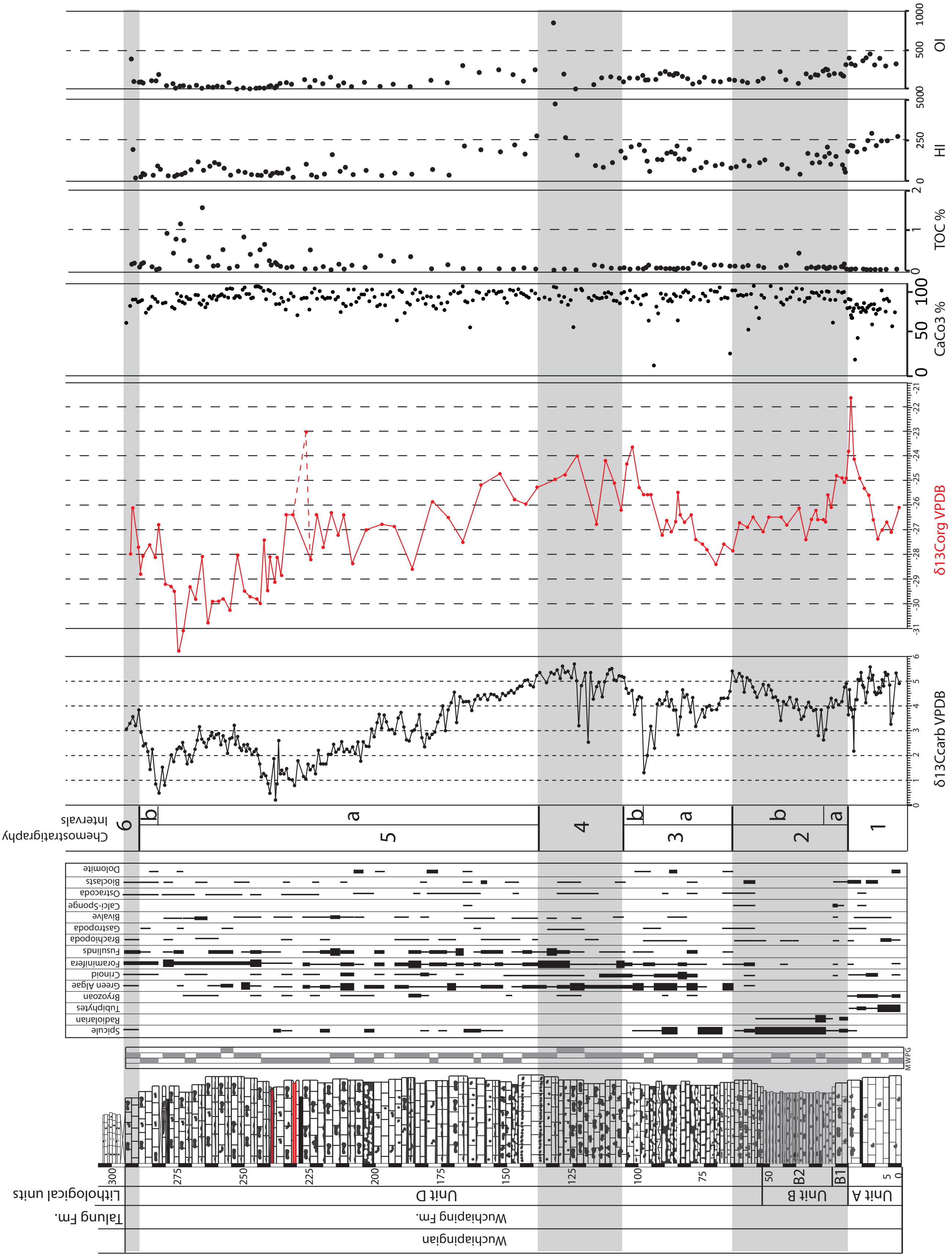

Fig. 4 Detailed stratigraphic log of the Guantan section with microfacies (M: Mudstone, W: Wackestone, P: Packstone, G: Grainstone), $\delta^{13}C_{carb}$, $\delta^{13}C_{org}$, carbonate content, TOC, hydrogen index (HI), and oxygen index (OI) data. Grey and white bands highlight different chemostratigraphic intervals. See figures 3 and 8 for legend.

the total inorganic carbon (MINC) content, free hydrocarbons (S1), residual petroleum potential (S2), generate CO2 (S3) and the temperature of maximum hydrocarbon evolution from kerogen (*T*max) are used to calculate the Hydrogen Index (HI), and the Oxygen Index (OI). The HI and OI are proportional to the H/C and O/C ratios of the organic matter, respectively, and can be used to identify different types of kerogen (I to IV) in Van-Krevelen-like diagrams (Espitalié et al., 1985, 1986).

Palynofacies analysis was used in order to evaluate terrestrial and marine fraction of the particulate OM. 15 samples (8 from Guantan, 7 from Layin) were selected for palynofacies analysis. Samples were cleaned and surfaces were trimmed off, then crushed to mm-size particles and treated with hydrochloric and hydrofluoric acid according to the standard techniques described by Traverse, (2007). The unoxidized residues were sieved over a 15 µm mesh screen and strew mounted on slides for analysis of the particulate organic matter (POM, kerogen, or palynofacies) using a transmitted light microscope Olympus BX51. The POM was subdivided into terrestrial and marine OM fractions. The terrestrial POM mainly consists of translucent and opaque woody particles and rare spores and pollen grains, inertinite, cuticles, and membranes. The marine POM mainly consists of amorphous organic matter (AOM) and a minor fraction of foraminiferal test linings.

One hundred samples were selected for the preparation of thin sections and petrographic analyses. In order to distinguish between calcite and dolomite thin sections were stained with Alizarin red S.

5. RESULTS

5.1. Facies Analysis

Facies analyses of different lithostratigraphic units from early Late Permian to basal Early Triassic of the Pingtang syncline are summarized in Table 1.

Thick-bedded and massive limestones of Unit A are characterized by wackestone-packstone texture with abundant benthic fauna including brachiopods, *Tubiphytes ?obscurus*, bryozoans, calcareous sponges, crinoids, and less abundant ostracods, smaller foraminifera, rugose corals and bivalves (Fig. 11a). Fusulinids and calcareous algae were not observed in this unit. Minor secondary dolomitization is occasionally observed in the lower part of this unit.

The lower part of Unit B (Subunit B1) is dominated by medium-bedded, dark grey, pyritic, wackestone-packstone limestone containing radiolarian and sponge spicules and subordinate fragments of benthic bioclasts (Fig. 11b). Bioturbation is occasionally observed in Subunit B1. Intercalations of thin storm deposits are present in Subunit B1 at Mapojiao (Bagherpour

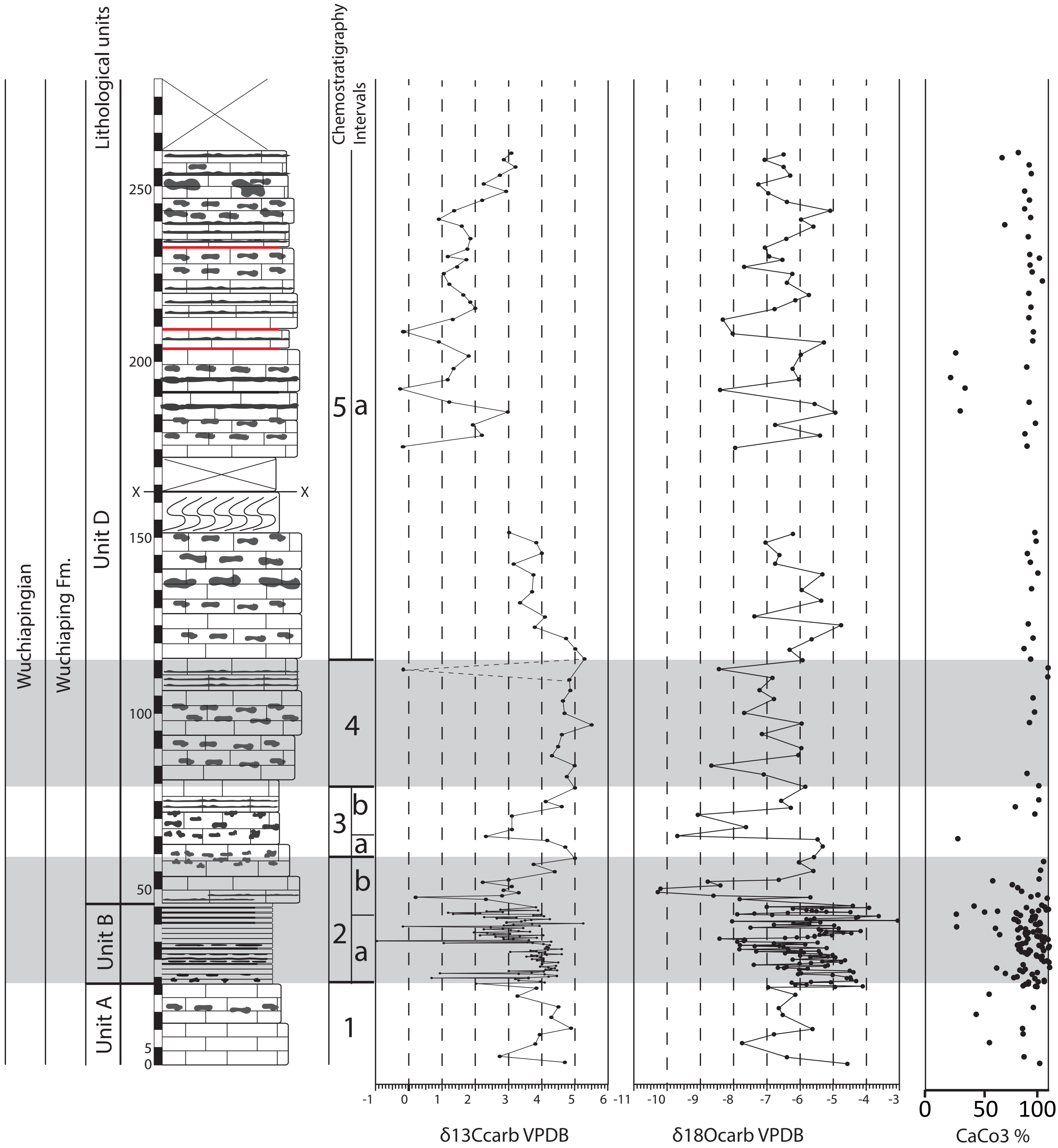

Fig. 5 Detailed stratigraphic log of the Layin section with $\delta^{13}C_{carb}$, $\delta^{18}O_{carb}$ and carbonate content data. Grey and white bands highlight different chemostratigraphic intervals. See Fig. 3 for legend.

et al., under revision a). The upper part of Unit B (Subunit B2) is dominated by thin-bedded, black, pyritic, wackestone-packstone limestone containing abundant radiolarian and sponge spicules and rare smaller foraminifers, ostracods and laterally transported brachiopods (Fig. 11c).

The overlying Unit C is represented by a stack of 20 volcanogenic distal turbidites.

The lowermost part of Unit D is characterized by limestone with wackestone texture rich in sponge spicules whose abundance progressively decrease upward and which are replaced by shallow marine benthic bioclasts (e.g. fusulinids, smaller foraminifera, calcareous algae (Fig. 11d)). The basal 40 m of Unit D are characterized by alternation of sponge spicule-dominated facies with foraminifera- and algae-dominated facies. The upper part of Unit D is characterized by thick-bedded, grey, bioclastic, wackestone and packstone rich in diverse shallow marine benthos, including fusulinids, smaller foraminifers, calcareous algae, crinoids, brachiopods, bivalves, gastropods, and ostracods. Two horizons with grainstone texture are intercalated in the middle and upper part of this unit. Minor secondary dolomitization that selectively altered bioclasts, such as calcareous sponge or algae, is also observed in some horizons. Hydrodynamic sedimentary structures are absent, and burrows are seldom seen.

Thick-bedded limestone of Unit D is interrupted by deposition of a synsedimentary breccia (Fig. 7a, b) near the top of the Wuchiaping Fm. The uppermost 2 m of the Wuchiaping Fm. (above the breccia) are characterized by medium to thin-bedded limestone with wackestone texture and a marked decrease in the abundance of shallow marine bioclasts.

The Talung Fm. conformably overlies the Wuchiaping Fm. and is dominated by thin-bedded, dark-grey, laminated, siliceous mudstone with abundant radiolarians and subordinate sponge spicules (Fig. 11e). Disseminated pyrite crystals are commonly present. Organic rich, thin (2 cm) horizons are frequently present within beds.

The basal part of the conformably overlying Daye Fm. is characterized by thin-bedded, laminated, carbonaceous black shales (Fig. 11f). Bioclasts and bioturbation are absent, and calcareous nodules are frequently present. Dolomitization is also observed in this interval.

5.2. Carbon ($\delta^{13}C_{carb,}$ $\delta^{13}C_{org}$) And Oxygen ($\delta^{18}O_{carb}$) Isotopes

The $\delta^{13}C_{carb}$ record (Supplementrary material S1) has been subdivided into seven chemostratigraphic intervals (“1” to “7”, see Figs. 3, 4, 5, 6 and 8) defined by trends in the time series (increasing, decreasing, or stable succession of values). The first five intervals and the base of the sixth interval are recognized in Guantan (and in the auxiliary Layin section), and the sixth and seventh intervals are recognized in Potuo and

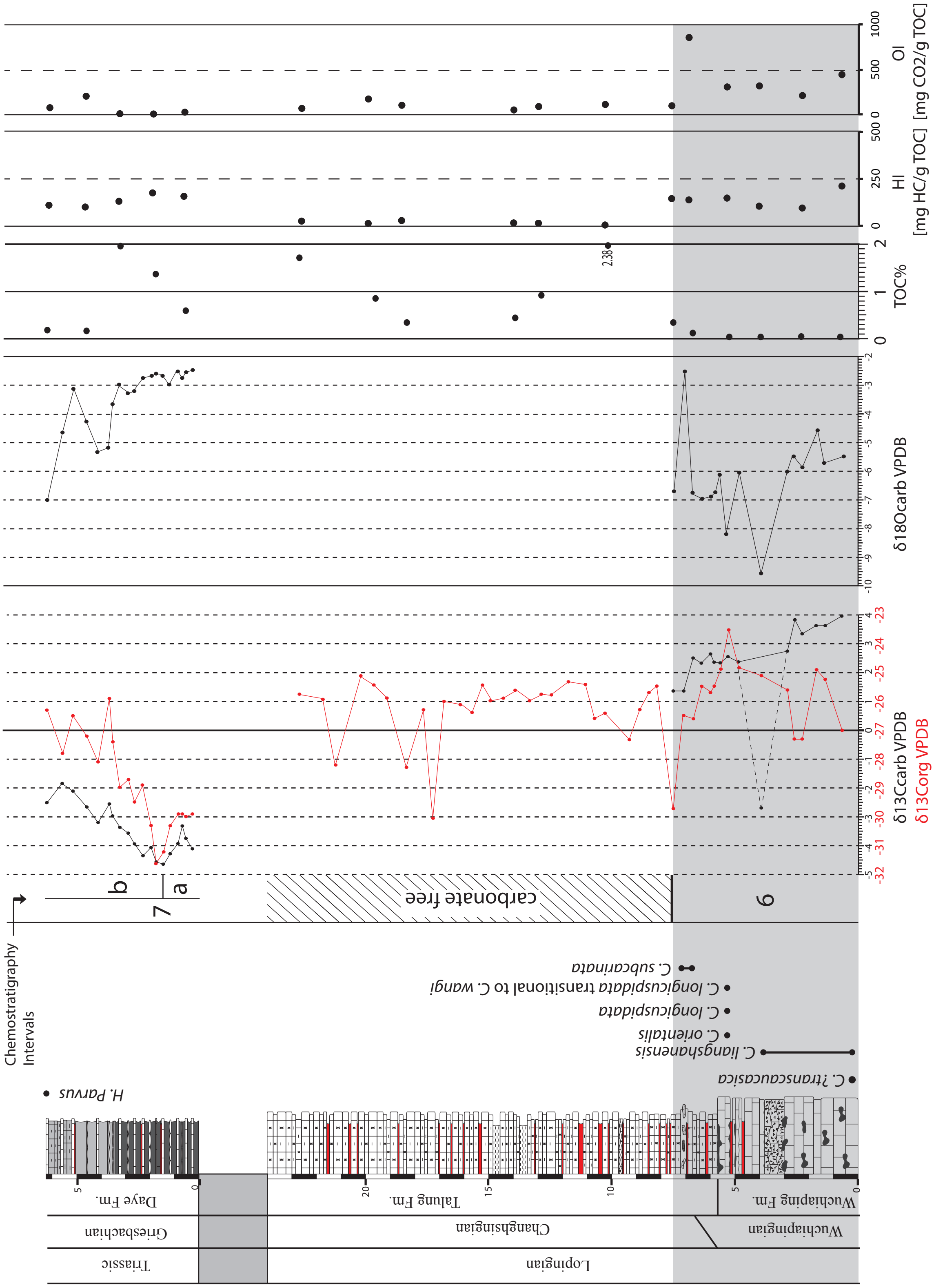

Fig. 6 Detailed stratigraphic log of the Potuo section with the stratigraphic range of conodont taxa, $\delta^{13}C_{carb}$, $\delta^{18}O_{carb}$, $\delta^{13}C_{org}$, TOC, hydrogen index (HI), and oxygen index (OI) data. Grey and white areas highlight different chemostratigraphic intervals. See figures 3 and 8 for legend.

Laxian. $\delta^{13}C_{carb,}$ $\delta^{13}C_{org}$ and $\delta^{18}O_{carb}$ time series are described for each of these intervals.

5.2.1. *Guantan*

Interval 1 is characterized by a plateau of heavy $\delta^{13}C_{carb}$ values around 5‰, followed by a sharp 1‰ drop (Fig. 4). The $\delta^{18}O_{carb}$ values in interval 1 vary between -4 and -9‰ and show a minor covariation with $\delta^{13}C_{carb}$ (Supplementrary material S2). An abrupt negative shift in $\delta^{18}O_{carb}$ is also documented in the uppermost part of interval 1. The $\delta^{13}C_{org}$ data in this interval display a sharp excursion toward higher values (positive shift) from -27.5‰ to -21.5‰.

Interval 2a is defined by a prominent $\delta^{13}C_{carb}$ negative CIE of about 2.5‰ in Unit B. Interval 2b corresponds to a positive shift reaching maximum value of 5‰ in the lower part of Unit D. The $\delta^{18}O_{carb}$ values in interval 2a and in the lower part of interval 2b range from -5‰ to -9‰, whereas the upper half of interval 2b is characterized by heavier values between -3‰ to -6‰. The base of interval 2 is marked by a rapid negative CIE in $\delta^{13}C_{org}$ values from -21.5‰ to -27.5‰. After a succession of rather stable values around -27‰, the $\delta^{13}C_{org}$ curve drops to -28‰ in the upper part of this interval.

In interval 3a, the $\delta^{13}C_{carb}$ profile shows a negative trend from 5‰ to 2‰, with superimposed fluctuations (Fig. 4). This negative shift is followed by a rapid increase to values of 5‰ in interval 3b. The $\delta^{18}O_{carb}$ values in interval 3 vary between -4 and -9‰. Although there is small negative $\delta^{18}O_{carb}$ shift at the base of this interval, no covariation with the $\delta^{13}C_{carb}$ is observed. Interval 3 also corresponds to a clear increasing trend in $\delta^{13}C_{org}$ values from -28‰ to -24‰.

Interval 4 is marked by a relatively stable plateau of heavy $\delta^{13}C_{carb}$ values around 5.5‰. The $\delta^{18}O_{carb}$ values range from -5‰ to -8‰. Most of interval 4 is also characterized by $\delta^{13}C_{org}$ values spreading around -25‰ in average.

Interval 5a is defined by a long and protracted negative trend in $\delta^{13}C_{carb}$ CIE from ca. 5.5‰ to 0.5‰. The upper part of this interval shows two distinct negative peaks (at 238 m and 282 m from the base of the section). It is followed by the abrupt 3‰ positive shift defining interval 5b. The $\delta^{18}O_{carb}$ values range from -4‰ to -9‰ and do not show any covariation with $\delta^{13}C_{carb}$ values for most of this interval, although the second negative peak of $\delta^{13}C_{carb}$ correlates with a parallel negative peak in $\delta^{18}O_{carb}$. Interval 5a shows a prominent 7‰ negative shift in $\delta^{13}C_{org}$ values throughout 140 m of the section, decreasing from -25‰ to -32‰ with superimposed 2‰ noise. The very end of interval 5a and interval 5b are characterized by a ~4‰ positive shift of $\delta^{13}C_{org}$.

The base of interval 6 is characterized by a 1‰ negative shift of $\delta^{13}C_{carb}$ values.in the uppermost part of Wuchiaping Fm.

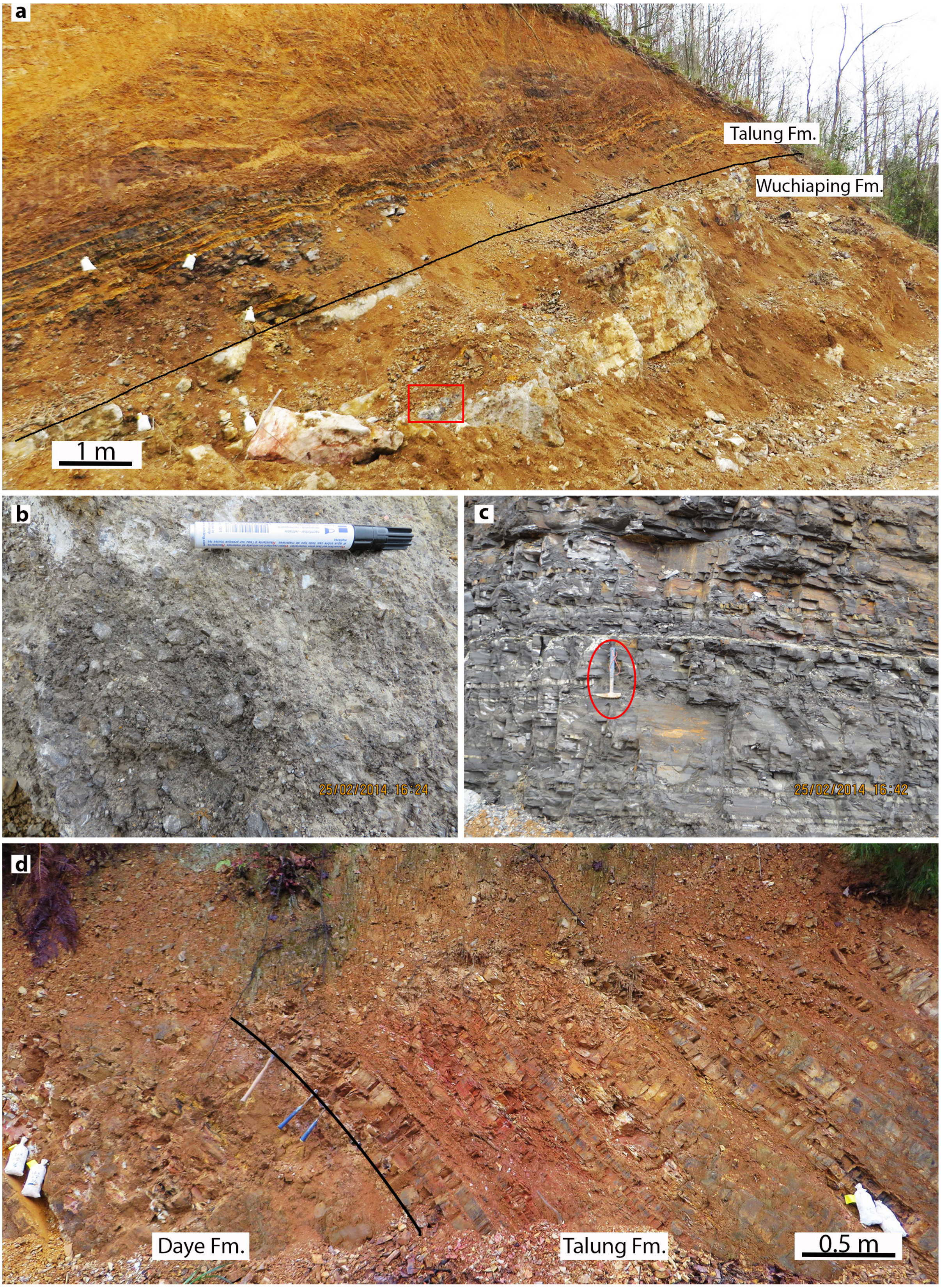

Fig. 7 Field photographs of Potuo and Laxian sections. **a**, Outcrop photograph of the Wuchiaping-Talung formational boundary at Potuo. **b**, Close-up picture of the breccia in the uppermost part of the Wuchiaping Fm. (red rectangle in Fig. 7a). **c,** Black shales in the base of Early Triassic Daye Fm. at Potuo. **d,** Exposure of Talung-Daye formational boundary (PTB) at Laxian.

5.2.2. *Layin*

The plateau of heavy $\delta^{13}C_{carb}$ values (4-5‰) characteristic of interval 1 can be recognized despite the low sampling resolution. The top of interval 1 is marked by a 1.5‰ negative CIE. The $\delta^{18}O_{carb}$ values in this interval vary between -4 and -8‰ and show a minor covariation with $\delta^{13}C_{carb}$ (Fig. 5).

The very high sampling resolution of interval 2 reveals a series of outliers ranging from -1 to +1‰. The same outliers have been detected at Mapojiao (Fig. 3), and their diagenetic origin has been previously discussed by Bagherpour et al. (under revision b). They are typically associated with OM-rich limestone immediately adjacent to ash layers. Absence of such outliers in Guantan results from the coarser sampling resolution. If ignoring these outliers, interval 2a is characterized by an episode of steady $\delta^{13}C_{carb}$ values around 4‰ in the lower part followed by a 2‰ negative CIE in the upper part of Unit B. This interval is succeeded by a positive CIE with substantial noise (interval 2b) reaching a maximum of 5‰ in the lower part of Unit D. The $\delta^{18}O_{carb}$ values in interval 2a are ranging from -4‰ to -8‰ and do not show any covariation with $\delta^{13}C_{carb}$values. The $\delta^{18}O_{carb}$ values in interval 2b are ranging from -3‰ to -11‰ and co-vary with $\delta^{18}O_{carb}$ values (Fig. 5).

Interval 3a is characterized by a $\delta^{13}C_{carb}$ negative CIE down to 2.2‰, switching back to a maximum of 5‰ in interval 3b. The $\delta^{18}O_{carb}$ values in interval 3 vary between -5 and -10‰ and display a strong covariation with $\delta^{13}C_{carb}$ (Fig. 5).

Interval 4 corresponds to a plateau of heavy $\delta^{13}C_{carb}$ values around 5‰ and variation of $\delta^{18}O_{carb}$ from -6‰ to -9‰.

Interval 5a shows a protracted 4-5‰ negative CIE of $\delta^{13}C_{carb}$ values. Although detailed reconstruction of the $\delta^{13}C_{carb}$ record of this interval is precluded by a fault, a substantial drop from 5‰ to 1‰ is clear. The $\delta^{18}O_{carb}$ values within the 30 m above the sheared zone show substantial fluctuations between -5‰ and -9‰, which co-vary with $\delta^{13}C_{carb}$ values. The upper part of interval 5 shows a 2‰ positive CIE $\delta^{13}C_{carb}$ uncorrelated with $\delta^{18}O_{carb}$ Values.

5.2.3. *Potuo And Laxian*

The uppermost part of the Wuchiaping Fm. (Unit D) and the lowermost part of the Talung Fm. are characterized by a negative shift of $\delta^{13}C_{carb}$ values from 4‰ to 1.5‰ (interval 6) (Fig. 6). The absolute values and magnitude of change at Potuo perfectly match with the uppermost part of the $\delta^{13}C_{carb}$ curve at Guantan. At Potuo, the $\delta^{18}O_{carb}$ values range from -2‰ to -10‰ and do not show covariation with $\delta^{13}C_{carb}$. Reconstruction of the $\delta^{13}C_{carb}$ record in the higher part of the Talung Fm. is precluded by the absence of carbonate. The $\delta^{13}C_{org}$ record in the uppermost part of the Wuchiaping Fm. shows a positive shift from -27‰ to -24‰,

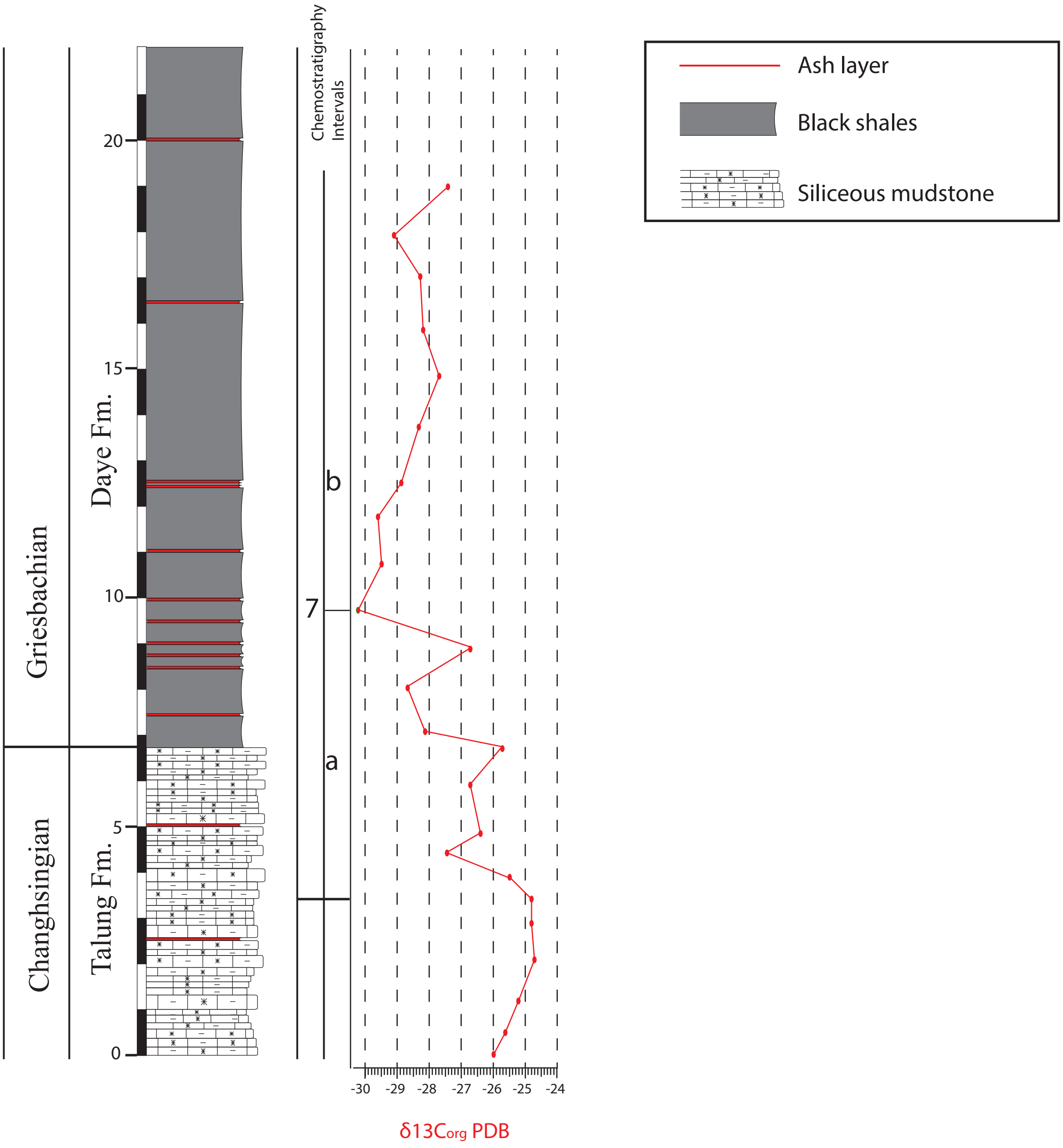

Fig. 8 Detailed stratigraphic log of the Laxian section with $\delta^{13}C_{org}$ data.

whereas the basal part of Talung Fm. displays a prominent negative shift from -23.5‰ to -29.5‰ (interval 6). The $\delta^{13}C_{org}$ values in the basal part of overlying carbonate free Talung Fm. increase to -25.5‰ and remain stable higher up.

At Potuo, above the covered interval that conceals the formational boundary between the Talung and Daye formations, the visible black shales of the Daye Fm. are characterized by the end of a negative shift in $\delta^{13}C_{carb}$ around -4.5‰ (interval 7a). It is followed by a 2.5‰ increase defining the base of interval 7b. The $\delta^{18}O_{carb}$ record displays an overall negative trend from -2.5‰ to -7‰ and do not show any covariation with $\delta^{13}C_{carb}$. Interval 7a corresponds to a negative shift (from -30‰ to -31.5‰) in $\delta^{13}C_{org}$ record succeeded by a 5.5‰ positive shift in interval 7b. Throughout interval 7, there is a remarkable covariation between carbonate and organic carbon values.

In Laxian, a gradual negative trend in $\delta^{13}C_{org}$ begins in the uppermost 3.5 m of the Talung Fm. with values around -25‰. Minimum values around -30‰ are reached 3 m above the formational boundary (interval 7a) (Fig. 8). This negative peak is followed by a gradual 2.5‰ positive shift in interval 7b, with little or no noise in comparison to the lower part of the section.

5.3. Rock-Eval And Palynofacies

TOC values are generally low in the lower part of the Guantan section (intervals 1– 4 and lower 30 m of interval 5) (Supplementrary material S1; Fig. 4). The TOC values slightly increase in the upper part of the section (upper half of interval 5a) to reach a maximum value of 1.58% and drop back abruptly near the end of the section (Fig. 4). In Potuo, the base of the Talung Fm. is marked by a second rise of TOC values up to a maximum of 2.38% in the carbonate free interval. The basal part of the Daye Fm. is also characterized by high TOC values (up to 2%), with a decrease down to 0.12% in the uppermost part of interval 7b (Fig. 6).

The HI values are generally low (<300) and follow a negative trend throughout the Guantan section (Fig. 4). These values show higher variability in the lower part of the section where lower TOC values are also documented. The base of the section (intervals 1, 2a and lower half of 2b) is characterized by a decreasing trend of HI values from 274 to 41. This episode is followed by an increasing trend with superimposed fluctuations up to 30 m above the base of interval 5 where it ends abruptly and remains low higher up. Within this rising trend a peak value of 475 is documented at 132 m. The overlying Talung Fm. is characterized by very low HI values (10–30), and the studied part of the Daye Fm. shows a rise in HI values to around 150 (Fig. 6).

The OI record follows the same general trend as HI. The base of the Guantan section (intervals 1, 2a and lower half of 2b) shows a decreasing trend in OI values from ca. 450 to 71, followed by a gradual increase to ca. 300 in the lower 30 m of interval 5 and with a marked peak of 847 at 132 m (Fig. 4). The OI values are very low in the upper part of the Wuchiaping (expect interval 6), Talung, and Daye formations (Fig. 4, 6).

The HI-OI cross-plot shows that almost all the samples fall between OI values <500 and HI values <300 (Fig. 12a). Intervals 2 to 6 have largely overlapping distributions, whereas intervals 1 and 7 have distinct signatures. Interval 1 has a mixed Kerogen composition between marine and terrestrial. Interval 7 shows the highest proportion of marine OM. The S2/TOC cross-plot shows a linear relationship between the two factors and also indicates a separation between samples from

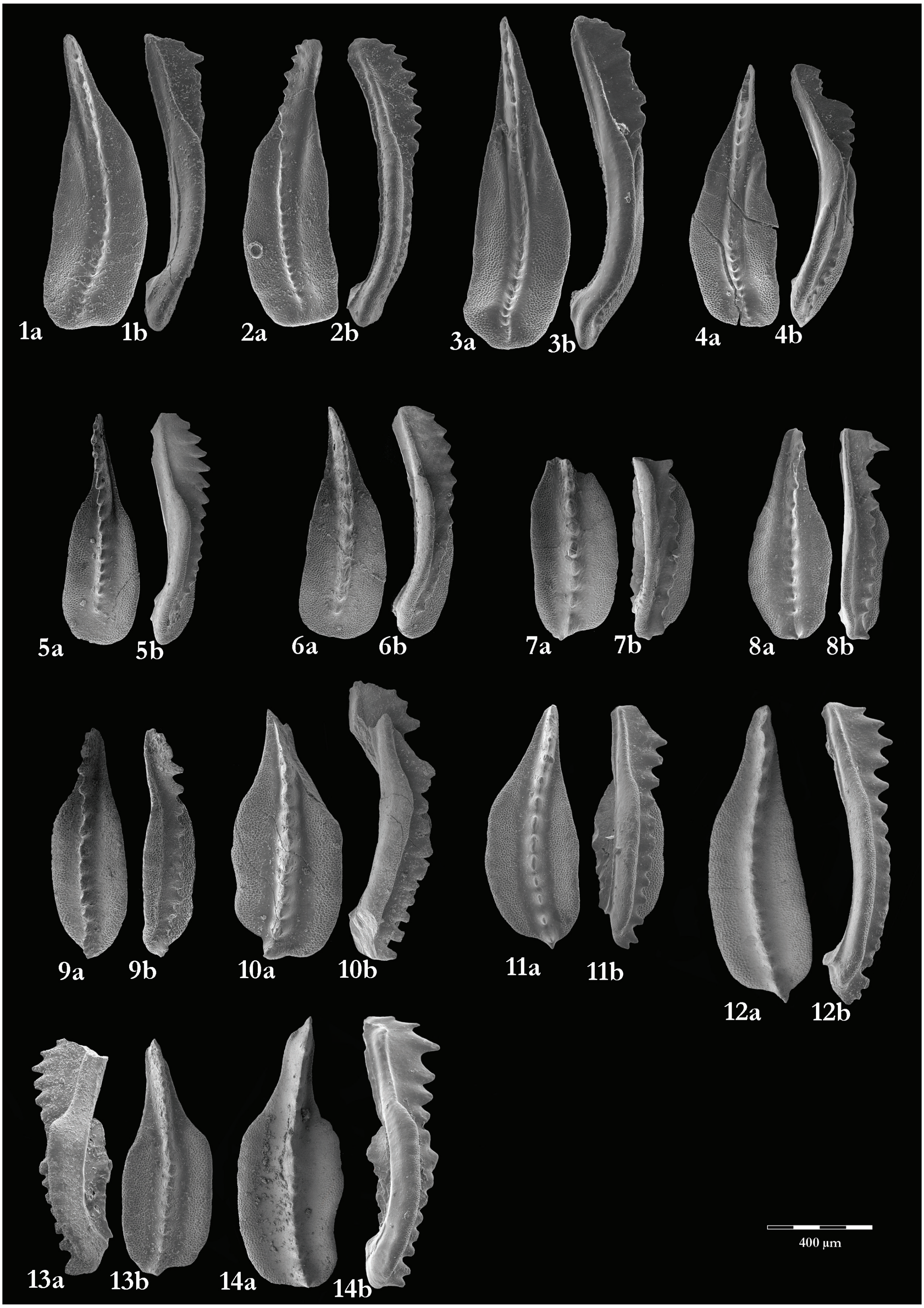

Fig. 9 Conodont P_1 elements from the Potuo section. 1, *Clarkina ?transcaucasica* (collection n°). 2-4, *Clarkina liangshanensis* (2, collection n°; 3, collection n°; 4, collection n°). 5-6, *Clarkina orientalis* (5, collection n°; 6, collection n°). 7-8, *Clarkina longicuspidata* (7, collection n°; 8, collection n°; 9, collection n°). 9-10, *Clarkina longicuspidata* to *Clarkina Wangi* (collection n°). 11-14, *Clarkina subcarinata* (11, collection n°; 12, collection n°; 13, collection n°; 14, collection n°).

the base of the Daye (interval 7) and the rest of the section (Fig. 12b). The OI-TOC and HI-TOC cross-plots both show negative logarithmic relationships (Fig. 12 c, d). With the exception of interval 7, these diagrams indicate that highest TOC values are always associated with a dominance of terrestrial OM. The $\delta^{13}C_{org}$-TOC cross-plot shows that the most negative $\delta^{13}C_{org}$ values correspond to the highest TOC values (Fig. 12e), and hence, to the dominance of terrestrial OM. The $\delta^{13}C_{org}$ - $\delta^{13}C_{carb}$ cross-plot shows the clearest positive correlation for interval 7 and to a lesser degree for interval 5 (Fig. 12f). Based on the palynofacies analysis, POM assemblages are dominated by terrestrial OM (>80%) with high abundances of woody particles throughout the Wuchiaping and Talung formations (Fig. 13b, c). However, the palynofacies analysis of interval 1 (lithological Unit A in Guantan) is hampered by very low abundances of POM. In addition, strong contamination with recent OM is observed in this interval and at the base of interval 5 (Fig. 13).

The basal part of the Daye Fm. (interval 7a) is characterized by a remarkable increase in marine OM (50-90%), whereas the overlying interval 7b shows an increase of terrestrial OM.

6. DISCUSSION

6.1. Sedimentary Setting

The abundant and diverse shallow marine fauna in thick-bedded and massive limestone of Unit A indicates a shallow marine, subtidal depositional setting. Intercalation of packstone-dominated beds implies occasional influences of waves and/or storms. In Unit B, the replacement of shallow-marine organisms by deep-water and pelagic organisms (siliceous sponge spicules and radiolarian, respectively) in thin-bedded, dark, laminated, organic-rich limestone indicates a major drowning. In Subunit B1, intercalation of thin beds containing fragmented shallow-marine fauna mixed with radiolarian-sponge spicules facies are interpreted as storm deposits on the slope. The exclusive presence of radiolarians and sponge spicules in the upper part of this unit (Subunit B2) suggests an even deeper basinal setting. Unit C is interpreted as a distal lobe of volcanogenic turbidites. The absence of Unit C in Guantan and Layin suggests a moderate (kilometric) lateral extension of this submarine turbiditic lobe (Bagherpour et al., under revision a). In the Nanpanjiang Basin, thick volcanogenic turbidites are known from the Luolou Fm. where greywacke and associated depositional mechanisms occurred during mid Griesbachian and latest Spathian time. These Early Triassic rocks were interpreted as indicative of major earth quakes related to bursts of subsidence (Bagherpour et al., 2017; Baresel et al., 2017c; Ovtcharova et al., 2015). Facies evolution from Units A to C suggests a rapid and protracted regional flexuration that ended with the sudden relaxation of the accumulated bending stress. The next overlying and strongly

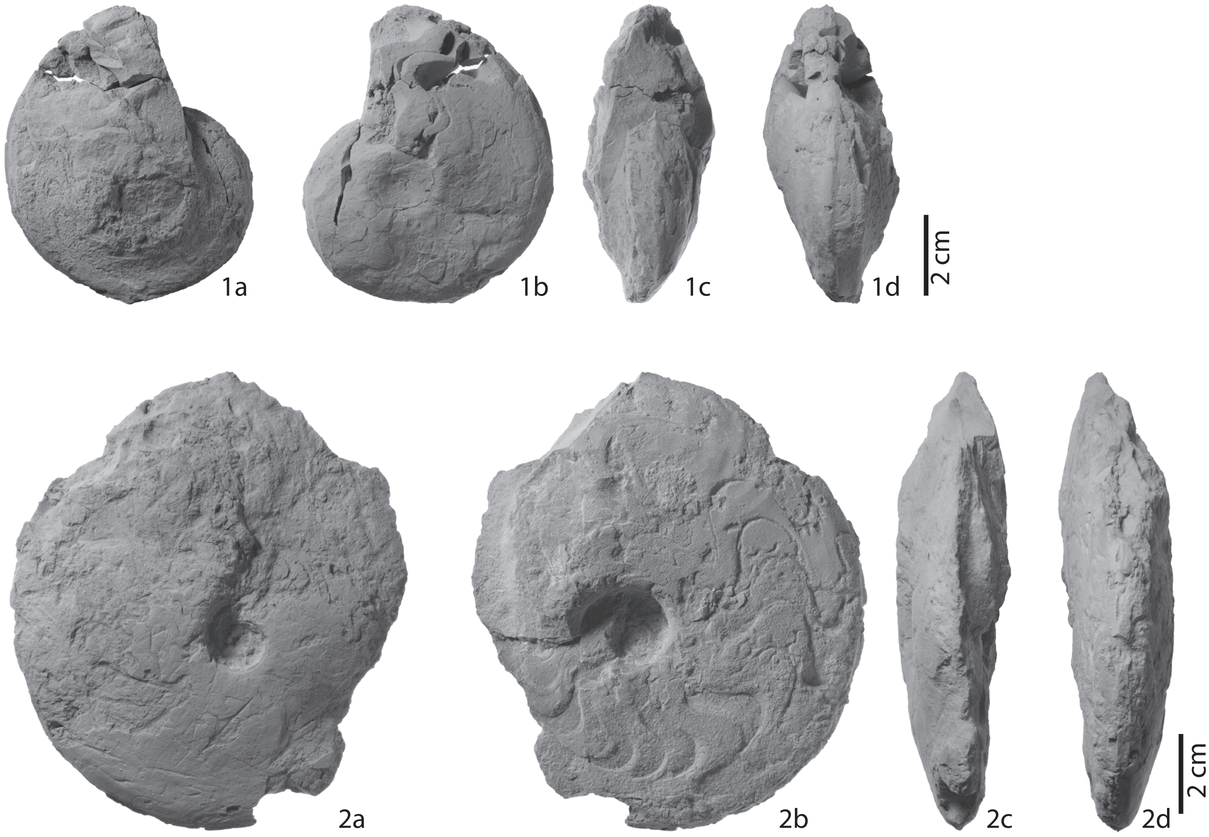

Fig. 10 Ammonites from top of the Wuchiaping Fm. 1a-d, *Avushoceras* sp. (collection n°). 2a-d, *Prototoceras* sp. (collection n°).

asymmetrical shallowing upward indicates a fast return to shallow water depositional settings immediately after the relaxation of the tectonic stress.

Bagherpour et al. (under review a) compiled the sedimentary records across the G-L interval in South China and concluded that such drowning events, with the same facies architecture, occurred within three distinct time intervals; 1- in early to middle Capitanian (in Xiong jia chang and Chaotian sections, Sun et al., 2010), 2- in latest Capitanian (in Maoershan and Dukou sections), 3- in early Wuchiapingian (in Mapojiao, Guantan and Layin sections). The youngest was discovered and named the Mapojiao Event by Bagherpour et al. (under revision a). The deep-marine sediments of the first two drowning events are overlain by Emeishan Large Igneous Province (ELIP) volcanic rocks or derived volcanogenic clastics of ELIP origin. The first drowning event has been related to a rapid subsidence phase prior to the ELIP volcanism (e.g. Utskins-Peate and Bryan, 2008; Sun et al., 2010). The strikingly similar architecture of the Mapojiao Event with that of earlier Capitanian examples suggests a similar driving mechanism for these three phases of drowning/eruptive events (Bagherpour et al., under revision a). The hypothesis of concomitant ELIP volcanism as the main cause for the drowning event during the early Wuchiapingian in the

Pingtang syncline is also supported by strontium isotope data. The Sr-isotope record of the Mapojiao section (Fig. 3) shows a transient shift in $^{87}Sr/^{86}Sr$ from 0.70715 to 0.70694, concomitant with the Mapojiao Event, superimposed on the prolonged global positive trend in the Wuchiapingian. This transient excursion argues in favor of enhanced hydrothermal flux related to a short pulse of ELIP-related volcanic activity (Bagherpour et al., under revision b).

Higher up section, the alternation of sponge spicule wackestone facies with foraminiferal algal facies in the lower 40 m of Unit D represents temporal oscillation of a shallower sea level. The dominance of typical shallow marine bioclasts in the overlying part (210 m) of Unit D shows the long term re-establishment of a carbonate platform. Deposition of shallow marine limestone of Unit D ended with a 0.8 m-thick breccia in Potuo, a drowning event caused by block faulting that consistently occurs at the transition between the Wuchiaping and Talung formations throughout the basin.

Next above, radiolarian-rich siliceous mudstone of Talung Fm. was deposited in a deep-marine, low energy basinal and restricted setting, with an estimated water depth of 200-500 m (He et al., 2007; Yin et al., 2007).

The conformably overlying laminated, black shale at the base of Early Triassic Daye Fm. also represents a deep-marine basinal setting similar to the Permian Talung Fm. However, in lithologically similar PTB sections in the basin, sedimentation rate underwent a substantial six-fold decrease across the PTB as inferred from U-Pb ages, thus supporting a lower weathering rate related to cooler and drier climate during the Griesbachian (Baresel et al., 2017b). The conformable formational boundary shows that the global glacio-eustatic regression across the PTB had no effect on the completeness of deep marine records.

6.2. Carbon Isotope Chemostratigraphy

6.2.1. *Composite Carbon Isotope Record And Diagenetic Alteration*

Carbon isotope data of bulk carbonate rocks provide an essential proxy for studying ancient changes in carbon cycling. The proxy is based on the assumption that $\delta^{13}C_{carb}$ values record the $\delta^{13}C$ composition of ancient Dissolved Inorganic Carbon (DIC) in the ocean. However, $\delta^{13}C_{carb}$ values can be altered by diagenesis. Therefore, measured $\delta^{13}C_{carb}$ data might represent a combination of primary and secondary signals (e.g. Given and Lohmann, 1985; Weissert et al., 2008; Tomazo et al. 2016). In comparison to $\delta^{13}C_{carb}$, $\delta^{18}O_{carb}$ values are even more prone to diagenetic alteration and the covariation of $\delta^{13}C_{carb}$ and $\delta^{18}O_{carb}$ in sedimentary records may reveal the magnitude of diagenetic alteration of the $\delta^{13}C_{carb}$ data (e.g. Brand and Veizer, 1981). Moreover,

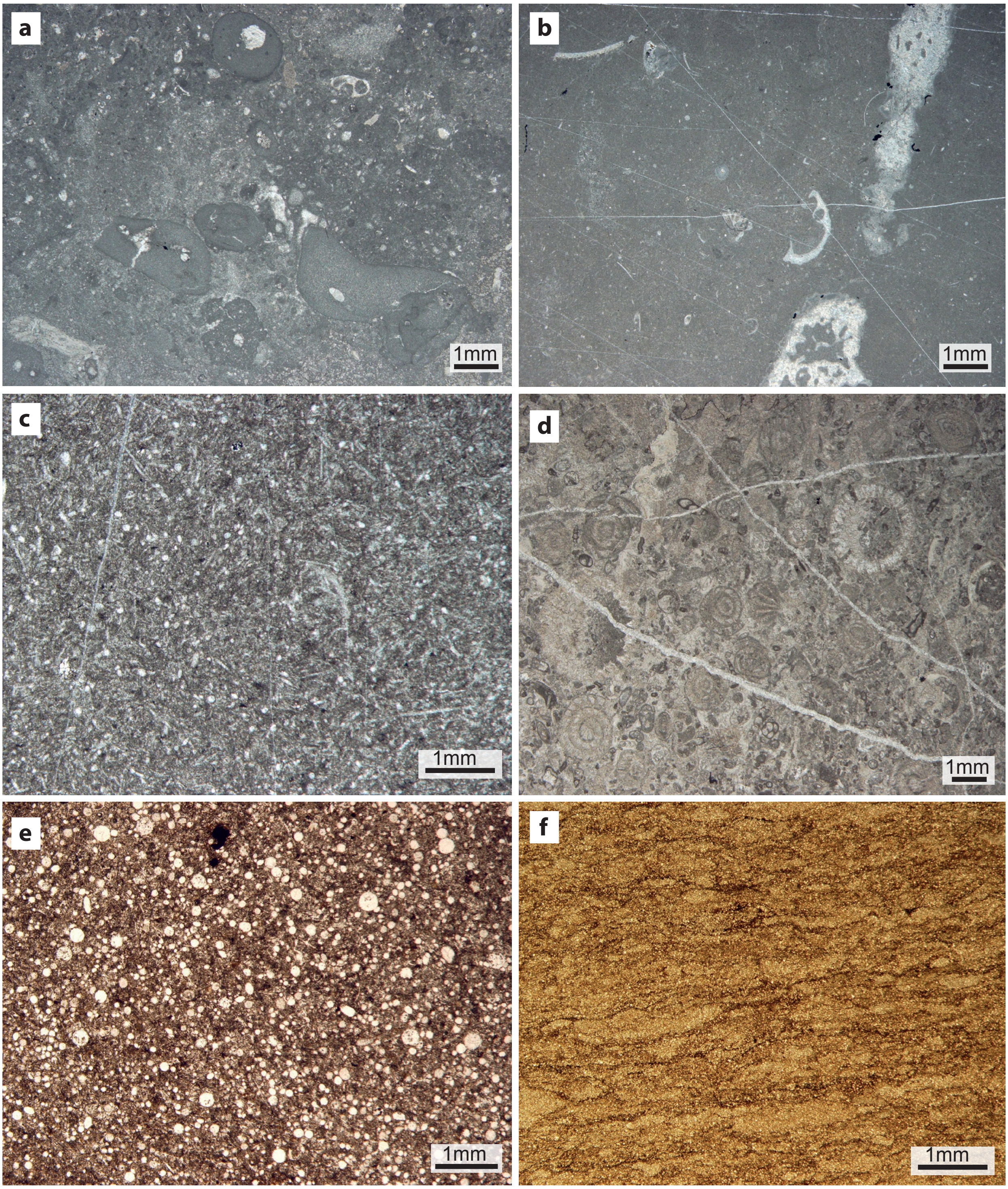

Fig. 11 Photomicrographs of microfacies of Wuchiaping, Talung and Daye formations. **a**, Bioclastic packstone of Unit A of Wuchiaping Fm. (Guantan section). **b**, Fragmented shallow-marine bioclasts in a radiolarian wackestone groundmass (Subunit B1 of Wuchiaping Fm.; Guantan section). **c**, Spiculite-radiolarian packstone-wackestone of Subunit B2 of Wuchiaping Fm. (Guantan section). **d**, Fusulinids-algal packstone of Unit D of Wuchiaping Fm. (Guantan section). **e**, Radiolarian packstone of Talung Fm. (Potuo section). **f,** Laminated black-shale of Daye Fm. (Potuo section).

limestones with $\delta^{18}O_{carb}$ less than -7‰ would indicate precipitation at temperatures >45˚C (Hays and Grossman, 1991). Hence, samples with $\delta^{18}O_{carb}$ <-7‰ are most likely affected by diagenetic alteration (Jost et al., 2014). Hence, in order to disentangle the primary $\delta^{13}C_{carb}$ signal from diagenetic overprint in the late Permian-earliest Triassic records of the Pingtang syncline, all $\delta^{13}C_{carb}$ values with $\delta^{18}O_{carb}$ <-7‰ have been removed in Figure 14. After applying this filter, the general shape of the $\delta^{13}C_{carb}$ does not change. However, intervals with abrupt negative peaks in $\delta^{13}C_{carb,}$ which are also characterized by strong covariation with $\delta^{18}O_{carb,}$ do disappear (upper part of interval 2a, base of interval 3b and middle of interval 5a in Layin; upper part of interval 3a in Guantan).

The $\delta^{13}C_{carb}$ and $\delta^{13}C_{org}$ time series obtained from the studied sections in the Pingtang syncline display good lateral reproducibility (Fig. 14). In Layin, a 1‰ negative offset of $\delta^{13}C_{carb}$ values within ca. 30 m below and above the fault zone can be noticed when compared to the lateral equivalent in Guantan. However, why any late circulation of fluids along this fault zone did not simultaneously alter the associated $\delta^{18}O_{carb}$ values remains unknown.

6.2.2. *Correlation Of $\delta^{13}C_{carb}$ Record Around The Guadalupian-Lopingian Boundary*

Although this time interval is not included in the present study of the Pingtang Syncline, a comparison of previously published C-isotope records round the GLB is nevertheless relevant here. Compilations of available $\delta^{13}C_{carb}$ data around the GLB show that the magnitude and biostratigraphic position of the CIEs are highly variable within South China and elsewhere (Jost et al., 2014; Bagherpour et al., under revision b). The Chaotian (Saitoh et al., 2013) and Xiong jia chang (Wignall et al., 2009) sections document the oldest negative CIEs with a magnitude of 7‰ in the early-middle Capitanian interval. In Penglaitan, no early-middle Capitanian correlative CIE has been detected. In Penglaitan, the entire Capitanian interval is characterized by a plateau of high values (4‰) and only a minor 1‰ negative CIE is documented in the earliest Wuchiapingian (Jost et al., 2014). In the nearby but shallower Tieqiao section, the same earliest Wuchiapingian negative CIE reaches a magnitude of 6‰ (Yan et al., 2013). A recent study (Jost et al., 2014) on coupled $\delta^{13}C_{carb}$ and calcium isotope (from Chaotian and Penglaitan) revealed the absence of any co-variation between these two proxies, which strongly suggests the influence of “local burial conditions or diagenetic effects” rather than perturbations in carbon and calcium cycles.

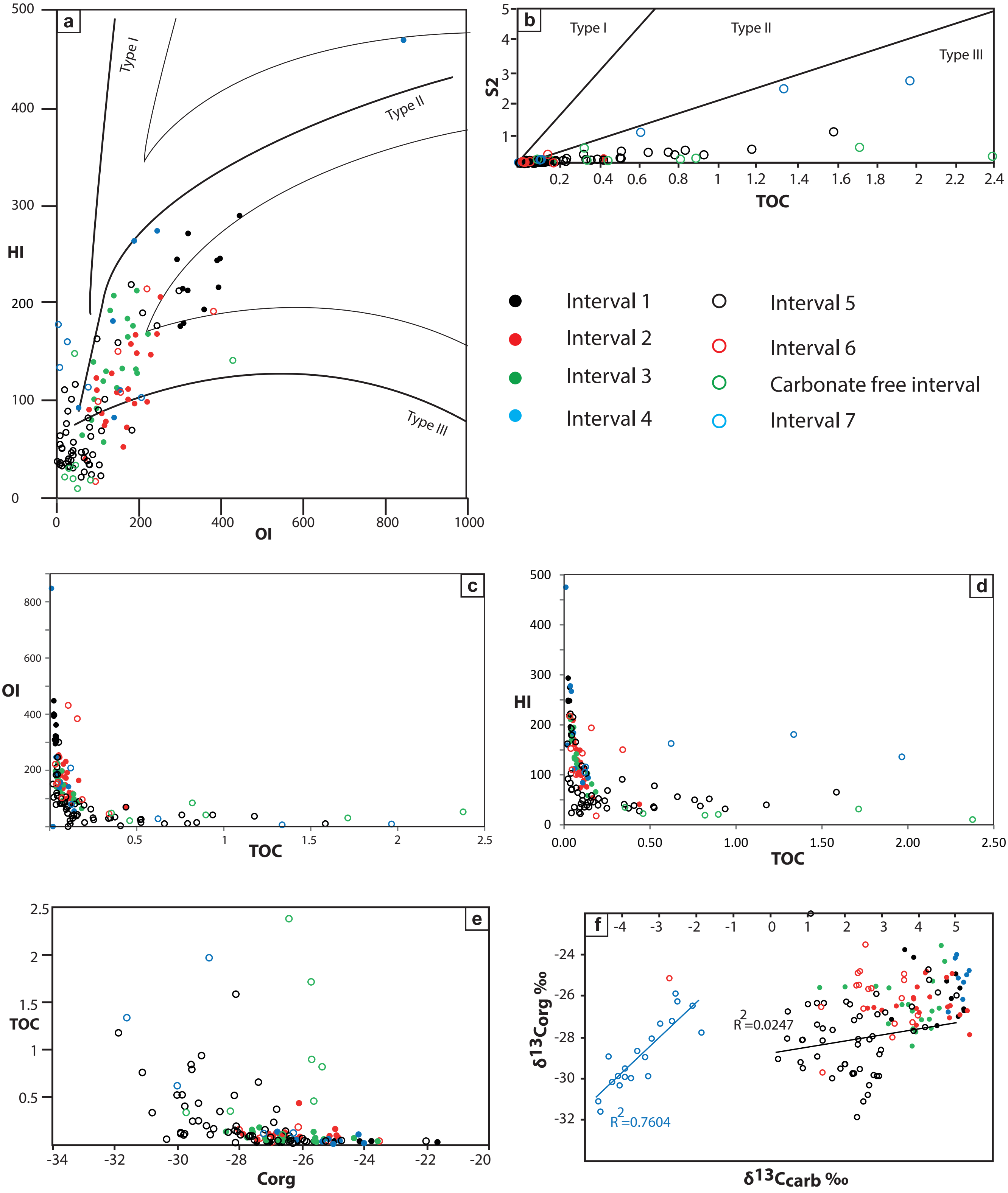

Fig. 12 a, Oxygen index (OI) and hydrogen index (HI) cross-plot, and the kerogen types fields as defined in Tyson (1995). **b**, S2 and TOC cross-plot (Langford & Blanc-Valleron, 1990). **c**, OI and TOC cross-plot. **d,** HI and TOC cross-plot. **e**, TOC and $\delta^{13}C_{org}$ cross-plot. **f**, $\delta^{13}C_{carb}$ and $\delta^{13}C_{org}$ cross-plot.

6.2.3. *Correlation Of The Pingtang $\delta^{13}C_{carb}$ Record Within South China And Elsewhere*

The high-resolution composite $\delta^{13}C_{carb}$ curve obtained from the Pingtang syncline documents only three main genuine negative CIEs not resulting from diagenetic alteration. The first negative CIE is early Wuchiapingian in age, the second one is around the WCB, and the third one immediately above the PTB. These three prominent excursions are discussed and compared with coeval events in South China and other Tethyan records.

6.2.3.1. *Early Wuchiapingian Negative CIE (Interval 2a)*

With a magnitude of ca. 3‰ (Interval 2a), the Pingtang syncline yields the only known early Wuchiapingian negative CIE, as established by conodont ages at Mapojiao (Bagherpour et al. under revision a). The much more modest drowning (beds 15 and 16) that occurs somewhat later (base of *Clarkina orientalis* IZ) in Dukou (Mei et al. 1994 a, b; Shen et al., 2013) coincides with minimal values (2‰) of a very shallow negative CIE of much longer duration (see Fig. 2 of Shen et al. 2013,). In Shangsi, the interval with the same biostratigraphic age (*C. guangyuanensis* IZ) as the Mapojiao Event does not display any drowning and is within an extended and monotonous negative trend from 5 to 2‰ (see Fig. 2 of Shen et al., 2013). Independent of their precise age around the GLB, the recurrent associations of local negative CIEs with ELIP eruptive phases and drowning (e.g. Xiong jia chang, Chaotian, and Pingtang) suggest a genetic link between these. However, negative CIEs of the Mapojiao type consistently co-occur with the intercalation of terrestrial OM-rich deep water facies in the drowned part of a vast carbonate platform argues against volcanism as a main overprinting source of light carbon. The absence of such CIEs in shallow water sections of similar age disqualifies the release of volcanogenic light carbon as an explanation for observed CIEs. Therefore, CIEs of the Mapojiao type can only be explained by local changes in bathymetry leading to restricted water circulation, and/or local increased burial and remineralization of mostly terrestrial OM.

In contrast to the remarkable time and space of scattered CIEs in S. China, the coeval C-isotope records from western Tethyan sections (Iran) are characterized by a stable plateau of heavy values around ca. 4‰ (Shen et al., 2013; Liu et al., 2013). This observation supports again the absence of any global scale perturbation of the C-cycle during the early Wuchiapingian.

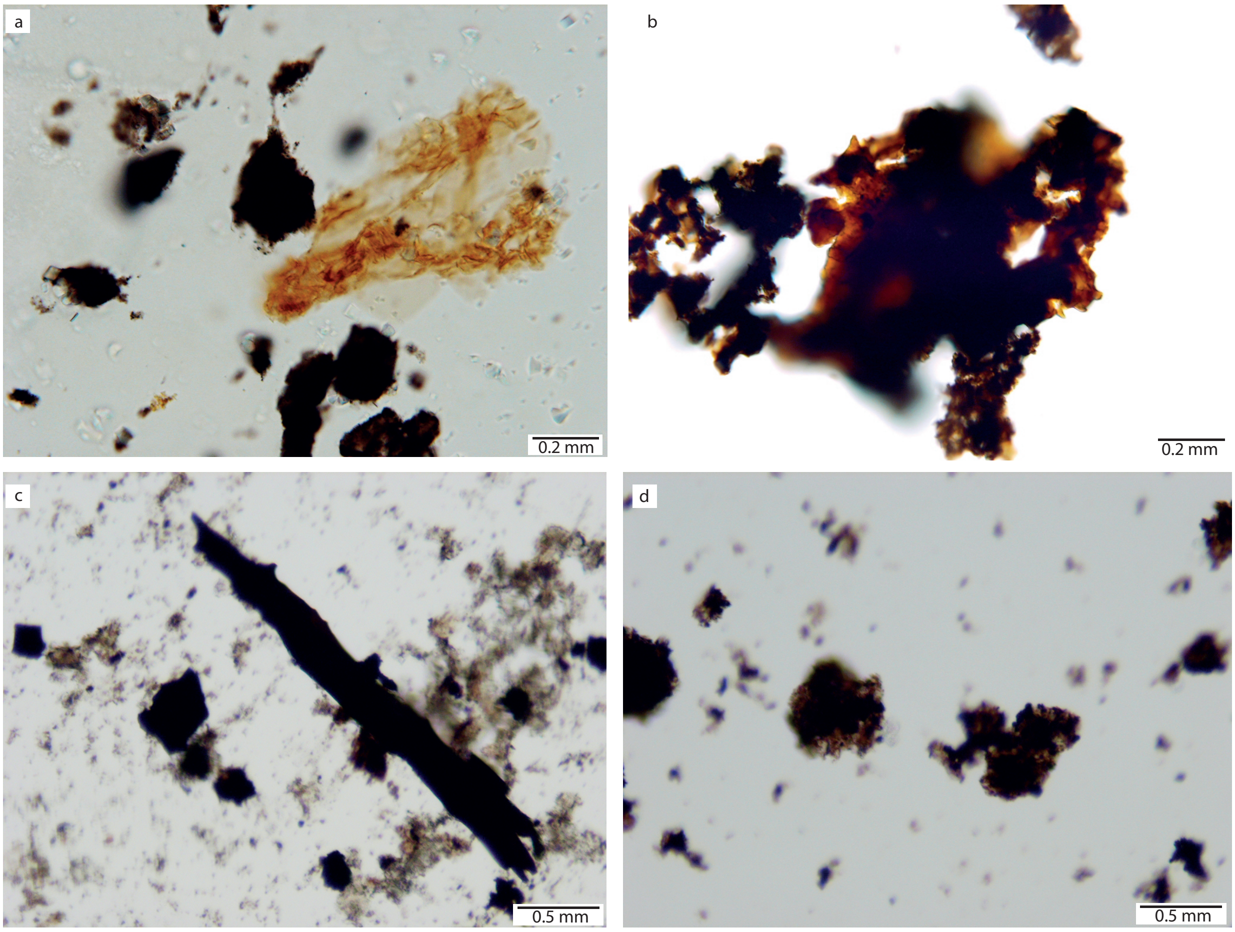

Fig. 13 Photomicrographs of sieved palynofacies slides from the Wuchiaping, Talung, and Daye formations. **a,** Contamination with recent OM in Unit A of the Wuchiaping Fm. (Guantan section). **b**, Terrestrial POM dominated palynofacies from Unit D of the Wuchiaping Fm. (Guantan section) **c,** Terrestrial POM dominated palynofacies from Talung Fm. (Potuo section). **d,** AOM (marine OM) dominated palynofacies from base of the Daye Fm. (Potuo section).

6.2.3.2. *WCB negative CIE (Intervals 5a, 6)*

The second major negative and long term CIE in $\delta^{13}C_{carb}$ is marked by a protracted 5‰ negative shift that includes two distinct short-lived negative peaks in the upper part of the Wuchiaping Fm. (interval 5a). The youngest of these two short lived peak ends with a rapid 2.5‰ positive shift immediately before the WCB (interval 5b), and a subsequent 2.5‰ negative CIE straddling the WCB (interval 6). The same protracted 4.5 Ma long negative CIE with a magnitude of 6‰, including the two negative peaks closely bracketing the WCB, is also reported from Shangsi (Shen et al., 2013). The first of the two negative peaks in interval 5a has been explained above by diagenetic alteration (see paragraph 6.2.4.2) and it is therefore not surprising that it is not recorded in Shangsi.

In contrast, the $\delta^{13}C_{carb}$ record of Dukou does not display any clear short term CIE around the WCB. Shen et al. (2013) correlated a very broad 2‰ negative CIE starting in the lower part of the Wuchiaping Fm. (*Clarkina guangyuanensis*

IZ) (the purple interval in their Fig. 2) with the negative WCB CIE in Shangsi. The transition from the Lungtan Fm. (latest Wuchiapingian) to the Changhsing Fm. in Meishan does not display any comparable negative CIE around the WCB. According to Shen et al. (2013), the different carbon isotope record around the WCB in Meishan is obscured by oxidation of organic matter.

In well dated sections from the western Tethys, the $\delta^{13}C_{carb}$ profiles show hardly any perturbation across the WCB. At the Shahreza (Korte et al., 2004) and Zal (Richoz, 2006; Schobben et al., 2014) sections, no CIE is documented. Only a weak (ca.1‰) negative shift is documented at the WCB in Abadeh (Liu et al., 2013). Shen et al. (2013) reported a 4‰ negative CIE from Kuh-e-Alibashi section, however, a more recent study by Schobben et al. (2014) could not reproduce this CIE. In addition, $\delta^{13}C_{carb}$ profiles around the assumed WCB (i.e. without independent age control) at Wadi Sahtan (Oman) and Cürük Dag (Turkey) again only show a minor (ca. 1‰) negative shift (Richoz, 2006).

From a global perspective, comparison of $\delta^{13}C_{carb}$ records around the WCB reveals disparate trends and magnitudes. The negative CIE around WCB is absent from western Tethys and is even highly variable across sections in S. China. Therefore, we conclude that no significant global perturbation of the carbon cycle can be recognized at the WCB and that both DIC and atmospheric reservoirs were not subject to substantial changes that would override all local noisy signals.

6.2.3.3. ***PTB negative CIE (Interval 7a)***

The PTB is globally associated with a pronounced negative CIE in wide range of depositional settings (e.g. Hermann et al., 2010; Cao et al., 2010; Korte and Kozur, 2010). The negative CIE begins in the *Clarkina yini* IZ, continues in the *C. meishanensis* IZ, and ends within the Early Triassic *Hindeodus parvus* IZ (Burgess et al., 2014; Yuan et al., 2014), assuming that the First Occurrence (FO) of *H. parvus* is not diachronous (but see Brosse et al. 2016 for numerous counter examples). This gradual trend toward lighter $\delta^{13}C_{carb}$ values is also documented to be synchronous in Iran, where there is also an independent paleontological age control and no significant hiatus straddling the PTB (Shen and Mei, 2010; Shen et al., 2013). However, $\delta^{13}C_{carb}$ records from S. China and western Tethys (Iran and Oman) reveal some discrepancy in the magnitude of the negative CIE. The most negative PTB values in Iran and Oman are higher than -1‰ (Richoz et al., 2010; Shen et al., 2013; Schobben et al., 2014), whereas the lowest values at Potuo (interval 7a), Meishan and Shangsi reach ca. -4‰.

In subtidal shallow-marine settings, C-isotope records across the PTB are generally characterized by a ca. 1.5‰ negative jump from latest Permian bioclastic limestone to the basal Early Triassic

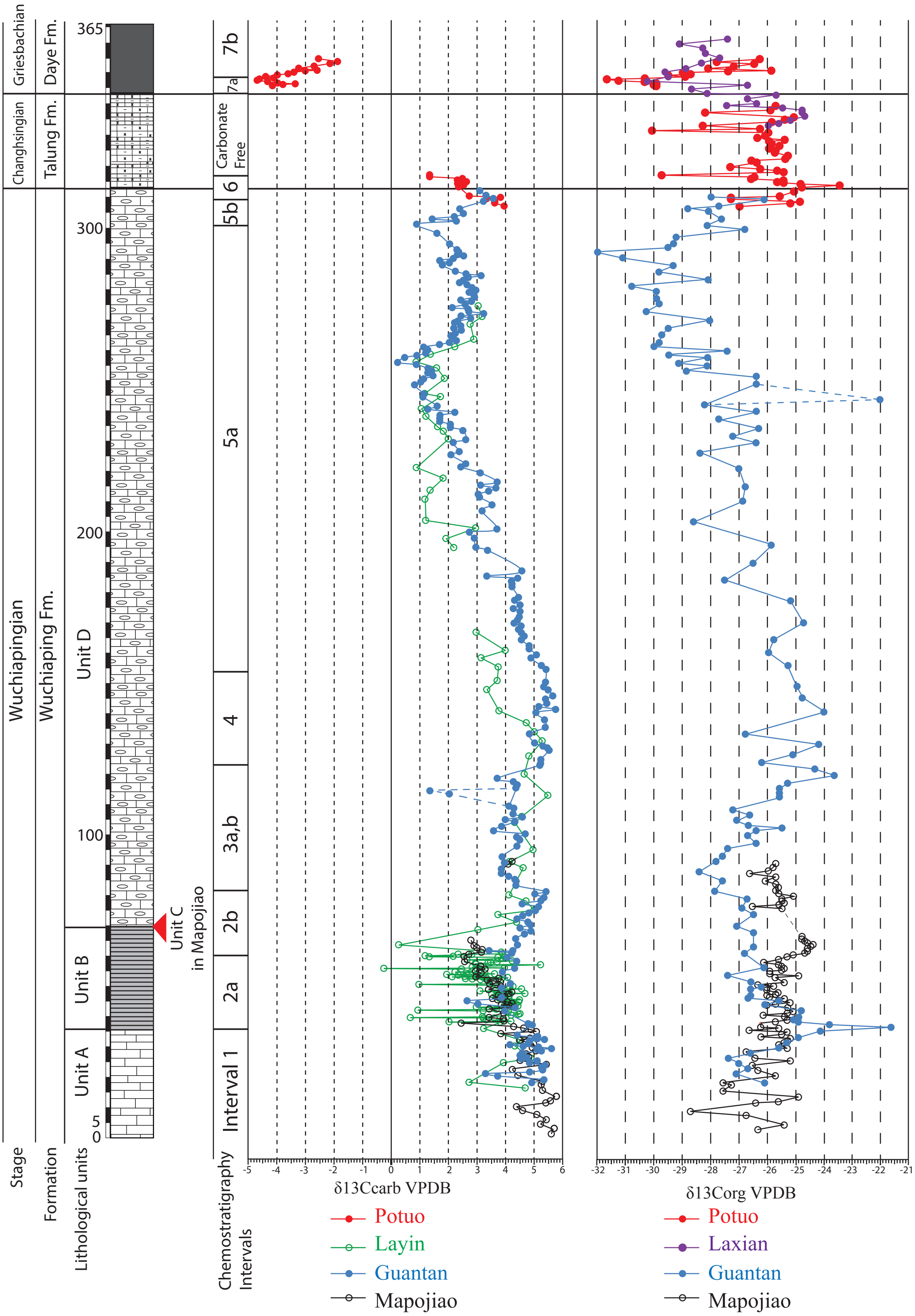

Fig. 14 $\delta^{13}C_{carb}$ and $\delta^{13}C_{org}$ data of the Pingtang syncline composite section. $\delta^{13}C_{carb}$ data points with $\delta^{18}O_{carb}$ <-7 are removed.

shallow marine sediments (e.g. microbialites). Hence, comparison of δ^{13}C$_{carb}$ profiles from deep-marine with shallow-marine sections highlights a stratigraphic gap straddling the PTB and, consequently, the incompleteness of C-isotope records in such settings because of a substantial unconformity (Yin et al., 2014; Baresel et al., 2017b; Bagherpour et al., 2017). This hiatus is also confirmed by means of conodont biochronology (Brosse et al., 2016) and radiometric ages (Baresel et al., 2017b). This global hiatus suggests a glacio-eustatic regression synchronous with the onset of the Siberian Traps volcanism and "a short-lived ice age responsible for the global regression and a brief but intense acidification" (Baresel et al., 2017b).

6.2.4. *Correlation Of The Pingtang δ^{13}C$_{org}$ Record Within South China And Elsewhere*

A reliable approach to discriminate primary signals from secondary diagenetic overprint in δ^{13}C$_{carb}$ data resides in the comparison of δ^{13}C$_{org}$ and δ^{13}C$_{carb}$ time series from the same section. Since no diagenetic alteration can offset the δ^{13}C$_{org}$ and δ^{13}C$_{carb}$ in a parallel fashion, a covariation of δ^{13}C$_{org}$ and δ^{13}C$_{carb}$ most likely reflects primary variations of the DIC C-isotope composition (Meyer et al., 2013). However, interpreting δ^{13}C$_{org}$ data also requires checking for respective contributions of terrestrial and marine OM or contamination by recent OM in low TOC intervals, where recent OM can obscure the genuine δ^{13}C$_{org}$ profile.

6.2.4.1. *Early Wuchiapingian decoupled CIE (Interval 2)*

In Guantan and Mapojiao, the early Wuchiapingian δ^{13}C$_{carb}$ values in Units A and B do not co-vary with δ^{13}C$_{org}$ values (interval 2). In Guantan, δ^{13}C$_{org}$ values in this interval show a 6‰ positive spike that most likely results from extremely low TOC content (<0.1%) and poor preservation of OM (Korte and Kozur, 2010; Margaritz, 1992). Moreover, contamination with recent OM (Fig. 13a) may also contribute to the signal in this interval. Rock-Eval data and palynofacies analysis of the same interval in Mapojiao, where OM is better preserved, revealed a substantial terrestrial input concomitant with the deposition of Unit B in comparison to the marine OM dominated underlying Unit A. Based on differences in the isotopic composition of marine and terrestrial isotopic end-members, Bagherpour et al. (under revision b) concluded that the decoupling of δ^{13}C$_{org}$ and δ^{13}C$_{carb}$ there is due to changing OM rather than a diagenetic alteration of δ^{13}C$_{carb}$.

6.2.4.2. *WCB coupled negative CIE (Intervals 5a, 6)*

Both carbon isotopes display a more or less parallel protracted negative trend prior to the WCB. The coupled negative CIE in $\delta^{13}C_{carb}$ and $\delta^{13}C_{org}$ (interval 5a) indicates that this CIE is a primary signal and represent variation in the isotopic composition of DIC. However, the older negative short-lived shift within interval 5a is not reflected in the $\delta^{13}C_{org}$ record, which suggests a diagenetic overprint. The long term coupled negative CIE is followed by a positive shift in both carbon isotope records (interval 5b), but with a contrasted magnitude, twice larger in the $\delta^{13}C_{org}$. It is followed by a further negative CIE with less amplitude (interval 6) straddling the WCB, which is at or slightly above the base of the Talung Fm. Palynofacies and Rock-Eval data indicate dominance of terrestrial OM (Fig. 13b) throughout the protracted negative CIE, implying that this CIE is not resulting from variable contributions of the different organic carbon pools. Negative CIEs of the organic carbon record associated with the WCB are also reported from Zhaojiaba (W. Hubei) and Niushan (SE. Anhui), but both sections lack independent biostratigraphic or radio-isotopic age controls (Wei et al., 2015; Liao et al., 2016) that would firmly establish a WCB age. The only available $\delta^{13}C_{org}$ profile documenting a possible WCB outside south China, the Buday'ah section in Oman (Baud et al., 2012), shows no contemporaneous perturbation of the C_{org} record at the suggested WCB, above which only mid-late Changhsingian rocks are recognized.

The gradual and protracted pattern of this CIE can exclude short lived geologic drivers such as methane release from the sea floor (Shen et al., 2013). Unlike the PTB, which is temporally associated with large igneous provinces, the CIE at the WCB is not associated with known large volcanic activities. Moreover, the conodont apatite $\delta^{18}O$ record across the WCB (in a composite section from S. China) is characterized by an increasing trend, which precludes a concomitant warming episode (Chen et al., 2012). In terms of sea level changes, neither our detailed facies analysis nor any published data indicate substantial variations in bathymetry. As mentioned above, the composition of terrestrial dominated OM during this CIE also remains constant, which excludes the role of increased marine OM. We conclude that, although the coupled negative CIE in this interval represent a primary variation in the $\delta^{13}C$ of DIC, the driving mechanisms remains equivocal because this trend is not known from well dated sections outside of south China.

6.2.4.3. ***PTB coupled negative CIE (interval 7a)***

The $\delta^{13}C_{org}$ record indicates a rapid return to heavy values (-26‰) in the carbonate free interval of the Talung Fm., before the substantial 5‰ negative CIE crossing the PTB (interval 7a). The negative CIE in both organic and inorganic

C-isotope records across the PTB in the Pingtang syncline, as well as the coeval negative CIE in globally distributed PTB sections indicates that this C-isotope record reflects a global variation in contemporaneous exogenic carbon reservoir. The gradual decline of C-isotope profile across the PTB in the Pingtang is in contrast with the abrupt ca. 1.5‰ negative jump observed in shallow-water sections. This confirms again that in deep enough water settings, the global regression did not affect the completeness of the record (e.g. Baresel et al 2017b). The negative CIE at Meishan is extremely compacted because of condensation and possible hiatuses (Shen et al. 2013; Burgess et al., 2014). In Pingtang (Laxian section, Fig. 8), this negative CIE is expanded and has a magnitude of 5‰ and spans a stratigraphic thickness of 6.5 m across the formational boundary between the Talung and Daye formations.

Palynofacies and Rock-Eval data indicate an increased contribution of marine OM in the lower part of the black shales of the Daye Fm. (Fig. 13d, 6). HI values rise above the PTB and cross-plot of HI/OI and TOC/S2 shows changes from type-III to type-II kerogen across the formational boundary (Fig. 12a, Fig. 12b). Because Permian and Triassic marine OM is depleted in ^{13}C relative to terrestrial OM (e.g. Hermann et al., 2010), the absolute $\delta^{13}C_{org}$ values of the basal black shales of the Daye Fm. could be potentially offset toward lighter values.

Rock-Eval data shows that both the Talung and Daye formations are characterized by high TOC values (up to 2.38%), indicating that oxygen-poor conditions in troughs with restricted water circulation in the Changhsingian persisted during the deposition of earliest Triassic black shales. Following Wignall and Hallam (1993), increased burial rates of earliest Triassic organic matter is customarily interpreted as the result of an expanded oxygen minimum zone (OMZ) accompanying a global sea-level rise. However, in Pingtang, as well as in other deep water marine sections in the Nanpanjiang Basin, inception of oxygen-poor bottom waters and rising TOC first occurred at the Wuchiaping-Talung formational boundary. Both oxygen depletion and TOC remained constant within the first few meters of the basal Triassic black shales. Because sedimentation rate of the basal Triassic black shales represents a 6 fold decrease with respect to that of the Talung Fm. (Baresel et al 2017b), fluxes of terrestrial OM into local tectonic troughs must have dropped simultaneously, thus shifting the kerogen balance from type III to type II. Moreover, differences in bathymetry between the upper Talung Fm. and the basal black shales of the Daye Fm. are negligible, thus undermining any causal relation between a sea-level rise and a relative increase of the marine contribution to OM burial. A simple change in the relative contributions of terrestrial *vs*. organic matter through reduced fluxes from continent into ocean provides a much more parsimonious explanation in perfect agreement with the decreasing sedimentation rates across the PTB. Interestingly, this new scenario requires no changes in the net production of the terrestrial biomass.

6.3. Local Vs. Global Significance Of Late Permian CIEs

Comparison of worldwide C-isotope records with suitable and independent age control indicates that perturbation around the GLB and WCB are only documented in south China. Moreover, the accurate biostratigraphic position and magnitude of CIEs around the GLB are highly variable within South China, and the occurrence of CIEs is obviously related to changes in bathymetry. Pingtang and Shangsi are the only two sections where a protracted negative CIE ends shortly after the WCB. In both sections, this long term negative CIE is unrelated to any major facies change. Comparison with Iranian sections analyzed by Shen et al. (2013) does not reveal any coeval CIE around the WCB. Moreover, facies remains constant around the WCB in Iranian sections. In contrast to the inconsistent Lopingian C-isotope records, the negative CIE associated with the PTB and subsequent Early Triassic CIEs have a consistent distribution in time and occur across a broad range of different paleogeographic and depositional settings (e.g. Payne et al., 2004; Galfetti et al., 2007b; Horacek et al., 2009; Hermann et al., 2011; Grasby et al., 2013; Meyer et al., 2013). Pulses of volcanic activity of the Siberian Traps have been the most invoked proximal trigger for the global Permian-Triassic negative CIE and Early Triassic CIEs. Massive amounts of volatiles degassed from the Siberian Traps reached the stratosphere (e.g. Wei et al., 2014) and caused a series of global environmental upheavals such as acid rain (Hinojosa et al., 2012, Black et al., 2014) and a latest Permian warming (Joachimski et al., 2012; Chen et al., 2016) ending with a 89 ± 38 kyr global hiatus due to a glacio-eustatic regression (Baresel et al., 2017b). The ultimate cause of this ice age straddling the PTB is to be sought in the formation of S-rich aerosols of volcanic origin (Baresel et al., 2017b). A stepwise return to greenhouse conditions was not completed prior to the Griesbachian-Dienerian boundary (Hochuli et al. 2016). Ozone depletion has also been proposed by Beerling et al., (2007), but the production of teratological pollen only requires exposure to atmospheric pollutants of volcanic origin (Hochuli et al. 2017). A comparison of the Siberian Traps, as the primary cause for the PTB and Early Triassic CIEs, with the Emeishan LIP, may help us to understand the striking absence of global late Permian CIEs. First, the Emeishan LIP with an estimated volume of ~0.3×10^6 km^3 (Ali et al., 2005) represents a much smaller LIP (about one-tenth) than the Siberian Tarps, with volume estimates ranging between 3 and 4×10^6 km^3 (Courtillot et al., 1999). This consequently implies a smaller amount of released volatiles by ELIP. Svensen et al. (2009) estimated that Siberian Traps (with metamorphism of OM and petroleum) could generate >100,000 Gt CO_2, whereas the maximum amount of released CO_2 from Emeishan LIP is estimated to be much smaller at 16.800 Gt CO_2 (Ganino and Arndt, 2009). Second, the buffering effect of sea-water must be factored in submarine LIP volcanism, as is the case for ELIP (Coffin and Eldholm, 1994). Widely recognized mafic hydromagmatic deposits and submarine extrusions in the early phases of the Emeishan LIP indicate emplacement at or below sea-level (Ukstins Peate and Bryan, 2009; Jerram et al., 2016a). In contrast, most of the Siberian Traps was emplaced on the land with restricted connection to marine environments (Jerram et al., 2016b). Third, the paleolatitude of eruptions influences the global dispersion of volcanogenic volatiles (e.g. Ganino and Arndt, 2009). Emeishan LIP occupied an equatorial position (Ali et al., 2002), whereas the Siberian Traps were emplaced at ~ 60°N (Cocks and Torsvik, 2007). Volcanogenic volatiles can ascend into the middle to upper troposphere if their source is located at low or mid latitude, whereas these can reach as high as the stratosphere if ejected at high latitude (Self et al., 2005, 2006), where the troposphere is thinner. Along the same lines, Saunders and Reichow, (2009) suggested that the high latitude of the Siberian Traps may have facilitated the global dispersion of released S-compounds. Hence, the equatorial paleolatitude of the Emeishan LIP may also have contributed to the less efficient dispersal of released volatiles. This scenario is still speculative and ignores several other factors such as wind patterns, residence time of gasses in the atmosphere and the location of the LIP with respect to the position of continents.

A global dispersion of massive amounts of thermogenic light carbon derived from the Siberian Traps (e.g. Wei et al., 2014) overriding all local controls of the C-cycle provides a reasonable explanation for the global character of the PTB and Early Triassic CIEs. Conversely, a less effective dispersion of a comparatively smaller amount of thermogenic light carbon degassed by the Emeishan LIP may not overprint local controls (e.g. bathymetry)

6.4. Perturbation In C-Isotope And Extinctions

The late Permian has been interpreted as an epoch bracketed between the end-Guadalupian (e.g. Stanley and Yang et al., 1994) and end-Permian (e.g. Raup, 1979) biotic crises. According to Lucas, (2017) the end-Guadalupian mass extinction occurred coevally in both marine and nonmarine realms. Recent studies showed that extinction rates during the Capitanian were very low in the marine realm (Clapham et al., 2009). In contrast, Bond et al. (2010) suggested that the end-Guadalupian extinction occurred abruptly in middle Capitanian time, and that it coincided with a global negative CIE and with the initial and main eruptive phase of Emeishan LIP.

However, significant variation in magnitude and stratigraphic position of negative CIEs around the GLB within S. China, and the absence of any clear perturbation in other parts of the world (Chen et al., 2011; Jost et al., 2014; Bagherpour et al., under revision b) does not support any causal relationship between the South Chinese CIEs and an abrupt extinction phase around GLB. In addition, a comprehensive dataset compilation by Shen et al. (2011) and Wang et al. (2014) did not uncover any extinction phase during the late Permian that would correlate with negative CIEs during the early Wuchiapingian and/or around the WCB. The common timing shared by the PTB and Early Triassic CIEs with global pulses of extinctions in the marine realm at the PTB, during the Dienerian (Ware et al., 2015) and the late Smithian (Galfetti et al., 2007b) again represents a fundamentally different situation than that of the Late Permian during which no intervening extinction peaks are known.

7. CONCLUSION

High-resolution early Late Permian to earliest Triassic $\delta^{13}C_{org}$ and $\delta^{13}C_{carb}$ records from the Pingtang syncline uncovers substantial local fluctuations prior to the PTB. A short negative CIE is recorded in the early Wuchiapingian, a protracted negative CIE spanning the upper part of the Wuchiaping Fm. and ending shortly after the WCB, and a negative short CIE spanning the PTB. The early Wuchiapingian CIE only occurs when associated with a drowning event (the Mapojiao Event). This drowning is not generated by block faulting, but by gradual flexure and an abrupt return to a shallow water depositional environment. We hypothesize that such tectonic events could be among the local rheological consequences of ELIP eruptive phases, but the actual underlying mechanism is still in need of explanation. The same type of CIEs accompanied by ELIP-related drowning events is also known from some other sections (Xiong jia chang and Chaotian) prior to the GLB in South China. These CIEs are again not laterally reproducible in time, which indicates the influence of local environmental factors such as bathymetry and the accumulation of terrestrial OM rather than any global change in the carbon cycle. The only CIE with a modest lateral reproducibility, without any concomitant facies change, is found in Pingtang and Shangsi. It is a protracted negative CIE that ends shortly after the WCB. Hence, comparison of our new Pingtang C-isotope record with published data highlight the lack of reproducibility of documented CIEs during the late Permian in south China. Comparison with other Tethyan sections (e.g. Iran) indicates that none of the detected late Permian CIEs can be recognized in central Tethys or beyond. This result stands in marked contrast with the well documented global CIE that spans the PTB worldwide and which is found in all depositional environments. The lack of lateral reproducibility in the late Permian C-isotope record implies an insufficient amount of released thermogenic CO_2 from Emeishan volcanism to override local factors controlling the C-isotope record, even if ELIP activity did extend into the late Permian. Modest volume of erupted basalts, equatorial position, and submarine volcanism may all contribute to the absence of ELIP-related global signals in the C-isotope record. The opposite case is found with the younger Siberian Traps, whose global C signals resulted from a ten-fold larger volume of basalt combined with - water unbuffered - subaerial volcanism and high latitude emplacement of the Siberian Traps, allowing injection of volatiles as high as the troposphere. The PTB and Early Triassic global CIE are accompanied by either massive diversity and/or ecological fluctuations on land and in the ocean, an attribute still unknown during Late Permian time.

ACKNOWLEDGMENTS: This work is supported by the Swiss NSF projects 135446 and 160055 (to H.B.). SSZ and DXY's work is supported by NSFC 41420104003 and 41290260. Comments on an earlier version of the manuscript by Spencer Lucas are highly acknowledged. Constructive reviews by XXX, XXX, and editor XXX are deeply acknowledged. Dieter Korn is thanked for identifying the ammonites. Morgane Brosse is thanked for taking SEM pictures of conodonts.

References:

Algeo, T.J., Twitchett, R.J., 2010. Anomalous Early Triassic sediment fluxes due to elevated weathering rates and their biological consequences. Geology, 38, 1023–1026, doi:10.1130/G31203.1.

Ali, J.R., Thompson, G.M., Song, X.Y., Wang, Y., 2002. Emeishan basalts (SW China) and the 'end-Guadalupian' crisis: magnetobiostratigraphic constraints. Journal of the Geological Society London 159, 21-29.

Ali, J.R., Thompson, G.M., Zhou, M.-F., Song, X.Y., 2005. Emeishan large igneous

province, SW China. Lithos 79, 475-489.

Bagherpour, B., Bucher, H., Yuan, D.X., Leu, M., Zhang, C., Shen, C.Z., under revision a. Early Wuchiapingian (Lopingian, Late Permian) drowning event in the South China Block related to a late eruptive phase of Emeishan Large Igneous Province? Global and Planetary Change xxx.

Bagherpour, B., Bucher, H., Schneebeli-Hermann, E., Vennemann, T., Chiaradia, M., Shen, S.Z., under revision b. A new late eruptive phase of Emeishan Large Igneous Province: Evidence from facies, C and Sr isotopes chemostratigraphy. Gondwana Research xxx.

Bagherpour, B., Bucher, H., Baud, A., Brosse, M., Vennemann, T., Martini, R., Goudun, K., 2017. Onset, development, and cessation of basal Early Triassic microbialites (BETM) in the Nanpanjiang pull-apart Basin, South China Block. Gondwana Research 44, 178–204.

Baresel, B., Bucher, H., Brosse, M., Cordey, F., Guodun, K., Schaltegger, U., 2017a. Precise age for the Permian–Triassic boundary in South China from high-precision U-Pb geochronology and Bayesian age–depth modelling. Solid Earth 8, 361–378.

Baresel, B., Bucher, H., Bagherpour, B., Brosse, M., Guodun. K., Schaltegger, U., 2017b. Timing of global regression and microbial bloom linked with the Permian-Triassic boundary mass extinction: implications for driving mechanisms. Scientific Reports 7, 43630.

Baresel, B., d'Abzac, F.X., Bucher, H., Schaltegger. 2017c. High-precision time-space correlation through coupled apatite and zircon tephrochronology: an example from the Permian-Triassic boundary in South China. Geology 45 (1), 83-86. doi:10.1130/G38181.1

Baud, A., Richoz, S., Beauchamp, B., Cordey, F., Grasby, S., Henderson, C.M., Krystyn, L., Nicora, A., 2012. The Buday'ah Formation, Sultanate of Oman: a Middle Permian to Early Triassic oceanic record of the Neotethys and the late Induan microsphere bloom. J. AsianEarthSci. 43, 130–144.

Beerling, D.J., Harfoot, M., Lomax, B.H., Pyle, J.A., 2007. The stability of the stratospheric ozone layer during the end-Permian eruption of the Siberian Traps. Royal Society of London Philosophical Transactions 365, 1843–1866.

Behar, F., Beaumont, V., De, B., Penteado, H.L., 2001. Technologie Rock-Eval 6: performances et développements. Oil & Gas Science and Technology - IFP Energies nouvelles 56 (2), 111–134.

Black, B.A., Lamarque, J.-F., Shields, C.A., Elkins-Tanton, L.T., Kiehl, J.T., 2014. Acid rain and ozone depletion from pulsed Siberian Traps magmatism. Geology 42 (1), 67–70.

Bond, D.P.G., Hilton, J., Wignall, P.B., Ali, J.R., Stevens, L.G., Sun, Y.D., Lai, X.L., 2010. The Middle Permian (Capitanian) mass extinction on land and in the oceans. Earth-Science Reviews 102, 100–116.

Bottjer, D.J., Clapham, M.E., Fraiser, M.L., Powers, C.M., 2008. Understanding mechanisms for the end-Permian mass extinction and the protracted Early Triassic aftermath and recovery. GSA Today 18, 4–10.

Brand, U., Veizer, J., 1981. Chemical diagenesis of a multicomponent carbonate system — 2: stable isotopes. Journal of Sedimentary Petrology 51, 987–997.

Brosse, M., Bucher, H., Goudemand, N., 2016. Quantitative biochronology of the Permian–

Triassic boundary in South China based on conodont unitary associations. Earth-Science Reviews 155, 153–171.

Burgess, S.D., Bowring, S., Shen, S.Z., 2014. High-precision timeline for Earth's most severe extinction. Proceedings of the National Academy of Sciences 111, 3316–3321.

Cao, C.Q., Love, G.D., Hays, L.E., Wang, W., Shen, S.Z., Summons, R.E., 2009. Biogeochemical evidence for euxinic oceans and ecological disturbance presaging the end-Permian mass extinction event. Earth and Planetary Science Letters 281, 188-201.

Cao, C.Q., Yang, Y.C., Shen, S.Z., Wang, W., Zheng, Q.F., Summons, R.E., 2010. Pattern of $\delta^{13}C_{carb}$ and implications for geological events during the Permian–Triassic transition in South China. Geological Journal 45,186–194.

Chen, B., Joachimski, M.M., Sun, Y.D., Shen, S.Z., Lai, X.L., 2011. Carbon and conodont apatite oxygen isotope records of Guadalupian–Lopingian boundary sections: climatic or sea-level signal? Palaeogeography, Palaeoclimatology, Palaeoecology 311, 145–153.

Chen, B., Joachimski, M.M., Shen, S.Z., Lambert, L.L., Lai, X.L., Wang, X.D., Chen, J., Yuan, D.X., 2012. Permian ice volume and palaeoclimate history: Oxygen isotope proxies revisited. Gondwana Research 24 (1), 77-89.

Chen, J., Shen, S.Z., Li, X.H., Xu, Y.G., Joachimski, M.M., Bowring, S.A., Erwin, D.H., Yuan, D.X., Chen, B., Zhang, H., Wang, Y., 2016. High-resolution SIMS oxygen isotope analysis on conodont apatite from South China and implications for the end-Permian mass extinction. Palaeogeography, Palaeoclimatology, Palaeoecology 448, 26-38.

Clapham, M.E., Shen, S., Bottjer, D.J., 2009. The double mass extinction revisited: reassessing the severity, selectivity, and causes of the end-Guadalupian biotic crisis (LatePermian). Paleobiology 35, 32–50.

Cocks, L.R.M., Torsvik, T.H., 2007. Siberia, the wandering northern terrane, and its changing

geography through the Palaeozoic. Earth-Science Reviews 82, 29–74.

Coffin, M.F., Eldholm, O., 1994. Large igneous provinces: Crustal structure, dimensions and external consequences. Reviews of Geophysics 32, 1–36. doi: 10.1029/93RG02508.

Courtillot, V., Jaupart, C., Manighetti, I., Tapponier, P., Besse, J., 1999. On causal links

between flood basalts and continental breakup. Earth and Planetary Science Letters 166, 177-195.

Ehiro, M. Bando, Y., 1985. Late Permian ammonoids from the southern Kitakami Massif, northeast Japan. Nihon Koseibutsu Gakkai hokoku, kiji 137, 25-49.

Espitalié, J., Deroo, G., Marquis, F., 1985. La pyrolyse Rock-Eval et ses applications: Première partie. Revue de l'Institut Francais du Petrole 40, 563–579.

Espitalié, J., Deroo, G., Marquis, F., 1986. La pyrolyse Rock-Eval et ses applications: Troisième partie. Revue de l'Institut Francais du Petrole 41, 73–89.

Galfetti, T., Bucher, H., Ovtcharova, M., Schaltegger, U., Brayard, A., Brühwiler, T., Goudemand, N., Weissert, H., Hochuli, P.A., Cordey, F., Guodun, K., 2007a. Timing of the Early Triassic carbon cycle perturbations inferred from new U–Pb ages and ammonoid biochronozones. Earth and Planetary Science Letters 258, 593–604.

Galfetti, T., Hochuli, P.A., Brayard, A., Bucher, H., Weissert, H., Vigran, J.O., 2007b. Smithian/Spathian boundary event: evidence for global climatic change in the wake of the end-Permian biotic crisis. Geology 35, 291–294.

Ganino, C., Arndt, N.T., 2009. Climate changes caused by degassing of sediments during the emplacement of large igneous provinces. Geology 37, 323–326.

Given, R.K., Lohmann, K.C., 1985. Derivation of the original isotopic composition of Permian marine cements. Journal of Sedimentary Petrology 55(3), 430-439.

Grasby, S.E., Beauchamp, B., Embry, A., Sanei, H., 2013. Recurrent Early Triassic anoxia. Geology 41, 175–178.

Hays, P.D., Grossman, E.L., 1991. Oxygen isotopes in meteoric calcite cements as indicators of continental paleoclimate. Geology19(5), 441.

He, W.H., Shi, G.R., Feng, Q.L., Campi, M.J., Gu, S.Z., Bu, J.J., Peng, Y.Q., Meng, Y.Y., 2007. Brachiopod miniaturization and its possible causes during the Permian-Triassic crisis in deep water environments, South China. Palaeogeography, Palaeoclimatology, Palaeoecology 252, 145–163.

Hermann, E., Hochuli, P.A., Bucher, H., Vigran, J.O., Weissert, H., Bernasconi, S.M., 2010.

Close-up view on the Permian–Triassic boundary based on extended organic carbon isotope records from Norway (Trøndelag and Finnmark Platform). Global and Planetary Change 74, 156-167.

Hermann, E., Hochuli, P.A., Méhay, S., Bucher, H., Brühwiler, T., Ware, D., Hautmann, M., Roohi, G., Ur-Rehman, K., Yaseen, A., 2011. Organic matter and palaeoenvironmental signals during the Early Triassic biotic recovery: the Salt Range and Surghar Range records. Sedimentary Geology 234, 19–41.

Hinojosa, J.L., Brown, S.T., Chen, J., DePaolo, D.J., Paytan, A., Shen, S.Z., Payne, J.L., 2012. Evidence for end-Permian ocean acidification from calcium isotopes in biogenic apatite. Geology 40(8), 743-746.

Hochuli, P.A., Hermann, E., Vigran, J.S., Bucher, H., Weissert, H., 2010. Rapid demise and recovery of plant ecosystems across the end-Permian extinction event, Global and Planetary Change 74, 144–155.

Hochuli, P.A., Sanson-Barrera, A., Schneebeli-Hermann, E., Bucher, H., 2016. Severest crisis overlooked-Worst disruption of terrestrial environments postdates the Permian-Triassic mass extinction. Nature Scientific Reports. DOI: 10.1038/srep28372.

Hochuli, P.A., Schneebeli-Hermann, E., Mangerud, G., Bucher, H., 2017. Evidence for atmospheric pollution across the Permian-Triassic transition. Geology. doi.org/10.1130/G39496.1.

Horacek, M., Koike, T., Richoz, S., 2009. Lower Triassic d13C isotope curve from shallow-marine carbonates in Japan, Panthalassa realm: confirmation of the Tethys d13C curve. Journal of Asian Earth Sciences 36, 481–490.

Isozaki, Y., Kawahata, H., Minoshima, K., 2007. The Capitanian (Permian) Kamura cooling event: the beginning of the Paleozoic–Mesozoic transition. Palaeoworld 16, 16–30.

Jerram, D.A., Widdowson, M., Wignall, P.B., Sun, Y., Lai, X., Bond, D.P.G., Torsvik, T.H., 2016a. Submarine palaeoenvironments during Emeishan flood basalt volcanism, SW China: Implications for plume–lithosphere interaction during the Capitanian, Middle Permian (‘end Guadalupian’) extinction event. Palaeogeography, Palaeoclimatology, Palaeoecology 441, 65–73.

Jerram, D.A., Svensena, H.H., Planke, S., Polozov, A.G., Torsvik, T.H., 2016b. The onset of flood volcanism in the north-western part of the Siberian Traps: Explosive volcanism versus effusive lava flows. Palaeogeography, Palaeoclimatology, Palaeoecology 441, 38–50.

Jin, Y.G.,Wang, Y., Henderson, C. M.,Wardlaw, B.R., Shen, S.Z., Cao, C.Q. 2006. The Global Boundary Stratotype Section and Point (GSSP) for the base of Changhsingian Stage (Upper Permian). Episodes 29, 175–182.

Joachimski, M.M., Lai, X., Shen, SZ., Jiang, H., Luo, G., Chen, B., Chen, J., Sun, Y., 2012. Climate warming in the latest Permian and the Permian–Triassic mass extinction. Geology 40(3), 195-198.

Jost, B. A., Mundil, R., He, B., Brown, T. S., Altiner, D., Sun, Y., DePaolo, D. J., Payne L. L., 2014. Constraining the cause of the end-Guadalupian extinction with coupled records carbon and calcium isotopes. Earth and Planetary Science Letters 396, 201-212.

Kershaw, S., Crasquin, S., Li, Y., Collin, P.Y., Forel, M.B., Mu, X., Baud, A., Wang, Y., Xie, S., Mauer, F., Guo, L., 2012. Microbialites and global environmental change across the

Permian–Triassic boundary: a synthesis. Geobiology 10, 25–47.

Korte, C., Kozur, H.W., Mohtat-Aghai, P., 2004. Dzhulfian to lowermost Triassic $\delta^{13}C$ record at the Permian/Triassic boundary section at Shahreza, Central Iran. Hallesches Jahrbuch fur Geowissenschaften B Beiheft 18, 73–78.

Korte, C., Kozur, H.W., 2010. Carbon-isotope stratigraphy across the Permian–Triassic boundary: A review. Journal of Asian Earth Sciences 39. 215–235.

Langford, F.F., Blanc-Valleron, M.M., 1990. Interpreting Rock-Eval Pyrolysis data using graphs of pyrolizable hydrocarbons versus total organic carbon. American Association of Petroleum Geologists 74(6), 799–804.

Lehrmann, D.J., Jiayong, W., Enos, P., 1998. Controls on facies architecture of a large Triassic carbonate platform: the Great Bank of Guizhou, Nanpanjiang Basin South China. Journal of sedimentary research 68 (2), 311–326.

Liao, Z., Hu, W., Cao, J., Wang, X., Yao, S., Wan Y., 2016. Permian–Triassic boundary (PTB) in the Lower Yangtze Region, southeastern China: A new discovery of deep-water archive based on organic carbon isotopic and U–Pb geochronological studies. Palaeogeography, Palaeoclimatology, Palaeoecology 451, 124–139.

Liu, X.C., Wang, W., Shen, S.Z., Gorgij, M.N., Ye, F.C., Zhang, Y.C., Furuyama, S., Kano, A., Chen,X.Z., 2013. Late Guadalupian to Lopingian (Permian) carbon and strontium isotopic chemostratigraphy in the Abadeh section, central Iran. Gondwana Research 24, 222–232.

Lucas, S., 2017. Permian tetrapod extinction events. Earth-Science Reviews 170, 31–60.

Magaritz, M., Krishnamurthy, R.V., Holser, W.T., 1992. Parallel trends in organic and inorganic carbon isotopes across the Permian/Triassic boundary. American Journal of Science 292, 727–739.

Meyer, K.M., Yu, M., Lehrmann, D., van de Schootbrugge, B., Payne, J.L., 2013. Constraints on Early Triassic carbon cycle dynamics from paired organic and inorganic carbon isotope records. Earth and Planetary Science Letters 361, 429–435.

Ovtcharova, M., Goudemand, N., Hammer, Ø., Kuang Guodun, Cordey, F., Galfetti, T., Schaltegger, U., Bucher, H. 2015. Developing a strategy for accurate definition of a geological boundary through radio-isotopic and biochronological dating: the Early-Middle Triassic boundary (South China). Earth Science Reviews 146, 65-76.

Payne, J.L., Lehrmann, D.J., Wei, J., Orchard, M.J., Schrag, D.P., Knoll, A.H.,

2004. Large perturbations of the carbon cycle during recovery from the end-Permian extinction. Science 305, 506–509.

Raup, D.M., 1979. Size of the Permo-Triassic bottleneck and its evolutionary implications. Science 206, 217–218.

Richoz, S., 2006. Stratigraphie et variations isotopiques du carbone dans le permien supérieur et le trias inférieur de quelques localités de la Néotéthys (Turquie, Oman et Iran). Mémoires de Géologie Lausanne 46, 1–275.

Richoz, S., Krystyn, L., Baud, A., Brandner, R., Horacek, M., Mohtat-Aghai, P., 2010. Permian–Triassic boundary interval in the Middle East (Iran and N.Oman): Progressive environmental change from detailed carbonate carbon isotope marine curve and sedimentary evolution. Journal of Asian Earth Sciences 39, 236–253.

Saitoh, M., Isozaki, Y., Ueno, Y., Yoshida, N., Yao, J., Ji, Z., 2013. Middle–Upper Permian carbon isotope stratigraphy at Chaotian, South China: pre-extinction multiple upwelling of oxygen-depleted water onto continental shelf. Journal of Asian Earth Sciences 67–68, 51–62.

Sanson-Barrera, A., Hochuli, P.A., Bucher, H., Schneebeli-Hermann, E., Meier, M.,Weissert, H., Bernasconi, S., 2015. Late Permian-earliest Triassic high resolution organic carbon isotope and palynofacies records from Kap Stosch (northeast Greenland). Global and Planetary Change 133, 149–166.

Saunders, A., Reichow, M., 2009. The Siberian Traps and the End-Permian mass extinction: a critical review. Chinese Science Bulletin 54(1), 20-37.

Schneebeli-Hermann, E., Kürschner, W.M., Kerp, H., Bomfleur, V., Hochuli, P.A., Bucher, H., Ware, D., Roohi, G. 2015. Vegetation history across the Permian-Triassic boundary in Pakistan (Amb section, Salt Range). Gondwana Research 27, 911-924.

Schneebeli-Hermann, E., Hochuli , P.A., Bucher, H. 2017. Plant associations before and after the Permian-Triassic mass extinction. Global and Planetary Change 155, 178-195.

Schobben, M., Joachimski, M.M., Korn, D., Leda, L., Korte, C., 2014. Palaeotethys seawater temperature rise and an intensified hydrological cycle following the end-Permian mass extinction. Gondwana Research 26, 675–683.

Self, S., Thordarson, T., Widdowson, M., 2005. Gas fluxes from flood basalt eruptions, Elements 1, 283–287.

Self, S., Widdowson, M., Thordarson, T., Jay, A., 2006. Volatile f luxes during f lood basalt eruptions and potential effects on the global environment: A Deccan perspective. Earth and Planetary Science Letters 24, 518–532.

Sepkoski, J.J., Jr., 1989. Periodicity in extinction and the problems of catastrophism in the

history of life. Journal of the Geological Society (London) 146, 7-19.

Shellnutt, J.G., 2014. The Emeishan large igneous province: A synthesis. Geoscience Frontiers 5, 369-394.

Shen, S.Z., Shi G.R., 1996. Diversity and extinction patterns of permian brachiopoda of South China. Historical Biology 12, 93-110. DOI: 10.1080/08912969609386558

Shen, S.Z., Shi, G.R., 2002. Paleobiogeographical extinction patterns of Permian brachiopods in the Asian-western Pacific region. Paleobiology 28(4), 449-463.

Shen, S.Z., Mei, S.L., 2010. Lopingian (Late Permian) high-resolution conodont biostratigraphy in Iran with comparison to South China zonation. Geological Journal 45, 135–161.

Shen, S.Z., Crowley, J.L., Wang, Y., Bowring, S.A., Erwin, D.H., Sadler, P.M., Cao, C.Q., Rothman, D.H., Henderson, C.M., Ramezani, J., Zhang, H., Shen, Y., Wang, X.D., Wang, W., Mu, L., Li, W.Z., Tang, Y.G., Liu, X.L., Liu, L.J., Zeng, Y., Jiang, Y.F., Jin, Y. G., 2011.Calibrating the end-Permian mass extinction. Science 334, 1367–1372.

Shen, S.Z., Cao, C.Q., Zhang, H., Bowring, S.A., Henderson, C.H., Payne, J.L., Davydov,

V.I., Chen, B., Yuan, D.X., Zhang, Y.C., Wang, W., Zheng, Q.F., 2013. High-resolution

$\delta^{13}C_{carb}$ chemostratigraphy from latest Guadalupian through earliest Triassic in South China and Iran. Earth and Planetary Science Letters 375, 156–165.

Spötl C., and Vennemann T.W., 2003. Continuous-flow IRMS analysis of carbonate minerals. Rapid Communications in Mass Spectrometry 17, 1004-1006.

Stanley, S.M., Yang, X., 1994. A double mass extinction at the end of the Paleozoic era.

Science 266, 1340–1344.

Stanley, S.M., 2016. Estimates of the magnitudes of major marine mass extinctions in earth history. Proceedings of the National Academy of Sciences 113(42), E6325–E6334.

Sun, Y., Lai, X., Wignall, P.B., Widdowson, M., Ali, J.R., Jiang, H., Wang, W., Yan, C., Bond, D.P.G., Vedrine, S., 2010. Dating the onset and nature of the Middle Permian Emeishan large igneous province eruptions in SW China using conodont biostratigraphy and its bearing on mantle plume uplift models. Lithos 119, 20–33.

Svensen, H., Planke, S., Polozov, A.G., Schmidbauer, N., Corfu, F., Podladchikov, Y.Y., Jamtveit, B., 2009. Siberian gas venting and the end-Permian environmental crisis.

Earth and Planetary Science Letters 277, 490–500.

Thomazo, C., Vennin, E., Brayard, A., Bour, I., Mathieu, O., Elmeknassi, S., Olivier, N., Escarguel, G., Bylund, K.G., Jenks, J. and Stephen, D.A., 2016. A diagenetic control on the Early Triassic Smithian–Spathian carbon isotopic excursions recorded in the marine settings of the Thaynes Group (Utah, USA). Geobiology 14(3), 220-236.

Traverse, A., 2007. Paleopalynology. Topics in Geobiology 28. Springer.

Ukstins Peate, I., Bryan, S.E., 2008. Re-evaluating plume-induced uplift in the Emeishan large igneous province. Nature Geoscience 1, 625–629.

Ukstins Peate, I., Bryan, S.E., 2009. Pre-eruptive uplift in the Emeishan? Nature Geoscience 2, 531–532.

Wang, X.D., Sugiyama, T., 2000. Diversity and extinction patterns of Permian coral faunas of China. Lethaia 33, 285–294.

Wang, Y., Sadler, P.M., Shen, S.Z., Erwin, D.H., Zhang, Y.C., Wang, X.D., Wang, W., Crowley, J.L., Henderson, C.M., 2013. Quantifying the process and abruptness of the end-Permian mass extinction. Paleobiology 40(1), 113-129.

Ware, D., Bucher, H., Brayard, A., Schneebeli-Hermann, E., Brühwiler, T., 2015. High-resolution biochronology and diversity dynamics of the Early Triassic ammonoid recovery: The Dienerian faunas of the Northern Indian Margin. Palaeogeography, Palaeoclimatology, Palaeoecology 440, 363–373.

Wei, H., Shen, J., Schoepfer, S.D., Krystyn, L., Richoz, S., Algeo, T., 2014. Environmental controls on marine ecosystem recovery following mass extinctions, with an example from the Early Triassic. Earth-Science Reviews 149, 108–135.

Wei, H.Y., Yu, H., Wang, J.G., Qiu, Z., Xiang, L., Shi, G., 2015. Carbon isotopic shift and its cause at the Wuchiapingian–Changhsingian boundary in the Upper Permian at the Zhaojiaba section, South China: evidences from multiple geochemical proxies. Journal of Asian Earth Sciences 105, 270–285.

Weissert, H., Joachimski, M.M., Sarnthein, M., 2008. Chemostratigraphy. Newsletters on Stratigraphy 42, 145–179.

Wignall, P.B., Hallam, A., 1993. Griesbachian (Earliest Triassic) palaeoenvironmental changes in the Salt Range, Pakistan and southeast China and their bearing on the Permo-Triassic mass extinction. Palaeogeography, Palaeoclimatology, Palaeoecology 102, 215–237.

Wignall, P.B., Sun, Y., Bond, D.P.G., Izon, G., Newton, R.J., Védrine, S., Widdowson, M., Ali, J.R., Lai, X., Jiang, H., Cope, H., Bottrell, S.H., 2009. Volcanism, mass extinction, and carbon isotope fluctuations in the Middle Permian of China. Science 324, 1179–1182.

Yan, D., Zhang, L., Qiu, Z., 2013. Carbon and sulfur isotopic fluctuations associated with the end-Guadalupian mass extinction in South China. Gondwana Research 24, 1276–1282.

Yin, H.F., Zhang, K.X., Tong, J.N., Yang, Z.Y., Wu, S.B., 2001. The Global Stratotype Section and Point (GSSP) of the Permian−Triassicboundary. Episodes, 24275–275.

Yin, H.F., Feng, Q.L., Lai, X.L., Baud, A., Tong, J.N., 2007. The protracted Permo-Triassic crisis and multi-episode extinction around the Permian-Triassic boundary. Global and Planetary Change 55, 1–20. doi:10.1016/j.gloplacha.2006.06.005.

Yin, H.F., Jiang, H.S., Xia,W.C., Feng, Q.L., Zhang, N., Shen, J., 2014. The end-Permian regression in South China and its implication on mass extinction. Earth-Science Reviews 173, 19–33.

Yuan, D.X., Shen, S.Z., Henderson, C.M., Chen, J., Zhang, H., Feng, H.Z., 2014. Revised conodont-based integrated high-resolution timescale for the Changhsingian Stage and end-Permian extinction interval at the Meishan sections, South China. Lithos 204, 220–245.

Zhang, H., Cao, C. Q., Liu, X. L., Mu, L., Zheng, Q. F., Liu, F., Xiang, L., Liu, L. J., Shen, S. Z., 2016. The terrestrial end-Permian mass extinction in South China: Palaeogeography, Palaeoclimatology, Palaeoecology 448, 108-124.

Sample	Position	Formation	Ccarb	Ocarb	CaCo3	TOC	Corg	PC [%]	RC [%]	TOC [%]	MINC [%]	HI [mg HC/g TOC]	OI [mg CO2/g TOC]	Tmax [°C]	S1 [mg HC/g]	S2a [mg HC/g]	S2b [mg HC/g]	S3
GUA 735	1	Wuchiaping	4.88	-5.12	76	0.5	-26.1	0.01	0.02	0.03	10.36	275	322	458	0.02	0.09	0.00	0.11
GUA 734	2	Wuchiaping	5.31	-4.80	59													
GUA 733	3.2	Wuchiaping	3.70	-5.81	89													
GUA 732	4	Wuchiaping	3.27	-5.96	92	0.7	-27.1	0.01	0.02	0.03	11.08	248	295	458	0.02	0.08	0.00	0.10
GUA 731	4.5	Wuchiaping	4.81	-5.37	77													
GUA 730	5.2	Wuchiaping	5.26	-4.46	91													
GUA 729	6.1	Wuchiaping	5.22	-4.65	102	0.5	-26.7	0.01	0.02	0.02	10.22	247	393	461	0.02	0.06	0.00	0.10
GUA 728	6.75	Wuchiaping	5.34	-4.74	80													
GUA 727	7.5	Wuchiaping	4.80	-5.13	78													
GUA 726	8.25	Wuchiaping	5.07	-4.38	74	0.4	-27.0	0.01	0.02	0.03	9.97	217	309	454	0.01	0.06	0.00	0.09
GUA 725	8.9	Wuchiaping	4.51	-5.78	85													
GUA 724	9.2	Wuchiaping	4.72	-4.60	80													
GUA 723	9.7	Wuchiaping	4.50	-5.58	61	0.4	-27.4	0.01	0.01	0.02	10.22	293	447	455	0.02	0.07	0.00	0.11
GUA 722	10	Wuchiaping	4.47	-5.37	85													
GUA 721	10.8	Wuchiaping	4.55	-5.12	83													
GUA 720	11.5	Wuchiaping	5.22	-4.24	81	0.4	-26.6	0.01	0.02	0.02	9.65	249	400	462	0.01	0.06	0.00	0.10
GUA 719	12	Wuchiaping	5.06	-4.75	76													
GUA 718	12.25	Wuchiaping	5.57	-5.13	77													
GUA 717	12.75	Wuchiaping	5.11	-5.10	87	0.4	-25.6	0.01	0.03	0.04	11.20	196	361	425	0.02	0.07	0.00	0.13
GUA 716	13	Wuchiaping	4.58	-5.56	79													
GUA 715	13.5	Wuchiaping	4.12	-5.80	81													
GUA 714	14	Wuchiaping	4.76	-5.87	76	0.3	-25.3											
GUA 713	14.8	Wuchiaping	4.81	-5.81	81													
GUA 712	15.2	Wuchiaping	5.33	-5.54	45													
GUA 711	15.5	Wuchiaping	5.08	-5.45	85													
GUA 710	15.75	Wuchiaping	5.00	-5.31	85	0.2	-24.9	0.01	0.03	0.04	10.36	179	303	454	0.02	0.07	0.00	0.12
GUA 709	16.25	Wuchiaping	5.09	-4.65	19													
GUA 708	16.7	Wuchiaping	4.38	-6.25	81													
GUA 707	17	Wuchiaping	4.23	-7.06	77													
GUA 706	17.25	Wuchiaping	3.87	-7.26	69	0.3	-24.1	0.01	0.03	0.04	11.10	216	321	463	0.03	0.08	0.00	0.12
GUA 705	17.5	Wuchiaping	2.19	-8.40	69													
GUA 704	17.75	Wuchiaping	3.56	-8.45	72													

Supplementary material S1 δ $^{13}C_{carb}$, δ $^{18}O_{carb}$, δ $^{13}C_{org}$, carbonate content, and Rock-Eval data measured at Guantan (GUA), Potuo (PUT), Layin (LAY), and Laxian (LAX) sections.

Sample	Position		Ccarb	Ocarb	CaCo3	TOC	Corg	PC [%]	RC [%]	TOC [%]	MINC [%]	HI [mg HC/g TOC]	OI [mg CO2/g TOC]	Tmax [°C]	S1 [mg HC/g]	S2a [mg HC/g]	S2b [mg HC/g]	S3
		Wuchiaping																
GUA 702	18	Wuchiaping	3.91	-7.20	91	0.1	-21.6	0.01	0.02	0.03	9.98	219	396	464	0.02	0.06	0.00	0.11
GUA 703	18.25	Wuchiaping	3.81	-8.91	81													
GUA 701	18.75	Wuchiaping	4.66	-7.15	92													
GUA 700	19.2	Wuchiaping	3.63	-9.39	81	0.1	-23.8	0.01	0.03	0.04	10.34	182	311	463	0.02	0.07	0.00	0.12
GUA 500	20	Wuchiaping	4.90	-6.66	88	0.9	-24.9	0.02	0.15	0.17	10.12	53	164	420	0.05	0.09	0.00	0.27
GUA 501	20.5	Wuchiaping	4.75	-5.80	100	0.9	-25.1	0.01	0.08	0.09	10.36	74	172	422	0.03	0.07	0.00	0.16
GUA 502	21.2	Wuchiaping	4.18	-8.06	99	1.0	-24.9	0.02	0.08	0.10	11.11	98	192	430	0.04	0.10	0.00	0.19
GUA 503	22.7	Wuchiaping	4.02	-7.20	100													
GUA 504	23.7	Wuchiaping	4.21	-8.27	90	0.9	-24.8	0.02	0.05	0.07	10.75	151	197	426	0.06	0.11	0.00	0.14
GUA 505	24.7	Wuchiaping	3.94	-6.94	63													
GUA 506	25.7	Wuchiaping	4.30	-5.01	91	4.5	-26.1	0.01	0.07	0.09	11.28	103	176	425	0.03	0.09	0.00	0.15
GUA 507	26.3	Wuchiaping	3.96	-8.20	100	1.0	-25.6	0.01	0.04	0.06	11.03	171	246	461	0.03	0.10	0.00	0.14
GUA 508	27	Wuchiaping	3.01	-6.80	101	1.9	-26.7	0.01	0.04	0.05	10.58	209	254	459	0.02	0.11	0.00	0.13
GUA 509	28	Wuchiaping	2.63	-6.76	92	0.6	-26.6	0.02	0.07	0.09	10.36	149	231	450	0.04	0.14	0.00	0.22
GUA 510	29	Wuchiaping	3.83	-5.45	100													
GUA 511	30	Wuchiaping	2.80	-8.04	96	0.7	-26.6	0.01	0.07	0.09	10.88	113	176	454	0.03	0.10	0.00	0.15
GUA 512	31	Wuchiaping	3.87	-9.05	99	1.7	-26.2	0.01	0.05	0.06	11.14	160	183	459	0.02	0.10	0.00	0.11
GUA 513	32.2	Wuchiaping	3.83	-6.50	99													
GUA 514	32.8	Wuchiaping	3.94	-7.44	100	0.4	-26.6	0.01	0.08	0.09	9.74	110	148	456	0.03	0.10	0.00	0.13
GUA 515	33.7	Wuchiaping	4.14	-5.97	93													
GUA 516	34.5	Wuchiaping	3.94	-7.93	93	0.3	-27.4	0.01	0.05	0.06	10.29	170	194	460	0.02	0.10	0.00	0.11
GUA 517	35.5	Wuchiaping	3.59	-8.90	88													
GUA 518	36.5	Wuchiaping	3.45	-9.03	104													
GUA 519	37.5	Wuchiaping	3.86	-6.42	91	1.2	-26.1	0.03	0.41	0.44	8.79	41	71	465	0.07	0.18	0.00	0.31
GUA 520	38.7	Wuchiaping	4.29	-6.33	104													
GUA 521	40	Wuchiaping	3.93	-8.18	100													
GUA 522	41	Wuchiaping	4.35	-4.87	94													
GUA 523	42.3	Wuchiaping	4.02	-5.05	91	0.4	-26.8	0.02	0.12	0.13	10.86	76	118	426	0.04	0.10	0.00	0.16
GUA 524	43.7	Wuchiaping	4.19	-3.83	85													
GUA 525	44.5	Wuchiaping	3.40	-5.49	88	6.0	-26.5	0.01	0.07	0.08	9.88	100	222	469	0.02	0.08	0.00	0.18
GUA 527	44.5	Wuchiaping	4.22	-4.65	104													
GUA 526	46.4	Wuchiaping	4.39	-4.09	94													

Sample	Position		Ccarb	Ocarb	CaCo3	TOC	Corg	PC [%]	RC [%]	TOC [%]	MINC [%]	HI [mg HC/g TOC]	OI [mg CO2/g TOC]	Tmax [°C]	S1 [mg HC/g]	S2a [mg HC/g]	S2b [mg HC/g]	S3
		Wuchiaping																
GUA 528	48.5	Wuchiaping	4.32	-4.21	107													
GUA 529	50	Wuchiaping	4.63	-2.94	111													
GUA 530	51	Wuchiaping	4.85	-2.79	93	0.8	-26.5	0.01	0.06	0.08	9.44	130	136	453	0.03	0.10	0.00	0.10
GUA 531	52	Wuchiaping	4.47	-4.23	96													
GUA 532	53	Wuchiaping	4.83	-4.84	69	1.0	-27.1	0.02	0.10	0.12	10.44	112	99	435	0.06	0.13	0.00	0.12
GUA 533	54	Wuchiaping	4.74	-3.75	82													
GUA 534	55	Wuchiaping	4.37	-3.67	107													
GUA 535	56	Wuchiaping	4.56	-5.81	98													
GUA 536	57	Wuchiaping	4.78	-6.03	55	0.4	-26.5	0.02	0.11	0.13	8.40	92	80	437	0.04	0.12	0.00	0.11
GUA 537	57.7	Wuchiaping	5.01	-3.84	97													
GUA 538	59	Wuchiaping	5.12	-3.94	95	17.8	-26.9	0.02	0.08	0.10	11.45	125	98	436	0.03	0.12	0.00	0.09
GUA 539	60	Wuchiaping	4.55	-5.71	96													
GUA 540	61	Wuchiaping	5.19	-4.02	96													
GUA 541	62	Wuchiaping	5.31	-2.89	102	1.6	-26.7	0.02	0.10	0.11	10.47	88	111	433	0.04	0.10	0.00	0.13
GUA 542	63.2	Wuchiaping	4.99	-3.44	102													
GUA 543	64	Wuchiaping	5.38	-4.27	27	0.4	-27.9	0.01	0.10	0.11	10.53	80	121	431	0.03	0.09	0.00	0.14
GUA 544	65	Wuchiaping	4.53	-7.43	93													
GUA 545	66	Wuchiaping	4.33	-5.61	94													
GUA 546	67.4	Wuchiaping	4.34	-6.11	92	3.2	-27.6	0.02	0.12	0.14	10.98	103	93	436	0.04	0.14	0.00	0.13
GUA 547	68	Wuchiaping	4.30	-5.30	105													
GUA 548	69	Wuchiaping	4.08	-5.52	100													
GUA 549	70	Wuchiaping	3.83	-6.21	101	1.5	-28.4	0.02	0.12	0.14	10.80	93	99	438	0.03	0.13	0.00	0.14
GUA 550	71.4	Wuchiaping	3.82	-5.84	102													
GUA 551	72.4	Wuchiaping	4.02	-7.40	89													
GUA 552	73.5	Wuchiaping	3.93	-4.79	95	2.3	-27.8	0.01	0.07	0.08	10.52	115	148	459	0.02	0.09	0.00	0.12
GUA 553	74.5	Wuchiaping	3.55	-7.20	98													
GUA 554	75.5	Wuchiaping	3.85	-4.10	91	1.8	-27.6	0.02	0.14	0.16	11.29	81	86	434	0.04	0.13	0.00	0.14
GUA 555	78	Wuchiaping	3.18	-9.19	94	7.6	-27.4	0.02	0.17	0.18	11.05	66	64	453	0.04	0.12	0.00	0.12
GUA 556	79	Wuchiaping	4.36	-5.31	90													
GUA 557	80	Wuchiaping	3.72	-8.79	99	2.9	-26.4	0.01	0.04	0.06	10.75	195	132	454	0.02	0.11	0.00	0.08
GUA 558	81	Wuchiaping	4.46	-6.04	102													
GUA 559	82	Wuchiaping	4.36	-6.21	99	0.4	-26.7	0.01	0.05	0.06	10.55	135	161	460	0.02	0.08	0.00	0.10

Sample	Position		Ccarb	Ocarb	CaCo3	TOC	Corg	PC [%]	RC [%]	TOC [%]	MINC [%]	HI [mg HC/g TOC]	OI [mg CO2/g TOC]	Tmax [°C]	S1 [mg HC/g]	S2a [mg HC/g]	S2b [mg HC/g]	S3
		Wuchiaping																
GUA 560	83	Wuchiaping	4.65	-5.45	94													
GUA 561	84	Wuchiaping	3.55	-6.88	66	0.1	-26.4	0.01	0.05	0.06	7.01	134	195	423	0.04	0.08	0.00	0.12
GUA 562	84.7	Wuchiaping	2.85	-8.12	95	0.1	-25.5	0.01	0.02	0.03	10.09	215	197	462	0.02	0.07	0.00	0.06
GUA 563	85.5	Wuchiaping	3.83	-5.85	98	1.1	-26.7	0.01	0.03	0.04	9.97	167	175	462	0.02	0.07	0.00	0.07
GUA 564	86.3	Wuchiaping	3.81	-6.39	89													
GUA 565	87	Wuchiaping	4.29	-6.21	91	1.3	-27.1	0.01	0.04	0.05	10.81	179	188	453	0.02	0.09	0.00	0.09
GUA 566	87.7	Wuchiaping	3.96	-6.85	89													
GUA 567	88.6	Wuchiaping	4.56	-4.34	97	0.5	-26.6	0.01	0.04	0.05	10.01	170	224	428	0.03	0.08	0.00	0.11
GUA 568	89.6	Wuchiaping	4.23	-4.47	92													
GUA 569	90.5	Wuchiaping	4.08	-7.32	98	1.1	-27.2	0.01	0.06	0.07	11.03	130	198	460	0.03	0.09	0.00	0.14
GUA 570	91.5	Wuchiaping	4.25	-5.88	74													
GUA 571	92.2	Wuchiaping	4.09	-6.91	82													
GUA 572	93.2	Wuchiaping	2.31	-7.08	12													
GUA 573	95.2	Wuchiaping	3.20	-7.26	66	0.3	-25.6	0.01	0.12	0.14	7.22	58	116	475	0.03	0.08	0.00	0.16
GUA 574	96.2	Wuchiaping	2.02	-6.32	97	1.3	-25.6	0.01	0.06	0.07	11.54	122	115	422	0.03	0.09	0.00	0.09
GUA 575	97.2	Wuchiaping	1.33	-6.00	96	3.5	-25.6	0.01	0.03	0.04	11.07	186	174	467	0.02	0.08	0.00	0.08
GUA 576	98.2	Wuchiaping	4.33	-5.51	85													
GUA 577	99.2	Wuchiaping	4.38	-6.49	92	8.9	-25.3	0.01	0.05	0.06	7.13	132	122	431	0.04	0.08	0.00	0.07
GUA 578	100.2	Wuchiaping	4.24	-6.80	95													
GUA 579	101.3	Wuchiaping	3.67	-5.66	88													
GUA 580	102.3	Wuchiaping	4.61	-7.64	102	0.9	-23.6	0.01	0.03	0.04	10.52	210	141	461	0.02	0.08	0.00	0.05
GUA 581	103.5	Wuchiaping	4.50	-7.84	92													
GUA 582	104.6	Wuchiaping	4.70	-8.08	100	5.6	-24.3	0.01	0.06	0.07	10.72	141	91	435	0.03	0.10	0.00	0.07
GUA 583	105.6	Wuchiaping	5.16	-4.86	98													
GUA 584	106.2	Wuchiaping	5.19	-5.64	86	1.6	-26.2	0.01	0.04	0.06	11.77	184	139	425	0.05	0.10	0.00	0.08
GUA 585	107.5	Wuchiaping	5.20	-5.64	89													
GUA 586	108.5	Wuchiaping	5.03	-8.45	90													
GUA 587	109.5	Wuchiaping	5.07	-8.38	98	7.6	-25.1	0.01	0.05	0.06	11.09	112	156	426	0.02	0.07	0.00	0.10
GUA 588	110.6	Wuchiaping	5.49	-5.98	100													
GUA 589	111.4	Wuchiaping	5.42	-6.64	94													
GUA 590	112	Wuchiaping	5.28	-5.01	99													
GUA 591	113	Wuchiaping	4.99	-5.72	93	0.8	-24.2	0.01	0.09	0.11	10.41	84	141	431	0.03	0.09	0.00	0.15

Sample	Position		Ccarb	Ocarb	CaCo3	TOC	Corg	PC [%]	RC [%]	TOC [%]	MINC [%]	HI [mg HC/g TOC]	OI [mg CO2/g TOC]	Tmax [°C]	S1 [mg HC/g]	S2a [mg HC/g]	S2b [mg HC/g]	S3
		Wuchiaping																
GUA 592	114	Wuchiaping	4.36	-7.66	92													
GUA 593	115	Wuchiaping	4.98	-7.05	93													
GUA 594	116	Wuchiaping	4.80	-5.07	95	1.2	-26.8	0.02	0.13	0.14	10.53	94	55	456	0.03	0.13	0.00	0.08
GUA 595	117	Wuchiaping	4.22	-8.70	90													
GUA 596	118.1	Wuchiaping	5.36	-6.86	93													
GUA 598	120.6	Wuchiaping	5.32	-6.60	102													
GUA 599	121	Wuchiaping	4.81	-7.68	104													
GUA 601	123	Wuchiaping	5.03	-6.90	103	3.4	-24.0	0.00	0.02	0.02	9.63	159	0	497	0.01	0.03	0.00	0.00
GUA 602	124	Wuchiaping	5.72	-5.61	58													
GUA 603	125	Wuchiaping	5.13	-5.94	90													
GUA 604	126	Wuchiaping	5.41	-6.09	85													
GUA 605	127.5	Wuchiaping	5.36	-6.04	94	3.8	-24.8	0.01	0.03	0.04	10.96	267	190	459	0.02	0.11	0.00	0.08
GUA 606	128.5	Wuchiaping	5.62	-6.43	88													
GUA 607	129.5	Wuchiaping	5.11	-7.70	96													
GUA 608	130.5	Wuchiaping	5.45	-5.53	105													
GUA 609	131.5	Wuchiaping	5.30	-6.52	106	7.1	-25.0	0.01	0.00	0.01	10.55	475	847	445	0.01	0.05	0.00	0.09
GUA 610	133	Wuchiaping	5.36	-5.97	91													
GUA 611	135	Wuchiaping	4.91	-7.18	94													
GUA 615	137.2	Wuchiaping	5.38	-6.69	92													
GUA 617	138.5	Wuchiaping	5.21	-6.89	98	2.2	-25.3	0.01	0.02	0.04	10.88	277	247	459	0.02	0.10	0.00	0.09
GUA 619	140	Wuchiaping	4.81	-7.25	101													
GUA 621	141	Wuchiaping	4.85	-6.57	93													
GUA 623	142	Wuchiaping	5.05	-5.41	95													
GUA 625	143	Wuchiaping	5.02	-7.07	97	3.3	-26.0	0.01	0.06	0.07	9.54	165	100	431	0.02	0.11	0.00	0.07
GUA 627	144	Wuchiaping	4.79	-6.57	99													
GUA 629	145	Wuchiaping	4.79	-6.24	103													
GUA 631	146	Wuchiaping	4.67	-7.20	96													
GUA 633	147	Wuchiaping	4.52	-5.04	102	2.1	-25.8	0.01	0.03	0.04	10.81	222	184	459	0.01	0.08	0.00	0.07
GUA 635	148.2	Wuchiaping	4.62	-6.03	103													
GUA 637	149.3	Wuchiaping	4.52	-4.86	87													
GUA 639	150.4	Wuchiaping	4.42	-4.56	93													
GUA 641	151.5	Wuchiaping	4.51	-4.85	100													

Sample	Position		Ccarb	Ocarb	CaCo3	TOC	Corg	PC [%]	RC [%]	TOC [%]	MINC [%]	HI [mg HC/g TOC]	OI [mg CO2/g TOC]	Tmax [°C]	S1 [mg HC/g]	S2a [mg HC/g]	S2b [mg HC/g]	S3
		Wuchiaping																
GUA 643	152.5	Wuchiaping	4.26	-5.11	100	14.2	-24.7	0.01	0.03	0.05	11.00	179	246	433	0.02	0.08	0.00	0.11
GUA 645	153.5	Wuchiaping	4.39	-5.44	98													
GUA 647	154.5	Wuchiaping	4.45	-5.75	101													
GUA 649	156.3	Wuchiaping	4.48	-5.82	101													
GUA 651	157.3	Wuchiaping	4.24	-6.88	97													
GUA 653	158.5	Wuchiaping	4.47	-4.81	92													
GUA 655	160	Wuchiaping	4.29	-4.96	99	1.7	-25.2	0.01	0.03	0.04	11.21	192	211	431	0.02	0.08	0.00	0.09
GUA 657	161	Wuchiaping	4.42	-5.18	101													
GUA 659	162.4	Wuchiaping	4.24	-7.21	90													
GUA 661	163.5	Wuchiaping	3.79	-7.56	58													
GUA 663	164.5	Wuchiaping	4.19	-4.91	88													
GUA 665	165.4	Wuchiaping	4.19	-4.96	89													
GUA 667	166.3	Wuchiaping	4.17	-5.35	107	2.2	-27.5	0.02	0.04	0.05	10.90	215	300	430	0.03	0.11	0.00	0.16
GUA 669	167.3	Wuchiaping	4.39	-4.83	100													
GUA 671	168	Wuchiaping	3.31	-5.47	98													
GUA 673	169.7	Wuchiaping	4.54	-6.66	101													
GUA 675	171	Wuchiaping	4.12	-7.22	98													
GUA 120	172.2	Wuchiaping	3.82	-7.83	88	7.7	-26.5	0.01	0.14	0.15	11.06	35	80	479	0.01	0.05	0.00	0.12
GUA 118	173.3	Wuchiaping	2.99	-9.97	78													
GUA 116	174.5	Wuchiaping	4.01	-7.05	86													
GUA 114	175.5	Wuchiaping	3.62	-7.08	94													
GUA 112	176.5	Wuchiaping	3.35	-6.25	80													
GUA 110	177.5	Wuchiaping	2.94	-6.59	83													
GUA 108	178.5	Wuchiaping	2.86	-9.21	94	2.5	-25.9	0.00	0.04	0.04	11.72	70	111	483	0.01	0.03	0.00	0.05
GUA 106	179.9	Wuchiaping	2.70	-8.12	95													
GUA 104	180.5	Wuchiaping	2.88	-6.45	86													
GUA 102	181.5	Wuchiaping	2.36	-7.43	92													
GUA 100	182.5	Wuchiaping	2.71	-6.27	99													
GUA 98	183.5	Wuchiaping	3.67	-6.46	90													
GUA 96	184.5	Wuchiaping	3.20	-7.72	103													
GUA 94	185.5	Wuchiaping	3.01	-8.11	98													
GUA 92	186.5	Wuchiaping	2.98	-7.38	85	22.5	-28.6	0.02	0.33	0.35	11.51	41	31	485	0.06	0.14	0.00	0.11

Sample	Position		Ccarb	Ocarb	CaCo3	TOC	Corg	PC [%]	RC [%]	TOC [%]	MINC [%]	HI [mg HC/g TOC]	OI [mg CO2/g TOC]	Tmax [°C]	S1 [mg HC/g]	S2a [mg HC/g]	S2b [mg HC/g]	S3
		Wuchiaping																
GUA 90	187.5	Wuchiaping	2.60	-7.45	87													
GUA 88	188.5	Wuchiaping	2.63	-8.60	75													
GUA 86	189.5	Wuchiaping	3.15	-6.48	100													
GUA 84	190.5	Wuchiaping	3.73	-9.97	102													
GUA 82	191.5	Wuchiaping	3.50	-5.96	66													
GUA 80	193	Wuchiaping	2.89	-9.09	94	3.1	-26.9	0.02	0.22	0.24	10.44	48	62	484	0.03	0.11	0.00	0.15
GUA 79	194	Wuchiaping	3.06	-6.33	100													
GUA 78	195	Wuchiaping	3.02	-5.35	97													
GUA 77	196	Wuchiaping	3.38	-6.87	84													
GUA 76	197	Wuchiaping	3.63	-5.90	97													
GUA 75	198	Wuchiaping	3.10	-5.29	85	5.0	-26.8	0.02	0.36	0.38	11.46	33	34	491	0.05	0.12	0.00	0.13
GUA 74	199	Wuchiaping	3.68	-6.77	83													
GUA 73	200	Wuchiaping	3.35	-7.57	94													
GUA 72	201	Wuchiaping	2.81	-8.80	103													
GUA 71	202	Wuchiaping	3.09	-5.08	89													
GUA 70	203	Wuchiaping	2.39	-7.15	102													
GUA 69	204	Wuchiaping	2.41	-5.58	97	14.3	-27.0	0.01	0.07	0.08	12.17	64	85	483	0.01	0.05	0.00	0.07
GUA 68	205	Wuchiaping	2.58	-5.67	97													
GUA 67	206	Wuchiaping	1.78	-7.00	93													
GUA 66	207	Wuchiaping	2.53	-8.12	88													
GUA 65	208	Wuchiaping	2.07	-6.18	103													
GUA 64	209	Wuchiaping	2.36	-5.84	85	6.0	-28.4	0.01	0.13	0.13	11.63	39	29	483	0.02	0.05	0.00	0.04
GUA 63	210	Wuchiaping	2.15	-7.22	103													
GUA 62	211	Wuchiaping	2.24	-5.99	83													
GUA 61	212	Wuchiaping	2.15	-6.01	86	6.0	-26.4	0.00	0.03	0.04	10.53	83	78	483	0.01	0.03	0.00	0.03
GUA 60	213	Wuchiaping	2.58	-5.72	76													
GUA 59	214	Wuchiaping	2.26	-8.71	94	10.7	-27.2	0.01	0.15	0.16	11.79	58	42	481	0.04	0.09	0.00	0.07
GUA 58	215	Wuchiaping	2.12	-7.60	91													
GUA 57	216	Wuchiaping	2.48	-6.59	100													
GUA 56	217	Wuchiaping	2.05	-5.93	93	4.2	-26.3	0.00	0.02	0.02	0.06	162	151	481	0.01	0.03	0.00	0.03
GUA 55	218	Wuchiaping	2.05	-6.32	93													
GUA 54	219	Wuchiaping	1.68	-6.16	92													

Sample	Position		Ccarb	Ocarb	CaCo3	TOC	Corg	PC [%]	RC [%]	TOC [%]	MINC [%]	HI [mg HC/g TOC]	OI [mg CO2/g TOC]	Tmax [°C]	S1 [mg HC/g]	S2a [mg HC/g]	S2b [mg HC/g]	S3
		Wuchiaping																
GUA 53	220	Wuchiaping	1.68	-5.57	94	8.4	-27.7	0.01	0.09	0.10	11.25	42	68	483	0.02	0.04	0.00	0.07
GUA 52	221	Wuchiaping	1.69	-5.18	101													
GUA 51	222	Wuchiaping	2.20	-6.65	92													
GUA 50	223	Wuchiaping	1.26	-5.91	104	4.4	-26.4	0.00	0.04	0.04	11.46	23	109	482	0.00	0.01	0.00	0.05
GUA 49	224	Wuchiaping	1.59	-6.35	99													
GUA 48	225	Wuchiaping	1.41	-8.29	79	8.0	-28.2	0.03	0.50	0.52	11.08	36	24	484	0.07	0.19	0.00	0.13
GUA 47	226	Wuchiaping	1.63	-8.14	93													
GUA 46	227	Wuchiaping	1.09	-6.37	93	1.0	-22.0	0.01	0.03	0.04	11.52	103	119	482	0.01	0.04	0.00	0.05
GUA 45	228	Wuchiaping	1.12	-6.87	92													
GUA 44	229.5	Wuchiaping	1.58	-7.21	72													
GUA 43	231	Wuchiaping	0.80	-4.78	95													
GUA 42	232	Wuchiaping	1.01	-4.10	98	1.1	-26.4	0.01	0.09	0.10	11.19	22	61	339	0.04	0.02	0.00	0.06
GUA 41	233	Wuchiaping	1.12	-3.59	91													
GUA 40	234	Wuchiaping	1.44	-5.73	79	2.2	-26.4	0.01	0.06	0.07	11.46	74	82	420	0.03	0.05	0.00	0.06
GUA 39/1	235	Wuchiaping	1.26	-6.68	89													
GUA 39	235.7	Wuchiaping	1.40	-4.06	93													
GUA 38/1	236.4	Wuchiaping	1.27	-5.24	86	0.8	-28.9	0.01	0.10	0.11	11.87	49	72	487	0.02	0.05	0.00	0.08
GUA 37/1	237.7	Wuchiaping	0.86	-5.04	86	17.9	-28.1	0.01	0.14	0.15	12.10	47	37	481	0.04	0.07	0.00	0.06
GUA 37	238.4	Wuchiaping	0.21	-3.66	98	29.2	-29.1	0.01	0.19	0.20	11.69	52	14	485	0.05	0.11	0.00	0.03
GUA 36	240	Wuchiaping	0.46	-4.90	101	9.0	-28.1	0.01	0.13	0.14	11.07	45	42	492	0.03	0.06	0.00	0.06
GUA 35/1	240.7	Wuchiaping	0.88	-5.35	102	27.5	-29.5	0.01	0.24	0.25	11.88	33	31	483	0.04	0.08	0.00	0.08
GUA 35	241.5	Wuchiaping	1.19	-6.50	91													
GUA 34/1	242.5	Wuchiaping	1.26	-4.43	101	262.9	-27.4	0.05	0.61	0.66	12.79	56	10	515	0.24	0.37	0.00	0.07
GUA 34	243.5	Wuchiaping	1.12	-5.83	105													
GUA 33/1	244.3	Wuchiaping	1.67	-5.74	106	37.4	-30.0	0.03	0.50	0.53	11.92	34	14	492	0.11	0.18	0.00	0.08
GUA 33	245	Wuchiaping	2.01	-5.21	107													
GUA 32/1	245.6	Wuchiaping	2.26	-6.12	106	18.8	-29.8	0.01	0.11	0.12	12.08	35	9	484	0.03	0.04	0.00	0.01
GUA 32	246.5	Wuchiaping	2.14	-6.24	93													
GUA 31/1	247.2	Wuchiaping	2.07	-6.19	92													
GUA31	248	Wuchiaping	2.22	-6.09	97	25.8	-29.7	0.02	0.38	0.41	11.53	38	3	485	0.11	0.16	0.00	0.01
GUA 30/1	249	Wuchiaping	2.43	-5.84	98													
GUA 30	249.7	Wuchiaping	2.17	-6.39	105													

Sample	Position		Ccarb	Ocarb	CaCo3	TOC	Corg	PC [%]	RC [%]	TOC [%]	MINC [%]	HI [mg HC/g TOC]	OI [mg CO2/g TOC]	Tmax [°C]	S1 [mg HC/g]	S2a [mg HC/g]	S2b [mg HC/g]	S3
		Wuchiaping																
GUA 29/1	250.5	Wuchiaping	2.41	-5.98	103	66.7	-29.5	0.05	0.79	0.85	11.11	52	14	493	0.16	0.44	0.00	0.12
GUA 29	251.5	Wuchiaping	2.20	-5.24	93													
GUA 28/1	252	Wuchiaping	2.30	-5.60	95													
GUA 28	253	Wuchiaping	2.76	-6.28	95	124.8	-28.0	0.01	0.10	0.11	11.57	59	0	484	0.04	0.06	0.00	0.00
GUA 27/1	253.7	Wuchiaping	2.42	-6.48	93													
GUA 27	254.5	Wuchiaping	3.21	-6.41	104													
GUA 26/1	255.2	Wuchiaping	2.69	-6.09	104													
GUA 26	256	Wuchiaping	2.67	-6.24	93	9.0	-30.3	0	0.05	0.06	11.45	35	82	483	0.02	0.02	0.00	0.05
GUA 25/1	256.5	Wuchiaping	2.11	-6.33	103													
GUA 25	257.5	Wuchiaping	2.56	-6.07	95													
GUA 24/1	258.5	Wuchiaping	2.79	-6.49	97	18.6	-29.8	0.05	0.48	0.53	11.45	78	25	444	0.13	0.41	0.00	0.13
GUA 24	259	Wuchiaping	2.41	-6.09	96													
GUA 23/1	259.9	Wuchiaping	2.89	-6.16	95													
GUA 23	260.5	Wuchiaping	2.87	-5.90	91	9.4	-29.9	0.02	0.11	0.13	11.97	103	38	442	0.04	0.13	0.00	0.05
GUA 22/1	261.5	Wuchiaping	2.70	-6.04	96													
GUA 22	262.2	Wuchiaping	2.93	-6.43	92	99.8	-29.9	0.02	0.10	0.12	11.58	113	21	442	0.04	0.13	0.00	0.02
GUA 21/1	263.1	Wuchiaping	2.80	-6.17	95													
GUA 21	264	Wuchiaping	2.63	-6.85	86	16.0	-30.8	0.03	0.30	0.34	11.62	90	29	449	0.08	0.31	0.00	0.10
GUA 20/1	264.7	Wuchiaping	2.37	-6.02	82													
GUA 20	265.5	Wuchiaping	2.50	-6.36	90													
GUA 19/1	266.4	Wuchiaping	2.68	-6.35	85	135.5	-28.1	0.11	1.47	1.58	11.29	65	10	499	0.30	1.03	0.00	0.16
GUA 19	267	Wuchiaping	3.12	-5.97	86													
GUA 18/1	267.6	Wuchiaping	2.59	-5.64	96													
GUA 18	268.5	Wuchiaping	2.22	-6.47	96	1.1	-29.8	0.01	0.09	0.10	12.01	118	47	451	0.03	0.12	0.00	0.05
GUA 17	270.5	Wuchiaping	1.76	-5.82	91													
GUA 16/1	271.2	Wuchiaping	2.01	-5.68	92	7.8	-29.3	0.02	0.23	0.25	12.01	68	24	452	0.05	0.17	0.00	0.06
GUA 16	272	Wuchiaping	1.68	-6.02	94													
GUA 15/1	272.7	Wuchiaping	2.15	-6.51	86													
GUA 15	273.5	Wuchiaping	2.51	-6.31	88	32.3	-31.1	0.05	0.71	0.76	11.15	50	42	447	0.11	0.38	0.00	0.32
GUA 14/1	274	Wuchiaping	2.29	-6.51	95													
GUA 14	274.8	Wuchiaping	2.34	-6.81	89	35.7	-31.9	0.06	1.12	1.18	11.02	40	36	500	0.10	0.47	0.00	0.43
GUA 13/1	275.6	Wuchiaping	2.28	-6.97	98													

Sample	Position		Ccarb	Ocarb	CaCo3	TOC	Corg	PC [%]	RC [%]	TOC [%]	MINC [%]	HI [mg HC/g TOC]	OI [mg CO2/g TOC]	Tmax [°C]	S1 [mg HC/g]	S2a [mg HC/g]	S2b [mg HC/g]	S3
		Wuchiaping																
GUA 13	276.5	Wuchiaping	1.89	-7.70	80	31.0	-29.5	0.04	0.75	0.79	12.66	37	11	492	0.14	0.29	0.00	0.08
GUA 12/2	277.5	Wuchiaping	2.02	-6.93	82	47.3	-29.3	0.02	0.42	0.44	12.53	27	69	489	0.03	0.12	0.00	0.30
GUA 12/1	280	Wuchiaping	0.81	-8.09	87	55.8	-29.2	0.04	0.89	0.94	11.49	31	41	491	0.11	0.30	0.00	0.39
GUA 12	281	Wuchiaping	1.58	-6.81	87													
GUA 11	283	Wuchiaping	0.47	-7.37	88	2.5	-26.8	0.01	0.04	0.05	11.31	71	185	483	0.01	0.03	0.00	0.09
GUA 10	284	Wuchiaping	0.87	-5.91	92	1.2	-28.1	0.00	0.02	0.02	10.71	92	103	484	0.01	0.02	0.00	0.02
GUA 9	285	Wuchiaping	2.26	-6.33	94													
GUA 8/1	285.7	Wuchiaping	1.41	-5.72	82	9.6	-27.6	0.01	0.09	0.09	10.68	35	105	481	0.02	0.03	0.00	0.10
GUA 8	286.5	Wuchiaping	2.19	-6.79	80													
GUA 7	287.5	Wuchiaping	2.50	-5.39	75													
GUA 6	289	Wuchiaping	2.37	-5.24	90	14.4	-28.1	0.01	0.18	0.20	10.19	39	76	483	0.03	0.08	0.00	0.15
GUA 5/1	289.7	Wuchiaping	2.95	-7.10	89	14.7	-28.8	0.01	0.16	0.17	10.78	45	90	480	0.03	0.08	0.00	0.15
GUA 5	290.5	Wuchiaping	3.86	-7.26	88	41.3	-27.7	0.01	0.08	0.09	10.90	25	86	484	0.02	0.02	0.00	0.08
GUA 4	291.5	Wuchiaping	3.20	-5.23	91													
GUA 3	292.5	Wuchiaping	3.54	-4.55	91	3.0	-26.1	0.01	0.18	0.19	10.87	18	96	510	0.04	0.03	0.00	0.18
GUA 2	293.5	Wuchiaping	3.29	-5.25	83	2.1	-28.0	0.05	0.11	0.16	10.50	194	384	400	0.10	0.31	0.00	0.61
GUA 1	295	Wuchiaping	3.07	-6.77	63													

Sample No.	Position	Formation	Ccarb	Ocarb	CaCo3
Lay484	0.1	Wuchiaping	4.70	-4.56	101
Lay483	2	Wuchiaping	2.73	-6.40	88
Lay482	6	Wuchiaping	3.79	-7.76	57
Lay632	8.5	Wuchiaping	3.94	-6.79	86.98
Lay481	10	Wuchiaping	4.90	-5.62	86
Lay480	14	Wuchiaping	4.34	-6.52	46
Lay479	16	Wuchiaping	4.54	-6.64	96
Lay478	19.8	Wuchiaping	3.24	-6.14	57
Lay477	21.9	Wuchiaping	3.83	-6.96	99
Lay901	22	Wuchiaping	2.02	-4.93	98
Lay900	22.2	Wuchiaping	4.20	-4.09	87
Lay899	22.6	Wuchiaping	3.90	-6.14	89
Lay898	22.7	Wuchiaping	3.33	-5.81	91
Lay896	23.2	Wuchiaping	3.23	-6.25	92
Lay895	23.3	Wuchiaping	3.61	-5.06	100
Lay894	23.4	Wuchiaping	0.67	-5.67	105
Lay893	23.7	Wuchiaping	3.20	-4.29	105
Lay892	24.2	Wuchiaping	4.21	-4.45	97
Lay891	24.5	Wuchiaping	4.46	-4.58	79
Lay890	24.7	Wuchiaping	4.51	-4.47	82
Lay889	25.4	Wuchiaping	4.11	-5.01	95
Lay888	25.65	Wuchiaping	3.22	-6.06	71
Lay887	25.9	Wuchiaping	0.93	-5.96	99
Lay886	26.2	Wuchiaping	3.69	-4.38	87
Lay885	26.6	Wuchiaping	4.07	-4.48	84
Lay884	26.9	Wuchiaping	2.99	-6.02	89
Lay883	27.2	Wuchiaping	4.45	-5.76	64
Lay882	27.4	Wuchiaping	3.98	-6.48	110
Lay881	27.5	Wuchiaping	4.05	-6.67	113
Lay880	27.7	Wuchiaping	4.16	-6.41	112
Lay879	27.9	Wuchiaping	4.36	-5.24	113
Lay878	28.15	Wuchiaping	4.21	-5.15	87
Lay877	28.3	Wuchiaping	3.97	-7.40	114
Lay876	28.6	Wuchiaping	4.48	-6.01	112
Lay875	28.8	Wuchiaping	4.02	-5.67	110
Lay874	29.1	Wuchiaping	3.96	-4.75	105
Lay873	29.3	Wuchiaping	4.50	-5.31	108
Lay872	29.6	Wuchiaping	4.12	-4.63	103
Lay871	29.8	Wuchiaping	3.79	-6.23	113
Lay800	30.4	Wuchiaping	4.12	-4.92	101
Lay801	30.55	Wuchiaping	3.68	-5.68	103
Lay802	30.65	Wuchiaping	4.14	-5.15	99
Lay803	30.9	Wuchiaping	3.89	-6.00	98
Lay804	31.1	Wuchiaping	3.52	-5.00	90
Lay805	31.4	Wuchiaping	4.69	-5.37	91
Lay806	31.6	Wuchiaping	4.16	-6.45	88
Lay807	31.8	Wuchiaping	3.89	-5.88	85
Lay808	32.1	Wuchiaping	4.14	-7.33	93
Lay809	32.2	Wuchiaping	3.11	-5.42	105
Lay810	32.3	Wuchiaping	3.85	-5.97	92
Lay811	32.5	Wuchiaping	3.66	-6.35	83
Lay812	32.7	Wuchiaping	4.16	-7.85	85
Lay813	32.9	Wuchiaping	4.58	-6.37	109
Lay814	33.1	Wuchiaping	4.12	-5.19	104
Lay815	33.4	Wuchiaping	4.16	-6.50	110

Sample No.	Position	Formation	Ccarb	Ocarb	CaCo3
Lay816	33.6	Wuchiaping	4.11	-7.37	101
Lay817	33.7	Wuchiaping	4.27	-6.62	82
Lay818	33.9	Wuchiaping	4.07	-7.82	83
Lay819	34.1	Wuchiaping	3.72	-5.84	86
Lay820	34.4	Wuchiaping	0.96	-6.79	89
Lay821	34.6	Wuchiaping	3.58	-5.46	105
Lay822	34.9	Wuchiaping	4.36	-7.91	104
Lay823	35.1	Wuchiaping	-0.97	-7.71	104
Lay824	35.3	Wuchiaping	3.62	-7.67	109
Lay825	35.5	Wuchiaping	3.12	-7.68	91
Lay826	35.75	Wuchiaping	2.86	-8.44	83
Lay827	35.95	Wuchiaping	3.13	-6.45	106
Lay828	36.1	Wuchiaping	3.86	-6.09	100
Lay829	36.2	Wuchiaping	2.83	-5.76	103
Lay830	36.3	Wuchiaping	2.60	-5.55	99
Lay831	36.5	Wuchiaping	3.34	-5.56	90
Lay832	36.7	Wuchiaping	4.08	-5.03	66
Lay833	36.9	Wuchiaping	2.13	-5.40	89
Lay834	37.1	Wuchiaping	2.57	-5.25	89
Lay835	37.3	Wuchiaping	3.06	-4.44	91
Lay836	37.45	Wuchiaping	2.36	-4.68	96
Lay837	37.7	Wuchiaping	1.94	-5.19	102
Lay838	37.9	Wuchiaping	3.62	-4.16	100
Lay839	38.1	Wuchiaping	3.29	-5.36	82
Lay840	38.3	Wuchiaping	3.07	-5.42	89
Lay841	38.5	Wuchiaping	2.24	-5.42	63
Lay842	38.7	Wuchiaping	2.82	-4.83	85
Lay843.1	38.9	Wuchiaping	3.45	-7.50	29
Lay844	39.5	Wuchiaping	2.46	-4.96	100
Lay845	39.7	Wuchiaping	-0.27	-6.79	98
Lay846	39.9	Wuchiaping	3.97	-5.72	102
Lay847	40.1	Wuchiaping	2.83	-6.20	101
Lay848	40.4	Wuchiaping	3.13	-5.38	83
Lay849	40.7	Wuchiaping	3.70	-8.06	94
Lay850	40.9	Wuchiaping	5.24	-3.03	81
Lay851	41.1	Wuchiaping	2.97	-5.68	79
Lay852	41.3	Wuchiaping	2.94	-5.80	97
Lay853	41.5	Wuchiaping	3.39	-5.56	96
Lay854	41.7	Wuchiaping	3.49	-4.29	95
Lay855	41.9	Wuchiaping	3.71	-4.23	98
Lay856	42.2	Wuchiaping	4.25	-3.60	84
Lay857	42.5	Wuchiaping	2.65	-6.84	28
Lay858	42.7	Wuchiaping	3.23	-7.90	82
Lay859	42.9	Wuchiaping	2.38	-7.38	81
Lay860	43.1	Wuchiaping	4.03	-6.37	53
Lay861	43.3	Wuchiaping	3.75	-4.47	95
Lay862	43.4	Wuchiaping	3.99	-5.20	64
Lay863	43.55	Wuchiaping	1.33	-5.50	100
Lay864	43.7	Wuchiaping	2.17	-5.64	107
Lay865	43.9	Wuchiaping	1.19	-5.80	109
Lay866	44.3	Wuchiaping	2.82	-6.21	110
Lay867	44.4	Wuchiaping	2.34	-5.33	90
Lay868	44.55	Wuchiaping	3.90	-3.90	106
Lay869	44.8	Wuchiaping	2.77	-7.01	44
Lay870	45.1	Wuchiaping	3.87	-4.39	103
Lay492	47	Wuchiaping	2.35	-7.83	108

Sample No.	Position	Formation	Ccarb	Ocarb	CaCo3
Lay491	47.5	Wuchiaping	0.26	-5.69	94
Lay490	48	Wuchiaping	2.88	-8.63	100
Lay489	49	Wuchiaping	3.29	-10.32	86
Lay488	50	Wuchiaping	2.89	-10.24	82
Lay487	50.9	Wuchiaping	3.10	-8.42	77
Lay486	52	Wuchiaping	2.23	-8.81	60
Lay485	52.5	Wuchiaping	3.04	-6.64	101
Lay473	55	Wuchiaping	4.40	-5.59	102
Lay472	57.5	Wuchiaping	3.74	-6.03	105
Lay471	59	Wuchiaping	5.01	-5.57	113
Lay470	62	Wuchiaping	4.73	-5.31	115
Lay625	64	Wuchiaping	4.13	-5.46	29.73
Lay469	65	Wuchiaping	2.35	-9.73	111
Lay468	67.5	Wuchiaping	3.12	-7.64	116
Lay467	71	Wuchiaping	3.16	-9.11	97
Lay624	73	Wuchiaping	4.63	-6.28	80.09
Lay466	75	Wuchiaping	4.14	-6.57	101
Lay465	79	Wuchiaping	4.98	-5.84	101
Lay464	82.5	Wuchiaping	4.77	-7.10	90
Lay463	85	Wuchiaping	5.02	-8.69	116
Lay462	88	Wuchiaping	4.33	-6.05	112
Lay461	90	Wuchiaping	4.58	-5.95	111
Lay460	94	Wuchiaping	4.62	-7.16	117
Lay459	97	Wuchiaping	5.50	-5.95	92
Lay458	100	Wuchiaping	4.69	-7.69	97
Lay457	104	Wuchiaping	4.66	-6.79	96
Lay456	106.5	Wuchiaping	4.87	-7.23	112
Lay455	110	Wuchiaping	4.83	-6.84	108
Lay454	112.5	Wuchiaping	-0.84	-8.46	109
Lay453	115	Wuchiaping	5.30	-5.92	94
Lay452	118	Wuchiaping	5.02	-6.31	88
Lay451	121	Wuchiaping	4.74	-5.64	96
Lay450	125	Wuchiaping	3.78	-4.75	91
Lay449	127.5	Wuchiaping	4.09	-7.39	111
Lay448	132	Wuchiaping	3.35	-5.35	113
Lay447	135	Wuchiaping	3.71	-5.95	94
Lay446	139.5	Wuchiaping	3.75	-5.32	100
Lay445	142.5	Wuchiaping	3.15	-6.75	93
Lay444	145	Wuchiaping	4.00	-6.63	91
Lay443	148.5	Wuchiaping	3.83	-7.05	98
Lay442	151	Wuchiaping	2.97	-6.21	97
LAY436	172	Wuchiaping	0.90	-5.90	
LAY435	175.5	Wuchiaping	-2.10	-7.97	90
LAY434	179	Wuchiaping	2.19	-5.39	88
LAY433	182	Wuchiaping	1.92	-6.75	98
LAY432	185.5	Wuchiaping	2.96	-4.93	32
LAY431	188	Wuchiaping	1.21	-5.55	92
LAY430	192	Wuchiaping	-0.21	-8.42	36
LAY429	195	Wuchiaping	1.18	-6.03	23
LAY428	198	Wuchiaping	1.36	-6.23	90
LAY427	202	Wuchiaping	1.82	-5.98	28
LAY426	205.5	Wuchiaping	0.88	-5.27	95
LAY425	208	Wuchiaping	-6.06	-8.05	96
LAY424	212	Wuchiaping	1.32	-8.35	92
LAY423	215	Wuchiaping	2.00	-6.77	94
LAY421	217.5	Wuchiaping	1.83	-6.14	115

Sample No.	Position	Formation	Ccarb	Ocarb	CaCo3
LAY420	219	Wuchiaping	1.62	-5.73	92
LAY419	222.5	Wuchiaping	1.21	-6.39	104
LAY418	225	Wuchiaping	1.05	-6.23	95
LAY417	227	Wuchiaping	1.44	-7.69	93
LAY416	229	Wuchiaping	1.73	-6.53	101
LAY415	230	Wuchiaping	1.17	-6.94	93
LAY414	232.5	Wuchiaping	1.75	-7.06	117
LAY413	235	Wuchiaping	1.86	-6.41	91
LAY412	238.5	Wuchiaping	1.59	-5.59	71
LAY410	240.5	Wuchiaping	0.87	-5.97	93
LAY409	243	Wuchiaping	1.37	-5.08	88
LAY408	245.5	Wuchiaping	2.22	-6.39	93
LAY407	248	Wuchiaping	2.89	-6.96	88
LAY406	250.5	Wuchiaping	2.37	-7.26	112
LAY405	253	Wuchiaping	2.77	-6.30	94
LAY403	255.5	Wuchiaping	3.18	-6.50	92
LAY402	257.5	Wuchiaping	2.82	-7.08	69
LAY400	259	Wuchiaping	3.04	-6.50	83

Sample No	Position	Formation	Corg	$d^{13}C$ VPDB	$d^{18}O$ VPDB	Yield % as CaCO3	PC [%]	RC [%]	TOC [%]	MINC [%]	HI [mg HC/g TOC]	OI [mg CO2/g TOC]	Tmax [°C]	S1 [mg HC/g]	S2a [mg HC/g]	S2b [mg HC/g]	S3
POT22	0.6m	Wuchiaping	-26.95	3.98	-5.55	105	0.01	0.02	0.03	10.41	217	222	457	0.01	0.07	0.00	0.07
POT23	1.3m	Wuchiaping	-25.24	3.61	-5.73	84											
POT24	1.8m	Wuchiaping	-24.9	3.61	-4.66	94											
POT25	2.2m	Wuchiaping	-27.3	3.35	-5.98	87	0.01	0.06	0.07	9.29	100	102	419	0.03	0.07	0.00	0.07
POT26	2.55m	Wuchiaping	-27.3	3.83	-5.51	88											
POT27	2.9m	Wuchiaping	-25.6	2.73	-6.02	97											
POT28	3.95m	Wuchiaping	-25.1	-2.72	-9.55	102	0.01	0.04	0.05	10.98	110	157	465	0.02	0.05	0.00	0.07
POT29	4.9m	Wuchiaping	-24.8	2.42	-6.07	91											
POT30	5.25m	Wuchiaping	-23.5	2.57	-8.24	105	0.01	0.03	0.04	10.38	152	151	459	0.01	0.06	0.00	0.06
POT31	5.6m	Wuchiaping	-24.9	2.36	-6.04	88											
POT32	5.9m	Talung	-25.5	2.39	-6.79	40											
POT33	6m	Talung	-25.7	2.65	-6.90	37											
POT34	6.3m	Talung	-25.5	2.32	-6.98	36											
POT35	6.8m	Talung	-26.6	2.51	-6.80	65	0.03	0.08	0.11	5.63	143	431	399	0.08	0.15	0.00	0.46
POT36	7.05m	Talung	-26.5	1.37	-2.51	108											
POT37	7.5m	Talung	-29.7	1.41	-6.72	5	0.05	0.29	0.34	0.10	150	45	257	0.08	0.51	0.00	0.15
POT38	8.15m	Talung	-25.5	NA	NA	0											
POT39	8.5m	Talung	-25.7	NA	NA	0											
POT40	8.9m	Talung	-26.3	NA	NA	0											
POT41	9.25m	Talung	-27.2	NA	NA	0											
POT42	10.2m	Talung	-26.4	NA	NA	0	0.08	2.30	2.38	0.10	10	52	536	0.29	0.25	0.00	1.24
POT43	10.8m	Talung	-26.6	NA	NA	0											
POT44	11.1m	Talung	-25.4	NA	NA	0											
POT45	11.85m	Talung	-25.3	NA	NA	0											
POT46	12.45m	Talung	-25.8	NA	NA	0											
POT47	12.9m	Talung	-25.7	NA	NA	0	0.03	0.87	0.90	0.05	20	41	501	0.06	0.18	0.00	0.37
POT48	13.4m	Talung	-26.0	NA	NA	0											
POT49	13.9m	Talung	-25.6	NA	NA	0	0.02	0.44	0.46	0.03	22	21	466	0.08	0.10	0.00	0.10
POT50	14.45m	Talung	-25.9	NA	NA	0											
POT51	14.9m	Talung	-26.0	NA	NA	0											
POT52	15.2m	Talung	-25.4	NA	NA	0											
POT53	15.8m	Talung	-26.4	NA	NA	0											
POT54	16.2m	Talung	-26.1	NA	NA	0											
POT55	16.8m	Talung	-26.0	NA	NA	0											
POT56	17.2m	Talung	-30.1	NA	NA	0											

Sample No	Position	Formation	Corg	$d^{13}C$ VPDB	$d^{18}O$ VPDB	Yield % as CaCO3	PC [%]	RC [%]	TOC [%]	MINC [%]	HI [mg HC/g TOC]	OI [mg CO2/g TOC]	Tmax [°C]	S1 [mg HC/g]	S2a [mg HC/g]	S2b [mg HC/g]	S3
POT57	17.7m	Talung	-26.3	NA	NA	0											
POT58	18.45m	Talung	-28.3	NA	NA	0	0.03	0.33	0.36	0.03	34	48	428	0.13	0.12	0.00	0.17
POT59	19.2m	Talung	-25.9	NA	NA	0											
POT60	19.8m	Talung	-25.4	NA	NA	0	0.03	0.79	0.82	0.08	19	84	495	0.01	0.16	0.00	0.69
POT61	20.2m	Talung	-25.1	NA	NA	0											
POT62	21.2m	Talung	-28.2	NA	NA	0											
POT63	21.8m	Talung	-25.9	NA	NA	0											
POT64	22.5m	Talung	-25.7	NA	NA	0	0.06	1.65	1.71	0.07	31	31	452	0.02	0.53	0.00	0.53
POT69	0.2m	Daye	-29.9	-4.11	-2.47	48											
POT70	0.5m	Daye	-30.0	-3.76	-2.54	50	0.10	0.53	0.62	6.11	162	28	448	0.08	1.01	0.00	0.17
POT71	0.6m	Daye	-29.9	-3.29	-2.74	53											
POT72	0.8m	Daye	-29.9	-3.92	-2.54	51											
POT73	1.2m	Daye	-30.2	-4.26	-2.99	60											
POT74	1.4m	Daye	-31.1	-4.64	-2.79	24											
POT75	1.8m	Daye	-31.6	-4.58	-2.66	63	0.22	1.12	1.34	6.39	180	6	454	0.18	2.41	0.00	0.07
POT76	2m	Daye	-30.3	-4.07	-2.79	63											
POT77	2.25m	Daye	-28.9	-4.36	-2.75	47											
POT78	2.55m	Daye	-29.5	-3.92	-3.20	57											
POT79	2.9m	Daye	-28.7	-3.59	-3.24	45											
POT80	3.2m	Daye	-29.0	-3.37	-2.93	32	0.24	1.73	1.97	3.47	136	9	449	0.12	2.67	0.00	0.17
POT81	3.5m	Daye	-27.4	-2.97	-3.67	72											
POT82	3.7m	Daye	-25.9	-2.56	-5.15	75											
POT83	4.1m	Daye	-28.1	-3.20	-5.33	77											
POT84	4.6m	Daye	-27.2	-2.65	-4.22	79	0.02	0.10	0.12	5.91	105	208	411	0.01	0.13	0.00	0.25
POT85	5.1m	Daye	-26.5	-2.10	-3.18	45											
POT86	5.5m	Daye	-27.8	-1.86	-4.61	84											
POT87	6.1m	Daye	-26.3	-2.51	-7.02	35	0.02	0.11	0.13	4.45	115	78	396	0.01	0.15	0.00	0.10

Sample No	Position	Formation	Corg
LAX 20	0.01	Talung	-26.0294
LAX 21	0.5	Talung	-25.6404
LAX 22	1.15	Talung	-25.1707
LAX 23	2.05	Talung	-24.7077
LAX 24	2.8	Talung	-24.8401
LAX 25	3.45	Talung	-24.8294
LAX 26	3.95	Talung	-25.475
LAX 27	4.45	Talung	-27.4621
LAX 28	4.95	Talung	-26.3933
LAX 29	5.95	Talung	-26.7204
LAX 30	6.8	Talung	-25.7254
LAX 31	7.05	Daye	-28.1486
LAX 32	8	Daye	-28.724
LAX 33	8.95	Daye	-26.6731
LAX 34	9.9	Daye	-30.2103
LAX 35	10.85	Daye	-29.531
LAX 36	11.8	Daye	-29.5998
LAX 37	12.5	Daye	-28.9412
LAX 38	13.8	Daye	-28.3113
LAX 39	14.9	Daye	-27.6985
LAX 40	15.9	Daye	-28.2049
LAX 41	17	Daye	-28.2578
LAX 42	18	Daye	-29.1128
LAX 43	19	Daye	-27.3643

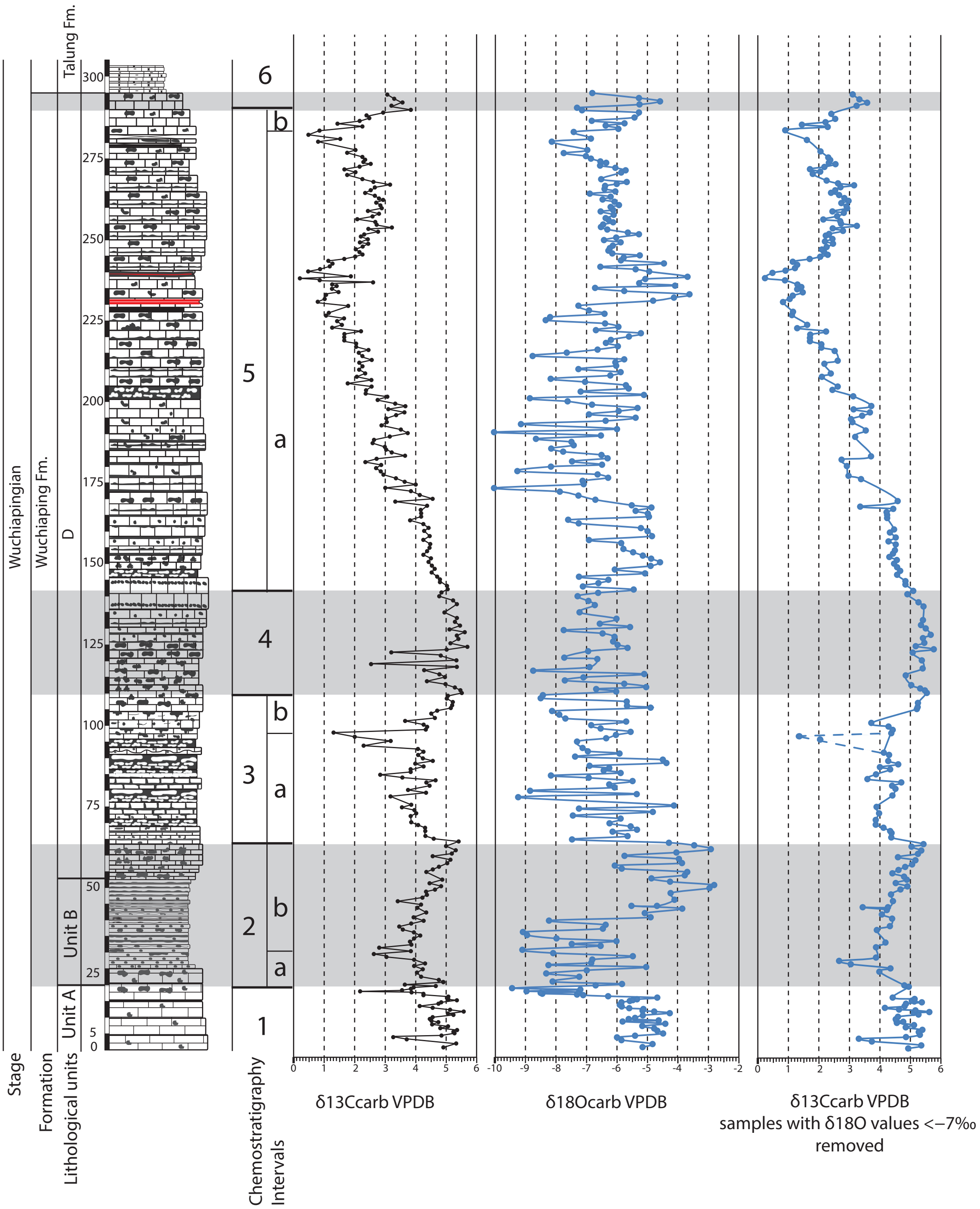

Supplementary Material S2 Stratigraphic log of the Guantan section with $\delta^{13}C_{carb}$, $\delta^{18}O_{carb}$ and $\delta^{13}C_{carb}$ data after removing samples with $\delta^{18}O_{carb}$ values < −7 ‰. Grey and white bands highlight different chemostratigraphic intervals.

Chapter IV

ONSET, DEVELOPMENT, AND CESSATION OF BASAL EARLY TRIASSIC MICROBIALITES (BETM) IN THE NANPANJIANG PULL-APART BASIN, SOUTH CHINA BLOCK

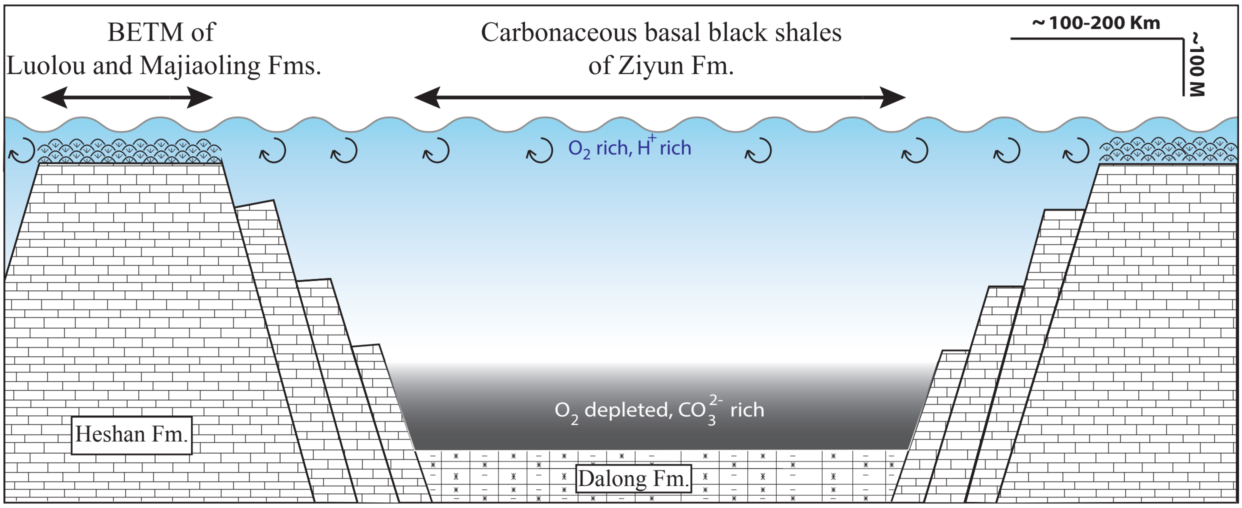

Gondwana Research 44 (2017) 178–204

Gondwana Research 44 (2017) 178–204

Contents lists available at ScienceDirect

Gondwana Research

journal homepage: www.elsevier.com/locate/gr

Onset, development, and cessation of basal Early Triassic microbialites (BETM) in the Nanpanjiang pull-apart Basin, South China Block

Borhan Bagherpour [a,*], Hugo Bucher [a], Aymon Baud [b], Morgane Brosse [a], Torsten Vennemann [c], Rossana Martini [d], Kuang Guodun [e]

[a] Paleontological institute, University of Zürich, Karl Schmid-Strasse 4, 8006 Zürich, Switzerland
[b] BCG Parc de la Rouvraie 28, 1018 Lausanne, Switzerland
[c] Institute of Earth Surface Dynamics, University of Lausanne, Géopolis, 1015 Lausanne, Switzerland
[d] Department of Earth Sciences, University of Geneva, 13 rue des Maraîchers, 1205 Geneva, Switzerland
[e] Guangxi Bureau of Geology and Mineral Resources, Jiangzheng Road 1, 530023 Nanning, China

ARTICLE INFO

Article history:
Received 21 June 2016
Received in revised form 23 November 2016
Accepted 24 November 2016
Available online 23 December 2016

Keywords:
Permian-Triassic boundary
Microbialites
Bathymetry
Oxygen
Alkalinity

ABSTRACT

New investigations in the Nanpanjiang Basin indicate that the onset of the iconic microbialites associated with the Paleozoic-Mesozoic boundary was Early Triassic in age. Bathymetry (water agitation, oxygenation, light penetration) and clastic load are shown to have exerted a direct control on the growth of microbialites. Carbonate supersaturation is also required for the deposition of the microbialites. Bathymetric control is further corroborated by the inheritance of the topography of a latest Permian pull-apart basin into Early Triassic times, with a distribution of basal Early Triassic microbialites (BETM) restricted to uplifted blocks and the accumulation of carbonaceous black shales in adjacent troughs. The geographically most extensive Nanpanjiang BETM bloomed on a large NW–SE trending uplifted block exceeding 12,000 km^2 (Luolou Platform) centered on northwestern Guangxi. Post-Triassic displacements along the Youjiang Fault obscure the paleogeographic relation of BETM exposed west of this fault.

Triassic foraminifers occur in the basal most BETM episode, which is locally bracketed by high-energy grainstones made of reworked Permian foraminifers. Therefore, the Permian-Triassic boundary (PTB) is within the unconformity that separates the Late Permian Heshan Fm. from the basal most BETM. Where accommodation space was sufficient, up to five event surfaces are associated with the unconformity. Microfacies analysis supports chemical dissolution but did not reveal evidence for subaerial erosion, although intercalated grainstone made of Permian foraminifers indicate reworking. Chemical dissolution and mechanical erosion both conceivably contributed to the genesis of the unconformity. The upward shift from tabulated to domical microbial build-ups is accompanied by accumulation of coquinoid lenses between domes, which indicates deepening of the Luolou Platform BETM. The main drowning resulting from both regional tectonic subsidence and a global sea-level rise led to the cessation of the BETM that were buried under predominant fine siliciclastics. Any concomitant change in sea water chemistry appears unlikely.

1. Introduction

The widespread deposition of microbial limestone in equatorial shallow seas is a hallmark of the Permian-Triassic transition. Deposition of the microbial limestone is intimately related to the largest mass-extinction of the Phanerozoic (Raup, 1979; Sepkoski, 1984), which coincides with the Permian-Triassic transition between 251.941 ± 0.037 and 251.880 ± 0.031 Ma (Burgess et al., 2014). In equatorial shallow waters, the Late Permian skeletal carbonate production ended with a global regression coinciding with the PTB (Yin et al., 2014) and was replaced by the production of microbialites during the earliest Early Triassic (BETM) (e.g. Lehrmann et al., 2003, 2015a). Although microbialite deposits are recurrent during Early Triassic times (e.g. Lehrmann, 1999; Baud et al., 2007; Brayard et al., 2011), their abundance typically peaked during the Griesbachian (basal Early Triassic), as exemplified by records from the South China Block (Lehrmann et al., 2003; Ezaki et al., 2008; Yang et al., 2011; Jiang et al., 2014),Turkey (Baud et al., 1997, 2005) and Iran (Taraz et al., 1981; Kozur, 2005, 2007; Baud et al., 2007; Richoz et al., 2010; Leda et al., 2014). The BETM have a distinctive equatorial distribution, and have been commonly interpreted as devastated ecosystems (Awramik, 1990; Schubert and Bottjer, 1992) and/or anachronistic facies reminiscent of Precambrian or Early Paleozoic shallow water microbe-dominated biota (Sepkoski et al., 1991; Baud et al., 1997, 2002, 2007; Kershaw et al., 1999, 2007; Pruss et al., 2006; Ezaki et al., 2008). The resurgence of

---

[*] Corresponding author.
E-mail address: borhan.bagherpour@pim.uzh.ch (B. Bagherpour).

http://dx.doi.org/10.1016/j.gr.2016.11.013
1342-937X/

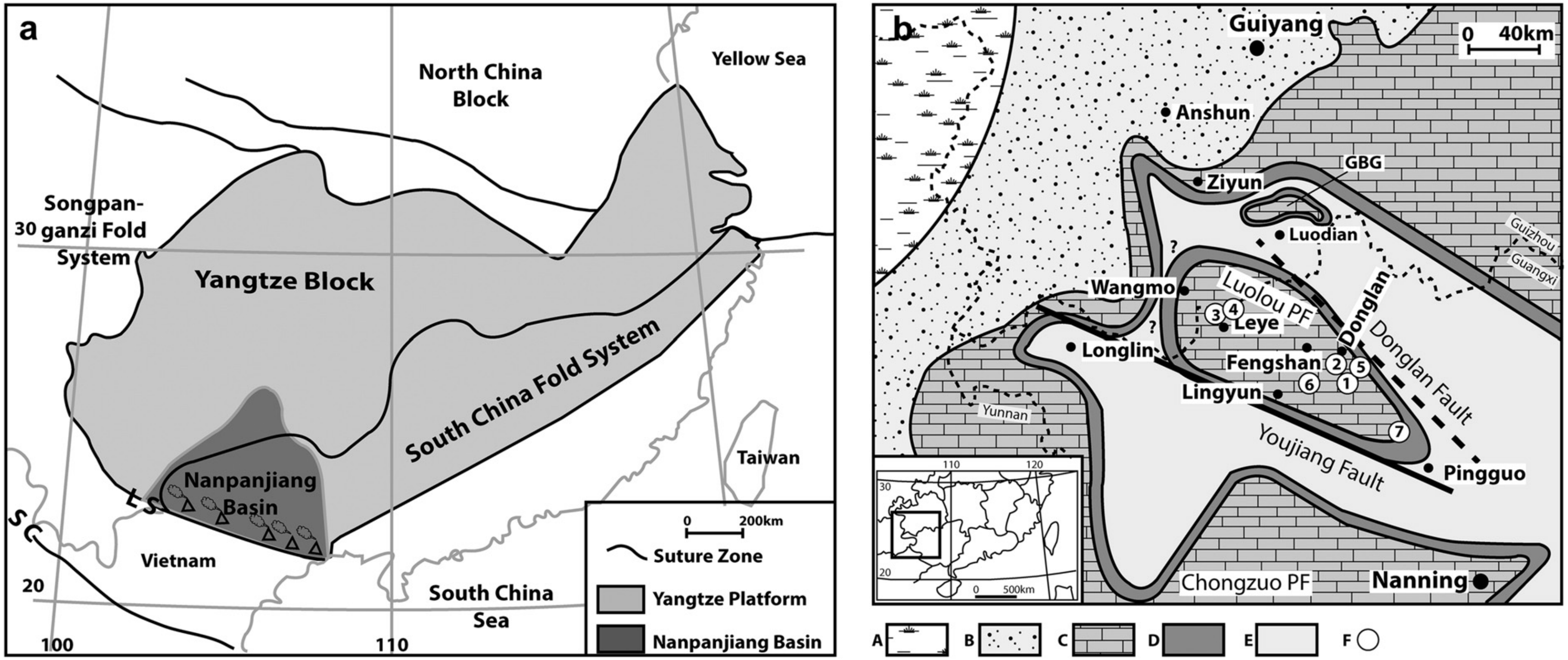

Fig. 1. Tectonic map of South China and paleogeographic map of the Nanpanjiang Basin. a, Tectonic map of South China Block including Yangtze Craton, South China fold system and the Nanpanjiang Basin (modified from Lehrmann et al., 1998) (LS: Lang Son Arc, SC: Song Chay suture). b, Palaeogeographic map and the locations of the studied sections in the Nanpanjiang Basin (Luolou Platform) (modified from Fan et al., 2014). A - flood alluvial facies, B - shallow-water siliciclastic deposit, C - carbonate platform, D - slope, E - basin, F - studied sections (1 - Wuzhuan, 2 - Nanem, 3 - Tienbao, 4 - Youping, 5 - Longyuan, 6 - Shanmenhai, 7 - Taiping) (GBG: Great Bank of Guizhou).

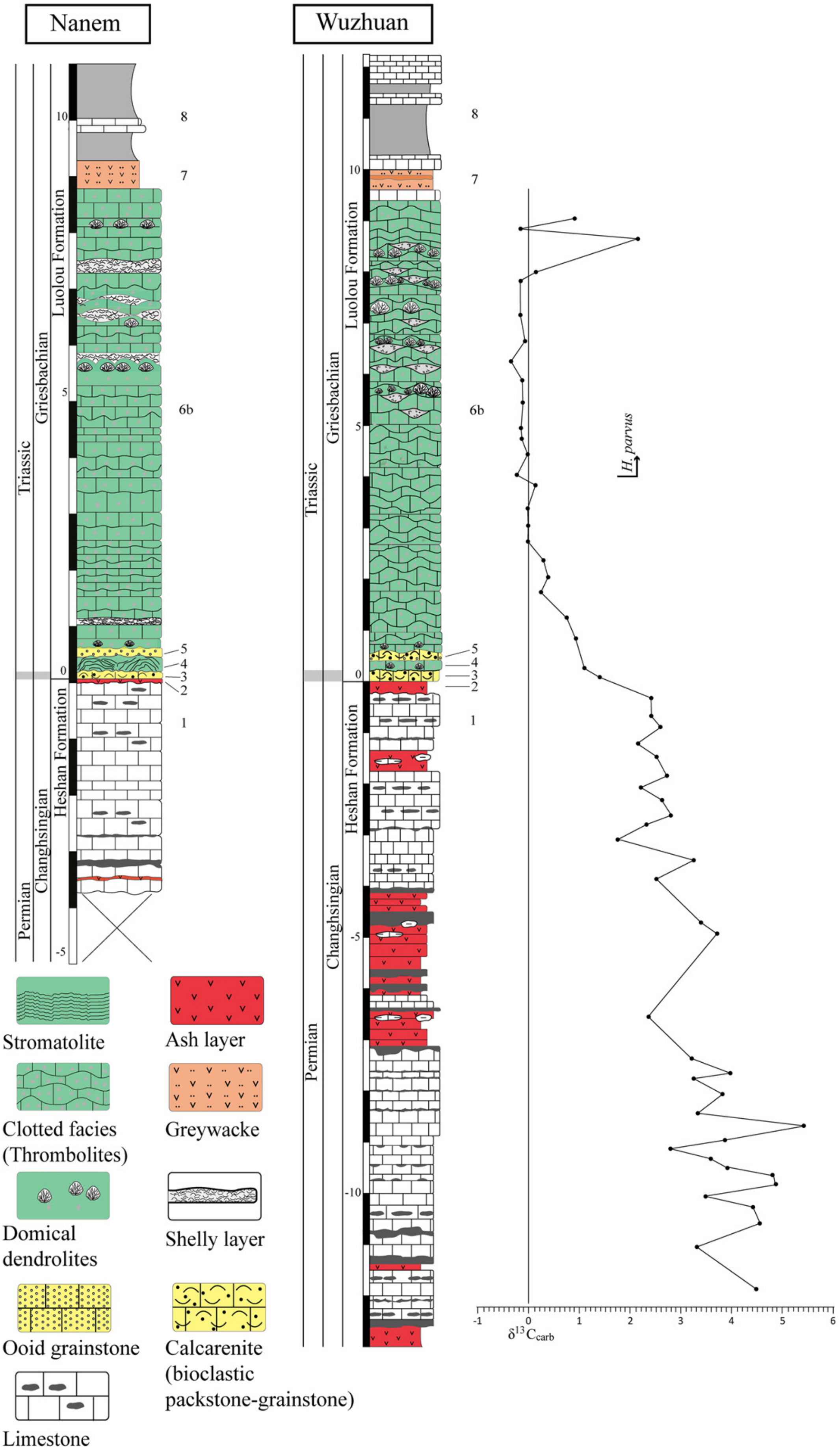
Nanem
Wuzhuan
Triassic
Griesbachian
Luolou Formation
Permian
Changhsingian
Heshan Formation
10
5
0
-5
-10
8
7
6b
5
4
3
2
1
H. parvus
-1
0
1
2
3
4
5
6
δ13Ccarb
Stromatolite
Ash layer
Clotted facies (Thrombolites)
Greywacke
Domical dendrolites
Shelly layer
Ooid grainstone
Calcarenite (bioclastic packstone-grainstone)
Limestone

microbe-dominated shallow-water environments has been tentatively explained by a temporary absence of predation pressure from grazing metazoans that were removed by the Permian-Triassic mass extinction (Schubert and Bottjer, 1992; Lehrmann, 1999; Pruss et al., 2006). Alternative explanations include ocean carbonate supersaturation, as well as upwelling of alkaline waters from deeper oxygen-depleted water masses within the intertropical convergence zone (Kershaw et al., 1999, 2007). Subsequently, Kershaw et al. (2012a) downplayed their earlier interpretations about upwelling and emphasized the importance of relative sea-level changes and clastic input as local controls on the formation of BETM for sections mainly located on the northern edge of the South China Block. Lehrmann et al. (2015a) also interpreted a lack of thickening of the microbialite unit towards platform margins as evidence against an upwelling of anoxic alkaline waters.

A detailed investigation of onset, development, and cessation of the BETM may improve the understanding of the underlying processes that fostered the deposition of microbial limestone. The distinction between global and local factors that enabled or impeded the deposition of microbialites is crucial for distinguishing the various processes that may have been at play. The South China Block offers the largest concentration of sections across the BETM and the Nanpanjiang Basin in the present-day southern part of the block includes many such well-exposed sections. The new data from the Nanpanjiang Basin presented in this paper add to the results from previous studies of the BETM (Lehrmann et al., 2003; Ezaki et al., 2008; Kershaw et al., 2011; Yang et al., 2011; Deng et al., 2016) and newly integrate observations from a broad range of scales, from micro-textures to basin geodynamic regime. Special emphasis is also placed on the cessation of microbialites deposition.

The nature of the unconformable boundary between the Late Permian skeletal limestone and the BETM is a matter of diverging interpretations. In South China, Payne et al. (2007), Song et al. (2009a) and Lehrmann et al. (2015a) interpreted the truncation of Upper Permian limestone as a submarine chemical dissolution surface resulting from acidification of the upper water column. Alternatively, the same surface was interpreted as the result of subaerial erosion by Liu et al. (2007), Collin et al. (2009) and Wignall et al. (2009). As reviewed by Yin et al. (2014), both processes are not mutually exclusive and their expression in the rock record may vary laterally as a function of uneven paleotopography and accommodation space. However, diagenetic microfabrics observed in thin sections in support of subaerial erosion by Liu et al. (2007), Collin et al. (2009) and Wignall et al. (2009) were subsequently questioned by Lehrmann et al. (2015a). The duration of the hiatus separating the Late Permian skeletal limestone from the Early Triassic microbialites was also a matter of debate. Payne et al. (2007) argued that “the contact between skeletal packstone and microbialite in south China…is also biostratigraphically complete, suggesting that erosion did not remove a substantial thickness of sediment or corresponding time”. On the basis of a previous calibration of conodont interval zones assumed to be of equal duration and calibrated against supposed astronomical cycles in the Germanic Basin, Yin et al. (2014) proposed a duration of ca. 50–100 ky for the unconformity between latest Permian skeletal limestone and earliest Triassic microbialites they assigned to the latest *Clarkina yini* to *C. meishanensis–Hindeodus changxingensis* interval zones in Meishan. Yet, apatite and zircon tephrochronology (Baresel et al., 2016a) coupled with high-resolution U-Pb dates indicate a duration of 90 ± 38 kyr for the Permian part of the hiatus straddling the PTB in BETM sections of the Nanpanjiang Basin (Baresel et al., 2016b; Baresel et al., in revision).

Comparisons of the detailed facies evolution that can be extracted from the BETM may also contribute to distinguish between local and global controls. Both shallowing and deepening trends have been inferred from facies analysis of various BETM sections (e.g. Ezaki et al., 2003; Kershaw et al., 2011; Deng et al., 2016). Comparisons within and across different Tethyan equatorial transit blocks (Ricou, 1994), such as South China and Turkey, may also help extracting the commonalities and differences of BETM sections, provided that enough information is available for reconstructing the paleogeographic and geodynamic context in which they were deposited. Similarly, patterns of cessation of the BETM may shed light on the relative roles of global versus local controls. Two diverging interpretations have been proposed, with either an abrupt (Kershaw et al., 2002; Ezaki et al., 2003; Deng et al., 2016) or a step-wise cessation (Ezaki et al., 2008).

In this study, the BETM is compared from seven different sections of the northwestern Guangxi part of the Nanpanjiang Basin in the South China Block. These results are then discussed in the larger context of the South China Block and of other Tethyan transit blocks such as Turkey. In order to gain a better understanding of the BETM within the Nanpanjiang Basin, this work focusses on: i) sedimentary features and facies analyses of the transition between Late Permian skeletal carbonates and the BETM; ii) the development and formation of different types of microbialites; and iii) the cessation of microbialites deposition. Robust conodont age constraints are only available for the upper part of the BETM (Brosse et al., 2016a) and are also utilized for assessing the timing of cessation. The BETM is further considered in the Early Triassic paleogeographic and geodynamic context of the Nanpanjiang Basin, a scale that is also required for screening among paleoceanographic hypotheses. Finally, a comparison with other low-paleolatitude basal Early Triassic records can clarify the role of paleogeography and associated paleoceanographic aspects for the production of the BETM.

2. Paleogeographic setting

During the Late Permian and Early Triassic, the Nanpanjiang Basin (Fig. 1a) evolved as a pull-apart basin in a back-arc context (HB ongoing work), resulting from the oblique convergence between the Indochina and South China blocks. The related volcanic Lang Son Arc is exposed in a belt near the present-day Vietnam-Guangxi border (Thanh et al., 2014; Halpin et al., 2016). Further to the southwest, the Song Chay ophiolite-bearing suture represents the convergence zone between the South Chinese upper plate and the Indochinese lower plate (Faure et al., 2016). As we consistently observe in the Nanpanjiang Basin, the basal Early Triassic (Griesbachian) paleotopography is typically inherited from the latest Permian one, thus indicating a permanent and similar regional geodynamic control of the basin across the Permian-Triassic Boundary (HB, ongoing work). Our field data indicate that occurrences of the BETM are strictly restricted to sections where the latest Permian is represented by shallow-water facies (essentially skeletal packstones). In the Nanpanjiang Basin, the northwest Guangxi-south Guizhou BETM platform exceeds a 12,000 km^2 surface area that precisely matches with the extent of the underlying latest Permian shallow-water carbonate rocks (Fig. 1b). This large and laterally continuous BETM platform, here named the Luolou Platform, includes the following areas: southwestern part of Donglan County, most of Fengshan, Leye, and Lingyun counties, northwestern part of Bama County (all northwestern Guangxi), and southern Wangmo County (southern Guizhou). In all these areas, the BETM represents the lowermost and shallowest part of the Luolou Formation, which otherwise encompasses younger and deeper water facies representing outer platform settings (Galfetti et al., 2008). Yet, how the BETM of the Pingguo area paleogeographically relates to the Luolou Platform to the northwest is uncertain. It was interpreted as an isolated platform by Lehrmann et al. (2007a), but it

Fig. 2. Nanem and Wuzhuan PTB sections and carbonate carbon isotope data from Wuzhuan section. Numbers on the right side of each section refer to lithological units as discussed in the text: Unit 1 - Bioclastic wackestone-packstone of Heshan Fm., Unit 2 - Ash layer, Unit 3 - Bioclastic packstone-grainstone, Unit 4 - Thin layer of microbialites, Unit 5 - Thin layer of ooid-bioclastic packstone, Unit 6a - Stromatolite microbialite (absent in Nanem and Wuzhuan sections), Unit 6b - Thrombolite microbialite, Unit 7 - Volcanogenic greywacke, Unit 8 - lime mudstone. *H. parvus* – FO of index conodont *Hindeodus parvus.*

more probably represents the southern tip of the Luolou BETM platform, just east of the Youjiang Fault. The BETM in Pingguo County occurs at the base of the Majiaoling Formation (Fig. 1, Supplementary material), which is essentially an upper slope lateral equivalent of the outer platform Luolou Fm. East of the Youjiang Fault, the distribution of late Permian and Early Triassic depositional environments in the Wangmo area and northwestern Guangxi delineates a clear NW–SE orientation of depositional environments distinguished by contrasted bathymetry (Fig. 1b). We observe that the main structural phase of the basin took place during the deposition of the upper part of the Late Permian Wujiaping Fm., as indicated by intercalated kilometric wedges of breccia along the Donglan Fault that demarcates the eastern edge of the Luolou Platform (Fig. 1b). This structural configuration governed the subsequent lateral and coeval deposition of the Heshan Fm. on horsts and of the Dalong Fm. in grabens during the Changhsingian (Fig. 1, Supplementary material). The eastern edge of the Luolou Platform typically runs along a NW–SE line that passes near Donglan. The deepest facies of the Dalong Fm. are represented by radiolarian cherts immediately east of the Donglan Fault, suggesting a depth contrast $>10^3$ m with the Heshan Fm. to the west. Hence, the Luolou Platform on which the BETM bloomed obviously extends far back into the late Permian. Unlike the Youjiang Fault, the Donglan Fault was not reactivated in post-Triassic times and allows a robust paleogeographic reconstruction which is at variance with previous models of isolated small platforms. In the southwestern part of the Nanpanjiang Basin, the paleogeographic position of the BETM of the Chongzuo, Debao and Jinxi platforms (Lehrmann et al., 2007b; Algeo et al., 2007) is difficult to restore with respect to the Luolou Platform because of substantial post-Triassic displacements along of the Youjiang Fault as well as in western part of the basin. These displacements have been omitted in previous reconstructions (e.g. Lehrmann et al., 2015a). Further north, a smaller tilted horst (ca. 2000 km^2), christened the “Great Bank of Guizhou” (GBG) by Lehrmann et al. (1998, 2007a), displays an exceptionally long-lived (Late Permian to Late Triassic) shallow-water carbonate succession that includes the BETM episode (Li et al., 2012). This misleading labelling that alludes to present-day carbonate banks has been recently criticized by Feng et al. (2015), who recommended using a more realistic appellation such as the “Luodian Carbonate Platform”. All these tectonic highs with shallow water BETM were laterally limited by slope and basinal deposits in Guangxi and southern Guizhou (Fig. 1b). The role of regional tectonics and of the broader geodynamic frame in the spatial distribution of the BETM in the Nanpanjiang Basin has therefore been commonly overlooked. Primary control has customarily been placed on biological calcification that was considered to be the main controlling agent involved in the construction of carbonate “low-relief banks” during the Early Triassic (e.g. Lehrmann et al., 2003). Moreover, bearing in mind that the studied sections were deposited in a pull-apart basin also puts further limitation on the intensity of water mass exchanges with the open ocean. The isolated “low-relief banks” model during the deposition of the BETM and later Early Triassic times (Lehrmann et al., 2003) was subsequently emended by adding isolated “drowned Upper Permian-basal Triassic platforms” in northwestern Guangxi (Lehrmann et al., 2015a, Fig. 1). However, the lateral continuity shown by the BETM within a single and much larger shallow-water platform (namely the Luolou Platform) was also ignored. Occasional and more or less coeval deposition of black shales or oxygen-poor sediments on Griesbachian shelves are generally assumed to represent an expansion of the oxygen minimum zone brought about by a global sea-level rise (Wignall and Hallam, 1993). However, the depth of the oxygen minimum zone in a silled basin such as the Nanpanjiang may be unrelated to global sea-level changes and may only reflect weak local circulation. Moreover, the absence of any anoxia during Griesbachian time on Tethyan off shore sea-mounts (Krystyn et al., 2003; Baud et al., 2014; Brosse et al., 2016b), on the northern Indian Margin (Hermann et al., 2011; Schneebeli-Hermann et al., 2013) and in the NE Greenland rift (Sanson-Barrera et al., 2015) notably undermine the mantra of a global expansion of the oxygen minimum zone at that time. The partly coeval deposition of black shales in troughs adjacent to these tectonic highs is better assigned to a local and stable stratification of the water column, rather than to any equivocal global rise of the oxygen minimum zone. Circulation between the Nanpanjiang Basin and the open ocean was essentially surficial, the intervening volcanic Lang Song Arc and silled topography of the Nanpanjiang back-arc basin precluding efficient mixing of deeper water masses. The general setting of the Nanpanjiang BETM advocated here is that of tectonic troughs with restricted circulation separated by horsts reaching above fair-weather wave-base depth, which permitted the BETM to thrive in clastic-free and oxygenated waters. This paleotopographic setting is diagnostic of a pull-apart basin, whose structuration initiated in the late Permian and which ended near the Early-Middle Triassic boundary (Galfetti et al., 2008; Ovtcharova et al., 2015), with a drastic change from a trans-tensional to a compressional regime manifested by the deposition of several kilometers of siliciclastic turbidites. Within the Luolou Platform, the new BETM sections studied here include Wuzhuan, Nanem, Longyuan, Youping, Tienbao, and Shanmenhai. In the Pingguo area, the Taiping section (Lehrmann et al., 2003) is also re-investigated (Figs. 2, 3 and 4).

3. Age and duration of the microbialites

The accuracy of conodont age control in microbialites and elsewhere depends on two criteria: a) the quality and density of the faunal record (i.e. the combined effects of sampling effort and ecological control on occurrence of taxa) and b) the method used to build biochronozones. A recent and comprehensive study of the basal Triassic conodont faunas from South China highlighted inconsistencies inherent to interval zones and proposed a robust and reliable zonation based on a revised taxonomic data set and the utilization of Unitary Association Zones (Brosse et al., 2016a,c), which is followed here. This work also pointed out the diachronous first local occurrence (FO) of *Hindeodus parvus* (the index species of the first Triassic interval zone) within the microbialites. One of the absurd consequences of the utilization of the diachronous FO of *H. parvus* as a base Triassic index is that despite the absence of Permian taxa, the base of the BETM is often assigned a default Permian age (e.g. Xie et al., 2010), only because age-diagnostic conodonts have not been recovered from the microbialites underlying a delayed FO of *H. parvus*. The frequent lack of age-diagnostic conodonts in the base of the microbialites is no indication of a Permian age.

The Permian-Triassic biochronological boundary falls within the interval of separation between the conodont UAZ2 and UAZ3 as defined by Brosse et al. (2016a) in the more fossiliferous record of Meishan. The second Triassic UA zone, UAZ4, was identified by Brosse et al. (2016a) at the very base of the microbial limestone at Dajiang in the GBG, thus indicating that the gap observed at the base of this lithological unit ranges well into the Early Triassic. Additionally, the youngest Permian UA zone, UAZ2, was identified at the very top of the Permian skeletal limestone in the nearby Dawen section. The unconformity separating the Permian skeletal limestone and the Early Triassic microbial limestone thus includes UAZ3 in the Dajiang-Dawen area. Hence, any previous statement of absence of biochronologic gap at the base of microbialites is unsound. UA zone correlations (Brosse et al., 2016a) with Meishan and its U-Pb age calibration indicated that the time interval between UAZ2 and UAZ4 is 61 ± 48 ky. Hence, the hiatus in Dajiang-Dawen precisely corresponds to the timing of the extinction interval in Meishan (Burgess et al., 2014). Therefore, the base of the microbialites in the sections described here must be assigned a Triassic age, as independently indicated by the presence of Triassic foraminifers and the carbon isotope record. As shown by Brosse et al. (2016a), the top of the microbial limestone falls within UAZ5 at Wuzhuan and is below UAZ6 at Dajiang and Dawen. This leaves the question of the synchronicity or diachronism of the cessation of the microbial limestone unanswered at this stage. Using an actualistic approach based on the growth rate of

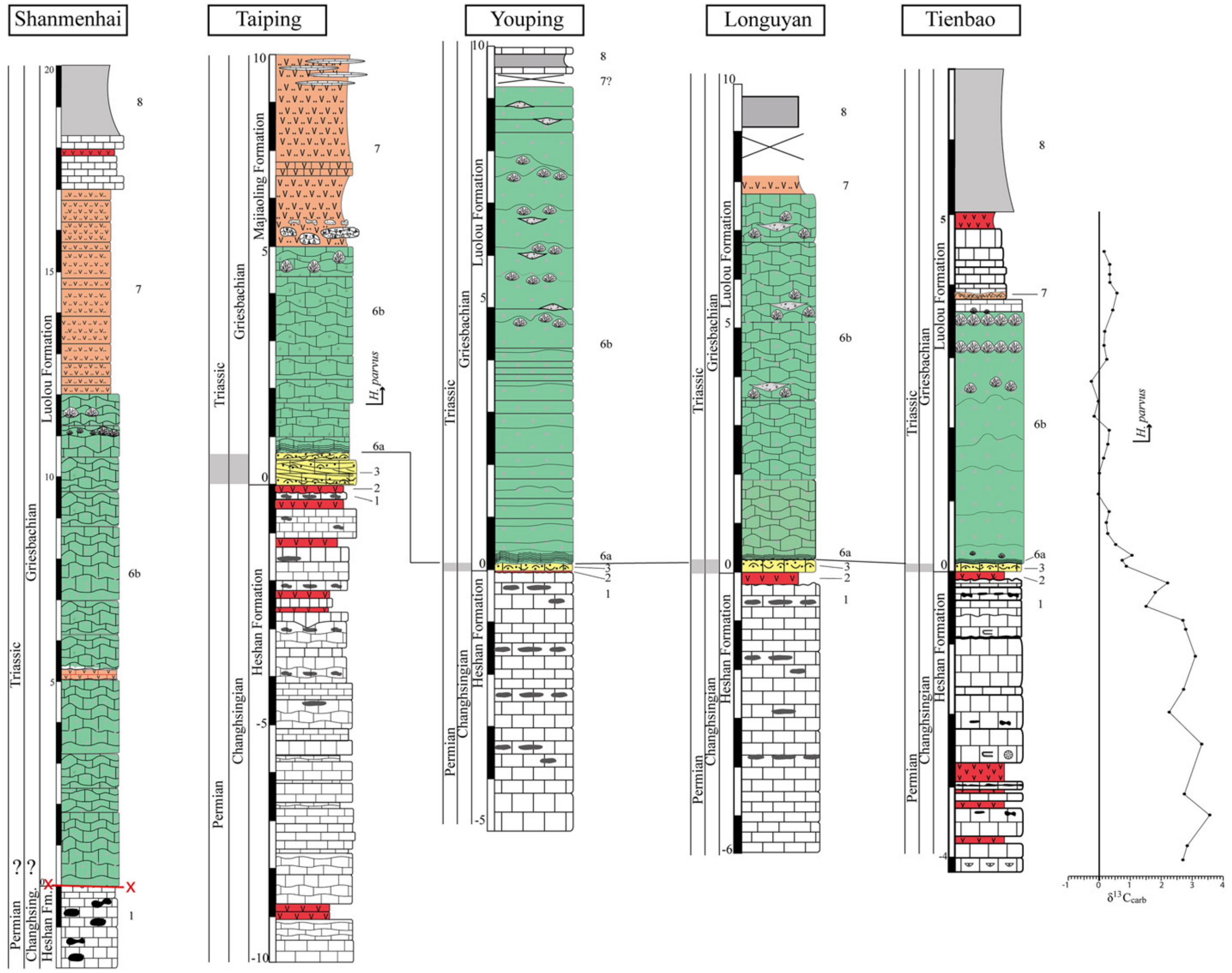

Fig. 3. Shanmenhai, Taiping, Youping, Longyuan, and Tienbao PTB sections. See Fig. 2 for legend and unit numbers. The correlation line indicates the base of the Triassic (as defined by base of Unit 6).

marine stromatolite, Hautmann et al. (2015) estimated a *minimum* duration of 25–30 ky for the ca. 9.5 m-thick microbial limestone in Wuzhuan. New high resolution U-Pb age dates (Baresel et al., in revision) indicate a duration of 13 ± 57 kyr for the BETM in the Luolou Platform. Hence, the order of magnitude of the growth rate of the BETM in our sections is close to 0.7 mm y^{-1}, a value which is in perfect agreement with the known 0.4 mm y^{-1} for living stromatolite in Shark Bay (Chivas et al., 1990).

4. Material and methods

Sections were logged and sampled bed by bed in the field and were sampled for the preparation of 30 polished slabs and 120 thin sections for further within-bed details. Using a Leica M165C microscope, petrographic classification of the skeletal limestone samples is based on Dunham (1962) classification system. Grainstones close to the PTB were studied under cathodoluminescence microscopy (CL) for detecting successive potential diagenetic phases and preservation state of skeleton microstructures. CL analyses were completed with an ERI-MRTech-optical cathodoluminescence microscope with a cold cathode that was mounted on an Olympus BX41 petrological microscope. The beam conditions were 18 kV at 120–200 microA with an unfocused beam of approximately 1 cm. The observation chamber has a residual pressure of about 80 mTorr. The samples were not coated.

For the microbialites, we follow the classification and the four scales of observation of fabrics (1 - mega-, 2 - macro-, 3 - meso-, and 4 - microstructure) given by Shapiro (2000). This author defined: 1 - megastructures as large-scale landscapes of microbialites (e.g., biohermal or biostromal buildups), 2 - macrostructures as growth form of the microbialites ranging from tens of centimeters to a few meters (e.g. tabular, columnar or domes), 3 - mesostructures as internal textures of macrostructural elements, which are visible to the naked eye (e.g., clotted, dendritic or digitated), and 4 - microstructures as fabrics observed under the microscope. In this classification, three types of mesostructures can be distinguished: laminated (stromatolites), clotted (thrombolites) and dendritic (dendrolites) (see also Riding, 2000, 2005, 2011 for further details).

High-resolution sampling was carried out in the Wuzhuan and Tienbao (Figs. 1b, 2, 3) sections for stable isotope measurements (C and O) of bulk micrite ($\delta^{13}C_{carb}$, $\delta^{18}O_{carb}$). Samples were carefully cleaned, cut and drilled with a diamond-tipped drill to produce a fine

Fig. 4. Exposures of the studied PTB sections at a, Wuzhuan, b, Nanem, c, Tienbao.

powder. The C- and O-isotope composition of the carbonates were measured with a GasBench II connected to a Finnigan MAT DeltaPlus XL mass spectrometer, using a He-carrier gas system according to a method adapted after Spötl and Vennemann (2003). For calcite samples, a reaction temperature of 70 °C is used and samples are reacted for 1 h. In-house standards of calcite are treated in the same way run interspersed with the samples in the same sequence. Samples are normalized using our in-house Carrara Marble standard calibrated against $\delta^{13}C$ and $\delta^{18}O$ values of NBS-19 (+1.95 and −2.20‰, relative to VPDB). External reproducibility for the analyses estimated from replicate analyses of the in-house standard ($n = 8$ per run) was better than ±0.08‰ for $\delta^{13}C$ and ±0.1‰ for $\delta^{18}O$ values.

5. Results

The Permian-Triassic boundary (PTB) in all studied sections is included in a hiatus marked by the abrupt facies change that characterizes the boundary between the Heshan and the Luolou formations. It is associated with a change in the $\delta^{13}C_{carb}$ values by about 1 per mil towards lower values (Figs. 2 and 3). The first local occurrences of the index conodont *Hindeodus parvus* in the Nanpanjiang Basin are known to be diachronous (Brosse et al., 2015, 2016a,c, see Figs. 2 and 3) and to largely postdate the base of the Triassic in many BETM sections. For the Wuzhuan section, the reader is referred to Brosse et al. (2015) for thorough information on the stratigraphic succession of conodonts and to

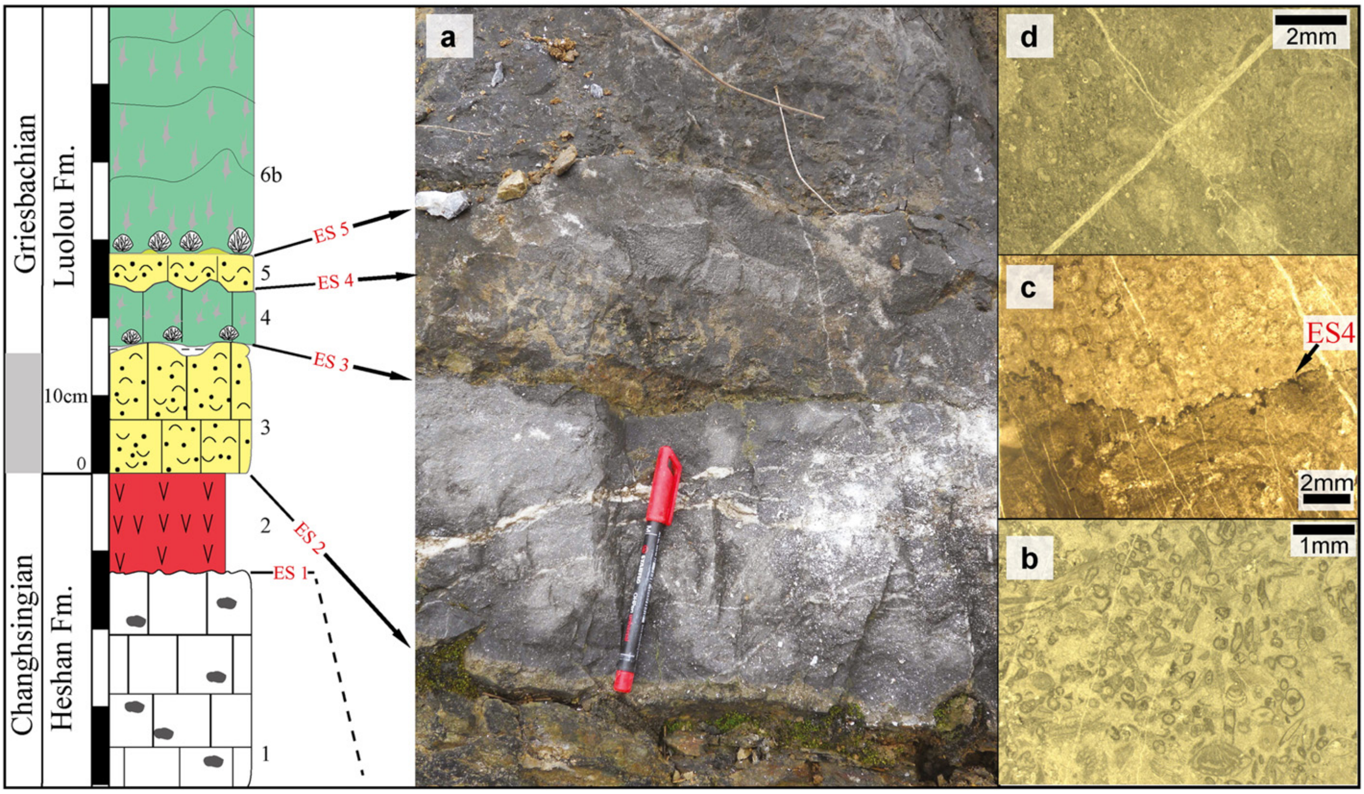

Fig. 5. Close-up view of the boundary between Heshan and Luolou formations, Wuzhuan section. Unit numbers: see Fig. 2. Event Surface 1–5: ES1 to ES5, see explanation in text. a, Close-up view of the PTB interval, boundaries between units are marked by black arrows. b, Photomicrograph of the foraminifer grainstone of Unit 3. c, Photomicrograph of the contact between microbialites facies of Unit 4 and foraminifer ooid packstone of Unit 5. d, Photomicrograph of the foraminifer ooid packstone of Unit 5.

Hautmann et al. (2015) for the diversified benthic molluscan fauna and its ecological significance. Other sections have only limited information on conodont occurrences. High-resolution $\delta^{13}C_{carb}$ data are given here for Wuzhuan and Tienbao (Table 1, Supplementary material). C-isotope data are also available for Taiping (Krull et al., 2004; Luo et al., 2014a; Lehrmann et al., 2015a).

Thin sections studied under CL indicate that all carbonate rocks have been uniformly overprinted by a late diagenetic phase that erased the earlier diagenetic history. This late phase includes the growth of microcrystalline dolomite rhombs. However, in some cases, it is possible to reconstruct part of the early diagenetic history.

5.1. Wuzhuan

This section (24°21′44.6″N; 107°20′02.00″E) is located south-east of Fengshan (No. 1 in Fig. 1b). The shallow-water limestone of the Permian Heshan Fm. is characterized by medium to thick (20–100 cm) wackestone beds (intercalated occasionally with packstone beds) rich in diagenetic chert nodules and interbedded with numerous ash layers (Figs. 2, 4a). These limestones are rich in shallow marine benthic fauna represented by corals, crinoids, brachiopods, bryozoans, fusulinids and small foraminifers.

The boundary between the Heshan (Unit 1) and Luolou formations at Wuzhuan (Fig. 5) immediately overlies a 12 cm-thick ash layer (Unit 2, Fig. 5a). Five Event Surfaces (ES1–5) are recognized between the youngest limestone bed of the Heshan Fm. and the main body of the microbial limestone. The first Event Surface (ES1) is an irregular contact between limestone of the Heshan Fm. and the last Permian ash layer. The second Event Surface (ES2) separates the top of the ash layer from the basal calcarenite bed (Unit 3, Fig. 5b) of the Luolou Fm., which is a bioclastic grainstone containing abundant foraminifers of exclusively Late Permian age (*Rectostipulina quadrata* Jenny-Deshusses, 1985; *Rectostipulina pentamerata* Groves et al., 2005a; *Dagmarita chanakchiensis* Reitlinger, 1965; *Louisettita ?elegantissima* Altiner and Brönnimann, 1980; *Dagmarita* sp.; *Ichthyofrondina* cf. *I. palmata* (Wang, 1974); *Ichthyofrondina* sp.; *Paraglobivalvulinoides septulifer* (Zaninetti and Altiner, 1981); *Nankinella* sp.; *Globivalvulina* sp.; *Climacammina* sp.; *Glomomidiella* sp.; ?*Midiella* sp.). Thin sections reveal that bioclasts were first coated by marine radiaxial fibrous cement (Fig. 6a, b and c). The habitus of these crystals suggests that this early phase consisted of aragonitic cement that formed prior to any compaction of the bioclasts whose original shape is preserved. Such aragonitic fibrous cement is known to develop in the upper intertidal to supra-tidal zone (Bartley et al., 2000). A second phase is represented by the filling of the remaining space between the coated bioclasts by blocky calcite (Fig. 6b and c). A third and late phase includes the development of stylolites (Fig. 6d), of tiny dolomite rhombs and an almost general recrystallization of the carbonate as highlighted by CL (Fig. 6e and f). The basal calcarenite (Unit 3) is separated from the first overlying clotted microbialites (8 cm thick, Unit 4) by a very thin lenticular clay bed and an irregular truncation surface (ES3). The interstitial micrite of Unit 4 yielded the Triassic foraminifers *Globivalvulina* sp. and ?*Cornuspira mahajeri* Brönnimann, Zaninetti and Bozorgnia, 1972 (=*Postcladella kahlori* n. comb. Krainer and Vachard, 2011). The uneven upper surface of this bed (ES4, Fig. 5c) is overlain by a 6–7 cm-thick packstone (Unit 5, Fig. 5d) containing superficial ooids and foraminifers exclusively of Late Permian age (*Dagmarita chanakchiensis* Reitlinger, 1965; *Globivalvulina vonderschmitti*, Reichel, 1946; *Ichthyofrondina* sp.; ?*Nankinella* sp.; *Paraglobivalvulina mira* Reitlinger, 1965; *Paraglobivalvulinoides septulifer* (Zaninetti and Altiner, 1981). The occurrence of Triassic foraminifers in Unit 4 suggests that all Permian foraminifers found in Unit 5 were reworked. Another alternative scenario is that Late Permian foraminifers from Unit 5 are survivors of the first phase of foraminiferal extinction as advocated by Song et al. (2009a, b). However, the faunal compositions of Units 3 and 5 unambiguously reflect pre-extinction assemblages, thus supporting the reworking

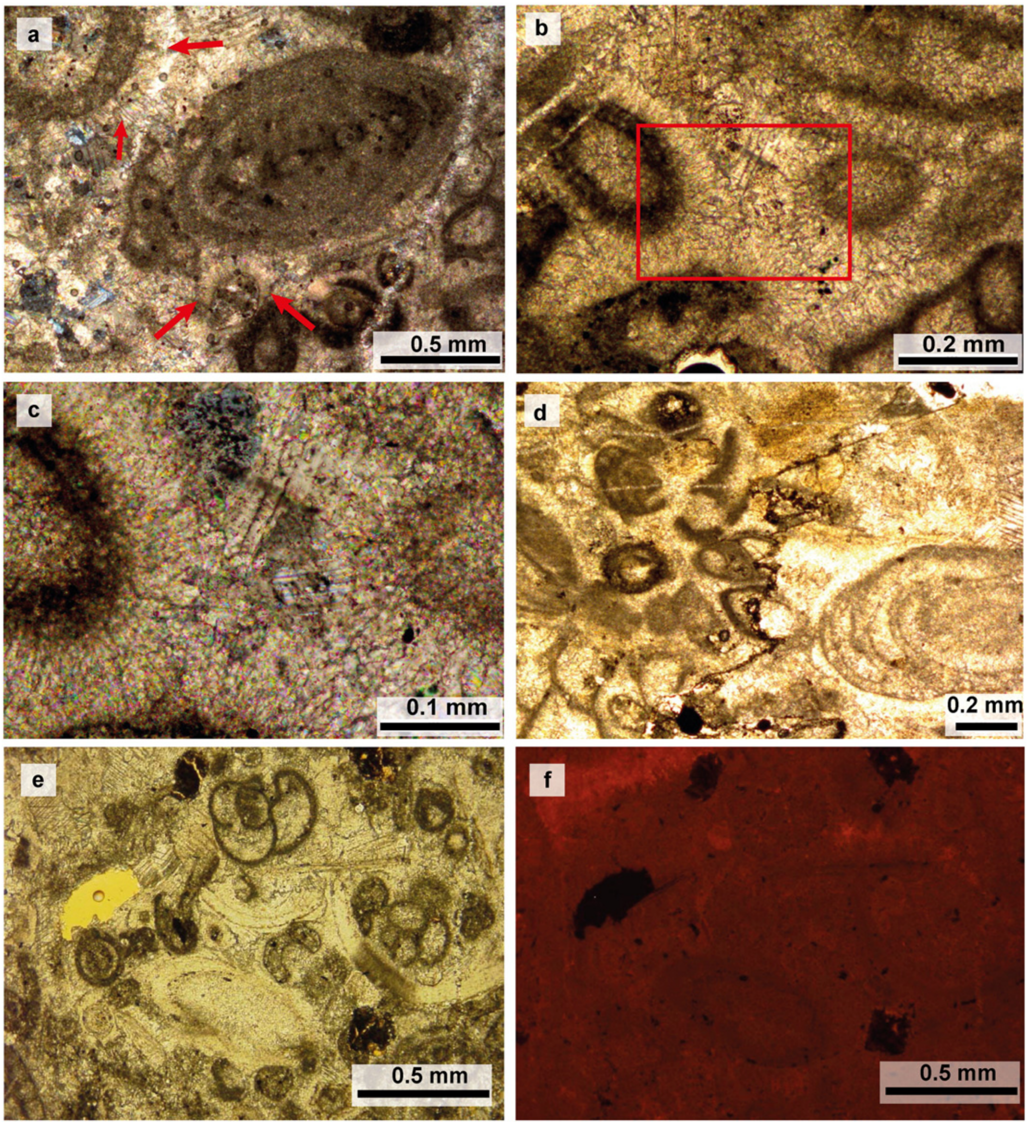

Fig. 6. Photomicrographs of marine cements and stylolites in the Wuzhuan section. a, Bioclasts coated by marine cement, Unit 3 (red arrows indicate fibrous cement). b, Bioclasts coated by marine radiaxial fibrous cement, Unit 3. Space between coated grains filled with blocky calcite. c, Enlargement of red rectangle in Fig. 6b. d, Example of stylolite cutting across Permian grains and cements, Unit 3. e, Bioclastic grainstone of Unit3 in natural light. f, Cathodoluminescence image of the sample illustrated in Fig. 6e. Bioclastic grains display similar luminescence as cements, indicating a late diagenetic overprint. (For interpretation of the references to colour in this figure legend, the reader is referred to the web version of this article.)

interpretation. The overlying main microbialite body (Unit 6b) is separated from this second grainstone bed (Unit 5) by an irregular truncation surface (ES5).

The main microbialite unit (Unit 6b) displays tabular constructions with a clotted fabric (thrombolite) in its lower half and domical buildups with a digitate (dendrolite) fabric in its upper half (Figs. 2 and 7b). In tabular thrombolites, centimetric and isolated mesoclots made of sparitic masses are embedded in a micritic matrix. These sparitic masses have an irregularly indented outline without any preferred orientation (Figs. 8a, b and 9a). This spotted texture is the main texture of the tabular thrombolite. Domical dendrolites, centimetric digitate mesoclots embedded in a micritic groundmass display a distinctive vertical to radial orientation. These digitate mesoclots are separated from the micritic groundmass by a sharp and regular outline. No spheroidal elements or coccoid structures were recognized in the digitate mesoclots. A large portion of these sparitic mesoclots is also dolomitized. Observed dolomite rhombs in this thrombolites are of secondary origin and probably formed during the late diagenetic overprint mentioned earlier. The interstitial micrite between the digitate mesoclots yielded small gastropods and *Cornuspira* sp. (Fig. 9f), the latter being reported from other basal Early Triassic microbialites in South China by Song et al. (2015) and Yang et al. (2011).

Shelly lenses with mainly packstone-grainstone textures occur between the domical microbialites (Figs. 2 and 7b). These coquinoid lenses contain highly diverse and abundant bivalves and subordinate brachiopods and gastropods (Hautmann et al., 2015). Similar lenses reported from other BETM sections (Shanggan) in the Luolou Platform (3 km north of Leye in Fig. 1b) also contain abundant and diverse bivalves (Hautmann et al., 2011), gastropods (Kaim et al., 2010), conodonts (Brosse et al., 2015), and occasional ammonoids (Brühwiler et al., 2008). It is worth noting that ostracods and echinoderm ossicles also occur in these lenses (Hautmann et al., 2015). The intraskeletal or shelter cavities of bivalves and gastropods are occasionally filled with peloids, micrite, and geopetal structures. Such peloids have been related to bacterial activities (Adachi et al., 2004).

The top of the microbialites Unit 6b is capped by thin-bedded bioclastic wackestone beds yielding sparse small-sized gastropods, thin-shelled bivalves, and occasional ostracods. This unit is overlain by a 50 cm-thick volcanogenic greywacke bed (Unit 7, Fig. 2). The greywacke interval is in turn overlain by brown-weathering

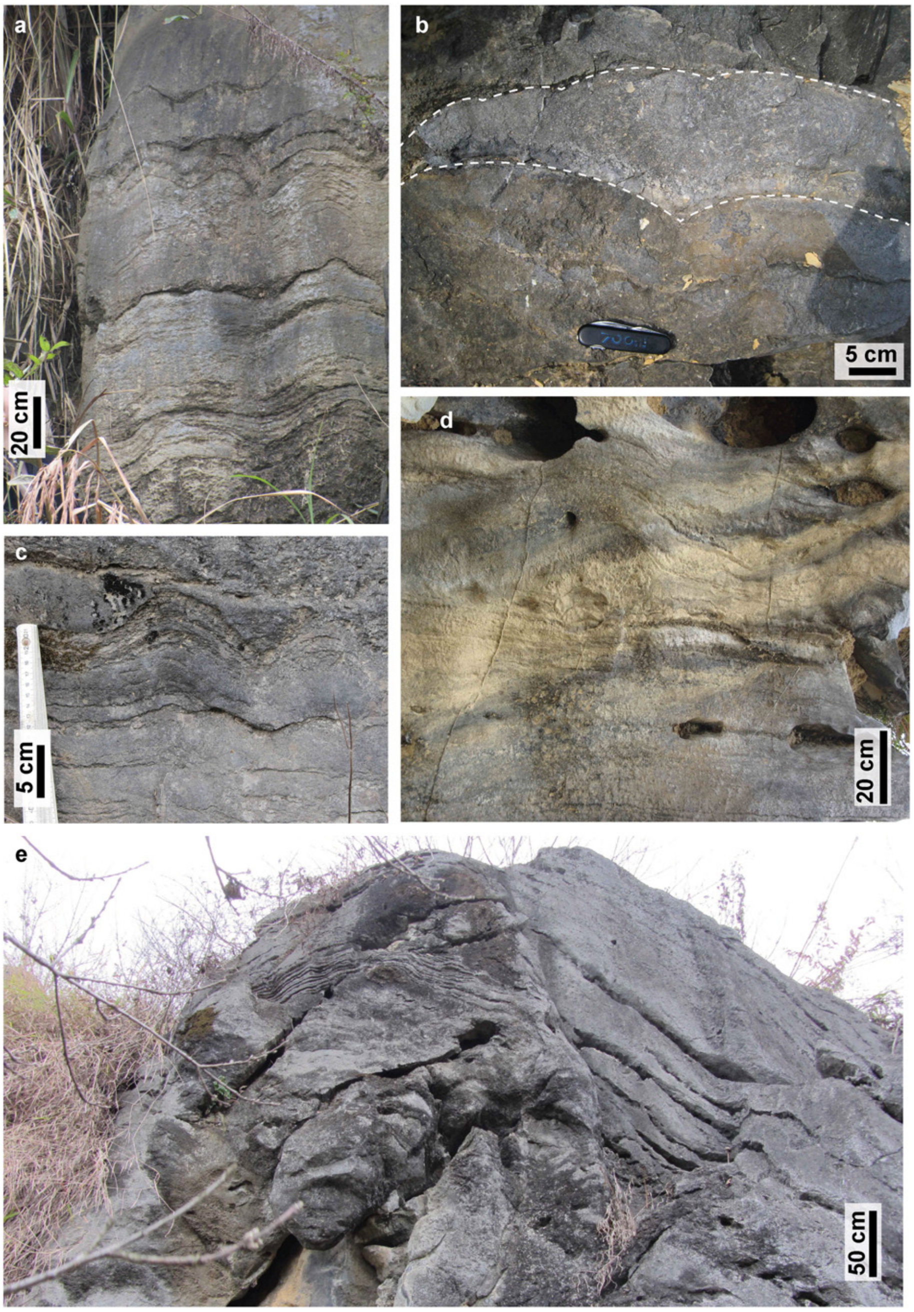

Fig. 7. Field photographs of domical structures in the microbialites. a, Upper part of microbialites at Tienbao section. b, Domical microbialites (dark) and a shelly lens (light) in the upper part of Wuzhuan section. c and e, Upper part of Youping section. d, Upper part of Nanem section.

carbonaceous, black, laminated mudstones intercalated with medium grey wackestone beds (Unit 8, Fig. 2).

The high-resolution $\delta^{13}C_{carb}$ record from the Wuzhuan section can be divided into three different stages (Fig. 2). The Late Permian Heshan Fm. has positive $\delta^{13}C_{carb}$ values with substantial fluctuations superimposed onto a protracted negative shift of 2‰ (from ca. 4.5‰ to 2.5‰). This first phase ends with an abrupt decrease of 1‰ around the first grainstone (Unit 3) at the base of the Luolou Fm. In addition to the significance of the detailed facies changes described above, this negative jump of 1‰ is an additional indication of a stratigraphic gap. The second phase shows a short negative shift from ca. 1.5 to 0‰ spanning Units 4, 5, and the first two meters of Unit 6. The third phase is characterized by a steady state with $\delta^{13}C_{carb}$ values around 0‰. The $\delta^{18}O_{carb}$ values are ranging from −5‰ to −12‰ in the Heshan Fm. and display a stable plateau near −6‰ in the microbialite unit (Table 1, Supplementary material). Although an anomaly in $\delta^{18}O_{carb}$ (with no correlative change in $\delta^{18}C_{carb}$) around a thick volcanic ash layer in Heshan Fm. is observed, no correlation between carbon and oxygen isotope values that would suggest a diagenetic overprinted on $\delta^{13}C_{carb}$ can be detected.

5.2. Nanem

The Nanem section (24°24′02.8″N; 107°19′28.1″E) is located 4 km north of the Wuzhuan section (No. 2 in Figs. 1b, 4b) and the lithological succession is very similar to that of Wuzhuan (Fig. 2). The contact

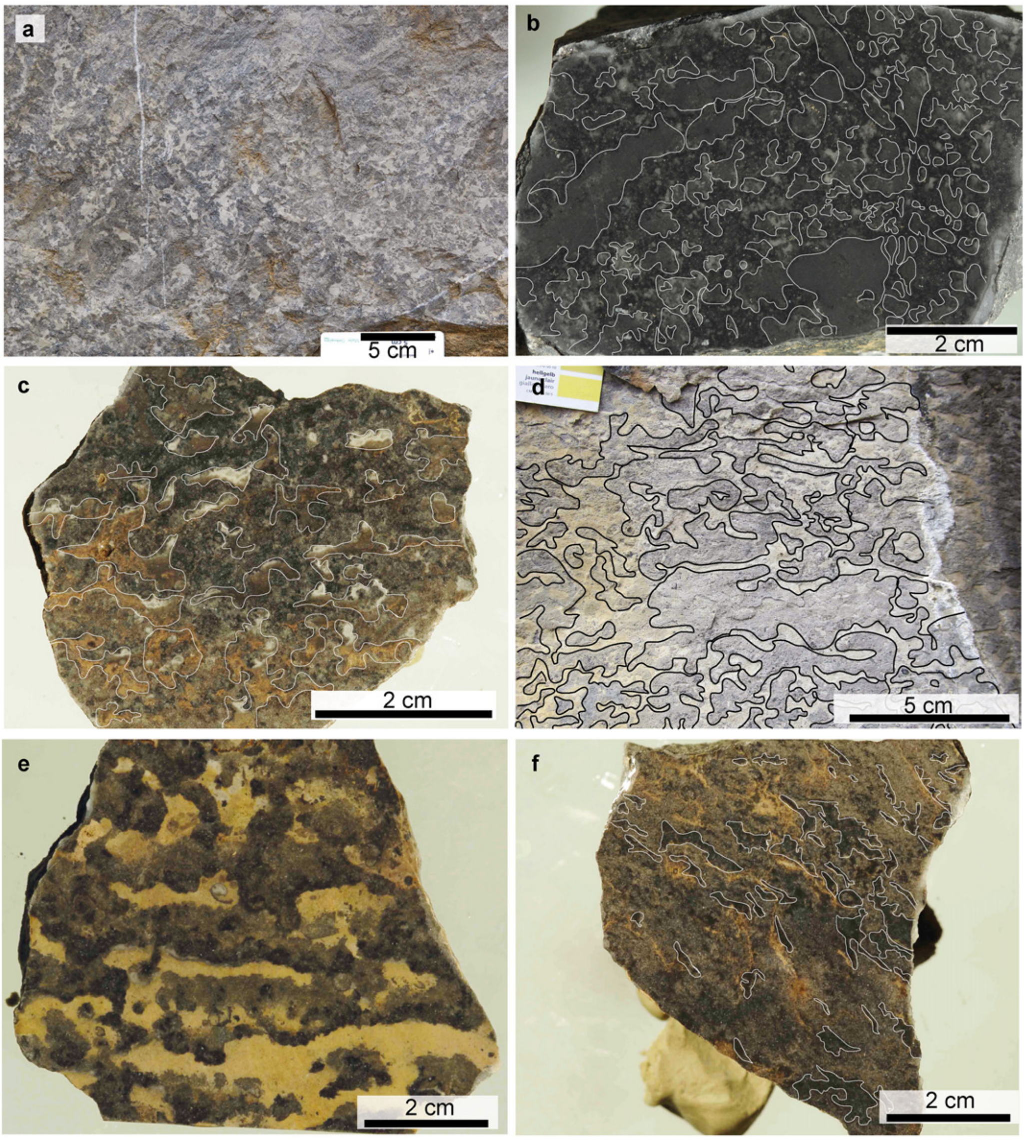

Fig. 8. Mesostructures of the microbialites. a, Field photograph of spotted mesostructures, Nanem section. b, Polished slab photograph of the spotted mesostructures, Nanem section. c, Polished slab of the layered mesostructure with stromatactis-type fenestral structures, Youping section. d, Field photograph of labyrinthic mesostructure, Youping section. e, Polished slab photograph of labyrinthic mesostructure, Youping section. f, Polished slab of layered vesicular mesostructure (outlined), Youping section.

between the limestones (Unit 1) and the last ash layer (Unit 2) of the Permian Heshan Fm. is an irregular surface (ES1). The topmost ash layer is overlain by a basal calcarenite, which is here a thin bioclastic packstone-wackestone limestone bed (Unit 3, Fig. 10a, b). This calcarenite is overlain by a first episode of the microbial limestone, which is represented by a 6 cm-thick stromatolite (Unit 4, see Figs. 10b, 11a, b, c) containing millimetric carbonate crystal fans (Fig. 12a). The interstitial micrite between stromatolite columns (decimetric domes) contains the Triassic *Cornuspira* sp. The contact between the basal calcarenite (Unit 3) and the thin stromatolite bed (Unit 4) is an irregular truncation surface (ES3) underlined by a crust of iron oxide (Fig. 11a). The upper boundary of the stromatolite bed is also an irregular truncation surface (ES4), which is overlain by a superficial ooid grainstone bed (Unit 5, Figs. 10b and 12b, c). The main microbialite body (Unit 6b) is again separated from the ooid grainstone (Unit 5) by an irregular truncation surface (ES5).

The lower part of the main microbialites (Unit 6b) exhibits tabular forms of thrombolite with common spotted texture while the upper part displays domes (Fig. 7d) associated with a predominant digitate fabric. Shelly lenses are intercalated between the domes in the upper part of Unit 6b. At Nanem, the volcanogenic greywacke (Unit 7) directly overlies the microbial limestone and is in turn followed by back laminated mudstones intercalated with medium (20–30 cm) grey wackestone beds (Unit 8).

5.3. Tienbao

This section is located north-west of Leye, in the northwestern part of Guangxi Province (No. 3 in Figs. 1b, 24°50′03.4″N; 106°29′20.9″E, 4c). The Permian Heshan Fm. consists of medium- to thick-bedded (20–100 cm) limestone with dark chert nodules and intercalated ash layers. The Heshan Fm. displays a wackestone-packstone microfacies and contains a rich benthic fauna including brachiopods, bivalves, corals, sponges, algae, and foraminifers (Unit 1). It is separated from a 10 cm-thick ash layer by an irregular surface (ES1; Fig. 13).

The topmost layer of the Heshan Fm. is again an ash layer (Unit 2) that ends with ES2. It is then overlain by an 8 cm-thick calcarenite (Unit 3, Fig. 13), corresponding to a packstone with fragmented skeletal

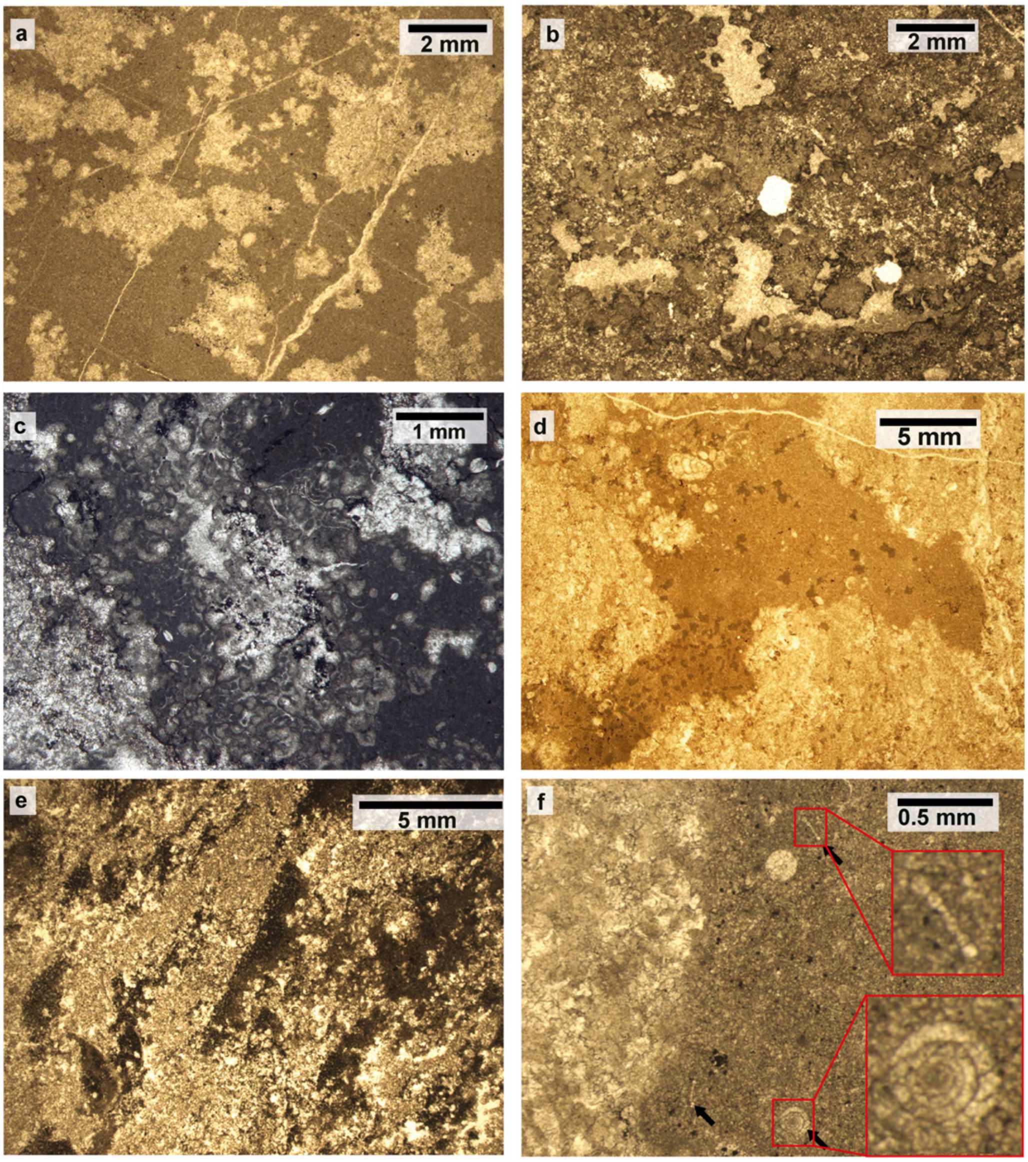

Fig. 9. Photomicrographs of different structures of microbialites. a, Spotted structure, Nanem section. b, Layered structure with stromatactis-type fenestral texture, Youping section. c, Aggregated globular renalcid-group calcimicrobes (micritic-wall spherical structures) and sparite-filled cavities, Youping section. d, Labyrinthic structure, Youping section. e, Vesicular structure, Youping section. f, Digitate structure. The micritic part shows axial and equatorial sections of *Cornuspira* sp. (= *Postcladella* Krainer and Vachard, 2011), Tienbao section.

grains including bivalves, gastropods, bryozoans, green algae and foraminifers (Fig. 11g) (*Paraglobivalvulina mira* Reitlinger, 1965; *Pseudovermiporella sodalica* Elliott, 1958; *Nodosinelloides* sp.; *Dagmarita* sp.; *Climacammina* sp.; ?*Deckerella* sp.; *Palaeotextularia* sp.; *Eotuberitina* sp.; *Ichthyofrondina* sp.) of Permian age. Above Unit 3, ES3 and 4 cannot be distinguished and are probably amalgamated with ES5. The main microbialite body (Unit 6) is thus resting on an undulating truncation surface (ES3–5) that cuts through calcarenite grains and groundmass of Unit 3 (Figs. 11g, h, i). Thin sections and polished slabs reveal evidence of bioerosion as well as abundant iron oxide lining the truncation of the amalgamated surface ES3–5. Burrows are filled with sparry calcite and the positive reliefs are encrusted with stromatolites containing disseminated pyrite crystals (Figs. 11g, h, i). The interstitial sediment between stromatolite columns contains millimetric carbonate crystal fans with a micritized envelope, gastropods, foraminifers, echinoid spines and unidentified bioclasts (Fig. 12d).

The microbialite body (Unit 6) is 3.5 m thick only. The base of the microbialites shows a thin (4 cm), discontinuous but distinctive stromatolite layer (Unit 6a) (Figs. 11g, 13). The contact between stromatolite crusts of Unit 6a and the overlying thrombolites (Unit 6b) is conformable, without any signs of an erosional surface.

The main part of the microbialites (Unit 6b) consists of tabular clotted thrombolites with spotted texture followed by domical digitate dendrolites (Figs. 4c, 7a, 14). The FO of *H. parvus* is 1.8 m above the base Unit 6.

The uppermost domical digitate dendrolites of Unit 6b are overlain by ca. 1 m of thin-bedded wackestone (Fig. 14c, d). Twenty-five centimeters above the base of the wackestone, a thin greywacke (Unit 7) is intercalated. The vertical growth of the topmost dendrolites was largely controlled by the variable ratio between sedimentation rate and growth rate as shown in Fig. 14d. Cessation of the microbialites in Tienbao clearly resulted from rapid burial of the digitate dendrolites by increased fluxes of shaly micritic limestone. The locally expanded record immediately following the microbial limestone shows that the ubiquitous volcanogenic greywacke (Unit 7) is in fact included within mudstone-wackestone limestone (Fig. 3), as is also the case in Wuzhuan (Fig. 2). In Tienbao, the greywacke has a reduced thickness of ca. 20 cm and yields poorly preserved bivalves of several centimeters in shell length,

Fig. 10. Close-up view of the boundary between Heshan and Luolou formations, Nanem section. Unit numbers: see caption of Fig. 2. Event Surface 1–5: ES1 to ES5, see explanation in text. a, Close-up view of the PTB interval, boundaries between units are marked by black arrows. b, Polished slab of the contacts between Units 3, 4 and 5. Note the erosional lower and upper limits (ES3 and ES4) of stromatolites (Unit 4).

thus contrasting with the much smaller size of bivalves specimens observed in the older coquinoid lenses intercalated between the microbial domes. The next overlying volcanic ash layer is in turn followed by an at least 12 m-thick, dark grey to black, laminated calcareous mudstone unit containing abundant specimens of *Claraia* sp. indet. (top of Unit 8).

The $\delta^{13}C_{carb}$ record in this section also shows a change in values from 3.5 to 1.5‰ with relatively large superimposed fluctuations in the Heshan Fm. In the base of the Luolou Fm., a negative jump of 1.5‰ is again observed in the basal calcarenite, which is in turn followed by a gradual negative shift in the first 0.8 m of the microbial limestone. Upsection, the $\delta^{13}C_{carb}$ isotopic values reach a 0‰ plateau extending throughout the rest of the microbialite unit. The $\delta^{13}C_{carb}$ record of Tienbao is in perfect agreement with that of Wuzhuan (compare Figs. 2 and 3). In addition, it demonstrates that the 0‰ plateau extends further up section into the shaly micritic limestone blanketing the BETM, thus recording that the cessation of the microbialites deposition is unrelated to any isotopic change of the regional carbonate carbon reservoir. Almost all $\delta^{18}O_{carb}$ values are between −5‰ and −9‰ and no correlation between carbon and oxygen isotope values can be detected (Table 1, Supplementary material). Hence $\delta^{13}C_{carb}$ values are most likely unaffected by diagenetic overprint.

5.4. Youping

The Youping section is located north of Leye, in the northern part of the Guangxi Province (24°57′28.0″N; 106°39′13.2″E, No.4 in Fig. 1b). The Heshan Fm. consists of the usual bioclastic wackestone-packstone beds (Unit 1). The topmost Permian ash layer (Unit 2) is very thin (1–2 cm) and overlain by a 20 cm-thick bioclastic limestone (Unit 3). ES1 is an irregular surface that separates Unit 1 from Unit 2, whereas ES2 is a planar surface between Units 2 and 3. ES3 and 4 as exposed in the Wuzhuan and Nanem sections have not been recognized in Youping and are likely amalgamated with ES5 (as arbitrarily chosen here, see Figs. 15 and 18). ES3–5 is a gently undulating surface (Fig. 15) that separates the bioclastic limestone (Unit 3) from the overlying microbialites (Unit 6).

The microbial limestone reaches a thickness of 9.2 m in Youping. The base of the microbialites typically consists of a 20 cm-thick stromatolite bed (Unit 6a). The main part of the microbialites (Unit 6b) comprises clotted thrombolites in its lower part and domes of digitate dendrolites in its upper part (Figs. 3 and 7c–e). The contact between Unit 6a and 6b is a conformable bedding plane without any indication of erosion. Four different textures can be recognized within the clotted thrombolites of this section: layered with stromatactis-type fenestral, labyrinthic, vesicular, and spotted. Thrombolites with layered and fenestral textures (Figs. 8c and 9b, c) consists of a sponge-like groundmass of ellipsoidal spheroids (?*Renalcis*) strewn with highly irregular cavities filled with microcrystalline calcite and dolomite rhombs. Spheroids are usually filled with microcrystalline calcite and cavities resemble stromatactis-type fenestral structures with geopetal fillings. These textures associated with diagenetically-altered sponge spicules are also found in the stromatactis-bearing basal Triassic microbial limestone at Shanggan section (Leye area), which represents a local and small tectonic uplift within the Luolou Platform (Baud et al., 2013). These cavities are probably results of decomposition of sponges, cyanobacteria, or algae (Monty, 1976; Flugel, 2004; Vennin et al., 2015). These textures document a close ecological association between sponges and microbialites, as frequently encountered in the latest Permian, newly found in the earliest Triassic (Baud et al., 2013; Friesenbichler et al., 2016) and in later episodes during the Early Triassic (Brayard et al., 2011; Marenco et al., 2012; Vennin et al., 2015; Olivier et al., 2016).

Small-sized gastropods, thin-shelled bivalves, and ostracods are abundant in the groundmass, while serpulid worm tubes (assigned to microconchids, Zaton et al., 2013; Yang et al., 2015a,b) are present mostly in the sparite-filled cavities. Ezaki et al. (2008), Lehrmann et al. (2015a) and Baud et al. (2005) described a similar facies in earliest Triassic microbialites from the Nanpanjiang Basin and from western Taurus (SW Turkey). Similar facies were also described from later episodes of the Early Triassic, e.g. in the western USA basin (Brayard et al., 2011; Zaton et al., 2013; Vennin et al., 2015; Olivier et al., 2014, 2016). Labyrinthic textures (Figs. 8d, e and 9d) contain abundant, millimetric carbonate crystal fans in a micritic groundmass. Only the micritic part of this texture contains bioclasts (e.g. ostracods and small gastropods). Vesicular mesostructures (Figs. 8f and 9e) contain aligned masses of peloids in a sparitic groundmass showing intense recrystallization and dolomitization.

Shelly lenses in the microbialites are essentially composed of bivalves, but also include gastropods and ostracods; coquinoid lenses at the top of the section occasionally contain small-sized ammonoids. A thin exposure gap above the upper limit of the microbial limestone likely corresponds to a weathered volcanogenic greywacke (Unit 7). Above the gap, dark laminated mudstones are interbedded with bioclastic

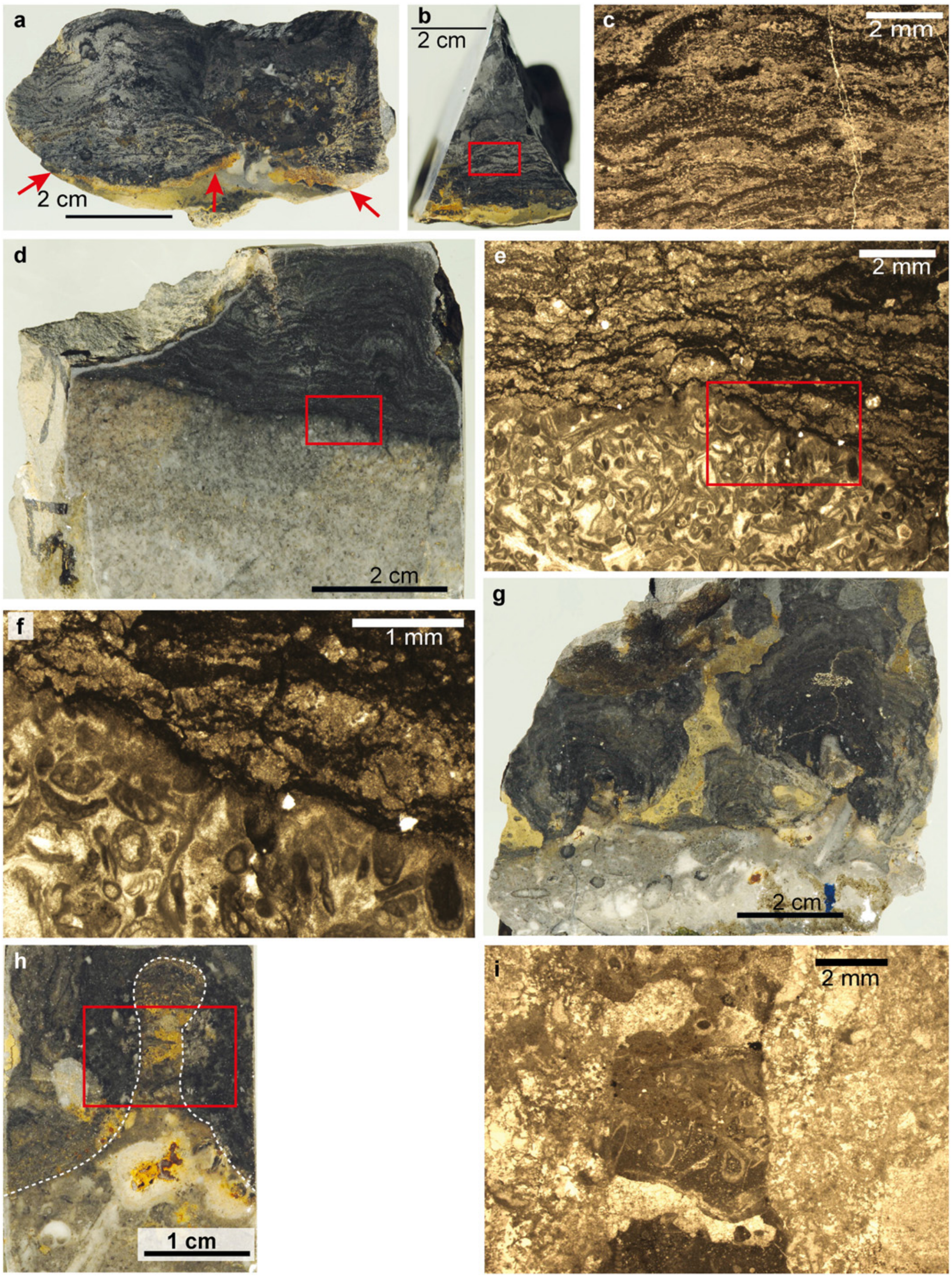

Fig. 11. Photographs of the contact between skeletal limestones and microbialites at Nanem, Longyuan and Tienbao sections. a and b, Polished slabs of the contact at Nanem section, red arrows show undulating surface with iron oxide crust. c, Photomicrographic enlargement of the red rectangle in Fig. 11b showing the millimetric lamination of a stromatolite. d, Polished slabs of the contact at Longyuan section showing the contact between the skeletal grainstone of Unit 3 and the stromatolite of Unit 6a. e, Photomicrographic enlargement of the red rectangle in Fig. 11d, showing the sharp contact between Units 3 and 6a. f, Photomicrographic enlargement of the red rectangle area in Fig. 11e showing the upper truncation of the bioclasts (mainly foraminifers, calcareous algae, crinoids) of Unit 3. g, Polished slab of the contact between Units 3 and 6a, Tienbao section. Note the growth of stromatolite (dark) atop of the erosional upper limit of the packstone. Note iron oxide remains and undulating irregular relief. h, Close-up view of the high relief contact between Units 3 and 6a, Tienbao section. The top of Unit 3 shows patches of iron oxide. i, Photomicrographic enlargement of the red rectangle of Fig. 11h. The dark central protuberance belongs to Unit 3. The light coloured left and right parts are recrystallized stromatolite of Unit 6a. Note burrows cutting across Unit 3. (For interpretation of the references to colour in this figure legend, the reader is referred to the web version of this article.)

wackestone yielding rare and poorly preserved ammonoids (Unit 8, Fig. 12e).

5.5. Longyuan

This section is located south-east of Fengshan (24°25′54.3″N; 107°22′24.2″E, No. 5 in Fig. 1b). The Heshan Fm. is similar to that described in the previous sections. ES1 is also an uneven surface. The topmost Permian ash layer (Unit 2) is 12 cm thick and is separated from the next overlying bioclastic grainstone (Unit 3) by a nearly planar surface (ES2). Unit 3 is only 7 cm thick and contains a shallow marine benthic fauna, with fragmented skeletal grains (Figs. 11d, e, f and 16) and abundant Permian foraminifers (*Dagmarita chanakchiensis* Reitlinger, 1965; *Climacammina* sp.; *Midiella* sp.; *Pachyphloia* sp.;

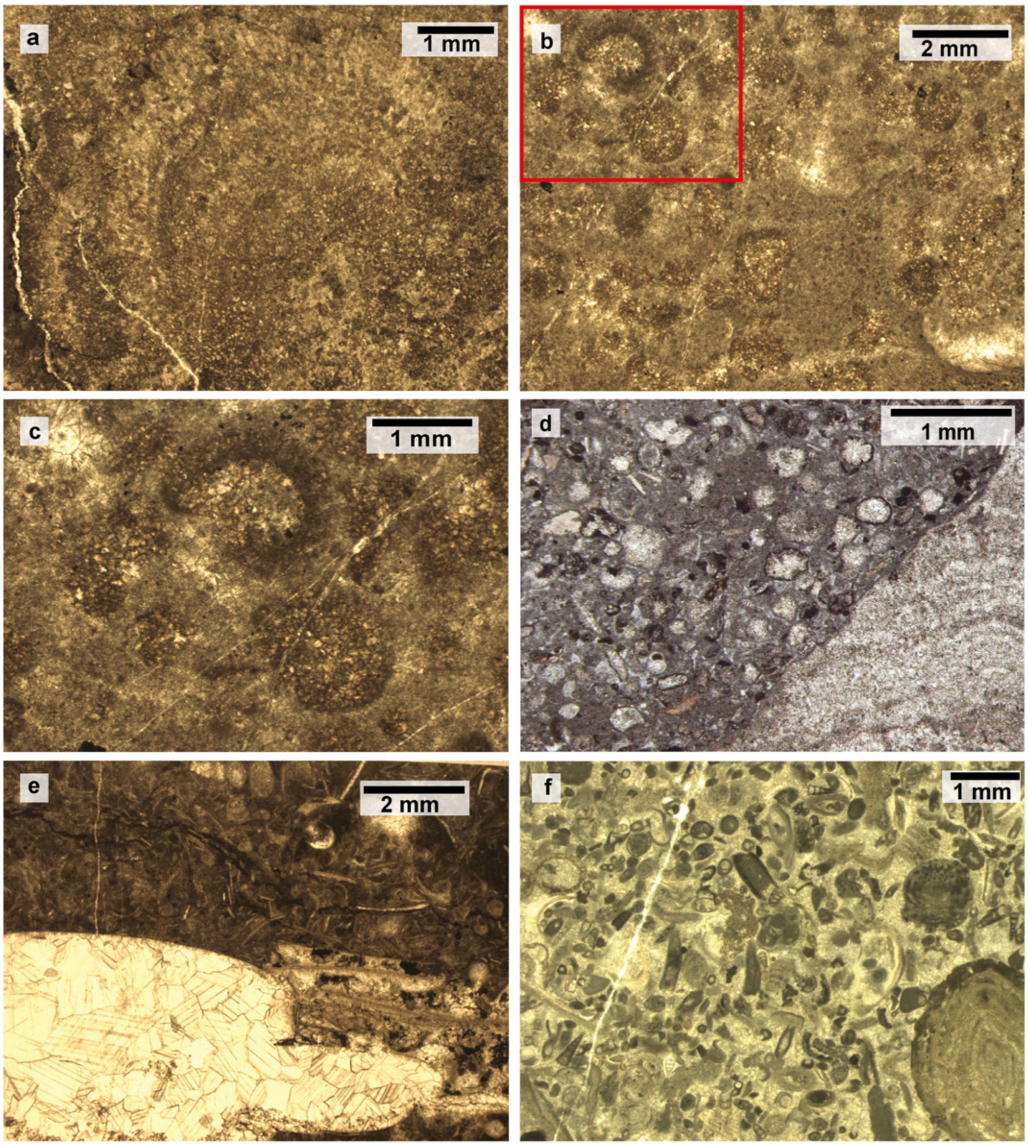

Fig. 12. Photomicrographs of limestones associated with microbialites. a, Millimetric calcite fan in Unit 4, Nanem section. b, Ooid grainstone, Unit 5, Nanem section. c, Enlargement of the red rectangle in Fig. 12b, showing superficial ooid grainstone, Nanem section. d, The interstitial skeletal-rich sediment between stromatolite columns, Tienbao section. The light coloured right part is a stromatolite of Unit 6a. e, Ammonoid-bearing wackestone-packstone on top of microbialites, Unit 8,Youping section. f, Bioclastic grainstone (including, foraminifers, calcareous algae, crinoids, ostracods and bivalves) directly overlain by microbialites, Unit 3, Taiping section. (For interpretation of the references to colour in this figure legend, the reader is referred to the web version of this article.)

Geinitzina sp.; *Ichthyofrondina* sp.; *Reichelina* sp.; ?*Cribrogenerina* sp.; ?*Sphaerulina* sp.; *Agathammina pusilla* (Geinitz, 1848)). Here, ES3 and 4 are not visible and are probably amalgamated with ES5. The microbialites (Unit 6) rests on top of the basal calcarenite bed with a sharp and undulating truncation surface (ES3–5, Fig. 11d). Cement and grains of the underlying calcarenite bed (Unit 3) are clearly cut by ES3–5, a surface molded by a 4 cm-thick wavy stromatolite (Unit 6a), as illustrated in Fig. 11e and f. The contact between Unit 6a and 6b is a wavy but conformable surface generated by the inception of domical structures at the top of bed 6a.

The total thickness of the microbialites is 7.7 m. This unit exhibits tabular constructions in the lower part of Unit 6b and domical constructions in its upper part. Spotted and layered textures with stromatactis-type fenestrae are visible in the clotted thrombolites of the lower part of Unit 6b. Three horizons of shelly lenses occur in the domical microbialites. A volcanogenic greywacke (Unit 7) rests directly on top of the microbialites. Above a ca. 1 m-thick exposure gap, dark grey to black, laminated calcareous mudstones of Unit 8 crop out (Fig. 3).

5.6. Shanmenhai

The Shanmenhai section is located 14 km south of Fengshan (24°24′ 51.90″N; 107° 2′27.50″E, No. 6 in Fig. 1b). The Permian part of this section also consists of medium- to thick-bedded (20–100 cm) limestone of the Heshan Fm., with dark chert nodules and a rich shallow marine benthic fauna. It is overlain by a 12 m-thick microbialite unit at the base of the Luolou Fm. In this section, the detailed transition between the Heshan and the Luolou formations is obscured by small-scale low-angle faults between the two formations. The lower part of the microbialites consists of tabular thrombolites with clotted facies. Vesicular and spotted textures were recognized in the clotted thrombolites. A thinner upper part is characterized by domical structures with a

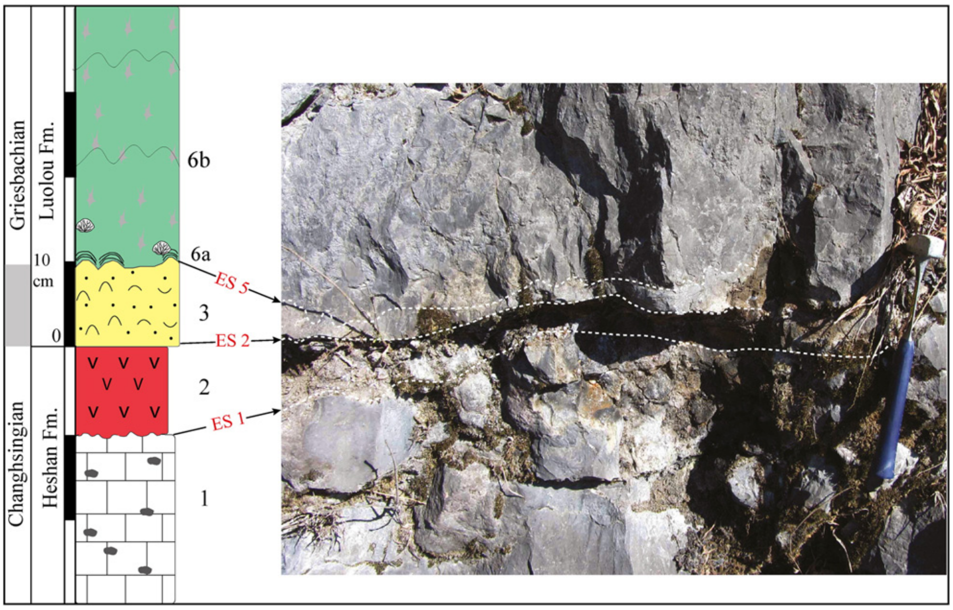

Fig. 13. Close-up view of the boundary between Heshan and Luolou formations, Tienbao section. Unit numbers: see caption of Fig. 2. Event Surface 1–5: ES1 to ES5, (ES3-ES4 are missing here) see explanation in text. Boundaries between units are marked by black arrows and dashed white lines.

predominant digitate fabric. A 15 cm-thick impure limestone bed containing volcanic material occurs 5 m above the base of the microbial unit. The microbialite unit is directly capped by a 5 m-thick volcanogenic greywacke (Unit 7), followed by an ammonite- and *Claraia* sp. indet.-bearing lime-mudstone, including an intercalated ash layer. Dark laminated mudstones (Unit 8) occur again at the top of this section (Fig. 3).

5.7. Taiping

This section is located north of Pingguo (23°29′98.9″N; 107°31′57.7″ E, No. 7 in Fig. 1b). Here, the Permian Heshan Fm. consists of medium to thick limestone (20–100 cm) beds containing dark chert nodules intercalated with numerous ash layers. It contains a rich shallow-water marine benthic fauna composed of bivalves, gastropods, foraminifers, corals, algae, and echinoderms (Unit 1). It ends with an undulated surface (ES1) capped by a volcanic ash layer (Unit 2). It is overlain by a 40-cm thick bioclastic grainstone (Fig. 12f) rich in Late Permian foraminifers (*Nankinella* sp.; *Dagmarita chanakchiensis* Reitlinger, 1965; *Tubiphytes* ex gr. *obscurus* Maslov, 1956; *Frondinodosaria* sp.; *Pachyphloia* sp.; *Agathammina pusilla* (Geinitz, 1848); *Pseudovermiporella* sp.; *Paraglobivalvulina mira* Reitlinger, 1965; *Midiella* sp.) with high-angle cross-bedding (Unit 3) at the base of the Majiaoling Fm. ES3 and 4 are also merged with ES5. A 4.7 m-thick microbial limestone (Unit 6) overlies Unit 3 with a truncation surface (ES3–5, Fig. 17). The calcimicrobial unit is here a basal member common to the Majiaoling and the Luolou formations. Yang et al. (1999) and subsequent authors placed the biostratigraphical Permian-Triassic boundary approximately 1 m above the base of the microbialite unit on the basis of the FO of *H. parvus* (see also discussion in Yin et al., 2014). Petrographic and facies analyses are documented by Lehrmann et al. (2003, 2015a). The carbon isotope record is given by Krull et al. (2004) and Lehrmann et al. (2015a). The $\delta^{13}C_{carb}$ shows a ca. 2‰ negative shift at the Heshan-Majiaoling boundary and a steady plateau around 0.5‰, which are both consistent with the Wuzhuan and Tienbao records.

New observations also reveal that the microbial limestone is directly overlain by a volcanogenic sandstone, which is at least 5 m thick (Unit 7). This greywacke was interpreted as an ash layer by Lehrmann et al. (2015b). Decimetric lenses of angular clasts of microbial limestone are laterally intercalated within the lowermost meter of the greywacke. These breccias indicate block-faulting activity coeval with deposition of the volcanogenic greywacke and are incompatible with any air-born transportation of the volcanogenic material of the enclosing bed. Inner molds of centimetric bivalves were found in the upper part of the exposed greywacke, below intercalated thin lenses of limestone displaying the typical vermiculate facies generated by intense bioturbation.

At Taiping, Lehrmann et al. (2015b) used two volcanoclastic ash layers to linearly extrapolate an age of 251.985 ± 0.097 Ma for what they interchangeably labelled as the "Permian-Triassic boundary" or "Permian-Triassic event horizon". Lehrmann et al. (2003, 2015a) used the FO of *H. parvus* for placing the PTB approximately 1 m above the base of the microbial limestone in Taiping. Yet, Lehrmann et al. (2015b) stated that "the ash layer TP Tuff-3 is ca. 0.5 m below the PTB at the Taiping section", thus implying that the PTB was newly and correctly moved at the base of the calcarenite and that the reference to the FO of *H. parvus* as a marker for the base of Triassic was abandoned.

6. Discussion

6.1. Heshan Formation (Units 1 to 2)

In all investigated sections, the Permian Heshan Fm. is uniform and is characterized by medium- to thick-bedded limestone with wackestone-packstone texture, chert nodules, presence of lime mud, bioclasts of brachiopods, bivalves, bryozoans, crinoids, algae, sponges and foraminifers, and a lack of terrigenous sediments (Unit 1). The high diversity of skeletal grains, the presence of lime mud and the extreme scarcity of hydrodynamic sedimentary structures indicate deposition in a subtidal open-marine platform in low-energy conditions (e.g. Wilson, 1975; Flugel, 2004). However, occasional horizons with a packstone texture suggest sporadic wave and/or storm influences. This part of Heshan Fm. shows no sign of lateral change in bathymetry, except in the Shanggan uplift (3 km north of Leye in the Luolou Platform) where it is replaced by reefal limestone (Baud et al., 2013). According to Yin et al. (2014), the upper Heshan Fm. (our Unit 1) yields the *Colaniella–Palaeofusulina* biota, including *Codonofusulina* and

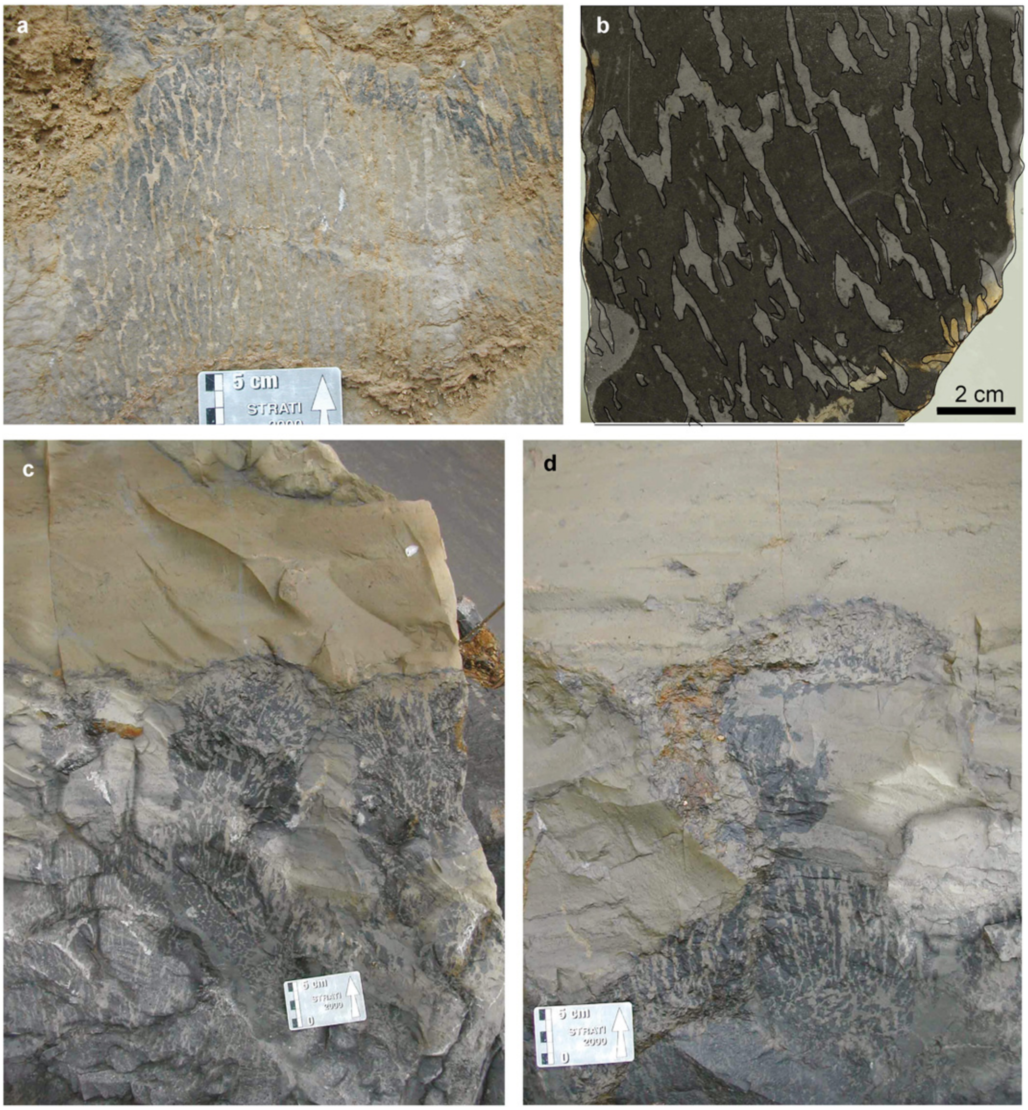

Fig. 14. Digitate microbialites in upper part of Teinbao section a, Field photograph and b, polished slab photograph. c, Contact between the microbialites and base of the overlying Unit 7 (note the sharp contact). d, Vertical growth and burial of dendrolites (Unit 6b) within the overlying wackestone (intercalated between Units 6b and 7).

Nankinella fusulinids. In our sections, we also identified *Colaniella* sp., *Palaeofusulina* sp., *Nankinella* sp. and other diagnostic Late Permian foraminifers such as *Paraglobivalvulina mira* and *Dagmarita chanakchiensis* in the upper Heshan Fm. Despite intensive sampling and processing of a substantial number of large samples (4 to 5 kg each) from the uppermost beds of the Permian Heshan Fm., no age-diagnostic conodont elements were obtained.

In all the sections reported here (Figs. 2, 3), the subtidal Heshan Fm. ends with an ash layer (Unit 2, Fig. 18), whose apatite chemical composition and U-Pb age demonstrate that it originated from the same eruption (Baresel et al., 2015, 2016a). This ash layer can thus be used as reliable synchronous time line (Fig. 18). This marker is lacking in some sections such as Laren (Galfetti et al., 2008) or Wangmo area (HB unpubl. observations) in the same Luolou Platform. It nevertheless opens up the possibility that it may have acted as a chemically-resistant barrier against dissolution caused by a submarine acidification event that would have removed younger Permian carbonate rocks. The planar bedding plane (ES2 Fig. 18) that separates this ash layer from the basal calcarenite and the absence of reworked Heshan-derived lithoclasts in the calcarenite are in better agreement with chemical dissolution than with mechanical erosion.

In Laolongdong section (Eastern Sichuan), Chongyang section (Southeast Hubei Province) (Yang et al., 2011), and in the Great Bank of Guizhou (e.g. Dajiang, Dawen and Heping sections) (Lehrmann et al., 2003, 2015a; Chen et al., 2009; Song et al., 2009a; Yin et al., 2014), the boundary between the Permian bioclastic limestone and the microbial limestone is a sharp surface, with no equivalents of Units 2 to 5. This contact is called the "skeletal packstone-calcimicrobial framestone (SP-CF)" boundary by Song et al. (2009a) and differs from all our sections by the absence of a terminal ash layer and of foraminiferal-rich grainstones.

6.2. Onset of the BETM (Units 3 to 5)

Dating the base of the microbial limestone by means of conodonts is difficult because of i) the generally impoverished conodont record in the lower half of the microbialites (Brosse et al., 2016a); ii) the diachronous FO of *H. parvus* (Baud, 1996); and iii) the generally long

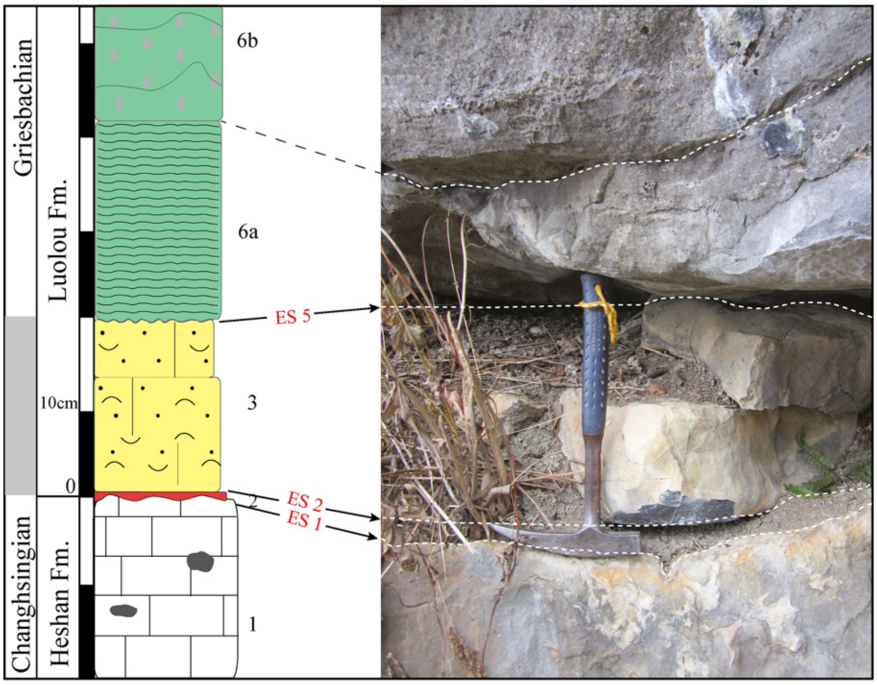

Fig. 15. Close-up view of the boundary between Heshan and Luolou formations, Youping section. Unit numbers: see caption of Fig. 2. Event Surface 1–5: ES1 to ES5 (ES3 and ES4 are missing here) see explanation in text. Boundaries between units are marked by black arrows and dashed white lines.

ranges of conodonts around the PTB (e.g. *H. typicalis* and *H. praeparvus* (Jiang et al., 2011)). The FO of *H. parvus* has even been documented immediately below the base of the microbialites at Dajiang section (Jiang et al., 2014), but in most BETM sections, this FO occurs at any depth within the microbialites (e.g. Chen et al., 2009; Mu et al., 2009; Yang et al., 2011). In Wuzhuan, the conodont record is only adequate

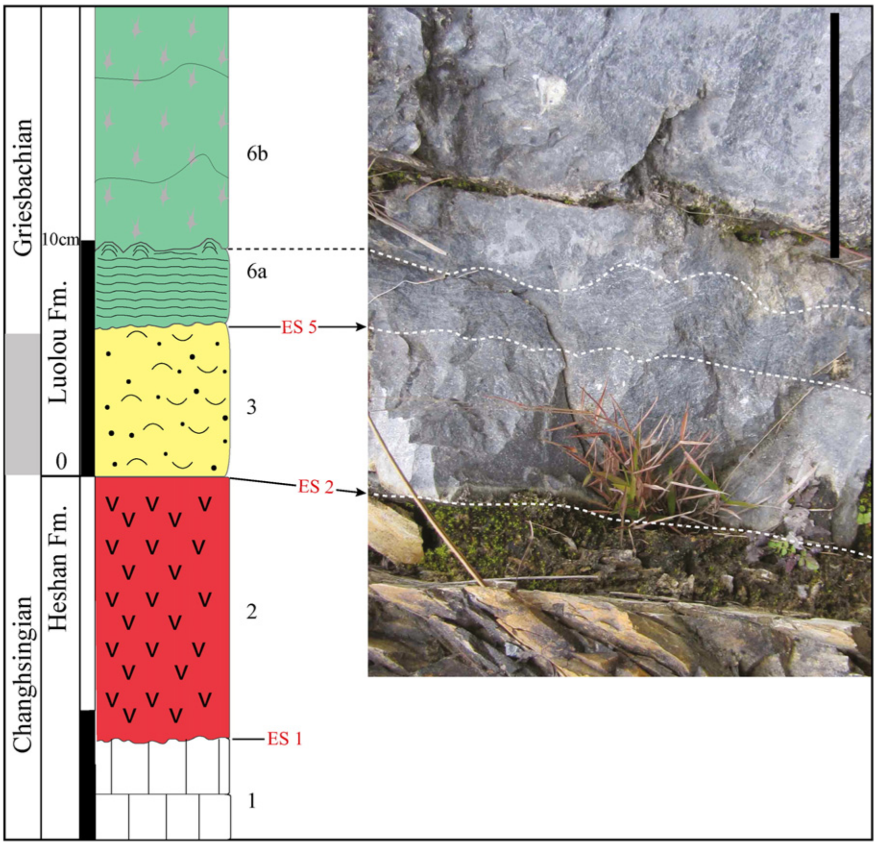

Fig. 16. Close-up view of the boundary between Heshan and Luolou formations, Longyuan section. Unit numbers: see caption of Fig. 2. Event Surface 1–5: ES1 to ES5 (ES3 and ES4 are missing here) see explanation in text. Boundaries between units are marked by black arrows and dashed white lines.

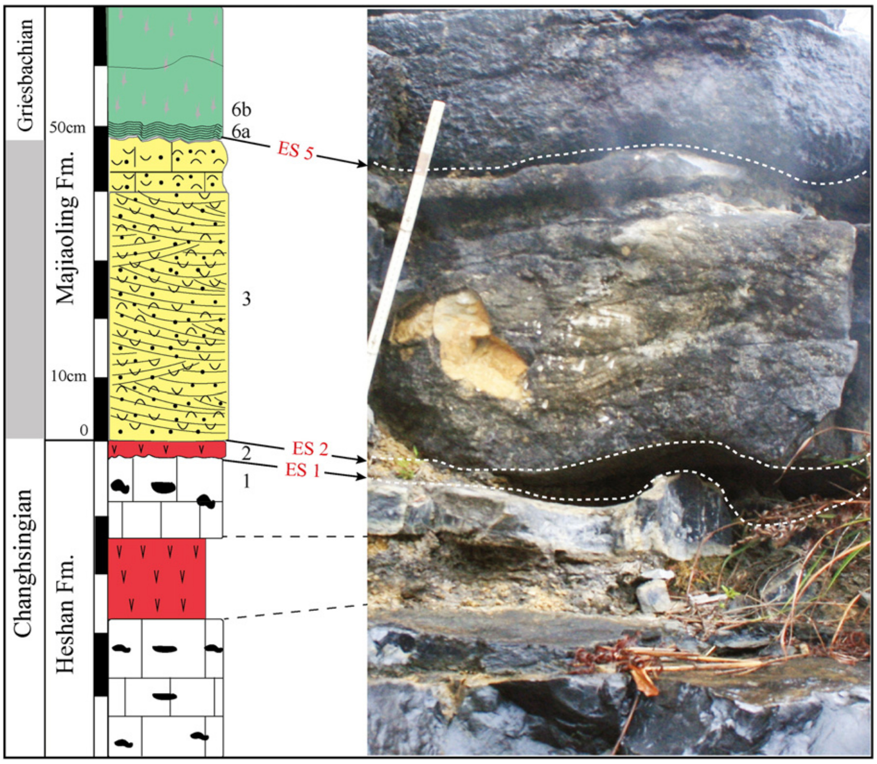

Fig. 17. Close-up view of the boundary between Heshan and Luolou formations, Taiping section. Unit numbers: see caption of Fig. 2. Event Surface 1–5: ES1 to ES5 (ES3 and ES4 absent) see explanation in text. Boundaries between units are marked by black arrows and dashed white lines. Note the cross-beddings in Unit 3.

in the upper part of the microbialites, the lower part being too poor for any robust and reliable dating by means of maximal associations (Brosse et al., 2015). Hence, the C-isotope record temporarily offers a convenient alternative approach for dating the onset of the BETM by means of correlation with conodont-rich PTB sections (e.g. Shangsi and Meishan).

Both $\delta^{13}C_{carb}$ records from Tienbao and Wuzhuan show a negative shift of ca. 1‰ between the topmost limestone beds (Unit 1) of the Heshan Fm. and the basal calcarenite (Unit 3) of the Luolou Fm. (Figs. 2, 3). This shift interrupts the protracted negative trend that spans the upper part of the Heshan Fm. and the lower part of the main body of the microbial limestone. Compared to the compressed succession of negative shifts in deeper water sections straddling the PTB (e.g., Xie et al., 2007 for Meishan), this 1‰ drop indicates a substantial hiatus within ES1 and/or within ES2.

The most commonly observed succession involves only a single bioclastic calcarenite (Unit 3 in Taiping, Longyuan, Tienbao and Youping). This basal calcarenite marks the base of the Triassic transgressive sequence above the PTB unconformity. Contradictory interpretations about ES 3 and ES 5 have been proposed either in support of submarine dissolution (e.g. Payne et al., 2007; Song et al., 2009a; Lehrmann et al., 2015a, 2016) or in support of subaerial erosion (e.g. Collin et al., 2009; Wignall et al., 2009; Kershaw et al., 2016). In our sections, any subaerial erosion prior to chemical dissolution cannot be excluded because i): the latter may conceivably erase all traces of the former one as argued by Kershaw et al. (2012b) and ii): both mechanisms do not need to be mutually exclusive. The pendant or meniscus cements are absent in our bioclastic calcarenites and sediments trapped between domical microbialites contain marine fossils. This is in agreement with the absence of traces indicative of subaerial diagenesis as noticed by Lehrmann et al. (2015a). Yet, deposition of a second bioclastic ooid packstone grainstone (Unit 5) characterized by concentration of Late Permian foraminifers (Fig. 5d) indicates a renewed episode of winnowing and reworking. The absence of Heshan Fm.-derived lithoclasts within all calcarenites suggests reworking of incompletely lithified Heshan sediments. The upper boundary of the calcarenite is an irregular surface and the transgressive base of the microbialites does not contain any clasts derived from the underlying foraminiferal-rich grainstone. Hence, ES3–5 (Fig. 18) suggests that chemical dissolution took place again shortly before the onset of the microbialites. The interval of uncertainty containing the PTB ranges from ES2 to ES3 in Nanem and Wuzhuan, and from ES2 to ES5 in other sections. Both Nanem and Wuzhuan provide more expanded records of the base of the BETM. There, the oldest bed of microbial limestone (Unit 4) contains Triassic foraminifers and is bracketed by two beds of calcarenite (Units 3 and 5), both of them yielding exclusively Late Permian foraminifers accompanied by ooids. This alternation of shallow water (upper intertidal to supratidal), high-energy calcarenite with subtidal, deeper water microbial limestone suggests that short term eustatic oscillations within a transgressive phase could be a viable mechanism for the succession of Units 3, 4, 5 and 6. An alternative explanation calling upon high frequency tectonic uplift and subsidence appears unlikely. Absence of such alternation of contrasted depositional environments in other sections may result from insufficient accommodation space.

At Nanem and Tienbao, the irregular truncation surface (ES3 or ES5, Fig. 18) between the basal calcarenite and oldest microbialites is underlined by a thin crust of iron oxide and bioerosion. These could have formed either in subaerial exposures or in submarine hardgrounds. However, the absence of any reworked clasts that would normally be expected along a subaerial erosional surface argues in favor of a submarine dissolution. At Tienbao, burrows cutting through the calcarenite confirm that this unit was lithified or consolidated and thus, provided a suitable substrate for the growth of microbialites. At Longyuan, ES5 is a smoother wavy surface, without bioerosion, root casts, iron oxide, meniscus cement, vadose cement or dissolution residual products that would suggest subaerial exposure.

We suggest that deposition of cross-bedded grainstone and interludes of microbial limestone before the onset of the main microbialite unit are at variance with any long-lasting acidification event of the sea-water. Our observations support brief pulses of acidification only,

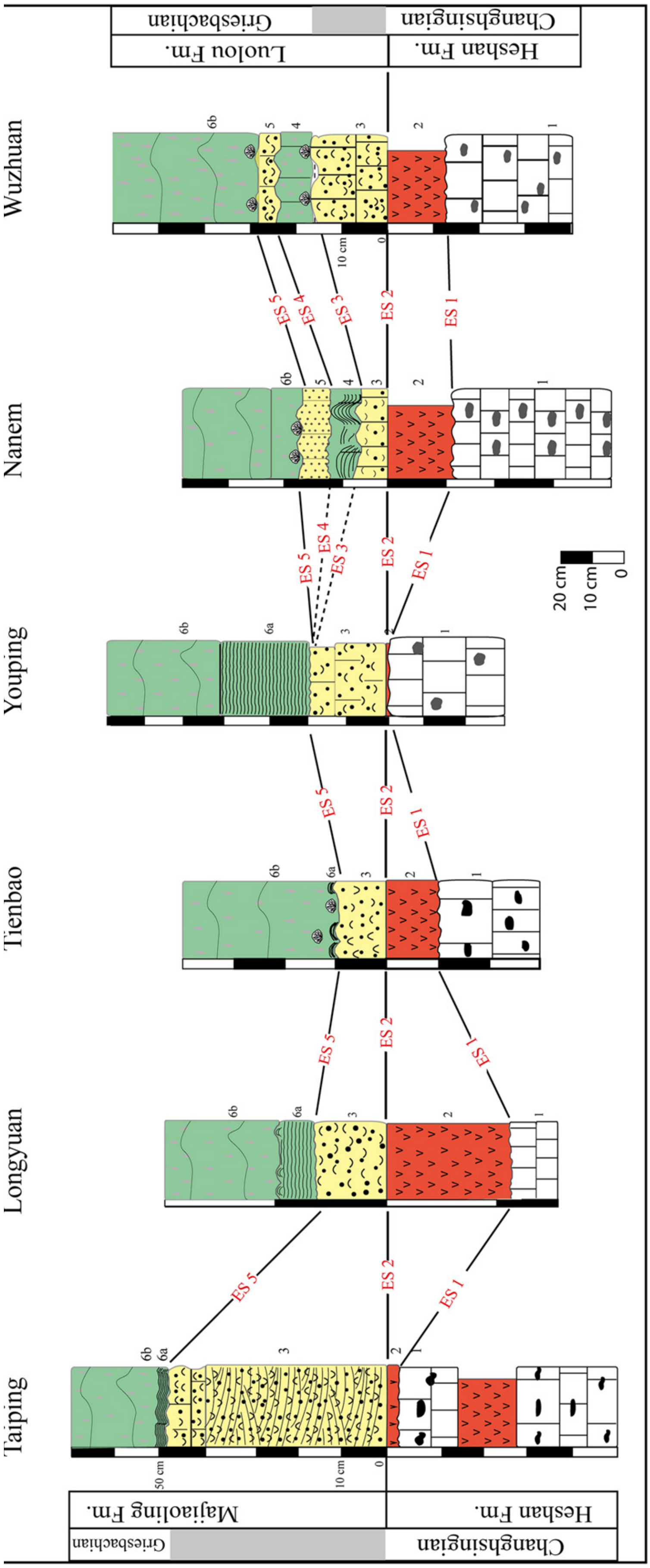

Fig. 18. Correlations of the Event Surfaces (ES) at the boundary between Heshan and Luolou formations. See text for description of Event Surfaces.

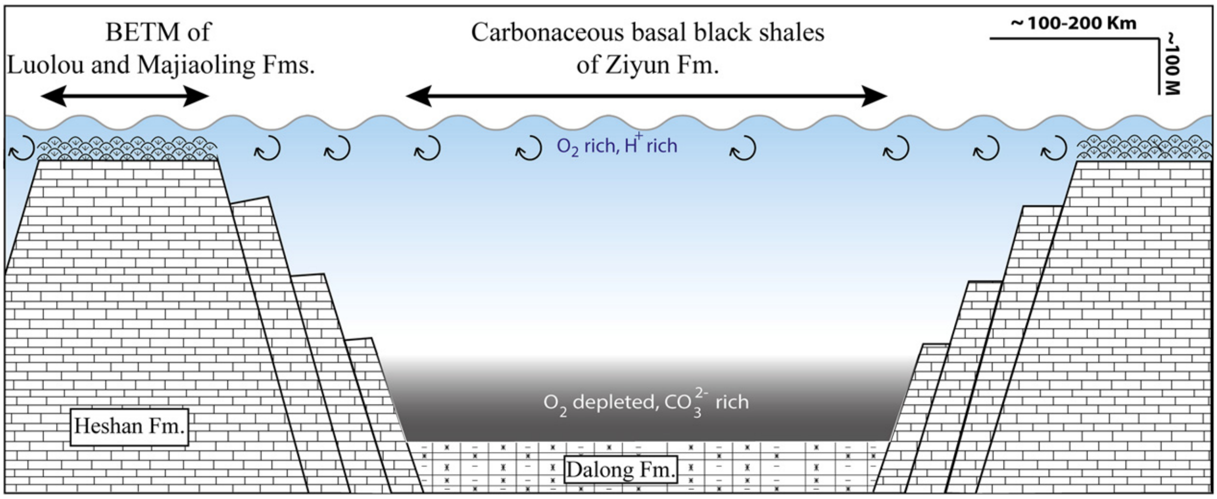

Fig. 19. Reconstruction of the spatial relations between basal Early Triassic depositional environments in the Nanpanjiang Basin. Downthrown blocks are characterized by the deep water stratigraphic succession including the latest Permian Dalong Fm. and Early Triassic Ziyun Fm. Upthrown blocks typically display a shallow water succession comprising the latest Permian Heshan Fm. and the basal Early Triassic microbialites of the Luolou Fm. The main structuration phase of the Nanpanjiang pull-apart basin occurred around the Wujianpingian-Changsinghian boundary and is manifested by thick wedges of synsedimentary breccias along the footwalls of uplifted blocks (not shown in this reconstruction).

coeval with some of the described event surfaces. The absence of any intraclasts in the basal calcarenite also lends support to such acidification pulses. The combined global eustatic and local tectonic controls of bathymetry, carbonate supersaturation and local absence of any significant siliciclastic load in shallow waters played a leading role in the onset of the BETM.

Evidence supporting a widespread regression at the PTB in South China is documented in previous studies. In the NE Sichuan Basin, a late Permian dolomitized skeletal grainstone was interpreted as a relative sea-level drop down by Ezaki et al. (2003). North of our study area, Ezaki et al. (2008) also reported a "conglomeratic fusulinid grainstone" in the Longbai section. Moreover, Collin et al. (2009) described a thin grainstone bed bounded by two truncation surfaces in the Langbai section that resemble our basal cross-bedded grainstone made of Permian foraminifers (Unit 3, Figs. 12f, 17). Similarly, other sections from South China where bioclastic grainstone is reported include Laolongdong (E Sichuan), Cili (NW Hunan), and Chongyang (SE Hubei) (Yang et al., 2011). Yin et al. (2014) also argued in favor of a widespread regression in South China on the basis of other additional PTB sections in shallow marine settings. Algeo et al. (2007) reported a 12 cm-thick oolitic–pisolitic grainstone at the base of the microbialites from the North Vietnamese part of the Jingxi Platform (Nhi Tao section), which may correlate with the same regressive phase.

Indications of a sea-level fall are also documented in Western Tethys, as reported from Turkey by Marcoux and Baud (1986) and from the Southern Alps where the rocks at the base of the Tesero oolites were labelled "the current event" by Brandner (1988) and Brandner et al. (2013). Baud et al. (1997, 2005 and 2009) described the same event in detail from the Çuruk Dag section (Turkey), which is also discussed by Kershaw et al. (2011). In the Demirtas section, Groves et al. (2003, 2005b) and Groves and Calner (2004) labelled this horizon the "disaster oolites". In Turkey, a lens-shaped thrombolite bed is reported at the top of the oolitic calcarenite just below the main microbial stromatolite body by Baud and Richoz (2009). More recently, Abdolmaleki and Tavakoli (2016) also reported a large-ooid facies intercalated within basal Early Triassic microbialites in the Persian Gulf Basin. Thus, the alternating oolites and microbialites is a widespread pattern at the Permian-Triassic transition in shallow marine carbonate settings across the Tethys and Panthalassa oceans (Li et al., 2015a,b), which strengthens the role of carbonate saturation and eustatic sea-level changes among the parameters that influenced the onset of the microbial limestone. However, by no means does this exclude the intercalation of short acidification events. In the Luolou Platform, the main acidification event may have dissolved the youngest Permian carbonate until the very same underlying ash layer (Horizon 1 of Baresel et al 2016a) was reached. This ash layer may have reacted with acidic sea water to form a chemical shield against dissolution (Schaltegger, Baresel, and Widmann, oral com. 2016).

6.3. Development of the BETM (Units 6a and b)

In Taiping, Longyuan, Tienbao and Youping, Unit 6a consists of stromatolites whose thickness varies laterally between 2 and 20 cm (Figs. 13, 15, 16, 17, 18). They are absent from Nanem and Wuzhuan, where tabular clotted microbialites (base of Unit 6b) rests directly on top of the second calcarenite.

Tabular clotted microbialites typically occur in the lower part of Unit 6b. In contrast, domical microbialites characterize the upper half of Unit 6b, where coquinoid lenses of benthic open-marine faunas dominated by bivalves accumulated between the domes (Hautmann et al., 2015). Exquisite preservation of these fossils suggests a short transport and quick burial. Micritic fringes of the shells also support the interpretation of carbonate supersaturated waters (Hautmann et al., 2015). The uppermost lenses in Shanggan (Brühwiler et al., 2008) and Youping yielded small-sized specimens of *Ophiceras* sp. indet. This observation also indicates increasing open marine conditions. A modest deepening within Unit 6b at Wuzhuan is also corroborated by the scarcity of conodonts in the tabular clotted microbialites compared to their diversity and relative abundance within the domical microbialites (Brosse et al., 2015).

The frequent development of domical microbialite in the upper part of the BETM is documented in other sections from South China (e.g. Ezaki et al., 2003, 2008; Yang et al., 2011). However, this change in morphology from tabular to domical thrombolites of South Chinese BETM does not occur in all sections and tabular microbialites may be the persistent macrostructure (Kershaw, 2004). The distribution of these different macrostructures is usually related to bathymetry in equatorial shallow marine settings. However, how tabular versus domical morphologies are controlled by water depth has led to diverging interpretations. On one hand, Ezaki et al. (2003) argued that planar (or tabular) thrombolites grew in low energy, shallow to deep subtidal settings, and domical microbialites grew in intertidal environments. This led Ezaki et al. (2003) to infer a shallowing-upward trend. On the other hand, Kershaw et al. (2011) favored a deepening-upward model on the basis of this change in macrostructure. Based on the ecological significance of the observed faunal content as outlined above, our data indicate that the transition from tabular to domical microbialites within Unit 6b coincides with deepening.

6.4. Cessation of the BETM (Units 7 and 8)

The cessation of the BETM yields highly relevant constraints about what environmental parameters played a role in the deposition of the BETM or not. The transition of the top of the microbial limestone to the next overlying mudstone-wackestone in Tienbao (Fig. 14c, d) and Wuzhuan indicates that the growth of microbial buildups was interrupted by a rapid burial that marks a drowning event throughout the Luolou Platform. Very few sections (e.g. Dajiang and Dawen) lack this drowning event and these typically belong to long-lived horsts (e.g. the GBG). In most sections of the Luolou Platform, the drowning event is also accompanied by deposition of a volcanogenic sandstone (Unit 7, which is labeled as Horizon 2 in Baresel et al. 2016a). In Tienbao and Wuzhuan sections, the mudstone-wackestone episode does not exceeds one meter in thickness and is overlain by the volcanogenic sandstone marker (Fig. 14c, d). It is abruptly followed by thin- to medium-bedded (10–30 cm) shaly micritic limestone and dark, laminated, more or less calcareous mudstone (Unit 8). This unit laterally expands to the adjacent troughs where it grades upward from the basal Triassic carbonaceous black shales. Where not weathered, the black mudstone part of Unit 8 resembles the basal Griesbachian carbonaceous black shales of the base of the Ziyun Fm. that was deposited in the intervening deeper water downthrown blocks (Fig. 19). In contrast with the Luolou Platform, the boundary between the Late Permian deep-water Dalong Fm. and the Early Triassic Ziyun Fm. shows no detectable unconformity. The new Bayesian age model of Baresel et al. (2016b) indicates that the Dalong-Ziyun boundary overlaps within errors with the age calibration of the PTB in Meishan GSSP. In the Luolou Fm., volcanogenic sandstones are exceptional and form basin-wide laterally continuous markers such as the Green Bean Rock of late Spathian age (Galfetti et al., 2007; Ovtcharova et al., 2006, 2015). Hence, the volcanogenic sandstone that caps the microbial limestone likely represents a single depositional event considered as a synchronous marker with respect to the cessation of the microbial limestone. The thickness of this volcanogenic greywacke of Griesbachian age varies laterally from a few centimeters up to five meters, suggesting that deposition of remobilized ash layer(s) was largely controlled by local submarine topography. In Wuzhuan, the greywacke occurs between the Griesbachian conodont unitary associations UAZ5 and UAZ6 (Brosse et al., 2015, 2016a). The genesis of such greywackes implies the presence of shallower depositional settings where unconsolidated volcanic ashes can be raised in suspension before settling down again or before being transported as gravity flows at greater depth. Genesis of such greywacke was likely triggered by quakes that release tectonic stress that accumulates in pull-apart basins. In Taiping, the base of the greywacke contains lenses of brecciated microbial limestone, thus highlighting the role of block faulting in this drowning event. This marker bed is not reported from persistently uplifted blocks (e.g. Dawen, see Chen et al., 2009 and Dajiang, see Payne et al., 2004).

Thickness of microbial limestone also varies laterally, from <4 m in Tienbao and Taiping (Fig. 3) to ca. 17 m in Dawen (Chen et al., 2009). Making the simplistic assumption of an approximately constant sedimentation rate for this unit, these lateral variations open up the possibility that cessation of the microbialites within the Nanpanjiang Basin is diachronous. However, all our sections within the Luolou Platform show that the microbial limestone, whatever its thickness, is always capped by the same volcanogenic sandstone as identified by the chemistry of accessory volcanic minerals and U-Pb ages (Baresel et al.,2016a). The presence of this laterally widespread marker bed gives an upper age limit for the cessation of the microbialites and suggests variable sedimentation rates of the microbialites across the different sections. The poor conodont record of Dawen (Chen et al., 2009; see Brosse et al., 2016a) does not allow detecting a diachronous cessation between the GBG and the Luolou Platform. However, correlation of the carbon isotope record between the Luolou Platform and the GBG indicates a diachronous cessation of the microbialites. In Tienbao and Wuzhuan, the $\delta^{13}C_{carb}$ values remain stable and close to 0‰ across the upper limit of the microbial limestone. Although the precise position of this upper boundary in Dajiang and Dawen is at variance between different authors (compare Payne et al., 2004 with Chen et al., 2009 and Jiang et al., 2014), this boundary is nevertheless associated with a $\delta^{13}C$ values close to 1‰ and within a positive trend unknown from sections outside the GBG. Pending improvements of the conodont record, the carbon isotope record suggests that cessation of the microbial limestone occurred later in the GBG than in the Luolou Platform. Here again, the pattern of this diachronism in time and space was shaped by the submarine paleotopography directly controlled by regional geodynamic constraints. In other words, microbialites thrived longer on shallow-water horsts (e.g. GBG) that escaped blanketing by clastic sediments, while their cessation was concomitant with the earlier drowning and clastic blanketing of the Luolou Platform. Hence, any instantaneous changes in the chemical composition of the water column or in upwelling being turned on or off (Kershaw et al., 2007) are not likely to be among the potential causes that led to the diachronous cessation of the microbial limestone throughout the Nanpanjiang Basin. A further observation compatible with the absence of causal relation with water chemistry is found in the deposition of black shales in intervening troughs (Baresel et al., in revision) that outlasted that of the microbialites on the horsts.

Some authors (e.g. Schubert and Bottjer, 1992; Lehrmann, 1999; Pruss et al., 2006) advocated that microbialites flourished in equatorial shallow waters because of the lack of predation pressure, most grazers having supposedly gone extinct. Main grazer groups in the Early Triassic include echinoids and gastropods. Gastropods do frequently occur and were already diversified within the microbialites of the Nanpanjiang Basin (Payne et al., 2006; Kaim et al., 2010; Hautmann et al., 2011, 2015). Hence, the blooming of microbialites cannot be readily assigned to the absence of grazers. Along the same line of thought, the cessation of the BETM did not coincide with any detectable increase in the abundance of grazers.

The cessation of the microbialites does not display a unique pattern within the South China Block. In the Luodian area, its cessation is stepwise rather than abrupt (Ezaki et al., 2008), while it is abrupt and sudden in eastern Sichuan Province (Kershaw et al., 2002; Ezaki et al., 2003). Moreover, there are other sections where the microbialite unit is capped by oolitic limestone, thus suggesting that shallowing was the cause of the cessation. For instance at Yudongzi (Sichuan Province), the microbialite unit is overlain by a regressive oncolitic and oolitic limestone (Kershaw et al., 2012a). In addition, microbialite units in Chongyang (Hubei Province), Cili (Hunan Province), Xiushui (Jiangxi Province) (Yang et al., 2011; Li et al., 2015b) and Hochang (GBG) (Lehrmann et al., 2015a) are also overlain by oolitic limestone (Yang et al., 2011; Li et al., 2015b). In such sections with oolitic limestone, cessation of the microbial limestone cannot be assigned to a change in carbonate supersaturation, but resulted again from a change in bathymetry.

Although microbial limestone of Griesbachian age was deposited during a global sea-level rise that followed the PTB regressive event and its associated hiatus (Kershaw et al., 2012a; Yin et al., 2014), cessation of microbialites was largely controlled by regional subsidence or uplift superimposed to a global sea-level rise. Western Tethyan sections show differences in the mode of cessation of microbialites. Stromatolites from Bükk Mountains (Hungary) are gradually diminishing upward. While increasing clastic supply through intensified weathering may equally have contributed to the end of the BETM, a sea-level rise is the most likely explanation for the deposition of overlying calcareous mudstone (Hips and Haas, 2006). In the Çürük Dag section (Turkey), the microbialites are overlain by ca. 25 m of oolitic grainstone-packstone and followed by Early Triassic shale (Baud et al., 2005, 2009). Grouped with the underlying microbialites, this carbonate unit has been labelled as "calcimicrobial caprock" by Baud et al. (2005). Here again, reduced bathymetry leading to oolite deposition precedes drowning and deposition of siliciclastics. Kershaw et al. (2011) suggested that local tectonic uplift might have been overridden by the first-order sea-level rise for this succession.

In agreement with Kershaw et al. (2012a), the comparison between different sections from South China and from western Tethys suggests that the global sea-level rise during upper Griesbachian times should be the primary controlling factor for the cessation of the BETM, regardless of the variability induced by local tectonics. Time and space distribution of the BETM indicate that bathymetry controlled by regional subsistence or uplift locally modulated the development and cessation of the BETM.

6.5. Water chemical composition

The chemical composition of the water in which the BETM was bathed can be indirectly assessed by the ecological significance of its faunal content. Microbialites are known to be relatively immune to salinity changes (e.g. Dill et al., 1986; Riding, 2000; Kershaw et al., 2011). However, mass abundances of low-diversity assemblages that are a common signature for abnormal salinity (Fürsich, 1993) are unknown from the BETM, thus suggesting normal salinity. The highly diversified benthos recovered from the domical microbialites (Kaim et al., 2010; Hautmann et al., 2011, 2015; Forel et al., 2013) provides a robust argument in support of normal oxygen content and pH. Furthermore, the fine preservation of these benthic faunas also supports the presence of carbonate supersaturated water (Hautmann et al., 2015). The presence of millimetric to centimetric calcite fans (Fig. 12a, d) in Unit 6 also supports a carbonate supersaturation of the upper part of the water column. In Turkey and Iran (Kershaw et al., 2011; Heydari et al., 2013), basal Triassic microbialites are associated with volumetrically more important calcite fans than in the Nanpanjiang Basin. In addition, carbonate supersaturation is known to favor different types of microbialites (Riding, 2005), as observed in the basal Early Triassic. In conjunction with reduced bathymetry and higher energy, carbonate supersaturation (Groves and Calner, 2004; Calner, 2005; Li et al., 2015a,b; Deng et al., 2016) also contributed to the local production of oolites overlying the BETM.

Facies distribution and conodont age constraints of Griesbachian rocks in the Nanpanjiang Basin indicate that anoxic conditions (black shales) straddled the sediment-water interface only in grabens adjacent to the microbialite-bearing horsts. The paleogeographic proximity of carbonaceous ($CaCO_3$ yield comprised between 30 and 50%) and anoxic black shales in the neighboring troughs (Fig. 19) suggests a strong stratification of the water column, somewhat reminiscent of the present-day Black Sea (Kershaw, 2015). It also suggests that carbonate deposition was not restricted to the horsts, but that a modest carbonate flux was exported from the horsts into the grabens. Absence of fine siliciclastics on the microbialite-bearing horsts stands in sharp contrast with their accumulation in lateral anoxic troughs. Wave and storm agitation in the uppermost part of the water column precluded the deposition of siliciclastics on microbialite-bearing horsts and maintained normal oxygen levels in the upper water column. Whether the production of oxygen by microbial photosynthesis alone (Forel et al., 2013) was quantitatively sufficient to sustain the diversified benthos remains an open question. Carbonate supersaturation probably did not cease with the termination of the BETM, as shown by the occasional overlying oolitic and oncolitic grainstone (e.g. Deng et al., 2016) or by the recurrence of later Early Triassic microbialites (Baud et al., 2007; Brayard et al., 2011; Luo et al., 2014b; Saito et al., 2015; Liu et al., 2016). Nor did the isotopic composition of the carbonate carbon reservoir undergo any detectable change with the transition from the BETM to the overlying shaly micritic limestone (see Tienbao section, Fig. 3). Payne et al. (2007) hypothesized that the origin of the Early Triassic carbonate saturation could be sought in the dissolved underlying shallow water carbonates of late Permian age. Kershaw et al. (2012a) suggested that the carbonate supersaturation did not undergo drastic changes across the PTB on the basis of the respective amounts of inorganic cement in pre- and post-extinction carbonate. On the whole, any long term change in supersaturation before, during and after the BETM remains elusive. However, brief undersaturation of the ocean is nevertheless needed during any episode of acidification and dissolution of Permian carbonate. A global sea-level rise, the regional tectonic drowning, and the transition to a more humid global climate (Algeo and Twitchett, 2010; Hochuli et al., 2016) may all have contributed to the sharp transition from the BETM to a siliciclastic-dominated sedimentation on the Luolou Platform.

7. Conclusions

1- Within the Nanpanjiang pull-apart basin, contrasted paleotopography directly inherited from Late Permian times controlled the spatial distribution of basal Early Triassic sediments, microbialites blooming on horsts and carbonaceous black shales simultaneously accumulating in adjacent troughs. The BETM of the Luolou Platform extended over a large uplifted block exceeding 12,000 km^2 (Luolou Platform) centered on northwestern Guangxi.

2- On the Luolou Platform, the youngest preserved Permian bed is frequently an ash layer whose identity and uniqueness was established by means of apatite chemistry and U-Pb ages (Baresel et al., 2015, 2016a). This ash layer likely acted as a shield against dissolution caused by any episode(s) of acidification. This maker places a regional lower boundary to the hiatus associated with PTB.

3- The next overlying layer is a bioclastic grainstone essentially composed of winnowed and reworked Late Permian foraminifers, showing evidence of early cementation. This high- energy episode contrasts with the underlying Heshan Fm. and documents a regressive episode. A negative ca.1‰ jump associated with the bioclastic grainstone is superimposed to the overall decreasing trend in carbonate carbon isotope composition. It indicates a substantial stratigraphic hiatus coincident with the PTB formational change on horsts, as previously detected by conodont Unitary Associations (Brosse et al., 2016a). Any chemical dissolution of the youngest Permian carbonate rocks would equally contribute to this discontinuous pattern of the carbon isotope record.

4- Before deposition of the main microbialite body, up to five Event Surfaces are recognized in sections where accommodation space was available. These surfaces amalgamated where accommodation space was insufficient. These Event Surface place a regional upper boundary to the PTB hiatus.

5- The contact between the bioclastic grainstone and the overlying microbialites shows different characteristics in the studied sections. At Tienbao and Nanem, the contact is characterized by an undulating irregular relief, the presence of an iron oxide crust, bioerosion, and cuts through Permian grains and groundmass, which can be common features to both subaerial exposures and submarine hardgrounds. However, no direct evidence of subaerial exposure could be detected at the level of microfabrics, but deposition of reworked grainstone containing exclusively Permian foraminifers implies mechanical erosion. The contact at Longyuan is represented by a smooth surface and is lacking any evidence in support of subaerial exposure or submarine hardground. Triassic foraminifers (e.g. *Cornuspira* (= *Postcladella*)) occur within the basal microbial episode, thus excluding any Permian age assignment of the base of the BETM.

6- In Nanem and Wuzhuan, a second bioclastic ooid packstone-grainstone is intercalated between the first microbial bed and the main microbialite body. It also yields reworked Permian bioclasts and foraminifers. These two sections document cycles of deposition of reworked Permian material followed by microbial growth. This alternation indicates that minor bathymetric fluctuations may have controlled the detailed onset of microbialites. Where accommodation was insufficient, these cycles are replaced by an amalgamation surface.

7- In all studied sections, microbialites are generally represented by stromatolites, tabular and domical thrombolites, and dendrolites. Domical microbialites are restricted to the upper part of the BETM. The open marine benthic fauna that typically occurs between the domes, as well as the relative abundance of conodonts and the earliest occurrence of ammonoids all indicate that the change from tabular to domical microbialtes was a response to a stepwise increase in bathymetry.

8- An abrupt regional drowning, largely controlled by synsedimentary faulting, is involved in the cessation of microbialites in the Luolou Platform. Alternatively, smaller scale tectonic uplifts also led to the cessation of the BETM and its capping by oolitic grainstone as documented in the GBG (Lehrmann et al., 2015a). Although the conodont record is not dense enough to demonstrate synchronicity or diachronism of the cessation of the BETM, blanketing by a laterally widely distributed volcanogenic sandstone provides a synchronous marker that may (Shanmenhai, Taiping, Longyuan, Nanem) or may not (e.g. Wuzhuan, Tienbao) directly rest on top of the microbialites. This minor lateral variation suggest that cessation of microbialites was not perfectly synchronous within in the Luolou Platform, as would be expected if their deposition was exclusively controlled by water chemistry at the basin scale. Comparison with other equatorial BETM sections from the northern Yangtze Platform and from outside South China nevertheless suggests that a concomitant global sea-level rise was involved in the cessation of the BETM, as well. The combined effects of regional tectonics and of a global sea-level rise, possibly coupled with increasing weathering rates, shaped the detailed pattern of the cessation of the BETM in time and space.

9- Biota associated with the BETM in the Nanpanjiang Basin indicates normal oxygenation and salinity. Presence of calcite fans and ooids support carbonate supersaturation of the upper part of the water column where microbialites thrived. Absence of siliciclastics on the microbialite-harboring horsts indicates high energy levels that also insured sufficient oxygenation. Adjacent anoxic troughs indicate very limited or no vertical mixing in the water column. The Early Triassic massive reduction of calcifying metazoans has been listed among the potential causes that would have increase the alkalinity of oceanic waters (Clarkson et al., 2015). Dissolution of Permian carbonates has also been evoked as a possible contribution to supersaturation (Payne et al., 2007). However, carbonate supersaturation did not significantly changed across the PTB as shown by the respective amounts of inorganic cement in pre- and post-extinction carbonate (Kershaw et al., 2012a; Baud et al., 2013). Although deep anoxic waters restricted to neighboring grabens may have been an alkaline source, the normal metazoan biota documented from the microbialite-bearing horsts does not support any sustained upwelling of anoxic waters. The occasional deposition of oolitic grainstone capping the BETM also indicates that carbonate supersaturation did equally persist after microbialites ceased blooming. Therefore, a close relation between deposition of microbialites and a coeval change in supersaturation state remains unsubstantiated. Only very short episodes of undersaturation must have accompanied any carbonate dissolution involved into the genesis of the PTB hiatus in shallow water platforms.

Supplementary data to this article can be found online at http://dx.doi.org/10.1016/j.gr.2016.11.013.

Acknowledgments

Comments on an earlier version of the manuscript by Michael Hautmann and very constructive reviews by Arnaud Brayard, Steve Kershaw, Sylvain Richoz, and editor Ian D. Somerville are deeply acknowledged. Urs Schaltegger is thanked for long term scientific discussions. This research is supported by the Swiss NSF project 200021_135446 (to H.B.) and 200020_156422 (to R.M.). We thank James Neenan for improving the English Text. Jiang Dayong (Peking University) kindly helped with administrative constraints and logistics.

References

Abdolmaleki, J., Tavakoli, V., 2016. Anachronistic facies in the early Triassic successions of the Persian Gulf and its palaeoenvironmental reconstruction. Palaeogeogr. Palaeoclimatol. Palaeoecol. 446, 213–224.

Adachi, N., Ezaki, Y., Liu, J., 2004. The fabrics and origins of peloids immediately after the end-Permian extinction, Guizhou Province, South China. Sediment. Geol. 164, 161–178.

Algeo, T.J., Twitchett, R.J., 2010. Anomalous Early Triassic sediment fluxes due to elevated weathering rates and their biological consequences. Geology 38, 1023–1026.

Algeo, T.J., Ellwood, B., Thoa Nguyen, T.K., Rowe, H., Maynard, J.B., 2007. The Permian–Triassic boundary at Nhi Tao, Vietnam: evidence for recurrent influx of sulfidic watermasses to a shallow-marine carbonate platform. Palaeogeogr. Palaeoclimatol. Palaeoecol. 252, 304–327.

Altiner, D., Brönnimann, P., 1980. Louisettita elegantissima, nov. gen. nov. sp., un nouveau foraminifère du Permien supérieur du Taurus oriental (Turquie). Notes du Laboratoire de Paléontologie de l'Université de Genève 6 (3), 39–43.

Awramik, S.M., 1990. Stromatolites. In: Briggs, D.E.G., Crowther, P.R. (Eds.), Palaeobiology: A Synthesis. Blackwell Scientific Publications, London, pp. 336–341.

Baresel, B., Bucher, H., Brosse, M., Bagerphour, B., Schaltegger, U., 2015. Ultra-high precision dating of mass extinction events: a combined zircon geochronology, apatite tephrochronology, and Bayesian age modelling approach of the Permian-Triassic boundary extinction. 13th Swiss Geoscience Meeting, Basel.

Baresel, B., d'Abzac, F.X., Bucher, H., Schaltegger, U., 2016a. High-precision time-space correlation through coupled apatite and zircon tephrochronology: an example from the Permian-Triassic boundary in South China. Geology http://dx.doi.org/10.1130/G38181.1 (in press).

Baresel, B., Bucher, H., Brosse, M., Cordey, F., Guodun, K., Schaltegger, U., 2016b. Precise age for the Permian-Triassic boundary in South China from high precision U-Pb geochronology and Bayesian age-depth modelling. Solid Earth http://dx.doi.org/10.5194/se-2016-145 (in review).

Baresel, B., Bucher, H., Bagherpour, H., Brosse, M., Guodun, K., Schaltegger, U., From icehouse to hothouse: timing of the global regression marking the Permian-Triassic boundary crisis and of the following microbial bloom. Sci. Rep. (in revision)

Bartley, J.K., Knoll, A.H., Grotzinger, J.P., Sergeev, V.N., 2000. Lithification and fabric genesis in precipitated stromatolites and associated peritidal carbonates, Mesoproterozoic Billyakh Group, Siberia. In: Grotzinger, J.P., James, N.P. (Eds.), Precambrian Carbonates, 65. Society of Economic Paleontologists and Mineralogists Special Publication, Tulsa, Oklahoma, pp. 59–74.

Baud, A., 1996. The Permian-Triassic boundary: recent developments, discussion and proposals. Albertiana 18, 6–9.

Baud, A., Richoz, S., 2009. The Permian-Triassic transition at the Demirtas section. In: Crasquin, et al. (Eds.), IGCP 572 Field Guide Book: The Permian-Triassic Transition in the Southwestern Taurus Mountains (South Turkey), Volume Field Guide Book 1: Antalya, pp. 29–35.

Baud, A., Cirilli, S., Marcoux, J., 1997. Biotic response to mass extinction: the Lowermost Triassic microbialites. Facies 36, 238–242.

Baud, A., Richoz, S., Cirilli, S., Marcoux, J., 2002. Basal Triassic carbonate of the Tethys: a microbialite world. 16th International Sedimentological Congress, Johannesburg, Abstract Volume, 24–25.

Baud, A., Richoz, S., Marcoux, J., 2005. Calcimicrobial cap rocks from the basal Triassic units: western Taurus occurrences (SW Turkey). C.R. Palevol 4, 569–582.

Baud, A., Richoz, S., Pruss, S., 2007. The Lower Triassic anachronisitic carbonate facies in space and time. Glob. Planet. Chang. 55, 81–89.

Baud, A., Crasquin, S., Forel, M.B., Richoz, S., 2009. The Permian-Triassic transition at the Çürük dag section (South Turkey). In: Craquin, et al. (Eds.), IGCP 572 Field Guide Book: The Permian-Triassic Transition in the Southwestern Taurus Mountains (South Turkey), Antalya, pp. 19–28.

Baud, A., Bucher, H., Brosse, M., Frisk, A., Guodun, K., 2013. Stromatactis limestone below and above the Permian-Triassic boundary event: evidence of sponge microbial build-up. In: Zhong-Qiang, C., Hao, Y., Genming, L. (Eds.), World Summit on P-Tr Mass Extinction & Extreme Climate Change. State Key Laboratory of Biogeology and Environmental Geology, China University of Geosciences, Wuhan, China, pp. 8–9.

Baud, A., Goudemand, N., Brosse, M., Frisk, Å.M., Bucher, H., Richoz, S., 2014. Oman oases: contrasting carbonates sediments on the Gondwana margin in the immediate aftermath of the Permian-Triassic boundary mass extinction. In 19th International Sedimentological Congress 2014, Geneva, Switzerland, Abstract Book, 54.

Brandner, R., 1988. The Permian-Triassic Boundary in the Dolomite (Southern Alp, Italy), San Antonio Section. Ber. Geol. Bundesanst. 15, 49–56.

Brandner, R., Horacek, M., Keim, L., 2013. Permian-Triassic-boundary and Lower Triassic in the Dolomites, Southern Alps (Italy), field trip guide. J. Alp. Geol. 54, 379–404.

Brayard, A., Vennin, E., Olivier, N., Bylund, K.G., Jenks, J., Stephen, D.A., Bucher, H., Hofmann, R., Goudemand, N., Escarguel, G., 2011. Transient metazoan reefs in the aftermath of the end-Permian mass extinction. Nat. Geosci. 4, 693–697.

Brönnimann, P., Zaninetti, L., Bozorgnia, F., 1972. Triassic (Skythian) smaller foraminifera from the Elika Formation of the central Alborz, northern Iran, and from the Siussi

Formation of the Dolomites, northern Italy. Mitteilung Gesellschaft geologische Bergsbaustudien, Innsbruck 21 pp. 861–864.

Brosse, M., Bucher, H., Bagherpour, B., Baud, A., Frisk, Å., Guodun, A., Goudemand, N., 2015. Conodonts from the Early Triassic microbialite of Guangxi (South China): implications for the definition of the base of the Triassic System. Palaeontology 58 (3), 563–584.

Brosse, M., Bucher, H., Goudemand, N., 2016a. Quantitative biochronology of the Permian–Triassic boundary in South China based on conodont unitary associations. Earth Sci. Rev. 155, 153–171.

Brosse, M., Baud, A., Bucher, H., Goudemand, N., Nützel, A., Ware, D., Frisk, A., Hagdorn, H., 2016b. Basal Triassic exotic blocks from Oman: the promised land, no raft of the medusa. 14th Swiss Geoscience Meeting, Geneva.

Brosse, M., Bucher, H., Goudemand, N., 2016c. Reply to the comment on “Quantitative biochronology of the Permian-Triassic boundary in South China based on conodont unitary associations”. Earth-Sci. Rev. http://dx.doi.org/10.1016/j.earscirev.2016.07.015.

Brühwiler, T., Brayard, A., Bucher, H., Guodun, K., 2008. Griesbachian and Dienerian (Early Triassic) ammonoid faunas from northwestern Guangxi and southern Guizhou (south China). Palaeontology 51 (5), 1151–1180.

Burgess, S.D., Bowring, S., Shen, S.Z., 2014. High-precision timeline for Earth's most severe extinction. Proc. Natl. Acad. Sci. 111, 3316–3321.

Calner, M., 2005. A Late Silurian extinction event and anachronistic period. Geology 33, 305–308.

Chen, J., Beatty, T.W., Henderson, C.M., Rowe, H., 2009. Conodont biostratigraphy across the Permian-Triassic boundary at the Dawen section, Great Bank of Guizhou, Guizhou Province, South China: implications for the late Permian extinction and correlation with Meishan. J. Asian Earth Sci. 36 (2), 442–458.

Chivas, A.R., Torgersen, T., Polach, H.A., 1990. Growth rates and Holocene development of stromatolites from Shark Bay, Western Australia. Aust. J. Earth Sci. 37, 113–121.

Clarkson, M.O., Kasemann, S.A., Wood, R.A., Lenton, T.M., Daines, S.J., Richoz, S., Ohnemueller, F., Meixner, A., Poulton, S.W., Tipper, E.T., 2015. Ocean acidification and the Permo-Triassic mass extinction. Science 348 (6231), 229–232.

Collin, P.Y., Kershaw, S., Crasquin, S., Feng, Q., 2009. Facies changes and diagenetic processes across the Permian-Triassic boundary event horizon, Great Bank of Guizhou, South China: a controversy of erosion and dissolution. Sedimentology 56, 677–693.

Deng, B., Wang, Y., Woods, A., Li, S., Li, G., Chen, W., 2016. Evidence for rapid precipitation of calcium carbonate in South China at the beginning of Early Triassic. Palaeogeogr. Palaeoclimatol. Palaeoecol. http://dx.doi.org/10.1016/j.palaeo.2016.06.007 (in press).

Dill, R.F., Shinn, E.A., Jones, A.T., Kelly, K., Steinen, R.P., 1986. Giant subtidal stromatolites forming in normal salinity waters. Nature 324, 55–58.

Dunham, R.J., 1962. Classification of carbonate rocks according to depositional texture. AAPG Mem. 1, 108–121.

Elliott, G.F., 1958. Fossil microproblematica from the Middle East. Micropaleontology 4, 419–428.

Ezaki, Y., Liu, J., Adachi, N., 2003. Earliest Triassic microbialite micro to megastructures in the Huaying area of Sichuan Province, south China: implications for the nature of oceanic conditions after the end-Permian extinction. PALAIOS 18, 388–402.

Ezaki, Y., Liu, J., Nagano, T., Adachi, N., 2008. Geobiological aspects of the earliest Triassic microbialites along the southern periphery of the tropical Yangtze Platform: initiation and cessation of a microbial regime. PALAIOS 23, 356–369.

Fan, G., Wang, Y., Kershaw, S., Li, G., Meng, Z., Lin, Q., Yuan, Z., 2014. Recurrent breakdown of Late Permian reef communities in response to episodic volcanic activities: evidence from southern Guizhou in South China. Facies 60, 603–613.

Faure, M., Lin, W., Chu, Y., Lepvrier, C., 2016. Triassic tectonics of the southern margin of the South China Block. Compt. Rendus Geosci. 348, 5–14.

Feng, Z.Z., Bao, Z.D., Zheng, X.J., Wang, Y., 2015. There was no “Great Bank of Guizhou” in the Early Triassic in Guizhou Province, South China. J. Palaeogeogr. 4 (1), 99–108.

Flugel, E., 2004. Microfacies of Carbonate Rocks. Springer.

Forel, M.B., Crasquin, S., Kershaw, S., Collin, P.Y., 2013. In the aftermath of the end-Permian extinction: the microbialite refuge? Terra Nova 25, 137–143.

Friesenbichler, E., Baud, A., Krystyn, L., Sahakyan, L., Richoz, S., 2016. Basal Induan (Early Triassic) giant sponge-microbial build-ups in Armenia: microfacies analyses and carbon isotope studies. GSA Annual Meeting in Denver, Colorado, USA (Paper No. 225-11).

Fürsich, F.T., 1993. Palaeoecology and evolution of Mesozoic salinity-controlled benthic macroinvertebrate associations. Lethaia 26 (4), 327–346.

Galfetti, T., Bucher, H., Ovtcharova, M., Schaltegger, U., Brayard, A., Brühwiler, T., Goudemand, N., Weissert, H., Hochuli, P.A., Cordey, F., Goudun, K., 2007. Timing of the Early Triassic carbon cycle perturbations inferred from new U–Pb ages and ammonoid biochronozones. Earth Planet. Sci. Lett. 258, 593–604.

Galfetti, T., Bucher, H., Martini, R., Hochuli, P.A., Weissert, H., Crasquin, S.S., Brayard, A., Goudemand, N., Brühwiler, T., Guodun, K., 2008. Evolution of Early Triassic outer platform paleoenvironments in the Nanpanjiang Basin (South China) and their significance for the biotic recovery. Sediment. Geol. 204, 36–60.

Geinitz, H.B., Gutbier, A., 1848. Die Versteinerungen des Zechsteingebirges und Rothliegenden. 26 pp. (Heft 1). Arnold, Dresden.

Groves, J.R., Calner, M., 2004. Lower Triassic oolites in Tethys: a sedimentologic response to the end-Permian mass extinction. Geol. Soc. Am. Abstr. Programs 36 (5), 336.

Groves, J.R., Altiner, D., Boyce, M., Craig, B.J., 2003. “Disaster oolites” in the Permian-Triassic boundary interval, Tauride Mountains (Turkey). Geological Society of America, North-Central Section Meeting, Abstracts with Programs. Vol. 35 (2), p. 48.

Groves, J.R., Altiner, D., Rettori, R., 2005a. Extinction, survival, and recovery of Lagenide foraminifers in the Permian-Triassic boundary interval, Central Taurides, Turkey. Paleontological Society Memoir, Journal of Paleontology (supplement), 1–38.

Groves, J.R., Altiner, D., Rettori, R., 2005b. Decline and recovery of lagenide foraminifers in the Permian-Triassic boundary interval (Central Taurides, Turkey). Paleontol. Soc. Mem. 62 ([supplement to Journal of Paleontology, 79(4)]38 pp.).

Halpin, J.A., Tran, H.T., Lai, C.K., Meffre, S., Crawford, A.J., Zaw, K., 2016. U–Pb zircon geochronology and geochemistry from NE Vietnam: a ‘tectonically disputed’ territory between the Indochina and South China blocks. Gondwana Res. 34, 254–273.

Hautmann, M., Bucher, H., Brühwiler, T., Goudemand, N., Kaim, A., Nützel, A., 2011. An unusually diverse mollusc fauna from the earliest Triassic of South China and its implications for benthic recovery after the end-Permian biotic crisis. Geobios 44 (1), 71–85.

Hautmann, M., Bagherpour, B., Brosse, M., Frisk, A., Hofmann, R., Baud, A., Nützel, A., Goudemand, N., Bucher, H., 2015. Competition in slow motion: the unusual case of benthic marine communities in the wake of end-Permian mass extinction. Palaeontology 58 (5), 871–901.

Hermann, E., Hochuli, P.A., Méhay, S., Bucher, H., Brühwiler, T., Hautmann, M., Ware, D., Roohi, G., Rehman, K., Yaseen, A., 2011. Organic matter and palaeoenvironmental signals in the Early Triassic of the Salt Range and Surghar Range. Sediment. Geol. 234, 19–41.

Heydari, E., Arzani, N., Safaei, M., Hassanzadeh, J., 2013. Ocean's response to a changing climate: clues from variations in carbonate mineralogy across the Permian–Triassic boundary of the Shareza Section, Iran. Glob. Planet. Chang. 105, 79–90.

Hips, K., Haas, J., 2006. Calcimicrobial stromatolites at the Permian–Triassic boundary in a western Tethyan section, Bükk Mountains, Hungary. Sediment. Geol. 185, 239–253.

Hochuli, P.A., Sanson-Barrera, A., Schneebeli-Hermann, E., Bucher, H., 2016. Severest crisis overlooked-Worst disruption of terrestrial environments postdates the Permian-Triassic mass extinction. Nat. Sci. Rep. 6, 28372.

Jenny-Deshusses, C., 1985. Rectostipulina n. gen. (= Stipulina LYS, 1978), unorganisme incertae sedis du Permien supérieur de la Téthys moyen-orientale: description morphologique et remarques stratigraphiques. Revue de Paléobiologie 4 (1), 153–158.

Jiang, H., Aldridge, R.J., Lai, X., Yan, C., Sun, Y., 2011. Phylogeny of the conodont genera *Hindeodus* and *Isarcicella* across the Permian–Triassic boundary. Lethaia 44 (4), 374–382.

Jiang, H., Lai, X., Sun, Y., Wignall, P.B., Liu, J., Yan, C., 2014. Permian–Triassic conodonts from Dajiang (Guizhou, South China) and their implication for the age of microbialite deposition in the aftermath of the End-Permian mass extinction. J. Earth Sci. 25 (3), 413–430.

Kaim, A., Nützel, A., Bucher, H., Brühwiler, T., Goudemand, N., 2010. Early Triassic (Late Griesbachian) gastropods from South China (Shanggan, Guangxi). Swiss J. Geosci. 103 (1), 121–128.

Kershaw, S., 2004. Comment-Earliest Triassic microbialite micro- to megastructures in the Huaying area of Sichuan Province, south China: implications for the nature of oceanic conditions after the end-Permian extinction (Ezaki et al., 2003). PALAIOS 19, 414–416.

Kershaw, S., 2015. Modern Black Sea oceanography applied to the end-Permian extinction event. J. Palaeogeogr. 4 (1), 52–62.

Kershaw, S., Zhang, T., Lan, G., 1999. A ?microbialite crust at the Permian-Triassic boundary in south China, and its palaeoenvironmental significance. Palaeogeogr. Palaeoclimatol. Palaeoecol. 146, 1–18.

Kershaw, S., Guo, L., Swift, A., Fan, J., 2002. ?Microbialites in the Permian–Triassic boundary interval in central China: structure, age and distribution. Facies 47, 83–90.

Kershaw, S., Li, Y., Crasquin, S.S., Feng, Q., Mu, X., Collin, P.Y., Reynolds, A., Guo, L., 2007. Earliest Triassic microbialites in the South China block and other areas: controls on their growth and distribution. Facies 53, 409–425.

Kershaw, S., Crasquin, S., Forel, M.B., Randon, C., Collin, P.Y., Kosun, E., Richoz, S., Baud, A., 2011. Earliest Triassic microbialites in Cürük Dag, southern Turkey; composition, sequences and controls on formation. Sedimentology 58, 739–755.

Kershaw, S., Crasquin, S., Li, Y., Collin, P.Y., Forel, M.B., Mu, X., Baud, A., Wang, Y., Xie, S., Mauer, F., Guo, L., 2012a. Microbialites and global environmental change across the Permian–Triassic boundary: a synthesis. Geobiology 10, 25–47.

Kershaw, S., Crasquin, S.D., Li, Y., Collin, P.Y., Forel, M.B., 2012b. Ocean acidification and the end-Permian mass extinction: to what extent does evidence support hypothesis? Geosciences 2, 221–234.

Kershaw, S., Collin, P.Y., Crasquin, S., 2016. Comment to Lehrmann et al. New sections and observations from the Nanpanjiang Basin, South China. PALAIOS 31, 111–117.

Kozur, H., 2005. Pelagic uppermost Permian and the Permian–Triassic boundary conodonts of Iran. Part II: investigated sections and evaluation of the conodont faunas. Hallesches Jahrb. Geowiss. Reihe B 19, 49–86.

Kozur, H.W., 2007. Biostratigraphy and event stratigraphy in Iran around the Permian Triassic Boundary (PTB): implications for the causes of the PTB biotic crisis. Glob. Planet. Chang. 55 (1–3), 155–176.

Krainer, K., Vachard, D., 2011. The Lower Triassic Werfen Formation of the Karawanken Mountains (Southern Austria) and its disaster survivor microfossils, with emphasis on Postcladella n. gen. (Foraminifera, Miliolata, Cornuspirida). Revue de Micropaleontologie 54 (2), 59–85.

Krull, E.S., Lehrmann, D.J., Druke, D., Kessel, B., Yu, Y., Li, R., 2004. Stable carbon isotope stratigraphy across the Permian–Triassic boundary in shallow marine carbonate platforms, Nanpanjiang Basin, South China. Palaeogeogr. Palaeoclimatol. Palaeoecol. 204, 297–315.

Krystyn, L., Richoz, S., Baud, A., Twitchett, R.J., 2003. A unique Permian-Triassic boundary section from the Neotethyan Hawasina Basin, Central Oman Mountains. Palaeogeogr. Palaeoclimatol. Palaeoecol. 191, 329–344.

Leda, L., Korn, D., Ghaderi, A., Hairapetian, V., Struck, U., Reimold, W.U., 2014. Lithostratigraphy and carbonate microfacies across the Permian–Triassic boundary near Julfa (NW Iran) and in the Baghuk Mountains (Central Iran). Facies 60 (1), 295–325.

Lehrmann, D.J., 1999. Early Triassic calcimicrobial mounds and biostromes of the Nanpanjiang Basin, South China. Geology 27, 359–362.

Lehrmann, D.J., Jiayong, W., Enos, P., 1998. Controls on facies architecture of a large Triassic carbonate platform: the Great Bank of Guizhou, Nanpanjiang Basin South China. J. Sediment. Res. 68 (2), 311–326.

Lehrmann, D.J., Payne, J.L., Felix, S.V., Dillett, P.M., Wang, H., Yu, Y.Y., Wei, J.Y., 2003. Permian–Triassic boundary sections from shallow marine carbonate platforms of the Nanpanjiang Basin, South China: implications for oceanic conditions associated with the end-Permian extinction and its aftermath. PALAIOS 18, 138–152.

Lehrmann, D.J., Donghong, P., Enos, P., Minzoni, M., Ellwood, B.B., Orchard, M.J., Jiyan, Z., Jiayong, W., Dillett, P., Koenig, J., Steffen, K., Druke, D., Druke, J., Kessel, B., Newkirk, T., 2007a. Impact of differential tectonic subsidence on isolated carbonate platform evolution: Triassic of the Nanpanjiang basin, south China. Am. Assoc. Pet. Geol. Bull. 91 (3), 287–320.

Lehrmann, D.J., Payne, J.L., Pei, D., Enos, P., Druke, D., Steffen, K., Zhang, J., Wei, J., Orchard, M.J., Ellwood, B., 2007b. Record of the end-Permian extinction and Triassic biotic recovery in the Chongzuo–Pingguo platform, southern Nanpanjiang Basin, Guangxi, South China. Palaeogeogr. Palaeoclimatol. Palaeoecol. 252, 200–217.

Lehrmann, D.J., Bentz, J.M., Wood, T., Goers, A., Dhillon, R., Akin, S., Li, X., Payne, J.L., Kelley, B.M., Meyer, K.M., Schaal, E.K., Suarez, M.B., Yu, M., Qin, Y., Li, R., Minzoni, M., Henderson, C.M., 2015a. Environmental controls on the genesis of marine microbialites and dissolution surface associated with the end-Permian mass extinction: new sections and observations from the Nanpanjiang basin, South China. PALAIOS 30, 529–552.

Lehrmann, D.J., Stepchinski, L., Altiner, D., Orchard, M.J., Montgomery, P., Enos, P., Ellwood, B.B., Bowring, S.A., Ramezani, J., Wangh, H., Wei, J., Yu, M., Griffiths, J.D., Minzoni, M., Schaal, E.K., Li, X., Meyer, K.M., Payne, J.L., 2015b. An integrated biostratigraphy (conodonts and foraminifers) and chronostratigraphy (paleomagnetic reversals, magnetic susceptibility, elemental chemistry, carbon isotopes and geochronology) for the Permian–Upper Triassic strata of Guandao section, Nanpanjiang Basin, south China. J. Asian Earth Sci. 108, 117–135.

Lehrmann, D.J., Bentz, J.M., Wood, T., Goers, A., Dhillon, R., Akin, S., Li, X., Payne, J.L., Kelley, B.M., Meyer, K.M., Schaal, E.K., Suarez, M.B., Yu, M., Qin, Y., Li, R., Minzoni, M., Henderson, C.M., 2016. Reply: Permian–Triassic microbialite and dissolution surface environmental controls on the genesis of marine microbialites and dissolution surface associated with the end-Permian mass extinction: new sections and observations from the Nanpanjiang Basin, South China. PALAIOS 31, 118–121.

Li, X., Yu, M., Lehrmann, D.J., Payne, J.L., Kelley, B.M., Minzoni, M., 2012. Factors controlling carbonate platform asymmetry: Preliminary results from the Great Bank of Guizhou, an isolated Permian–Triassic Platform in the Nanpanjiang Basin, south China. Palaeogeogr. Palaeoclimatol. Palaeoecol. 315-316, 158–171.

Li, T., Bottjer, D., Tong, J., Li, F., Yang, T., Song, H., Song, H., Liang, L., 2015a. Distribution and size variation of ooids in the aftermath of the Permian-Triassic mass extinction. PALAIOS 30 (9), 714–727.

Li, F., Yan, J., Chen, Z.Q., Ogg, J.G., Tian, L., Korngreen, D., Liu, K., Ma, Z., Woods, A.D., 2015b. Global oolite deposits across the Permian–Triassic boundary: a synthesis and implications for palaeoceanography immediately after the end-Permian biocrisis. Earth Sci. Rev. 149, 163–180.

Liu, J.B., Ezaki, Y., Yang, S.R., Wang, H.F., Adachi, N., 2007. Age and sedimentology of microbialites after the end-Permian mass extinction in Luodian, Guizhou Province. J. Palaeogeogr. 9, 473–486 (In Chinese).

Liu, S., Wang, J., Yin, F., Xie, T., Hu, S., Guan, X., Zhang, Q., Zhou, C., Cheng, W., Xu, J., 2016. Early Triassic stromatolites from the Xingyi area, Guizhou Province, southwest China: geobiological features and environmental implications. Carbonates Evaporites http://dx.doi.org/10.1007/s13146-016-0318-1.

Luo, G., Algeo, T.J., Huang, J., Zhou, W., Wang, Y., Yang, H., Richoz, S., Xie, S., 2014a. Vertical δ13Corg gradients record changes in planktonic microbial community composition during the end-Permian mass extinction. Palaeogeogr. Palaeoclimatol. Palaeoecol. 396, 119–131.

Luo, M., Chen, Z.Q., Zhao, L., Kershaw, S., Huang, J., Wu, L., Yang, H., Fang, Y., Huang, Y., Zhang, Q., Hu, S., Zhou, C., Wen, W., Jia, Z., 2014b. Early Middle Triassic stromatolites from the Luoping area, Yunnan Province, Southwest China: Geobiologic features and environmental implications. Palaeogeogr. Palaeoclimatol. Palaeoecol. 412, 124–140.

Marcoux, J., Baud, A., 1986. The Permo-Triassic boundary in the Antalya Nappes (western Taurides, Turkey). Mem. Soc. Geol. Ital. 34, 243–252.

Marenco, P.J., Griffin, J.M., Fraiser, M.L., Clapham, M.E., 2012. Paleoecology and geochemistry of Early Triassic (Spathian) microbial mounds and implications for anoxia following the end- Permian mass extinction. Geology 40 (8), 715–718.

Maslov, V.N., 1956. Iskopaemye izvestkovye vodorosli SSSR. Akademya nauk SSSR, Trudy instituta geologicheskikh Nauk, Vypusk (297 pp).

Monty, C., 1976. The origin and development of cryptalgal fabrics. In: Stromatolites (Ed. M.R. Walker). Dev. Sedimentol. 20, 193–250.

Mu, X., Kershaw, S., Yue, L., Guo, L., Qi, Y., Reynolds, A., 2009. High-resolution carbon isotope changes in the Permian–Triassic boundary interval, Chongqing, South China; implications for control and growth of earliest Triassic microbialites. J. Asian Earth Sci. 36 (6), 434–441.

Olivier, N., Brayard, A., Fara, E., Bylund, K.G., Jenks, J.F., Vennin, E., Stephen, D.A., Escarguel, G., 2014. Smithian Shoreline migrations and depositional settings in Timpoweap Canyon (Early Triassic, Utah, USA). Geol. Mag. 151, 938–955.

Olivier, N., Brayard, A., Vennin, E., Escarguel, G., Fara, E., Bylund, K.G., Jenks, J.F., Caravaca, G., Stephen, D.A., 2016. Evolution of depositional settings in the Torrey area during the Smithian (Early Triassic, Utah, USA) and their significance for the biotic recovery. Geol. J. 51, 600–626.

Ovtcharova, M., Bucher, H., Schaltegger, U., Galfetti, T., Brayard, A., Guex, J., 2006. New early to middle Triassic U-Pb ages from South China: calibration with the ammonoid biochronozones and implications for the timing of the Triassic biotic recovery. Earth Planet. Sci. Lett. 243, 463–475.

Ovtcharova, M., Goudemand, N., Hammer, Ø., Goudun, K., Cordey, F., Galfetti, T., Schaltegger, U., Bucher, H., 2015. Developing a strategy for accurate definition of a geological boundary through radio-isotopic and biochronological dating: the Early–Middle Triassic boundary (South China). Earth Sci. Rev. 146, 65–76.

Payne, J.L., Lehrmann, D.J., Wei, J., Orchard, M.J., Schrag, D.P., Knoll, A.H., 2004. Large perturbations of the carbon cycle during recovery from the end-Permian extinction. Science 305 (5683), 506–509.

Payne, J.L., Lehrmann, D.J., Wei, J., Knoll, A.H., 2006. The pattern and timing of biotic recovery from the end- Permian extinction on the Great Bank of Guizhou, Guizhou Province, China. PALAIOS 21, 63–85.

Payne, J.L., Lehrmann, D.J., Follett, D., Seibel, M., Kump, L.R., Riccardi, A., Altiner, D., Sano, H., Wei, J., 2007. Erosional truncation of uppermost Permian shallow-marine carbonates and implications for Permian–Triassic boundary events. Geol. Soc. Am. Bull. 119, 771–784.

Pruss, S.B., Bottjer, D.J., Corsetti, F.A., Baud, A., 2006. A global marine sedimentary response to the end-Permian mass extinction: examples from southern Turkey and the western United States. Earth-Sci. Rev. 78, 193–206.

Raup, D.M., 1979. Size of the Permo-Triassic bottleneck and its evolutionary implications. Science 206, 217–218.

Reichel, M., 1945. Sur quelques foraminifères nouveaux du Permien méditerranéen. Eclogae Geol. Helv. 38 (2), 524–560.

Reitlinger, E.A., 1965. Razvitie foraminifer v pozdnepermskogo i rannetriasovyuf epokhi na territorii Zakavkazya (Development of the foraminifers in the Late Permian and Early Triassic times in Transcaucasia). Voprosy Mikropaleontologii 9, 45–70 (in Russian).

Richoz, S., Krystyn, L., Baud, A., Brandner, R., Horacek, M., Mohtat-Aghai, P., 2010. Permian Triassic boundary interval in the Middle East (Iran and N. Oman): progressive environmental change from detailed carbonate carbon isotope marine curve and sedimentary evolution. J. Asian Earth Sci. 39, 236–253.

Ricou, L.E., 1994. Tethys reconstructed: plates, continental fragments and their boundaries since 260 Ma from central America to south-eastern Asia. Geodyn. Acta 7 (4), 169–218.

Riding, R., 2000. Microbial carbonates: the geological record of calcified bacterial-algal mats and biofilms. Sedimentology 47, 179–214.

Riding, R., 2005. Phanerozoic reefal microbial carbonate abundance: comparisons with metazoan diversity, mass extinction events, and seawater saturation state. Rev. Esp. Micropaleontol. 37, 23–39.

Riding, R., 2011. Reefalmicrobial crusts. In: Encyclopedia of Modern Coral Reefs. In: Hopley, D. (Ed.), Encyclopedia of Earth Science Series. Springer, Heidelberg, pp. 911–915.

Saito, R., Kaiho, K., Oba, M., Fujibayashi, M., Tong, J., Tian, L., 2015. Predominance of archaea-derived hydrocarbons in an Early Triassic Microbialite. Org. Geochem. 85, 66–75.

Sanson-Barrera, A., Hochuli, P.A., Bucher, H., Schneebeli-Hermann, E., Meier, M., Weissert, H., Bernasconi, S., 2015. Late Permian-earliest Triassic high resolution organic carbon isotope and palynofacies records from Kap Stosch (northeast Greenland). Glob. Planet. Chang. 133, 149–166.

Schneebeli-Hermann, E., Kürschner, W.M., Hochuli, P.A., Ware, D., Weissert, H., Bernasconi, S.M., Roohi, G., Rehman, K., Bucher, H., 2013. Evidence for atmospheric carbon injection during end-Permian extinction. Geology 41 (5), 579–582.

Schubert, J.K., Bottjer, D.J., 1992. Early Triassic stromatolites as post-mass extinction disaster forms. Geology 20, 883–886.

Sepkoski Jr., J.J., 1984. A kinetic-model of Phanerozoic taxonomic diversity 3. Post-Paleozoic families and mass extinctions. Paleobiology 10, 246–267.

Sepkoski Jr., J.J., Bambach, R.K., Droser, M.L., 1991. Secular changes in Phanerozoic event bedding and the biological overprint. In: Einsele, G., Ricken, W., Seilacher, A. (Eds.), Cycles and Events in Stratigraphy. Springer, Berlin, pp. 298–312.

Shapiro, R.S., 2000. A comment on the systematic confusion of thrombolites. PALAIOS 15, 166–169.

Song, H.J., Tong, J.N., Chen, Z.Q., Yang, H., Wang, Y.B., 2009a. End-Permian mass extinction of foraminifers in the Nanpanjiang Basin, South China. J. Paleontol. 83, 718–738.

Song, H., Tong, J., Chen, Z.Q., 2009b. Two episodes of foraminiferal extinction near the Permian–Triassic boundary at the Meishan section, South China. Aust. J. Earth Sci. 56 (6), 765–773.

Song, H., Yang, L., Tong, J., Chen, J., Tian, L., Song, H., Chu, D., 2015. Recovery dynamics of foraminifers and algae following the Permian-Triassic extinction in Qingyan, South China. Geobios 48 (1), 71–83.

Spötl, C., Vennemann, T.W., 2003. Continuous-flow IRMS analysis of carbonate minerals. Rapid Commun. Mass Spectrom. 17, 1004–1006.

Taraz, H., Golshani, F., Nakazawa, K., Shimizu, D., Bando, Y., Ishii, K.-I., Murata, M., Okimura, Y., Sakagami, S., Nakamura, K., Tukuoka, T., 1981. The Permian and the Lower Triassic systems in Abadeh region, central Iran. Mem. Fac. Sci. Kyoto Univ. Ser. Geol. Miner. 47, 62–133.

Thanh, N.X., Hai, T.T., Hoang, N., Lan, V.Q., Kwon, S., Itaya, T., Santosh, M., 2014. Backarc mafic–ultramafic magmatism in Northeastern Vietnam and its regional tectonic significance. J. Asian Earth Sci. 90, 45–60.

Vennin, E., Olivier, N., Brayard, A., Bour, I., Thomazo, C., Escarguel, G., Fara, E., Bylund, K.G., Jenks, J.F., Stephen, D.A., Hofmann, R., Pufahl, P., 2015. Microbial deposits in the aftermath of the end-Permian mass extinction; a diverging case from the Mineral Mountains (Utah, USA). Sedimentology 62 (3), 753–792.

Wang, Y.J., 1974. A handbook of the stratigraphy and paleontology in Southwest China. (454 pp.). Nanking Institute of Geology and PaleontologyAcademia Sinica. Science Press (in Chinese).

Wignall, P.B., Hallam, A., 1993. Griesbachian (Earliest Triassic) palaeoenvironmental changes in the Salt Range, Pakistan and southeast China and their bearing on the

Permo-Triassic mass extinction. Palaeogeogr. Palaeoclimatol. Palaeoecol. 102, 215–237.

Wignall, P.B., Kershaw, S., Collin, P.Y., Crasquin, S.S., 2009. Erosional truncation of uppermost Permian shallow-marine carbonates and implications for Permian-Triassic boundary events: comment. Geol. Soc. Am. Bull. 121 (5–6), 954–956.

Wilson, J.L., 1975. Carbonate Facies in Geological History. Springer.

Xie, S.C., Pancost, R.D., Huang, J.H., Wignall, P.B., Yu, J.X., Tang, X.Y., Chen, L., Huang, X.Y., Lai, X.L., 2007. Changes in the global carbon cycle occurred as two episodes during the Permian–Triassic crisis. Geology 35, 1083–1086.

Xie, S., Pancost, R.D., Wang, Y., Yang, H., Wignall, P.B., Luo, G., Jia, C., Chen, L., 2010. Cyanobacterial blooms tied to volcanism during the 5 my Permo-Triassic biotic crisis. Geology 38 (5), 447–450.

Yang, S., Hao, W., Wang, X., 1999. Conodont evolutionary lineages, zonation, and P-T boundary beds in Guangxi, China. In: Yao, A., Ezaki, Y., Hao, W., Wang, X. (Eds.), Biotic and Geological Developments in the Paleo-Tethys in China. Peking University Press, Beijing, pp. 81–95.

Yang, H., Chen, Z.Q., Wang, Y., Tong, J., Song, H., Chen, J., 2011. Composition and structure of microbialite ecosystems following the end-Permian mass extinction in South China. Palaeogeogr. Palaeoclimatol. Palaeoecol. 308, 111–128.

Yang, H., Chen, Z.Q., Ou, W., 2015a. Microconchids from microbialites near the Permian-Triassic boundary in the Zuodeng Section, Baise area, Guangxi Zhuang Autonomous Region, South China and their paleoenvironmental implications. J. Earth Sci. 26 (2), 157–165.

Yang, H., Chen, Z.Q., Wang, Y., Ou, W., Liao, W., Mei, X., 2015b. Palaeoecology of microconchids from microbialites near the Permian–Triassic boundary in South China. Lethaia 48, 497–508.

Yin, H.F., Jiang, H.S., Xia, W.C., Feng, Q.L., Zhang, N., Shen, J., 2014. The end-Permian regression in South China and its implication on mass extinction. Earth Sci. Rev. 173, 19–33.

Zaninetti, L., Altiner, D., 1981. Les Biseriamminidae (Foraminifères) dans le Permien supérieur mésogéen: évolution et biostratigraphie. Notes du Laboratoire de Paléontologie de l'Université de Genève 7 (2), 39–46.

Zaton, M., Taylop, P.D., Vinn, O., 2013. Early Triassic (Spathian) Post-extinction microconchids from Western Pangea. J. Paleontol. 87, 159–165.

Sample No.	Section	Elevation	d13C VPDB	d18O VSMOW Calcite
wuz1	Wuzhuan	-11.95	4.49	-5.60
wuz2	Wuzhuan	-11.1	3.32	-5.60
wuz3	Wuzhuan	-10.65	4.55	-5.60
wuz4	Wuzhuan	-10.35	4.42	-5.60
wuz5	Wuzhuan	-10.15	3.49	-5.60
wuz6	Wuzhuan	-9.9	4.87	-5.60
wuz7	Wuzhuan	-9.6	4.79	-5.60
wuz8	Wuzhuan	-9.6	3.92	-5.60
wuz9	Wuzhuan	-9.4	3.60	-5.60
wuz10	Wuzhuan	-9.2	2.80	-5.60
wuz11	Wuzhuan	-9	3.88	-5.60
wuz12	Wuzhuan	-8.6	5.41	-5.60
wuz13	Wuzhuan	-8.6	3.34	-5.60
wuz15	Wuzhuan	-8.15	3.82	-6.79
wuz16	Wuzhuan	-7.85	3.24	-9.60
wuz17	Wuzhuan	-7.7	3.97	-6.78
wuz18	Wuzhuan	-7.45	3.21	-8.22
wuz19	Wuzhuan	-6.75	2.35	-9.66
wuz20	Wuzhuan	-4.95	3.72	-5.91
wuz21	Wuzhuan	-4.8	3.39	-6.07
wuz22	Wuzhuan	-3.9	2.51	-11.47
wuz23	Wuzhuan	-3.6	3.25	-7.65
wuz24	Wuzhuan	-3.15	1.75	-11.22
wuz25	Wuzhuan	-2.85	2.31	-10.65
wuz26	Wuzhuan	-2.7	2.79	-11.14
wuz27	Wuzhuan	-2.4	2.62	-8.69
wuz28	Wuzhuan	-2.15	2.20	-10.14
wuz29	Wuzhuan	-1.9	2.71	-8.22
wuz30	Wuzhuan	-1.55	2.52	-9.01
wuz50	Wuzhuan	-1.25	2.13	-9.23
wuz31	Wuzhuan	-0.95	2.58	-7.54
wuz32	Wuzhuan	-0.8	2.38	-7.02
wuz33	Wuzhuan	-0.4	2.37	-8.38
wuz48	Wuzhuan	0.05	1.39	-6.21
wuz34	Wuzhuan	0.2	1.08	-6.28
wuz35	Wuzhuan	0.75	0.95	-6.33
wuz36	Wuzhuan	1.15	0.74	-4.97
wuz49	Wuzhuan	1.65	0.23	-6.38
wuz37	Wuzhuan	1.95	0.37	-6.28
wuz51	Wuzhuan	2.3	0.29	-6.10
wuz52	Wuzhuan	2.6	0.00	-6.67
wuz38	Wuzhuan	2.95	0.02	-6.27
wuz53	Wuzhuan	3.15	-0.01	-6.59
wuz39	Wuzhuan	3.75	0.12	-6.42
wuz54	Wuzhuan	3.95	-0.24	-6.48
wuz40	Wuzhuan	4.35	-0.07	-6.32
wuz55	Wuzhuan	4.65	-0.14	-6.68
wuz41	Wuzhuan	4.85	-0.15	-6.96
wuz56	Wuzhuan	5.35	-0.11	-6.39
wuz42	Wuzhuan	5.8	-0.12	-6.46
wuz57	Wuzhuan	6.15	-0.36	-6.51
wuz43	Wuzhuan	6.55	-0.07	-6.59
wuz58	Wuzhuan	7.1	-0.17	-5.75
wuz44	Wuzhuan	7.75	-0.17	-5.96
wuz45	Wuzhuan	7.95	0.12	-6.76
wuz59	Wuzhuan	8.55	2.13	-1.77
wuz46	Wuzhuan	8.75	-0.17	-6.75
wuz47	Wuzhuan	8.95	0.91	-5.65

Sample No.	Section	Elevation	d13C VPDB	d18O VSMOW Calcite
Tie7	Tieb bao	-4.1	**2.74**	-7.60
Tie8	Tieb bao	-3.8	**2.88**	-6.73
Tie9	Tieb bao	-3.4	**3.58**	-6.51
Tie10	Tieb bao	-3.1	**2.75**	-7.07
Tie11	Tieb bao	-2.2	**3.31**	-5.86
Tie12	Tieb bao	-2	**2.26**	-7.16
Tie13	Tieb bao	-1.6	**2.72**	-7.28
Tie14	Tieb bao	-1.2	**3.11**	-6.75
Tie15	Tieb bao	-0.8	**2.81**	-7.75
Tie16	Tieb bao	-0.6	**2.71**	-6.79
Tie17	Tieb bao	-0.4	**1.51**	-6.62
Tie18	Tieb bao	-0.2	**1.82**	-6.07
Tie19	Tieb bao	-0.1	**2.25**	-11.88
Tie 57.1	Tieb bao	0.02	**0.87**	-8.12
Tie57.3	Tieb bao	0.08	**0.79**	-7.91
TIE 100	Tieb bao	0.2	**1.04**	**-7.31**
TIE 101	Tieb bao	0.35	**0.51**	**-7.48**
TIE 102	Tieb bao	0.5	**0.29**	**-7.86**
TIE 103	Tieb bao	0.65	**0.21**	**-7.64**
TIE 104	Tieb bao	0.8	**0.31**	**-7.54**
TIE 105	Tieb bao	1.1	**-0.03**	**-7.57**
TIE 106	Tieb bao	1.4	**0.00**	**-7.49**
TIE 107	Tieb bao	1.6	**0.14**	**-7.98**
TIE 108	Tieb bao	1.8	**0.28**	**-7.75**
TIE 109	Tieb bao	2	**0.31**	**-7.61**
TIE 110	Tieb bao	2.2	**-0.18**	**-8.11**
TIE 111	Tieb bao	2.5	**-0.02**	**-8.27**
TIE 112	Tieb bao	2.7	**-0.26**	**-8.35**
TIE 113	Tieb bao	3	**0.26**	**-7.64**
TIE 114	Tieb bao	3.2	**0.15**	**-7.61**
TIE 115	Tieb bao	3.4	**0.17**	**-7.29**
TIE 116	Tieb bao	3.7	**0.42**	**-7.37**
TIE 117	Tieb bao	4	**0.56**	**-6.34**
TIE 118	Tieb bao	4.15	**0.36**	**-6.61**
TIE 119	Tieb bao	4.25	**0.34**	**-5.91**
TIE 120	Tieb bao	4.4	**0.32**	**-5.47**
TIE 121	Tieb bao	4.6	**0.11**	**-5.83**

Table 1 Supplementary material. δ13Ccarb and δ18Ocarb values measured from the Permian Heshan and Triassic Luolou formations at Wuzhuan and Tienbao sections.

APPENDIX A

Additional publication link to this thesis

CONODONTS FROM THE EARLY TRIASSIC MICROBIALITE OF GUANGXI (SOUTH CHINA): IMPLICATIONS FOR THE DEFINITION OF THE BASE OF THE TRIASSIC SYSTEM

Palaeontology, Vol. 58, Part 3, 2015, pp. 563–584

Palaeontology
The Palaeontological Association
www.palass.org

[Palaeontology, 2015, pp. 1–22]

CONODONTS FROM THE EARLY TRIASSIC MICROBIALITE OF GUANGXI (SOUTH CHINA): IMPLICATIONS FOR THE DEFINITION OF THE BASE OF THE TRIASSIC SYSTEM

by MORGANE BROSSE[1], HUGO BUCHER[1], BORHAN BAGHERPOUR[1], AYMON BAUD[3], ÅSA M. FRISK[1,4], KUANG GUODUN[2] *and* NICOLAS GOUDEMAND[1]

[1]Paläontologisches Institut der Universität Zürich, Karl Schmid-Strasse 4, 8006, Zürich, Switzerland; e-mail: morgane.brosse@pim.uzh.ch
[2]Guangxi Bureau of Geology and Mineral Resources, Jiangzheng Road 1, 530023, Nanning, China
[3]Geological Museum, Lausanne University, Quartier UNIL-Dorigny, Bâtiment Anthropole, CH-1015, Lausanne, Switzerland
[4]Palaeobiology, Department of Earth Sciences, Uppsala University, Villavägen 16, 753 36, Uppsala, Sweden

Typescript received 3 December 2014; accepted in revised form 20 February 2015

Abstract: We describe a new Early Triassic (Griesbachian) succession of conodont faunas from a high-resolution sampling of the basal Early Triassic microbial limestone and the base of the overlying unit at the Wuzhuan section (Nanpanjiang Basin, Guangxi, South China). The microbial limestone records the earliest phase of the Early Triassic biotic recovery after the end-Permian mass extinction. For the first time, rich conodont faunas are reported from within the microbialite. The faunas from Wuzhuan are largely dominated by anchignathodontids, including several *Isarcicella* species, which were previously documented only from strata above the microbialite. A total of 14 conodont species assigned to three genera is recorded from the Wuzhuan section. Starting from the base of the microbialite upwards, several species are sequentially added to the conodont assemblage. The alpha diversity peaks at the top of the microbialite. The conodont record in the considered microbialite interval at Wuzhuan is presumably unaffected by local ecological changes. It therefore more likely represents an evolutionary rather than an ecological pattern. We compare the Wuzhuan's conodont record with a well-supported phylogenetic model and suggest that the sequence of first occurrences at Wuzhuan is the closest to the 'true' sequence of evolutionary events that took place during this Griesbachian radiation of anchignathodontids. Based on comparisons with the GSSP section at Meishan, we suggest further that the first occurrence of *Hindeodus parvus* in Meishan does not correspond to its first appearance datum.

Key words: Permian–Triassic boundary, Nanpanjiang Basin, microbial limestone, calcarenite lenses, anchignathodontids.

THE end-Permian mass extinction (between 251.941 ± 0.037 and 251.880 ± 0.031 Ma, see Burgess *et al.* 2014) is known to be the largest biodiversity crisis in the history of life and was marked by the disappearance of many typical Palaeozoic organisms (e.g. trilobites, rugose and tabulate corals, fusulinid foraminifers). About 90% of all marine species on Earth disappeared during this event (Raup 1979), and major changes in plant communities have been documented (Retallack 1995; Hermann *et al.* 2011; Schneebeli-Hermann 2012; Schneebeli-Hermann *et al.* 2015). It has been argued that the end-Permian mass extinction was followed by a delayed biotic recovery (Erwin 2001). Marine communities throughout the Early Triassic are classically described as low-diversity assemblages typified by opportunistic, cosmopolitan taxa (Schubert and Bottjer 1992; Erwin 2001; Rodland and Bottjer 2001). Yet, more recent studies on benthic foraminifers (Song *et al.* 2009*a*, *b*, 2011), trace fossils (Hofmann *et al.* 2011), bivalves (Krystyn *et al.* 2003; Hautmann *et al.* 2011) and metazoan reefs (Brayard *et al.* 2011) have suggested that the recovery of benthic communities was more rapid than previously thought. The recovery of nekto-pelagic clades such as ammonoids and conodonts also was much faster than previously assumed (Orchard 2007; Brayard *et al.* 2009), with a succession of several extinction-recovery cycles. The brief resurgence of microbial limestone has been customarily interpreted as devastated environments and ecological and diversity collapses (Awramik 1990; Schubert and Bottjer 1992; Schubert and Bottjer 1995). In support of the classical view of a delayed

doi: 10.1111/pala.12162

recovery, palaeoequatorial microbialites of basal Triassic age were traditionally interpreted as representing an anachronistic facies (Baud *et al.* 1997, 2002, 2007; Kershaw *et al.* 1999, 2007; Erwin 2006; Pruss *et al.* 2006). However, this apocalyptic view needs to be revised: in several South Chinese sections, lenses with abundant and diverse benthic macrofaunas were discovered in shell coquinas that are trapped in-between domes of microbial limestone, such as in Shanggan, Guangxi (Kaim *et al.* 2010; Hautmann *et al.* 2011). Shell coquinas are also present in Wuzhuan, and their corresponding conodont faunas are here described in detail.

Owing to their abundance and high evolutionary rates, conodonts are of great importance for dating Early Triassic rocks. Although many marine organisms were decimated during the end-Permian mass extinction, conodonts remain comparatively unscathed and abundant through the Permian–Triassic boundary (PTB; Orchard 2007). Hence, high-resolution biostratigraphical correlations frequently utilize conodont elements. Yet, the conodont record from the earliest Triassic microbialite is poorly known, which has hitherto precluded high-resolution correlations between regions where the microbialite occurs and those with non-microbial basal Early Triassic rocks. Either the few available range charts lack descriptions and illustrations of conodonts (Ezaki *et al.* 2003, 2008), or only a few specimens of the index species (e.g. *Hindeodus parvus*) from very few samples are illustrated (Kershaw *et al.* 2002). In other cases, the quality of the illustrations is too poor for unambiguous verification of the determinations (Qi and Liao 2007). When illustrations and occurrences are adequately documented, most of the reported occurrences are restricted to beds located below or above the microbial limestone (Jiang *et al.* 2014); conodont occurrences within the microbialite are very scarce (Chen *et al.* 2008*a*). In this respect, the Wuzhuan section is remarkable because abundant conodont faunas were found within the microbial limestone itself. Hence, our study on the Wuzhuan section represents the first documentation of a detailed, high-resolution succession of diversified Griesbachian conodont faunas from the microbial limestone of South China. Abundant and diversified benthic macrofaunas of Permian and Triassic affinities were also discovered in the microbialite at neighbouring sections (Hautmann *et al.* 2011). In this study, we focus on the taxonomy of these conodonts. Their implications for basinwide correlations and comparisons between shallow-water and deeper-water settings will be addressed in a separate study.

GEOLOGICAL SETTING

The Nanpanjiang Basin in South China is of Palaeozoic to Early Mesozoic age, which extends across central and western Guangxi, southern Guizhou and eastern Yunnan

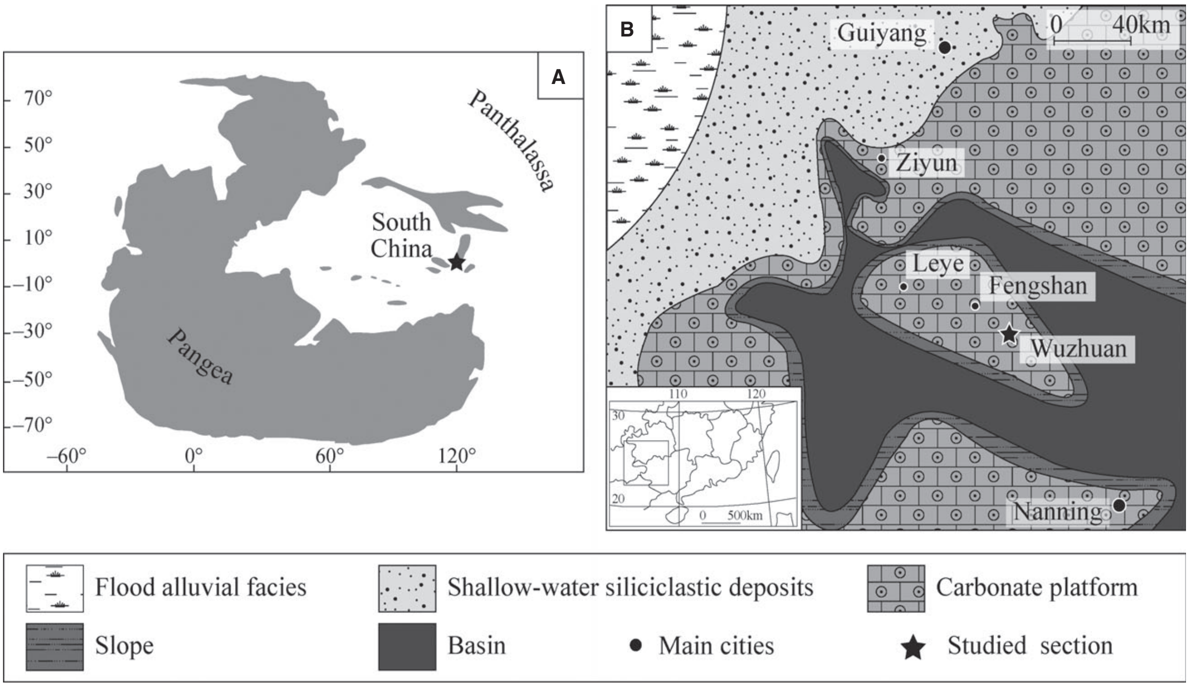

FIG. 1. A, palaeogeographical map of the studied area during Early Triassic. B, locality map indicating the position of Wuzhuan section in the Nanpanjiang Basin (modified from Fan *et al.* 2014).

provinces (Fig. 1). Differential subsidence controlled by block faulting initiated at the beginning of the Late Permian and persisted until the Early–Middle Triassic boundary (HB unpub. data). Where not blanketed by Middle Triassic flysch deposits, isolated shallow-water carbonate platforms persisted until the early Carnian. In shallow-water settings, the Late Permian is represented by the Heshan Formation and displays thick-bedded limestone with chert nodules containing abundant Permian faunas (predominantly represented by foraminifera, bryozoans, corals, brachiopods and bivalves) and locally intercalated with numerous ash layers.

Unconformably overlying the Heshan Formation, the Luolou Formation is of Early Triassic age. Its base records a microbial event of Griesbachian age (Kershaw *et al.* 1999, 2007; Lehrmann 1999; Lehrmann *et al.* 2001; Wang *et al.* 2005; Galfetti *et al.* 2008).

The Wuzhuan section (24°21′44.6″N; 107°20′02.00″E) is exposed along a road cut in the western Donglan County, northern Guangxi (Fig. 1). The PTB is well exposed in this section. The upper 12 m of the Permian medium grey, moderately thick-to-thick limestone is rich in diagenetic chert nodules. Typical Late Permian benthic communities including bryozoans, brachiopods, bivalves, crinoids, algae and foraminifera are well represented, however, conodonts and ammonoids are rare. Numerous ash layers are locally intercalated with the upper part of the Heshan Formation. An ash layer caps the top of the formation in a majority of sections and is the closest layer in time with the main extinction event (HB unpub. data). All following references to sample position refer to metres above the bottom level (0 m) at the top of the ash layer, that is, at the boundary between the Heshan and Luolou formations. The Luolou Formation at Wuzhuan is divided into two units as established by Galfetti *et al.* (2008). It is further subdivided here into six new subunits, as shown in Figure 2. The lowermost unit corresponds roughly to the microbialite.

The terminology of Shapiro (2000) is adopted here for the description of the microfacies of the microbialite. Subunit 1a consists of two thin fossiliferous calcarenites enclosing one layer of microbial limestone with clotted facies thrombolite and small isolated domes with a dendrolitic fabric; it is about 40 cm thick. In the calcarenites, we found Late Permian foraminifers. Their remarkable concentration and the grainstone fabric of their matrix suggest latest Permian or earliest Triassic reworking. Hence, the PTB at Wuzhuan is likely to lie within this 40-cm interval, above the last ash layer of the Heshan Formation. The lower part (Subunit 1b, 5 m) of the microbialite displays predominantly thrombolite in clotted facies, while the upper part of the microbialite (Subunit 1c, 4.5 m) displays dome-shaped dendrolites with the intercalation of coarse calcarenitic lenses. These calcarenitic lenses are fossiliferous and yield rich benthic faunas including bivalves, gastropods and brachiopods. Similar lenses have been reported in other sections of the Nanpanjiang Basin. These yielded abundant and diversified bivalves (Hautmann *et al.* 2011), gastropods (Kaim *et al.* 2010) and occasionally ammonoids (Brühwiler *et al.* 2008).

The top of the microbialite is capped by a 20-cm-thick bioclastic wackestone (Subunit 1d) containing a very abundant conodont fauna, overlain by a greywacke (Subunit 2a) and in turn followed by a succession of laminated, dark mudstones and silts with intercalated thin-bedded limestone beds (Subunit 2b). Table 1 shows the positions of these subunits with respect to the lithostratigraphical schemes of Ezaki *et al.* (2008) and Galfetti *et al.* (2008).

MATERIAL AND METHODS

A total of 27 carbonate samples, each weighing between 1 and 6 kg, were collected from units 1 and 2 (Table 1). In addition to samples from each of the nine coquinoid lenses from Subunit 1c, samples were collected at 50 cm spacing on average throughout the microbialite (Unit 1). Another sample was collected from the bioclastic wackestone lying directly on top of the microbialite (Subunit 1d), and uppermost samples were from the thin-bedded limestone beds at the top of the section (Subunit 2b).

The samples were dissolved with a ~10% buffered acetic acid solution following the procedure of Jeppsson *et al.* (1999). The insoluble residues were concentrated by heavy liquid separation using sodium polytungstate (Jeppsson and Anehus 1999). Concentrated residues were sieved with a 0.075-mm mesh, and handpicked and studied under a binocular microscope.

RESULTS

Of the 27 samples from the Luolou Formation that were processed, 15 yielded conodont elements. The Heshan Formation was also sampled but turned out to be barren.

FIG. 2. Detailed stratigraphical log of the Wuzhuan section showing the distribution of conodont taxa throughout the Griesbachian Luolou Formation (left), and corresponding phylogenetic tree (right; modified after Jiang *et al.* 2010, using the ranges in the left part). The boundary between the Heshan and the Luolou formations is the base of the scale. Black circles correspond to confirmed occurrences and white circles correspond to undetermined species. Only beds yielding conodont elements have been numbered. The thick line in the phylogenetic tree represents the estimated range of *H. parvus* as recorded in Meishan. At Wuzhuan, the FO of *H. parvus* appears older. *H*, *Hindeodus*; *N*, *Neogondolella*; *I*, *Isarcicella*.

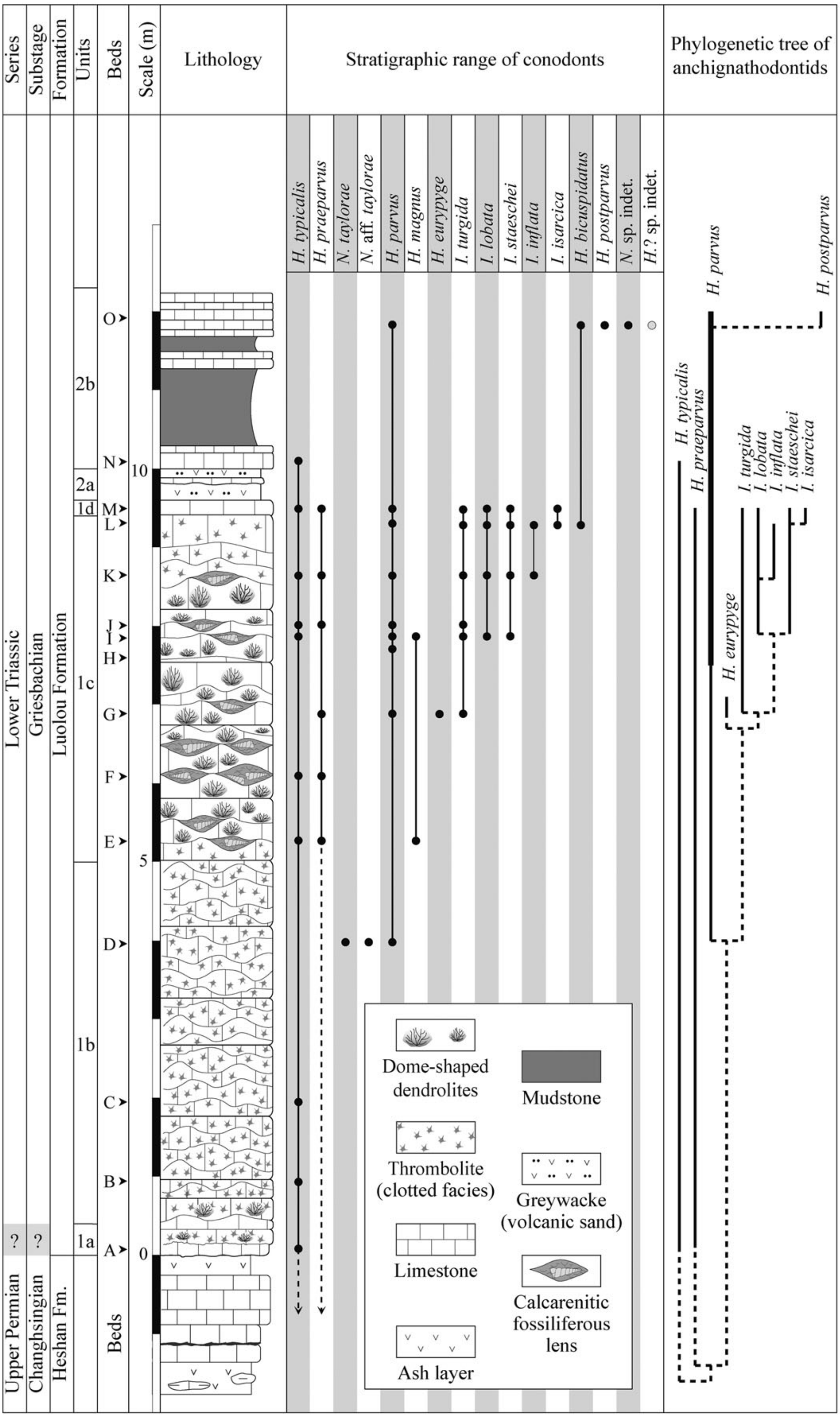
Series
Substage
Formation
Units
Beds
Scale (m)
Lithology
Stratigraphic range of conodonts
Phylogenetic tree of anchignathodontids
Lower Triassic
Griesbachian
Luolou Formation
Upper Permian
Changhsingian
Heshan Fm.
?
?
1a
1b
1c
1d
2a
2b
Beds
A
B
C
D
E
F
G
H
I
J
K
L
M
N
O
0
5
10
H. typicalis
H. praeparvus
N. taylorae
N. aff. taylorae
H. parvus
H. magnus
H. eurypyge
I. turgida
I. lobata
I. staeschei
I. inflata
I. isarcica
H. bicuspidatus
H. postparvus
N. sp. indet.
H.? sp. indet.
Dome-shaped dendrolites
Thrombolite (clotted facies)
Limestone
Ash layer
Mudstone
Greywacke (volcanic sand)
Calcarenitic fossiliferous lens
H. typicalis
H. praeparvus
H. parvus
H. postparvus
H. eurypyge
I. turgida
I. lobata
I. inflata
I. staeschei
I. isarcica

TABLE. 1. Occurrence of conodont species in the Luolou Formation at the Wuzhuan section.

Elevation (m) from base of Luolou Formation	Sample names	Lithological units (displayed in Fig. 2)	Corresponding units in Galfetti *et al.* (2008)	Corresponding units in Ezaki *et al.* (2008)	Quantity dissolved (kg)	*H. typicalis*	*H. parvus*	*N. taylorae*	*N.* aff. *taylorae*	*H. praeparvus*	*H. magnus*	*H. eurypyge*	*I. turgida*	*I. lobata*	*I. staeschei*	*I. inflata*	*I. isarcica*	*H. bicuspidatus*	*H. postparvus*	*N. sp. indet*	*H.?* sp. indet
11.8	WUZ.O	2b	2	3	5		9						1?	1?				4	33	1	1
10.1	WUZ.N	2a	2	3	1	4															
9.5	WUZ.M	1d	1	3	7	4	58			2			1	15	40		12				
9.3	WUZ.L	1c	1	2	4		42						1	9	21	1	9	6			
8.7	WUZ.K	1c	1	2	6	7	49			3			17	12	2	1					
8	WUZ.J	1c	1	2	4	5	10			2			2								
7.9	WUZ.I	1c	1	2	1	4	4			1	1		5	2	1						
7.6	WUZ.H	1c	1	2	3		2														
6.9	WUZ.G	1c	1	2	1		12			4		1	2								
6.1	WUZ.F	1c	1	2	13	2				2											
5.3	WUZ.E	1c	1	2	3	2				3	1										
4	WUZ.D	1b	1	2	9		2	1	1												
1.9	WUZ.C	1b	1	2	3	1															
1	WUZ.B	1b	1	2	4	2															
0.1	WUZ.A	1a	1	2	6	1															

The sample elevation is given as distance from the base of Luolou Formation.
H, *Hindeodus*; *N*, *Neogondolella; I, Isarcicella.*

Within the microbialite, the coquinoid lenses were not significantly richer in conodont elements than the rest of the unit, and several calcarenitic lenses did not contain conodonts.

Fourteen species assigned to three genera were identified from about 1000 P_1 and 600 ramiform elements (Table 1). Most of these elements are assigned to anchignathodontids (*Hindeodus* and *Isarcicella* in order of decreasing abundance), and only a few specimens to *Neogondolella*. The general preservation is moderate to good, but numerous fragmentary elements could not be determined at the species level. For this reason, we do not provide a table of relative abundances. The colour of the elements is black (CAI = 5). The illustrated specimens are presented in Figures 3–8.

Conodont occurrences are presented in Figure 2. Ranging almost throughout the entire section, the basal Triassic index species *H. parvus* (Fig. 4) first occurs 4 m above the formational boundary, where it is associated with a single P_1 element of *Neogondolella taylorae* (Fig. 7J). The first occurrence (FO) of *Isarcicella* species is in Subunit 1c, 7–8 m above the base of the microbialite. *Isarcicella* is reported for the first time within the microbialite. A very different assemblage dominated by *Hindeodus postparvus* occurs in Subunit 2b, 2–3 m above the top of the microbialite unit.

The conodonts collected from the Wuzhuan section (Fig. 2) also document an evolutionary radiation, with a taxonomic diversity peak at the top of the microbialite (sample L, top of Subunit 1c). Starting from the base of Unit 1 (microbialite), several species are sequentially added upwards to the conodont assemblage and only *N. taylorae*, *H. magnus* and *H. eurypyge* disappear before the top of the Unit 1. Only one specimen of *N. taylorae* is found in the entire section, and its exclusion from most samples (as for other neogondolellids) is attributed to ecological constraints as neogondolellids likely preferred colder environments (and hence, at the equator, deeper-water settings) than anchignathodontids (Joachimski *et al.* 2012). Indeed, in other sections (e.g. Dajiang section, Jiang *et al.* 2014), *N. taylorae*, *H. magnus* is known to occur also above the FO of *Isarcicella isarcica*.

DISCUSSION

Conodont elements are known from within the microbialite only in a few sections. Up to now, the best documented sections were as follows: Dongwan, Sichuan (Ezaki *et al.* 2003); Langpai, Guizhou (Ezaki *et al.* 2008); Dawen, Guizhou (Chen *et al.* 2008*a*); and Dajiang section, Guizhou (Jiang *et al.* 2014). Yet, none of these sections records a high-resolution sequence of abundant conodonts that compares with that of Wuzhuan.

The fossil record is always discontinuous, locally incomplete due to depositional gaps, and affected by taphonomic biases and selective preservation. Hence, a sequence of FOs does not necessarily reflect the true chronology of phylogenetic events and one may ask to what extent the evolutionary radiation of anchignathodontids recorded at Wuzhuan reflects a true evolutionary radiation. In the case of this study, however, invariance of microfacies and sedimentological features and virtually constant $\delta^{13}C_{carb}$ values throughout the upper half of Unit 1 (pers. obs.) indicate stable environmental conditions. Hence, the conodont record in this interval at Wuzhuan is unaffected by local ecological changes and is more likely to represent an evolutionary rather than an ecological pattern. The sequence of FOs of anchignathodontids (species of genera *Hindeodus* and *Isarcicella*, see Fig. 2) is indeed remarkably consistent with the phylogenetic hypothesis proposed by Jiang *et al.* (2010, fig. 4). Jiang *et al.* (2010) used the ranges of conodont taxa in the Meishan section (Sichuan, China), the most intensively documented PTB section, to calibrate a cladogram based on the analysis of 25 P_1 element characters for 22 species of anchignathodontids. Hence, Jiang *et al.*'s phylogeny is considered to be the best available model for conodonts around the PTB. It is also largely in agreement with the phylogenetic scheme proposed by Perri and Farabegoli (2003, fig. 7, p. 291). The most notable difference between Jiang *et al.*'s model and our phylogenetic tree (modified from Jiang *et al.* 2010, using the ranges of taxa in Wuzhuan, see Fig. 2) is that we can possibly resolve some of their ghost lineages: in Wuzhuan, *I. turgida* occurs already below the FOs of *I. lobata*, *I. inflata*, *I. staeschei* and *I. isarcica*, in agreement with the phylogenetic model; and *H. parvus* occurs also below the FO of *H. eurypyge* and *I. turgida*, which, if confirmed, would shorten the longest ghost lineage of Jiang *et al.* (2010). This suggests that the conodont record at Wuzhuan is the closest to the 'true' sequence of evolutionary events that took place during this Griesbachian radiation of anchignathodontids.

In particular, the FO of *H. parvus* in Wuzhuan is found about 3 m below the FOs of *H. eurypyge* and *I. turgida*, which, assuming a maximum of 0.4 mm/year growth rate of recent stromatolites (Chivas *et al.* 1990), suggests the age of origination of *H. parvus* is at least 7.5 kyr older than the ages of *H. eurypyge* and *I. turgida*. This would also imply that the FO of *H. parvus* is older in Wuzhuan than its supposed first appearance datum (FAD) in Meishan: indeed, based on the Meishan's record, it appears that the origination of *H. parvus* would have taken place anytime between the origination of *I. turgida* and the origination of *I. lobata* (Jiang *et al.* 2010, fig. 4; Fig. 2, the bold line in the stratigraphical range of *H. parvus*), markedly after the origination of *H. eurypyge*. In other words, the FO of *H. parvus* in Meishan does not correspond to its FAD.

CONCLUSION

We document the first high-resolution sequence of abundant and diverse conodonts from the microbialite unit at the base of the Luolou Formation in South China including the FOs of index species such as *I. lobata*, *I. staeschei* and *I. isarcica*. The conodont record at Wuzhuan supports the cladistics-based phylogeny of Jiang *et al.* (2010) and seems to better approximate the evolutionary radiation of anchignathodontids than other sections, including the GSSP section at Meishan. Comparisons with the latter suggest that the FO of *H. parvus* in Meishan is younger than the FO of *H. parvus* in Wuzhuan and thus does not correspond to its FAD.

SYSTEMATIC PALAEONTOLOGY
(Brosse and Goudemand)

The descriptions of species are exclusively based on P_1 elements. Synonymies are limited to key citations and are not intended to be exhaustive lists. All illustrated specimens are shown at the same scale. Figured elements are stored in PIMUZ, Paleontological Institute and Museum of the University of Zurich, Karl Schmid-Strasse 4, 8006 Zurich, Switzerland.

The terminology for the orientation of the element is the traditional one based on the orientation and curvature of the cusp; it refers to the element only, not to its natural orientation within the animal (Purnell *et al.* 2000). 'Lower' refers to the side of the element from which the basal cavity opens. 'Upper' refers to the opposite side. The

FIG. 3. A, *Hindeodus eurypyge* Nicoll *et al.*, 2002; bed WUZ.G, PIMUZ 30988. B–E, F?, *Hindeodus bicuspidatus* Kozur, 2004; B, bed WUZ.L, PIMUZ 31054; C, bed WUZ.O, PIMUZ 30989; D, bed WUZ.O, PIMUZ 31002; E, bed WUZ.L, PIMUZ 31045; F, (mirrored) bed WUZ.L, PIMUZ 31017. G, *Hindeodus*? sp. indet. (mirrored) bed WUZ.O, PIMUZ 31018. H–N, *Hindeodus postparvus* Kozur, 1989; H, (mirrored, juvenile) bed WUZ.O, PIMUZ 31004; I, (mirrored) bed WUZ.O, PIMUZ 31019; J, (mirrored) WUZ.O, PIMUZ 31020; K, (mirrored) bed WUZ.O, PIMUZ 31022; L, bed WUZ.O, PIMUZ 31023; M, (mirrored) bed WUZ.O, PIMUZ 31024; N, (mirrored) bed WUZ.O, PIMUZ 31021. Respectively, 'lateral' and 'upper' views, for some specimens additionally 'lower' and 'posterior' views. Scale bar represents 400 μm.

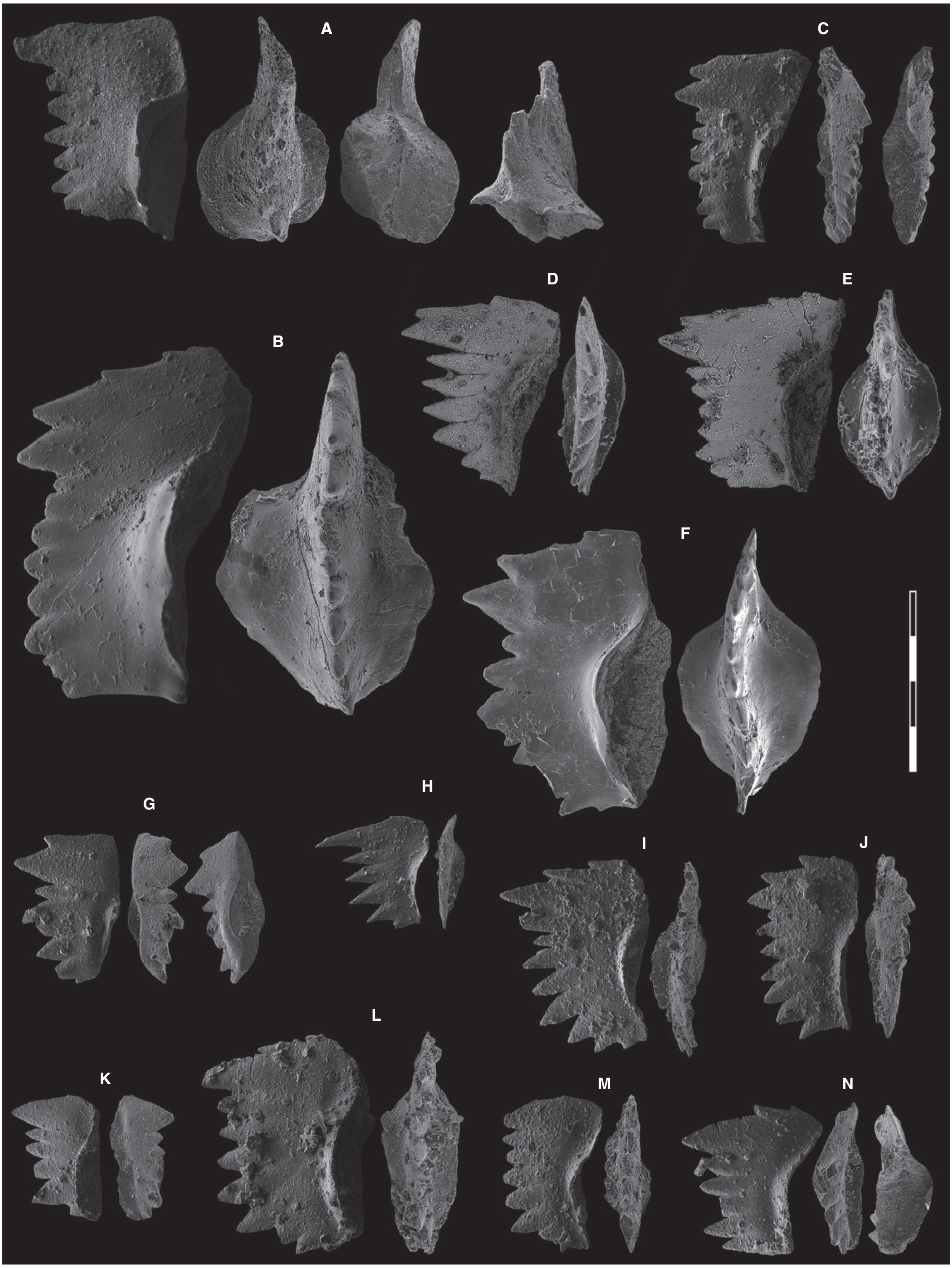
A
B
C
D
E
F
G
H
I
J
K
L
M
N

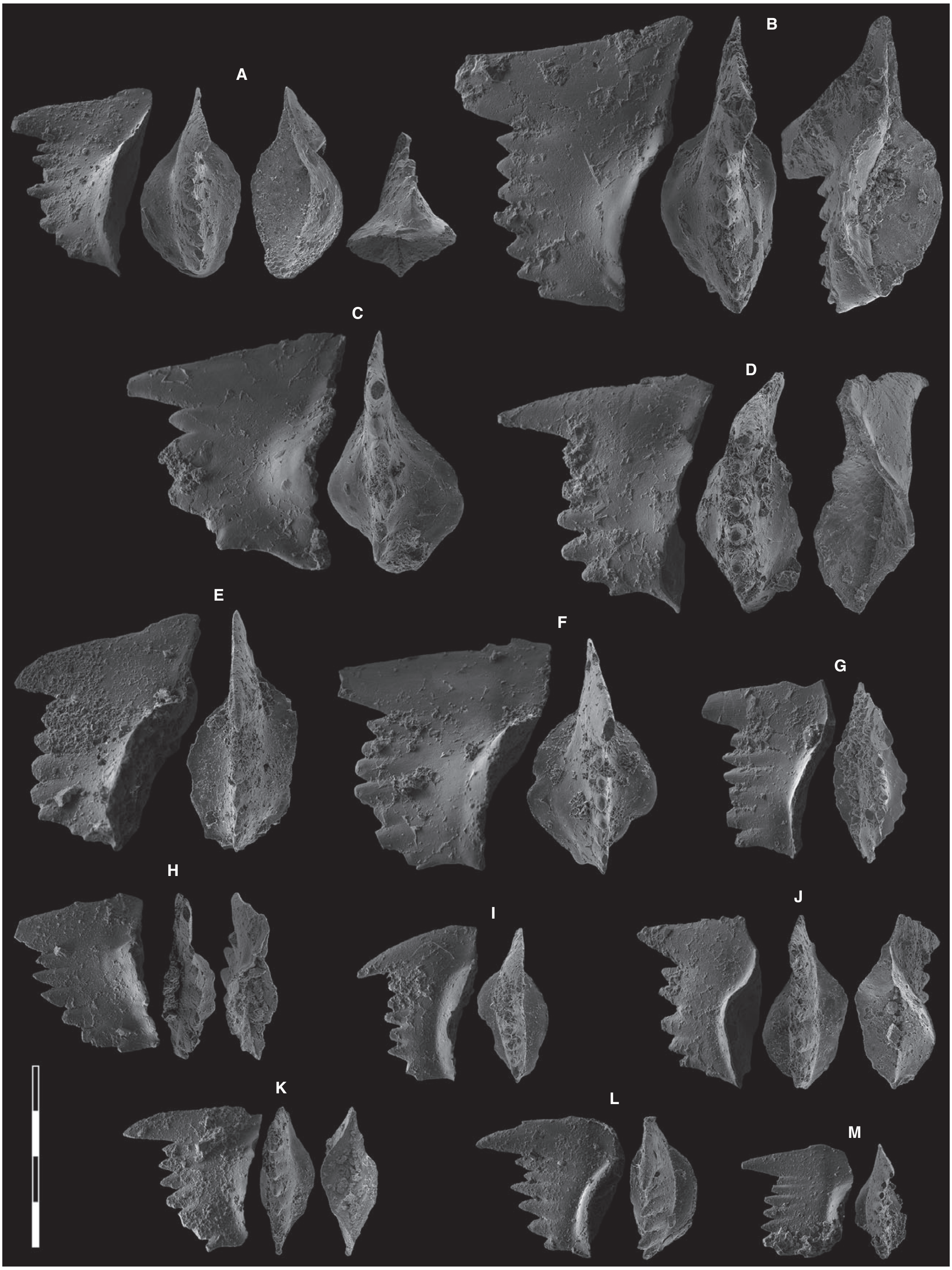
A
B
C
D
E
F
G
H
I
J
K
L
M

term 'cusp' refers only to the cusp *sensu stricto*. It represents the structure above the apex of the basal cavity (Klapper *et al.* 1973) and is homologous in distinct conodont elements. The cusp is often larger than the other denticles, but not necessarily. The big denticle that is found on the 'anterior' of carminiscaphate elements of anchignathodontids is appropriately termed 'distal denticle' (as in Agematsu *et al.* 2014).

Genus HINDEODUS Rexroad and Furnish, 1964

Type species. Hindeodus cristulus Youngquist and Miller, 1949.

Hindeodus bicuspidatus Kozur, 2004
Figure 3B–E, ?F

1991 *Hindeodus* n. sp.; Schönlaub, p. 88, pl. 1, fig. 6 (only).
*2004 *Hindeodus bicuspidatus* Kozur, p. 50, pl. 2, fig. 4.
2011 *Hindeodus anterodentatus* Dai and Tian; Jiang *et al.*, pl. 1, figs 3, 5.
2014 *Hindeodus bicuspidatus* Kozur; Zhang *et al.*, fig. 4: 22–24.

Diagnosis. Two large denticles of similar height instead of one single 'distal denticle' in the anterior part of the P_1 element.

Description. The most distal denticle is slightly smaller than the adjacent one, although both are considerably higher and larger than the other denticles. They can be inclined anteriorly and posteriorly. A few microdenticles are sometimes found on the anterior margin of the blade. Five to eight thickened denticles grow on the posterior part of the blade. The upper view of *H. bicuspidatus* is illustrated for the first time here, in Figure 3B, E. The basal cavity is large and asymmetrical. In upper view, the denticle line is discontinuous between the anteriormost denticles of the blade and the posterior denticles above the basal cavity.

Remarks. H. bicuspidatus differs from *H. anterodentatus* in the size of the anteriormost denticle, which is much bigger in *H. bicuspidatus*.

The two 'distal denticles' in *H. bicuspidatus* can be either inclined anteriorly (Kozur 2004, pl. 2, fig. 4, holotype; Zhang *et al.* 2014, fig. 4: 23; Schönlaub 1991, pl. 1, fig. 6) or posteriorly (Zhang *et al.* 2014, fig. 4: 22, 24; Jiang *et al.* 2011, pl. 5, fig. 3; Fig. 3B–E). The specimen illustrated in Figure 3F has an irregular denticulation reminiscent of *H. postparvus* or *H. sosioensis,* but its wide, deeply excavated and asymmetrical basal cavity is more typical of *H. bicuspidatus*.

Occurrence. Iran: Kuh-e-Hambast, section V, bed Aba V-3, lower *Clarkina meishanensis* – *Hindeodus praeparvus* Zone (Kozur 2004). China: Feixianguan Formation, Shangsi section, Sichuan, beds 28c, 30c, *H. parvus*, *I. lobata* and *I. isarcica* zones (Jiang *et al.* 2011); Zhongzhai section, Guizhou, bed 28 (Zhang *et al.* 2014); Luolou Formation, Wuzhuan section, Guangxi, beds WUZ.L and WUZ.O.

Hindeodus eurypyge Nicoll *et al.*, 2002
Figure 3A

1989 *Anchignathodus parvus* Kozur and Pjatakova; Dai and Zhang, pl. 39, figs 16, 17, pl. 45, figs 22–24.
*2002 *Hindeodus eurypyge* Nicoll *et al.*, pp. 616–620, figs 4, 5, 7–9.
2007 *Hindeodus eurypyge* Nicoll *et al.*; Metcalfe and Nicoll, pl. 1, figs 2–6.

Diagnosis. P_1 with a tall erect 'distal denticle' and 3–10 posterior blade denticles. Basal margin ovate with rounded posterior margin and basal margin flare. Basal cavity extending posteriorly of the 'distal denticle' with an ovate outline, deeply excavated with a groove extending anteriorly under the 'distal denticle'. Base of the basal cavity narrowed posteriorly to a rounded margin. Posterior end of the element high and rounded.

Description. P_1 with a rectangular lateral profile. In upper view, the blade of the specimen in Figure 3A is clearly S-shaped. The 'distal denticle' is higher than the adjacent denticles, erect and triangular. Like the holotype, the anterior margin of the 'distal denticle' is smooth. The denticles are triangular anteriorly until the mid-carina and become slightly chisel-like in the posterior half of the carina. They have an ovate section. The basal margin is very narrow anteriorly, but extends at the posterior edge of the 'distal denticle' in a wide and ovate outline with basal margin flare.

Occurrence. Meishan D, Zhejiang, discontinuous from bed 27a to bed D/C-2 in the Yinkeng Formation (Nicoll *et al.* 2002);

FIG. 4. *Hindeodus parvus* Kozur and Pjatakova, 1976. A, bed WUZ.D, PIMUZ 30990. B, (mirrored) bed WUZ.J, PIMUZ 30993. C, bed WUZ.L, PIMUZ 30995. D, bed WUZ.K, PIMUZ 30994. E, (mirrored) bed WUZ.J, PIMUZ 30992. F, (mirrored) bed WUZ.M, PIMUZ 30991. G, bed WUZ.I, PIMUZ 31001. H, bed WUZ.J, PIMUZ 31007. I, (mirrored) bed WUZ.K, PIMUZ 30996. J, bed WUZ.G, PIMUZ 31000. K, (mirrored) bed WUZ.G, PIMUZ 30999. L, (mirrored) bed WUZ.O, PIMUZ 30998. M, (mirrored) bed WUZ.J, PIMUZ 31003. Respectively, 'lateral' and 'upper' views, for some specimens additionally 'lower' and 'posterior' views. Scale bar represents 400 μm.

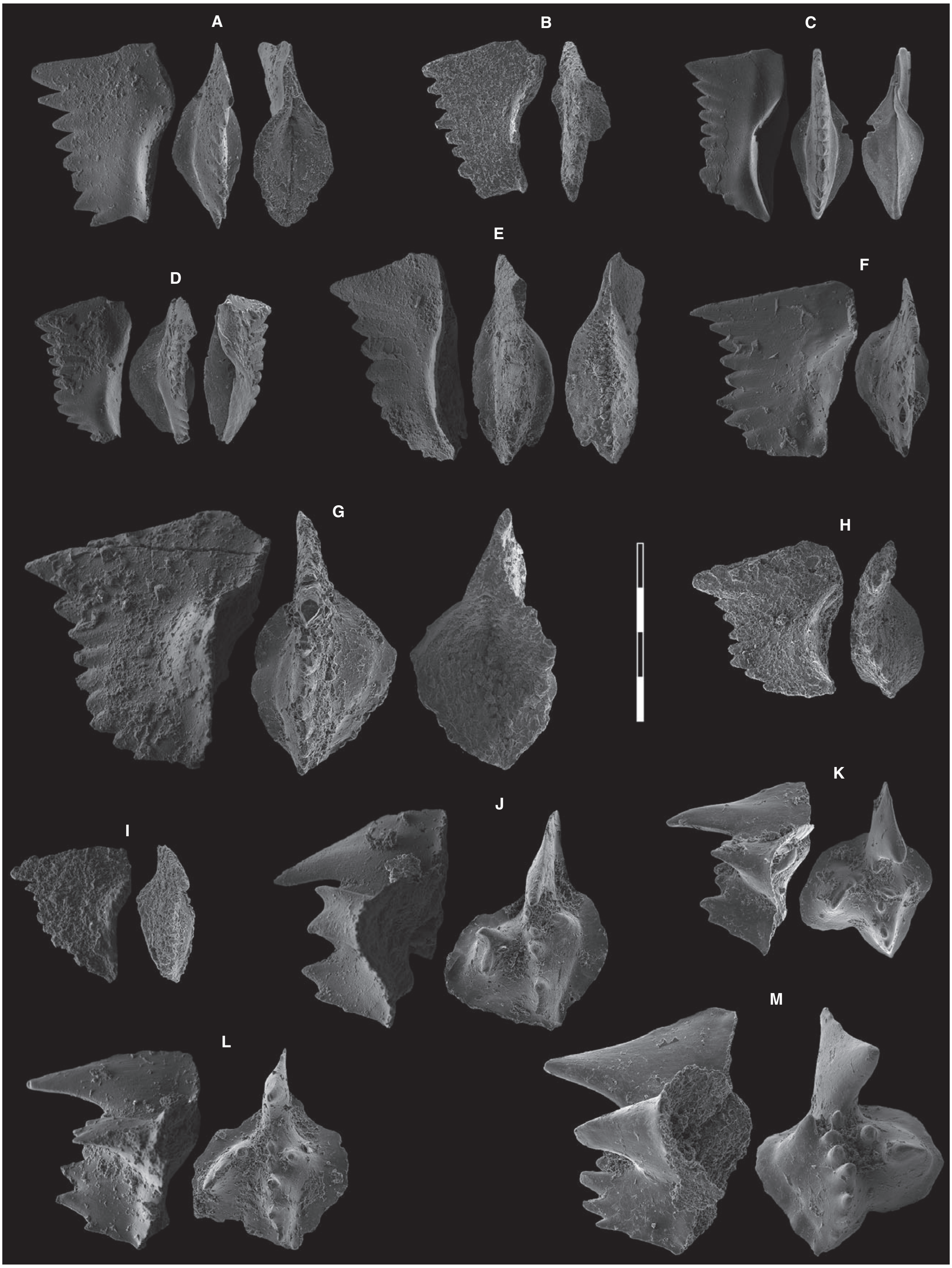
A
B
C
D
E
F
G
H
I
J
K
L
M

Shangsi, Sichuan, bed 6405548, *Merrillina ultima – Stepanovites? mostleri* Zone (Metcalfe and Nicoll 2007); Luolou Formation, Wuzhuan, Guangxi, bed WUZ. G.

Hindeodus magnus Kozur, 2004
Figure 7F–H

1993 *Hindeodus parvus* Kozur and Pjatakova; Tian, pl. 6, fig. 15 (only).
?1995 *Hindeodus latidentatus* Kozur *et al.*; Zhang *et al.*, pl. 2, fig. 12.
*2004 *Hindeodus magnus* Kozur, pl.1, fig. 14.

Diagnosis. Large P_1 element, with very large, broad ‘distal denticle’. Carina with 8–9 rather large and broad denticles. Cup broad, symmetrical, rounded at posterior end.

Description. ‘Distal denticle’ broad and erect, posteriorly followed by 7–10 more or less fused denticles with pointed-to-rounded tips.

Remarks. Kozur (2004) noted that the P_1 element in *H. magnus* is much larger that than in *H. parvus*, and its ‘distal denticle’ is comparatively broader than for *H. parvus*. Also, the denticles in *H. magnus* are broader and relatively shorter than those in *H. parvus*. *H. magnus* bears also some resemblance to *H. latidentatus*, notably in the shape of the posteriormost denticles, which are more discrete and less fused than the anterior ones. However, *H. magnus* does not display the U-shaped space between the denticles that is characteristic of *H. latidentatus*, and has a relatively broader ‘distal denticle’. In comparison with *H. magnus*, *H. praeparvus* has more discrete posterior denticles and a smaller ‘distal denticle’.

The specimen shown in Figure 7H is not typical in having a wide, symmetrical and subtrapezoidal basal cavity that expands under the entire element, is tapered under the blade and is rounded and flared at the posterior margin.

Occurrence. China: Luolou Formation, Wuzhuan, Guangxi, bed WUZ. E; Zhejiang, Meishan C, Bed 25. Iran: lowermost Elikah Formation, Abadeh and Zal sections.

Hindeodus parvus Kozur and Pjatakova, 1976
Figure 4

*1976 *Anchignathodus parvus* Kozur and Pjatakova, pp. 123–125, fig. 1a, b, e, h.
1981 *Hindeodus parvus* Kozur and Pjatakova; Matsuda, pp. 91–93, pl. 5, figs 1–3.
1981 *Hindeodus minutus* Ellison; Matsuda, pp. 78–84, pl. 1, figs 8–12 (only).
1996 *Hindeodus parvus* Kozur and Pjatakova; Koike, pp. 342–344, fig. 3: 3–15.
1996 *Hindeodus parvus* Kozur and Pjatakova; Mei, pp. 145–146, pl. 18.2, figs 2–4, 14.
1998 *Hindeodus parvus* Kozur and Pjatakova; Orchard and Krystyn, pl. 6, figs 9, 16, 17, 20.
2002 *Hindeodus parvus* Kozur and Pjatakova; Nicoll *et al.*, p. 628, fig. 15: 1–4, fig. 16: 1–3.
2007 *Hindeodus parvus* Kozur and Pjatakova; Jiang *et al.*, pl. 5, figs 1–7.
2008*a* *Hindeodus parvus* Kozur and Pjatakova; Chen *et al.*, fig. 10: 1–13.
2008*a* *Hindeodus parvus parvus* Kozur and Pjatakova; Chen *et al.*, pp. 11–12, fig. 10: 14–19, fig. 11: 1–5.
2008*b* *Hindeodus parvus* Kozur and Pjatakova; Chen *et al.*, p. 105, pl. 5, figs 1–5.
2013 *Hindeodus parvus* Kozur and Pjatakova; Yan *et al.*, fig. 5G–L, P, S, U (only).

Diagnosis. P_1 element with a ‘distal denticle’ whose height is considerably higher than the other denticles. It can be preceded by a small microdenticle. Carina often bearing 4–8 denticles. First denticles posterior to the ‘distal denticle’ subequal. Posterior denticles often but not always inclined posteriorly.

Description. ‘Distal denticle’ tall and erect, sometimes inclined posteriorly. Its anterior margin sometimes bears one or even two microdenticles (Fig. 4F, H, J, L). The ‘distal denticle’ is followed posteriorly by five to seven more or less fused denticles. The denticles are often broader on the posterior half of the carina.

Remarks. Kozur (1989, 1996) and Mei (1996) have established three morphotypes of *H. parvus*. *H. parvus erectus* (morphotype 1) has a subvertical posterior edge; *H. parvus parvus* (morphotype 2), including the holotype, has a steeply inclined posterior blade bearing a few denticles

FIG. 5. A–B, *Hindeodus typicalis* Sweet, 1970*a*, morphotype 1; A, (mirrored) bed WUZ.E, PIMUZ 31025; B, bed WUZ.K, PIMUZ 31026. C?, D?, E, *Hindeodus typicalis* Sweet, 1970*a*, morphotype 2; C, bed WUZ.B, PIMUZ 31027; D, (mirrored) bed WUZ.B, PIMUZ 31028; E, (mirrored) bed WUZ.J, PIMUZ 31029. F–I, *Hindeodus typicalis* Sweet, 1970*a*, morphotype 3; F, (mirrored) bed WUZ.M, PIMUZ 31031; G, bed WUZ.I, PIMUZ 31030; H, bed WUZ.F, PIMUZ 31032; I, bed WUZ.I, PIMUZ 31033. J–M, *Isarcicella isarcica* Huckriede, 1958; J, (mirrored) bed WUZ.M, PIMUZ 31034; K, (mirrored) bed WUZ.L, PIMUZ 31036; L, (mirrored) bed WUZ.M, PIMUZ 31035; M, bed WUZ.L, PIMUZ 31037. Respectively, ‘lateral’ and ‘upper’ views, for some specimens additionally ‘lower’ view. Scale bar represents 400 μm.

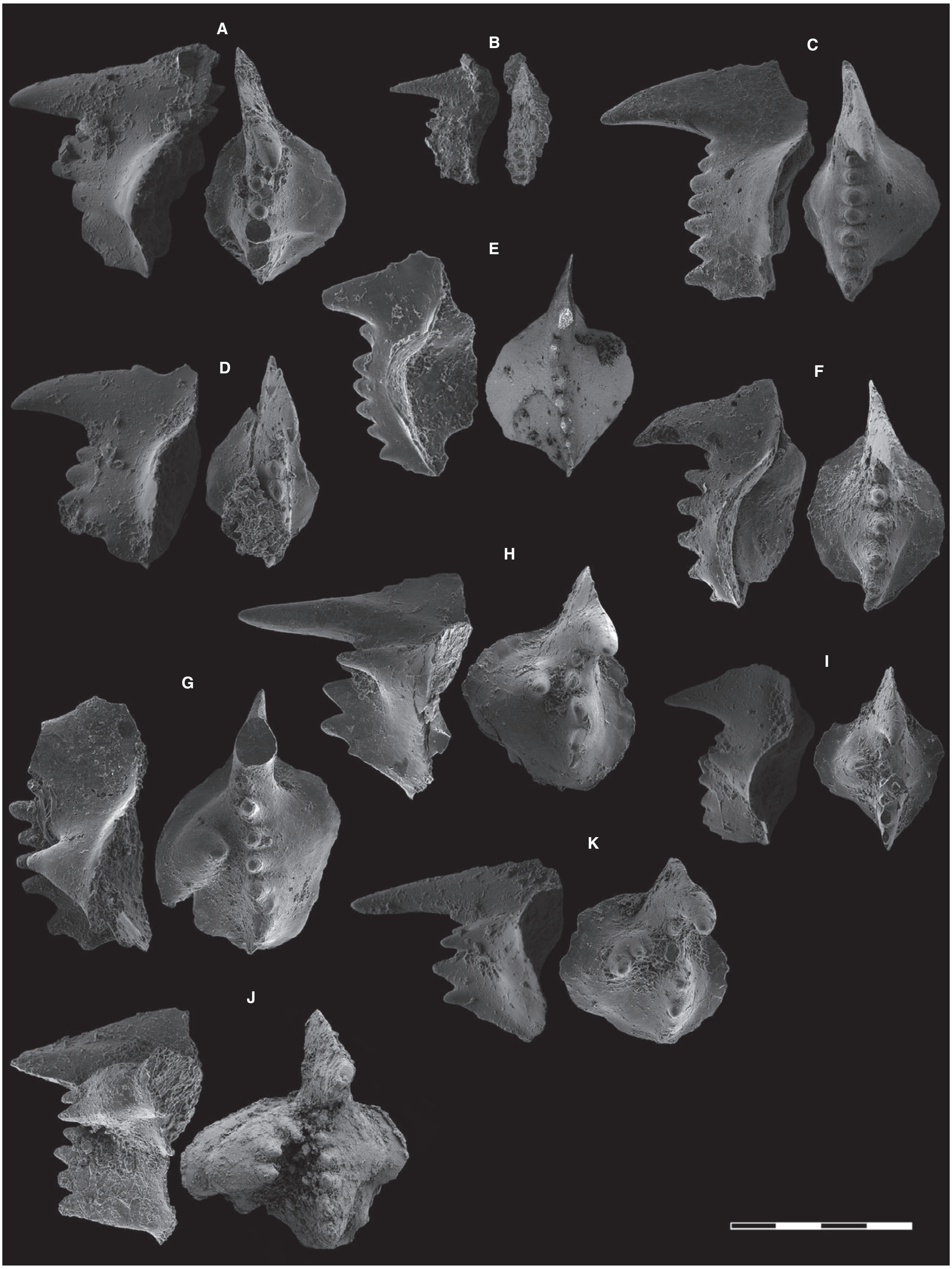
A
B
C
E
D
F
H
G
I
K
J

(Kozur 1989, 1996). A third morphotype, referred to as morphotype 3, was described in Meishan, with a less inclined, denticulate posterior edge (Mei 1996). We retain *H. parvus* for the three forms.

Occurrence. Tibet: *Otoceras latilobatum* Zone, Selong. Spiti: *Otoceras woodwardi* Zone, Guling, Lingti, Lalung. Canadian Arctic: *Otoceras boreale* Zone, Ellesmere Island (Henderson and Baud 1997). China: Meishan, Zhejiang, transition beds 25 (aff.), 27c, 27d (Yin *et al.* 1996); Luolou Formation, Wuzhuan, Guangxi, microbialite and thin-bedded limestone beds above. Kashmir: Khunamuh Formation, Guryul Ravine, beds 56–61 (E2–E3; beds number from Nakazawa *et al.* 1975). Salt Range: Kathwai Dolomite (Sweet 1970*b*). Griesbachian, Early Triassic worldwide.

Hindeodus postparvus Kozur, 1989
Figure 3H–N

1977 *Anchignathodus parvus* Kozur and Pjatakova; Kozur, figs 19, 20.
*1989 *Hindeodus postparvus* Kozur, p. 400.
1996 *Hindeodus postparvus* Kozur; Kozur, pl. 2, figs 9–10.
1998 *Hindeodus postparvus* Kozur; Orchard and Krystyn, pl. 6, fig. 1.
2008*a* *Hindeodus postparvus* Kozur; Chen *et al.*, fig. 11: 6–12.

Diagnosis. Carina with small, erected anterior denticles and strongly divergent posterior denticles. 'Distal denticle' only slightly bigger than other denticles. A small denticle can be present on the anterior edge of the 'distal denticle'. Basal cavity expands under most of the element's length, widest at mid-length.

Description. In lateral view, the element's margin is slightly arched at mid-length where the basal cavity is widest. There can be one or two small denticles on the anterior margin of the biggest elements (Fig. 3I, J, L, N). The blade posteriorly bears large denticles of unequal size which can be strongly divergent at the posterior end.

Remarks. Although displaying typical characteristics of *H. postparvus* (particularly the divergent posteriormost denticles), the specimens from Wuzhuan also bear similarities with *H. sosioensis*, such as small denticles on the anterior margin of the 'distal denticle' and unequally sized denticles. Yet, all lack the strongly unequal denticles of *H. sosioensis.* The specimen of *H. sosioensis* illustrated by Jiang *et al.* (2014, pl. 3, fig. 10) is an intermediate form between one of our specimens (Fig. 3I) and Kozur's holotype of *H. sosioensis.* Note that *H. sosioensis* and *H. postparvus* co-occur both in the floated block of Sicily (Kozur 1996, 1998) and in bed DJ-35 at Dajiang (Jiang *et al.* 2014, pl. 3, figs 10–13).

Occurrence. Southern Alps: Early Triassic of Sicily, floated block (Kozur, 1996); China: Wuzhuan section, Guangxi, bed WUZ.O.

Hindeodus praeparvus Kozur, 1996
Figure 7A–E

1994*a* *Hindeodus latidentatus* Kozur *et al.*; Wang, pl. 1, fig. 9.
1994*b* *Hindeodus latidentatus* Kozur *et al.*; Wang, pl. 2, figs 4, 5.
1996 *Hindeodus parvus erectus* Kozur; Kozur, pl. 4, fig. 7.
*1996 *Hindeodus latidentatus praeparvus* Kozur, pp. 93–94, pl. 2, figs 1–4 (only).
1996 *Hindeodus latidentatus* Kozur *et al.*; Yin *et al.*, pl. 2, fig. 3 (only).
1998 *Hindeodus praeparvus* Kozur; Orchard and Krystyn, p. 352, pl. 6, figs 22–23.
2002 *Hindeodus praeparvus* Kozur; Nicoll *et al.*, fig. 17.
2008*a* *Hindeodus praeparvus* Kozur; Chen *et al.*, fig. 9: 7–14.
2013 *Hindeodus praeparvus* Kozur; Zhao *et al.*, pl. 5, figs V–W.

Diagnosis. P_1 element with a moderately high 'distal denticle'. Anterior denticles slender and closely spaced. Posterior denticles broader and more widely spaced. V-shaped spaces between denticles.

Description. Our material agrees in all observable characters with the description of Kozur (1996).

Remarks. The distinction between the anterior and posterior denticles is shared with *H. latidentatus*, a species of which *H. praeparvus* was first described as a subspecies (Kozur 1996). Orchard and Krystyn (1998) elevated *H. latidentatus praeparvus* to the rank of species and noted that *H. latidentatus* has U-shaped posterior denticles, whereas those of *H. praeparvus* are V-shaped.

FIG. 6. A–D, *Isarcicella lobata* Perri and Farabegoli, 2003; A, bed WUZ.I, PIMUZ 31038; B, (mirrored, juvenile) bed WUZ.O, PIMUZ 31005; C, bed WUZ.K, PIMUZ 31039; D, bed WUZ.M, PIMUZ 31040. E, ?F, *Isarcicella inflata* Perri and Farabegoli, 2003; E, bed WUZ.L, PIMUZ 31053; F, bed WUZ.K, PIMUZ 31057. G–K, *Isarcicella staeschei* Dai and Zhang, 1989; G, (mirrored) bed WUZ.K, PIMUZ 31042; H, (mirrored) bed WUZ.M, PIMUZ 31043; I, (mirrored) bed WUZ.M, PIMUZ 31041; J, (mirrored) bed WUZ.I, PIMUZ 31063; K, (mirrored) bed WUZ.M, PIMUZ 31044. Respectively, 'lateral' and 'upper' views. Scale bar represents 400 μm.

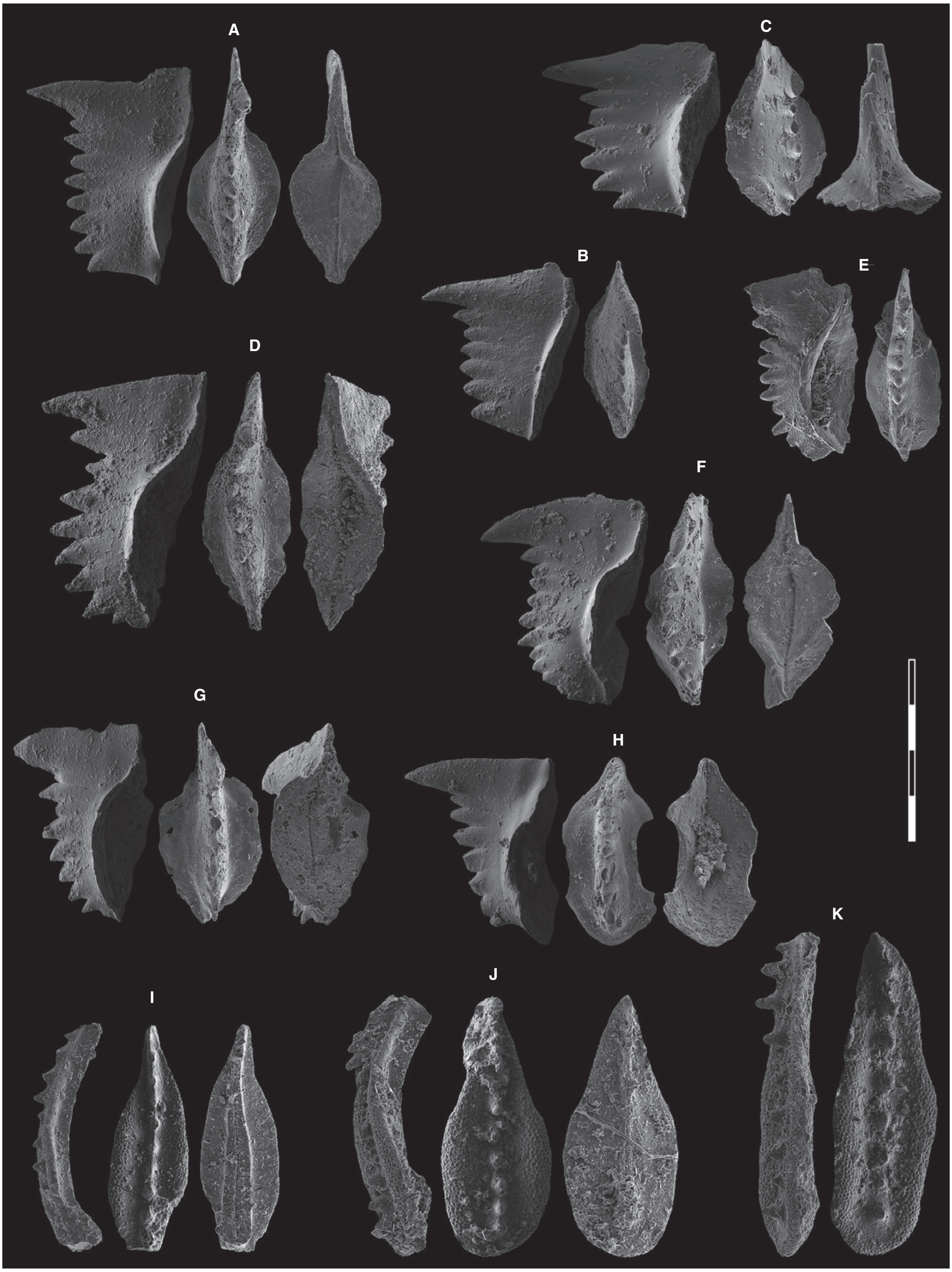
A
C
B
E
D
F
G
H
I
J
K

Occurrence. Spiti: *Otoceras woodwardi* Zone, Guling and Lingti. Kashmir: Khunamuh Formation, E2 (beds number from Nakazawa *et al.* 1975), Guryul Ravine (Bhatt and Arora 1984). China: lower and upper bed 27, Meishan, Zhejiang (Wang 1994*a*, *b*; Yin *et al.* 1996); Wuzhuan, Guangxi. Late Changhsingian and Griesbachian.

Hindeodus? sp. indet.
Figure 3G

Remarks. Owing to its resemblance to coeval forms assigned to *Hindeodus*, this element is retained tentatively within that genus although its P_1 element is carminate and not carminiscaphate. Its basal cavity is reduced and shallow. In lateral view, its unequal denticles remind those of *H. sosioensis* and it occurs in the same sample as *H. postparvus*.

Hindeodus typicalis Sweet, 1970*a*
Figure 5A–B, C?, D?, E–I

*1970*a* *Anchignathodus typicalis* Sweet, pp. 7–8, pl. 1, figs 13, 22.
1981 *Hindeodus minutus* Ellison; Matsuda, pp. 78–84, pl. 1, figs 1–7 (only).
1996 *Hindeodus typicalis* Sweet; Mei, p. 146, pl. 18.2, figs 6, 10, 11 (only).
1998 *Hindeodus typicalis* Sweet; Orchard and Krystyn, p. 354, pl. 6, figs 14, 18, 19, 25, 26.
2013 *Hindeodus typicalis* Sweet; Zhao *et al.*, fig. 5T–U.

Diagnosis. P_1 element with large 'distal denticle', but not very high compared with other denticles. Blade with four to eight subequal denticles. Outline of the blade slightly S-shaped in lateral view. Carina slightly arched posteriorly as a consequence of the monotonic decrease in the height of the denticles towards the posterior end.

Remarks. Sweet (1970*a*) differentiated *H. typicalis* from *H. minutus* (Ellison 1941) on the base of a much lower length:height ratio and a more gradual denticular margin. Specimens from Wuzhuan display a wide intraspecific variation and can be split into three morphotypes: morphotype 1 is short with a straight superior margin decreasing regularly to the posterior end, and it corresponds to *H. typicalis sensu stricto* (Fig. 5A–B); morphotypes 2 and 3 have an S-shaped denticular margin similar to that of *H. minutus*; morphotype 3 is short (length:height ratio is about 1, see Fig. 5F–I), whereas morphotype 2 is the longest of the three morphotypes (length:height ratio is 1.5–2; see Fig. 5C–E). Among the morphotype 2 specimens, those shown in Figure 5C–D are found in the same bed (WUZE B) and resemble *H. changxingensis* in having a straight carina in lateral view. However, the carina is not adenticulate, as it is described for the holotype of *H. changxingensis*.

Occurrence. Tibet: *Otoceras latilobatum* Zone, Selong. Spiti: *O. woodwardi* and *Ophiceras tibeticum* zones, Guling, Lingti, Lalung, Muth. Kashmir: Khunamuh Formation, Guryul Ravine, beds 53, 55–57, 61 (beds number from Nakazawa *et al.* 1975). Late Permian – Early Triassic worldwide.

Genus ISARCICELLA Kozur, 1975

Type species. Spathognathodus isarcicus Huckriede, 1958.

Isarcicella inflata Perri and Farabegoli, 2003
Figure 6E, ?F

1981 *Hindeodus parvus* Kozur and Pjatakova; Matsuda, p. 91, pl. 5, fig. 1.
1991 *Isarcicella isarcica* morphotype l; Perri, p. 42, pl. 4, fig. 10, pl. 5, fig. 5.
1991 *Isarcicella isarcica* morphotype 2; Perri, p. 42, pl. 5, fig. 4.
*2003 *Isarcicella inflata* n. sp.; Perri and Farabegoli pl. 4, figs 15–19 (only).
2007 *Isarcicella inflata* Perri and Farabegoli; Jiang, pl. 5, fig. 19.
2011 *Isarcicella inflata* Perri and Farabegoli; Jiang *et al.*, pl. 2, figs 10–12.
2011 *Isarcicella inflata* Perri and Farabegoli; Kolar-Jurkovšek *et al.*, pl. 5, fig. 5.
2014 *Isarcicella lobata* Perri and Farabegoli; Jiang *et al.*, pl. 4, fig. 2 (only).

Diagnosis. P_1 element with a very wide, asymmetrical, lobed, swollen and thickened cup lacking lateral nodes or denticles. 'Distal denticle' high, blade bearing 6–8 denticles.

Description. The 'distal denticle' is considerably higher than the other denticles, straight or arched posteriorward. The denticles

FIG. 7. A–E, *Hindeodus praeparvus* Kozur, 1996; A, bed WUZ.G, PIMUZ 31008; B, bed WUZ.G, PIMUZ 31009; C, bed WUZ.M, PIMUZ 31010; D, bed WUZ.J, PIMUZ 31014; E, bed WUZ.F, PIMUZ 31016. F–H, *Hindeodus magnus* Kozur, 2004; F, bed WUZ.I, PIMUZ 31015; G, bed WUZ.E, PIMUZ 31013; H, bed WUZ.E, PIMUZ 31056. I, *Neogondolella* sp. indet., bed WUZ.O, PIMUZ 31059. J, *Neogondolella taylorae* Orchard *in* Orchard *et al.*, 1994, bed WUZ.D, PIMUZ 31051. K, *Neogondolella* aff. *taylorae*, bed WUZ.D, PIMUZ 31058. Respectively, 'lateral' and 'upper' views, for some specimens additionally 'lower' or 'posterior' views. Scale bar represents 400 μm.

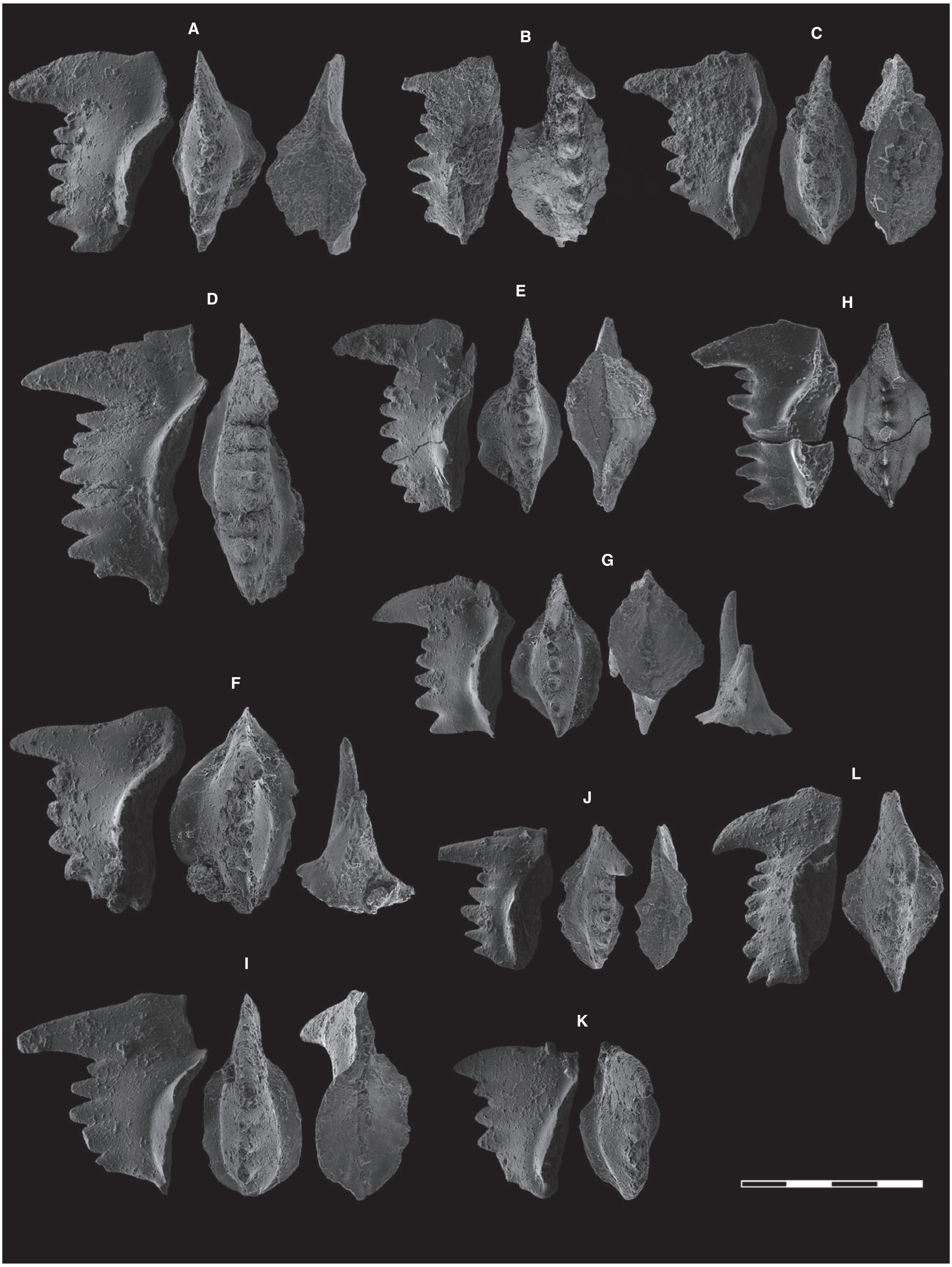
A
B
C
D
E
H
G
F
L
J
I
K

have rounded tips and can be very discrete (Fig. 6F), with a laterally compressed-to-rounded section. The cup is very wide with margin flares.

Remarks. Perri and Farabegoli (2003) differentiated this species from *I. lobata* in having a 'very much wider and inflated cup', whose outer side is 'always greatly expanded'. Perri and Farabegoli suggested that *I. inflata* derived from *I. lobata* and this hypothesis is retained here (see our phylogenetic tree, Fig. 2). The specimens of *I. inflata* from Wuzhuan have a more symmetrical basal cavity than the holotype (Fig. 6F).

Occurrence. Southern Alps: Werfen Formation, Mazzin Member, Bulla section, Tesero section, San Pellegrino Pass section, Agordo-Frassené section. China: Meishan, Zhejiang, beds 29; Shangsi, Sichuan, beds 31a–33; Luolou Formation, Wuzhuan, Guangxi, beds WUZ.K–L.

Isarcicella isarcica Huckriede, 1958
Figure 5J–M

*1958 *Spathognathodus isarcica* n. sp. Huckriede, p. 162, pl. 10, fig. 7a–b, e.
1970*b* *Anchignathodus isarcicus* Huckriede; Sweet, pp. 223–224, pl. 1, figs 18–19.
1975 *Isarcicella isarcicus* Huckriede; Kozur *et al.*, pl. 1, fig. 18.
1991 *Isarcicella isarcica* morphotype 3; Perri, pp. 42–43, pl. 4, fig. l, pl. 6, figs 1–3 (only).
1993 *Isarcicella isarcica* Huckriede; Wang and Cao, p. 254, pl. 55, figs 8–9.
1993 *Isarcicella isarcica* Huckriede; Tian, pl. 6, figs 19, 22 (only).
1994 *Isarcicella isarcica* Huckriede; Orchard *et al.*, pp. 832–833, pl. 2, figs 13–14.
1997 *Isarcicella isarcica* Huckriede; Wang and Wang, p. 165, pl. 2, fig. 1.
1999 *Isarcicella isarcica* Huckriede; Nicora and Perri, pl. 3, fig. 16.
2011 *Isarcicella isarcica* Huckriede; Jiang *et al.*, figs 7–9.

Diagnosis. An *Isarcicella* species in which the P_1 element has two lateral processes bearing nodes or denticles. P_1 element asymmetrical with two lateral node- or denticle-bearing processes, one on each side of the blade.

Description. Our material agrees in all observable characters with the description of Huckriede (1958).

Occurrence. Tibet: Selong. Southern Alps: Werfen Formation, Mazzin Member, Bulla section, Tesero section. China: widespread in the *I. isarcica* interval zone.

Isarcicella lobata Perri and Farabegoli, 2003
Figure 6A–D

1964 *Spathognathodus isarcicus* Huckriede; Staesche, text-fig. 61.
1981 *Hindeodus parvus* Kozur and Pjatakova; Matsuda, pp. 91–93, pl. 5, figs 1, 3 (only).
1991 *Isarcicella isarcica* Huckriede; Perri, pp. 42–43, pl. 3, fig. 7, pl. 4, fig. 8.
1995 *Hindeodus parvus-Isarcicella* transition?; Metcalfe pl. 1, figs 12–13.
1998 *Hindeodus parvus* morphotype 2; Farabegoli and Perri, pl. 4.3.1, fig. 13.
1999 *Hindeodus parvus erectus* Kozur; Nicora and Perri, pl. 3, fig. 7.
1999 *Hindeodus parvus parvus* Kozur and Pjatakova; Nicora and Perri, pl. 3, fig. 14.
*2003 *Isarcicella lobata*; Perri and Farabegoli, pp. 298–298, pl. 2, figs 1–3, pl. 3, figs 18–23 (only).
2004 *Isarcicella lobata* Perri and Farabegoli; Perri *et al.*, p. 475, pl. 1, figs 7, 9.
2007 *Isarcicella lobata* Perri and Farabegoli; Jiang *et al.*, pl. 5, figs 17, 18.
2011 *Isarcicella lobata* Perri and Farabegoli; Jiang *et al.*, pl. 3, figs 2–4 (only).
2014 *Isarcicella lobata* Perri and Farabegoli; Jiang *et al.*, pl. 4, figs 1, 3 (only).

Diagnosis. An *Isarcicella* species in which the P_1 element has no lateral node/denticle. P_1 element with an asymmetrical swollen and thickened cup with a lateral lobe. 'Distal denticle' higher than the other denticles, which are thickened.

Description. The 'distal denticle' is considerably higher than the other denticles, straight or arched posteriorward. The denticles have rounded tips and a rounded section. The cup is asymmetrical and swollen and lacks nodes or denticles. For the best preserved P_1 element (Fig. 6C), the denticles are bigger and more discrete posteriorly.

FIG. 8. A–J, ?K, ?L, *Isarcicella turgida* Kozur *et al.*, 1975; A, bed WUZ.I, PIMUZ 31012; B, bed WUZ.I, PIMUZ 31046; C, bed WUZ.G, PIMUZ 31047; D, bed WUZ.K, PIMUZ 31048; E, (mirrored) bed WUZ.K, PIMUZ 31049; F, (mirrored) bed WUZ.K, PIMUZ 31055; G, (mirrored) bed WUZ.K, PIMUZ 31050; H, bed WUZ.K, PIMUZ 31205; I, bed WUZ.I (element lost); J, (juvenile) bed WUZ.O, PIMUZ 30997; K, (mirrored) bed WUZ.J, PIMUZ 31006; L, bed WUZ.I, PIMUZ 31011. Respectively, 'lateral' and 'upper' views, for some specimens additionally 'lower' or 'posterior' views. Scale bar represents 400 μm.

Remarks. *Isarcicella lobata* is sometimes confused with *H. parvus* (Matsuda 1981, pl. 5, figs 1, 3), but it differs by the asymmetrical wide basal cavity. It shares with *I. turgida* a swelling of the base of the denticles, but the blade is not as swollen and its basal cavity is asymmetrical and more inflated.

Occurrence. Southern Alps: Werfen Formation, Mazzin Member, Bulla section, Tesero section, San Pellegrino Pass section, Agordo-Frassené section. Kashmir: Khunamuh Formation, Guryul Ravine, beds 56 and 57 (beds number from Nakazawa *et al.* 1975). China: Meishan, Zhejiang, beds 28 and 29; Shangsi, Sichuan, beds 30–33; Luolou Formation, Wuzhuan, Guangxi, beds WUZ.I-M.

Isarcicella staeschei Dai and Zhang, 1989
Figure 6G–K

1964 *Spathognathodus isarcicus* Huckriede; Staesche, p. 288, text-figs 62–63.
1981 *Isarcicella isarcica* Huckriede; Matsuda, pp. 93–94, pl. 5, figs 4–7.
1981 *Isarcicella*? sp.; Matsuda, pp. 94–95, pl. 5, fig. 8.
*1989 *Isarcicella staeschei* Dai and Zhang, pp. 430–431, pl. 45, figs 16–17; pl. 46, figs 4–7, 11–13, 18, 19; pl. 53, figs 13–14.
1996 *Isarcicella isarcica* Huckriede; Kozur, p. 100, pl. 5, figs 6, 9.
1998 *Isarcicella staeschei* Dai and Zhang; Orchard and Krystyn, p. 354, pl. 6, figs 4, 5, 10–12.
2003 *Isarcicella staeschei* Dai and Zhang; Perri and Farabegoli, p. 300, pl. 3, figs 1–14, pl. 4, figs 7–9.
2004 *Isarcicella staeschei* Dai and Zhang; Perri *et al.*, p. 475, pl. 1, figs 1–6, pl. 2, figs 3, 6–14.
2011 *Isarcicella staeschei* Dai and Zhang; Jiang *et al.*, pl. 3, figs 9–12.

Diagnosis. An *Isarcicella* species in which the P_1 element has one lateral process bearing nodes or denticles. P_1 element strongly asymmetrical with one lateral process bearing nodes or denticles. 'Distal denticle' twice as high as other denticles. Carina with 4–6 discrete denticles. Basal cavity expending almost under the entire element.

Description. Our material agrees in all observable characters with the description of Dai and Zhang (1989).

Remarks. Two distinct morphotypes of *I. staeschei* have been described: a 'single lateral denticle' morphotype (Fig. 6G–I) and a 'more than one lateral denticle' morphotype (Fig. 6J, K), the latter including the holotype. According to Kozur (1996), morphotype 2 occurs exclusively in the *I. isarcica* zone, while according to Perri and Farabegoli (2003), it is older than the FO of *I. isarcica* in the Southern Alps. At Wuzhuan, morphotype 2 also occurs before the FO of *I. isarcica*, extending Perri and Farabegoli's observation to Guangxi.

Occurrence. China: Feixianguan Formation, Shangsi, Xiaoba and Xikou, Sichuan; Lower Jinjiling Formation, Meishan, Zhejiang, beds 27d and 28; Luolou Formation, Wuzhuan, Guangxi, beds WUZ.I-M. Southern Alps: Werfen Formation, Mazzin Member, Bulla section, Tesero section, San Pellegrino Pass section, Agordo-Frassené section. Kashmir: Khunamuh Formation, Guryul Ravine, beds 61 and 63 (beds number from Nakazawa *et al.* 1975).

Isarcicella turgida Kozur *et al.*, 1975
Figure 8A–J, ?K, ?L

*1975 *Anchignathodus turgidus* n. sp. Kozur *et al.*, p. 5, pl. 7, figs 11–12.
1995 *lsarcicella*? *turgida* Kozur *et al.*; Kozur, p. 72, pl. 2, figs 5, 8.
1996 *Isarcicella*? *turgida* Kozur *et al.*; Kozur, p. 100, pl. 4, fig. 8.
2003 *Isarcicella turgida* Kozur *et al.*; Perri and Farabegoli, p. 245, pl. 2, figs 13–15.
2003 *Isarcicella lobata* Perri and Farabegoli; Perri and Farabegoli, pp. 298–298, pl. 3, figs 15–17, 24–29 (only).
2004 *Isarcicella turgida* Kozur *et al.*; Perri *et al.*, p. 475, pl. 1, fig. 8.
2011 *Isarcicella turgida* Kozur *et al.*; Jiang *et al.*, pl. 2, figs 3–6.

Diagnosis. P_1 element with a characteristic thickened carina. Basal cavity moderately excavated and slightly asymmetrical, extending over two-thirds of the overall length of the element.

Description. The carina is thickened with a relatively short blade. The broad denticles have a rounded (e.g. Fig. 8A) to marked laterally compressed section (e.g. Fig. 8D). They are sometimes broader and more discrete posteriorly (Fig. 8A, B, G). The basal cavity is moderately excavated and slightly asymmetrical to nearly symmetrical (Fig. 8C, F).

Remarks. In overall shape, *I. turgida* is very similar to *H. parvus*. It differs only by the swollen blade. Specimens from Wuzhuan can be intermediate (Fig. 8C, E). *I. lobata* also shows a swelling of the entire basal cavity, but *I. turgida* has a narrower and subsymmetrical basal cavity.

Occurrence. Iran: Elikah Formation, Unit 64. China: Feixianguan Formation, Shangsi, Sichuan, beds 31a–33; Luolou Formation, Wuzhuan, Guangxi¸ 7 m above the top of the microbialite (beds WUZ.I–L). Southern Alps: Werfen Formation, Mazzin Member, Bulla section, Tesero section, San Pellegrino Pass section, Agordo-Frassené section.

Genus NEOGONDOLELLA Bender and Stoppel, 1965

Type species. *Gondolella mombergensis* (Tatge, 1956).

Neogondolella taylorae Orchard *in* Orchard *et al.*, 1994
Figure 7J

*1994 *Neogondolella taylorae* n. sp. Orchard *et al.*, p. 833, pl. 3, fig. 15 (only).
1996 *Clarkina* aff. *planata* Clark; Mei, pl. 18.2, fig. 13.
1998 *Neogondolella taylorae* beta morphotype nov.; Orchard and Krystyn, p. 362, pl. 2, figs 5, 9, 13–16.
2013 *Clarkina taylorae* Orchard; Zhao *et al.*, pl. 5, figs J–L.

Diagnosis. P_1 element with an elongated and oval-shaped platform. Platform widest at mid-length, rounded well-developed posterior margin surrounding the cusp. Carina with discrete nodes terminated anteriorly in a blade and posteriorly in a rounded erect cusp.

Remarks. The platform outline bears some resemblance to *N. planata,* but it is less flat. The single specimen from Wuzhuan is similar to *N. nevadensis,* but has a distinct posterior platform margin. Orchard and Krystyn (1998) distinguished three morphotypes. Our specimen is similar to morphotype beta, but has a slightly larger posterior margin.

Occurrence. Tibet: *Otoceras latilobatum* Zone, Selong. Spiti: *Otoceras woodwardi* and *Ophiceras tibeticum* zones, Guling, Lingti, Lalung, Muth. China: Meishan, Zhejiang; Wuzhuan, Guangxi (bed WUZ.D).

Neogondolella aff. *taylorae*
Figure 7K

Description. P_1 element more elongated (length:width ratio is *ca.* 3:1) than *N. taylorae*. Platform symmetrical and widest at mid-length, tapered anteriorly extending to the anterior end. Cusp erect and surrounded by a very large platform margin. Denticles discrete, including the most anterior ones which are erect and taller than the others. Element very straight in lateral profile.

Occurrence. Co-occurs with *N. taylorae*, 4 m above the base of the microbialite at Wuzhuan, Guangxi (bed WUZ.D).

Neogondolella sp. indet.
Figure 7I

Description. P_1 element with asymmetrical, anteriorly tapered platform. It differs from *N. taylorae* in having fused anterior denticles. This specimen could be an element of *N. carinata*, but the broken posterior part prevents any confident determination at the species level.

Occurrence. In the thin-bedded limestone beds above the microbialite in Wuzhuan, 12 m above the PTB (bed WUZ.O).

Acknowledgements. This research is supported by the Swiss NSF project 200021_135446 (to HB). We are deeply grateful to Mike Orchard, Tea Kolar-Jurkovšek and Sally Thomas for reviewing the manuscript and making insightful comments and to Michael Hautmann for editing and critical reading of the manuscript. Lorena Tessitore and Marc Leu are thanked for their help in processing samples. Prof. Rossana Martini and Agathe Martinier (Université de Genève) are thanked for their help with the SEM.

Editor. Michael Hautmann

REFERENCES

AGEMATSU, S., SANO, H. and SASHIDA, K. 2014. Natural assemblages of Hindeodus conodonts from a Permian–Triassic boundary sequence, Japan. *Palaeontology*, **57** (6), 1277–1289.

AWRAMIK, S. M. 1990. Stromatolites. 336–341. *In* BRIGGS, D. E. G. and CROWTHER, P. R. *Palaeobiology: a synthesis*. Blackwell Scientific Publications, London.

BAUD, A., CIRILLI, S. and MARCOUX, J. 1997. Biotic response to mass extinction: the Lowermost Triassic microbialites. *Facies*, **36**, 238–242.

—— RICHOZ, S., CIRILLI, S. and MARCOUX, J. 2002. *Basal Triassic carbonate of the Tethys: a microbialite world.* 16th International Sedimentological Congress, Johannesburg, Abstract Volume, 24–25.

—— —— and PRUSS S. 2007. The lower Triassic anachronistic carbonate facies in space and time. *Global and Planetary Change*, **55** (1), 81–89.

BENDER, H. and STOPPEL, D. 1965. Perm-Conodonten. *Geologisches Jahrbuch der BGR, (Hannover)*, **82** (3), 331–364.

BHATT, D. K. and ARORA, R. K. 1984. Otoceras bed of Himalaya and Permian–Triassic boundary-assessment and elucidation with conodont data. *Journal of the Geological Society of India*, **25** (11), 720–727.

BRAYARD, A., ESCARGUEL, G., BUCHER, H. and BRÜHWILER, T. 2009. Smithian and Spathian (Early Triassic) ammonoid assemblages from terranes: paleoceanographic and paleogeographic implications. *Journal of Asian Earth Sciences*, **36** (6), 420–433.

—— VENNIN, E., OLIVIER, N., BYLUND, K. G., JENKS, J., STEPHEN, D. A., BUCHER, H., HOFMANN, R., GOUDEMAND, N. and ESCARGUEL, G. 2011. Transient metazoan reefs in the aftermath of the end-Permian mass extinction. *Nature Geoscience*, **4** (10), 693–697.

BRÜHWILER, T., BRAYARD, A., BUCHER, H. and GUODUN, K. 2008. Griesbachian and Dienerian (Early Triassic) ammonoid faunas from northwestern Guangxi and southern Guizhou (south China). *Palaeontology*, **51** (5), 1151–1180.

BURGESS, S. D., BOWRING, S. and SHEN, S. Z. 2014. High-precision timeline for Earth's most severe extinction.

Proceedings of the National Academy of Sciences, **111** (9), 3316–3321.

CHEN, J., BEATTY, T. W., HENDERSON, C. M. and ROWE, H. 2008*a*. Conodont biostratigraphy across the Permian–Triassic boundary at the Dawen section, Great Bank of Guizhou, Guizhou Province, South China: implications for the Late Permian extinction and correlation with Meishan. *Journal of Asian Earth Sciences*, **36** (6), 442–458.

—— HENDERSON, C. M. and SHEN, S. Z. 2008*b*. Conodont succession around the Permian–Triassic boundary at the Huangzhishan Section, Zhejiang and its stratigraphic correlation. *Acta Palaeontologica Sinica*, **7** (1), 91–114.

CHIVAS, A. R., TORGERSEN, T. and POLACH, H. A. 1990. Growth rates and Holocene development of stromatolites from Shark Bay, Western Australia. *Australian Journal of Earth Sciences*, **37** (2), 113–121.

DAI, J. and ZHANG, J. 1989. Study on the Permian–Triassic biostratigraphy and event stratigraphy of northern Sichuan and southern Shaanxi. *Ministry of Geology and Mineral Resources, Geological Memoirs, Series*, **2**, 435 pp.

ELLISON, S. 1941. Revision of the Pennsylvanian conodonts. *Journal of Paleontology*, **15** (2), 107–143.

ERWIN, D. H. 2001. Lessons from the past: biotic recoveries from mass extinctions. *Proceedings of the National Academy of Sciences*, **98** (10), 5399–5403.

—— 2006. *Extinction: how life on Earth nearly ended 250 million years ago*. Princeton University Press, 230 pp.

EZAKI, Y., LIU, J. and ADACHI, N. 2003. Earliest Triassic microbialite micro-to megastructures in the Huaying area of Sichuan Province, South China: implications for the nature of oceanic conditions after the end-Permian extinction. *Palaios*, **18** (4–5), 388–402.

—— —— NAGANO, T. and ADACHI, N. 2008. Geobiological aspects of the earliest Triassic microbialites along the southern periphery of the tropical Yangtze Platform: initiation and cessation of a microbial regime. *Palaios*, **23** (6), 356–369.

FAN, G., WANG, Y., KERSHAW, S., LI, G., MENG, Z., LIN, Q. and YUAN, Z. 2014. Recurrent breakdown of Late Permian reef communities in response to episodic volcanic activities: evidence from southern Guizhou in South China. *Facies*, **60** (2), 603–613.

FARABEGOLI, E. and PERRI, M. C. 1998. Permian/Triassic boundary and Early Triassic of the Bulla section (Southern Alps, Italy): lithostratigraphy, facies and conodont biostratigraphy. *Giornale di geologia*, **60** (Special Issue), 292–310.

GALFETTI, T., BUCHER, H., MARTINI, R., HOCHULI, P. A., WEISSERT, H., CRASQUIN-SOLEAU, S., BRAYARD, A., GOUDEMAND, N., BRÜHWILER, T. and GUODUN, K. 2008. Evolution of Early Triassic outer platform paleoenvironments in the Nanpanjiang Basin (South China) and their significance for the biotic recovery. *Sedimentary Geology*, **204** (1), 36–60.

HAUTMANN, M., BUCHER, H., BRÜHWILER, T., GOUDEMAND, N., KAIM, A. and NÜTZEL, A. 2011. An unusually diverse mollusc fauna from the earliest Triassic of South China and its implications for benthic recovery after the end-Permian biotic crisis. *Geobios*, **44** (1), 71–85.

HENDERSON, C. M. and BAUD, A. 1997. Correlation of the Permian–Triassic boundary in Arctic Canada and comparison with Meishan, China. *Stratigraphy*, **11**, 143–152.

HERMANN, E., HOCHULI, P. A., MÉHAY, S., BUCHER, H., BRÜHWILER, T., WARE, D., HAUTMANN, M., ROOHI, G., UR-REHMAN, K. and YASEEN, A. 2011. Organic matter and palaeoenvironmental signals during the Early Triassic biotic recovery: the Salt Range and Surghar Range records. *Sedimentary Geology*, **234** (1), 19–41.

HOFMANN, R., GOUDEMAND, N., WASMER, M., BUCHER, H. and HAUTMANN, M. 2011. New trace fossil evidence for an early recovery signal in the aftermath of the end-Permian mass extinction. *Palaeogeography, Palaeoclimatology, Palaeoecology*, **310** (3), 216–226.

HUCKRIEDE, R. 1958. Die Conodonten der mediterranen Trias und ihr stratigraphischer Wert. *Paläontologische Zeitschrift*, **32** (3–4), 141–175.

JEPPSSON, L. and ANEHUS, R. 1999. A new technique to separate conodont elements from heavier minerals. *Alcheringa*, **23** (1), 57–62.

—— —— and FREDHOLM D. 1999. The optimal acetate buffered acetic acid technique for extracting phosphatic fossils. *Journal of Paleontology*, **73** (5), 964–972.

JIANG, H., LAI, X., LUO, G., ALDRIDGE, R., ZHANG, K. and WIGNALL, P. 2007. Restudy of conodont zonation and evolution across the P/T boundary at Meishan section, Changxing, Zhejiang, China. *Global and Planetary Change*, **55** (1), 39–55.

—— ALDRIDGE, R. J., LAI, X., YAN, C. and SUN, Y. 2010. Phylogeny of the conodont genera *Hindeodus* and *Isarcicella* across the Permian–Triassic boundary. *Lethaia*, **44** (4), 374–382.

—— LAI, X., YAN, C., ALDRIDGE, R. J., WIGNALL, P. and SUN, Y. 2011. Revised conodont zonation and conodont evolution across the Permian–Triassic boundary at the Shangsi section, Guangyuan, Sichuan, South China. *Global and Planetary Change*, **77** (3), 103–115.

—— —— SUN, Y., WIGNALL, P. B., LIU, J. and YAN, C. 2014. Permian–Triassic conodonts from Dajiang (Guizhou, South China) and their implication for the age of microbialite deposition in the aftermath of the End-Permian mass extinction. *Journal of Earth Science*, **25** (3), 413–430.

JOACHIMSKI, M. M., LAI, X., SHEN, S., JIANG, H., LUO, G., CHEN, B., JUN, C. and SUN, Y. 2012. Climate warming in the latest Permian and the Permian–Triassic mass extinction. *Geology*, **40** (3), 195–198.

KAIM, A., NÜTZEL, A., BUCHER, H., BRÜHWILER, T. and GOUDEMAND, N. 2010. Early Triassic (Late Griesbachian) gastropods from South China (Shanggan, Guangxi). *Swiss Journal of Geosciences*, **103** (1), 121–128.

KERSHAW, S., ZHANG, T. and LAN, G. 1999. A ?microbialite carbonate crust at the Permian–Triassic boundary in South China, and its palaeoenvironmental significance. *Palaeogeography, Palaeoclimatology, Palaeoecology*, **146** (1), 1–18.

—— GUO, L., SWIFT, A. and FAN, J. 2002. ?Microbialites in the Permian–Triassic boundary interval in central China: structure, age and distribution. *Facies*, **47** (1), 83–89.

—— LI, Y., CRASQUIN-SOLEAU, S., FENG, Q., MU, X., COLLIN, P. Y., REYNOLDS, A. and GUO, L. 2007.

Earliest Triassic microbialites in the South China block and other areas: controls on their growth and distribution. *Facies*, **53** (3), 409–425.

KLAPPER, G., LINDSTRÖM, M., SWEET, W. C. and ZIEGLER, W. 1973. *In* ZIEGLER, W. (ed.). *Catalogue of Conodonts, 1*. E. Schweizerbart'sche Verlagsbuchhandlung, Stuttgart, 504 pp.

KOIKE, T. 1996. The first occurrence of Griesbachian conodonts in Japan. *Transactions and Proceedings of the Palaeontological Society of Japan*, **181**, 337–346.

KOLAR-JURKOVŠEK, T., JURKOVŠEK, B. and ALJINOVIĆ, D. 2011. Conodont biostratigraphy across the Permian–Triassic boundary at the Lukač section in western Slovenia. *Rivista Italiana di Paleontologia e Stratigrafia*, **117**, 115–133.

KOZUR, H. W. 1975. Beiträge zur Conodontenfauna des Perm. *Geologisch-Paläontologische Mitteilungen Innsbruck*, **5**, 1–44.

—— 1977. Revision der Conodontengattung Anchignathodus und ihrer Typusart. *Zeitschrift für Geologische Wissenschaften*, **5**, 1113–1127.

—— 1989. Significance of events in conodont evolution for the Permian and Triassic stratigraphy. *Courier Forschungsinstitut Senckenberg*, **117**, 385–408.

—— 1995. Permian conodont zonation and its importance for the Permian stratigraphic standard scale. *Geologisch-Paläontologische Mitteilungen Innsbruck*, **20**, 165–205.

—— 1996. The conodonts *Hindeodus*, *Isarcicella* and *Sweetohindeodus* in the uppermost Permian and lowermost Triassic. *Geologia Croatica*, **49** (1), 81–115.

—— 1998. Some aspects of the Permian–Triassic boundary (PTB) and of the possible causes for the biotic crisis around this boundary. *Palaeogeography, Palaeoclimatology, Palaeoecology*, **143** (4), 227–272.

—— 2004. Pelagic uppermost Permian and the Permian–Triassic boundary conodonts of Iran. Part 1: Taxonomy. *Hallesches Jahrbuch für Geowissenschaften, B Geologie, Paläontologie, Mineralogie*, **18**, 29–68.

—— and PJATAKOVA, M. 1976. Die Conodontenart *Anchignathodus parvus* n. sp., eine wichtige Leitform der basalen Trias. *Koninklijke Nederlandse Akademie van Wetenschappen, Amsterdam, Proceedings, Series B*, **79**, 123–128.

—— MOSTLER, H. and RAHIMI-YAZD, A. 1975. Beiträge zur Mikrofauna permotriadischer Schichtfolgen. Teil II: Neue Conodonten aus dem Oberperm und der basalen Trias von Nord-und Zentraliran. *Geologisch-Paläontologische Mitteilungen Innsbruck*, **5** (3), 1–23.

KRYSTYN, L., RICHOZ, S., BAUD, A. and TWITCHETT, R. J. 2003. A unique Permian–Triassic boundary section from the neotethyan Hawasina basin, Central Oman Mountains. *Palaeogeography, Palaeoclimatology, Palaeoecology*, **191** (3), 329–344.

LEHRMANN, D. J. 1999. Early Triassic calcimicrobial mounds and biostromes of the Nanpanjiang basin, South China. *Geology*, **27** (4), 359–362.

—— WAN, Y., WEI, J., YU, Y. and XIAO, J. 2001. Lower Triassic peritidal cyclic limestone: an example of anachronistic carbonate facies from the Great Bank of Guizhou, Nanpanjiang Basin, Guizhou province, South China. *Palaeogeography, Palaeoclimatology, Palaeoecology*, **173** (3), 103–123.

MATSUDA, T. 1981. Appendix to conodonts of Guryul Ravine. *Palaeontologia Indica*, **46**, 187–188.

MEI, S. 1996. Restudy of conodonts from the Permian–Triassic boundary beds at Selong and Meishan and the natural Permian–Triassic boundary. 141–148. *In* WANG, H. and WANG, X. (eds). *Centennial memorial volume of Professor Sun Yunzhu, palaeontology and stratigraphy*. China University of Geosciences Press, Beijing.

METCALFE, I. 1995. Mixed Permo-Triassic boundary conodont assemblages from Gua Sei and Kampong Gua, Pahang, Peninsular Malaysia. *Courier Forschungsinstitut Senckenberg*, **182**, 487–495.

—— and NICOLL, R. S. 2007. Conodont biostratigraphic control on transitional marine to non-marine Permian–Triassic boundary sequences in Yunnan-Guizhou, China. *Palaeogeography, Palaeoclimatology, Palaeoecology*, **252** (1), 56–65.

NAKAZAWA, K., KAPOOR, H. M., ISHII, K. I., BANDO, Y., OKIMURA, Y. and TOKUOKA, T. 1975. The upper Permian and the lower Triassic in Kashmir, India. *Memoirs of the Faculty of Science, Kyoto University, Series of Geology and Mineralogy*, **42**, 1–106.

NICOLL, R. S., METCALFE, I. and CHENG-YUAN, W. 2002. New species of the conodont genus *Hindeodus* and the conodont biostratigraphy of the Permian–Triassic boundary interval. *Journal of Asian Earth Sciences*, **20** (6), 609–631.

NICORA, A. and PERRI, M. C. 1999. The P/T boundary in the Tesero section, western Dolomites (Trento). 3.3. Bio- and chronostratigraphy. Conodonts. *In Stratigraphy and facies of the Permian deposits between Eastern Lombardy and the Western Dolomites*. Field Trip Guidebook, 23–25 September 1999, Earth Science Department, Pavia University, Brescia, Italy.

ORCHARD, M. J. 2007. Conodont diversity and evolution through the latest Permian and Early Triassic upheavals. *Palaeogeography, Palaeoclimatology, Palaeoecology*, **252** (1), 93–117.

—— and KRYSTYN, L. 1998. Conodonts of the lowermost Triassic of Spiti, and new zonation based on *Neogondolella* successions. *Rivista Italiana di Paleontologia e Stratigrafia*, **104** (3), 341–367.

—— NASSICHUK, W. W. and RUI, L. 1994. Conodonts from the lower Griesbachian *Otoceras Latilobatum* bed of Selong, Tibet and the position of the Permian–Triassic boundary. *Canadian Society of Petroleum Geologists, Memoir*, **17**, 823–843.

PERRI, M. C. 1991. Conodont biostratigraphy of the Werfen Formation (Lower Triassic), Southern Alps, Italy. *Bollettino della Società Paleontologica Italiana*, **30** (1), 23–46.

—— and FARABEGOLI, E. 2003. Conodonts across the Permian–Triassic boundary in the Southern Alps. *Courier Forschungsinstitut Senckenberg*, **245**, 281–313.

—— MOLLOY, P. D. and TALENT, J. A. 2004. Earliest Triassic conodonts from Chitral, northernmost Pakistan. *Rivista Italiana di Paleontologia e Stratigrafia*, **110** (2), 467–478.

PRUSS, S. B., BOTTJER, D. J., CORSETTI, F. A. and BAUD, A. 2006. A global marine sedimentary response to the end-Permian mass extinction: examples from southern

Turkey and the western United States. *Earth-Science Reviews*, **78** (3), 193–206.

PURNELL, M. A., DONOGHUE, P. C. and ALDRIDGE, R. J. 2000. Orientation and anatomical notation in conodonts. *Journal of Paleontology*, **74** (1), 113–122.

QI, Y. P. and LIAO, T. P. 2007. Discovery of the latest Permian gondolellid conodonts from the microbialites across the Permian–Triassic boundary in the Tudiya Section, Chongqing, South China and its implications. *Permophiles*, **49**, 28–31.

RAUP, D. M. 1979. Size of the Permo-Triassic bottleneck and its evolutionary implications. *Science*, **206** (4415), 217–218.

RETALLACK, G. J. 1995. Permian–Triassic life crisis on land. *Science*, **267** (5194), 77–80.

REXROAD, C. and FURNISH, W. M. 1964. Conodonts from the Pella Formation (Mississippian), south-central Iowa. *Journal of Paleontology*, **38** (4), 667–676.

RODLAND, D. L. and BOTTJER, D. J. 2001. Biotic recovery from the end-Permian mass extinction: behavior of the inarticulate brachiopod Lingula as a disaster taxon. *Palaios*, **16** (1), 95–101.

SCHNEEBELI-HERMANN, E. 2012. Extinguishing a Permian world. *Geology*, **40** (3), 287–288.

—— KÜRSCHNER, W. M., KERP, H., BOMFLEUR, B., HOCHULI, P. A., BUCHER, H., WARE, D. and ROOHI, G. 2015. Vegetation history across the Permian–Triassic boundary in Pakistan (Amb section, Salt Range). *Gondwana Research*, **27** (3), 911–924. doi:10.1016/j.gr.2013.11.007

SCHÖNLAUB, H. P. 1991. The Permian–Triassic of the Gartnerkofel-1 core (Carnic Alps, Austria): conodont biostratigraphy. *Abhandlungen der Geologischen Bundesanstalt Wien*, **45**, 79–98.

SCHUBERT, J. K. and BOTTJER, D. J. 1992. Early Triassic stromatolites as post-mass extinction disaster forms. *Geology*, **20** (10), 883–886.

—— —— 1995. Aftermath of the Permian–Triassic mass extinction event: paleoecology of Lower Triassic carbonates in the western USA. *Palaeogeography, Palaeoclimatology, Palaeoecology*, **116** (1), 1–39.

SHAPIRO, R. S. 2000. A comment on the systematic confusion of thrombolites. *Palaios*, **15** (2), 166–169.

SONG, H., TONG, J. and CHEN, Z. 2009*a*. Two episodes of foraminiferal extinction near the Permian–Triassic boundary at the Meishan section, South China. *Australian Journal of Earth Sciences*, **56** (6), 765–773.

—— —— —— YANG, H. and WANG, Y. 2009*b*. End-Permian mass extinction of foraminifers in the Nanpanjiang Basin, South China. *Journal of Paleontology*, **83**, 718–738.

—— WIGNALL, P. B., CHEN, Z. Q., TONG, J., BOND, D. P., LAI, X., ZHAO, X., JIANG, H., YAN, C., NIU, Z., CHEN, Z. and WANG, Y. 2011. Recovery tempo and pattern of marine ecosystems after the end-Permian mass extinction. *Geology*, **39** (8), 739–742.

STAESCHE, U. 1964. Conodonten aus dem Skyth von Südtirol. *Neues Jahrbuch für Geologie und Paläontologie, Abhandlungen*, **119** (3), 247–306.

SWEET, W. C. 1970*a*. Permian and Triassic conodonts from a section at Guryul Ravine, Vihi district, Kashmir. *University of Kansas Paleontological Contributions, Paper*, **49**, 1–10.

—— 1970*b*. Uppermost Permian and Lower Triassic conodonts of the Salt Range and Trans-Indus Ranges, West Pakistan. 207–275. *In* KUMMEL, B. and TEICHERT, C. (eds). *Stratigraphic boundary problems: Permian and Triassic of West Pakistan*, Special Publication **4**, University of Kansas.

TATGE, U. 1956. Conodonten aus dem germanischen Muschelkalk. *Paläontologische Zeitschrift*, **30** (3/4), 129–147.

TIAN, S. 1993. Evolution of conodont genera *Neogondolella*, *Hindeodus* and *Isarcicella* in northwestern Hunan, China. *Stratigraphy and Palaeontology of China*, **2**, 173–191.

WANG, C. 1994*a*. A conodont-based high-resolution eventostratigraphy and biostratigraphy for the Permian–Triassic boundaries in South China. *Palaeoworld*, **4**, 234–248.

—— 1994*b*. Conodonts of Permian–Triassic boundary beds and biostratigraphic boundary. *Acta Palaeontologica Sinica*, **34** (2), 129–151.

—— and WANG, S. 1997. Conodonts from Permian–Triassic boundary beds in Jiangxi, China and evolutionary lineage of *Hindeodus–Isarcicella*. *Acta Palaeontologica Sinica*, **36**, 151–178.

WANG, Y., TONG, J., WANG, J. and ZHOU, X. 2005. Calcimicrobialite after end-Permian mass extinction in South China and its palaeoenvironmental significance. *Chinese Science Bulletin*, **50** (7), 665–671.

WANG, Z. and CAO, Y. 1993. *In* WANG, C. 1993. *Conodonts of the Lower Yangtze Valley-an index to biostratigraphy and organic metamorphic maturity*. Science Press, Beijing, 326 pp. [in Chinese with English summary]

YAN, C., WANG, L., JIANG, H., WIGNALL, P., SUN, Y., CHEN, Y. and LAI, X. 2013. Uppermost Permian to Lower Triassic conodonts at Bianyang section, Guihzou province, South China. *Palaios*, **28**, 509–522.

YIN, H., SWEET, W. C., GLENISTER, B. F., KOTLYAR, G., KOZUR, H., NEWELL, N. D., SHENG, J., YANG, Z. and ZAKHAROV, Y. D. 1996. Recommendation of the Meishan section as Global Stratotype Section and Point for basal boundary of Triassic System. *Newsletters on Stratigraphy*, **34** (2), 81–108.

YOUNGQUIST, W. and MILLER, A. 1949. Conodonts from the Late Mississippian Pella Beds of South-Central Iowa. *Journal of Paleontology*, **23** (6), 617–622.

ZHANG, K., LAI, X., DING, M. and LIU, J. 1995. Conodont sequence and its global correlation of Permian–Triassic boundary in Meishan section, Changxing, Zhejiang Province. *Earth Science, Journal of China University of Geosciences*, **20** (6), 669–676. [in Chinese]

ZHANG, Y., ZHANG, K., SHI, G., HE, W., YUAN, D., YUE, M. and YANG, T. 2014. Restudy of conodont biostratigraphy of the Permian–Triassic boundary section in Zhongzhai, southwestern Guizhou Province, South China. *Journal of Asian Earth Sciences*, **80**, 75–83.

ZHAO, L., CHEN, Y., CHEN, Z. Q. and CAO, L. 2013. Uppermost Permian to Lower Triassic conodont zonation from Three Gorges area, South China. *Palaios*, **28** (8), 523–540.

APPENDIX B

Additional publication link to this thesis

COMPETITION IN SLOW MOTION: THE UNUSUAL CASE OF BENTHIC MARINE COMMUNITIES IN THE WAKE OF THE END-PERMIAN MASS EXTINCTION

Palaeontology, Vol. 58, Part 5, 2015, pp. 871–901

Palaeontology The Palaeontological Association www.palass.org

[Palaeontology, 2015, pp. 1–31]

COMPETITION IN SLOW MOTION: THE UNUSUAL CASE OF BENTHIC MARINE COMMUNITIES IN THE WAKE OF THE END-PERMIAN MASS EXTINCTION

by MICHAEL HAUTMANN[1], BORHAN BAGHERPOUR[1], MORGANE BROSSE[1], ÅSA FRISK[1,2], RICHARD HOFMANN[1], AYMON BAUD[3], ALEXANDER NÜTZEL[4], NICOLAS GOUDEMAND[1] *and* HUGO BUCHER[1]

[1]Paläontologisches Institut und Museum, Universität Zürich, Karl-Schmid Strasse 4, 8006, Zürich, Switzerland; e-mails: michael.hautmann@pim.uzh.ch, borhan.bagherpour@pim.uzh.ch, morgane.brosse@pim.uzh.ch, richard.hofmann@pim.uzh.ch, nicolas.goudemand@pim.uzh.ch, hugo.fr.bucher@pim.uzh.ch
[2]Department of Earth Sciences, Uppsala University, Villav. 16, 75236, Uppsala, Sweden; e-mail: asa.frisk@pim.uzh.ch
[3]Baud Geological Consultant, Parc de la Rouvraie 28, 1018, Lausanne, Switzerland; e-mail: aymon.baud@unil.ch
[4]SNSB-Bayerische Staatssammlung für Paläontologie und Geologie, GeoBio-Center LMU, Richard-Wagner-Str. 10, 80333, München, Germany; e-mail: a.nuetzel@lrz.uni-muenchen.de

Typescript received 13 March 2015; accepted in revised form 16 June 2015

Abstract: Changes of community structure in response to competition usually take place on timescales that are much too short to be visible in the geological record. Here we report the notable exception of a benthic marine community in the wake of the end-Permian mass extinction, which is associated with the microbial limestone facies of the earliest Triassic of South China. The newly reported fauna is well preserved and extraordinarily rich (30 benthic macroinvertebrate species, including the new species *Astartella*? *stefaniae* (Bivalvia) and *Eucochlis obliquecostata* (Gastropoda)) and stems from an environmentally stable setting providing favourable conditions for benthic organisms. Whereas changes in the taxonomic composition are negligible over the observed time interval of 10–100 ka, three ecological stages are identified, in which relative abundances of initially rare species continuously increased at the cost of previously dominant species. Concomitant with the changes of dominant species is an increase in faunal evenness and heterogeneity. In the absence of both environmental and taxonomic changes, we attribute this pattern to the long-term effects of interspecific competition, which acted at an unusually slow pace because the number of competing species and potential immigrants was dramatically reduced by the end-Permian mass extinction. We suggest that these non-actualistic conditions led to decreased rates of niche differentiation and hence to the delayed rediversification of benthos that characterizes the aftermath of the greatest Phanerozoic mass extinction event. A hyperbolic diversification model is proposed, which accounts for the positive relationship between the intensity of interspecific competition and the rate of niche differentiation and resolves the conundrum of delayed rediversification at a time when niche space was largely vacated.

Key words: diversification, competition, benthos, Early Triassic, China.

HOW fast can the world's biosphere recover from a global mass extinction? Palaeorecord data suggest a significant time lag between major extinction events and the onset of biotic recovery, conventionally termed the 'survival interval' during which surviving species persisted without an indication of rediversification (Kauffman and Harries 1996; Erwin 2001). Whereas the phenomenon itself is generally recognized, its possible causes are debated. Frequently discussed explanations include the following: (1) persistence of environmental stress (Hallam 1991); (2) incompleteness of the fossil record (Wignall and Benton 1999; Peters and Foote 2002); and (3) reduced evolutionary rates. Although the latter explanation has frequently been considered as a possible mechanism, few authors (e.g. Kirchner and Weil 2000) have explicitly invoked it as a major factor, possibly because a comprehensive understanding of drivers (both intrinsic and extrinsic) of evolutionary rates is still lacking. Erwin (2001) noted that the excess of ecological opportunities after a mass extinction should theoretically increase speciation rather than

doi: 10.1111/pala.12186

depressing it, and he suggested that the construction of a new ecological framework during recovery intervals was a more important process than refilling of vacant niches. Consumer–resource aspects, mutualism and ecosystem engineering are among the obvious ecological factors that may make speciation a self-augmenting process (Whittaker 1977; Erwin 2007). Accordingly, the reduced effects of these factors at times of low global diversity provide a possible explanation for the low diversification rates. However, the most important ecological determinant of diversification rates is competition, which may either impede diversification by niche pre-emption (Darwin 1859; Sepkoski 1996) or drive diversification by promoting niche differentiation (Mayr 1963; Schluter 1994; Emerson and Kolm 2005; Meyer and Kassen 2007; Bailey *et al.* 2013). The low intensity of competition-mediated niche differentiation after a global mass extinction is therefore a possible cause of decreased speciation rates during the survival interval, and conversely, competition may become the main driver of post-extinction diversification until a level of ecological saturation is reached where niche pre-emption becomes a dominant factor and options for further niche differentiation are exhausted. This changing role of competition in biodiversification is nearly completely ignored in existing models, probably because evolutionary thinking is still subtly influenced by Darwin's commitment to the principle of plenitude.

Testing for possible causes of the time lag in rediversification after global mass extinctions is not straightforward. The Lazarus phenomenon, that is the temporary absence of taxa from the fossil record after a major extinction event (Flessa and Jablonski 1983, p. 319), has been taken as evidence for the persistence of environmental stress that forced species into refuges that are unlikely to be discovered (Vermeij 1986), or alternatively as an indication of incompleteness of the fossil record after mass extinctions (Wignall and Benton 1999). Ecological factors are more difficult to detect, because they normally act at the timescale of several tens or hundreds of generations (Miller 1967), which is unlikely to be resolved by palaeorecord data (Sepkoski 1996). The possibility that the greatest Phanerozoic mass extinction (Raup 1979) could have reduced competition to such a low level that ecological processes were extended to the geologically observable timescale has not yet been explored. This is at least partly due to the manifold prerequisites that a sedimentary succession needs to fulfil as a potential archive for such processes, including exceptional preservation conditions, environmentally stable conditions throughout the interval of observation, and stratigraphic control. Our new data are unique in that they stem from a section that provides all these conditions for a time interval of 10–100 ka soon after the greatest mass extinction event in metazoan history.

GEOLOGICAL SETTING

Overview

The fossil material stems from lens-shaped, laterally discontinuous shell coquinas interbedded within microbial limestone (ML) that characterizes the basal part of the Lower Triassic Luolou Formation in northern Guangxi and southern Guizhou, South China (Figs 1, 2). The ML has been formed in an inner to mid-shelf setting and is generally dominated by *Renalcis*-type calcimicrobes (Kershaw *et al.* 2012). In the studied sections, the ML overlies an erosional surface above Changhsingian (late Permian) skeletal limestone and piles up to an 8- to 12-m-thick sequence that locally yields Griesbachian ammonoids (*Ophiceras* sp.) in its uppermost few metres (Brühwiler *et al.* 2008). Tabular-to-wavy thrombolites dominate in the lower half of the sections, whereas the upper half is dominated by dome-shaped dendrolites (Fig. 2). Shell coquinas occur usually in association with dome-shaped microbialites and are thus restricted to the upper half of the sections. Throughout this upper interval, invariance of microfacies and sedimentological features and constant $\delta^{13}C_{carb}$ values (Figs 2, 3) indicate constant environmental conditions.

Age control

A rich and abundant conodont fauna occurs in one of the studied sections (Wuzhuan; Figs 1, 2), which allows for a precise biostratigraphical age determination (Brosse *et al.* 2015). Accordingly, the macrofaunal succession discussed in this paper comprises three Griesbachian conodont interval zones: *Hindeodus parvus* interval zone, *Isarcicella lobata* interval zone and *I. staeschei* interval zone (Hautmann *et al.* 2015, appendix S1). The middle Griesbachian *I. isarcica* interval zone occurs above the stratigraphically highest macroinvertebrate sample. Given that: (1) the first Griesbachian conodont zone (*H. parvus* zone) extends stratigraphically below the lowest macroinvertebrate sample; and (2) the latest Griesbachian conodont zone is younger than the uppermost sample, the macroinvertebrate-bearing part of the section was deposited during a time interval notably shorter than the overall duration of the Griesbachian. A minimum duration of the deposition time can be estimated on the basis of maximum growth rates of Recent marine stromatolites (0.4 mm/a; Chivas *et al.* 1990), suggesting 25–30 ka minimum duration for the complete ML sequence (10–12 m thick) and 12.5 ka for the macrofaunal interval (5 m thick). Revised U–Pb ages from the GSSP at Meishan (Burgess *et al.* 2014) indicate 60 ± 48 ka duration for the interval between the main extinction horizon and the base

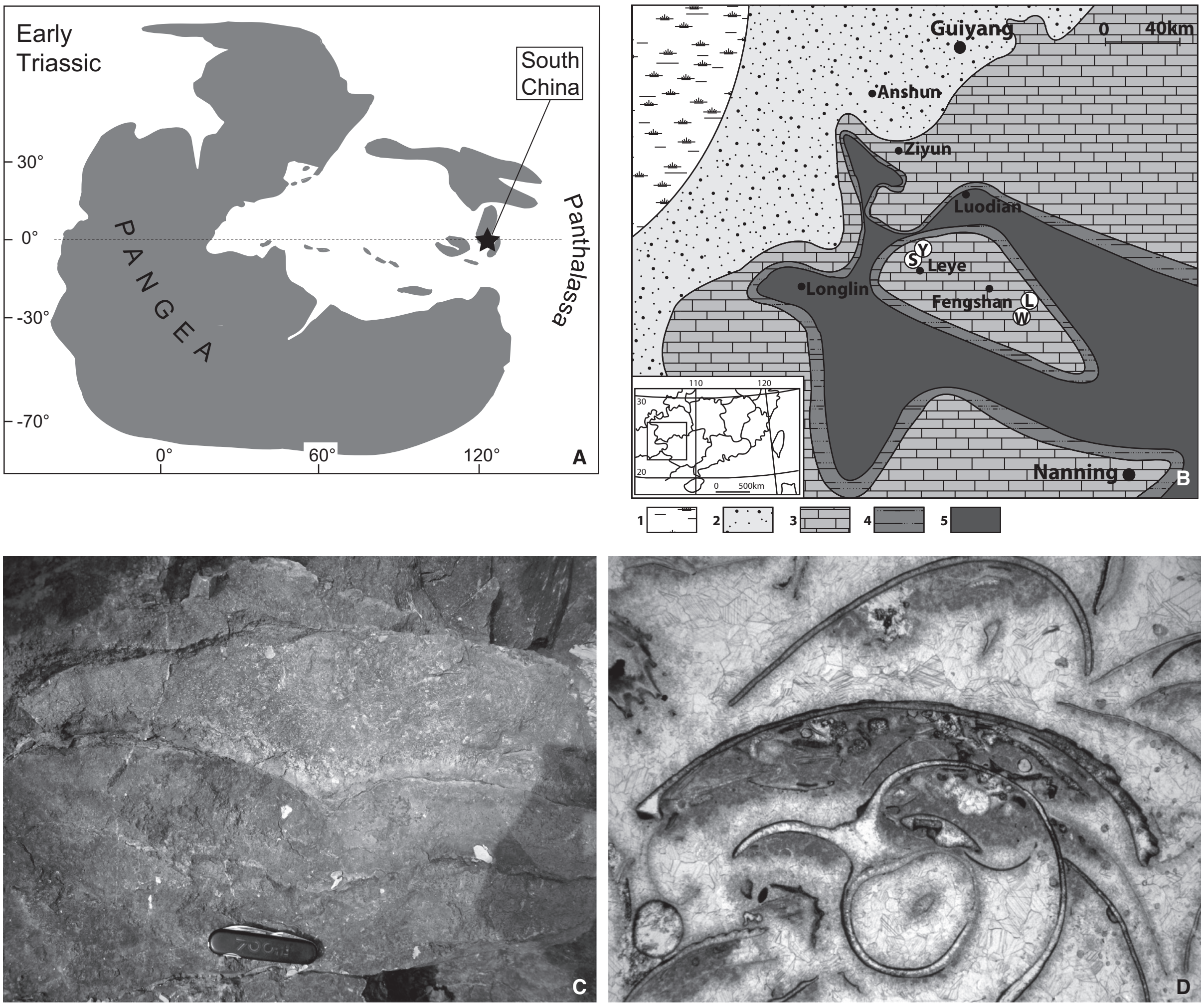

FIG. 1. Study area, field situation and microfacies of fossil occurrences. A, palaeo-position of the study area. B, locality map indicating position of sections in the Nanpanjiang Basin. *Abbreviations:* L, Longyuan; S, Shanggan; W, Wuzhuan; Y, Youping. *Legend*: 1, flood alluvial facies; 2, shallow-water siliciclastic deposits; 3, carbonate platform; 4, slope; 5, basin; modified from Fan *et al.* (2014). C, field photograph of lens-shaped shell concentration trapped between microbialitic dome structures in the Wuzhuan section; pen knife *c.* 9 cm long. D, thin section of shell-bearing sediments showing micritic envelopes (dark) that aided shell preservation; width of field is 12.5 mm.

of the *Isarcicella isarcica* zone, providing further evidence that the deposition time of the macrofaunal interval was most likely longer than 10 ka but shorter than 100 ka.

Microfacies

Generally, Permian–Triassic boundary microbialites were facies-limited, avoiding both the shallowest high-energy settings and the deeper shelf (Kershaw *et al.* 2012). They were also concentrated around the Early Triassic equator and restricted to waters devoid of clastic load. The microbialites of the studied sections overlay an early cemented high-energy post-extinction grainstone or packstone containing reworked latest Permian foraminifera. At the base of the ML interval, a stromatolitic facies is commonly (except for Wuzhuan) developed, varying in thickness between 20 cm at Youping and Longyuan and 5 m in Shanggan. The microbialites that follow above the stromatolites (or, in Wuzhuan, above the basal grainstone) are usually developed as thrombolites with a tabular-to-wavy-undulating morphology in the lower half and as dendrolites with dome-shaped morphologies in the upper half. The clotted mesostructures of the tabular thrombolites include labyrinthic (Fig. 3A), isolated-spotted and vesicular structures as well as layered structures with stromatactis-type fabric. In contrast, digitated mesoclots (Fig. 3B) build up domal morphologies that dominate in

FIG. 2. Lithological logs, stratigraphy, and position of samples. $\delta^{13}C_{carb}$ refers to the Wuzhuan section. Colour indicates assignment of samples to faunal intervals: FI 1 (red), FI 2 (orange), FI 3 (green) and the transitional sample (t.s.; light green) according to the cluster analysis (Fig. 4A).

the upper half of the sections. In Shanggan, the domal part contains centimetric cavities of stromatactis type filled with blocky calcite. The change from tabular to domal morphologies has been attributed to a change in water depth and sedimentation rate (Kershaw *et al.* 2012), but within the dome-dominated upper interval, no major changes in fabric, microfacies and carbon isotopes are observed (Fig. 2). The occurrence of shell lenses containing macrofauna is restricted to the stratigraphically upper part of the sections, where the dome-shaped morphologies allowed for the sedimentological concentration of shells in the troughs between neighbouring domes. The microfacies type of the shell coquinas is a poorly to well-washed mollusc rudstone (Hautmann *et al.* 2011). Main skeletal grains are bivalves and gastropods, augmented by echinoderm ossicles, ostracods and rare brachiopods. The original shells of molluscs are typically replaced by blocky sparite, which is surmounted by micrite envelopes (Fig. 1D).

Taphonomy

Skeletal elements are usually disarticulated, but in spite of their tiny nature and small size (generally <1 cm), they are usually neither fragmented nor abraded. This indicates a short transportation distance, most likely because the shells were hydrodynamically accumulated in troughs between dome structures formed by ML (Fig. 1C), which prevented them from further transportation and abrasion. Given the limited transportation distance and the absence of major lateral facies changes for distances of tens of kilometres around the fossil localities (Fig. 1B), a mixing of faunas from different habitats can be excluded. We therefore interpret the shell lenses as autochthonous to parautochthonous concentrations of skeletal remains within the former habitat of the animals.

The state of preservation of the shelly fossils is outstanding by Early Triassic standards, allowing for recognition of minute details of the shell surface such as delicate ornamentation and incremental lines (see figured material in Systematic Palaeontology below). We identified several factors that worked in concert to produce this exceptional preservation:

1. The fossils are from an environment that was locally supersaturated in $CaCO_3$, as evidenced by the presence of microbialite (Riding and Liang 2005). Although $CaCO_3$ supersaturation of sea water prevailed during most of the Phanerozoic, huge fluctuations due to volcanogenic ocean acidification have been described for the Early Triassic, with dissolution surfaces at the top of limestone beds stratigraphically adjacent to inorganic carbonate precipitations (Payne *et al.* 2007). Repeated intervals of $CaCO_3$ undersaturation could thus have prevented preservation of delicate shells in other settings.
2. Nearly all shells have micrite envelopes (Fig. 1D), which are more resistant to dissolution than the shell itself in primarily aragonitic molluscs (Flügel 2009). The non-micritized part of the molluscan shells generally consists of blocky sparite (Fig. 1D), indicating shell dissolution and subsequent vug filling. During this critical interval of fossil diagenesis, delicate details of external structures were preserved by the micrite envelopes until stabilized by the newly precipitated calcite.
3. The shells were trapped in-between domes of ML (Fig. 1C), which prevented further transport and abrasion. The shell lenses therefore represent a *Konzentrat-Lagerstätte* (Seilacher *et al.* 1985), which is extremely unusual in the Early Triassic.

MATERIAL AND METHODS

Locality information

GPS coordinates of the sections are as follows: Wuzhuan section: 24°21′44.6″ N 107°20′02.00″ E; Yuping section: 24°57′28.0″ N 106°39′13.20″ E; Shanggan section: 24°48′48.00″ N 106°32′52.30″ E; Longyuan section: 24°25′54.30″ N 107°22′24.20″ E.

Logging and sampling protocol

All sections have been logged in detail with respect to lithological and sedimentological features (Fig. 2). Lens-shaped shell coquinas that occur in the upper half of the sections have been quantitatively sampled in the field and mechanically disintegrated in the laboratory to a target size of 5–20 cm for individual rock fragments. Standard mechanical preparation techniques were applied where necessary. Fossils on the surfaces of the rock fragments were determined and quantitatively counted. For bivalved animals (bivalves and brachiopods), the number of individuals has been inferred by counting only the most numerous valve (left/right or dorsal/ventral) together with the articulated specimens. As an exception, the number of individuals of the lingulid *Sinolingularia*? has been obtained by dividing the overall number of valves by two, because features for distinguishing dorsal and ventral valves were not preserved in the majority of the specimens. The collected fauna comprises approximately 2500 specimens from twelve samples, representing *c.* 1800 individuals belonging to 30 species (Hautmann *et al.* 2015, appendices S2–S4).

Carbon isotope analysis

Carbon isotopes have been measured in the Wuzhuan section from samples taken each 20–50 cm, depending on lithology and outcrop conditions. Samples were cleaned and cut into slabs; homogenous parts (avoiding bioclasts, diagenetic calcite veins) were then identified, drilled and ground. Analyses were carried out at the isotope laboratories of ETH Zürich using a GasBench II (ThermoFisher

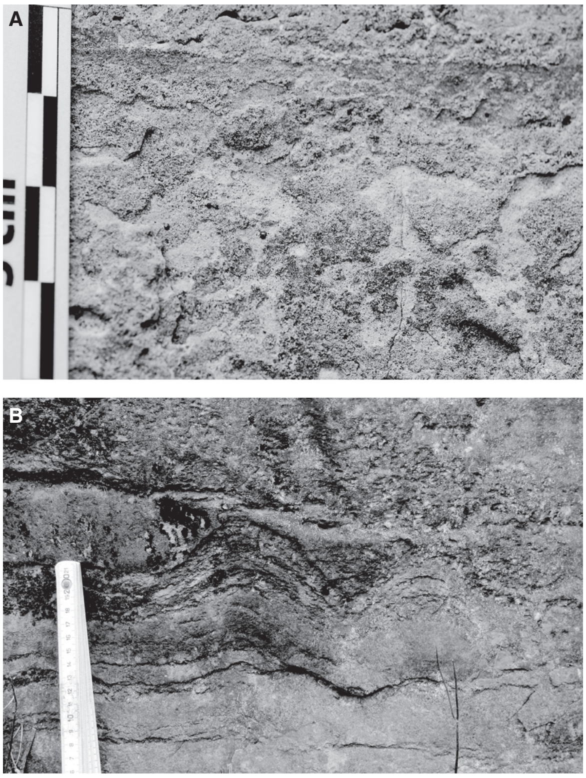

FIG. 3. Microbialites in the studied sections. A, field photograph of thrombolite with clotted mesostructure and labyrinthic fabric from the Youping section at 1.75 m. B, field photograph of dome-shaped structures from the Youping section; height of the domes varies from 10 to 20 cm. Both scale bars measured in cm.

Scientific, Bremen, Germany) equipped with a CTC autosampler (CTC Analytics AG, Zwingen, Switzerland), and coupled to a ConFlow IV interface and a Delta V Plus mass spectrometer (both ThermoFisher Scientific, Bremen, Germany).

Statistical analysis

Statistical analyses and diversity parameters were calculated with PAST (Hammer *et al.* 2001). Cluster analysis was applied to the quantitative data set using the paired group cluster algorithm and Morisita similarity index. The results of the cluster analysis indicate three stratigraphically successive faunal intervals (FIs) plus one transitional sample, which each contain between 188 and 980 individuals. We followed the standard procedure (e.g. Aberhan 1992) of pooling samples of statistically identified units (palaeocommunities or, herein, FIs) for the palaeoecological discussion (Figs 4–8), chiefly for clarity of presentation. It is noted that this procedure has no effect on the observed trends (e.g. increasing evenness), which are also seen in the raw data (individual samples; Hautmann *et al.* 2015, appendix S2). Rarefaction analysis was applied to account for the effects of sample size on taxonomic richness of the different FIs (Hautmann *et al.* 2015, appendix S4).

RESULTS

We identified a total of 30 benthic macroinvertebrate species, mostly bivalves (20 species) and, to a lesser extent, gastropods (five species) and brachiopods (three species) as well as serpulids and microconchids (one species each). Bivalves are also dominant in terms of relative abundance (84.1%), followed by gastropods (11.4%) and brachiopods (2.7%). Thin sections show that echinoderms were part of the benthic fauna as well. Microfossils that are not part of the analysis include ostracods (possibly more than 20 species for the time interval under consideration; Forel 2012) and conodonts (8 species within the *H. parvus*–*I. staeschei* interval zones; Brosse *et al.* 2015). Ammonoids (*Ophiceras* sp.) are locally observed near the top of the ML.

The diversity of the ML fauna is unmatched by any other coeval fauna. Twitchett *et al.* (2004) reported what they termed ‘an incredibly diverse benthic fauna’ from the Griesbachian of Oman, which comprises 16 benthic macroinvertebrate species. The well-studied Griesbachian – early Dienerian Dinwoody Formation of the Western US contains a total of 19 benthic macroinvertebrate species (Hofmann *et al.* 2013*a*), but this formation represents a longer time interval and more heterogeneous deposition environments. Taxonomic richness comparable to the ML fauna is not observed until the late Early Triassic, more than 1.5 Ma after the end-Permian mass extinction (Nützel and Schulbert 2005; Hautmann *et al.* 2013; Hofmann *et al.* 2014).

Cluster analysis of quantitative occurrence data identifies three groups of samples (Fig. 4A) that differ in their stratigraphical position (Fig. 2) and are referred to as faunal intervals (FI) in the following. The stratigraphically oldest samples (FI 1) are found *c.* 5–6 m above the base of the Luolou Formation in Youping, Longyan and Wuzhuan, where they appear soon after the onset of dome-shaped dendrolites that provided the topography for the concentration of shells. These samples are highly dominated by the flat clam *Claraia liuqiaoensis* (*c.* 50 %), followed by the bakevelliid bivalve *Towapteria scythica* (*c.* 34%). A stratigraphically intermediate interval (FI 2) that occurs stratigraphically higher in the Youping and Wuzhuan sections is still dominated by these two species, but *T. scythica* is now more abundant than *C. liuqiaoensis*, and cumulated abundance of these two taxa decreased to *c.* 57 %. In the stratigraphically

FIG. 4. Faunal intervals. A, Q-mode cluster analysis of species abundance data using paired group linkage and Morisita similarity index. Note the decreasing similarity between samples from faunal interval (FI) 1 to 3. *Abbreviations*: t.s., transitional sample; LON, Longyan; WUZE, Wuzhuan east; YUP, Youping; SHA, Shanggan; see Figure 2 for stratigraphic positions of individual samples. B, number of species in the trophic nucleus, effective richness, and number of species in successive faunal intervals. Note that whereas overall diversity was similar in all intervals, effective richness and diversity of the trophic nucleus continuously increased.

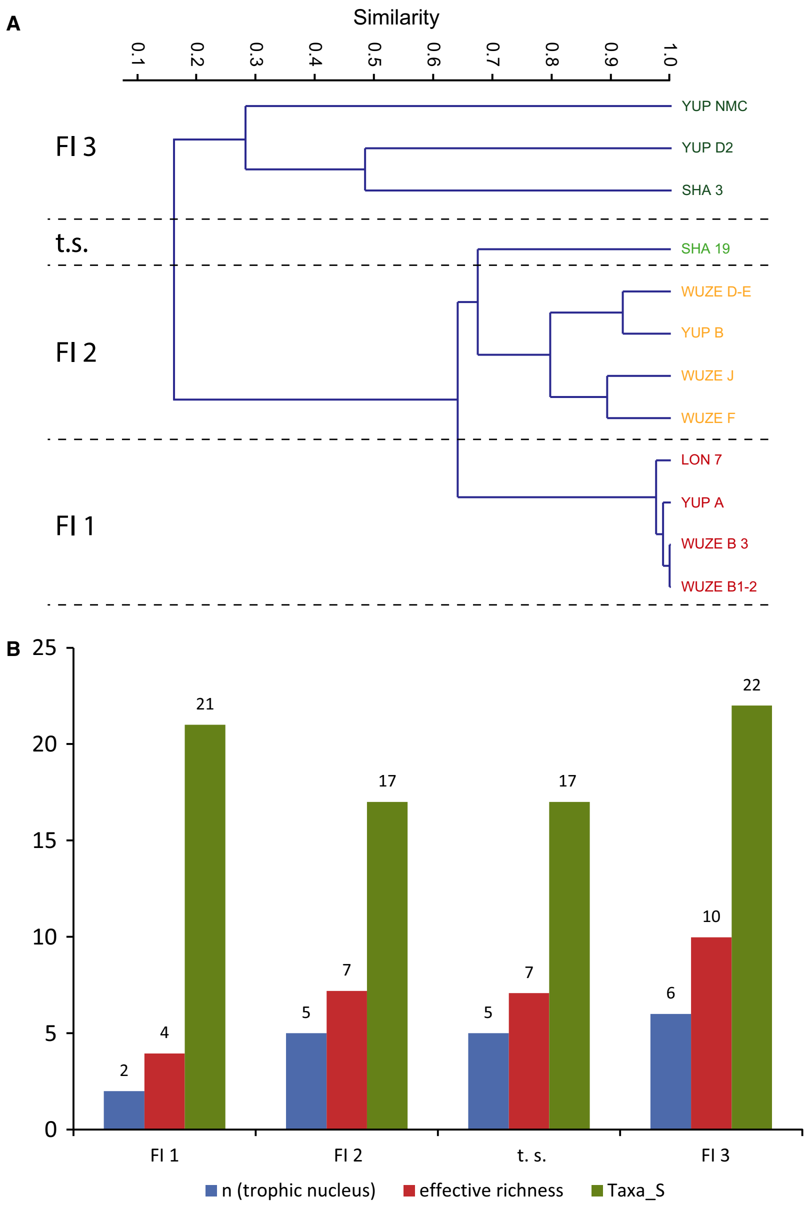

youngest samples (FI 3) that occur at the top of the Shanggan 1 and Youping sections, *C. liuqiaoensis* and *T. scythica* are only accessory elements or are missing, and each sample is dominated by a different species. One sample (SHA 19) is transitional between FI 2 and FI 3 in that a species of *Eumorphotis* is dominant but *Towapteria* and *Claraia* are still abundant, suggesting that denser sample spacing would probably reveal a gradual transition between these FIs.

In accordance with the gradual decline of the post-extinction bloom taxa *Claraia* and *Towapteria*, faunal evenness within samples and FIs notably increases (Hautmann *et al.* 2015, appendices S2–S4), as does effective richness (Jost 2006) and the richness of the trophic nucleus (Neyman 1967; Fürsich 1977), that is the number of species that contribute to 80% of the total specimen number in a given FI (Fig. 4B). Moreover, cluster analysis (Fig. 4A) indicates an increasing dissimilarity between individual samples from FI 1 to FI 3 in spite of a virtually constant facies. Species richness is more or less constant in the raw data (Fig. 4B), although rarefaction analysis suggests a moderate increase from FI 1 to FI 3 (Hautmann *et al.* 2015, appendix S4).

In each FI, 41–47% of the species are epibyssally attached filter feeders (Fig. 5A), accounting for 80–91% of the individuals in FI 1–FI 2 and in the transitional

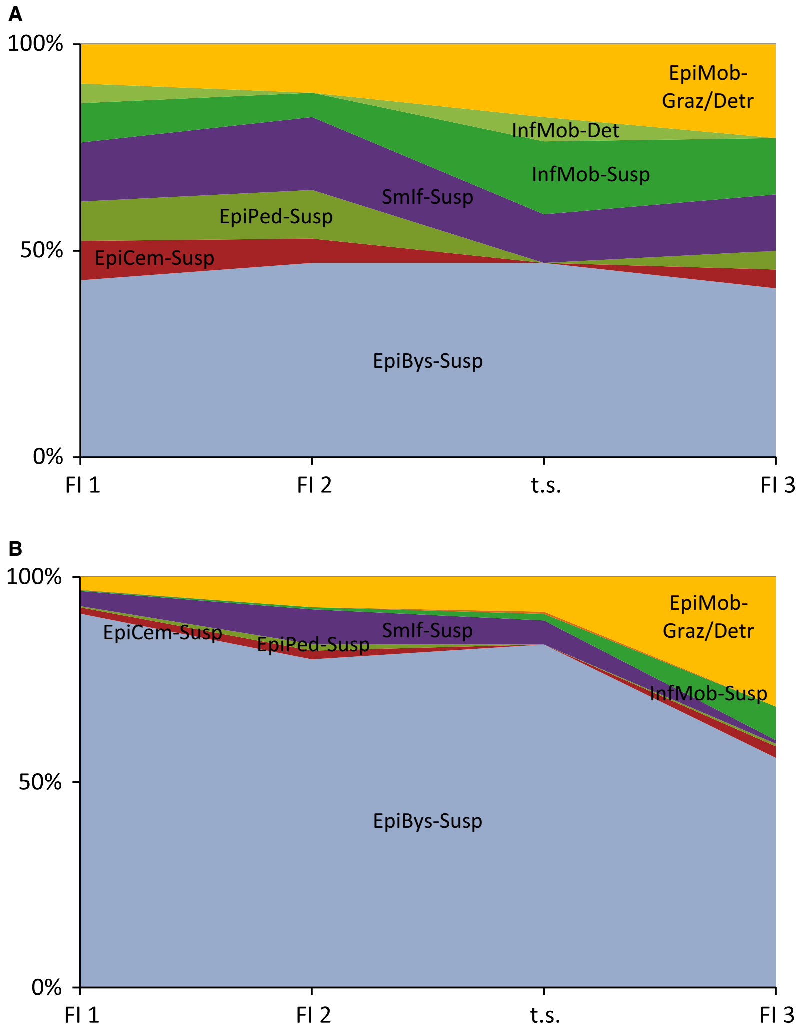

FIG. 5. Evolution of guild structure from faunal interval (FI) 1 to 3. A, species richness. B, relative abundances. Note the constancy in guild structure except for a moderate increase in the abundance of epifaunal mobile grazers/detritivores. See text for further explanations. *Abbreviations*: EpiBys-Susp, epibyssally attached suspension feeders; EpiCem-Susp, epifaunal, cemented suspension feeders; EpiPed-Susp, epifaunal, pedicle-attached suspension feeders; SmIf-Susp, semi-infaunal (endobyssate) suspension feeders; InfMob-Susp/Det, infaunal mobile suspension feeders/detritivores; EpiMob-Graz/Detr, epifaunal mobile grazers/detritivores.

sample and still 56% of the individuals in FI 3 (Fig. 5B). The decrease in relative abundance of this guild in the stratigraphically youngest FI is due to an increase in epifaunal grazers/detritivores (gastropods), which reflects the combined effects of the immigration of three gastropod species (*Dicellonema abrekensis*, *Palaeonarica guangxinensis* and *Eucochlis obliquecostata*) plus the proliferation of the autochthonous *Wannerispira shangganensis*. Whether this proliferation was caused by environmental changes that are not seen in the sedimentary record is difficult to assess; however, possible improvement in food supply that might have led to increased abundance of the epifaunal grazer/detritivore guild would have little impact on the ecology of the various types of filter feeders, to which all other guilds belong.

Another, minor trend is an increase in infaunal mobile suspension feeders at the costs of sessile, semi-infaunal suspension feeders in the stratigraphically youngest FI, which follows the immigration and proliferation of the heterodont bivalve *Astartella*? *stefaniae*.

DISCUSSION

Diversity

For ostracods associated with the ML facies, the case of an oxygen- and nutrient-rich refugium has been made (Forel 2012; Forel *et al.* 2013). Implicit to this interpretation is that the lack of the microbialite-related ostracod taxa in other settings is due to unfavourable environmental conditions that prevailed in the rest of the oceans. We do not reject this hypothesis *a priori*, but it is an unlikely explanation for the high diversity of the ML macroinvertebrate fauna, because the vast majority (75 %) of the genera also occurs at Griesbachian localities devoid of ML

(Hautmann *et al.* 2015, appendix S3), which contradicts the definition of a refugium as a place that provided favourable ecological conditions that were lacking elsewhere.

Related to the refugium hypothesis is the assertion that recovery may have started early where local environmental conditions were favourable, but was restrained in less privileged settings that prevailed in most other areas (Twitchett *et al.* 2004). Empirical recovery indices such as high overall diversity and low dominance values of FI 3 are in accordance with the quick recovery hypothesis, whether as a local or part of a global signal (Hautmann *et al.* 2011). However, two-thirds of the ML genera are Permian survivors (Hautmann *et al.* 2015, appendix S3), and the remaining genera are either closely related to Permian taxa or generally low in abundance and thus likely to be overlooked. The high diversity of the ML fauna is thus not the result of an early post-extinction diversification, contrary to a preliminary interpretation (Hautmann *et al.* 2011) that was based on limited data from the ecologically most advanced FI (3).

Some sort of taphonomic failure has repeatedly been invoked as a possible cause for the low diversity recorded in Lower Triassic strata (Wignall and Benton 1999; Peters and Foote 2002). Taphonomic data indicate exceptionally favourable preservation conditions for the ML, which is paralleled by a likewise exceptionally high diversity. We therefore assume that the high diversity of the ML fauna in comparison to other Griesbachian localities is primarily a Lagerstätten effect, but this interpretation does not provide the sole explanation for the low global diversity in the Griesbachian, because only six genera of the ML fauna have not been reported previously from the Griesbachian (three from the entire Early Triassic; Hautmann *et al.* 2015, appendix S3). It thus seems that whereas alpha-diversity of typical Griesbachian palaeocommunities might have been underestimated due to unfavourable preservation conditions, the effect of taphonomic failure on the global palaeorecord was minor.

Ecology

Identification of statistically related faunal samples is a standard procedure in palaeoecology, which mostly aims to infer palaeo-environmental conditions from ecological information of recurrent assemblages that are interpreted as palaeocommunities (Fürsich 1977, Aberhan 1992). In this concept, a predominantly environmental control of sample clusters is likely if complementary information from non-biological parameters of the host rocks confirms the following: (1) similar environmental conditions *within*; and (2) different environmental conditions *between* potential palaeocommunities.

Because the three sample groups (FI 1 – FI 3) identified by the cluster analysis (Fig. 4A) occur in stratigraphic succession, temporally changing environmental conditions within the basin are a potential explanation for the observed ecological differences. However, there is no indication of environmental differences between the three FIs and the transitional sample in the sedimentological, carbonate microfacies, and available $\delta^{13}C_{carb}$ data of the host rocks (Fig. 2), which is at variance with an environmental control. The only notable facies change in the studied sections occurs *below* the stratigraphically lowest faunal sample, with the transition from tabular or wavy thrombolites to dome-shaped dendrolites (see above). We therefore reject environmental shifts as an explanation for the observed trends. It is also highly unlikely that the pattern is stochastic, because the probability that 12 samples belonging to four categories (FI 1 (n = 4); FI 2 (n = 4); t.s. (n = 1); FI 3 (n = 3)) are arranged in the observed stratigraphic order is merely 1:138 600.

Given the lack of a plausible environmental or stochastic explanation for the differences between the FIs, the alternative possibility must be explored that the main changes in ecological parameters (Fig. 4B) result from the internal dynamic of the community. Three principal trends from FI 1 to FI 3 are observable: increasing faunal evenness within samples, increasing dissimilarity between samples, and the waxing of certain species at the cost of others (Figs 4–6). Although the proliferation of epifaunal grazers/detritivores and shallow-infaunal burrowing filter feeders in FI 3 partly contribute to these trends (see above), the main differences between the FIs reside in changes in species' abundances within the largest guild, which is formed by epifaunal filter feeders.

Figure 6 illustrates changes in relative abundances for those species of the epifaunal filter feeder guild that are part of the trophic nucleus in at least one of the three FIs and the transitional sample. Note that all of these species are already present in FI 1. The observed pattern conforms to a standard Lotka–Volterra situation of competitively interacting species, where species with higher rates of population growth are progressively suppressed by species that are better adapted to increasing their share of the resources of the system (Pianka 1970, 1972). This increase in competitive capabilities follows the sequence *Claraia liuqiaoensis* → *Towapteria scythica*, *Bakevellia ceratophaga* → *Myalinella newelli* → *Leptochondria albertii*, *Eumorphotis shajingengi*, *Scythentolium scutigerulus* (Fig. 6). A Lotka–Volterra framework is also in accordance with the concomitant increase of evenness and effective richness from FI 1 to FI 3 (Fig. 4B and Hautmann *et al.* 2015, appendix S4), which reflects the system's approach to a state of stable competitive coexistence of species with similar competitive abilities and carrying capacities in the given ecological context.

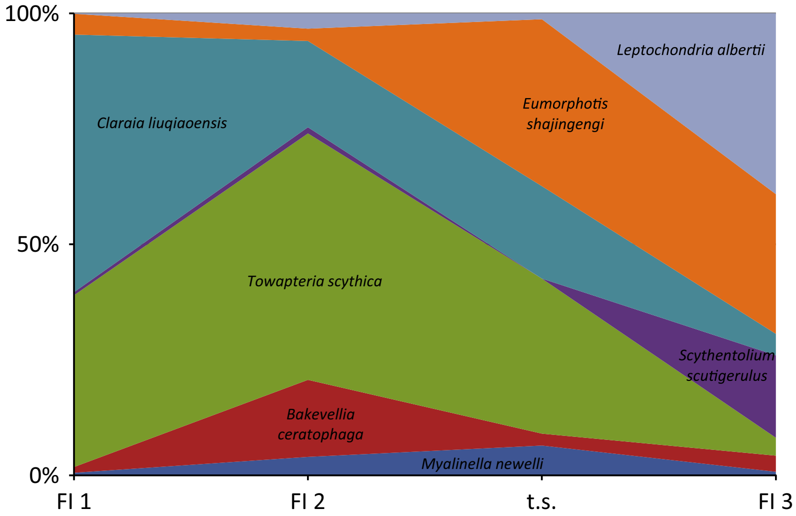

FIG. 6. Relative abundances of epifaunal filter feeders in stratigraphically successive faunal intervals (FI) and the transitional sample (t.s.). The trends conform to a competitive Lotka–Volterra situation where species with higher rates of population growth are increasingly suppressed by species that are more effective in the utilization of resources. See text for further details.

Finally, the increasing dissimilarity between individual samples from FI 1 to FI 3 (Fig. 4A) follows predictions on the long-term effect of interspecific competition on niche breadth and geographical range (Bolknik *et al.* 2010; Slatyer *et al.* 2013; Hautmann 2014). Overall, the faunal pattern recorded in the epifaunal filter feeder guild of the ML resembles ecological successions, but the process is different because it is not immigration-driven.

The surprising aspect of the described trends is the timescale at which they are observed. The macrofauna-bearing part of the section can be temporally constrained to 10–100 ka, whereas ecological changes as described above usually occur in the timescale of some tens to hundreds of generations (Miller 1967). The conundrum can be resolved by the assumption that the extension of ecological processes into the geologically observable timescale is due to extremely low competition as a result of the intensity of the end-Permian mass extinction. In other words, the manifestation of interspecific competition in the geological record is an indication of its low intensity.

Credibility of the low-competition model hinges on several factors. First, can a global mass extinction actually decrease competition to the low level postulated herein? Probably not generally, but marine level-bottom communities that are dominated by primary consumers are among the ecosystems with the lowest interspecific competition even in background times (Stanley 2008), and competition in such ecosystems occurs chiefly as diffuse competition (MacArthur 1972) that depends primarily on the overall number of competing species and not on the presence of few but strong competitors. Eliminating up to 95% of species (Jablonski 1994) from such low-competition communities could therefore realistically reduce the effects of interspecific competition to the low level assumed herein.

A second crucial aspect is the stability of the ecological context. As noted by Sepkoski (1996), the effects of extremely low competition are likely to be overridden by other factors such as environmental changes. The environmental stability of the ML setting is thus a prerequisite for recording long-term effects of low competition on community dynamics; another aspect is the stability of the biotic environment in terms of species composition (Hautmann *et al.* 2015, appendices S2–S3). This taxonomic stability results from scarcity of potential immigrants as an outcome of the global extinction, which constituted a setting different from well-studied cases of Recent island colonization or recolonization of defaunated areas, in which ecological changes are essentially driven by immigration dynamics (Simberloff and Wilson 1970).

Although reduced competition is an inevitable outcome of mass extinctions, its effects on post-extinction biota have rarely been addressed, apart from the recent studies of Hofmann *et al.* (2013*a*,*b*, 2014) that attributed the wide habitat range of many Early Triassic taxa to a lack of competitive exclusion from suboptimal habitats. The ML faunal data suggest an even more important effect of reduced competition. They demonstrate sluggish shifts in relative abundances and beginning divergence of communities without any evidence for speciation, which indicates that competition-mediated niche differentiation operated at an extremely slow pace. We argue in the following that the observed time extension of competition-driven processes due to the high extinction magnitude provides an intrinsic mechanism for the delayed diversification of the Early Triassic benthos.

A COMPETITION-DRIVEN MODEL OF DIVERSIFICATION

Interspecific competition is a potential main driver of diversification because it promotes niche differentiation (Stanley 1973; Schluter 1994; Pianka 2000; Emerson and Kolm 2005; Meyer and Kassen 2007; Bailey *et al.* 2013). Although this is ecological consensus, competition is mostly perceived in its opposite role as a factor that damps diversification (Sepkoski 1984, 1996), as evidenced by dynamic diversity equilibria in ecologically saturated islands (MacArthur and Wilson 1967). The apparent contradiction resolves because positive and negative effects of competition on diversity govern different stages of diversification. Promotion of niche differentiation is the dominant outcome of competition until a critical level of ecological saturation has been reached, at which further division of niche space requires increasingly elaborated adaptations that are more and more unlikely to evolve. Above such a saturation limit, outcompeting of existing species may be the prevalent effect of competition that damps further diversification, whether in geographically limited areas such as islands (MacArthur and Wilson 1967) or globally (Darwin 1859; Sepkoski 1984; but see Benton and Emerson 2007).

Translated into a mathematical model, the positive role of competition introduces a diversity-dependent factor in the growth equation (i.e. the per-taxon rate of diversification increases with the number of species), which produces an initially hyperbolic diversification curve. Combining the hyperbolic term for the early phase of diversification with a damping term for systems near their carrying capacities accounts for the changing role of competition in early and late stages of diversity build-up:

$$\frac{dS}{dt} = cS^2\left(1 - \frac{S}{K}\right) \tag{1}$$

where S = richness, t = time, c = proportionality factor, and K = carrying capacity. This model corresponds to the hyperbolic case in Solé *et al.* (2010), but it is based solely on a reversal in the role of competition. We note that the competition-based model of diversification is not meant as a full description of all aspects of diversification. Actual pathways of diversification are likely to differ between ecological groups and will additionally be superimposed by environmental changes. Moreover, the effects of predation reduce the intensity of competition at any stage of diversification, and evolutionary innovations may increase the carrying capacity. However, the model has a great explanatory power for some general aspects of diversification, particularly in predicting that the minimum duration of the lag phase is highly sensitive to the extinction magnitude. Figure 7 demonstrates that the duration of the lag phase disproportionally increases at higher extinction magnitudes, illustrated for starting diversities of 20%, 5% and 1% of the system's carrying capacity. The first two cases approximate the situations after the end-Triassic and the end-Permian mass extinctions (80% and

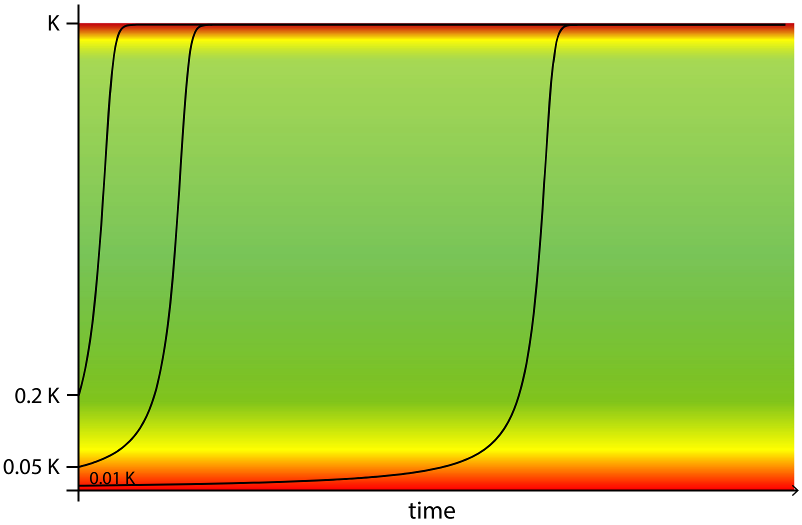

FIG. 7. Diversification pathways in a competition-driven model. The model assumes a positive feedback between the number of competing species and the rate of diversity increase until the system approaches its carrying capacity and the effect of competition reverses. Curves are calculated from Equation 1 using Euler's method; initial diversities (S_0) are given as fractions of a hypothetical carrying capacity (K); c = 0.3 for all curves. Colour indicates fields of positive (green), transitional (yellow) and negative (red) effects of different competition levels on diversity increase. Note that the delay of diversification increases disproportionally with decreasing initial diversity.

95% estimated species extinction, respectively; Jablonski 1994, table 1). The curves that were calculated from Equation 1 for these values (0.2 and 0.05 K in Fig. 7) correctly predict the marked contrast between the nearly instantaneous recovery of level-bottom benthos after the end-Triassic extinction (Hautmann *et al.* 2008) and the delayed recovery of benthic communities after the end-Permian crisis. No mass extinction with a species loss >95% is known, but model calculations for very low starting diversities (illustrated for 0.01 K in Fig. 7) might provide an adequate description of the Cambrian radiation of metazoans that followed a long Precambrian interval of extremely low diversity.

Because there are intrinsic differences in the intensity of competition between ecological groups, the duration of the lag phase does depend not only on the extinction magnitude of the group under consideration but also on its ecology: it is predicted that a higher intensity of competitive interactions (expressed by larger *c*-values in Eq. 1) results in a shorter duration of the lag phase (Fig. 8). However, even if the intensity of competition within a group is very high (large *c*-values), a lag phase can still be recognized in the diversification curves (Fig. 8), which is an important difference to the logistic model of Sepkoski (1979, 1984).

The effect of intrinsic differences in the intensity of competition is well illustrated by the differential rediversification of bivalves and ammonoids after the end-Permian mass extinction. As already suggested by Stanley (1973, p. 502), ammonoids (among other possible reasons) probably rediversified more quickly than bivalves because competition is more intense among nektonic predators than among sessile primary consumers. This is confirmed by empirical diversification curves, which show a quick rebound of ammonoid diversity after a short Griesbachian lag phase (Brayard *et al.* 2009, fig. 4), in contrast to a more sigmoidal diversification curve of Triassic bivalves that reached the maximum rate of diversification not before the Middle Triassic (Hautmann 2007, fig. 8; note however that cited data refer to the genus level). Although no curve fitting is intended in this paper because species-level data are unknown, a close resemblance of these empirical curves with the theoretical diversification curves for strongly and weakly competing groups (Fig. 8) is obvious.

CONCLUSIONS: SLOW DIVERSIFICATION IN A LOW-COMPETITION WORLD

We propose that interspecific competition is a main driver of diversification in early phases of diversity rebuilding and that low levels of competition correlate with low rates of diversification. The ML fauna provides a test case for this hypothesis. Thriving in the immediate aftermath of the greatest Phanerozoic mass extinction, it shows evidence for competitive interactions that took place at a timescale that is orders of magnitude longer than in background times. Incipient spatial separation of potentially competing species occurs in the latest of the three observed FIs, but competition remained too weak to promote speciation. The weakness of competitive interactions evidenced in the outcrop scale correlates with a delay of rediversification on the global scale, which for benthic communities is retarded until the late Early Triassic, >1.5 Ma after the extinction event. Although episodic deterioration of environmental conditions might have played an additional role in the overall delay of benthic recovery in this and other mass extinction events, we

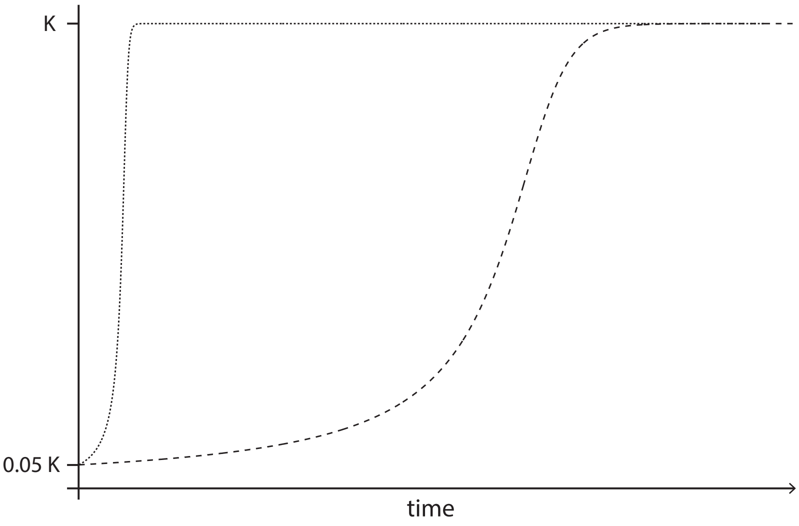

FIG. 8. Diversification curves for groups of organisms that differ in having intrinsically high ($c = 1$; dotted line) and low ($c = 0.1$; dashed line) levels of competition, calculated from Equation 1; starting diversity ($S_0 = 0.05$ K) is identical for both groups. Note the effect of the intrinsic difference in the intensity of competition on the duration of the lag phase. See text for further details.

infer that it is the extinction magnitude that determines the minimum amount of time that elapses until diversification actually resumes. The positive relationship between competition and diversification might also underlie the lagged correlation between extinction and diversification that pervades Phanerozoic diversity trends in general (Kirchner and Weil 2000).

SYSTEMATIC PALAEONTOLOGY

This published work and the nomenclatural acts it contains have been registered in ZooBank: http://zoobank.org/References/CCC41580-BC54-4AF9-8986-195BA51D76DE

The collected fossils are housed in the collection of the Palaeontological Institute and Museum of the University of Zurich (PIMUZ).

Occurrences and number of individuals in the analysed samples are documented in Hautmann *et al.* (2015, appendix S2).

Locality abbreviations. LON, Longyan; WUZE, Wuzhuan east; YUP, Youping; SHA, Shanggan.

Phylum MOLLUSCA Cuvier, 1797
Class BIVALVIA Linnaeus, 1758
Subclass PALAEOTAXODONTA Korobkov, 1954
Order NUCULOIDA Dall, 1889
Superfamily NUCULANOIDEA Adams and Adams, 1858
Family NUCULANIDAE Adams and Adams, 1858

Genus DACRYOMYA Agassiz, 1840

Type species. Nucula lacryma Sowerby, 1824, by subsequent designation (Herrmannsen 1846).

Dacryomya sp.
Figure 9A

Material. Two right valves.

Description. Relatively large nuculaniform shell with opisthogyrate umbo, broadly rounded anterior shell margin and rostrate posterior end with deeply impressed escutcheon.

Remarks. The shape of the shell agrees very well with typical *Dacryomya*, as revised by Cox (1940). The majority of Early Triassic nuculanids have been assigned to this genus (Nakazawa 1961; Dagys and Kanygin 1996), based chiefly on the absence of a pallial sinus, which however may be absent in *Nuculana* as well. We follow Cox (1940) in regarding the strongly opisthogyrate umbones and the deeply impressed escutcheon as characters that distinguish *Dacryomya* from *Nuculana*.

Subclass AUTOLAMELLIBRANCHIATA Grobben, 1894
Infraclass PTERIOMORPHIA Beurlen, 1944
Order MYTILOIDA Férussac, 1822
Superfamily MYTILOIDEA Rafinesque-Schmalz, 1815
Family MYTILIDAE Rafinesque-Schmalz, 1815
Subfamily MODIOLINAE Keen, 1958

Genus MODIOLUS Lamarck, 1799

Type species. Mytilus modiolus Linnaeus, 1758, by subsequent designation (Gray 1847).

Modiolus sp.
Figure 9B

2011 *Modiolus* sp.; Hautmann *et al.*, p. 75, fig. 4.1.

Material. Two right valves and two left valves.

Description and remarks. See Hautmann *et al.* (2011).

Order PTERIOIDA Newell, 1965
Suborder PTERIINA Newell, 1965
Superfamily AMBONYCHIOIDEA Miller, 1877
Family MYALINIDAE Frech, 1891

Genus ATOMODESMA Beyrich, 1865

Type species. A. exaratum Beyrich 1865, by subsequent designation (Wanner 1922).

Atomodesma sp.
Figure 9G

Material. Three right valves.

Description. Small shell with terminal, prosogyrate beak and straight posterior dorsal margin. Shell exterior covered with regularly arranged commarginal ribs.

Remarks. Assignment to *Atomodesma* is based on the characteristic outline, ornamentation, and form and position of the beak. *Atomodesma* was diverse and abundant in the Permian but has also been reported from the Early Triassic (Dagys and Kanygin 1996).

Genus PROMYALINA Kittl, 1904

Type species. Promyalina hindi Kittl, 1904, by original designation.

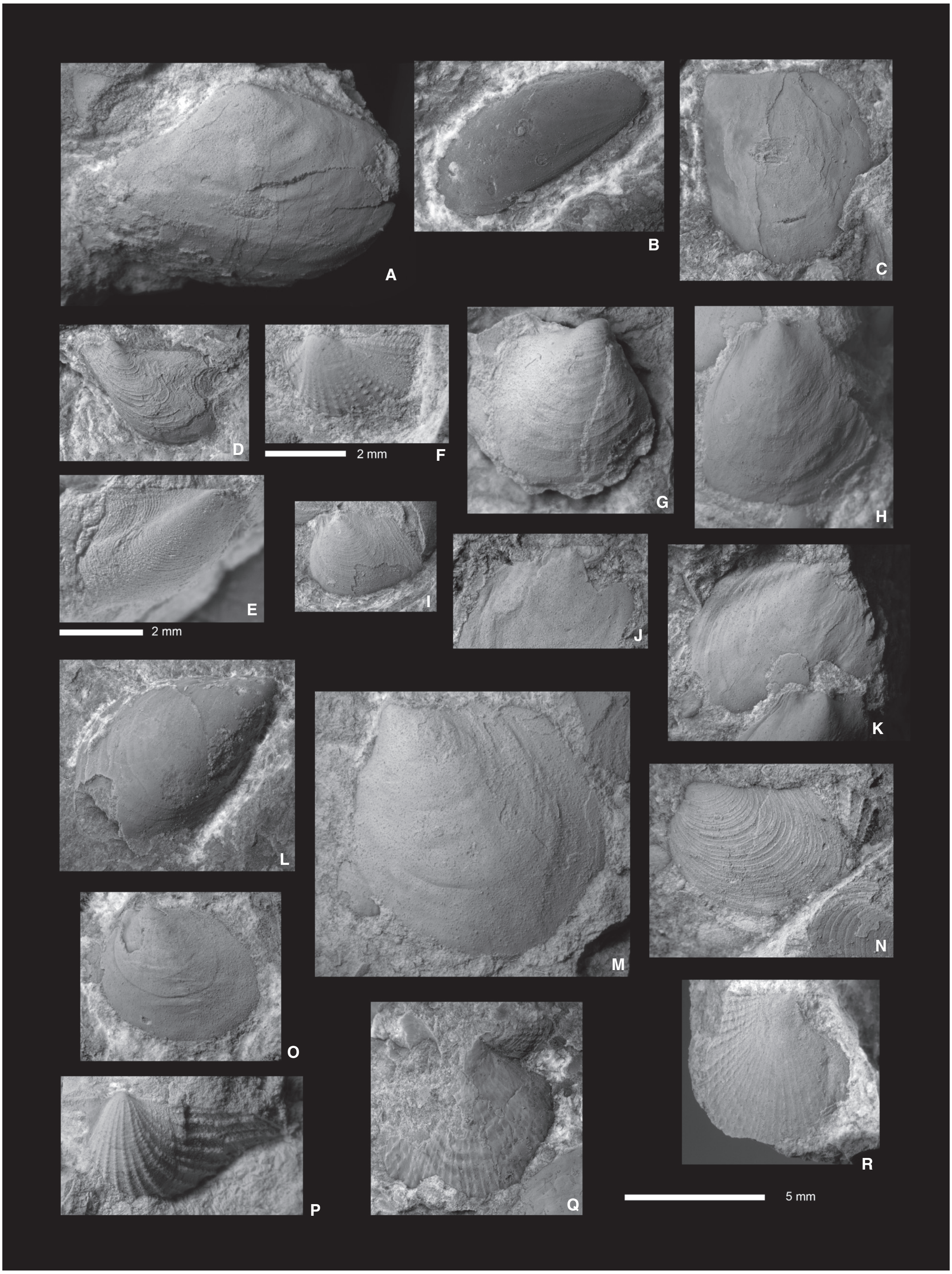
A
B
C
D
2 mm
F
G
H
E
2 mm
I
J
K
L
M
N
O
P
Q
R
5 mm

Promyalina putiatinensis (Kiparisova, 1938)
Figure 9C

1899 *Myalina vetusta* Benecke; Bittner, p. 17, pl. 4, figs 17–19.
*1938 *Myalina putiatinensis* Kiparisova, p. 261, pl. 6, fig. 9.
2011 *Promyalina* cf. *putiatinensis* (Kiparisova, 1938); Hautmann *et al.*, p. 77, fig. 4.5.
2013 *Promyalina putiatinensis* (Kiparisova, 1938); Hautmann *et al.*, p. 270, fig. 5C–H (*cum synonymis*).

Material. Four left valves.

Description and remarks. See Hautmann *et al.* (2011).

Genus MYALINELLA Newell, 1942

Type species. Myalina meeki Dunbar, 1924, by original designation.

Myalinella newelli Hautmann *et al.*, 2011
Figure 9L

*2011 *Myalinella newelli* Hautmann *et al.*, p. 75, fig. 4 (2–4).

Material. 15 right valves and 17 left valves.

Description. Shell inequivalved, with left valve being slightly more convex than right valve. Shell exterior of left valve with regularly spaced commarginal ribs, which are less pronounced and more irregular in the right valve. Umbo slender, prosogyrate, beak terminal or nearly so.

Remarks. This species was erected on limited material and has subsequently been synonymized with *Myalinella postcarbonica* (Girty, 1927; Hofmann et al. 2013*a*). However, with the much larger suite of specimens that is now available, some differences between *M. postcarbonica* and the Chinese species emerge that seem to justify at least provisionally the distinction of these two species. These differences include the near-terminal position of the beak, the less pronounced anterior shell lobe and, most importantly, the presence of regular commarginal ornamentation on the left valve of *M. newelli*. Although the ornamentation is prone to diagenetic loss (as demonstrated by the absence of ornamentation in some of the left valves in our samples), the absence of a comparable ornamentation in *M. postcarbonica* is likely to be primary, because this species is well documented from different localities where it has invariably been described as externally smooth (Hofmann *et al.* 2013*a*).

Myalinella newelli is very similar to juvenile specimens of early Permian *Septimyalina burmai* Newell, 1938, as figured in Newell (1938, pl. 12, fig. 5a–b). This similarity concerns both the general shape and the difference in rugosity between left and right valve, which according to Newell (1938, p. 60) is generally more pronounced in *Septimyalina* than in *Myalinella*. However, later growth stages of *S. burmai* differ from juveniles in the development of a differentiated posterior wing. Moreover, *Septimyalina* has a characteristic internal umbonal septum that is not documented in *M. newelli*, and the stratigraphical distance between *Septimyalina* and *Myalinella* is considerable. However, the similarity between *M. newelli* and juveniles of *S. burmai* may point to derivation of *Myalinella* from a *Septimyalina* stock by paedomorphism.

Family MYSIDIELLIDAE Cox, 1964

Genus PROMYSIDIELLA Waller, 2005

Type species. Mysidiella cordillerana Newton, 1987, by original designation.

Promysidiella? sp.

2011 *Promysidiella*? sp.; Hautmann *et al.*, p. 77, fig. 4 (6).

FIG. 9. Bivalve species of the microbial limestone fauna. A, *Dacryomya* sp., PIMUZ 31266, right valve from WUZE B3. B, *Modiolus* sp., PIMUZ 31267, right valve from LON 7. C, *Promyalina putiatinensis* (Kiparisova, 1938), PIMUZ 31268, left valve from LON 7. D–E, *Bakevellia ceratophaga* (Schlotheim, 1816); D, PIMUZ 31269, left valve from WUZE F; E, PIMUZ 31270, right valve from WUZE J. F, *Towapteria scythica* (Wirth, 1936), PIMUZ 31271, left valve from WUZE B3. G, *Atomodesma* sp., PIMUZ 31272, right valve from WUZE D. H–K, M–O, *Claraia liuqiaoensis* He *et al.*, 2007, showing intraspecific variability and different preservation states (see systematic description for details); H, PIMUZ 31273, left valve from WUZE B1 I, PIMUZ 31274, left valve from LON 7, showing commarginal ornamentation and anterior auricle; J, PIMUZ 31275, right valve from WUZE B3, showing detail of byssal notch; K, PIMUZ 31276, right valve from WUZE B1; M, PIMUZ 31278, left valve from WUZE B1; N, PIMUZ 31279, left valve from WUZE B2; O, PIMUZ 31280, left valve from WUZE B3. L, *Myalinella newelli* Hautmann *et al.*, 2011, PIMUZ 31277, right valve from LON 7. P–R, *Eumorphotis shajingengi* Hautmann *et al.*, 2011; P, PIMUZ 31281, left valve from SHA 19; Q, PIMUZ 31282, right valve from LON 7; R, PIMUZ 31283, right valve from WUZE D. Scale bar in lower right corner (representing 5 mm) refers to all figures except for E–F, which have individual scale bars representing 2 mm.

Material. Two right valves.

Description and remarks. See Hautmann *et al.* (2011).

Superfamily PTERIOIDEA Gray, 1847
Family BAKEVELLIIDAE King, 1850

Genus BAKEVELLIA King, 1848

Type species. Avicula antiqua Graf Zu Münster *in* Goldfuss, 1836 (*non A. antiqua* Defrance) = *Avicula binneyi* Brown, 1841 by original designation.

Bakevellia ceratophaga (Schlotheim, 1816)
Figure 9D–E

*1816 *Mytulites ceratophagus* Schlotheim, p. 30, pl. 5, fig. 2a–c.
1967 *Bakevellia* (*Bakevellia*) *ceratophaga* (Schlotheim); Logan, p. 35, pl. 4, figs 12–19 (*cum synonymis*).
2011 *Bakevellia* sp.; Hautmann *et al.*: 77, fig. 4 (7–9).

Material. 26 right and 37 left valves.

Description. Left valve moderately inflated, with acutely angulated posterior wing and regularly spaced and slightly scaly commarginal ribs. Right valve less convex than left valve, with small beak not projecting above hinge line. Commarginal ribs of right valve slightly weaker and more densely spaced.

Remarks. The Early Triassic material from South China agrees very well with the figures of the type series from the late Permian of Europe, as refigured by Logan (1967). The here-reported occurrence in the Griesbachian makes *Bakevellia ceratophaga* one of the few species that demonstrably survived the end-Permian mass extinction (see Wasmer *et al.* 2012).

Genus TOWAPTERIA Nakazawa and Newell, 1968

Type species. Towapteria nipponica, by original designation.

Towapteria scythica (Wirth, 1936)
Figure 9F

*1936 *Oxytoma scythicum* Wirth, p. 429, fig. 5a–b, pl. 14, fig. 3a–b.
1983 *Towapteria scythica* (Wirth, 1936); Broglio Loriga *et al.*, p. 566, fig. 23.

Material. 472 left valves.

Description. Shell small (>0.5 cm), left valve pteriiform, with beak located *c.* 30% of shell length behind anterior end. Anterior part of left valve anteriorly rounded and posteriorly set off by ventrally directed radial depression. Left posterior wing flat, posteriorly extending up to the distal end of the main body of shell. Ornament consisting of: (1) commarginal riblets on anterior part of shell; (2) *c.* seven narrow radial ribs on main body of shell; and (3) *c.* five radial ribs on posterior wing. Secondary ribs occasionally inserted by intercalation. Crests of radial ribs scaly where intersecting weaker commarginal ornamentation. Right valves unknown.

Remarks. The absence of right valves in our sample and elsewhere probably indicates its weak calcification.

Wirth (1936) described the ribs on the posterior wing as distinctly finer than that on the main body of the shell, which does not conform to our observation. However, we assume that this difference is due to the less perfect preservation in the material of Wirth; we therefore place our specimens within *Towapteria scythica.*

Suborder ENTOLIIDINA Hautmann *in* Carter *et al.*, 2011
Superfamily ENTOLIOIDEA Korobkov, 1960
Family ENTOLIIDAE Korobkov, 1960

Genus SCYTHENTOLIUM Allasinaz, 1972

Type species. Pecten tirolicus Wittenburg, 1908, by original designation.

FIG. 10. Bivalve species of the microbial limestone fauna. A–B, *Leptochondria albertii* (Goldfuss, 1838); A, PIMUZ 31284, left valve from YUP D2; B, PIMUZ 31285, left valve from YUP D2. C–D, *Scythentolium scutigerulus* Hautmann *et al.*, 2011; C, PIMUZ 31286, right valve from WUZE G; D, PIMUZ 31287, left valve from YUP D2, note microconchids. E, *Permophorus* cf. *similis* (Girty, 1927), PIMUZ 31288, left valve from SHA 19. F–G, *Permophorus* cf. *rotundus* (Girty, 1927); F, PIMUZ 31289, right valve from YUP D2; G, PIMUZ 31290, right valve from YUP D2. H, *Unionites* cf. *fassaensis* (Wissmann, 1841), PIMUZ 31291, left valve from WUZE B9. I, *Unionites*? sp., PIMUZ 31292, right valve from WUZE B3. J–N, *Astartella*? *stefaniae* sp. nov.; J–K, PIMUZ 31293, holotype, complete individual from YUP NMC; J, dorsal view, showing lunule, beaks and escutcheon; K, right valve showing commarginal shell folds; L, PIMUZ 31294, right valve from YUP D2; M, PIMUZ 31295, right valve from YUP NMC; N, PIMUZ 31296, left valve from YUP NMC, showing commarginal shell folds on shell exterior and steinkern. O–P, *Astartopis*? sp.; O, PIMUZ 312997, right valve from WUZE J; P, PIMUZ 31298, left valve from WUZE J. Q, *Astartella*? sp., PIMUZ 31299, right valve from SHA 19. Scale bar in lower right corner (representing 5 mm) refers to all figures except for J and O, which have individual scale bars representing 1 mm and 2 mm respectively.

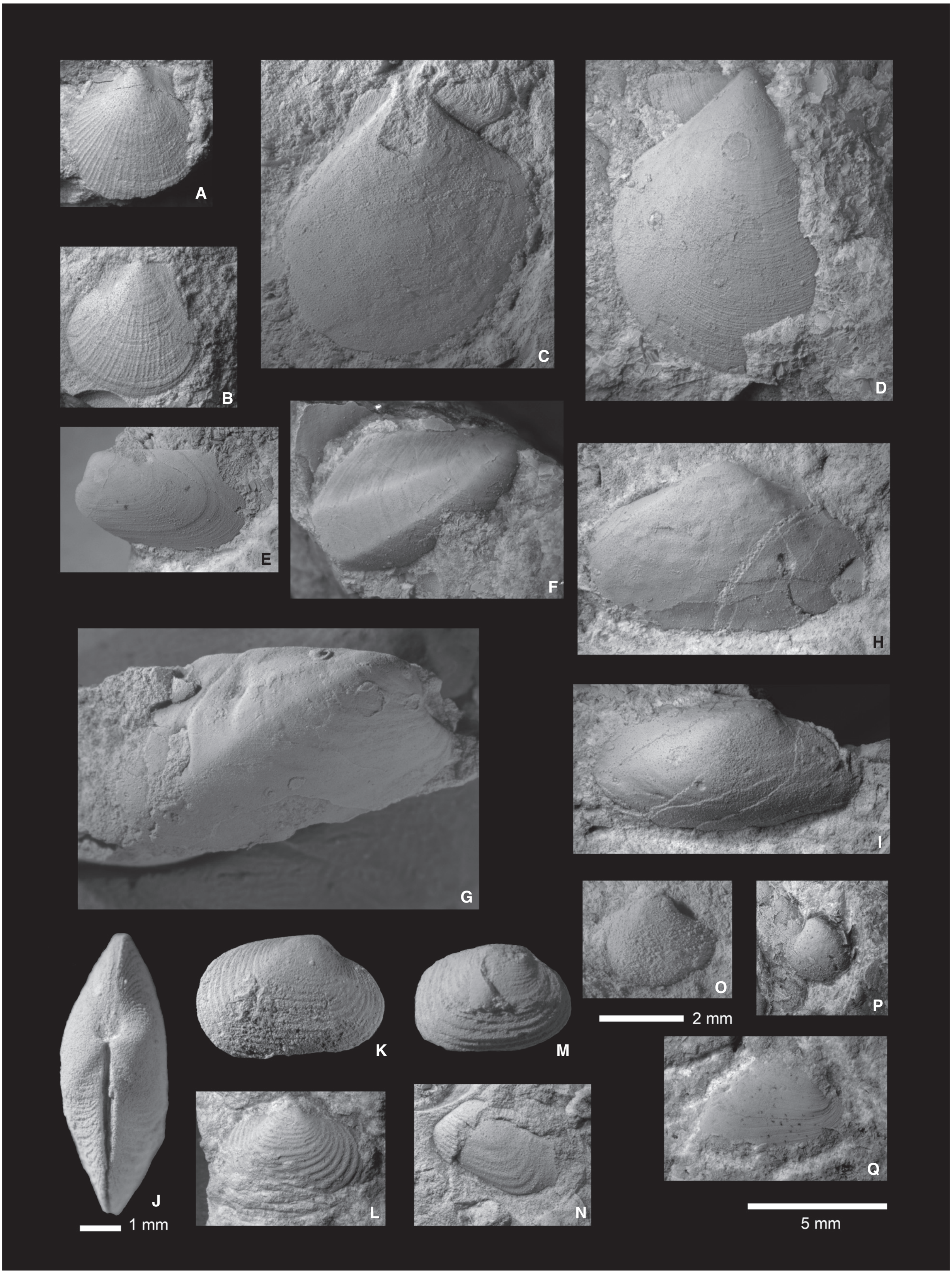
A
B
C
D
E
F
H
G
I
O
P
2 mm
J
K
M
Q
1 mm
L
N
5 mm

Scythentolium scutigerulus Hautmann *et al.*, 2011
Figure 10C–D

*2011 *Scythentolium scutigerulus* Hautmann *et al.*, p. 77, fig. 4 (10–19), fig. 5 (1–2).

Material. 7 right valves, 28 left valves and 32 fragments.

Description. For a general characterization, see Hautmann *et al.* (2011). The larger suite of specimens that is now available documents some variability in the general shape, in particular the presence of individuals in which the disc is higher than long (rather than circular) and the apical angle somewhat smaller (*c.* 80 degrees) than indicated in Hautmann *et al.* (2011).

Remarks. Scythentolium was recently placed in a newly erected family Entolioididae Waller, 2006, but it appears questionable whether morphological information justifies separation from the established family Entoliidae (Hautmann *et al.* 2013). We therefore follow Hautmann *et al.* (2013) in assigning *Scythentolium* to Entoliidae.

Scythentolium scutigerulus resembles *Pecten* (*Chlamys*?) *kryschtofowichi* Kiparisova, 1938 from the Lower Triassic of Ussuri (Far East Russia) but differs in having a larger posterior auricle. *Pleuronectites meeki* Newell and Boyd, 1995 is a possible younger synonym of the Russian species.

Suborder PECTININA Waller, 1978
Superfamily PTERINOPECTINOIDEA Newell, 1938
Family PTERINOPECTINIDAE Newell, 1938

Genus CLARAIA Bittner, 1901

Type species. Posidonomya clarai Emmrich, 1844, by subsequent designation (Diener 1923).

Claraia liuqiaoensis He *et al.*, 2007
Figure 9H–K, M–O

*2007 *Claraia liuqiaoensis* He *et al.*, p. 1010, fig. 3.7–3.16.

Material. 128 right valves and 566 left valves.

Description. Disc of left valve orbicular, convex, externally covered with regularly arranged commarginal riblets and occasionally very faint radial structures (Fig. 9M). Beak prominent, located *c.* 20–40% of shell length behind anterior end. Left anterior auricle small, with shallow auricular sinus (Fig. 9I). Disc of right valve flat, with wide rectangular byssal notch below anterior auricle (Fig. 9J–K). Posterodorsal segment of right valve flattened. Right valve exterior smooth or with very faint radial structure.

Remarks. Claraia liuqiaoensis was first reported from the topmost Permian and lowest Triassic of Dopang, southern Guangxi (He *et al.* 2007; see Fang Zong-Jie (2010, p. 171) for comments on stratigraphic occurrence). Although the original diagnosis essentially refers to the right valve, He *et al.* (2007) chose a left valve as the holotype. This is unfortunate, particularly because the material of He *et al.* (2007) is diagenetically flattened and this flattening chiefly affected the originally more convex left valve, as indicated by the unevenly distributed wrinkles that represent diagenetic shell breakage rather than original ornamentation. Our material, which is mostly preserved without significant shell compaction, shows that the left valve was considerably convex, not just ‘weakly inflated’, as indicated by He *et al.* (2007). Apart from this diagenetically caused difference, the morphology is in very good agreement with *Claraia liuqiaoensis*, particularly with respect to the wide, deep and rectangular byssal notch. The external ornamentation of the left valve is subject to secondary modifications due to abrasion and diagenetic modifications. More precisely, abrasion frequently removed the commarginal ribs (compare Fig. 9M and Fig. 9N), whereas diagenesis tends to accentuate a faint radial structure (Fig. 9M).

Superfamily AVICULOPECTINOIDEA Meek and Hayden, 1864
Family HETEROPECTINIDAE Beurlen, 1954

Genus EUMORPHOTIS Bittner, 1901

Type species. Pseudomonotis telleri Bittner, 1898, by subsequent designation (Cossmann 1902).

Eumorphotis shajingengi Hautmann *et al.*, 2011
Figure 9P–R

*2011 *Eumorphotis shajingengi* Hautmann *et al.*, p. 79, figs 5 (3–12) (*non* fig. 5 (13) = distorted right valve of *Scythentolium scutigerulus*?).

Material. 16 right valves and 178 left valves.

Description. Left valve strongly convex, externally covered with scaly radial ribs intercalated in two ranks. Hinge margin elongated, with shallow anterior and posterior auricular sinuses. Right valve slightly convex, with a well-differentiated anterior auricle and a short posterior wing, entirely covered with scaly radial ribs not differentiated in different ranks.

Remarks. Right valves as herein described have not been encountered in the type material of *Eumorphotis shajingengi*. A smooth right valve assigned to *E. shajingengi* by Hautmann *et al.* (2011, fig. 5(13)) is probably a distorted valve of *Scythentolium scutigerulus*. Although no specimens with conjoined valves are present, we assign right valves as described above to *E. shajingengi* because this is the only species in the ML fauna to which their shape and style of ornamentation fit and because they usually co-occur with the more common left valves in the same samples.

Family ASOELLIDAE Begg and Campbell, 1985

Genus LEPTOCHONDRIA Bittner, 1891

Type species. Pecten (*Leptochondria*) *aeolicus* Bittner, 1891, by monotypy.

Leptochondria albertii (Goldfuss, 1838)

Figure 10A–B

*1838 *Monotis albertii* Goldfuss, p. 138, pl. 120, fig. 6.
1928 *Pecten albertii* (Goldfuss, 1838); Schmidt, p. 161, fig. 346.
1972 *Leptochondria albertii* (Goldfuss, 1838); Allasinaz, p. 246, pl. 30, fig. 1.

Material. 109 left valves.

Description. Small *Leptochondria* with fine radial ribs intercalated in two ranks.

Remarks. Our material agrees well with this extensively documented species. It is externally similar to juvenile specimens of *Eumorphotis shajingengi*, from which it can be distinguished by a less broad hinge margin that lacks auricular sinuses.

The lack of right valves is a common phenomenon in *Leptochondria*, which is probably due to weak calcification (Newell and Boyd 1995).

Infraclass HETEROCONCHIA Hertwig, 1895
Superorder PALAEOHETERODONTA Newell, 1965
Order MODIOMORPHOIDA Newell, 1969
Superfamily MODIOMORPHOIDEA Miller, 1877
Family KALENTERIDAE Marwick, 1953

Genus PERMOPHORUS Chavan, 1954

Type species. Arca costata Brown, 1841, by monotypy.

Permophorus cf. *similis* (Girty, 1927)

Figure 10E

cf. 1927 *Pleurophorus similis* Girty, p. 446, pl. 30, figs 38–39.
2011 *Trigonodus*? sp.; Hautmann *et al.*, p.79, fig. 5 (15).

Material. 17 right valves and 13 left valves.

Description. Small, externally smooth *Permophorus* lacking angulations on the posterior slope of the shell.

Remarks. Girty (1927) described three species of '*Pleurophorus*' (= *Permophorus*) from the Induan Dinwoody Formation ('Woodside shale') of the Western US, based on differences in the general shape. In each of these species, posterior angulations of the shell might occur, which however was not regarded as a 'satisfactory differentiating character' (Girty 1927, p. 445). Ciriacks (1963, p. 83) later united the three species of Girty (1927) as *Permophorus*? *bregeri* (Girty, 1927), because he regarded the described differences as insignificant and *P. bregeri* 'appears to be the most variable and least specialized of his (= Girty's) three original forms'. Whereas the description of Girty (1927) suggests indeed little morphological differences between his three species, the present material of *Permophorus* comprises two morphologically clearly distinct forms: one that is posteriorly rounded and agrees well with the figured specimen of *P. similis* (Girty 1927, pl. 30, figs 38–39) and another that has two distinct posterior angulations as in *P. rotundus* of Girty (1927, pl. 30, figs 41–42). We therefore tentatively assign our material to these two species based on the absence/presence of two angulations on the posterior slope of the shell. This assignment is provisional because the type material of Girty (1927) has not been studied.

Permophorus cf. *rotundus* (Girty, 1927)

Figure 10F–G

cf. 1927 *Pleurophorus rotundus* Girty, p. 446, pl. 30, figs 41–42.

Material. Two left valves.

Description. Small *Permophorus* with two distinct angulations on the posterior slope of the shell.

Remarks. See remarks on *Permophorus* cf. *similis*.

Order UNIONOIDA Stoliczka, 1871
Superfamily ANTHRACOSIOIDEA Amalizky, 1892
Family ANTHRACOSIIDAE Amalizky, 1892

Genus *Unionites* Wissmann, 1841

Type species. Unionites muensteri Wissmann, 1841, by original designation.

Unionites cf. *fassaensis* (Wissmann, 1841)
Figure 10H

cf. 1841 *Myacites fassaensis* Wissmann, p. 9, pl. 16, fig. 2a–c.

Material. One left valve.

Description. Outline subelliptical; umbo prosogyrate, placed near midpoint of dorsal margin; blunt umbonal ridge extending from beak to posterorventral corner.

Remarks. The present specimen differs from 'typical' *Unionites fassaensis* in the median position of the beak, which is usually placed in a slightly more anterior position (Kumagae and Nakazawa 2009). However, *U. fassaensis* is highly variable in its general shape and the position of the beak (Broglio Loriga *et al.* 1986, pl. 3, fig. 5), and it seems even possible that several morphologically ill-defined species are currently united in this taxon. We therefore place the present specimen tentatively in *U. fassaensis* as currently understood. It is noteworthy that although *U. fassaensis* is among the most frequently reported species from the Induan, it is represented by just one questionable specimen in the ML fauna.

Unionites? sp.
Figure 10I

Material. One right valve.

Description. Shell elongated suboval, with strongly prosogyrate umbo that gives rise to posterior umbonal ridge.

Remarks. This taxon differs from *Unionites* cf. *fassaensis* described above in its more elongated shell and a more anteriorly placed umbo.

Order TRIGONIOIDA Dall, 1889
Superfamily MYOPHORIOIDEA Bronn, 1849
Family MYOPHORIIDAE Bronn, 1849

Genus NEOSCHIZODUS Giebel, 1855

Type species. Lyrodon laevigatum Goldfuss, 1837, by subsequently designation (Stoliczka, 1871).

Neoschizodus laevigatus (Ziethen, 1830)

2011 *Neoschizodus laevigatus* (Ziethen, 1830); Hautmann *et al.*, p. 79, fig. 5 (14).

Material. One right valve.

Description and remarks. See Hautmann *et al.* (2011).

Superorder HETERODONTA Neumayr, 1884
Order VENEROIDA Adams and Adams, 1856
Superfamily CRASSATELLOIDEA Férussac, 1822
Family ASTARTIDAE d'Orbigny, 1844

Genus ASTARTELLA Hall, 1858

Type species. Astartella vera Hall, 1858, by subsequent designation (Miller 1889).

Astartella? *stefaniae* Hautmann, sp. nov.
Figures 10J–N, 11

LSID. urn:lsid:zoobank.org:act:5E20C9FD-CD14-4305-B74E-36A5B29B3CEE

2011 *Astartella* sp.; Hautmann *et al.*, p. 79, fig. 5 (16–19).

Derivation of name. For my beloved wife Stefanie.

Material. 20 right valves, 22 left valves and 6 complete individuals.

Holotype. PIMUZ 31293 (Fig. 10J–K).

Diagnosis. Shell small, posteriorly slightly expanded; ventral margin straight; beak located at anterior 30–35% of dorsal margin; umbo prosogyrate, giving rise to blunt posterior diagonal carina; shell with regularly arranged commarginal folds, each bearing sets of up to six delicate exterior ribs.

Type locality. Yuping, sample YUP NMC.

Type stratum. Lower Triassic, Griesbachian, Luolou Formation.

Description. Shell length typically <7 mm; valves elongated; ventral margin straight; posterior part of valves higher than anterior part; umbo prosogyrate, located 30–35% of shell length behind anterior end; lunule poorly demarcated; escutcheon deep and narrow; nymphs long; ornamentation of valves with *c.* ten commarginal folds; sets of delicate commarginal ribs on external side of shell folds (Fig. 11); ornamentation occasionally worn away on dorsal part of shell.

Remarks. The generic assignment is based on the external shape of the valves and the characteristic ornamentation, both of which are suggestive of *Astartella*. There are genera with similar external shape in Astartidae and in related families within the superfamily Crassatelloidea, but all of these are stratigraphically very distant to the

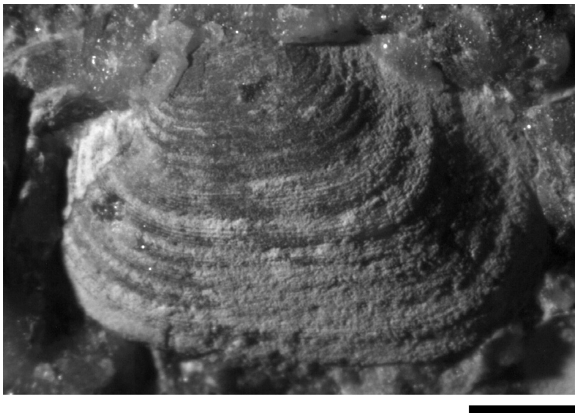

FIG. 11. *Astartella*? *stefaniae* sp. nov., PIMUZ 31300, exterior of left valve from YUP NMC, showing details of ornamentation. Scale bar represents 1 mm.

Lower Triassic except for the myophoricardiid *Sementiconcha* Hautmann *et al.*, 2013, which is similar in outline but lacks the regularly arranged commarginal shell folds. Although there is no plausible alternative to the placement in *Astartella*, generic assignment is indicated as uncertain because the hinge details are unknown.

A unique character of the new species is its ornamentation, which combines relatively coarse commarginal shell folds with delicate second-order ribs at the external side of the folds (Fig. 11). In addition, the new species is distinguished from similar Permian species such as *Astartella vallisneriana* (King, 1848) and the possibly synonymous *A. tunstallensis* (King, 1848) by its straight ventral margin.

Astartella? sp.
Figure 10Q

Material. One right valve.

Description. This species differs from *Astartella*? *stefaniae* sp. nov. in its more anteriorly located beak, in a more expanded height of the posterior part of the shell, and in lacking prominent commarginal ribs.

Remarks. We exclude the possibility that the lack of external commarginal ribs is a preservational effect because delicate incremental lines are clearly visible on the shell surface. In its general morphology, this taxon resembles Ladinian *Balantioselena* Speden, 1962, which might have descended from an *Astartella* stock.

Genus ASTARTOPIS von Wöhrmann, 1889

Type species. Myophoria richthofeni Stur, 1868, by monotypy.

Astartopis? sp.
Figure 10O–P

2011 *Astartopis*? sp.; Hautmann *et al.*, p. 80, fig. 5 (20–22).

Material. Three right valves and four left valves.

Description and remarks. See Hautmann *et al.* (2011).

Class GASTROPODA Cuvier, 1798
Order AMPHIGASTROPODA Simroth, 1906
Superfamily BELLEROPHONTOIDEA M'Coy, 1852
Family BELLEROPHONTIDAE M'Coy, 1852

Genus DICELLONEMA Yü and Wang *in* Yü, 1975

Type species. Bellerophon (*Dicellonema*) *dicellonematum* Yü and Wang *in* Yü, 1975, by original designation.

Dicellonema abrekensis (Kaim, 2009)
Figure 12A

*2009 *Bellerophon abrekensis* Kaim, p. 147, figs 145–136.
2010 *Bellerophon abrekensis* Kaim; Kaim *et al., p.* 123, fig. 2 (*cum synonymis*).

Material. 46 specimens.

Description. See Kaim *et al.* (2010).

Remarks. This well-defined species has been transferred from *Bellerophon* to *Dicellonema* by Kaim and Nützel (*in* Kaim *et al.* 2010), based on the presence of bundles of growth lines at the lateral borders of the selenizone.

Order VETIGASTROPODA Salvini-Plawen, 1980
Superfamily EOTOMARIOIDEA Wenz, 1938
Family EOTOMARIIDAE Wenz, 1938
Subfamily NEILSONIINAE Knight, 1956

Genus WANNERISPIRA Kaim and Nützel *in* Kaim *et al.*, 2010
(= *Pagodina* Wanner, 1942 (type species *Pagodina typus* Wanner, 1942 by original designation); *non Pagodina* Van Beneden (1853) (Crustacea))

Wannerispira shangganensis Kaim and Nützel *in* Kaim *et al.*, 2010
Figure 12B, D

*2010 *Wannerispira shangganensis* Kaim and Nützel *in* Kaim *et al.*, p. 124, fig. 3.

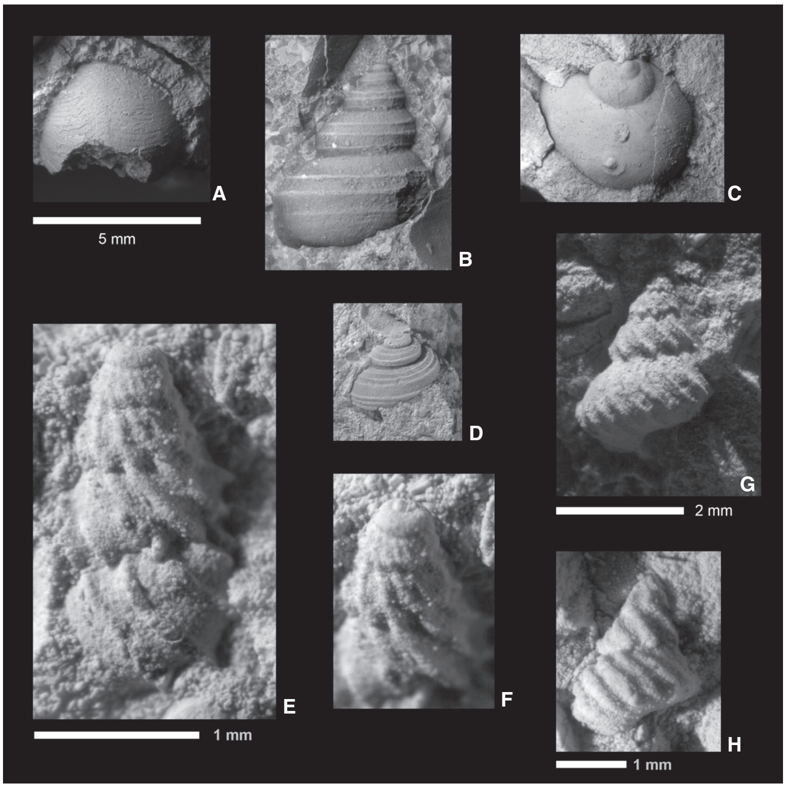

FIG. 12. Gastropod species of the microbial limestone fauna. A, *Dicellonema abrekensis* (Kaim, 2009), PIMUZ 31301, from YUP D2. B, D, *Wannerispira shangganensis* Kaim and Nützel; B, PIMUZ 31302, from YUP D2; D, PIMUZ 31304, from LON 7. C, *Naticopsis* sp., PIMUZ 31303, from WUZE B3; note microconchids. E–H, *Eucochlis obliquecostata* sp. nov., from YUP NMC; E–F, PIMUZ 31305, note protoconch; G, PIMUZ 31306, holotype; H, PIMUZ 31307. Scale bar in upper left corner (representing 5 mm) refers to A–D; scale bar in lower left corner (representing 1 mm corner) refers to E–F.

Material. 120 specimens.

Description and remarks. See Kaim *et al.* (2010).

Superfamily TROCHOIDEA Rafinesque-Schmalz, 1815
Family EUCOCHLIDAE Bandel, 2002

Genus EUCOCHLIS Knight, 1933

Type species. Eucochlis perminutus Knight, 1933, by original designation, Pennsylvanian, USA.

Eucochlis obliquecostata Nützel, sp. nov.
Figure 12E–H

LSID. urn:lsid:zoobank.org:act:EFD5CFA3-8679-462C-A150-FD04CCB74E55

Derivation of name. Obliquely ribbed, as to teleoconch ornament.

Material. Five specimens.

Holotype. PIMUZ 31306 (Fig. 12G).

Diagnosis. Conical, trochiform *Eucochlis* species with strongly prosocline and backward curving, sharp axial ribs.

Type locality. Yuping, sample YUP NMC.

Type stratum. Lower Triassic, Griesbachian, Luolou Formation.

Description. Shell acutely trochiform, small, a specimen consisting of *c.* five whorls 2.8 mm high, 2.2 mm wide; first 1.5 whorls including incomplete protoconch smooth, convex, low-spired; earliest teleoconch whorls with almost straight whorl face with periphery somewhat above abapical suture; early teleoconch whorl with about 20 sharp, densely spaced axial ribs; ribs straight, orthocline on whorl face but curve sharply backward somewhat above abapical suture; later whorls more convex with pendant whorl profile; periphery well below mid-whorl formed by rounded edge; these whorls ornamented with strong, narrow axial ribs running orthocline below adapical suture then curving in a distinctly prosocline/prosocyrt direction; overall course of axial ribs strongly prosocline; about 10 axial ribs, sharp, separated by wide interspaces; last preserved whorl again with more ribs per whorls (*c.* 17 ribs); axial ribs continue on convex base.

Remarks. The described species is the first record of the minute gastropod genus *Eucochlis* from the Triassic.

Eucochlis perminutus Knight, 1933, the Pennsylvanian type species of the genus, has a cyrtoconoid shape and a denser and finer ribbing. Moreover, the ribs are straight in *Eucochlis perminutus*. The oldest known *Eucochlis* species, *Eucochlis withnalli* Cook and Nützel, 2005 from the Givetian Papilio Mudstone (Australia), is much more low-spired than the Triassic species. *Eucochlis depressa* Yoo, 1994, *E. australis* Yoo 1988 and *E. umbiliparva* Yoo, 1994, all described from the Early Carboniferous of Australia, are stouter and have a denser and finer ribbing. *Eucochlis costatus* Bandel, Gründel and Maxwell, 2000 from the Early/Middle Jurassic of New Zealand has a finer axial ribbing and conspicuous spiral cords on the base which is untypical for the genus; the presence of spiral ribs on the base renders doubt whether this Jurassic species really belongs to *Eucochlis*. Fine spiral lirae have also been reported from the Early Carboniferous *Eucochlis* species reported by Yoo (1988, 1994). It cannot be excluded that this type of ornament was also present in the herein-reported species but is not preserved due to recrystallization. However, an original presence of strong spiral ornaments can be excluded for this species as well as for the Carboniferous type species of *Eucochlis*.

Trochomorph vetigastropods are generally rare in the Early Triassic (Wittenburg 1908; Pan 1982; Batten and Stokes 1986); only five genera have been reported worldwide, among them outdated assignments to the modern genus *Turbo*. In their study on gastropod diversity pattern of the Permian–Triassic of South China, Pan and Erwin (1994) listed not a single trochomorph occurrence for the Griesbachian. Later, in the Middle and Late Triassic, this group experienced a major radiation, but Early Triassic diversity was very low.

Order NERITIMORPHA Koken, 1896
Superfamily NERITOIDEA Rafinesque-Schmalz, 1815
Family NATICOPSIDAE Waagen, 1880

Genus NATICOPSIS M'Coy, 1844

Type species. Naticopsis phillipsii M'Coy, 1844, by subsequent designation (Meek and Worthen 1866).

Naticopsis sp.
Figure 12C

2010 *Naticopsis* sp.; Kaim *et al.*, p. 125, fig. 4a, b, d, e (*cum synonymis*).

Material. 31 specimens.

Description and remarks. See Kaim *et al.* (2010).

Superfamily NERITOPSOIDEA Gray, 1847
Family PALAEONARICIDAE Bandel, 2007

Genus PALAEONARICA Kittl, 1892

Type species. Naticella pyrulaeformis Klipstein, 1843, by subsequent designation (Cossmann 1915).

Palaeonarica guangxinensis Kaim and Nützel *in* Kaim *et al.*, 2010

*2010 *Palaeonarica guangxinensis* Kaim and Nützel *in* Kaim *et al.*, p. 125, fig. 4c, f.

Material. Six specimens.

Description and remarks. See Kaim *et al.* (2010).

Phylum BRACHIOPODA Duméril, 1806
Class LINGULATA Goryansky and Popov, 1985
Order LINGULIDA Waagen, 1885
Family LINGULIDAE Menke, 1828

Genus SINOLINGULARIA Peng and Shi, 2008

Type species. Sinolingularia huananensis Peng and Shi, 2008, by original designation.

Sinolingularia? sp.
Figure 13C

Material. 82 disarticulated valves (ventral/dorsal valve mostly not distinguishable).

Description. Shell small (maximum length <4 mm) and oval in outline. Interior of dorsal valve with triangular shell thickening on the posterior part of the valve bearing a central linear impression, which is anteriorly terminated by a round, undivided muscle impression. Traces of the mantle canals present on the dorsal valve of one specimen, not well resolved but possibly bifurcating. Vascula media lacking. Length of lophophoral cavity *c.* 45% of overall length of dorsal valve. Interior of ventral valve unknown.

Remarks. The relatively large lophophoral cavity and the undivided anterior muscle impression resemble *Lingularia* Biernat and Emig, 1993, but the shell thickening and the linear shell impression in the interior of the dorsal valve have not been reported from this genus and need further examination. *Sinolingularia* Peng and Shi, 2008 is also similar to the present material but differs in having two clearly separated antero-lateral muscle scars in the dorsal valve according to the original description. According to

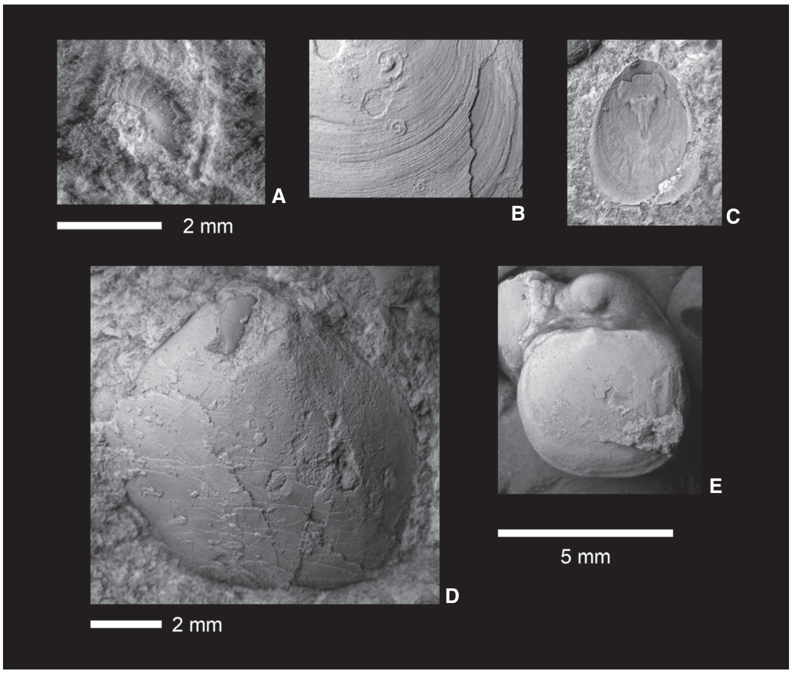

FIG. 13. Serpulid, microconchid and brachiopod species. A, serpulid indet., PIMUZ 31308, from WUZE B3. B, *Microconchus* sp., PIMUZ 31309, from YUP D2, fixed on a left (upper) valve of *Scythentolium scutigerulus*. C, *Sinolingularia*? sp., PIMUZ 31310, interior of dorsal valve from LON 7. D, brachiopod indet., PIMUZ 31311, pedicle (ventral) valve from WUZE B3. E, *Orbicoelia speciosa* (Wang, 1955), PIMUZ 31312, from YUP D2. Scale bar in lower right corner (representing 5 mm) refers to B–C, E.

L. Popov (pers. comm. 18 May 2014), Early Triassic lingulids from China are oversplit and any determination requires a comprehensive revision of the group that accounts for intraspecific variability. Following his suggestion, the here-described lingulid is provisionally placed in *Sinolingularia*.

Class RHYNCHONELLATA Williams *et al.*, 1996
Order SPIRIFERIDA Waagen, 1883
Suborder SPIRIFERIDINA Waagen, 1883
Superfamily AMBOCOELIOIDEA George, 1931
Family AMBOCOELIIDAE George, 1931
Subfamily AMBOCOELIINAE George, 1931

Genus ORBICOELIA Waterhouse and Piyasin, 1970

Type species. Orbicoelia fraterculus Waterhouse and Piyasin, 1970, by original designation.

Orbicoelia speciosa (Wang, 1955)
Figure 13E

*1955 *Crurithyris speciosa* Wang, p. 146, pl. 83, figs 1–4.
2006 *Orbicoelia speciosa* (Wang, 1955); Chen *et al.*, p. 317, fig. 9 (*cum synonymis*).

Material. Seven specimens.

Description. Shell small, unequally biconvex, lacking a median sulcus on both valves. Ventral valve strongly convex; beak pointed, slightly incurved over relatively broad, open delthyrium; interarea rather low. Dorsal valve slightly convex to nearly flat; outline hemispheric to rounded-quadrate; triangular notothyrium present. Ornamentation with growth lines, no spines observed. Shell interior unknown.

Remarks. The few specimens at hand exclude serial sections; thus, our determination is based solely on external characters, which suggest assignment to *Orbicoelia speciosa*. *O. speciosa* is a common brachiopod species in the upper Permian and Permian–Triassic boundary beds in South China. Wang's (1955) *O. speciosa* externally resembles *O. extima* (Grant, 1970), from which it is distinguished by a more incurved ventral beak. In South China, *O. pusilla* (Zhan, 1979) is also present in the latest Changhsingian; however, the dorsal valve of *O. pusilla* is more flattened and has a sulcus on the pedicle valve, which is lacking in *O. speciosa*. The present specimen is within the lower range of the lengths measured for *O. speciosa* by Chen *et al.* (2006, table 4).

Jing and Sun (1981) suggested a new genus *Speciothyris* with *Crurithyris speciosa* as the type species, but this genus did not find general acceptance (Xu and Grant 1994).

brachiopod indet.
Figure 13D

Material. One pedicle valve.

Description. Pedicle valve relatively large (length *c.* 1 cm), rounded-pentagonal in outline, with strongly incurved beak.

Remarks. In spite of the incomplete preservation, this taxon can clearly be separated from *Orbicoelia speciosa* described above on grounds of the quite different outline and distinctly larger shell size.

incertae sedis
Class TENTACULITA Bouček, 1964
Order MICROCONCHIDA Weedon, 1991

Genus MICROCONCHUS Murchison, 1839

Type species. Microconchus carbonarius Murchison, 1839 by monotypy.

Microconchus sp.
Figure 13B

Material. 17 specimens.

Description. Tube small, planispirally and dextrally coiled, attached by its entire length.

Remarks. This taxon occasionally occurs in this fauna as an epizoan on epifaunal species such as *Scythentolium scutigerulus*. It resembles the recently described *Microconchus utahensis* Zaton *et al.*, 2013 from the Spathian of the Western US, but the preservation of the Chinese material is insufficient for a firm identification.

Phylum ANNELIDA Lamarck, 1809
Class POLYCHAETA Grube, 1850
Order SERPULIMORPHA Hatschek, 1893
Family SERPULIDAE Burmeister, 1837
serpulid indet.
Figure 13A

Material. 15 specimens.

Description. Tube fragments of a solitary serpulid that has an annulated ornamentation on the shell exterior.

Remarks. This taxon occasionally occurs in samples of FI 1, but no complete specimens are available that would allow for a precise determination.

Acknowledgements. This work was supported by the Swiss NSF projects 200021_132134 to H.B. and 200021-149152/1 to MH. The manuscript benefitted from comments of F. T. Fürsich and an anonymous reviewer.

Author contributions. MH determined the bivalves, constructed and analysed the palaeoecological data set, developed the diversification model and wrote the manuscript; BB and AB logged sections and contributed thin-section analyses and sedimentological interpretations; MB and NG provided the conodont biostratigraphy; ÅF logged sections, sampled the fauna, determined the brachiopods and carried out the carbon isotope analysis; RH provided palaeoecological data; AN determined the gastropods; HB discovered and sampled the sections, coordinated the project, and contributed the geological and geochronological framework; all authors commented on the manuscript.

DATA ARCHIVING STATEMENT

Data for this study are available in the Dryad Digital Repository: http://dx.doi.org/10.5061/dryad.g3s10

Editor. Arnaud Brayard

REFERENCES

ABERHAN, M. 1992. Palökologie und zeitliche Verbreitung benthischer Faunengemeinschaften im Unterjura von Chile. *Beringeria*, **5**, 1–174.

ADAMS, H. and ADAMS, A. 1854–1858. *The genera of Recent Mollusca, arranged according to their organisation*, Vol. 2. John van Vorst, London, 661 pp.

AGASSIZ, L. 1840. Mémoire sur les moules des mollusques vivans et fossiles. *Mémoires de la Société des Sciences Naturelle de Neuchâtel*, **2** (4), 1–48.

ALLASINAZ, A. 1972. Revisione dei Pettinidi Triassici. *Rivista Italiana di Paleontologia e Stratigrafia*, **78**, 189–428.

AMALIZKY, W. 1892. Ueber die Anthracosien der Permformation Russlands. *Palaeontographica*, **39**, 125–213.

BAILEY, S. F., DETTMAN, J. R., RAINEY, P. B. and KASSEN, R. 2013. Competition both drives and impedes diversification in a model adaptive radiation. *Proceedings of the Royal Society B*, **280**, 1471–2954.

BANDEL, K. 2002. Reevaluation and classification of Carboniferous and Permian Gastropoda belonging to the Caenogastropoda and their relation. *Mitteilungen aus dem Geologisch-Paläontologischen Institut der Universität Hamburg*, **86**, 81–188.

—— 2007. Description and classification of Late Triassic Neritomorpha (Gastropoda, Mollusca) from the St Cassian Formation, Italian Alps. *Bulletin of Geosciences*, **82**, 215–274.

—— GRÜNDEL, J. and MAXWELL, P. 2000. Gastropods from the Upper Jurassic/early Middle Jurassic of Kaiwara Valley, North Canterbury, New Zealand. *Freiberger Forschungshefte C*, **490**, 67–132.

BATTEN, R. L. and STOKES, W. L. 1986. Early Triassic gastropods from the Sinbad Member of the Moenkopi Formation, San Rafael Swell, Utah. *American Museum Novitates*, **2864**, 1–33.

BEGG, J. G. and CAMPBELL, H. J. 1985. *Etalia*, a new Middle Triassic (Anisian) bivalve from New Zealand, and its relationship with other pteriomorphs. *New Zealand Journal of Geology and Geophysics*, **28**, 725–741.

BENTON, M. J. and EMERSON, B. C. 2007. How did life become so diverse? The dynamics of diversification according to the fossil record and molecular phylogenetics. *Palaeontology*, **50**, 23–40.

BEURLEN, K. 1944. Beiträge zur Stammesgeschichte der Muscheln. *Sitzungsberichte der Bayerischen Akademie der Wissenschaften*, **1944** (1–2), 133–145.

—— 1954. As faunas de lamellibranquios do sistema genduanico no Parana. 107–136. *In* LANGE, F. W. (ed.). *Paleontologia do Parana*. Comissao de Comemoracoes do Centenario do Parana, Curitiba, 210 pp.

BEYRICH, E. 1865. Über eine Kohlenkalk-Fauna von Timor. *Abhandlungen der Königlichen Akademie der Wissenschaften zu Berlin, Physikalische Klasse*, **1864**, 61–98.

BIERNAT, G. and EMIG, C. C. 1993. Anatomical distinctions of the Mesozoic brachiopods. *Acta Palaeontologica Polonica*, **38**, 1–20.

BITTNER, A. 1891. Triaspetrefakten von Balia in Kleinasien. *Jahrbuch der Kaiserlich-Königlichen Geologischen Reichsanstalt*, **41**, 97–116.

—— 1898. Beiträge zur Paläontologie, insbesondere der triadischen Ablagerungen centralasiatischer Hochgebirge. *Jahrbuch der Kaiserlich-Königlichen Geologischen Reichsanstalt*, **48**, 689–718.

—— 1899. Trias-Ablagerungen des Süd-Ussuri-Gebietes in der ostsibirischen Küstenprovinz. *Mémoires du Comité Géologique*, **7**, 1–35.

—— 1901. Ueber *Pseudomonotis Telleri* und verwandte Arten der unteren Trias. *Jahrbuch der k.k. Geologischen Reichsanstalt*, **50**, 559–592.

BOLKNIK, D. I., INGRAM, T., STUTZ, W. E., SNOWBERG, L. K., LAU, O. L. and PAULL, J. S. 2010. Ecological release from interspecific competition leads to decoupled changes in population and individual niche width. *Proceedings of the Royal Society B*, **277**, 1789–1797.

BOUČEK, B. 1964. *The Tentaculites from Bohemia. Their Morphology, Taxonomy, Ecology, Phylogeny and Biostratigraphy*. Publishing House of the Czechoslovak Academy of Sciences, Prague, 215 pp.

BRAYARD, A., ESCARGUEL, G., BUCHER, H., MONNET, C., BRÜHWILER, T., GOUDEMAND, N., GALFETTI, T. and GUEX, J. 2009. Good genes and good luck: ammonoid diversity and the end-Permian mass extinction. *Science*, **325**, 1118–1121.

BROGLIO LORIGA, C., MASETTI, D. and NERI, C. 1983. La Formazione di Werfen (Scitico) delle Dolomiti occidentali: sedimentologia e biostratigrafia. *Rivista Italiana di Paleontologia e Stratigrafia*, **58**, 501–598.

—— NERI, C., PASINI, M. and POSENATO, R. 1986. Marine fossil assemblages from Upper Permian to lowermost Triassic in the western Dolomites (Italy). *Memorie della Società Geologica Italiana*, **34**, 5–44.

BRONN, H. G. 1849. *Index Palaeontologicus oder Übersicht der bis jetzt bekannten fossilen Organismen. Zweite Abtheilung. Enumerator palaeontologicus: Systematische Zusammenstellung und geologische Entwickelungs-Gesetze der organischen Reiche*. Schweizerbart, Stuttgart, 776 pp.

BROSSE, M., BUCHER, H., BAGHERPOUR, B., BAUD, A., FRISK, Å. M., GUODUN, K. and GOUDEMAND, N. 2015. Conodonts from the Early Triassic microbialite of Guangxi (South China): implications for the definition of the base of the Triassic System. *Palaeontology*, **58**, 563–584.

BROWN, T. 1841. Description of some new species of fossil shells, found chiefly in the Vale of Todmorden, Yorkshire. *Transactions of the Manchester Geological Society*, **1**, 212–229.

BRÜHWILER, T., BRAYARD, A., BUCHER, H. and KUANG, G. D. 2008. Griesbachian and Dienerian (Early Triassic) ammonoid faunas from northwestern Guangxi and southern Guizhou (South China). *Palaeontology*, **51**, 1151–1180.

BURGESS, S. D., BOWRING, S. and SHEN, S.-Z. 2014. High-precision timeline for Earth's most severe extinction. *Proceedings of the National Academy of Sciences, USA*, **111**, 3316–3321.

BURMEISTER, H. 1837. *Handbuch der Naturgeschichte [Part 2]*. Enslin, Berlin, 858 pp.

CARTER, J. G. *et al.* 2011. A synoptical classification of the Bivalvia (Mollusca). *Paleontological Contributions*, **4**, 1–47.

CHAVAN, A. 1954. Les *Pleurophorus* et genres voisins. *Cahier Géologiques Seyssel*, **22**, 200.

CHEN, Z. Q., KAIHO, K., GEORGE, A. D. and TONG, J. 2006. Survival brachiopod faunas of the end-Permian mass extinction from north Italy and south China. *Geological Magazine*, **143**, 301–327.

CHIVAS, A. R., TORGERSEN, T. and POLACH, H. A. 1990. Growth rates and Holocene development of stromatolites from Shark Bay, Western Australia. *Australian Journal of Earth Sciences*, **37**, 113–121.

CIRIACKS, K. W. 1963. Permian and Eotriassic bivalves of the middle Rockies. *Bulletin of the American Museum of Natural History*, **125**, 1–100.

COOK, A. G. and NÜTZEL, A. 2005. New Devonian gastropods from the Broken River and their palaeoecology. *Memoirs of the Queensland Museum*, **51**, 391–397.

COSSMANN, M. 1902. Rectification de nomenclature. *Revue Critique de la Nomenclature*, **6**, 233 pp.

—— 1915. Étude complementaire sur le Charmoutien de la Vendée. *Mémoires de la Société Linnéenne de Normandie, Section Geologique*, **33**, 113–159.

COX, L. R. 1940. The Jurassic lamellibranch fauna of Kuchh (Cutch). *Memoirs of the Geological Survey of India, Palaeontologia Indica, Series 9*, **3**, 1–157.

—— 1964. Notes concerning the taxonomy and nomenclature of fossil Bivalves (mainly Mesozoic). *Proceedings of the Malacological Society of London*, **36**, 39–48.

CUVIER, G. 1797–1798. *Tableau élémentaire de l'histoire naturelle des animaux*. Baudouin, Paris, 710 pp.

DAGYS, A. S. and KANYGIN, A. V. 1996. *The Triassic fauna of the north-east of Asia*. Sibirskaj Isdatelskaj Firma Ran, Novosibirsk, 168 pp. [In Russian]

DALL, W. H. 1889. On the hinge of pelecypods and its development with an attempt toward a better subdivision of the group. *American Journal of Science*, **38**, 445–462.

DARWIN, C. 1859. *On the origin of species by means of natural selection*. John Murray, London, 502 pp.

DIENER, C. 1923. *Lamellibranchiata triadica. Fossilium catalogus I: Animalia. Pars 19, W.* Junk, Berlin, 257 pp.

DUMÉRIL, A. M. C. 1806. *Zoologie analytique ou méthode naturelle de classification des animaux.* Allais, Paris, xxiv + 364 pp.

DUNBAR, C. O. 1924. Kansas Permian insects, part 1. The geologic occurrence and the environment of the insects. *American Journal of Science*, **7**, 171–208.

EMERSON, B. C. and KOLM, N. 2005. Species diversity can drive speciation. *Nature*, **434**, 1015–1017.

EMMRICH, H. 1844. Über die Schichten-Folge der Flötz-Gebirge des Gader-Thales, der Seisser-Alpe und insbesondere bei St. Cassian. *Neues Jahrbuch für Mineralogie*, **1844**, 791–803.

ERWIN, D. H. 2001. Lessons from the past: biotic recoveries from mass extinctions. *Proceedings of the National Academy of Sciences, USA*, **98**, 5399–5403.

—— 2007. Increasing returns, ecological feedback and the Early Triassic recovery. *Palaeoworld*, **16**, 9–15.

FAN, G., WANG, Y., KERSHAW, S., LI, G., MENG, Z., LIN, Q. and YUAN, Z. 2014. Recurrent breakdown of Late Permian reef communities in response to episodic volcanic activities: evidence from southern Guizhou in South China. *Facies*, **60**, 603–613.

FANG Z.-J. 2010. Generic demarcation of permo-triassic claraia-like species and their biogeographic significance. *Alcheringa*, **34**, 161–178.

FÉRUSSAC, A. E. de 1822. *Tableaux systématiques des animaux mollusques classés en familles naturelles, dans lesquels on a établi la concordance de tous les systèmes; suivis d'un prodrome général pour tous les mollusques terrestres ou fluviatiles, vivants ou fossiles*. Bertrand, Paris, 111 pp.

FLESSA, K. W. and JABLONSKI, D. 1983. Extinction is here to stay. *Paleobiology*, **9** (4), 315–321.

FLÜGEL, E. 2009. *Microfacies of carbonate rocks: analysis, interpretation and application*. Springer, Berlin, 984 pp.

FOREL, M.-B. 2012. Ostracods (Crustacea) associated with microbialites across the Permian–Triassic boundary in Dajiang (Guizhou Province, South China). *European Journal of Taxonomy*, **19**, 1–34.

—— CRASQUIN, S., KERSHAW, S. and COLLIN, P.-Y. 2013. In the aftermath of the end-Permian extinction: the microbialite refuge? *Terra Nova*, **25**, 137–143.

FRECH, F. 1891. Die devonischen Aviculiden Deutschlands, ein Beitrag zur Systematik und Stammesgeschichte der Zweischaler. *Abhandlungen zur Geologischen Spezialkarte von Preußen und den Thüringischen Staaten*, **9**, 1–253.

FÜRSICH, F. T. 1977. Corallian (Upper Jurassic) marine benthic associations from England and Normandy. *Palaeontology*, **20**, 337–385.

GEORGE, T. N. 1931. *Ambocoelia* Hall and certain similar British Spiriferidae. *Quarterly Journal of the Geological Society of London*, **87**, 30–61.

GIEBEL, C. 1855. Kritisches über die Myophorien des Muschelkalkes. *Zeitschrift für die Gesamten Naturwissenschaften*, **5**, 34–36.

GIRTY, G. H. 1927. Descriptions of new species of Carboniferous and Triassic fossils. 411–453. *In* MANSFIELD, G. R. *Geography geology and mineral resources of part of southeastern Idaho With descriptions of Carboniferous and Triassic fossils*. Geological Survey Professional Paper, **152**, 453 pp.

GOLDFUSS, A. 1833–1840. *Petrefacta Germaniae. Abbildungen und Beschreibungen der Petrefacten Deutschlands und der angränzenden Länder, unter Mitwirkung des Herrn Grafen Georg zu Münster, herausgegeben von August Goldfuss. Zweiter Teil*. Arnz and Co., Düsseldorf, 211 pp.

GORYANSKY, V. Y. U. and POPOV, L. 1985. Morphology, systematic position and origin of the inarticulate brachiopods with calcareous shells. *Paleontologicheskii Zhurnal*, **1985**, 3–14.

GRANT, R. E. 1970. Brachiopods from Permian–Triassic boundary beds and age of Chhidru Formation, West Pakistan. 117–151. *In* KUMMEL, B. and TEICHERT, C. (eds). *Stratigraphic boundary problems: Permian and Triassic of West Pakistan*. University of Kansas, Department of Geology, Special Publication, **4**, 474 pp.

GRAY, J. E. 1847. A list of the genera of Recent Mollusca, their synonyms and types. *Proceedings of the Zoological Society of London*, **15**, 129–219.

GROBBEN, K. 1894. Zur Kenntnis der Morphologie, der Verwandtschaftsverhältnisse und des Systems der Mollusken. *Sitzungsberichte der Akademie der Wissenschaften in Mathematisch–Naturwissenschaftliche Klasse, Wien*, **103**, 61–86.

GRUBE, A. E. 1850. Die Familien der Anneliden. *Archiv für Naturgeschichte*, **16**, 249–364.

HALL, J. 1858. Palaeontology of Iowa. 473–724. *In* HALL, J. and WHITNEY, J. D. (eds). *Report on the geological survey of the state of Iowa: embracing the results of investigations made during portions of the years 1855, 56 and 57*. Authority of the legislature of Iowa, Des Moines, 724 pp.

HALLAM, A. 1991. Why was there a delayed radiation after the end-Palaeozoic extinctions? *Historical Biology*, **5**, 257–262.

HAMMER, Ø., HARPER, D. A. T. and RYAN, P. D. 2001. PAST: Paleontological Statistics Software Package for Education and Data Analysis. *Palaeontologia Electronica*, **4** (1), 4A.

HATSCHEK, B. 1893. System der Anneliden, ein vorläufiger Bericht. *Lotos*, **13**, 123–126.

HAUTMANN, M. 2007. Steuerungsfaktoren globaler Biodiversifizierungsmuster am Beispiel frühmesozoischer Muscheln. *Beringeria*, **37**, 61–74.

—— 2014. Diversification and diversity partitioning. *Paleobiology*, **40**, 162–176.

—— STILLER, F., CAI, H. and SHA, J. 2008. Extinction-recovery pattern of level-bottom faunas across the Triassic-Jurassic boundary in Tibet: implications for potential killing mechanisms. *Palaios*, **23**, 711–718.

—— BUCHER, H., BRÜHWILER, T., GOUDEMAND, N., KAIM, A. and NÜTZEL, A. 2011. An unusually diverse mollusc fauna from the earliest Triassic of South China and its implications for benthic recovery after the end-Permian biotic crisis. *Geobios*, **44**, 71–85.

—— SMITH, A. B., McGOWAN, A. J. and BUCHER, H. 2013. Bivalves from the Olenekian (Early Triassic) of southwestern Utah: systematics and evolutionary significance. *Journal of Systematic Palaeontology*, **11**, 263–293.

—— BAGHERPOUR, B., BROSSE, M., FRISK, Å., HOFMANN, R., BAUD, A., NÜTZEL, A., GOUDEMAND,

N. and BUCHER, H. 2015. Data from: Competition in slow motion: the unusual case of benthic marine communities in the wake of the end-Permian mass extinction. *Dryad Digital Repository*. doi:10.5061/dryad.g3s10

HE, W. H., FENG, Q. L., WELDON, E. A., GU, S. Z., MENG, Y. Y., ZHANG, F. and WU, S. B. 2007. A Late Permian to Early Triassic bivalve fauna from the Dongpan section, southern Guangxi, south China. *Journal of Paleontology*, **81**, 1009–1019.

HERRMANNSEN, A. N. 1846–1852. *Indicis Generum Malacozoorum primordia*, vol. 1 (1846–1847) 637 pp., vol. 2 (1847–1849) 717 pp., Suppl. (1852), 140 pp. Fischer, Kassel.

HERTWIG, C. W. T. R. 1895. *Lehrbuch der Zoologie*, 3rd edn. Fischer, Jena, 599 pp.

HOFMANN, R., HAUTMANN, M. and BUCHER, H. 2013*a*. A new paleoecological look at the Dinwoody Formation (Lower Triassic, Western U.S.): intrinsic versus extrinsic controls on ecosystem recovery after the end-Permian mass extinction. *Journal of Paleontology*, **87**, 854–880.

—— —— WASMER, M. and BUCHER, H. 2013*b*. Palaeoecology of the Virgin Formation (Utah, USA) and its implications for the Early Triassic recovery. *Acta Palaeontologica Polonica*, **58**, 149–173.

—— —— BRAYARD, A., NÜTZEL, A., BYLUND, K. G., JENKS, J. F., VENNIN, E., OLIVIER, N. and BUCHER, H. 2014. Recovery of benthic marine communities from the end-Permian mass extinction at the low-latitudes of Eastern Panthalassa. *Palaeontology*, **57**, 547–589.

JABLONSKI, D. 1994. Extinctions in the fossil record. *Philosophical Transactions of the Royal Society of London, Series B*, **344**, 11–17.

JING, Y. G. and SUN, D. L. 1981. Palaeozoic Brachiopods from Xizang. 127–171. *In* NANJING INSTITUTE OF GEOLOGY AND PALEONTOLOGY (ed.). *Palaeontology of Xizang. Book III. The Series of the Scientific Expedition to the Qinghai–Xizang Plateau*. Beijing Science Press, Beijing, 254 pp.

JOST, L. 2006. Entropy and diversity. *Oikos*, **113**, 363–375.

KAIM, A. 2009. Gastropods. 141–156. *In* SHIGETA, Y., ZAKHAROV, Y. U. D., MAEDA, H. and POPOV, A. M. (eds). *The Lower Triassic system in the Abrek Bay area, south Primorye, Russia*. National Museum of Nature and Science Monographs, **38**, 218 pp.

—— NÜTZEL, A., BUCHER, H., BRÜHWILER, T. and GOUDEMAND, N. 2010. Early Triassic (Late Griesbachian) gastropods from South China (Shanggan, Guangxi). *Swiss Journal of Geosciences*, **103**, 121–128.

KAUFFMAN, E. G. and HARRIES, P. J. 1996. The importance of crisis progenitors in recovery from mass extinction. 15–39. *In* HART, M. B. (ed.). *Biotic recovery from mass extinction events*. Geological Society Special Publication, **102**, 393 pp.

KEEN, A. M. 1958. *Marine shells of the tropical West America*. Stanford University Press, Stanford, 624 pp.

KERSHAW, S., CRASQUIN, S., LI, Y., COLLIN, P.-Y., FOREL, M.-B., MU, X., BAUD, A., WANG, Y., XIE, S., MAURER, F. and GUO, L. 2012. Microbialites and global environmental change across the Permian–Triassic boundary: a synthesis. *Geobiology*, **10**, 25–47.

KING, W. 1848. *A catalogue of the organic remains of the Permian rocks of Northumberland and Durham*. Published by the author, Newcastle-Upon-Tyne, 16 pp.

—— 1850. *A monograph of the Permian Fossils of England*. Palaeontographical Society, London, 258 pp.

KIPARISOVA, L. D. 1938. Nizhnetriasovye plastinchatozhabernye Ussurijskogo kraya. *Trudy Geologicheskogo Instituta*, **7**, 197–311. [In Russian]

KIRCHNER, J. W. and WEIL, A. 2000. Delayed biological recovery from extinctions throughout the fossil record. *Nature*, **404**, 177–180.

KITTL, E. 1892. Die Gastropoden der Schichten von St. Cassian der südalpinen Trias. II. Theil. *Annalen des Kaiserlich-Königlichen Naturhistorischen Hofmuseums*, **7**, 35–97.

—— 1904. Geologie der Umgebung von Sarajevo. *Jahrbuch der Kaiserlich-Königlichen Geologischen Reichsanstalt*, **53**, 707–738 [for 1903].

KLIPSTEIN, A. VON 1843. *Beiträge zur geologischen Kenntnis der östlichen Alpen*. Heyer, Gießen, 311 pp.

KNIGHT, J. B. 1933. The Gastropods of the St. Louis, Missouri, Pennsylvanian outlier: the Trocho-Turbinidae. *Journal of Paleontology*, **7**, 30–58.

—— 1956. New families of Gastropoda. *Journal of the Washington Academy of Sciences*, **46**, 41–42.

KOKEN, E. 1896. Die Gastropoden der Trias um Hallstadt. *Jahrbuch der Kaiserlich-Königlichen Geologischen Reichsanstalt*, **46**, 37–126.

KOROBKOV, I. A. 1954. *Spravochnik i metodicheskoe rukovodstvo po tretichnym molliuskam. Plastinchatozhabernye [Handbook and methodical manual on Tertiary mollusks: Lamellibranchiates]*. Gostoptekhizdat, Leningrad, 444 pp. [In Russian]

—— 1960. Anisomyaria. 83. *In* EBERZIN, A. G. (ed.). *Osnovy Paleontologii*, Vol. 3. Academy Nauk USSR, Moscow, 300 pp.

KUMAGAE, T. and NAKAZAWA, K. 2009. Bivalves. 156–173. *In* SHIGETA, Y., ZAKHAROV, Y. U. D., MAEDA, H. and POPOV, A. M. (eds). *The Lower Triassic system in the Abrek Bay area, south Primorye, Russia*. National Museum of Nature and Science Monographs, **38**, 218 pp.

LAMARCK, J. B. de, 1799. Prodrome d'une nouvelle classification des coquilles, comprenant une rédaction appropriée des caractères génériques et l'établissement d'un grand nombre de genres nouveaux. *Mémoires de la Société d'Histoire Naturelle de Paris*, **1**, 63–91.

—— 1809. *Philosophie zoologique, ou, Exposition des considérations relative à l'histoire naturelle des animaux*. Dentu, Paris, 2 vols, 422 and 473 pp.

LINNAEUS, C. 1758. *Systema naturae per regna tria naturae, secundum classes, ordines, genera, species, cum characteribus, differentiis, synonymis, locis. Tomus I. Editio Decima*. Laurentius Salvius, Stockholm, 824 pp.

LOGAN, A. 1967. The Permian Bivalvia of northern England. *Monograph of the Palaeontographical Society, London*, **121**, 1–72.

MACARTHUR, R. H. 1972. *Geographical ecology*. Harper and Row, New York, 269 pp.

—— and WILSON, E. O. 1967. *The theory of island biogeography*. Princeton University Press, 215 pp.

MARWICK, J. 1953. Divisions and faunas of the Hokonui system (Triassic and Jurassic). *New Zealand Geological Survey, Paleontological Bulletin*, **21**, 1–141.

MAYR, E. 1963. *Animal species and evolution*. Harvard University Press, Cambridge, 797 pp.

M'COY, F. 1844. *A synopsis of the characters of Carboniferous Limestone Fossils of Ireland*. McGloshan and Gill, Dublin, 274 pp.

—— 1852. *A synopsis of the classification of the of the British Palaeozoic rocks [By the Rev. Adam Sedgwick] with a systematic description of the British Palaeozoic fossils in the Geological Museum of the University of Cambridge [by Frederick M'Coy] with figures of the new and imperfectly known species*. Parker and Son, London, 661 pp.

MEEK, F. B. and HAYDEN, F. V. 1864. Palaeontology of the Upper Missouri. *Smithsonian Contributions to Knowledge*, **14**, 1–135.

—— and WORTHEN, A. H. 1866. Description of Paleozoic fossils from the Silurian, Devonian and Carboniferous rocks of Illinois, and other western states. *Chicago Academy of Sciences Proceedings*, **1**, 11–23.

MENKE, C. T. 1828. *Synopsis methodica Molluscorum generum omnium et specierum earum, quae in Museo Menkeano adservantur*. Published by the author, Pyrmont, 91 pp.

MEYER, J. R. and KASSEN, R. 2007. The effects of competition and predation on diversification in a model adaptive radiation. *Nature*, **446**, 432–435.

MILLER, S. A. 1877. *The American Paleozoic fossils: a catalogue of the genera and species*. Published by the author, Cincinnati, 334 pp.

—— 1889. *North American geology and palaeontology for the use of amateurs, students, and scientists*. Western Methodist Book Concern, Cincinnati, 664 pp.

MILLER, R. S. 1967. Pattern and process in competition. *Advances in Ecological Research*, **4**, 1–74.

MURCHISON, R. I. 1839. *The Silurian System, founded on geological researches in the counties of Salop, Hereford, Radnor, Montgomery, Caermarthen, Brecon, Pembroke, Monmouth, Gloucester, Worcester, and Stafford, with descriptions of the coal-fields and overlying formations*. John Murray, London, 768 pp.

NAKAZAWA, K. 1961. Early and Middle Triassic pelecypod–fossils from the Maizuru Zone, Southwest Japan. *Memoirs of the College of Science, University of Kyoto, Series B*, **27**, 249–279.

—— and NEWELL, N. D. 1968. Permian bivalves of Japan. *Memoirs of the Faculty of Science, Kyoto University, Series of Geology and Mineralogy*, **35**, 1–108.

NEUMAYR, M. 1884. Zur Morphologie des Bivalvenschlosses. *Sitzungsberichte der Akademie der Wissenschaften in Wien, Mathematisch–Naturwissenschaftliche Klasse, Abteilung, 1*, **88**, 385–418.

NEWELL, N. D. 1938. Late Paleozoic pelecypods: Pectinacea. *State Geological Survey of Kansas Publications*, **10**, 1–123 [for 1937].

—— 1942. Systematic palaeontology. 953–961. *In* NEWELL, N. D. and KUMMEL, B. (eds). *Lower Eo-Triassic stratigraphy, western Wyoming and southeast Idaho*. GSA Bulletin, **53**, 937–996.

—— 1965. Classification of the Bivalvia. *American Museum Novitates*, **2206**, 1–25.

—— 1969. Order Modiomorphoida Newell, new order. N393. *In* MOORE, R. C. (ed.). *Treatise on invertebrate paleontology, Part N, Mollusca* 6, Vol. 1. Geological Society of America, Boulder, CO & University of Kansas Press, Lawrence, KS, 952 pp.

—— and BOYD, D. W. 1995. Pectinoid bivalves of the Permian–Triassic crisis. *American Museum of Natural History Bulletin*, **227**, 1–95.

NEWTON, C. R. 1987. Systematic paleontology. 13–78. *In* NEWTON, C. R., WHALEN, M. T., THOMPSON, J. B., PRINS, N. and DELALLA, D. (eds). *Systematics and paleoecology of Norian (Late Triassic) bivalves from a tropical isaland arc: Wallowa terrane, Oregon*. Journal of Paleontology Memoir, **22**, 83 pp.

NEYMAN, A. A. 1967. Limits to the application of the trophic group concept in benthic studies. *Oceanology, Academy of Sciences of the USSR*, **7**, 149–155.

NÜTZEL, A. and SCHULBERT, C. 2005. Facies of two important Early Triassic gastropod lagerstätten: implications for diversity patterns in the aftermath of the end-Permian mass extinction. *Facies*, **51**, 495–515.

ORBIGNY, A. d' 1844–1848. *Paléontologie française. Description zoologique et géologique de tous les animaux mollusques et rayonnés fossiles de France. Terrains crétacés. Vol. 3, Mollusques*. Masson, Paris, 807 pp.

PAN, H. Z. 1982. Triassic marine gastropods from SW China. *Bulletin of the Nanjing Institute of Geology and Paleontology*, **4**, 153–188.

—— and ERWIN, D. H. 1994. Gastropod diversity patterns in South China during the Chihsia-Ladinian and their mass extinction. *Palaeoworld*, **4**, 249–262.

PAYNE, J. L., LEHRMANN, D. J., FOLLETT, D., SEIBEL, M., KUMP, L. R., RICCARDI, A., ALTINER, D., SANO, H. and WEI, J. 2007. Erosional truncation of uppermost Permian shallow-marine carbonates and implications for Permian–Triassic boundary events. *Geological Society of America Bulletin*, **119**, 771–784.

PENG, Y. Q. and SHI, G. R. 2008. New Early Triassic Lingulidae (Brachiopoda) genera and species from South China. *Alcheringa*, **32**, 149–170.

PETERS, S. E. and FOOTE, M. 2002. Determinants of extinction in the fossil record. *Nature*, **416**, 420–424.

PIANKA, E. R. 1970. On r-and K-selection. *American Naturalist*, **104**, 592–597.

—— 1972. r and K selection or b and d selection? *American Naturalist*, **106**, 581–588.

—— 2000. *Evolutionary ecology*. Addison-Wesley, San Francisco, 512 pp.

RAFINESQUE-SCHMALZ, C. S. 1815. *Analyse de la nature ou tableau de l'a Univers et des corps organisés*. Jean Barravecchia, Palermo, 224 pp.

RAUP, D. M. 1979. Size of the Permo-Triassic bottleneck and its evolutionary implications. *Science*, **206**, 217–218.

RIDING, R. and LIANG, L. 2005. Geobiology of microbial carbonates: Metazoan and seawater saturation state influences on secular trends during the Phanerozoic. *Palaeogeography, Palaeoclimatology, Palaeoecology*, **219**, 101–115.

SALVINI-PLAWEN, L. V. 1980. A reconsideration of systematics in the Mollusca (phylogeny and higher classification). *Malacologica*, **19**, 249–278.

SCHLOTHEIM, E. F. VON 1816. Beiträge zur Naturgeschichte der Versteinerungen in geognostischer Hinsicht. *Denkschriften der Akademie der Wissenschaften München, Mathematisch-Naturwissenschaftliche Klasse*, **6**, 13–36.

SCHLUTER, D. 1994. Experimental evidence that competition promotes divergence in adaptive radiation. *Science*, **266**, 798–801.

SCHMIDT, M. 1928. *Die Lebewelt unserer Trias*. Hohenlohe'sche Buchhandlung Ferdinand Rau, Öhringen, 461 pp.

SEILACHER, A., REIF, W.-E. and WESTPHAL, F. 1985. Sedimentological, ecological and temporal patterns of fossil Lagerstätten. *Philosophical Transactions of the Royal Society of London, Series B*, **311**, 5–23.

SEPKOSKI, J. J. 1979. A kinetic model of Phanerozoic taxonomic diversity. II. Early Phanerozoic families and multiple equilibria. *Paleobiology*, **5**, 222–251.

—— 1984. A kinetic model of Phanerozoic taxonomic diversity. III. Post-Paleozoic families and mass extinctions. *Paleobiology*, **10**, 246–267.

—— 1996. Competition in macroevolution: the double wedge revisited. 211–255. *In* JABLONSKI, D., ERWIN, D. H. and LIPPS, J. H. (eds). *Evolutionary paleobiology*. University of Chicago Press, Chicago, 492 pp.

SIMBERLOFF, D. S. and WILSON, E. O. 1970. Experimental zoography of islands. A two-year record of colonization. *Ecology*, **51**, 934–937.

SIMROTH, H. 1906. Versuch einer neuen Deutung der Bellerophontidae. *Sitzungsberichte der Naturforschenden Gesellschaft zu Leipzig*, **32**, 3–8 (for 1905).

SLATYER, R. A., HIRST, M. and SEXTON, J. P. 2013. Niche breadth predicts geographical range size: a general ecological pattern. *Ecology Letters*, **16**, 1104–1114.

SOLÉ, R. V., SALDAÑA, J., MONTOYA, J. M. and ERWIN, D. H. 2010. Simple model of recovery dynamics after mass extinction. *Journal of Theoretical Biology*, **267**, 193–200.

SOWERBY, J. de C. 1823–1825. *The mineral conchology of Great Britain or, coloured figures and descriptions of those remains of testaceous animals or shells, which have been preserved at various times and depths in the earth*, Vol. 5. Published by the author, London, 168 pp.

SPEDEN, I. G. 1962. The faunas of the Corbies Creek localities and description of two new species, in Triassic fossils from Corbies Creek, north Otago. *New Zealand Journal of Geology and Geophysics*, **5**, 95–111.

STANLEY, S. M. 1973. Effects of competition on rates of evolution, with special reference to bivalve mollusks and mammals. *Systematic Zoology*, **22**, 486–506.

—— 2008. Predation defeats competition on the seafloor. *Paleobiology*, **34**, 1–21.

STOLICZKA, F. 1870–1871. Cretaceous fauna of southern India. 3. The Pelecypoda, with a review of all known genera of this class, fossil and Recent. *Paleontologica Indica, Memoirs*, **6**, 1–537.

STUR, D. 1868. Eine Excursion in die Umgegend von St. Cassian. *Jahrbuch der kaiserlich-königlichen Geologischen Reichsanstalt*, **18**, 509–572.

TWITCHETT, R. J., KRYSTYN, L., BAUD, A., WHEELEY, J. R. and RICHOZ, A. 2004. Rapid marine recovery after the end-Permian mass-extinction event in absence of marine anoxia. *Geology*, **32**, 805–808.

VAN BENEDEN, P. J. 1853. Note sur un nouveau genre de Crustace′ parasite (Pagodina). *Bulletins de l'Académie Royale des Sciences de Belgique*, **20**, 1–482.

VERMEIJ, G. J. 1986, Survival during biotic crisis: the properties and evolutionary significance of refuges. 231–246. *In* ELLIOT, D. K. (ed.). *Dynamics of extinction*. Wiley, New York, 304 pp.

WAAGEN, W. 1880. Salt Range fossils. Vol. I. Productus Limestone fossils, part II. *Palaeontologia Indica*, **13**, 73–183.

—— 1883. Salt Range fossils. Vol. I. Productus Limestone fossils, part IV, fas. 2. *Palaeontologia Indica*, **13**, 391–546.

—— 1885. Salt Range fossils. Vol. I. Productus Limestone fossils, part IV, fas. 5. *Palaeontologia Indica*, **13**, 729–770.

WALLER, T. R. 1978. Morphology, morphoclines and a new classification of the Pteriomorphia (Mollusca: Bivalvia). *Philosophical Transactions of the Royal Society of London, Series B*, **284**, 345–365.

—— 2005. Systematic Palaeontology. 7–50. *In* WALLER, T. R. and STANLEY, G. D. (eds). *Middle Triassic pteriomorphian bivalvia (Mollusca) from the New Pass Range, west-central Nevada: systematics, biostratigraphy, paleoecology, and paleobiogeography*. Journal of Paleontology, **79**, 1–58.

—— 2006. Phylogeny of families in the Pectinoidea (Mollusca: Bivalvia): importance of the fossil record. *Zoological Journal of the Linnean Society*, **148**, 313–342.

WANG, Y. 1955. Phylum Brachiopoda. 109–171. *In* WANG, Y. and YANG, J. Z. (eds). *Index fossils of China, Book 2*. Science Press, Beijing, 171 pp.

WANNER, C. 1922. Die Gastropoden und Lamellibranchiaten der Dyas von Timor. *Paläontologie von Timor*, **18**, 1–160.

—— 1942. Neue Beiträge zur Gastropodenfauna des Perm von Timor. *Geological Expedition to the Lesser Sunda Islands*, **4**, 1–71.

WASMER, M., HAUTMANN, M., HERMANN, E., WARE, D., ROOHI, G., UR-REHMAN, K., YASEEN, A. and BUCHER, H. 2012. Olenekian (Early Triassic) bivalves from the Salt Range and Surghar Range, Pakistan. *Palaeontology*, **55**, 1043–1073.

WATERHOUSE, J. B. and PIYASIN, S. 1970. Mid-Permian brachiopods from Khao Phrik, Thailand. *Palaeontographica Abteilung A*, **135**, 83–197.

WEEDON, M. J. 1991. Microstructure and affinity of the enigmatic Devonian tubular fossil Trypanopora. *Lethaia*, **24**, 227–234.

WENZ, W. 1938–1944. Gastropoda. 1–240. *In* SCHINDEWOLF, O. H. (ed.). *Handbuch der Paläozoologie, Band 6*, Borntraeger, Berlin, 1639 pp.

WHITTAKER, R. H. 1977. Evolution of species diversity in land communities. 1–67. *In* HECHT, M. K., STEERE, W. C. and WALLACE, B. (eds). *Evolutionary biology*, Vol. 10. Plenum Press, New York, 486 pp.

WIGNALL, P. B. and BENTON, M. J. 1999. Lazarus taxa and fossil abundances at times of biotic crises. *Journal of the Geological Society, London*, **156**, 453–456.

WILLIAMS, A., CARLSON, S. J., BRUNTON, C. H. C., HOLMER, L. E. and POPOV, L. 1996. A supra-ordinal classification of the Brachiopoda. *Philosophical Transactions of the Royal Society of London, Series B*, **35**, 1171–1193.

WIRTH, E. 1936. Beiträge zur Kenntnis der Trias in Provinz Szechuan, West China. *Neues Jahrbuch für Mineralogie, Geologie und Paläontologie, Beilage-Band*, **75**, 412–446.

WISSMANN, H. L. 1841. Beiträge zur Geognosie und Petrefactenkunde des südöstlichen Tirols. 1–24. *In* WISSMANN, H. L. and MÜNSTER, G. GRAF ZU (eds). *Beiträge zur Petrefactenkunde*. Buchner'sche Buchhandlung, Bayreuth, 152 pp.

WITTENBURG, P. VON 1908. Neue Beiträge zur Geologie und Paläontologie der Werfener Schichten Südtirols, mit Berücksichtigung der Schichten von Wladiwostok. *Centralblatt für Mineralogie, Geologie und Paläontologie*, **1908**, 67–89.

WÖHRMANN, S. VON 1889. Die Fauna der sogenannten Cardita und Raibler Schichten in den Alpen Nordtirols und in den Bayerischen Alpen. *Jahrbuch der kaiserlich–königlichen Geologischen Reichsanstalt*, **39**, 180–258.

XU, G. and GRANT, R. E. 1994. Brachiopods near the Permian–Triassic Boundary in South China. *Smithsonian Contributions to Paleobiology*, **76**, 1–68.

YOO, E. K. 1988. Early Carboniferous Mollusca from Gundy, Upper Hunter, New South Wales. *Records of the Australian Museum*, **40**, 233–264.

—— 1994. Early Carboniferous Gastropoda from the Tamworth Belt, New South Wales, *Australia*. *Records of the Australian Museum*, **46**, 63–110.

YÜ, W. 1975. The gastropod fossils from Qomolangma Feng Region. 129–238. *In* WU, T. S. (ed.). *A report of a scientific expedition in the Qomolangma Feng Region (Paleontology)*. Science Press, Peking. [In Chinese]

ZATON, M., TAYLOR, P. D. and VINN, O. 2013. Early Triassic (Spathian) Post-extinction microconchids from Western Pangea. *Journal of Paleontology*, **87**, 159–165.

ZHAN, L. P. 1979. Brachiopoda. 61–100. *In* HOU, H. F., ZHAN, L. P. and CHEN, B. W. (eds). *The coalbearing strata and fossils of Late Permian from Guangdong*. Geological Publishing House, Beijing, 166 pp.

ZIETHEN, C. H. VON 1830. *Die Versteinerungen Württembergs*. Verlag and Lithographie des Werkes Unsere Zeit, Stuttgart, 102 pp.

APPENDIX C

Additional publication link to this thesis

TIMING OF GLOBAL REGRESSION AND MICROBIAL BLOOM LINKED WITH THE PERMIAN-TRIASSIC BOUNDARY MASS EXTINCTION: IMPLICATIONS FOR DRIVING MECHANISMS

Scientific Reports | 7:43630 | DOI: 10.1038/srep43630

www.nature.com/scientificreports

SCIENTIFIC REPORTS

OPEN

Received: 12 October 2016
Accepted: 26 January 2017
Published: 06 March 2017

Timing of global regression and microbial bloom linked with the Permian-Triassic boundary mass extinction: implications for driving mechanisms

Björn Baresel[1], Hugo Bucher[2], Borhan Bagherpour[2], Morgane Brosse[2], Kuang Guodun[3] & Urs Schaltegger[1]

New high-resolution U-Pb dates indicate a duration of 89 ± 38 kyr for the Permian hiatus and of 14 ± 57 kyr for the overlying Triassic microbial limestone in shallow water settings of the Nanpanjiang Basin, South China. The age and duration of the hiatus coincides with the Permian-Triassic boundary (PTB) and the extinction interval in the Meishan Global Stratotype Section and Point, and strongly supports a glacio-eustatic regression, which best explains the genesis of the worldwide hiatus straddling the PTB in shallow water records. In adjacent deep marine troughs, rates of sediment accumulation display a six-fold decrease across the PTB compatible with a dryer and cooler climate as indicated by terrestrial plants. Our model of the Permian-Triassic boundary mass extinction (PTBME) hinges on the synchronicity of the hiatus with the onset of the Siberian Traps volcanism. This early eruptive phase released sulfur-rich volatiles into the stratosphere, thus simultaneously eliciting a short-lived ice age responsible for the global regression and a brief but intense acidification. Abrupt cooling, shrunk habitats on shelves and acidification may all have synergistically triggered the PTBME. Subsequently, the build-up of volcanic CO_2 induced a transient cool climate whose early phase saw the deposition of the microbial limestone.

Since the early days of stratigraphy, mass extinctions were noticed to coincide with major and global sea-level changes[1,2] that significantly alter extinction patterns and time-series of geochemical proxies. In the case of the Permian-Triassic boundary mass extinction (PTBME), the system boundary itself has been initially placed during a global eustatic regression[3], but was subsequently placed during a global transgression[4]. The sea-level rise scenario naturally paved the way for a concomitant rise of the oxygen minimum zone as a kill mechanism, to which "lethally" hot sea-surface temperatures were recently added[5,6]. With the exceptions of deep oceanic settings (e.g., Arrow Rocks, New Zealand[7]; Mino Tamba Terrane, Japan[8,9]), of few deep water shelves (e.g., Dongpan, South China[10]) and of extremely rare shallow shelves (Musandam, United Arab Emirates[11]), an overwhelming majority of globally distributed Permian-Triassic boundary (PTB) sections are affected by an unconformity separating the last Permian rocks from the first Triassic ones (e.g., Armenia[12]; Canada[13]; Pakistan[14]; Norway[15]; China[16]). Intensively studied shallow water sections from South China follow this rule and the origin of this hiatus is intensively debated. Two competing mechanisms are frequently proposed: submarine dissolution through acidified waters[17] or subaerial erosion[18]. However, both mechanisms are not mutually exclusive and may conceivably have acted simultaneously[19]. In this respect, we emphasize here that climate-driven eustatic sea-level changes are commonly at the decamillennial timescale, an order of magnitude compatible with the duration of the world-wide regression that coincides with the PTB. The base of the Triassic in the equatorial shallow water sections is usually represented by the iconic microbial limestone[16], which has been interpreted as the hallmark of ecosystem

[1]Department of Earth Sciences, University of Geneva, Rue des Maraîchers 13, 1205 Geneva, Switzerland. [2]Paleontological Institute and Museum, University of Zurich, Karl Schmid-Strasse 4, 8006 Zurich, Switzerland. [3]Guangxi Bureau of Geology and Mineral Resources, Jiangzheng Road 1, 530023 Nanning, China. Correspondence and requests for materials should be addressed to Bj.B. (email: bjoern@heldenepos.de)

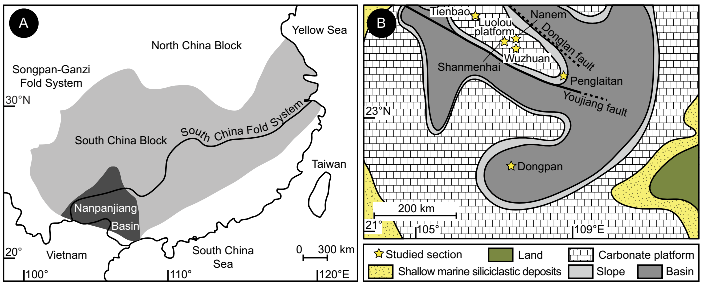

Figure 1. Tectonic map of South China and palaeogeographic map of the Nanpanjiang Basin. (**A**) Tectonic map of South China indicating the position of the North China Block, the South China Block, the Nanpanjiang Basin and the South China Fold System. (**B**) Late Permian to Early Triassic palaeogeographic map of the Nanpanjiang Basin showing the locations of the Shanmenhai, Nanem, Wuzhuan and Tienbao sections in the Luolou carbonate platform and of the deeper water Penglaitan and Dongpan sections. Both maps are created with Adobe Illustrator CS4 (https://helpx.adobe.com/creative-suite/kb/cs4-product-downloads.html).

devastation in the immediate aftermath of the PTBME. This "devastated" view is questioned by the recent discovery of diversified Triassic (Griesbachian) shelly faunas that mechanically accumulated between domical microbialites[20–22]. Although carbonate super-saturation, warm waters and absence of clastic input were all prerequisites for the development of microbial limestone in the >12000 km^2 Luolou Platform of the Nanpanjiang Basin[19], how to switch swiftly from acidic to alkaline and $CaCO_3$ super-saturated waters remains open. However, a sudden increase of accommodation space leading to the burial of microbialite-bearing fault bounded blocks under siliciclastic sediments is the most likely explanation for the abrupt cessation of the microbial limestone in the Nanpanjiang Basin (South China). No evidence in support of a concomitant change in sea water chemistry has been documented[19].

How much time is represented by the hiatus and the microbial limestone was still unknown. A new thorough revision of the conodont biochronology by means of Unitary Association Zones (UAZs) highlighted that the conodont record around the PTB in shallow water sections is still insufficient for reliable age control[23]. Correlation by means of carbon isotope stratigraphy with the radio-isotopically well calibrated Global Stratotype Section and Point (GSSP) in Meishan[24] is hindered by the extreme condensation of this section[25]. However, the carbonate carbon isotope record from Musandam[11] allows positing that the peak segment of the negative carbon isotope excursion (CIE) straddling the PTB is erased by the hiatus in shallow water records of South China[19]. Hence, the respective timings of the unconformity and of the microbial limestone are highly relevant for constraining the underlying mechanisms during the extinction and its immediate aftermath.

Here, we propose a new, precise and accurate timescale for the regressive event that generated the hiatus, and for the overlying microbial bloom and its cessation, based on high-resolution U-Pb ages from 11 volcanic samples obtained from four shallow water boundary sections in the Nanpanjiang Basin (Fig. 1). The chronology can be directly compared to U-Pb ages from deep water records of juxtaposed troughs of the same basin[25]. Some of the underlying key mechanisms are then discussed in the light of this new time-space framework.

High-precision U-Pb dates

The full data table and analytical details are given in the supplement. The detailed descriptions of the sampled sections are available in the supplement and in ref. 19, respectively. Th-corrected $^{206}Pb/^{238}U$ dates are presented as weighted mean ages of selected zircon populations and their associated ±2σ internal (analytical) uncertainties (±x) in Figs 2 and 3, and as single zircon grain $^{206}Pb/^{238}U$ age ranked distribution plots in Supplementary Fig. S1. Uncertainty of $^{206}Pb/^{238}U$ weighted mean ages in Supplementary Fig. S1 is reported as 2σ internal uncertainty (±x), 2σ external uncertainty including tracer calibration (±y), and 2σ external uncertainty including tracer calibration and ^{238}U decay constant uncertainty (±z).

Five volcanic ash layers were sampled within the uppermost ~4 m of the Late Permian Heshan Fm. and six volcanic samples in the lowermost ~18 m of the Early Triassic Luolou Fm. (Fig. 2) in shallow water PTB sections from the Nanpanjiang Basin. Unlike in Shanmenhai where the PTB is obscured by low angle small scale faults, the topmost Permian bed immediately underlying the hiatus in Nanem (NAN-8), Wuzhuan (WUZ-4) and Tienbao (TIE-6) is represented by an ash layer (Fig. 2). This ash layer has been correlated in Wuzhuan, Tienbao and the deeper water section of Penglaitan by similar zircon and apatite chemistry and identical U-Pb zircon ages, suggesting origin from the same volcanic eruption (ref. 26 and see Supplementary Figs S3a and S4a). WUZ-4 and TIE-6 yield respective dates of 252.033 ± 0.067 Ma (N = 6; MSWD = 0.33) and 252.022 ± 0.076 Ma (N = 3; MSWD = 0.63), which overlap within internal errors. Based on this temporal coincidence and identical zircon and apatite chemistry, a pooled weighted mean age of 252.048 ± 0.033 Ma (N = 16; MSWD = 0.46), also including PEN-28, has thus been proposed for this last Permian marker bed in Wuzhuan, Tienbao and Penglaitan (referred to as Horizon 1[26]). Identical origin of NAN-8 due to similar zircon age (252.060 ± 0.067 Ma; N = 4;

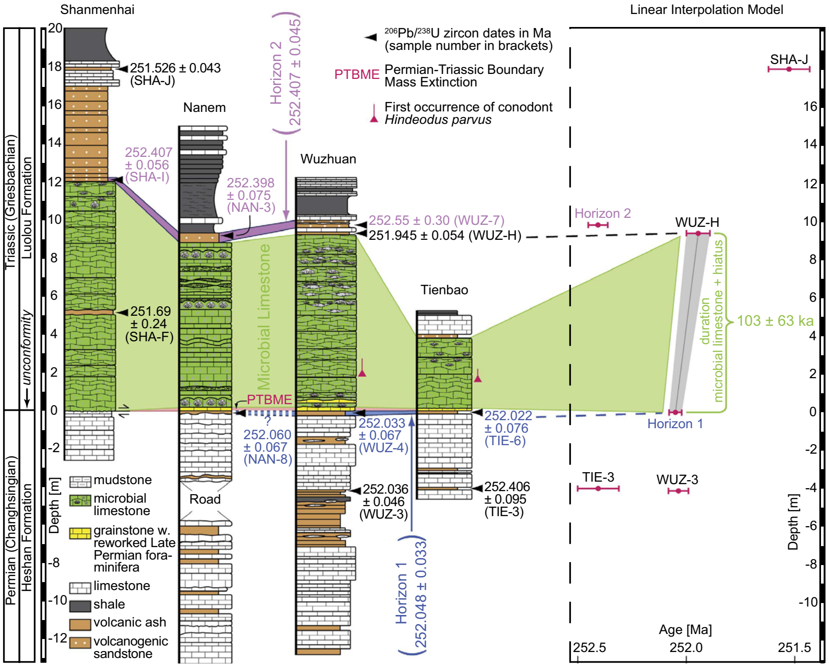

Figure 2. Stratigraphy and geochronology for the Shanmenhai, Nanem, Wuzhuan and Tienbao sections from late Changhsingian to Griesbachian showing ^{206}Pb/^{238}U weighted mean ages (in Ma; uncertainties are given by 2σ internal errors) of the investigated volcanic ashes and volcanogenic sandstone beds. Pooled ^{206}Pb/^{238}U weighted mean zircon population ages from ref. 26 for Horizon 1 (indicated in blue) and Horizon 2 (indicated in purple) are also given (see Supplementary Fig. S3). Though NAN-8 shows identical ^{206}Pb/^{238}U weighted mean age and similar zircon chemistry (see Supplementary Fig. S4a), the lack of apatite hampers definite correlation with Horizon 1. The first occurrences of the index conodont *Hindeodus parvus* are shown in their stratigraphic positions in Wuzhuan and Tienbao. The combined duration of the Triassic microbial limestone (indicated in green) and the underlying hiatus (marked by the arrows) of 103 ± 63 kyr is calculated by linear interpolation between Horizon 1 and WUZ-H, which bracket this period in Wuzhuan. The linear interpolation model is presented with its median (middle grey line) and its associated 95% confidence interval (grey area). In the linear interpolation model, red horizontal bars indicate ^{206}Pb/^{238}U weighted mean ages of dated volcanic levels in their stratigraphic position. MSWD = mean square of weighted deviates.

MSWD = 0.53) and chemistry is plausible (Supplementary Fig. S4a). It is also worth noting that WUZ-4 and TIE-6 are ca. 100 km far apart, which illustrates the lateral extension of this marker bed (Fig. 1).

The next underlying Permian ash sample occurs 4 m below the hiatus in Wuzhuan (WUZ-3) and represents the youngest layer of a 3 m thick succession of ash falls intercalated with subordinate limestone beds and lenses (Fig. 2). WUZ-3 yields a date of 252.036 ± 0.046 Ma (N = 6; MSWD = 0.05). The next underlying Permian ash sample in Tienbao (TIE-3) is also 4 m below the hiatus, but yields a date of 252.406 ± 0.095 Ma (N = 4; MSWD = 0.36). This indicates lower sediment accumulation rates for the Heshan Fm. at Tienbao, which is consistent with the modest (3.8 m) thickness of the microbial limestone at the base of the overlying Luolou Fm.

The lowermost Triassic ash layer occurs ~5 m above the base of the microbial limestone at Shanmenhai (SHA-F). SHA-F is not a typical air-fall tuff since its volcaniclastic material is diluted in a 0.1 m thick limestone bed intercalated in the microbial limestone. SHA-F yields a comparatively lower precision date of 251.69 ± 0.24 Ma (N = 3; MSWD = 0.99). The top of the microbial limestone is capped by an ash layer in Wuzhuan (WUZ-H) that is rarely preserved between the microbial limestone and an ubiquitous volcanogenic sandstone. WUZ-H provides an age of 251.945 ± 0.054 Ma (N = 8; MSWD = 0.54). At Shanmenhai, Nanem and Tienbao, this intervening ash layer is missing and the volcanogenic sandstone directly rests on top of the microbial limestone. Zircon and apatite chemistry were shown to have a uniform signature for all samples (SHA-I, NAN-3, WUZ-7) from this volcanogenic sandstone, which was labeled Horizon 2 (ref. 26; see Supplementary Fig. S3b). The re-deposited nature of Horizon 2 is confirmed by its ca. 400 ka too old U-Pb age, which violates the chronological succession imposed by air-fall tuffs. However, U-Pb ages of SHA-I (252.407 ± 0.056 Ma; N = 6; MSWD = 0.84), NAN-3 (252.398 ± 0.075 Ma; N = 5; MSWD = 0.53), and WUZ-7 (252.55 ± 0.30 Ma, youngest zircon date) all

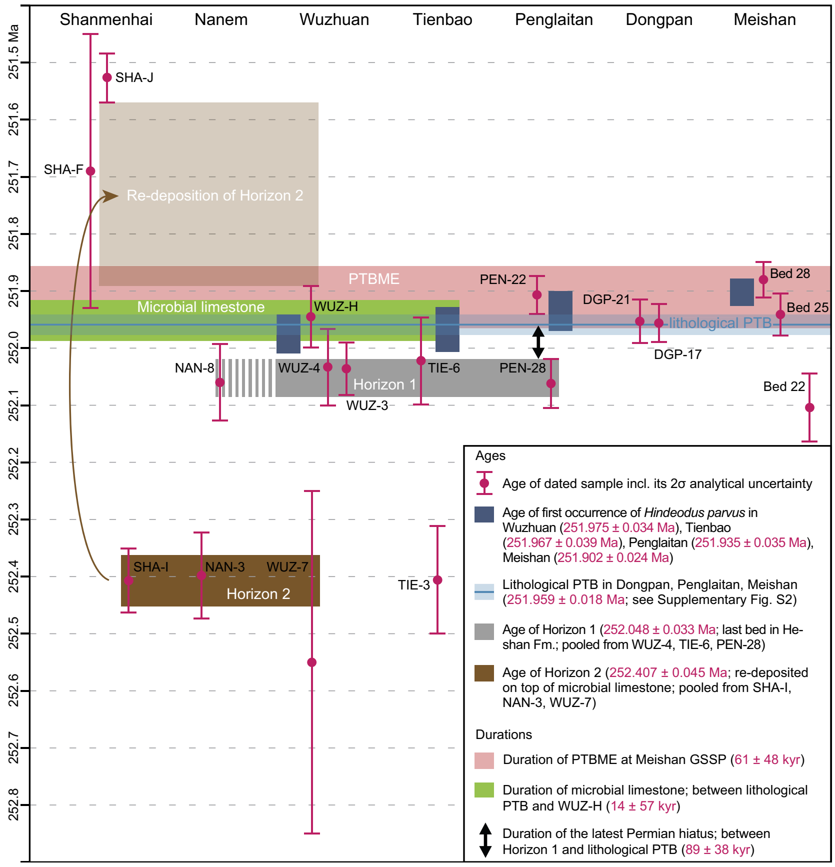

Figure 3. Comparison of ^{206}Pb/^{238}U weighted mean ages of volcanic ashes and volcanogenic sandstones from the shallow-marine Shanmenhai, Nanem, Wuzhuan and Tienbao sections with those from the deeper marine Dongpan and Penglaitan sections[25] and the Meishan GSSP[24]. The ages of the first occurrence (FO) of *Hindeodus parvus* in Wuzhuan and Tienbao are from this study, the FOs of *H. parvus* in Penglaitan and Meishan are taken from ref. 25. The weighted mean age (see calculation in Supplementary Fig. S2) of the lithological Permian-Triassic boundary (PTB) in China is inferred from model ages of the boundary in Dongpan (bracketed by DGP-17 and DGP-21), in Meishan (bracketed by Bed 22 and Bed 25) and in Penglaitan (bracketed by PEN-28 and PEN-22)[25]. Ages of Horizon 1 and Horizon 2 are from ref. 26. The duration of the Permian-Triassic boundary mass extinction (PTBME; bracketed by Bed 25 and Bed 28) interval is taken from ref. 24. The respective durations of the hiatus and the microbial limestone are calculated from the time gap between Horizon 1 and the lithological PTB, and the time gap between the lithological PTB and WUZ-H. Uncertainty on durations is added in quadrature from 2σ analytical uncertainty on Horizon 1 (252.048 ± 0.033 Ma; N = 16; MSWD = 0.46), on the lithological PTB (251.959 ± 0.018 Ma; N = 3; MSWD = 2.2) and on WUZ-H (251.945 ± 0.054 Ma; N = 8; MSWD = 0.54). All associated uncertainties are given as 2σ analytical uncertainties.

overlap within internal errors. Given the cogenetic nature of the volcanogenic beds, zircon U-Pb dates can be pooled, and a weighted mean age of 252.407 ± 0.045 Ma (N = 12; MSWD = 0.67) can be calculated for Horizon 2 (ref. 26; see Supplementary Fig. S3b).

The stratigraphically youngest ash bed (SHA-J) is ~6 m above the top of the microbial limestone and ~0.8 m above the top of the volcanogenic sandstone interval at Shanmenhai. It yields a date of 251.526 ± 0.043 Ma (N = 10; MSWD = 0.23). This age gives an upper limit for the deposition of the volcanogenic sandstone, which represents the main and abrupt drowning event that ended the deposition of the microbial limestone[19].

Duration of the hiatus and microbial bloom

Figure 3 compares the new chronological constraints from the shallow water sections of the Luolou Platform to those of the deeper water sections at Penglaitan and Dongpan[25], and to the Meishan GSSP[24]. The lithological PTB is well constrained in terms of U-Pb dates at Dongpan, Penglaitan and Meishan[25]. The application of probabilistic age-depth models revealed the synchronicity of the formational PTBs in these sections, allowing to calculate a weighted mean age of 251.959 ± 0.018 Ma (N = 3; MSWD = 2.2; see Supplementary Fig. S2) for the PTB in China, as shown by the reference time line in Fig. 3. With the exception of its younger first occurrence (FO) in Meishan, all FOs of *Hindeodus parvus* intersect within errors with the age of the lithological PTB (Fig. 3). Furthermore, all FOs are either included or intersect with the extinction interval in Meishan, thus highlighting that the extinction interval and the system boundary cannot be resolved within the 40 ka uncertainty of the U-Pb dates. Hence, the end-Permian mass extinction (e.g., ref. 5) as previously defined and referred to in the literature is here more accurately named the Permian-Triassic *boundary* mass extinction (PTBME). The duration of the PTBME interval at Meishan has been estimated to 61 ± 48 kyr[24].

A duration of 89 ± 38 kyr for the hiatus in shallow marine sections is derived from the late Permian Horizon 1 and the lithological PTB (Fig. 3). Based on the correlation of conodont UAZs, the inferred duration for the hiatus at the formational PTB in the Great Bank of Guizhou is 61 ± 48 kyr[23], which is in agreement with our new estimate of 89 ± 38 kyr for the shallow water sections of the Luolou Platform. Another independent line of evidence is found in the carbon isotope records of Wuzhuan and Tienbao (Supplementary Fig. S5a). These indicate that a large segment of the negative CIE of the PTB in deeper water sections of Meishan and Dongpan is within the hiatus in Tienbao and Wuzhuan shallow water sections (Supplementary Fig. S5b). Subtracting the duration of 89 ± 38 kyr for the hiatus from the combined, linear interpolated duration of the hiatus and the microbial limestone of 103 ± 63 kyr (as inferred by linear interpolation between the pooled weighted mean ages of Horizon 1 and the weighted mean age of WUZ-H; Fig. 2), yields a duration of 14 ± 57 kyr for the microbial limestone alone (Fig. 3).

The microbial limestone shows striking lateral changes in thickness. It varies from 3.8 m at Tienbao to 9.1 m at Wuzhuan, although its duration may not depart significantly from 14 ± 57 kyr. Therefore, estimates of growth rate of the basal Triassic microbial limestone vary from >5.4 cm/ka at Tienbao to >13.0 cm/ka at Wuzhuan (Supplementary Fig. S5a). These estimates are all in agreement with the maximum growth rate of recent marine stromatolites (40 cm/ka; ref. 27) and with the duration of the microbial limestone in Wuzhuan recently proposed by ref. 21. The bathymetric differentiation of the microbial limestone is also corroborated by the carbonate carbon isotope records from Wuzhuan and Tienbao, whose basal Triassic end of the youngest negative shift is more expanded in Wuzhuan than in Tienbao (Supplementary Fig. S5a). Absence of the negative CIE in microbial limestone bearing sections[20] supports the extension of the PTB hiatus into basal Griesbachian shallow water records (see Supplementary Fig. S5b). The presence of the widespread volcanogenic sandstone (Horizon 2) blanketing the microbial limestone also demonstrates that the cessation of this peculiar facies was nearly synchronous within the Luolou Platform. The pooled weighted mean age of Horizon 2 (252.407 ± 0.045 Ma) is also in agreement with the age of the volcanogenic sandstone DGP-18 from the deeper water section of Dongpan (252.56 ± 0.26 Ma; N = 1; youngest zircon date), where it occurs 0.5 m above the PTB (ref. 25 and see also Supplementary Fig. S4b). Additionally, DGP-18 shows identical zircon chemistry with Horizon 2, but apatite chemistry reveals a large spread of halogen and trace element composition. This spread either reflects different apatite composition than Horizon 2–thus precluding origin from a single source–or indicates alteration of the primary apatite chemical fingerprint. Assuming that the alteration hypothesis is correct, we infer that the first 0.5 m of basal Triassic black shales in Dongpan correlate with the first 9.5 m basal Triassic strata in Wuzhuan, which translates into a sediment accumulation rate of >0.6 cm/ka for the black shales at the base of the Ziyun Fm. in Dongpan (Supplementary Fig. S5b). An additional line of evidence in support of this inferred sediment accumulation rate of >0.6 cm/ka is found in the compatible >0.19 cm/ka sediment accumulation rate based on the age difference between the lithological PTB (251.959 ± 0.018 Ma) and the first basal Triassic ash bed DGP-21 (251.953 ± 0.038 Ma) in Dongpan[25]. In comparison to the >3.6 cm/ka obtained for the uppermost two meters of the Permian Dalong Fm. in Dongpan[25], the minimum sediment accumulation rate of the basal Triassic black shales shows a six-fold decrease across the PTB. As there are no fundamental differences in bathymetry between the Dalong Fm. and the base of the Ziyun Fm., the strongly reduced sediment accumulation rate of the basal Triassic black shales of the Ziyun Fm. likely relates to a lower weathering rate, in agreement with the dry and cool Griesbachian climate drawn from the terrestrial plant record[28]. This climatic interpretation is also supported by clay mineralogy of the Shangsi section (northwestern South China Block) that revealed an accelerated aridification at the PTB[29].

Since the time interval during which microbial limestone thrived on uplifted blocks only correlates with the basal 0.5 m of the >5 m black shale interval of adjacent downthrown blocks, the much later cessation of black shale deposition does not support common underlying paleoceanographic causes or relations for these two contrasted depositional environments (e.g., upwelling of nutrient-rich and alkaline waters[30]). Moreover, this correlation does not support a cessation of the microbial limestone caused by the disruption of a regionally stratified water column, or by any change in water chemistry common to both uplifted blocks and intervening troughs.

Discussion

In the Nanpanjiang pull apart Basin, Late Permian to Early Triassic lateral changes in depositional setting and sediment accumulation rate were controlled by both eustatic sea-level changes and episodes of regional synsedimentary faulting[19]. Disentangling the effects of eustatic sea-level changes from those of regional tectonics is always delicate. However, dense U-Pb age control along with chemistry of accessory minerals allows recognition of synchronous tephrostratigraphic markers and the construction of a reliable absolute time framework[26].

The new U-Pb dates presented here question the view that the main extinction event is older than the PTB (e.g., refs 31 and 32). Within our decamillennial age uncertainty, the main episode of the mass extinction, as recorded in the Meishan GSSP and elsewhere, can neither be distinguished from the revised paleontological definition of the PTB[23], nor from formational boundaries associated with the PTB[25]. A converging conclusion was also reached by ref. 33. This revised timing has direct implications for the identification of the mechanistic causes of the PTBME.

The mainstream claim that the mass extinction occurred "during the transgressive pulse when anoxic bottom waters often became extensive"[4] is untenable in the view of our timing from the South Chinese record with its locally restricted occurrences of Griesbachian anoxic marine deposits[15,20,34–36]. The duration of 89 ± 38 kyr for the hiatus in the Luolou Platform can only be explained by a short term marine regression of glacio-eustatic origin possibly combined with submarine dissolution of carbonate through acidification of surface waters. In the studied sections, both mechanical and chemical erosion can be called upon for the genesis of the hiatus. Mechanical erosion is supported by occasional deposition of high-energy grainstone, which exclusively contains reworked Permian faunas, within the base of the microbial limestone[19]. A new argument supporting shallow marine dissolution of the uppermost part of the Heshan Fm. is provided by the wide lateral extension of Horizon 1, the youngest preserved bed of the Permian Heshan Fm. In all sections where this horizon was recognized, it rests directly beneath the PTB hiatus without intervening Permian sedimentary rocks. Assuming that the obtained sediment accumulation rate of >6.6 cm/ka for the last preserved 4 m of the Heshan Fm. (Supplementary Fig. S5b) remained constant and considering the duration of the Permian part of the hiatus (89 ± 38 kyr), at least 3.4 m to 8.4 m of missing latest Permian rocks can be inferred. Generating the 89 ± 38 kyr gap - corresponding to a minimum of 3.4 m to 8.4 m of strata–with preservation of the same lower limit (i.e. Horizon 1) can hardly be explained by non-deposition or by mechanical erosion only. Ash layers such as Horizon 1 are extremely unlikely to resist subaerial and submarine mechanical erosion. The peculiar stratigraphic position of this bed as well as its remarkable lateral extension into the deeper water Penglaitan section[26] some 300 km to the ESE from the Luolou Platform strongly suggests that it may have acted as a chemical shield against submarine dissolution caused by acidic waters. In the Luolou Platform, we obtain a duration of 14 ± 57 kyr for the deposition of the basal Triassic microbial limestone, whose growth and associated metazoan fauna excludes any coeval acidic and oxygen-deficient surface waters. The cessation of the microbial limestone in the Luolou Platform was caused by a sharp increase in base level that was manifested by a siliciclastic blanketing that deposited both volcanogenic sandstone (Horizon 2) and mudstone[19]. An episode of regional tectonic subsidence and the global sea-level rise may have jointly led to this cessation, but a concomitant change of water chemistry lacks any evidence[19]. Yet, the water depth, siliciclastic free and alkaline waters required for microbialite growth are in marked contrast with the earlier acidic and low stand conditions that prevailed during the 89 ± 38 kyr hiatus.

All these observations from the Nanpanjiang Basin as well as from other relevant sections world-wide must be integrated into a coherent causes and effects model. In this endeavor, the volcanogenic sulfur aerosol-driven model proposed by refs 37 and 38 provides the most parsimonious working frame, with the greatest explanatory power. Stratospheric injection of volcanogenic sulfur volatiles and subsequent condensation into aerosols are seen as the proximal cause for brief climate cooling[39,40] and ensuing global regression[41], provided that the cooling was profound enough to store water as terrestrial ice. Sulfur volatiles also provide a direct mechanism for ocean acidification. Abrupt cooling likely resulted from the atmospheric injection of both volcanogenic and remobilized SO_2 and H_2S from early Paleozoic evaporites by the initial emplacement of dykes and sills of the Siberian Traps[42,43]. This scenario simultaneously accounts for acidification of ocean surface waters and for the global regression. The synergistic effects of shrunken marine habitats on continental shelves through a global eustatic regression, of fast temperature drop down, and of substantial acidification are all compatible with the new timing proposed here. Moreover, paleontological evidence (e.g., ref. 44), facies interpretations and sediment accumulation rates are all compatible with the volcanogenic sulfur aerosol-driven model for the PTBME.

Subsequent and slower accumulation of CO_2 derived from the basaltic effusions of the Siberian Traps and from burned Permian coal best account for successive warming and stepwise eustatic sea-level rise that first saw the deposition of the microbial limestone. The order of magnitude of the initial stage of the transgression in the Nanpanjiang Basin can be derived from the water depth (0 to 30 m) of present-day most common habitat of stromatolites[27]. Average Griesbachian pCO_2 levels documented from plant cuticles[45] may also have stimulated $CaCO_3$ fixation via photosynthesis by cyanobacteria in equatorial surface waters, thus promoting the deposition of microbialites where normally oxygenated and clastic-free surface waters prevailed[19]. A subsequent and more substantial build up of pCO_2 is needed to account for the following sea-level rise around the Griesbachian-Dienerian boundary[34,46], for increased weathering rates[47], for more frequent anoxia on continental shelves[34,48], and for the largest ecological and concomitant change of terrestrial plants[30]. Our revised model is at striking variance with the long held mantra of an expanded oxygen minimum zone (e.g., ref. 6) as a leading kill mechanism for the PTBME. It must also be stressed that in our model large scale anoxia first comes into the play during Dienerian times. The "lethally" hot temperatures that were subsequently proposed as second kill mechanism[5,6] are also irreconcilable with our model that involves a glacio-eustatic low-stand at the PTB. It is worth noting that these extremely hot temperatures are all derived from the South Chinese record[49,50], whose equatorial position is the least climate sensitive configuration. It is also worth noting that all PTB sections[46], from which temperature estimates were obtained, suffer from extreme condensation and hiatuses. Moreover, fractionation coefficients used for reconstructing sea-surface temperatures from oxygen isotopic values of biogenic phosphate[51] rest on the multiple assumptions of an ice-free world, constant salinity and stable pH[49], irrespective of the utilized analytical method (isotope ratio mass spectrometry or *in situ* secondary ion mass spectrometry). Yet, none of these prerequisites is valid within the frame of the volcanogenic sulfur aerosol-driven model. For all these reasons, available PTB temperature reconstructions based on oxygen isotopes from biogenic phosphate cannot be taken at face value. Abrupt drop down of sea surface temperature, shrunken habitats on shelves resulting from a global low stand, and short-term acidification may all have synergistically triggered the PTBME. In many aspects, the environmental upheavals linked with the PTBME (i.e. short-lived cooling followed by longer term warming) tend to parallel the most recent model proposed for the Triassic-Jurassic boundary mass extinction event[52], thus leading to a more unifying view of causes and effects of large igneous provinces.

References

1. Brongniart, A. & Cuvier, G. Essai sur la géographie minéralogique des environs de Paris. *Journal des mines* **23,** 421–458 (1808).
2. Cuvier, G. *Discourse on the revolutionary upheavals on the surface of the globe and on the changes which they have produced in the animal kingdom* (G. Defour & Eduard D'Ocagne, 1825).
3. Newell, N. D. Revolutions in the history of life. *The Geological Society of America Special Paper* **89,** 63–91 (1967).
4. Hallam, A. & Wignall, P. B. Mass extinctions and sea-level changes. *Earth-Science Reviews* **48,** 217–250, doi: 10.1016/s0012-8252(99)00055-0 (1999).
5. Sun, Y. *et al.* Lethally hot temperatures during the Early Triassic greenhouse. *Science* **338,** 366–370, doi: 10.1126/science.1224126 (2012).
6. Song, H. *et al.* Anoxia/high temperature double whammy during the Permian-Triassic marine crisis and its aftermath. *Scientific Reports* **4,** 4132, doi: 10.1038/srep04132 (2014).
7. Takemura, A. *et al.* Preliminary report on the lithostratigraphy of the Arrow Rocks, and geologic age of the northern part of the Waipapa Terrane, New Zealand. *News of Osaka Micropaleontologists* **11,** 47–57 (1998).
8. Sano, H. Permian oceanic rocks of Mino terrane, central Japan. Part I. Chert facies. *Journal of the Geological Society of Japan* **94,** 697–709, doi: 10.5575/geosoc.94.697 (1988).
9. Sugiyama, K. Lower and Middle Triassic radiolarians from Mt. Kinkazan, Gifu prefecture, central Japan. *Transactions and Proceedings of the Palaeontological Society of Japan* **167,** 180–223 (1992).
10. Zhang, F. *et al.* Multidisciplinary stratigraphy across the Permian-Triassic boundary in deep-water environment of Dongpan section, south China. *Norwegian Journal of Geology* **86,** 125–131 (2006).
11. Clarkson, M. O. *et al.* Ocean acidification and the Permo-Triassic mass extinction. *Science* **348,** 229–232, doi: 10.1126/science.aaa0193 (2015).
12. Tozer, E. T. Xenodiscacean Ammonoids and their bearing on the discrimination of the Permo-Triassic boundary. *Geological Magazine* **106,** 348–361, doi: 10.1017/S0016756800058209 (1969).
13. Tozer, E. T. Marine Triassic faunas In *Biochronology: Standard of Phanerozoic time* (ed. Bamber, E. W. *et al.*) 633–640 (Economic Geology Report, 1970).
14. Kummel, B. & Teichert, C. The Permian-Triassic boundary beds in central Tethys In *The Permian and Triassic systems and their mutual boundary* (eds Logan, A. & Hills, L. V.) 17–34 (Canadian Society of Petroleum Geologists, 1973).
15. Hermann, E. *et al.* A close-up view of the Permian-Triassic boundary based on expanded organic carbon isotope records from Norway (Trøndelag and Finnmark Platform). *Global and Planetary Change* **74,** 156–167, doi: 10.1016/j.gloplacha.2010.10.007 (2010).
16. Yin, H. F. *et al.* The end-Permian regression in South China and its implication on mass extinction. *Earth-Science Reviews* **173,** 19–33, doi: 10.1016/j.earscirev.2013.06.003 (2014).
17. Payne, J. L. *et al.* Erosional truncation of uppermost Permian shallow-marine carbonates and implications for Permian-Triassic boundary events. *Geological Society of America Bulletin* **119,** 771–784, doi: 10.1130/b26091.1 (2007).
18. Kershaw, S. *et al.* Ocean acidification and the end-Permian mass extinction: to what extent does evidence support hypothesis? *Geosciences* **2,** 221–234, doi: 10.3390/geosciences2040221 (2012).
19. Bagherpour, B. *et al.* Onset, development, and cessation of basal Early Triassic microbialite in the Nanpanjiang pull-apart Basin, South China Block. *Gondwana Research*, in press, doi: 10.1016/j.gr.2016.11.013 (2016).
20. Hautmann, M. *et al.* An unusually diverse mollusc fauna from the earliest Triassic of South China and its implications for benthic recovery after the end-Permian biotic crisis. *Geobios* **44,** 71–85, doi: 10.1016/j.geobios.2010.07.004 (2011).
21. Hautmann, M. *et al.* Competition in slow motion: The unusual case of benthic marine communities in the wake of the end-Permian mass extinction. *Palaeontology* **58,** 871–901, doi: 10.1111/pala.12186 (2015).
22. Kaim, A. *et al.* Early Triassic (Late Griesbachian) gastropods from South China (Shanggan, Guangxi). *Swiss Journal of Geosciences* **103,** 121–128, doi: 10.1007/s00015-010-0005-5 (2010).
23. Brosse, M., Bucher, H. & Goudemand, N. Quantitative biochronology of the Permian-Triassic boundary in South China based on conodont Unitary Associations. *Earth-Science Reviews* **155,** 153–171, doi: 10.1016/j.earscirev.2016.02.003 (2016).
24. Burgess, S. D., Bowring, S. A. & Shen, S. Z. High-precision timeline for Earth's most severe extinction. *Proceedings of the National Academy of Sciences of the United States of America* **111,** 3316–3321, doi: 10.1073/pnas.1317692111 (2014).
25. Baresel, B. *et al.* Precise age for the Permian-Triassic boundary in South China from high precision U-Pb geochronology and Bayesian age-depth modelling. *Solid Earth Discussions*, doi: 10.5194/se-2016-145 (2016).
26. Baresel, B., D'Abzac, F.-X., Bucher, H. & Schaltegger, U. High-precision time-space correlation through coupled apatite and zircon tephrochronology: An example from the Permian-Triassic boundary in South China. *Geology* **45,** 83–86, doi: 10.1130/g38181.1 (2016).
27. Chivas, A. R., Torgersen, T. & Polach, H. A. Growth rates and Holocene development of stromatolites from Shark Bay, Western Australia. *Australian Journal of Earth Sciences* **37,** 113–121, doi: 10.1080/08120099008727913 (1990).
28. Hochuli, P. A., Sanson-Barrera, A., Schneebeli-Hermann, E. & Bucher, H. Severest crisis overlooked-Worst disruption of terrestrial environments postdates the Permian-Triassic mass extinction. *Scientific Reports* **6,** 28372, doi: 10.1038/srep28372 (2016).
29. Xu, G. *et al.* Clay mineralogical characteristics at the Permian–Triassic Shangsi section and their paleoenvironmental and/or paleoclimatic significance. *Palaeogeography, Palaeoclimatology, Palaeoecology*, in press, doi: 10.1016/j.palaeo.2016.07.036 (2016).
30. Kershaw, S. *et al.* Earliest Triassic microbialites in the South China block and other areas: controls on their growth and distribution. *Facies* **53,** 409–425, doi: 10.1007/s10347-007-0105-5 (2007).
31. Hallam, A. & Wignall, P. B. *Mass Extinctions and their Aftermath*, doi: 10.1017/s0016756898258985 (Oxford University Press, 1997).
32. Xie, S. *et al.* Cyanobacterial blooms tied to volcanism during the 5 m.y. Permo-Triassic biotic crisis. *Geology* **38,** 447–450, doi: 10.1130/G30769.1 (2010).
33. Shen, S. & Bowring, S. A. The end-Permian mass extinction: a still unexplained catastrophe. *National Science Review* **1,** 492–495, doi: 10.1093/nsr/nwu04 (2014).
34. Hermann, E. *et al.* Organic matter and palaeoenvironmental signals during the Early Triassic biotic recovery: The Salt Range and Surghar Range records. *Sedimentary Geology* **234,** 19–41, doi: 10.1016/j.sedgeo.2010.11.003 (2011).
35. Hofmann, R. *et al.* New trace fossil evidence for an early recovery signal in the aftermath of the end-Permian mass extinction. *Palaeogeography, Palaeoclimatology, Palaeoecology* **310,** 216–226, doi: 10.1016/j.palaeo.2011.07.014 (2011).
36. Schneebeli-Hermann, E. *et al.* Palynofacies analysis of the Permian-Triassic transition in the Amb section (Salt Range, Pakistan): Implications for the anoxia on the South Tethyan Margin. *Journal of Asian Earth Sciences* **60,** 225–234, doi: 10.1016/j.jseaes.2012.09.005 (2012).
37. Campbell, I. H. *et al.* Synchronism of the Siberian Traps and the Permian-Triassic Boundary. *Science* **258,** 1760–1763, doi: 10.1126/science.258.5089.1760 (1992).

38. Renne, P. R. *et al.* Synchrony and Causal Relations between Permian-Triassic Boundary Crises and Siberian Flood Volcanism. *Science* **269,** 1413–1416, doi: 10.1126/science.269.5229.1413 (1995).
39. Robock, A. Volcanic eruptions and climate. *Reviews of Geophysics* **38,** 191–219, doi: 10.1029/1998rg000054 (2000).
40. Raible, C. C. *et al.* Tambora 1815 as a test case for high impact volcanic eruptions: Earth system effects. *Wiley Interdisciplinary Reviews: Climate Change* **7,** 569–589, doi: 10.1002/wcc.407 (2016).
41. Milne, G. A. *et al.* Identifying the causes of sea-level change. *Nature Geoscience* **2,** 471–478, doi: 10.1038/ngeo544 (2009).
42. Courtillot, V. *et al.* On causal links between flood basalts and continental breakup. *Earth and Planetary Science Letters* **166,** 177–195, doi: 10.1016/s0012-821x(98)00282-9 (1999).
43. Svensen, H. *et al.* Siberian gas venting and the end-Permian environmental crisis. *Earth and Planetary Science Letters* **277,** 490–500, doi: 10.1016/j.epsl.2008.11.015 (2009).
44. Knoll, A. H. *et al.* Paleophysiology and end-Permian mass extinction. *Earth and Planetary Science Letters* **256,** 295–313, doi: 10.1016/j.epsl.2007.02.018 (2007).
45. Schneebeli-Hermann, E. *et al.* Evidence for atmospheric carbon injection during end-Permian extinction. *Geology* **41,** 579–582, doi: 10.1130/G34047.1 (2013).
46. Galfetti, T. *et al.* Evolution of Early Triassic outer platform paleoenvironments in the Nanpanjiang Basin (South China) and their significance for the biotic recovery. *Sedimentary Geology* **204,** 36–60, doi: 10.1016/j.sedgeo.2007.12.008 (2008).
47. Algeo, T. J. & Twitchett, R. J. Anomalous Early Triassic sediment fluxes due to elevated weathering rates and their biological consequences. *Geology* **38,** 1023–1026, doi: 10.1130/G31203.1 (2010).
48. Ware, D. *et al.* Dienerian (Early Triassic) ammonoids from the Candelaria Hills (Nevada, USA) and their significance for palaeobiogeography and palaeoceanography. *Swiss Journal of Geosciences* **104,** 161–181, doi: 10.1007/s00015-011-0055-3 (2011).
49. Joachimski, M. M. *et al.* Climate warming in the latest Permian and the Permian-Triassic mass extinction. *Geology* **40,** 195–198, doi: 10.1130/G32707.1 (2012).
50. Chen, J. *et al.* High-resolution SIMS oxygen isotope analysis on conodont apatite from South China and implications for the end-Permian mass extinction. *Palaeogeography, Palaeoclimatology, Palaeoecology* **448,** 26–38, doi: 10.1016/j.palaeo.2015.11.025 (2016).
51. Pucéat, E. *et al.* Revised phosphate-water fractionation equation reassessing paleotemperatures derived from biogenic apatite. *Earth and Planetary Science Letters* **298,** 135–142, doi: 10.1016/j.epsl.2010.07.034 (2010).
52. Guex, J. *et al.* Thermal erosion of cratonic lithosphere as a potential trigger for mass-extinction. *Scientific Reports* **6,** 23168, doi: 10.1038/srep23168 (2016).

Acknowledgements

The authors acknowledge the support from the Swiss National Science Foundation (projects 137630 to U.S. and 160055 to H.B.). Special thanks go to the technical and scientific members of the Geneva and Zurich research groups who helped at all stages of this study. H.B. thanks Peter Hochuli (University of Zurich), Jean Guex and Torsten Vennemann (both University of Lausanne), and Helmut Weissert and Stefano Bernasconi (both ETH Zurich) for long term and highly stimulating scientific discussions.

Author Contributions

Bj.B., H.B. and U.S. designed the research and wrote the manuscript. Bj.B. performed the analyses. Field work was carried out by H.B., Bo.B., Bj.B., M.B. and K.G. All authors contributed to the interpretation of the results and the discussion.

Additional Information

Supplementary information accompanies this paper at http://www.nature.com/srep

Competing Interests: The authors declare no competing financial interests.

How to cite this article: Baresel, B. *et al.* Timing of global regression and microbial bloom linked with the Permian-Triassic boundary mass extinction: implications for driving mechanisms. *Sci. Rep.* **7**, 43630; doi: 10.1038/srep43630 (2017).

ACKNOWLEDGMENTS

This work would have not been possible to be completed without help of my supervisor Prof. Dr. Hugo Bucher (University of Zurich). His expertise and valuable guidance during this thesis has made the foundations of this work.

I wish to deeply thank Prof. Dr. Torsten Vennemann (University of Lausanne) for carbon isotope measurements, his insightful constructive comments during the preparation of the manuscripts, and being member of dissertation committee. Dr. Elke Schneebeli-Hermann (University of Zurich) is thanked for her great contribution to preparing and interpreting palynofacies slides. Her great help for preparing the German abstract is also appreciated. Dr. Dong-xun Yuan and Prof. Dr. ShuZhong Shen (both Nanjing Institute of Geology and Palaeontology) are highly thanked for identification of conodonts and brachiopods.

I am very thankful to Dr. Maria Ovtcharova and Dr. Massimo Chiaradia (both University of Geneva) for measuring U-Pb ages and Sr isotope, respectively.

Many thanks go to Dr. Sylvain Richoz (Lund University) for reviewing this thesis. Prof. Dr. Marcelo Sánchez and Prof. Dr. Peter Linder are thanked for being part of my dissertation committee.

This work has greatly benefited from my collaborator and colleagues (alphabetical order):

Dr. Åsa Frisk, Dr. Aymon Baud, Prof. Dr. Christian Klug, Heike Götzmann, Prof. Dr. Jean-Pierre Burg, Kuang Guodun, Lydia Zehnder, Marc Leu, Markus Hebeisen, Dr. Michael Hautmann, Dr. Morgane Brosse, Prof. Dr. Rossana Martini, and Remy Lüchinger.

Last but not least, special thanks to my family for their constant supports.

CURRICULUM VITAE

BAGHERPOUR Borhan

Date of birth: 09.09.1982

Nationality: Iranian

Education

2012-2017: PhD: Paleontological Institute and Museum, University of Zurich, Switzerland.

Thesis: Late Permian and Basal Triassic Paleoenvironments and Stable Isotope Geochemistry in the Nanpanjiang Basin (South China).

Supervisor: Prof. Dr. Hugo Bucher

2006-2009 Master of Science: S.B. University of Kerman, Geology (Palaeontology and Stratigraphy).

Thesis: Biostratigraphy, paleoecology, sedimentary environments and sequence stratigraphy of the Taleh zang Formation at the Lorestan area (S.W Iran).

Supervisors: Prof. Dr. Mohammad R. Vaziri; Dr. Ali Kheradmand

2001-2006 Bachelor: Isfahan University, Geology